Final Report

Grant NAG-1-882
UW 144-AH14

Lidar Observations of the Optical Properties and 3-Dimensional Structure of Cirrus Clouds

E.W.Eloranta
Principal Investigator

University of Wisconsin
Space Science and Engineering Center
1225 W. Dayton St.
Madison,Wis
Tel (608)-262-7327

1

The scientific results of research supported under this grant have been reported in a series of journal papers, dissertations, and conference presentations. This report is consists of a compilation of these publications.

2 Publications

2.1 Journal Papers

The following journal papers were published. Copies of these papers are included as part of this report.

- Grund, C. J., and E. W. Eloranta, 1990: *The 27-28 October 1986 FIRE IFO Cirrus Case Study: Cloud Optical Properties Determined by High Spectral Resolution Lidar*, Monthly Weather Review, **118**, 2344-2355.
- Minnis, P. D. F. Young, K. Sassen, J. M. Alvarez and J. Grund, 1990:*The 27-28 October 1986 FIRE IFO Cirrus Case Study: Cirrus Parameter Relationships Derived from Satellite and Lidar Data*, Monthly Weather Review, **118**, 2402-2425
- Sassen, K., Starr, D. O'C, G. G. Mace, M. R. Poellot, S. H. Melfi, W. L. Eberhard, J. D. Spinhirne, E. W. Eloranta, D. E. Hagen, and J. Hallett, 1995: *The 5-6 December 1991 FIRE IFO II Jet Stream Cirrus Case Study: Possible Influences of Volcanic Aerosols*, Journal of the Atmospheric Sciences, **52**, 97-123.

2.2 Dissertations

- Wolf, W., 1996: *Cirrus Cloud Optical and Morphological Variations within a Mesoscale Volume*, Master of Science Thesis, Dept. of Atmospheric and Oceanic Sciences, University of Wisconsin-Madison, Madison, WI
- Piironen, P. 1994: *A High Spectral Resolution Lidar Based on an Iodine Absorption Filter*, PhD Thesis, Dept. of Physics, Väisälä Laboratory, University of Joensuu, Joensuu, Finland.

2.3 Conference Presentations

The following is a list of conference papers presented with support of this grant. Abstracts of these presentations are attached to this report.

- Eloranta, E. W., D. Wylie and W. Wolf, *The Three-Dimensional Structure of Cirrus Clouds determined from Lidar and Satellite Observations*, Cloud Impact on Defense Operations and Systems, El Segundo, CA, 1991.

- Eloranta, E. W. and P. K. Piironen, *Adaptation of the University of Wisconsin High Spectral Resolution Lidar for Polarization and Multiple Scattering Measurements*, NASA Conference Publication 3158, Sixteenth International Laser Radar Conference, Cambridge, MA, July 20-24, 1992

- Wylie, D., W. Wolf, P. Piironen and E. W. Eloranta, *Visible/Infrared Optical Depths of Cirrus ans seen by Satellite and Scanning Lidar*, Cloud Impact on Defense Operations and Systems, Fort Belvoir, VA, November 15-19, 1993.

- Wylie, D., W. Wolf, and E. W. Eloranta, *Visible and Infrared Radiative Relationships as Measured by Satellite and Lidar*, American Meteorological Society, 74th Annual Meeting, Nashville TN, January 23-28, 1994

- Eloranta, E. W. and P. Piironen, *High Spectral Resolution Lidar Measurements of Multiple Scattering*, Seventeenth International Laser Radar Conference, Sendei, Japan, July 1994.

- Eloranta, E. W. and P. Piironen, *Depolarization Measurements with the High Spectral Resolution Lidar*, Seventeenth International Laser Radar Conference, Sendei, Japan, July 1994.

- Eloranta, E. W. and P. Piironen, *High Spectral Resolution Lidar Measurements using an I_2 Filter*, Seventeenth International Laser Radar Conference, Sendei, Japan, July 1994.

- Eloranta, E. W., *Ground Based Lidar Characterization of Cirrus Clouds*, IEEE International Geoscience and Remote Sensing Symposium, Pasadena, CA, August 1994

- Eloranta, E. W. and P. Piironen, *High Spectal Resolution Lidar Measurements of Extinction and Particle Size in Clouds*, Optical Society of America, Optical Remote Sensing of the Atmosphere, Topical Meeting , Salt Lake City, Utah, Feburary, 1995.

- Eloranta, E. W. and P. Piironen, *Measurement of Particle Size in Clouds with the High Spectral Resolution Lidar*, Eighth International Workshop on Multiple Scattering Lidar Experiments, Quebec, Canada, March 4-6, 1996.

- Eloranta, E. W. and P. Piironen, *Modification of the High Spectral Resolution Lidar for the Measurment of Multiply Scattered Lidar Returns*, IEEE Second Topical Symposium on Combined Optical-Microwave Earth and Atmosphere Sensing, April 3-6, 1995, Atlanta, GA

- Eloranta, E. W. and P. Piironen, *High Spectral Resolution Lidar Measurements of Extinction and Particle Size in Clouds*, Optical Society of America Topic Meeting on Optical Remote Sensing of the the Atmosphere, Feb 6-10, 1995, Salt Lake City, UT.

3 Participants

Edwin Eloranta	Principal Investigator
Chris Grund	Assistant Scientist
Dan Forrest	Programmer
Dick Sharkey	Instrumentation Specialist
Antti Piironen	Graduate Student
Paivi Piironen	Graduate Student
Walter Wolf	Graduate Student
Ralph Kuehn	Graduate Student
Chen Hui Sun	Graduate Student

- To be presented 18^{th} International Laser Radar Conference, Berlin Germany, July 22-26 1996.
- Presented Eighth International Workshop on Multiple Scattering Lidar Experiments, Quebec, Canada, March 4-6, 1996.
- Presented IEEE Second Topical Symposium on Combined Optical-Microwave Earth and Atmosphere Sensing, April 3-6, 1995, Atlanta, GA
- Presented Optical Society of America Topic Meeting on Optical Remote Sensing of the the Atmosphere, Feb 6-10, 1995, Salt Lake City, UT.

CDOS 1991

(1)
51-47

The three-dimensional spatial structure of cirrus clouds determined from lidar and satellite observations.

71198
032584
2P.

E. W. Eloranta, D. Wylie, and W. Wolf

Cirrus cloud fields exhibit complex spatial structure; only infrequently does the standard homogenous plane-parallel description used by most modelers provide a reasonable picture of real cirrus structure. Simultaneous imagery from the University of Wisconsin Volume Imaging Lidar (VIL) and Meteorological Satellites have been used to quantify spatial structure of cirrus clouds. The VIL data includes 120 km by 220 km 3-dimensional maps of cirrus cloud fields with 60 m resolution. This data has been used to compute quantities such as the spatial distributions of cloud base altitude, cloud top altitude, and mid-cloud altitude. Two-dimensional autocorrelation functions describing the mean shape of cirrus clouds have been computed. Because cirrus clouds seldom have distinct edges, these correlation functions are derived as a function of a threshold value which defines the cloud edge.

The lidar data and ray tracing algorithms have also been used to synthesis images of the cirrus cloud fields as they would appear at a wavelength of 1.06 microns observed from the vantage point of the GOES satellite. These images will be presented and compared with the simultaneous GOES imagery.

The complex spatial organization of cirrus makes measurements of area-averaged mean cloud properties difficult with fixed location instrumentation. It also suggests that statistics on the occurrence of clear lines of sight through the cloud fields are difficult to collect. Figure 1 illustrates this problem using a top-down image of a cirrus cloud field derived from VIL data. This image depicts the cirrus cloud as a solid object with edges defined by a backscatter threshold value. Plotted on this image are a series of sloping lines; these show the path of clouds passing over 12 zenith-pointing sensors placed along a north south line at 10 km intervals. Numbers on the right of the plot show the one-hour-average percentage cloud cover in the first hour of the data period and those on the left show the one-hour-average for the second hour. Notice that during the first hour of observation one-hour-average cloud cover varies from 0 to 73%. Interestingly, the maximum cloud cover the minimum would be observed only 10 km apart. Even in the second hour of observation, where the average cloud cover has increased, the one-hour-average cloud cover varies from 36 to 87%.

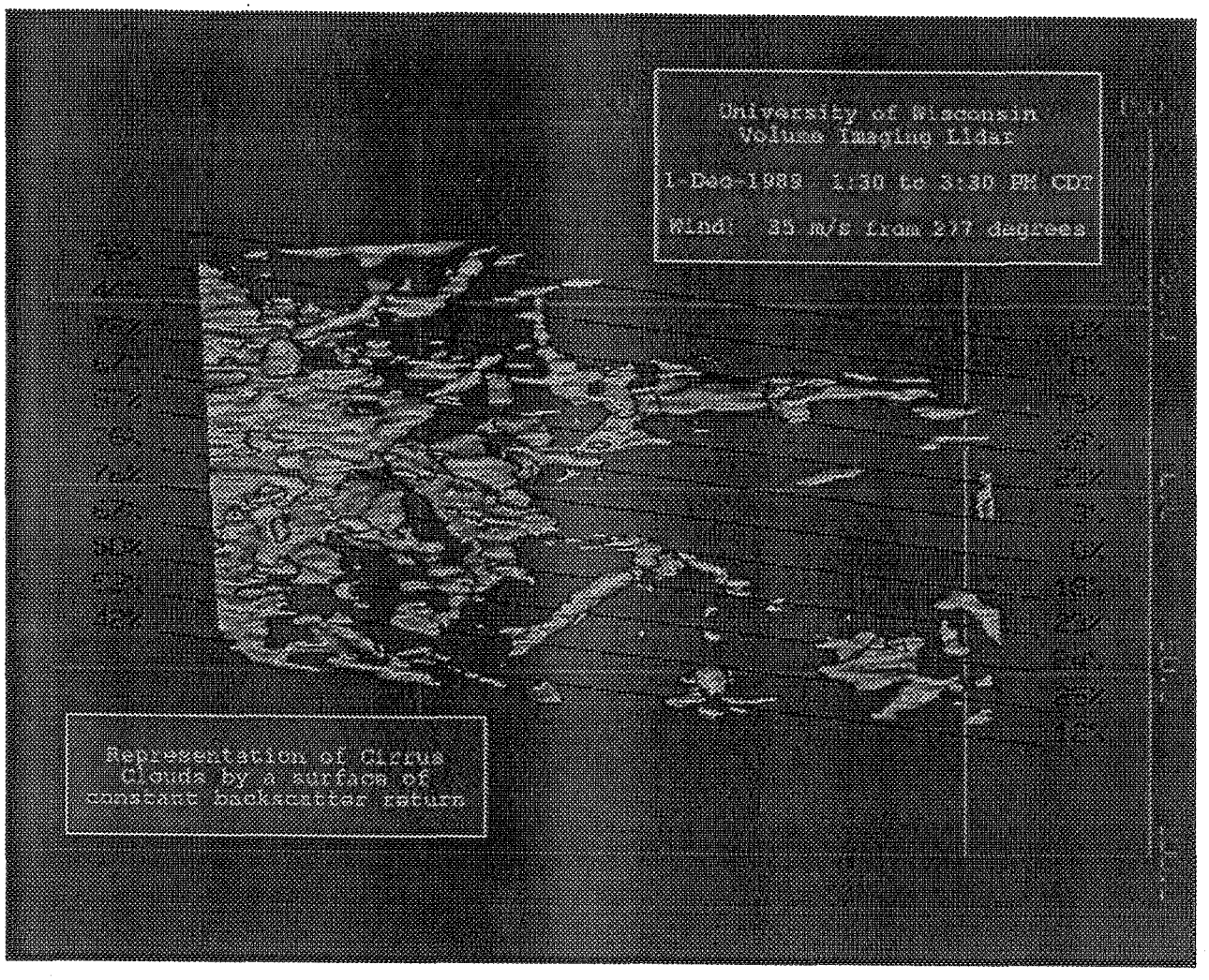

Figure 1:

A top-down view of the cirrus cloud field observed on Dec 1, 1989 with the Volume Imaging Lidar. The distance scale is given in kilometers. This image was constructed from two hours of VIL north-zenith-south image planes; the east-west dimension was constructed using loran-radiosonde winds. In the absence of temporal evolution of cloud elements this picture should be identical to a top-down picture of the cloud. The sloping black lines follow the cloud elements which would pass over 12 zenith-pointing radiometers placed at 10 km intervals along a north-south line. Figures at the right of the image represent the one-hour-average cloud cover seen by each radiometer in the first hour of observation and figures on the left for the second hour.

Eloranta, E. W., P. Piironen, "High spectral resolution lidar measurements using an I2-absorption filter", Seventeenth International Laser Radar Conference, Sendai, Japan, 1994.

HIGH SPECTRAL RESOLUTION LIDAR MEASUREMENTS USING AN I_2 ABSORPTION FILTER

E. W. Eloranta and P. Piironen
University of Wisconsin
1225 W. Dayton St., Madison, Wisconsin
Tel: 608-262-7327 Fax: 608-262-5974
email: eloranta@lidar.ssec.wisc.edu

The University of Wisconsin High Spectral Resolution Lidar (HSRL) measures optical properties of the atmosphere by separating the Doppler-broadened molecular backscatter return from the unbroadened aerosol return[1,2]. In the past, the HSRL employed a Fabry-Perot etalon with a 0.5 pm bandpass to separate the aerosol and molecular scattering. With careful control of the etalon[1], we were able to maintain a short term ($\sim$ 1 hour) calibration stability $\sim$ 0.1% in the inversion coefficients used to separate aerosol and molecular signals. This provided accurate measurements when the aerosol to molecular backscatter ratio was less than $\sim$ 100. However, in dense clouds the backscatter ratio often exceeds 10^3. The etalon provided only a factor of $\sim$ 2 rejection of the aerosol signal incident on the molecular phototube. Thus, the molecular channel signal from inside a dense cloud included $\sim$ 500 times as many photons scattered by aerosols as by molecules. In these cases, a 0.1% error in the inversion coefficients produced a 100% error in the separated molecular return.

She et al[3]. reported HSRL lidar observations of temperature and aerosol backscattering using a HSRL based on a barium absorption filter and a dye laser. Atomic absorption filters provide more complete rejection of the aerosol signal in the molecular channel. In addition, these filters are much less sensitive to temperature and have little sensitivity to the incidence angle or the divergence of the optical beam. Miles et al. [4] have used I_2 molecular filters to separate aerosol and molecular scattering for wind tunnel flow visualization and velocity measurements. Molecular iodine has several absorption lines which lie in the thermal tuning range of injection-locked, frequency-doubled Nd-Yag lasers[5]. This eliminates the frequency stabilized dye laser which is required when using a barium absorption cell. Even though the I_2 lines are broadened by hyperfine structure, room temperature operation provides linewidths similar to those provided by the barium cell which must be operated at $\sim$ 500°C.

The HSRL has been modified to use an I_2 absorption cell; the new receiver schematic is shown in figure 1. The signal detected by PMT1 contains both aerosol and molecular scattering. The I_2 filter inserted before PMT2 heavily attenuates aerosol contributions while transmitting the Doppler broadened wings of the molecular spectrum. PMT 3 is used to measure the angular field of view dependence of the signal. The transmitter switches the polarization between parallel and perpendicular on alternate laser pulses. Since the lidar operates at a 4 kHz repetition rate, ratios of alternate lidar returns can be used to accurately determine depolarization in all signal channels.

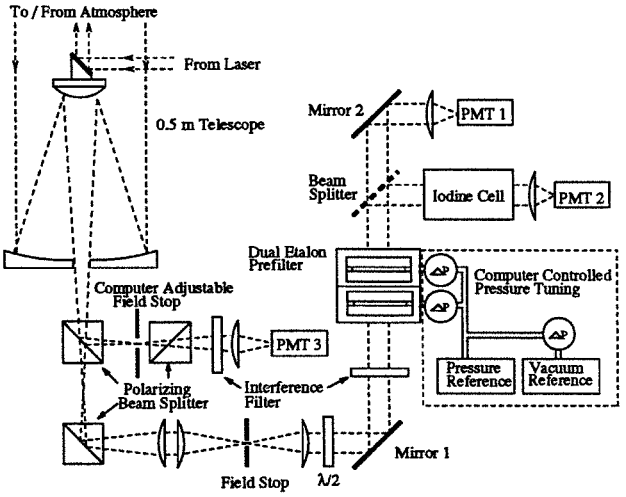

Figure 1. The modified HSRL receiver.

The HSRL transmitter uses a continuously pumped, Q-switched, injection seeded, frequency doubled Nd:YAG laser operating at a 4 kHz pulse repetition rate[1]. This laser is tunable over a 124 GHz frequency range by temperature tuning the seed laser under computer control.

An evacuated, 43 cm long cell containing I_2 crystals in a side arm serves as the absorption cell. The cell is maintained at a constant temperature of 27±0.1°C. Figure 2 shows the absorption spectrum of this cell.

For routine operation the HSRL is tuned to line 1109 which provides a large attenuation of the aerosol return and is well isolated from the neighboring lines. However, the laser is sometimes tuned to the notch between lines 1107 and 1108; this provides better separation of aerosol from molecular scattering when the molecular scattering is much larger than the aerosol scattering. Tuning is maintained by a digital servo which monitors the trans-

mission of laser light through a 4 cm long I_2 absorption cell.

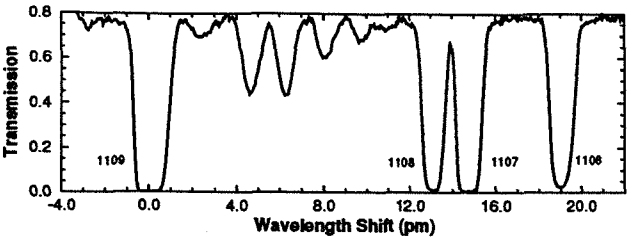

Figure 2. The I_2 absorption spectrum measured by thermally tuning the laser. Spectral lines are identified with numbers from Gerstenkorn and Luc[6].

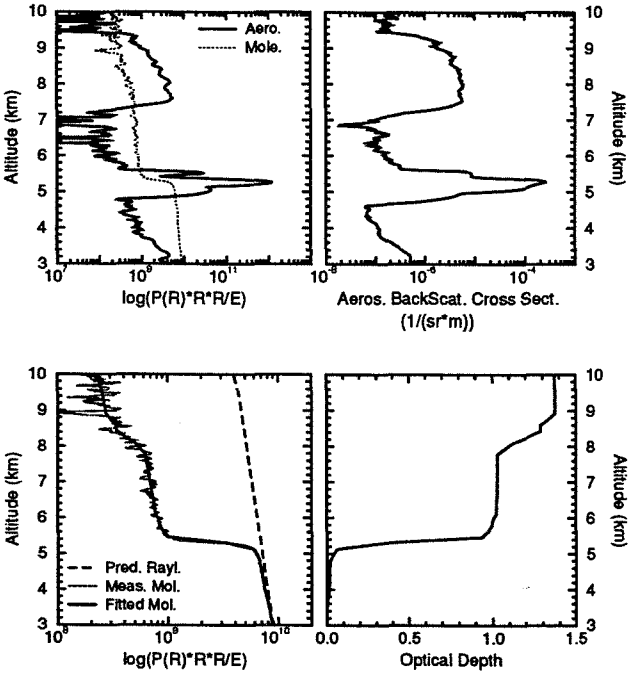

Figure 3. HSRL profiles showing signal returns from aerosols (below 4.8 km and 5.7 - 7.2 km), a water cloud (4.8 - 5.7 km) and an ice cloud (7.2 -9.5 km). The range-square corrected aerosol (solid line) and molecular (dotted) lidar returns are shown in the upper left. The measured particulate backscatter cross section is shown in the upper right. The measured molecular (thin solid), a constrained nonlinear regression fit to the molecular (bold solid) and the molecular density variation with altitude (dashed) are plotted in the lower left. The measured optical depth profile is plotted in the lower right.

Line 1109 of the I_2 filter provides very clean separation of the molecular lidar return. Only 0.08% of the aerosol return appears in the molecular return. Increasing the cell length does not increase the online rejection of the cell. The rejection may now be limited by the spectral purity of the laser output. Tests show that the spectral transmission of the cell is very stable. Separation of aerosol and molecular returns can be accomplished in dense clouds. In the past, the probing of dense clouds was limited by uncertainties in the calibration constants; currently, photon counting statistics appear to provide the dominant error.

The HSRL also includes a Wide-Field-of-View (WFOV) data channel which records the combined aerosol and molecular lidar return simultaneously with the spectrometer channels. The angular field of view of this channel is controlled by the system computer and it can be adjusted from 0.2 mr to 4 mr. This channel is rapidly sequenced between several apertures to record the FOV dependence of the multiply scattered lidar return. The system calibration and signals recorded in the spectrometer channels are sufficient to allow removal of the molecular return from the WFOV signal. The depolarization of light received in the WFOV channel is also measured.

Figure 3 provides an example of HSRL profiles measured between 1:29 and 1:34 UT on November 11, 1993. Notice that these measurements have been acquired through clouds with a total one-way optical depth of 1.38. With more uniform clouds, longer time averages have allowed measurements through clouds with an optical depth as large as 3.

ACKNOWLEDGMENTS

This work was supported by grants from the Office of Naval Research (N00014-91-J-1558) and the National Aeronautics and Space Administration (NAG-1-882).

REFERENCES

1. Grund, C.J., and E.W. Eloranta, 1991: University of Wisconsin High Spectral Resolution Lidar, *Optical Engineering*, **30**, 6-12.

2. Piironen, P. and E. W. Eloranta, 1994: Demonstration of an iodine absorption filter based high spectral resolution lidar, *Optics Letters*, **19**, 234.

3. She, C. Y., R. J. Alvarez II, L. M. Caldwell, and D. A. Krueger, 1992: High-spectral-resolution Rayleigh-Mie lidar measurements of aerosol and atmospheric profiles, *Optics Letters* **17**, 541-543 .

4. Miles, R.B., W.R. Lempert and J. Forkey, 1991: Instantaneous Velocity Fields and Background Suppression by Filter Rayleigh Scattering, *29th Aerospace Science Meeting*, AIAA paper 91-0357, Reno, NV.

5. J. A. Harrison, M. Zahedi, and J. W. Nibler, 1993: Use of seeded Nd:YAG lasers for high-resolution spectroscopy, *Optics Letters* **18**, 149-151.

6. S. Gerstenkorn and P. Luc, 1978: *Atlas du spectre d'absorption de la molecule d'iode* (Centre National de la Recherche Scientifigue, Paris.

Eloranta, E. W., P. Piironen, "Adaptation of the University of Wisconsin High Spectral Resolution lidar for polarization and multiple scattering measurements", NASA Conference Publication 3158, Sixteenth International Laser Radar Conference, Cambridge, Massachusetts, July 20-24, 1992.

Adaptation of the University of Wisconsin High Spectral Resolution Lidar for Polarization and Multiple Scattering Measurements

E. W. Eloranta and P. K. Piironen

University of Wisconsin
Dept. of Meteorology
Madison, WI 53706

Quantitative lidar measurements of aerosol scattering are hampered by the need for calibrations and the problem of correcting observed backscatter profiles for the effects of attenuation. The University of Wisconsin High Spectral Resolution Lidar(HSRL) addresses these problems by separating molecular scattering contributions from the aerosol scattering; the molecular scattering is then used as a calibration target which is available at each point in the observed profiles(Shipley et. al, Grund et al). This approach does not require knowledge of the backscatter/extinction ratio to correct for attenuation and thus avoids the uncertainties and numeric instabilities of schemes for inversion of single channel lidar profiles. Because the molecular backscatter cross section is approximately one thousand times larger than the Raman scattering cross section, the HSRL also holds a significant signal strength advantage over the use of Raman scattering approaches for measurement of aerosol backscatter cross sections.

While the HSRL approach has intrinsic advantages over competing techniques, realization of these advantages requires implementation of a technically demanding system which is potentially very sensitive to changes in temperature and mechanical alignments. This paper describes a new implementation of the HSRL in an instrument van which allows measurements during field experiments. The instrument has been modified to provide measurements of depolarization. In addition, both the signal amplitude and depolarization variations with receiver field of view are simultaneously measured. These modifications allow discrimination of ice clouds from water clouds and observation of multiple scattering contributions to the lidar return. In the past it has been very difficult to verify models of the multiply scattered lidar return. The ability to measure calibrated backscatter cross sections and optical depths while simultaneously measuring depolarization and field-of-view variations make the HSRL a unique instrument for these investigations.

Figure 1 provides a block diagram of the new HSRL transmitter and receiver. The depolarization measurement capability is implemented so as to provide extremely precise measurements. The transmitted polarization is rotated 90 degrees between alternate laser pulses by a Pockels cell. Calibrations show that with proper alignment the residual cross polarization in the transmitted beam can be reduced to approximately 0.1% of the parallel component. Separate depolarization measurements can be made in both the "molecular" and "aerosol" channels of the HSRL while simultaneously observing the depolarization in the wide field of view channel. Because both polarization components are observed with the same detector and receiver optics, no calibration is required to make accurate measurements of the depolarization ratio. Photon counting detection also provides linear detector response over a very large dynamic range. The small time separation between laser pulses (250 μs) insures that the both polarization components are measured from the same ensemble of scattering particles.

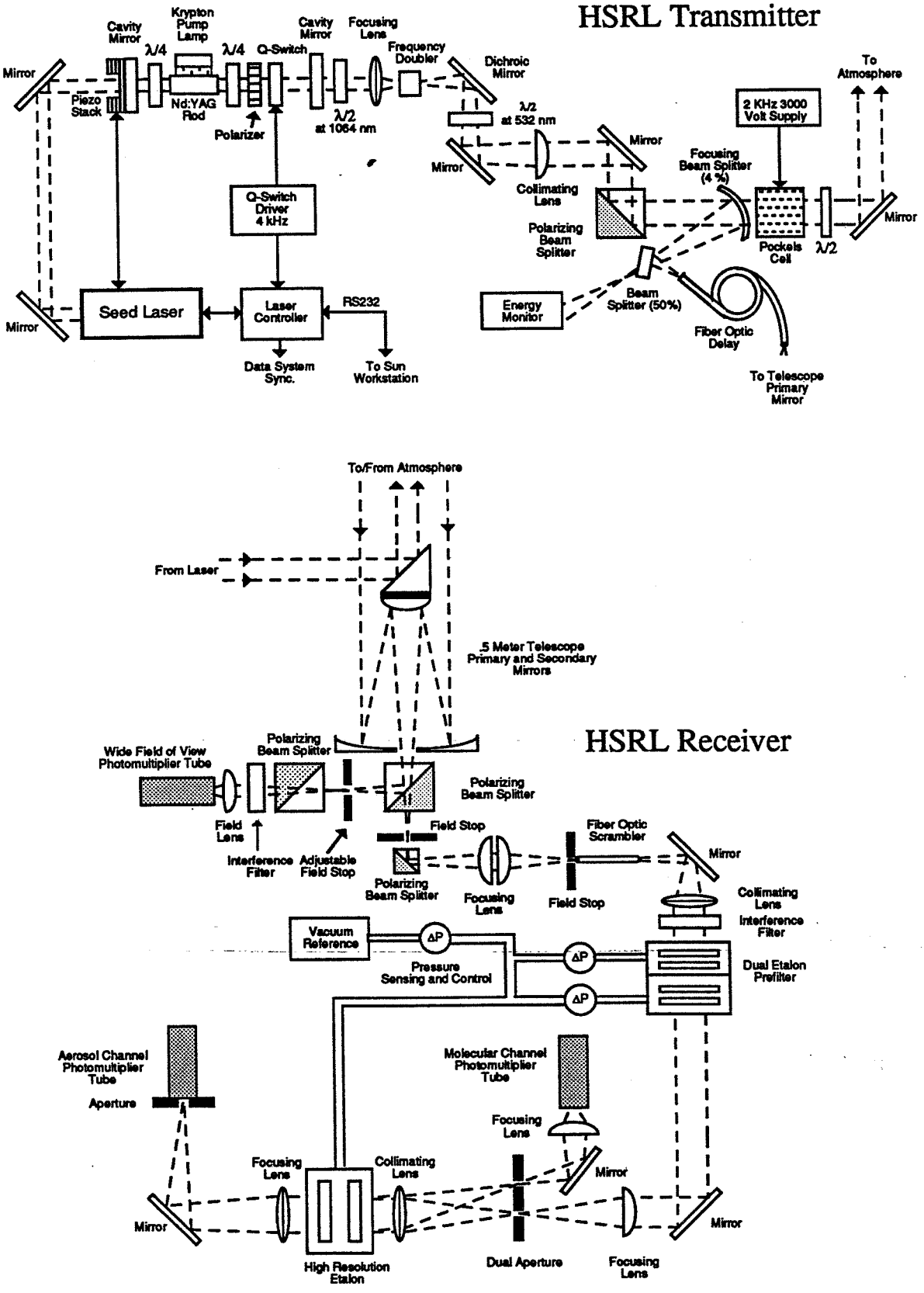
HSRL Transmitter
Cavity Mirror
Krypton Pump Lamp
λ/4
λ/4
Q-Switch
Cavity Mirror
Focusing Lens
Frequency Doubler
Dichroic Mirror
To Atmosphere
Mirror
Piezo Stack
Nd:YAG Rod
Polarizer
λ/2 at 1064 nm
λ/2 at 532 nm
2 KHz 3000 Volt Supply
Mirror
Mirror
Collimating Lens
Focusing Beam Splitter (4 %)
Q-Switch Driver 4 kHz
Polarizing Beam Splitter
Pockels Cell
λ/2
Mirror
Seed Laser
Laser Controller
RS232
Energy Monitor
Beam Splitter (50%)
Fiber Optic Delay
Mirror
Data System Sync.
To Sun Workstation
To Telescope Primary Mirror
To/From Atmosphere
From Laser
.5 Meter Telescope Primary and Secondary Mirrors
HSRL Receiver
Wide Field of View Photomultiplier Tube
Polarizing Beam Splitter
Polarizing Beam Splitter
Field Lens
Interference Filter
Adjustable Field Stop
Field Stop
Polarizing Beam Splitter
Focusing Lens
Fiber Optic Scrambler
Field Stop
Mirror
Collimating Lens
Interference Filter
Vacuum Reference
ΔP
Pressure Sensing and Control
ΔP
ΔP
Dual Etalon Prefilter
Aerosol Channel Photomultiplier Tube
Aperture
Molecular Channel Photomultiplier Tube
Focusing Lens
Focusing Lens
Collimating Lens
Mirror
Mirror
Mirror
High Resolution Etalon
Dual Aperture
Focusing Lens

Figure 1.

In order to increase the dynamic range of the HSRL we have designed new photon counting electronics to enable count rates near 1 GHz while accumulating counts in up to 8,192 range bins of 100 ns each. These counters have thus far been tested to count rates of over 250 MHz. Full utilization of these counters awaits the installation of phototubes providing shorter single photon pulses than the EMI model 9860 currently employed. A schematic of the HSRL data system is shown in figure 2.

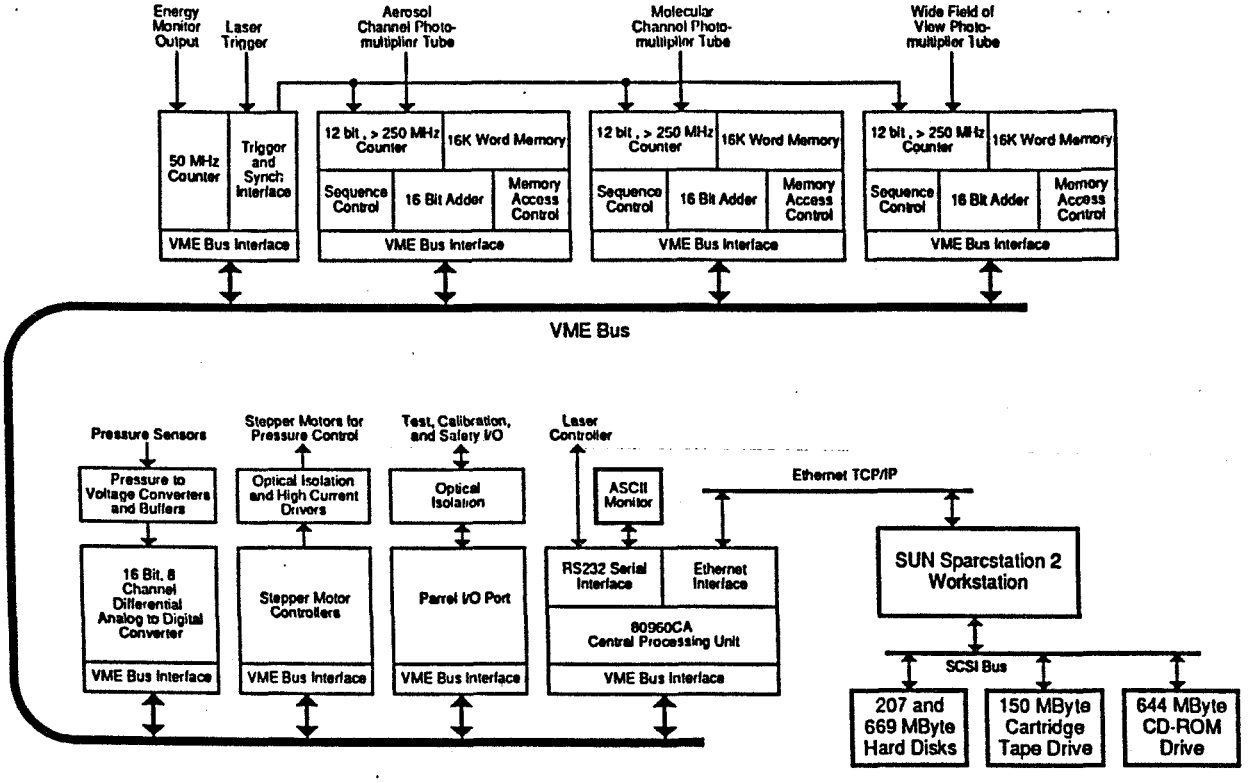

HSRL Data Acquisition System

Figure 2.

Figure 3 shows HSRL returns from a super-cooled water cloud(at an altitude of 5 km) and from ice crystal precipitation falling from this cloud(between altitudes of 3.3 and 4.8 km). The received signals polarized parallel and perpendicular to the transmitted polarization are shown along with the depolarization ratio. Notice that the depolarization observed in the clear air below the cloud is approximately 1% and thus very near the depolarization expected for molecular depolarization of the Cabannes line. Also note that the water cloud depolarization is approximately 2% indicating that for this cloud the 200 microradian field-of-view of the HSRL effectively suppresses depolarization caused by multiple scattering.

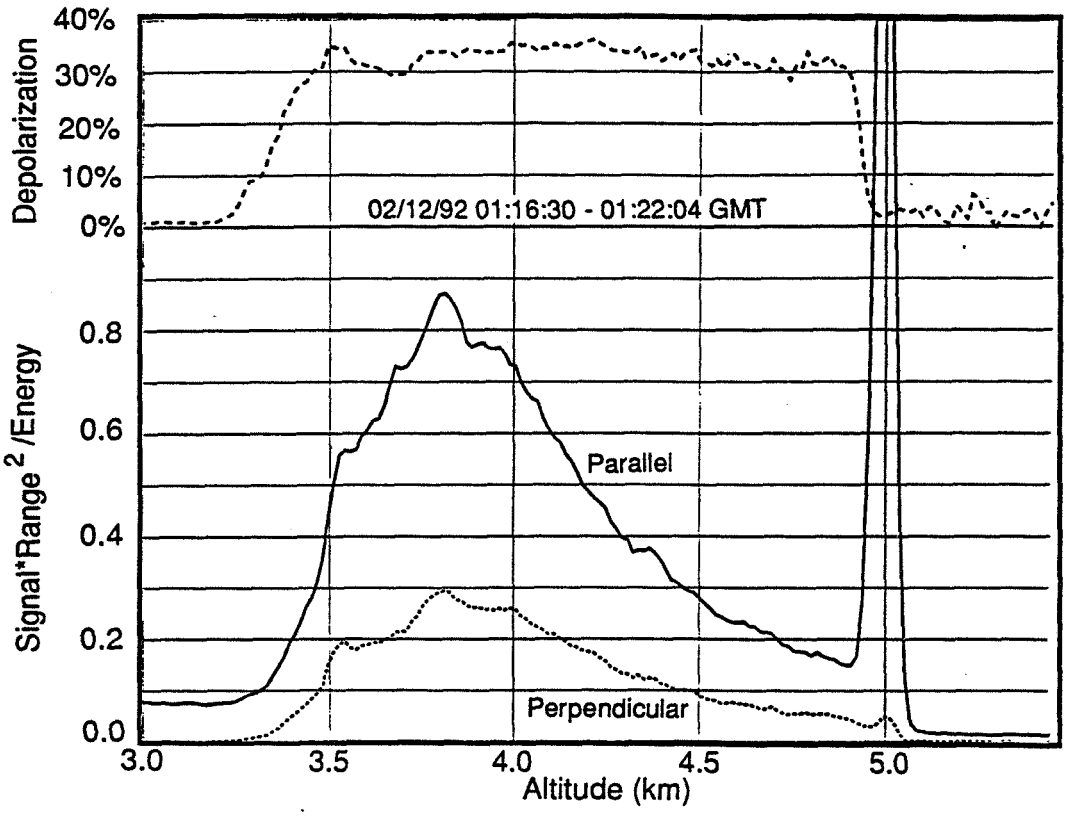

Figure 3.

Acknowledgements

This work was supported by grants from the Dept. of Energy(DE-FG01-90ER61058), the National Aeronautics and Space Administration(NAG-1-882) and the Office of Naval Research(N00014-91-J-1558). Support to P. K. Piironen was provided by Foundation of Maj and Tor Nessling, and University of Joensuu, Finland.

References

Shipley,S.T.,D.H.Tracy, E.W.Eloranta,J.T.Sorga,F.L.Roeseler, and J.W.Weinman, "High spectral resolution lidar to measure optical scattering properties of atmospheric aerosols. 1: theory and instrumentation," App.Optics, 22, 1983, p3716-3724.

Grund, C.J. and E.W.Eloranta, "University of Wisconsin high spectral resolution lidar", Optical Engineering, Vol 30, #1, p6-12, Jan 1991.

Eloranta, E. W., "Ground based lidar characterization of cirrus clouds", IEEE IGARS-94, Pasadena, CA, Aug., 1994.

GROUND BASED LIDAR CHARACTERIZATION OF CIRRUS CLOUDS

Edwin W. Eloranta
University of Wisconsin
1225 W. Dayton St. Madison, WI 53706
Tel 608-262-7327 FAX 262-5974

The optical properties and spatial coverage of cirrus clouds must be known for climate prediction. Lidar is capable of detecting tenuous cirrus clouds. Lidar is also able to make measurements through all except the thickest cirrus clouds. Traditional lidar systems provide insufficient information to allow unambiguous measurement of optical depth or backscatter cross sections. Furthermore, cirrus often includes structures which are elongated in the direction of the wind; this makes it difficult to estimate the area-averaged cloud coverage from temporally-averaged profiles measured with a vertically pointed lidar. These two problems are addressed with unique lidar systems developed at the University of Wisconsin.

The Volume Imaging Lidar (VIL) provides rapid high spatial resolution imaging of cirrus clouds. Typical images depict structure along a 120 km slice of the atmosphere with a 60 m spatial resolution. These images, which are recorded at a rate of two per minute, allow calculation of true spatial averages. The High Spectral Resolution Lidar (HSRL) divides aerosol and molecular scattering into separate profiles; the additional information provides absolutely calibrated measurements of optical depth, backscatter cross section, backscatter phase function and depolarization. Multiple scattering measurements are also recorded with the HSRL; these provide information on the size of cloud particles.

This paper presents cirrus cloud observations made with the HSRL and the VIL. The HSRL has been redesigned to use an iodine absorption filter in place of the Fabry-Perot etalon which was used for spectral separation of the aerosol and molecular lidar returns. These modifications, which improve both sensitivity and calibration stability, are described.

Eloranta, E. W., P. Piironen, " An error analysis for High Spectral Resolution Lidar Measurements", Optical Society of America, Optical Remote Sensing of the Atmosphere, Topical Meeting, Salt Lake City, Utah, February, 1995.

High Spectral Resolution Lidar

Measurements of Extinction and Particle Size in Clouds

E. W. Eloranta and P. Piironen
University of Wisconsin
1225 W. Dayton Street, Madison, Wisconsin 53706, USA
Phone: 608-262-7327 Fax: 608-262-5974
Email: eloranta@lidar.ssec.wisc.edu, paivi@hsrl.ssec.wisc.edu

The spectral width of light backscattered from molecules is increased due to Doppler shifts caused by the thermal motion of the molecules. The thermal motion of aerosol and cloud particles is much slower and the backscatter spectrum is nearly unchanged. The University of Wisconsin High Spectral Resolution Lidar (HSRL) measures optical properties of the atmosphere by separating the Doppler-broadened molecular backscatter return from the unbroadened aerosol return[1]. The molecular backscatter cross section can be calculated from the molecular density profile. Thus, observing the magnitude of the measured molecular signal relative to the computed profile allows unambiguous measurement of the atmospheric extinction profile. The ratio of the aerosol return to the molecular return along with the computed molecular cross section provides direct measurement of the aerosol backscatter cross section.

Past versions of the HSRL have employed a 150 mm diameter Fabry-Perot etalon to separate the aerosol and molecular signals. Recent replacement of the etalon with an I_2 absorption filter has significantly improved the ability of the HSRL to separate weak molecular signals inside dense clouds[2]. In dense water clouds the backscatter signal from droplets is often 100 to 1000 times larger than the molecular signal. The etalon based system was unable to reliably separate the weak molecular signal from the intense aerosol signal. Using the I_2 filter, it is now possible to acquire HSRL profiles extending upward from cloud base until the optical depth increases to ~ 6 for the two-way propagation path. Figure 1 provides an example of HSRL profiles measured between 1:29 and 1:34 UT on November 11, 1993.

In dense clouds, the single scatter lidar equation may not correctly describe the received signal. A substantial portion of the signal may be comprised of photons which have been scattered more than once. Calculations show that the multiply scattered signal is strongly dependent on both the angular Field Of View (FOV) of the receiving telescope and on the angular width of the forward diffraction peak in the scattering phase function.[3,4,5] Typical lidar receivers employ a FOV of 1 mrad or greater. Calculations show that when dense clouds are observed with these systems, most of the returned signal is often due to multiple scattering.[3] In order to minimize multiple scattering contributions, the HSRL employs a very small (160μrad) FOV.

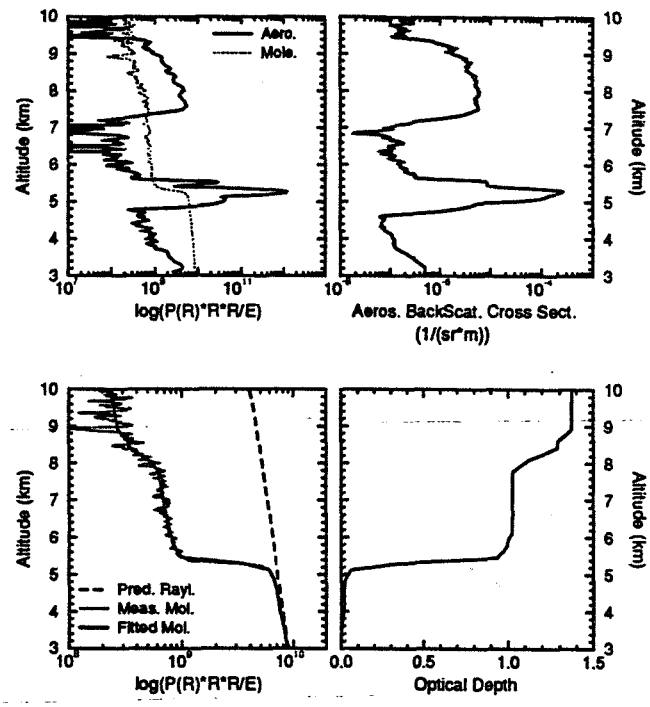

Figure 1. HSRL observations of a thin water cloud below a cirrus cloud on November 11, 1993 between 1:29 and 1:34 UT. The separated aerosol and molecular returns (left) and aerosol backscatter cross section (right) are shown in the upper panels. The molecular return predicted in the absence of aerosol attenuation and the measured molecular return are shown in the lower left hand panel. The derived optical depth profile is shown in the lower right panel.

The HSRL also includes a separate Wide Field Of View (WFOV) data channel with a computer controlled FOV (see figure 3) that can be adjusted from 0.22 mrad to 4 mrad. In operation, it is rapidly sequenced between several aperture sizes to record

the FOV dependence of the lidar return while the other HSRL channels measure the backscatter and extinction profiles. The system calibration and signals recorded in the spectrometer channels are sufficient to allow removal of the molecular return from the WFOV signal. The depolarization of light received in all HSRL channels is also measured.

The WFOV channel provides data similar to that of the multiple field of view lidar described by Hutt et al[6] with the added advantage of simultaneous extinction, backscatter and depolarization measurements.

Measurements from the WFOV channel, along with the optical depth profile derived from the observed molecular return, can be used to estimate the width of the forward diffraction peak in the scattering phase function. For particles which are large compared to the wavelength, λ, the angular width of the diffraction peak, $\Theta \sim \lambda/d$: where d is the particle diameter. Thus, it appears that the variation of the multiply scattered lidar return with angular field of view contains information on the size of the scattering particles[3]. In principle, the multiply scattered lidar return provides particle size information similar to that contained in measurements of the solar aureole. Previous studies of the solar aureole suggest that under favorable conditions as many as 5 independent pieces of information on the particle size distribution may be derived from measurements of the forward diffraction peak[7]. Much of this information is potentially available from the multiply scattered lidar return.

Figure 2 shows measurements acquired from a water cloud with the WFOV channel. Also plotted in this figure are calculations of the multiply scattered return using the model described in reference 3. The model results are highly sensitive to the assumed particle size and provide results which are consistant with particle sizes normally found in clouds of this type. When similar measurements are made in cirrus clouds, much larger particle sizes must be assumed to fit the observations. These sizes are consistant with expected values.

Measurements of particle size using the multiply scattered return are based on determination of the width of the forward diffraction peak. Models show that almost all multiply scattered photons have undergone only a single large angle scattering which directs them back towards the receiver. All other scatterings are small angle forward scatterings. Unfortunately, the large angle scattering event is not exactly at 180°. The backscatter phase function of the cloud is often quite variable and strongly dependent on particle size and shape at angles near 180°. Models for the multiply scattered lidar return must therefore include information on the angular variation of the backscatter phase function. This makes derivation of particle size from the WFOV data much more difficult.

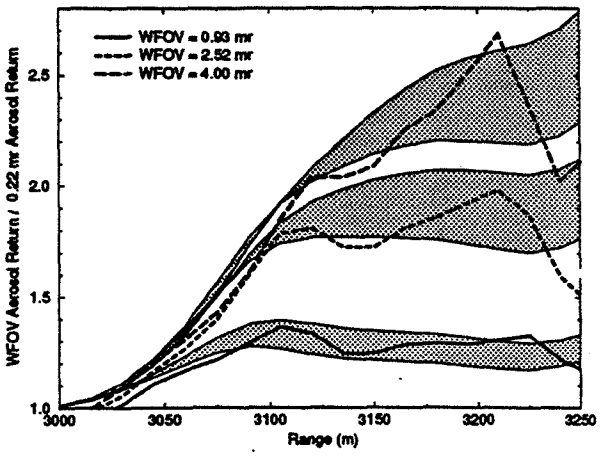

Figure 2. Ratios of the inverted aerosol signal measured in the WFOV channel to the inverted aerosol return derived from the 0.22 mrad spectrometer channels are compared to model results. Results derived from a May 30, 1993 data set are shown as bold lines. Model results are shown as shaded areas around the measured curves. The bottom boundary of the shaded area is computed for a diffraction peak width of 0.05 radians and the top boundary for a width of 0.034 radians. These correspond to effective particle diameters of $\sim 6\mu$m and $\sim 8\mu$m respectively.

In order to remove the dependence of the multiply scattered signal on the aerosol backscatter phase function, we are installing an additional channel on the HSRL (see figure 3). This employs an I_2 filter which removes photons which have not not been Doppler broadened by a molecular scattering near 180°. In addition, the singly scattered return is removed by reflection from a mirror with a small central aperture which defines the FOV of the normal HSRL data channels. Since multiply scattered photons which encounter more than one large angle scattering provide a neglibible contribution to the lidar return, this channel will observe photons which are deflected out of the laser beam by small angle scatterings and turned back to the receiver by a single molecular scattering. Thus, the signal depends on the backscatter phase function for molecular rather than aerosol scattering. Testing of this data channel is in progress and we expect to present sample data.

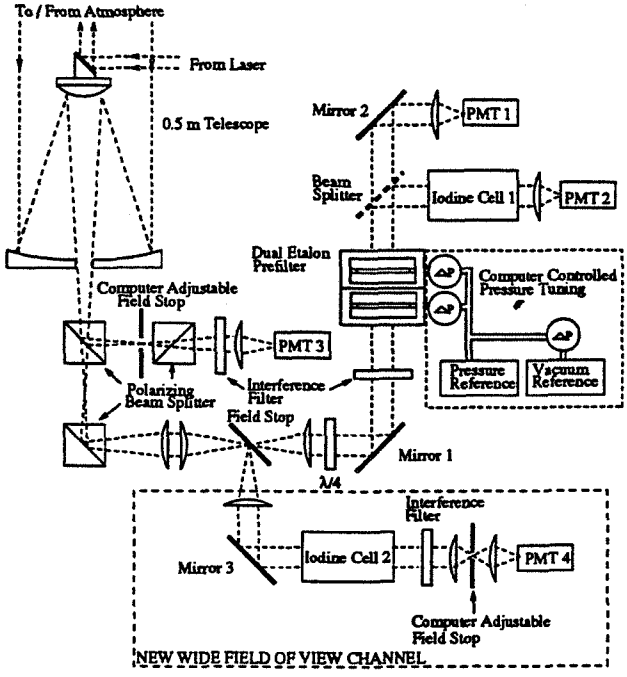

Figure 3. The HSRL receiver modified to use an I_2 absorption cell to separate aerosol and molecular signals. Photomultiplier 3 (PMT 3) is the WFOV channel used to measure the angular field of view dependence of the signal. Photomultiplier 4 (PMT 4) measures light which has been deflected out of the transmitted beam by small angle scattering and then Doppler broadened by molecular backscattering. The transmitter switches the polarization between parallel and perpendicular on alternate laser pulses. Since the lidar operates at a 4 kHz repetition rate, ratios of alternate lidar returns can be used to accurately determine depolarization in all signal channels.

ACKNOWLEDGMENTS

This work was supported by grants from the Office of Naval Research (N00014-91-J-1558) and the National Aeronautics and Space Administration (NAG-1-882).

REFERENCES

1. Grund, C.J., and E. W. Eloranta, 1991: University of Wisconsin High Spectral Resolution Lidar, *Optical Engineering*, **30**, 6-12.

2. Piironen, P, and E. W. Eloranta, 1994: Demonstration of an iodine absorption filter based high spectral resolution lidar, *Optics Letters*, **19**, 234.

3. Eloranta, E. W., 1993: A Practical model for the calculation of multiply scattered lidar returns, *Proceedings of Am. Optical Soc.*, Topical Meeting on Remote Sensing of the Atmosphere, Salt Lake City, UT, March 8-12.

4. Eloranta, E. W., 1972: Calculation of Doubly Scattered Lidar Returns, Ph.D. Thesis, University of Wis., Ann Arbor Press, Ann Arbor, MI.

5. Eloranta, E. W. and S.T. Shipley, 1982: A Solution for Multiple Scattering, *Atmospheric Aerosols*, Adarsh Depeek, Ed., Spectrum Press.

6. Hutt, D. L., L. R. Bissonnette, and L. Durand, 1994: Multiple field of view lidar returns from atmospheric aerosols. *Applied Optics*, **33**, 2338-2348.

7. Twitty, J., R.Parent, J.Weinman, E.Eloranta, 1976: The remote measurement of aerosol size distributions from airborne measurements of solar aureole, *Appl. Optics*, **15**, 980-989.

Wylie, D., W. Wolf, and E. W. Eloranta, "Visible and infrared radiative relationships as measured by satellite and lidar", American Meteorological Society, 74'th Annual Meeting, Nashville, Tennesee, January 23-28, 1994.

VISIBLE AND INFRARED RADIATIVE RELATIONSHIPS AS MEASURED BY SATELLITE AND LIDAR

Donald Wylie, Walt Wolf and Edwin Eloranta

University of Wisconsin-Madison
Madison, WI 53706

1. INTRODUCTION

The impact of cirrus clouds on the heat balance of the earth is dependent on their reflectivity of solar radiation and their absorptivity of terrestrial radiation. These clouds can either contribute to radiative warming or cooling depending on the ratio of their visible reflectance to their infrared absorption. Any prediction of cloud cover changes that accompany climate change, will have to know whether the visible/IR radiative characteristics of the clouds will also change. Few measurements of cirrus have been made where data from both the visible and IR were collected simultaneously. Most cloud studies have used only one portion of the spectrum.

The best studies of the visible and IR radiative properties of ice clouds have been Platt (1979) using a vertically pointing IR radiometer next to a visible lidar and Minnis et al. (1990) which combined satellite and lidar data. Platt (1979) studied several cases of cirrus clouds and found a ratio of the visible/IR optical depths of 2.0:1. Minnis et al. (1990) studied one case from the FIRE experiment and found the visible/IR ratio to be slightly higher, 2.1:1. Modelling of radiative properties of ice crystals suggest that the visible/IR ratio can vary from 1.8 to 4.0 (Minnis et al., 1993).

One of the largest problems for any cirrus cloud study is the large spatial variability of clouds. Vertically pointing lidars sample only the part of the cloud that drifted over them while satellites see the gradients in the horizontal field. Lidars have a vary narrow beam, <1 m in width while satellite radiometers have field of views (FOV) of 1 to 20 km. For this study, we used a scanning lidar to make volume imagery of cirrus clouds similar to the satellite view of the clouds.

2. MEASUREMENT TECHNIQUE

To obtain the visible optical depths of cirrus, the High Spectral Resolution Lidar (HSRL) and the Volume Imaging Lidar (VIL) of the University of Wisconsin-Madison were used. The HSRL is a unique instrument that measures the backscatter of the lidar pulse by particulate matter separately from the backscatter of air molecules. A spectrally narrow pulse of 0.6 μ from a NadYg lidar is transmitted. The returning radiation scattered by air molecules will be spectrally doppler broadened while that from particles will not. Measurements of both the doppler broadened and non-broadened backscatter are made. The backscatter from air molecules allows a direct determination of the strength of the lidar pulse reaching each level of the cloud. Extinction and optical depth of the cloud can be determined without assumptions of the attenuation along the beam path. More precise measurements of the visible radiative quantities of the clouds can be made this way.

To understand radiative scattering in clouds, the large horizontal and vertical variations in cloud structure have to be measured. The HSRL lidar samples only a small portion of the cloud - a column about 30 centimeters wide. The GOES satellite IR sensors have a horizontal resolution of 10.8 km at Madison, WI. To account for FOV differences, the horizontal structure of the clouds were measured by the VIL.

The VIL produced visible backscatter images of the clouds by scanning across the wind. Time advection was used to construct a horizontal image of visible backscatter from the VIL data over a one hour period. The HSRL was used to calibrate the VIL signal into backscatter cross sections of particulates. The backscatter cross sections were related to extinction by a constant backscatter phase function determined from the HSRL data. This process produced a three dimensional image of visible extinction in the cirrus clouds over a one hour period.

The extinction volume image was then transformed to an image of optical depth in the same viewing geometry as the

GOES satellite. Optical depths were formed from the integral of extinction along the path in which the GOES scanner view this volume. The optical depth image was originally produced with a 1 km (satellite nadir) resolution. This image was then shifted to align with the satellite IR image to account for error in the satellite registration system. The lidar visible optical depth image then was averaged to an 8 km (satellite nadir) image for direct comparison to the satellite IR image. This gave coincident fields of views from both satellite and lidars in the same geometry with a horizontal resolution of 10.8 km per pixel.

IR optical depths were extracted from the GOES image using calculations of the IR transmittance of the clouds using the IR radiance of the cloud, the radiance of cloud free FOV's and radiances calculated from the temperature of the mean vertical level of the cloud. The VIL data were used to determine the cloud level. Rawinsonde observations were made at Madison at the same time as these data.

All data were taken in the vicinity of Madison, WI on 1 December, 1989. The VIL was located 24 km west of the HSRL. The VIL scanned both crosswind and nearly downwind over the HSRL. Data were taken from 19:35 UTC (13:35 Local) to 21:20 UTC (15:20 L). During this time a large mass of cirrus clouds moved in from the west-northwest with an approaching cold front. Madison, WI was under cloud free sky during the morning and proceeded to total overcast by the end of this period. Two lidar images were constructed from 1 hour records. More details on the data taken can be found in Ackerman et al. (1993).

3. RESULTS

An example of the structure of the clouds from the VIL is shown in Figure 1. A thick cloud mass from 6.8 to 9.0 km is apparent from 8 km south to 20 km north of the VIL. Other thin broken layers are apparent both north and south of the large mass. This is typical of the different forms of cirrus sampled on 1 Dec, 89. The first clouds to reach Madison were vertically thin and horizontally broken. A few dense lines with evidence of precipitating virga also were found in the VIL volume. Later thicker cirrus moved in with virga that spanned the 2.2 km shown in Fig. 1.

The satellite and VIL image was divided into regions of similar cloud characteristics. The VIL cross sections were used as the primary division tool. The GOES image had little detail in the IR. The lidar visible optical depth image at 1 km showed many line and sheet structures. Cloud thickness, the presence of multiple layers and the intensity of precipitating virga were used to segregate different cloud forms.

The visible/IR optical depths are shown in Fig. 2. Most of the data are near the 2:1 line shown in the image. These data loosely agree with theory and the other past measurements. However, the visible/IR optical depth ratio appears to increase for thicker precipitating cirrus. Clouds with dense precipitating virga have ratios below the 2:1 line (visible/IR > 2). Cloud areas of highest reflectivity had solid lidar returns over 2 km depth with occasional embedded layers of extremely high reflectivity. The horizontal variations in cloud reflectivity were seen in the IR satellite imagery but with far less detail than the lidar images. The lower resolution of the satellite IR sensor smoothed some of these variations. However, the lidar data show that visible reflectivity had wide range of values with large vertical and horizontal detail.

4. REFERENCES

Ackerman, S. A., E. W. Eloranta, C. J. Grund, R. O. Knuteson, H. E. Revercomb, W. L. Smith and D. P. Wylie, 1993: University of Wisconsin Remote Sensing Pilot Experiment. Bull. A.M.S.

Minnis, P., D.F. Young, K. Sassen, J.M. Alvarez and C.J. Grund, 1990: The October 27-28 1986 FIRE IFO Cirrus Case Study: Cirrus parameter relationships derived from satellite and lidar data. Mon. Wea. Rev., 118, 2402 2425.

Minnis, P., K.N. Liou and Y. Takano, 1993: Inference of cirrus cloud properties using satellite-observed visible and infrared radiances. Part I: Parameterization of radiance fields, J. Atm. Sci., 50, 1279-1304.

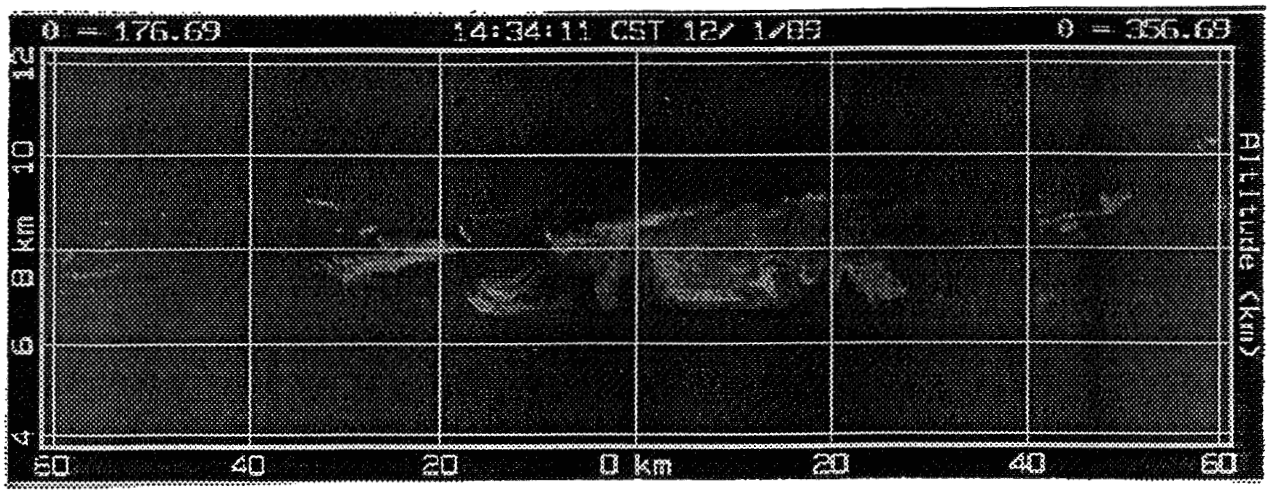

Figure 1: A Volume Imaging Lidar (VIL) cross wind section taken at 20:34 UTC (14:34 local). Scan directions were azimuths of 177° and 357°. Orientation is south to north.

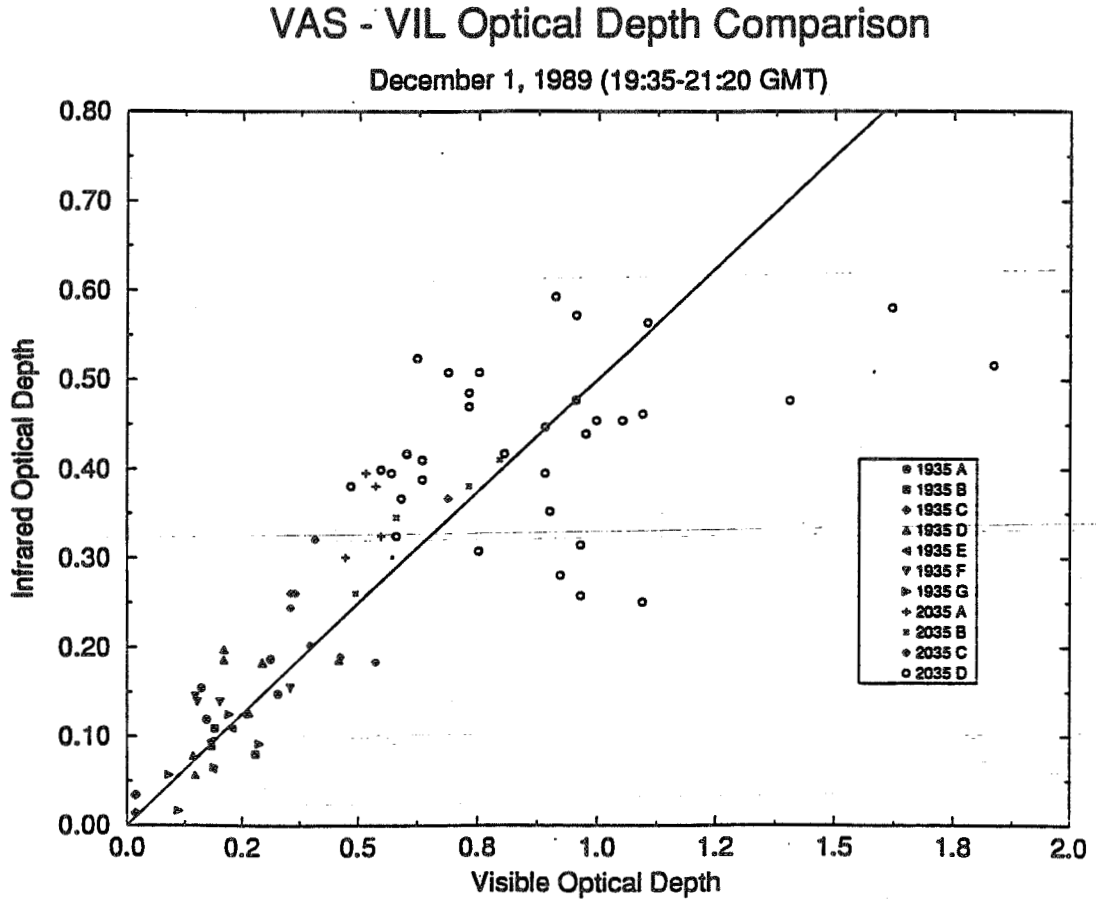

Figure 2: Scatter plot of the visible and IR optical depths of cirrus clouds using coincident lidar and satellite data.

Wylie, D., W. Wolf, P. Piironen, E. Eloranta, "Visible infrared optical depths of cirrus as seen by satellite and scanning lidar", Cloud Impact on Defence Operations and Systems, Fort Belvoir, Virginia, November 15-19, 1993.

VISIBLE/INFRARED OPTICAL DEPTHS OF CIRRUS AS SEEN BY SATELLITE AND SCANNING LIDAR

Donald Wylie, Walt Wolf, Paivi Piironen and Edwin Eloranta

University of Wisconsin-Madison
Madison, WI 53706

1. INTRODUCTION

A large body of cloud statistics have been recently compiled from satellite data, Schiffer and Rossow, (1983) and Wylie and Menzel, (1993). These are from infrared satellite sensors which can be added to the CFLOS data base which came primarily from visual observations. To quantitatively use the satellite data, the relationship between the visible and infrared optical depths of the clouds must be established. To study this relationship, we combined data of the visible scattering in cirrus from lidars with infrared emittance and transmission data from satellites.

Previous studies of the visible and IR radiative properties of ice clouds have been made by Platt (1979) using lidar with an IR radiometer and Minnis et al. (1990) using satellite and lidar data from a case study in FIRE. Platt (1979) collected several cases of cirrus clouds and found a ratio of the visible/IR optical depths of 2:1. The Minnis et al. (1990) FIRE case study found the visible/IR ratio to be slightly higher, 2.1:1. Modelling of radiative properties of ice crystals suggest that the visible/IR ratio can vary from 1.8 to 4.0 (Minnis et al., 1993).

The previous studies have been limited in scope because of the difficulty in obtaining visible and IR data together. To expand our knowledge of the visible and IR radiative properties of transmissive cirrus, we initiated our own study.

One of the largest problems for any cirrus cloud study is the large spatial variability of clouds. Vertically pointing lidars sample only the part of the cloud that drifted over them. They have a vary narrow beam, < 1 m in width. Satellites can see spatial gradients in clouds but have less resolution. Satellite radiometer field of views (FOV) vary from 1 to 20 km. To reduce the spatial sampling problem caused by this mix of instruments, a scanning lidar was used to make volume imagery of cirrus clouds similar to the satellite view of the same clouds.

2. MEASUREMENT TECHNIQUE

The High Spectral Resolution Lidar (HSRL) and the Volume Imaging Lidar (VIL) of the University of Wisconsin-Madison were combined to produce a quantitative image of the visible optical depth of cirrus clouds. The HSRL is a unique instrument that measures the extinction and optical depth of the cloud without assuming the extinction to backscatter ratio in clouds. Simple lidars require estimating extinction from the backscattered return measured by the lidar. The extinction to backscatter ratio varies depending on the constituents of the clouds. The HSRL directly measurements this radiative property of the clouds. Details of this system are given else where in these proceedings by Eloranta et al., (1993).

To understand radiative scattering in clouds, the large horizontal and vertical variations in cloud structure have to be measured. The HSRL samples only a small portion of the cloud - a column about 30 centimeters wide. The GOES satellite IR sensors have a horizontal resolution of 10.8 km at Madison, WI. To account for FOV differences, the horizontal structure of the clouds were measured by the VIL.

The VIL produced visible backscatter images of the clouds by scanning across the wind (see Figure 1). Time advection of the clouds was used to construct a horizontal image of visible backscatter from the VIL data over a one hour period. An example is shown in Figure 2. This image covers 100 km in the north-south direction. The location of the VIL is the center of the image. The image is skewed because it has been distorted to the projection of the GOES satellite image.

The HSRL was used to calibrate the VIL signal into backscatter cross sections of particulates. The backscatter cross sections were related to extinction by a constant backscatter phase function determined from the HSRL data. This process produced a

three dimensional image of visible extinction in the cirrus clouds over a one hour period.

The extinction volume image was then transformed to an image of optical depth in the same viewing geometry as the GOES satellite (Fig. 2). Optical depths were formed from the integral of extinction along the path in which the GOES scanner viewed this volume. The optical depth image was originally produced with a 1 km (satellite nadir) resolution. This image was then shifted to align with the satellite IR image to account for error in the satellite registration system. The lidar visible optical depth image then was averaged to an 8 km (satellite nadir) image for direct comparison to the satellite IR image. This gave coincident fields of views from both satellite and lidars in the same geometry with a horizontal resolution of 10.8 km per pixel.

IR optical depths were extracted from the GOES image using calculations of the IR transmittance of the clouds using the IR radiance of the cloud, the radiance of cloud free FOV's and radiances calculated from the temperature of the mean vertical level of the cloud. The VIL data were used to determine the cloud level. Rawinsonde observations were made at Madison at the same time as these data.

All dual lidar data were taken in the vicinity of Madison, WI on 1 December, 1989. The VIL was located 24 km west of the HSRL. The VIL scanned both crosswind and nearly downwind over the HSRL. Data were taken from 19:35 UTC (13:35 Local) to 21:20 UTC (15:20 L). During this time a large mass of cirrus clouds moved into the region from the west-northwest with an approaching cold front. Madison, WI was under cloud free sky during the morning and proceeded to total overcast by the end of this period. Two lidar images were constructed from 1 hour VIL crossection records. More details on the data taken can be found in Ackerman et al. (1993).

3. RESULTS

An example of the cirrus cloud structure viewed by the VIL is shown in Figure 1. A thick cloud mass from 6.8 to 9.0 km is apparent from 8 km south to 20 km north of the VIL. Other thin broken layers are apparent both north and south of the large mass. This is typical of the different forms of cirrus sampled on 1 Dec, 89. The first clouds to reach Madison were vertically thin and horizontally broken. A few dense lines with evidence of precipitating virga also were found in the VIL volume. Later thicker cirrus moved in with virga that spanned the 2.2 km shown in Fig. 1.

The satellite and VIL images were divided into regions of similar cloud characteristics. The VIL cross sections were used as the primary division tool. The GOES image had little detail in the IR, although the same general spatial pattern as the lidar image was seen. The lidar visible optical depth image at 1 km showed many line and sheet structures. Cloud thickness, the presence of multiple layers and the intensity of precipitating virga were used to segregate different cloud forms.

The visible and accompanying IR optical depths are shown in Fig. 3. Most of the data are near the 2:1 line shown in the image. These data loosely agree with theory and the other past measurements. However, the visible/IR optical depth ratio appears to increase for thicker precipitating cirrus. Clouds with dense precipitating virga have ratios below the 2:1 line (visible/IR > 2). Cloud areas of highest reflectivity had solid lidar returns over 2 km depth with occasional embedded layers of extremely high reflectivity. The horizontal variations in cloud reflectivity were seen in the IR satellite imagery but with far less detail than the lidar images. The lower resolution of the satellite IR sensor smoothed some of these variations. However, the lidar data show that visible reflectivity had a wide range of values with large vertical and horizontal detail.

More data have been added to Fig. 3 from 1993. HSRL data have been taken during polar orbiter NOAA satellite passes over Madison, WI. The VIL was not used with these data. An example of HSRL data from 12 October 93 is shown in Figure 4. NOAA 12 crossed the HSRL at 00:36 (UTC). The IR image is shown in Figure 5. Light cirrus from 7.8 to 10.5 km moved over the HSRL before the NOAA 12 overpass.

Some bright cells were apparent in the HSRL data (Fig. 4) that could not be seen in the NOAA 12 IR image (Fig. 5). The scanning resolution of the NOAA 12 image

was 1 km (HRPT) and has been remapped to a rectangular latitude-longitude coordinate projection. It appears that the bright cells apparent in the HSRL time section, are smoothed over in the satellite IR image.

A time record of the optical depth of this cloud measured by the HSRL is shown in Figure 6. The optical depth was very low, around 0.1 before the cirrus arrived. At about 0:06 UTC (0.1 decimal hour on absissa), the optical depth radically increased to 1.15 and then decreased to 0.9 at the time of the satellite overpass. Later, the visible optical depths dropped into a range from 0.25 to 0.6.

Also shown on Fig. 6 are equivalent IR optical depths taken from the satellite image. The spatial satellite image was converted to a time section using the wind at 9 km.

Some discrepancies between the satellite and the lidar optical depths are apparent. The large visible optical depth measured at 0.35 UTC by the lidar, 0.25 hour before the satellite overpass, did not appear in the satellite image. The satellite measured nearly consistent temperatures around 262 K. Later the satellite image follows the lidar time section with optical depths dropping at 1.35 UTC.

The cirrus was evaporating as it crossed the HSRL from the northwest. It appears that the intense cells that appeared in the HSRL time record decayed down wind by the time of the satellite overpass. These cells lasted for 0.1 hour over the lidar. The 9 km wind speed was 22.7 km/hr. This implies that the cells were at least 2.2 km long in the down wind direction which should have been visible on the 1 km satellite image. The cross wind scans of the VIL would have been useful in determining the areal coverage of these cells.

The HSRL and NOAA satellite data are shown on Fig 3. They fall near the 2:1 line inside the points taken from the HSRL, VIL and GOES data from 1 December 89.

4. CONCLUSION

These data appear to confirm the previous studies of Platt (1979) and Minnis et al. (1990). The visible/IR optical depth ratios have been in the range of 1:1 to 4:1.

The strength of the precipitating virga definitely affected the visible/IR optical depth ratio. This ratio was found to $\leq$ 2:1 for clouds with weak or no virga. While cirrus with dense virga had ratio's of > 2:1.

Some other trends are being investigated. The presence of water at the top of cirrus layers has been found in the 1993 data. The HSRL can identify water from ice by polarization measurements that have recently been added. These data have not been shown here, but are under study and the effects of water on the visible/IR optical depth will be reported at some later date.

There is a slight indication that the temperature of the cloud has some effect on the visible/IR optical depth ratio. The clouds studied in 1989 were warmer and of lower altitude than the 1993 data. The recently acquired data lack any points with visible/IR ratios > 2:1. We will look for this trend with future data.

5. REFERENCES

Ackerman, S. A., E. W. Eloranta, C. J. Grund, R. O. Knuteson, H. E. Revercomb, W. L. Smith and D. P. Wylie, 1993: University of Wisconsin Remote Sensing Pilot Experiment. Bull. A.M.S.

Eloranta, E.W., and P. Piironen, 1993: Remote measurements of cloud optical properties with a robust high spectral resolution lidar., CIDOS-93.

Minnis, P., D.F. Young, K. Sassen, J.M. Alvarez and C.J. Grund, 1990: The October 27-28 1986 FIRE IFO Cirrus Case Study: Cirrus parameter relationships derived from satellite and lidar data. Mon. Wea. Rev., 118, 2402 2425.

Minnis, P., K.N. Liou and Y. Takano, 1993: Inference of cirrus cloud properties using satellite-observed visible and infrared radiances. Part I: Parameterization of radiance fields, J. Atm. Sci., 50, 1279-1304.

Platt, C.M.R., 1979: Remote sounding of high clouds, I: Calculations of visible and infrared optical properties from lidar and radiometer measurements., J. Appl. Meteor., 18, 1130-1143.

Schiffer, R.A. and W.B. Rossow, 1983: The International Satellite Cloud Climatology Project (ISCCP): The first project of the World Climate Research Programme., Bull. Amer. Meteor. Soc., 64, 779-784.

Wylie, D.P. and W.P. Menzel, 1993: Four years of global cirrus cloud statistics using HIRS., Submitted to J. Climatology.

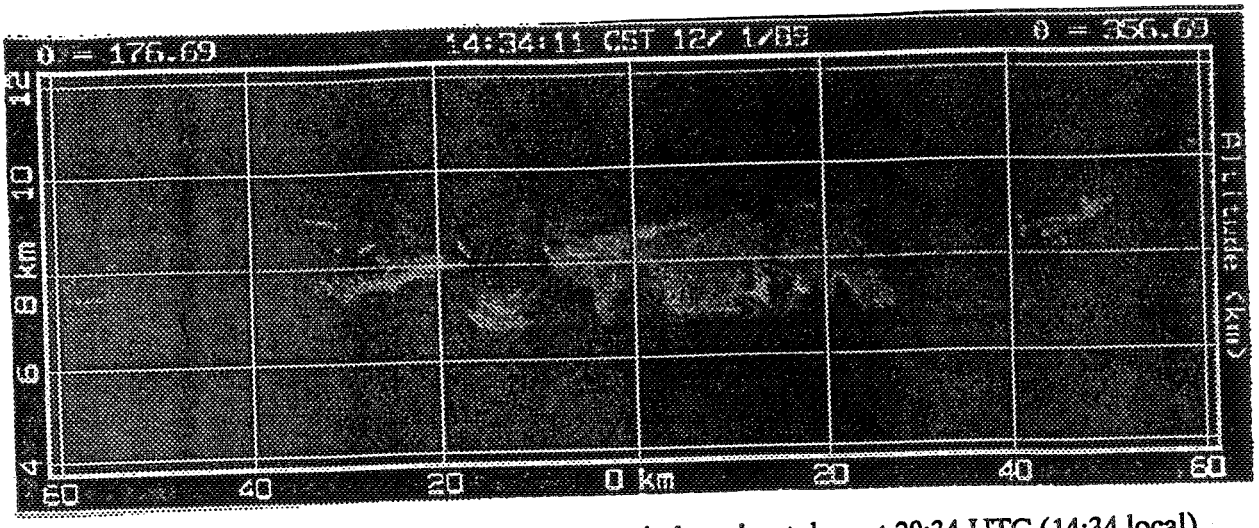

Figure 1: A Volume Imaging Lidar (VIL) cross wind section taken at 20:34 UTC (14:34 local). Scan directions were azimuths of 177° and 357°. Orientation is south to north.

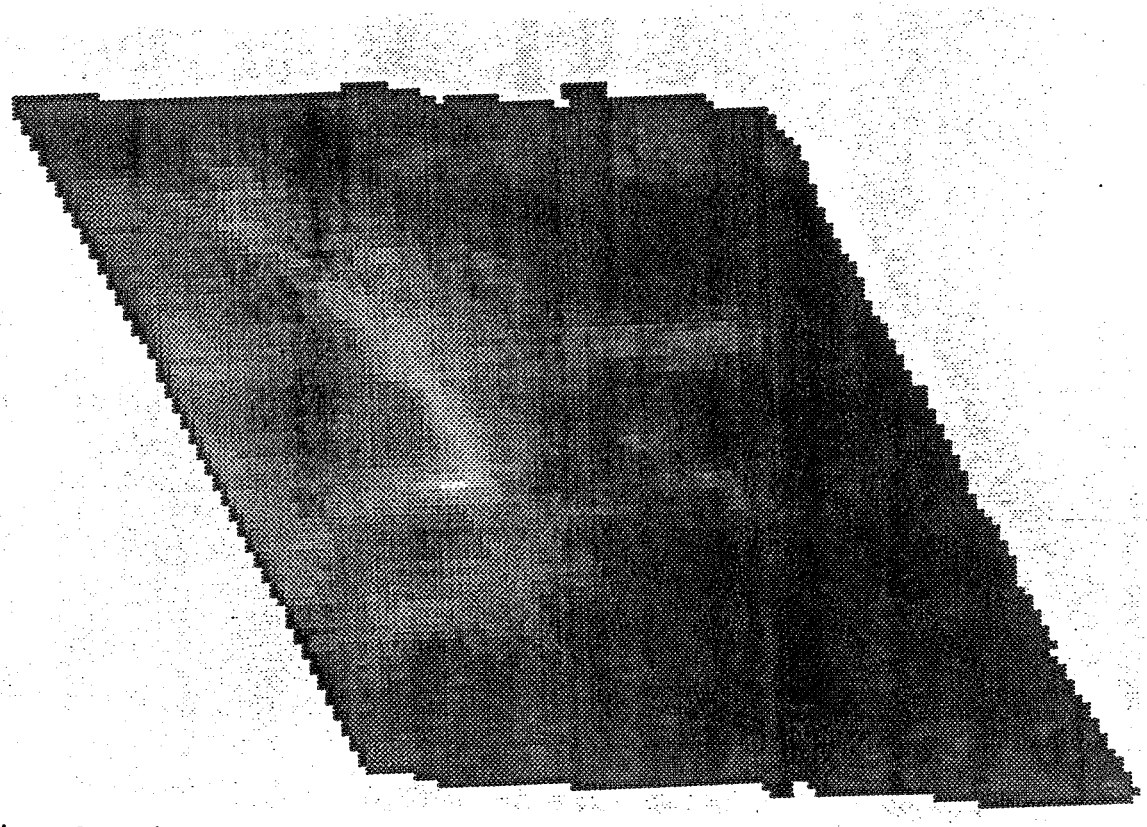

Figure 2: An image in the projection of the GOES satellite made from the cross wind scans of the VIL from 20:35 to 21:20 UTC, 1 December 1989. The VIL scan in Fig. 1 is near the center of the image. Boundaries of the image are north-south and east-west.

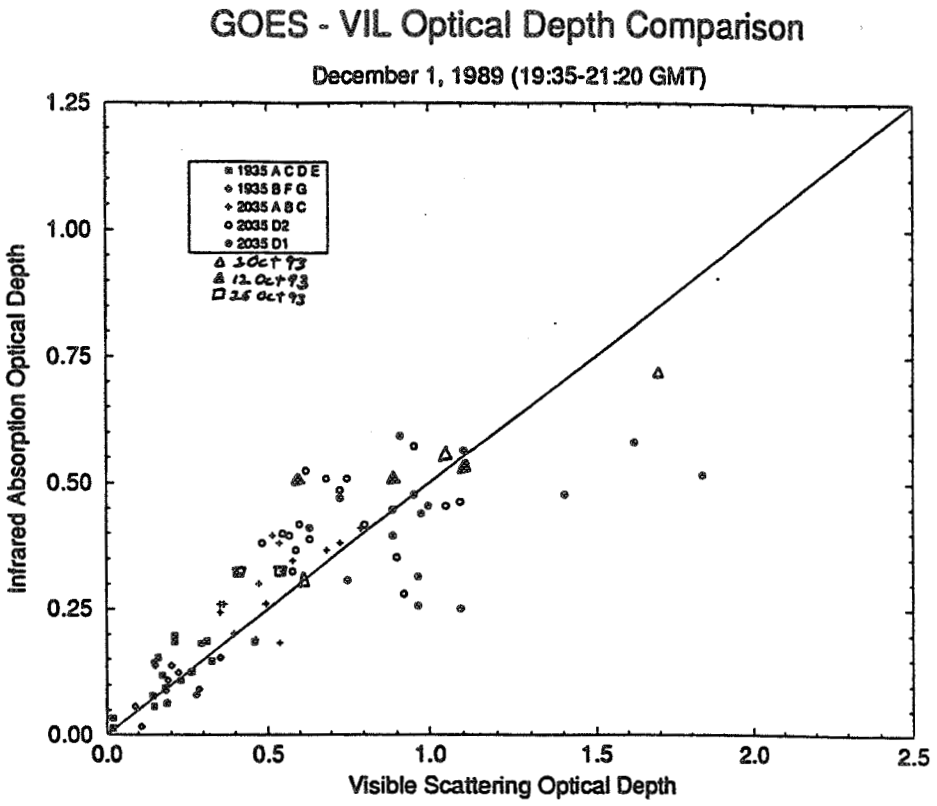

Figure 3: Scatter plot of the visible and IR optical depths of cirrus clouds using coincident lidar and satellite data.

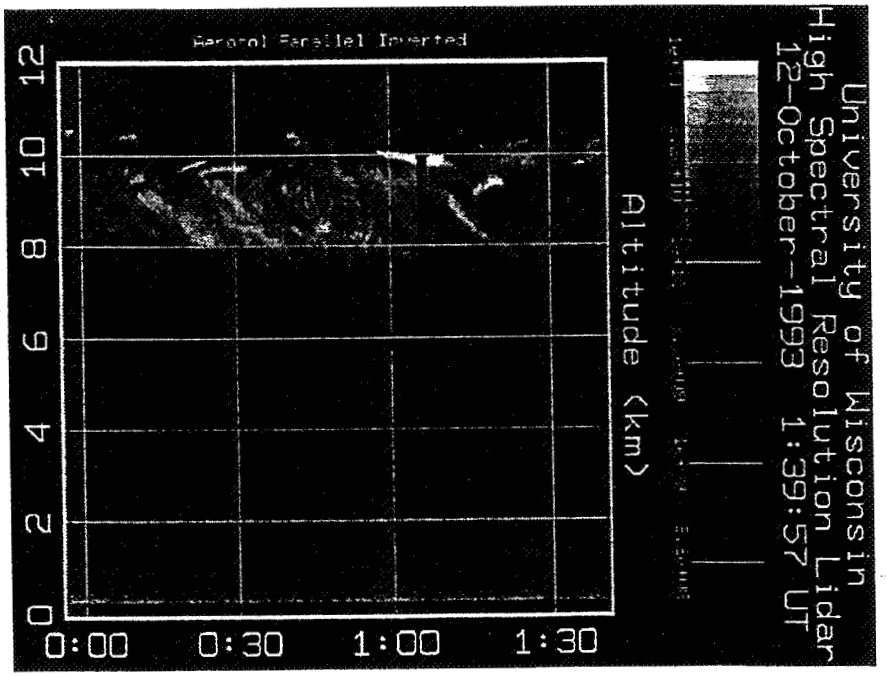

Figure 4: Time section of the HSRL lidar taken at Madison, WI on 12 October 93. The time scale is UTC.

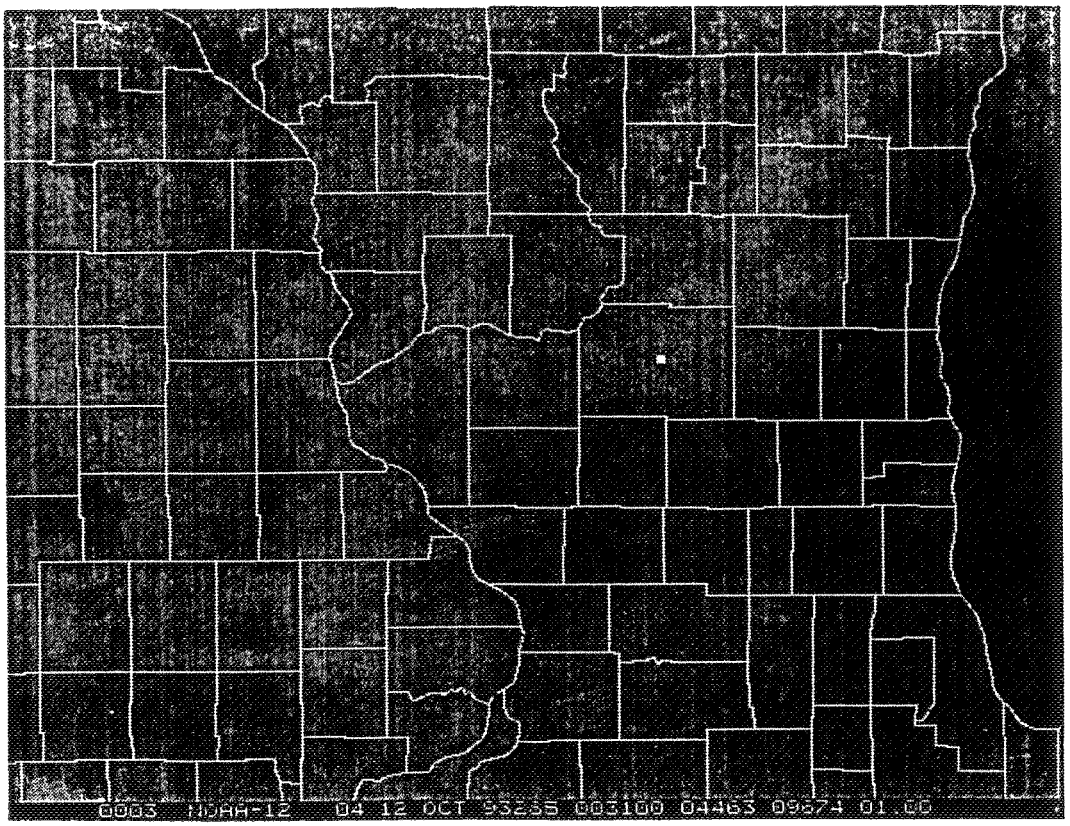

Figure 5: The NOAA 12 AVHRR HRPT channel 4 (11 micron) infrared image from 00:36 UTC, 12 October 93. This image has been rectified to an equal distance latitude-longitude projection.

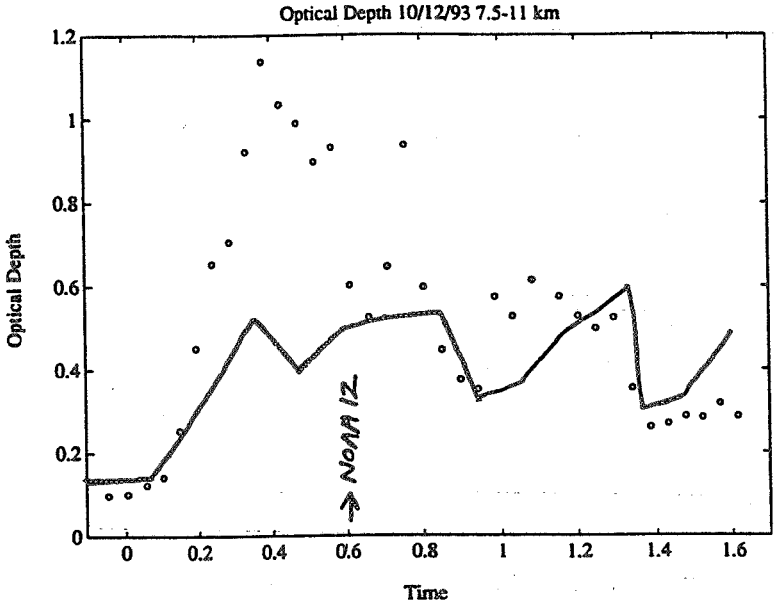

Figure 6: The optical depths measured by the HSRL on 12 October 93 (circles) and the from the NOAA 12 image (solid line).

Eloranta, E. W., P. Piironen, "Depolarization measurements with the high spectral resolution lidar", Seventeenth International Laser Radar Conference, Sendai, Japan, 1994.

DEPOLARIZATION MEASUREMENTS WITH THE HIGH SPECTRAL RESOLUTION LIDAR

E. W. Eloranta and P. Piironen
University of Wisconsin
1225 W. Dayton Street, Madison, Wisconsin 53706, USA
Phone: 608-262-7327 Fax: 608-262-5974
Email: eloranta@lidar.ssec.wisc.edu, paivi@hsrl.ssec.wisc.edu

Many investigators have used depolarization of lidar returns to characterize atmospheric particles[1]. This paper describes modifications to the University of Wisconsin High Spectral Resolution Lidar which permit very precise depolarization measurements in addition to optical depth, backscatter cross section, and extinction cross section measurements made by the instrument[2,3].

The HSRL rotates the polarization of the transmitted laser pulse by 90° on every other pulse (see figure 1). This allows measurement of the parallel and cross polarized lidar returns without the use of separate detectors for the two polarizations. The parallel return is measured on the first pulse and the perpendicular return on the second pulse. The HSRL operates at a pulse repetition rate of 4 kHz. The parallel and perpendicular returns are summed in separate buffers. Each profile consists of the sum of 4000 pulses of each polarization. Since only 250 μs separates individual laser pulses, it is possible to compute depolarizations from successive pulses without having the wind change the particles in the sample volume. Because the optical path and detector are the same for both polarizations, the depolarization ratios can be measured without the need to calibrate the relative sensitivity of the two channels.

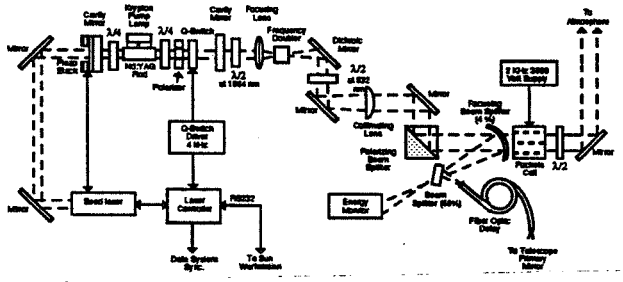

Figure 3. The transmitter section of the HSRL. The transmitted polarization is rotated by 90° between successive pulses by a Pockels cell.

Accurate measurements depend only on the linearity of the detector, the polarization purity of the transmitter, and the cross polarized leakage of the receiver polarization filter. The photon counting system of the HSRL is very linear. Pile-up and after-pulsing corrections are applied to all data; however, low after-pulsing photomultipliers and high bandwidth counting electronics make the corrections very small for all returns execpt those from dense low altitude water clouds. Measurements of the polarization of the laser output show residual cross-polarizations of $\sim 0.1\%$ when measured with a polarization cube which is specified to have a 0.1% cross polarization rejection. Model calculations suggest that the cross polarization response of the receiver is also less than 0.1% with the major portion of the error resulting from the ellipticity of light reflected from the primary and secondary aluminized mirrors of the 0.5 m diameter Dall-Kirkham receiving telescope. Thus, although we have not devised a rigorous experimental test of the total cross polarization leakage in the system, we expect that it is $\sim 0.1\%$.

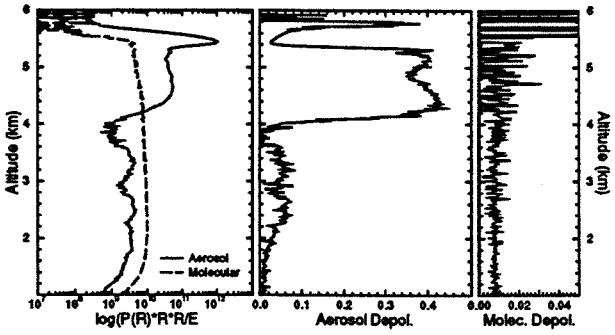

Figure 2. Range-squared corrected aerosol and molecular lidar returns from aerosols (0 - 4 km), ice crystal virga (4-5.2 km), a water cloud (5.4-5.7 km) and a cirrus cloud (5.7-5.8 km) are shown on the left. Particulate depolarizations are shown in the center and molecular depolarizations on the right.

Because the HSRL separates the lidar return into aerosol and molecular contributions, the aerosol and molecular depolarizations can be measured separately. Figure 2 shows separated aerosol and molecular profiles observed with the HSRL on November 11, 1993 between 1:55 and 2:01 UT. Ice crystal virga (at altitudes between 4.0 and 5.2 km) is falling out of a thin water cloud located at altitudes between 5.4 and 5.7 km. Below 4 km, the backscatter from aerosols is weaker than from molecules. The depolarization of the ice is nearly constant between 34% and 42%. At the base of the wa-

ter cloud the depolarization drops to 2% as result of scattering from spherical droplets. Higher in the cloud the depolarization increases, apparently as the result of multiple scattering and the presence of ice. Because the HSRL receiver field of view is only 160 μradians, multiple scattering depolarization appears to be under 10% in nearly all clouds we have observed. The 30% depolarization at the top of the water cloud is due to the presence of ice at the cloud top. Figure 3 summarizes the depolarizations measured in clouds on 14 days between Aug. 2 and Nov 11, 1993. High depolarization ratios easily distinguish ice clouds from water clouds which produce much smaller depolarization.

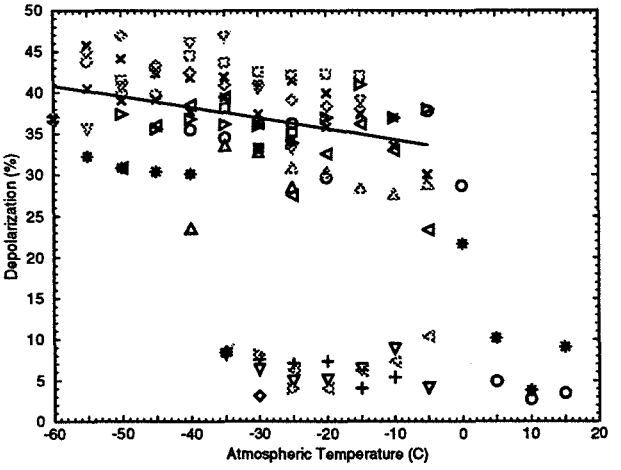

Figure 3. Depolarization as a function of temperature for particulate scattering in clouds.

Notice that all clouds colder than the -40°C homogeneous nucleation temperature of water are ice. Above 0°C all returns show low depolarizations. Although spherical water droplets are expected to yield no depolarization from single scattering, this plot shows depolarizations up to 10% in clouds which appear to be water clouds. Since many of these clouds are observed to have ice crystal virga falling from their bases, it is apparent that at least part of the increased depolarization is due to ice in mixed phase clouds. For mixed phase clouds the scattering from water droplets dominates the scattering cross section; thus, the depolarization is closer to that of pure water clouds than of cirrus. Inside water clouds we see a characteristic increase of depolarization with penetration depth caused by the presence of multiple scattering. For cases studied thus far, it appears that the 160 μradian angular field of view of the HSRL limits multiple scattering induced depolarization to less than 10% in water clouds. We are surprised to find no water cloud depolarizations less than 0.8%, although it is clear that the HSRL can detect smaller values.

The molecular depolarization measured by the HSRL is constant at a value of 0.7% to 0.8% when viewed with a 1 nm filter bandpass. This is larger than expected for Cabanne line depolarization since the filter admits a small fraction of the closest rotational Raman lines and the I_2 filter of HSRL blocks the center of the Cabanne line[3]. When the filter is removed and the laser is tuned off the I_2 filter, rotational Raman scattering increases the molecular depolarization increases to 1.5%.

With traditional lidars, aerosol depolarization measurements are complicated by the presence of molecular scattering which often dominates the received signal in clear air. Since the HSRL separately measures the aerosol depolarization, accurate measurements can be obtained. Figure 4 presents a histogram of aerosol depolarizations observed below the clouds from the data set used to compile figure 3.

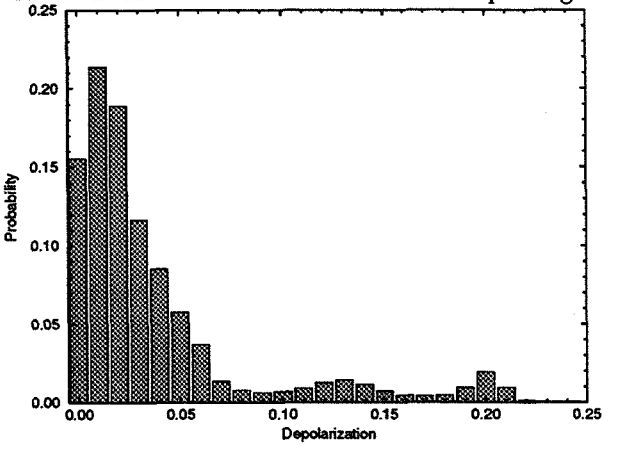

Figure 4. The probability of occurrence of depolarizations for aerosol scattering between altitudes of 500 m and cloud base. Data points consist of 5 min averages of data in 15 m range bins. Statistics include only points with backscatter ratios greater than 0.2.

ACKNOWLEDGMENTS

This work was supported by grants from the Office of Naval Research (N00014-91-J-1558) and the National Aeronautics and Space Administration (NAG-1-882).

REFERENCES

1. Sassen, K., 1991: The Polarization Lidar Technique for Cloud Research: A Review and Current Assessment,*Bulletin of Am. Meteor. Soc.*, **72**, 1848.
2. Grund, C.J., and E.W. Eloranta, 1991: University of Wisconsin High Spectral Resolution Lidar, *Optical Engineering*, **30**, 6-12.
3. Piironen, P. and E. W. Eloranta, 1994: Demonstration of an iodine absorption filter based high spectral resolution lidar, *Optics Letters*, **19**, 234.
4. Eloranta, E. W. and P. Piironen, 1994: *Proceedings of the 17th ILRC*, July 25-29, 1994, Sendei Japan.

Eloranta, E. W., P. Piironen, "High spectral resolution lidar measurements of particle size", Seventeenth International Laser Radar Conference, Sendai, Japan, 1994.

HIGH SPECTRAL RESOLUTION LIDAR MEASUREMENTS OF MULTIPLE SCATTERING.

E. W. Eloranta and P. Piironen
University of Wisconsin
1225 W. Dayton Street, Madison, Wisconsin 53706, USA
Phone: 608-262-7327 Fax: 608-262-5974
Email: eloranta@lidar.ssec.wisc.edu, paivi@hsrl.ssec.wisc.edu

Calculations show that the multiply scattered lidar signal is strongly dependent on: 1) the angular Field Of View (FOV) of the receiving telescope, 2) the small angle forward peak in the scattering phase function and 3) the scattering cross section profile in the cloud. If the scattering cross section profile can be measured, multiple scattering measurements may allow measurement of the forward diffraction peak width. This would provide particle size information. Traditional aerosol lidar systems do not provide sufficient information to measure the extinction or backscatter cross section without using assumed relationships between the backscatter and extinction cross section. A boundary value specifying the extinction at one point in the cloud is also required.

The University of Wisconsin High Spectral Resolution Lidar (HSRL) provides unambiguous measurements of backscatter cross section, backscatter phase function, depolarization, and optical depth[1,2]. This is accomplished by dividing the lidar return into separate particulate and molecular contributions. The molecular return is then used as a calibration target. We have modified the HSRL to use an I_2 molecular absorption filter to separate aerosol and molecular signals[2]. This allows measurements in dense clouds. Useful profiles extend above the cloud base until the two-way optical depth reaches values between 5 and 6; beyond this, photon counting errors become large. The spectrometer channels have a 0.16 mr FOV; the small FOV suppresses multiple scattering errors in the retrieved optical parameters.

In order to observe multiple scattering, the HSRL includes a channel which records the combined aerosol and molecular lidar return simultaneously with the spectrometer channel measurements of optical properties. The angular field of view of this Wide Field Of View (WFOV) channel is controlled by the system computer and it can be adjusted from 0.22 mr to 4 mr. This channel is rapidly sequenced between several aperture sizes to record the FOV dependence of the lidar return. The system calibration and signals recorded in the spectrometer channels are sufficient to allow removal of the molecular return from the WFOV signal. The depolarization of light received in the WFOV channel is also measured.

HSRL measurements from a water cloud are shown in figure 1. The lidar returns in the WFOV channeldivided by the return in the 0.16 mr spectrometer channel are plotted. The measured backscatter cross section profile is also shown. The increased contribution of multiple scattering with increased field of view is easily seen.

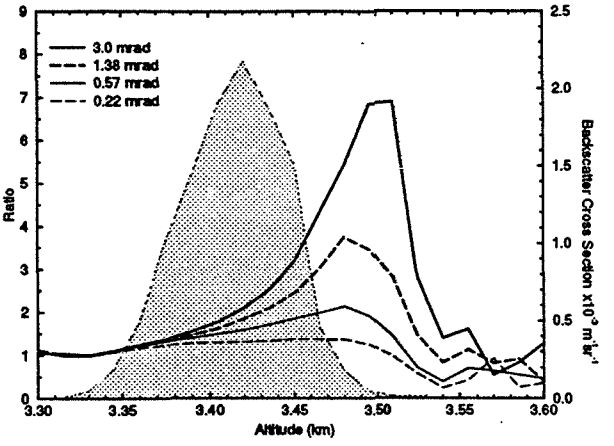

Figure 1. Ratios of the WFOV signals to the signal in the 0.16 mrad spectrometer channel. WFOV acceptance angles of 0.22, 0.57, 1.38 and 3.0 mrad are shown. The backscatter cross section is shaded.

This paper describes HSRL multiple scattering measurements from both water and ice clouds. These include signal strengths and depolarizations as a function of receiver field of view. All observations include profiles of extinction and backscatter cross sections. Measurements are also compared to predictions of a multiple scattering model based on small angle approximations.

Acknowledgements

This work was supported by grants from the Office of Naval Research (N00014-91-J-1558) and the National Aeronautics and Space Administration (NAG-1-882).

References

1. Grund, C.J., and E.W. Eloranta, 1991: University of Wisconsin High Spectral Resolution Lidar, *Optical Engineering*, **30**, 6-12.

2. Piironen, P, and E. W. Eloranta, 1994: Demonstration of an iodine absorption filter based high spectral resolution lidar, *Optics Letters*, **19**, 234.

Reprinted from MONTHLY WEATHER REVIEW, Vol. 118, No. 11, November 1990
American Meteorological Society

The 27–28 October 1986 FIRE IFO Cirrus Case Study: Cirrus Parameter Relationships Derived from Satellite and Lidar Data

PATRICK MINNIS*, DAVID F. YOUNG†, KENNETH SASSEN,**
JOSEPH M. ALVAREZ* AND CHRISTIAN J. GRUND‡

*Atmospheric Sciences Division, NASA Langley Research Center, Hampton, Virginia,
†Lockheed Engineering and Sciences Company, Hampton, Virginia,
**Department of Meteorology, University of Utah, Salt Lake City, Utah,
‡Department of Meteorology, University of Wisconsin, Madison, Wisconsin

(Manuscript received 24 March 1989, in final form 12 June 1990)

ABSTRACT

Cirrus cloud radiative and physical characteristics are determined using a combination of ground-based, aircraft, and satellite measurements taken as part of the FIRE Cirrus Intensive Field Observations (IFO) during October and November 1986. Lidar backscatter data are used with rawinsonde data to define cloud base, center, and top heights and the corresponding temperatures. Coincident GOES 4-km visible (0.65 μm) and 8-km infrared window (11.5 μm) radiances are analyzed to determine cloud emittances and reflectances. Infrared optical depth is computed from the emittance results. Visible optical depth is derived from reflectance using a theoretical ice crystal scattering model and an empirical bidirectional reflectance model. No clouds with visible optical depths greater than 5 or infrared optical depths less than 0.1 were used in the analysis.

Average cloud thickness ranged from 0.5 km to 8.0 km for the 71 scenes. Mean vertical beam emittances derived from cloud-center temperatures were 0.62 for all scenes compared to 0.33 for the case study (27–28 October) reflecting the thinner clouds observed for the latter scenes. Relationships between cloud emittance, extinction coefficients, and temperature for the case study are very similar to those derived from earlier surface-based studies. The thicker clouds seen during the other IFO days yield different results. Emittances derived using cloud-top temperature were ratioed to those determined from cloud-center temperature. A nearly linear relationship between these ratios and cloud-center temperature holds promise for determining actual cloud-top temperatures and cloud thicknesses from visible and infrared radiance pairs.

The mean ratio of the visible scattering optical depth to the infrared absorption optical depth was 2.13 for these data. This scattering efficiency ratio shows a significant dependence on cloud temperature. Values of mean scattering efficiency as high as 2.6 suggest the presence of small ice particles at temperatures below 230 K. The parameterization of visible reflectance in terms of cloud optical depth and clear-sky reflectance shows promise as a simplified method for interpreting visible satellite data reflected from cirrus clouds. Large uncertainties in the optical parameters due to cloud reflectance anisotropy and shading were found by analyzing data for various solar zenith angles and for simultaneous AVHRR data. Inhomogeneities in the cloud fields result in uneven cloud shading that apparently causes the occurrence of anomalously dark, cloudy pixels in the GOES data. These shading effects complicate the interpretation of the satellite data. The results highlight the need for additional study of cirrus cloud scattering processes and remote sensing techniques.

1. Introduction

Accurate quantification of cirrus cloud properties from satellite measurements is particularly important to the understanding of the role of cirrus in climate change. The nonblackness of cirrus at thermal infrared wavelengths renders the interpretation of satellite data taken over cirrus more difficult than measurements over most water clouds. The International Satellite Cloud Climatology Project (ISCCP; see Schiffer and Rossow 1983) is making an ambitious effort to derive daytime cirrus coverage, altitudes, and optical depths over the globe during a 5-year period. The ISCCP analysis algorithm (Rossow et al. 1988) relies entirely on bispectral data taken at visible (VIS: ~0.65 μm) and infrared (IR: ~11.5 μm) wavelengths. Although VIS–IR bispectral techniques have been suggested as feasible methods for determining bulk cirrus properties (e.g., Shenk and Curran 1973; Reynolds and Vonder Haar 1977), there has been very little application of these techniques to real data prior to the ISCCP.

The basic premise for using the bispectral approach is that the VIS extinction coefficient is related to the IR absorption coefficient. This relationship implies that the cloud VIS reflectance may be used to infer the cloud's IR emittance. Having a value for the clear-sky IR radiance, it is possible to correct the observed cloudy radiance for cloud emittance resulting in an estimate

Corresponding author address: Patrick Minnis, Atmospheric Sciences Division, NASA/Langley Research Center, Hampton, VA 23665-5225.

of the radiance emanating from a specified level in the cloud. The equivalent blackbody temperature of this level, usually the cloud center, is then converted to cloud altitude using a vertical sounding of temperature. The critical relationship required for this approach is the dependence of IR emittance on VIS reflectance through the IR and VIS optical depths. Since clouds scatter radiation anisotropically, this relationship is also influenced by the viewing and illumination conditions.

The ISCCP cirrus analysis (Rossow et al. 1988) utilizes a combination of theoretical and empirical models to determine the cloud visible optical depth from the observed reflectance; the cloud emittance from the visible optical depth; and finally, the cloud-top temperature from the cloud emittance and the observed infrared radiance. The theoretical cloud model is a radiative transfer scheme that simulates the scattering and absorption of visible radiation by water droplets with an effective radius of 10 μm. For water droplets of this size, the ratio of VIS extinction to infrared absorption optical depths is ~2.4. An analysis of coincident satellite and lidar data by Platt et al. (1980) and theoretical calculations employing cylinders (Platt 1979) suggest that this ratio is approximately equal to 2.0 for cirrus. The ISCCP algorithm utilizes the latter value to provide a link between the water droplet model and actual cirrus clouds.

Cirrus clouds are primarily composed of ice crystals with various shapes having maximum dimensions ranging from about 20 μm to 2000 μm (e.g., Heymsfield and Platt 1984). The scattering properties of hexagonal ice crystals differ considerably from spherical particles (Liou 1986). Because of the complexities involved in computing scattering by hexagonal solids, cylindrical columns have been used to approximate hexagonal crystals in radiative transfer calculations (e.g., Liou 1973). More recently, however, Takano and Liou (1989a) have solved the radiative transfer equations for randomly oriented hexagonal plates and columns. Their results are the most realistic to date in that they reproduce certain well-known cirrus optical phenomena.

Absorption plays the dominant role in IR extinction in cirrus clouds. Some theoretical investigations (Liou and Wittman 1979; Stephens 1980), however, have shown that scattering effects may also be significant at IR optical depths greater than ~0.1. An IR radiance measured by a satellite over cirrus clouds, therefore, is the product of both absorption and scattering processes in the cloud, as well as the transmission of radiation from below the cloud (Platt and Stephens 1980). It is generally assumed, however, that scattering effects are negligible so that the observed emittance is considered to be the absorption beam emittance.

Empirical studies have also shed some light on the VIS reflectance–IR emittance relationship. Platt (1973) developed techniques for deriving cloud visible and infrared properties from a ground-based lidar and an upward-looking infrared radiometer. The backscatter intensities measured with the lidar are used to defi cloud base and top heights. Cloud emittance was d rived from the observed downwelling IR radiance. Pl and Dilley (1979) presented emittance results from set of observations taken over Australia. Platt et (1980) used lidar and satellite VIS–IR data to estima the dependence of beam emittance on VIS cloud r flectance for a limited set of viewing and illuminati conditions over Colorado. Their results are more co sistent with theoretical scattering from ice cylind than with scattering from ice spheres. Aircraft radi metric measurements taken over New Mexico (P tridge and Platt 1981) have also been used to determi the radiative characteristics of cirrus clouds as relat to the cloud ice water path. Those results provide fi ther evidence that real clouds scatter more like cylind than spheres. Platt (1983) combined the results fro previous studies and used them to explain the ch acteristics of two-dimensional bispectral histograms VIS–IR data observed from a geostationary satelli Theoretical calculations of reflectance and emittan for typical cirrus clouds were consistent with the s ellite data taken over areas of suspected cirrus clou While that study provided encouragement for usin bispectral approach to retrieving cirrus properties fro bispectral data, it also highlighted some of the di culties that are likely to be encountered with such technique. Platt and Dilley (1984) used lidar and so radiation measurements to measure part of the sing scattering phase function of real cirrus clouds. Th results fell within the range of laboratory measureme and theoretical calculations for hexagonal crystals. A analysis of a large sample of ground-based lidar a infrared data taken over Australia (Platt et al. 198 showed that the average emissivity of cirrus clouds primarily a function of the midcloud temperatu Though fraught with significant uncertainties, th study also indicated that the theoretical value of t ratio of visible extinction to infrared absorption f cirrus clouds may be too low.

From these previous studies, it appears that:

1) cirrus cloud scattering properties are similar those of hexagonal crystals resulting in reflectance p terns that are unlike those from spheres;

2) scattering of IR radiation may be important determinations of IR optical depths; and

3) the ratio of VIS extinction to IR absorption co ficients is between ~1.8 and 4.0.

The full impact of these results on using a VIS–IR spectral method for retrieving cirrus properties is u known. Differences between ice crystal and wa droplet bidirectional reflectance patterns will introdu errors into the retrieved VIS optical depth. Use of observed beam emittance with a theoretical model th assumes absorption only may affect the emittance timation. Finally, uncertainties in the extinction ra

(scattering efficiency) may cause significant errors in the estimation of IR optical depth.

In this paper, the relationship between VIS reflectance and IR emittance is examined using data taken during the First ISCCP Regional Experiment (FIRE) Cirrus Intensive Field Observations (IFO; see Starr 1987). Ground-based and aircraft lidars are used to define the vertical locations of the cirrus clouds, while satellites provide measurements of VIS and IR radiances. Both VIS and IR optical depths are computed from the reflectance and emittance data covering a range of solar zenith angles missed in previous studies. These relationships are derived to provide a means for the application of a bispectral cirrus parameter retrieval algorithm over the FIRE IFO region. Results are presented for the entire IFO period with emphasis on 27–28 October 1986, the case study period. The data presented here also constitute an initial source for developing cirrus bidirectional reflectance models and may be used to help validate the models employed in the ISCCP algorithm.

2. Data

a. Lidar measurements

Lidar backscatter data were taken from four different sources—three surface and one airborne. The lidars and their operating systems and data products have been described elsewhere. Thus, only a brief description of sources and their uses in this study are given here.

The University of Utah mobile polarization lidar (see Sassen et al. 1990) was located at Wausau, Wisconsin (WAU; 45.0°N, 89.7°W). The NASA Langley ground lidar (Sassen et al. 1990) was situated at Ft. McCoy, Wisconsin (FMC; 43.9°N, 90.8°W), while the University of Wisconsin High-Spectral Resolution Lidar (Grund and Eloranta 1990) was in Madison, Wisconsin (MAD; 43.1°N, 89.4°W). These ground systems acquired nearly continuous lidar backscatter profiles during the cirrus days of the IFO with especially good coverage during the case study period. The lidar returns are used to define the cloud base and physical thickness. Under conditions of small attenuation and constant backscatter-phase function, the backscatter intensity profiles indicate the vertical distribution of cloud extinction. A time series of these lidar returns shown in Fig. 1 define the outlines of the cirrus clouds as they passed over FMC during the afternoon of 28 October. Solid black areas define the most intense cloud backscatter. Grey denotes less backscatter and white indicates no cloud. Vertical stripes represent missing data. Cloud-top altitude is fairly constant at ~11 km. Cloud base changes from ~8 km to 10 km approximately every half hour. In the morning, cloud base was observed at ~7 km, while cloud top varied between 8 km and 11 km. A similar variation is also seen in the WAU estimated volume backscatter coefficients shown in Fig. 2 for the morning of 28 October. Darker portions

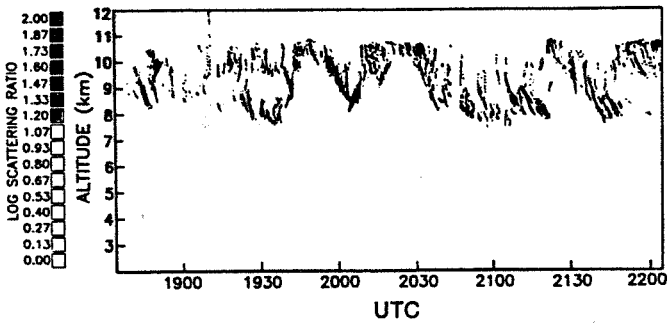

FIG. 1. Lidar backscatter ratios from cirrus clouds passing over Ft. McCoy during 28 October 1986.

of the plot correspond to higher backscatter coefficient values. The particle backscattering efficiency depends on cloud particle shape and phase. Further details of the lidar returns are reported in the cited references.

Three parameters are derived from plots like those in Figs. 1 and 2 by averaging the data within ±15 min of the UTC (Coordinated Universal Time) half hour plus 5 min. All times, however, will be given here to the nearest half hour. Cloud-top altitude, z_t, and cloud-base altitude, z_b, are defined as the average altitudes of the highest and lowest nonclear-air backscatter returns, respectively. Similarly, the cloud thickness is $h = z_t - z_b$. Mean cloud height (approximately cloud center height), z_c, is the backscatter-intensity weighted average height of the cloud. It corresponds roughly to the altitude below which 50% of the lidar backscatter is accumulated. These parameters were estimated graphically for the FMC and WAU sites, while a computer analysis was applied to the MAD results. The value of z_c for MAD corresponds to the midpoint in optical thickness independent of cloud attenuation (see Grund and Eloranta 1990). Since the clouds are advecting over the fixed surface sites, the averaged lidar data correspond to a thin vertical cross section taken out of some cloud volume. It is assumed that the cross-section-averaged data represent the mean conditions of that volume.

These same parameters were also derived from the down-looking lidar backscatter plots reported by Spinhirne et al. (1988) for selected flight tracks of the high-flying, NASA ER-2 aircraft over the IFO area. Shorter time averages were used since the plane's motion greatly increased the cirrus advection rates relative to the lidar. In some instances, the clouds were too thick for complete penetration by the ground-based lidars. To determine these occurrences, the cloud altitudes estimated from the ground were compared to those determined from the nearest aircraft flight. On most days, there was good agreement between the surface and airborne lidars. The thick clouds observed on 22 October required use of the aircraft lidar to estimate z_t. At other times when no aircraft data were available for comparison, a different approach was used to estimate z_t (see section 3a).

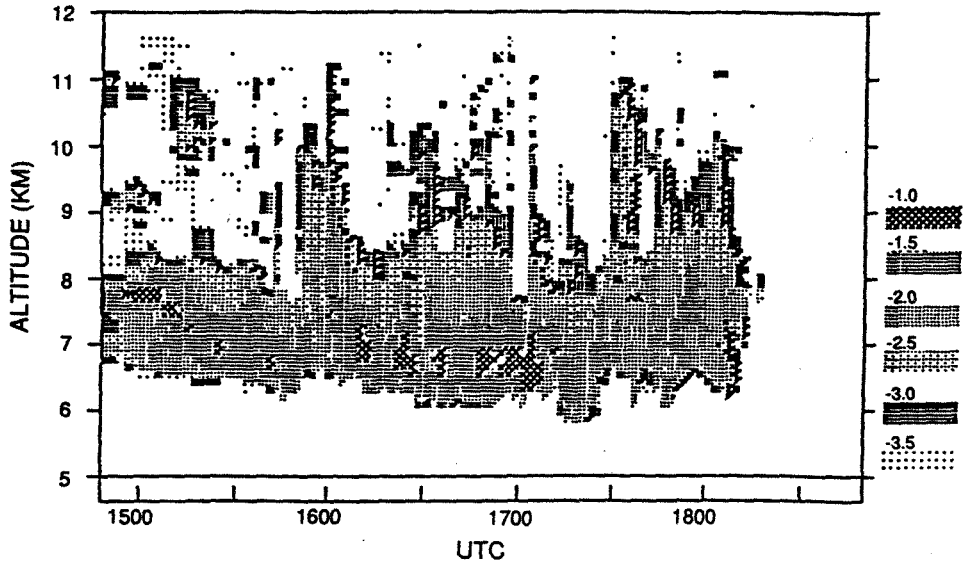

FIG. 2. Estimated lidar volume extinction efficiencies from cirrus clouds over WAU 28 October 1986.

b. Satellite radiances

Half-hourly VIS and IR data from the Geostationary Operational Environmental Satellite (GOES) were resolved to 4-km pixels by averaging and replication of 1-km VIS and 4-km × 8-km IR pixels, respectively, for most times. When the full-resolution data were not available, 8-km pixels derived by pixel averaging (VIS) and sampling (IR) were used. The pixels were navigated to ±8 km as in Minnis and Harrison (1984a). Pixel pairs were extracted for areas within 0.35° longitude and 0.25° latitude of the surface lidar sites. These areas correspond to cloud advection at wind speeds of ~30 m s^{-1} for a half-hour interval. Strips of pixels, 4(2) pixels wide, along the wind vector at z_c centered over the surface site were then taken from the 4 km(8 km) resolution areas. The satellite data corresponding to the ER-2 flight track were extracted for a strip centered on the flight track. This strip is approximately 30 km wide and 100 km long.

Two-dimensional histograms of the VIS and IR radiance pixel pairs were formed from the strips of extracted data. The VIS data, stored as counts, D (where $0 < D \leqslant 63$), in the histogram were converted to radiance and VIS reflectance, ρ, using the calibration of C. H. Whitlock (1989, personal communication) where

$$\rho = (0.1624D^2 - 8.3)(526.9\mu_0)^{-1},$$

and μ_0 is the cosine of the solar zenith angle θ_0. The raw IR data are given as equivalent blackbody temperatures, T, and are converted to radiance with the Planck function, $B(T)$, evaluated at 11.5 μm. Note that all radiometric quantities discussed in this study are spectral quantities, either VIS or IR, so no subscripts denoting spectral dependence are given.

A similar set of histograms was derived from the NOAA-9 Advanced Very High Resolution Radiom (AVHRR) Global Area Coverage (GAC) 4-km for the 0.35° × 0.25° areas over the surface sites. NOAA-9 daytime pass over the areas occurred betw 2000 and 2130 UTC (~1430 local time). Radia from channels 4 and 5 were averaged to produc IR radiance corresponding to the GOES 11.5- channel. The AVHRR VIS data were taken fi channel 1 and converted to reflectance using the brations of C. H. Whitlock (1989, personal comi nication) where

$$\rho = (0.6060D_A - 22.0)(519.4\mu_0)^{-1}$$

and D_A is AVHRR 10-bit count.

Solar zenith, satellite zenith θ, and relative azim ψ angles were computed for each set of measureme from GOES-6 located over the equator at appr mately 97°W. This location yielded a value of $\theta \sim$ for the ground sites. Relative azimuth angles were c fined to the backscattering hemisphere for GOES. orbital precession of the NOAA-9 produces a variati in θ between 0° and 70° over a given site every 4 days. Because of its cross-track scan pattern, AVHRR views a given site from relative azimuth ang that lie in both the forward and backward hemisph at a nearly constant skew to the solar plane. The sk depends on both the solar and site latitudes. Con quently, a range of solar zenith angles with consta viewing angles is covered using the GOES, while a ran of viewing angles at a relatively constant θ_0 is cover with the AVHRR.

Days when cirrus were observed over the IFO wi out substantial low-cloud interference are referred as cirrus days. The times used in this study when lid and satellite data coincided with cirrus are listed Table 1.

TABLE 1. Times and locations of lidar-satellite data used in this study.

Site	Day	Month	Times (UTC)
FMC	22	October	1300, 1330, 1400, 1600, 1630, 1700, 2000
	27		2030, 2100
	28		1330, 1400, 1430, 1500, 1600, 1700, 1900
			1930, 2000, 2030, 2100, 2130, 2200
	30		2000, 2030
	1	November	1800, 1900
	2		1900, 2000, 2100
MAD	28	October	1330, 1500, 1600, 1700, 1800, 1930, 2000
			2030, 2100, 2130, 2200
WAU	22	October	1300, 1330, 1400, 1430, 1600, 1630, 1700, 1800
			1830, 1900, 1930, 2130, 2200
	28		1500, 1600, 1700, 1800, 1900, 1930, 2000, 2030
			2100, 2130
	30		2130, 2200
	1	November	1800, 1900, 2000
	2		1700, 1800, 1900, 2000, 2100

c. *Temperature data*

Soundings from Green Bay, Wisconsin, determined the temperature–height relationships for all of the data. Linear interpolation was used to estimate half-hourly soundings from the six-hourly data. Cloud-top temperature, T_t, corresponds to z_t on the soundings. Mean cloud temperature, T_c, is found from z_c. Surface temperatures taken every six hours at MAD, WAU, and Lone Rock, Wisconsin (Hahn et al. 1988), and occasionally at the FMC site, were used to supplement the clear-sky temperatures derived from the satellite data as described below.

The clear-sky temperature, T_s, is the equivalent blackbody temperature for clear scenes. It is estimated in several different ways. The first order estimate is taken from the initial results of Minnis et al. (1990), which applies the techniques of Minnis et al. (1987) to 0.5° regions within the greater IFO area. That approach sets a VIS threshold ~2 counts above the clear-sky count, D_s (see section 3). All pixels considered to be clear must be darker than this threshold and have a temperature that is no more than 3 K colder than the maximum observed temperature. The 4 K range for clear pixels, roughly double the typical value over Wisconsin land areas, allows for shading effects in partly cloudy scenes. The average temperature of the clear pixels is the initial value of T_s. Surface air temperatures, T_g, are also taken from nearby ground stations. A rough correction is applied to these temperatures to adjust for atmospheric attenuation and the difference between the temperature of the surface skin and the air at shelter height. The resulting estimate of clear-sky temperature is T_a. An example of the relationship between T_s and T_g is shown in Fig. 3 for a region including FMC during 27 October 1986. Note that the difference between T_s and T_g constitutes the correction to determine T_a from T_g. It varies with local time (6 hours less than UTC) from positive values in the morning to negative values in the afternoon, behavior typical of land surfaces (e.g., Minnis and Harrison 1984a).

The initial value of T_s for the ground site is compared to the values for the surrounding regions to check for cirrus contamination of the clear-sky temperature. If T_s for the ground site is not within 2 K of the warmest value found for nearby regions, then its value is reset to that of the warmest value. The 2 K limit is typical of the range in T_s over relatively flat homogeneous areas. If extensive overcast prevents the calculation of T_s, $T_s = T_a$.

The AVHRR clear-sky temperatures are first estimated using T_s derived from the AVHRR data. If that result is lower than the corresponding GOES estimate of T_s by 2 K, then the AVHRR value of T_s is reset to the GOES value. It is assumed that the warmer of the two values is less cloud contaminated. Because of limb-darkening effects, the AVHRR value of T_s may be up to 2 K colder than the GOES value and still be valid. In warmer, moister atmospheres, greater limb-darkening effects are expected.

3. IR and VIS parameter analyses and results

a. *Emittance calculations*

Neglecting IR scattering effects, the observed cloud beam emittance is given here as

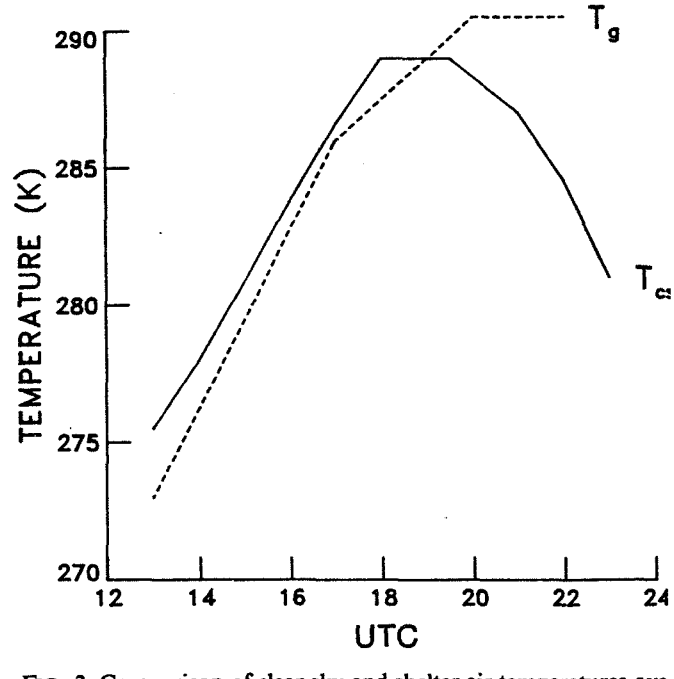

FIG. 3. Comparison of clear-sky and shelter air temperatures ove FMC 27 October 1986.

$$\epsilon_b(\theta) = [B(T) - B(T_s)][B(T_z) - B(T_s)]^{-1}, \quad (1)$$

where T_z is the temperature at some altitude z corresponding to the cloud. The mean clear-sky equivalent blackbody temperature over the area of interest, T_s, has a weak dependence on θ.

Cloud beam emittance is calculated twice for each set of lidar-radiance data using $T_z = T_c$ and $T_z = T_t$. The former value, which corresponds to the quantity used in most previous studies (e.g., Platt et al. 1980), may be more representative of the actual radiating part of the cloud. It does not necessarily correspond to the center of the cloud. The actual cloud-top temperature defines the vertical limit of the cloud. Emittances are computed using both temperatures to determine if there is a relationship between them that may be used to better define the physical boundaries of the cloud from the satellite data.

Due to angular effects, the values of T_c may require some adjustment from the initial lidar values. It is unlikely that a value of $\epsilon_b = 1$ will be measured at a useful satellite zenith angle using T_t because of the low density of particles in the upper portions of the cloud. On the other hand, $\epsilon_b(T_c)$ may be greater than one for some thick cirrus clouds. Although emittances greater than unity may be possible due to scattering enhancements of the upward radiance (Platt and Stephens 1980), the uncertainties in z_c for thick clouds preclude any definitive measurements of $\epsilon_b > 1$. Thus, if $\epsilon_b > 1$, T_c is decreased until the average value of ϵ_b for a given reflectance is less than or equal to one. While this limit is reasonable, it is somewhat arbitrary resulting in increased uncertainty in the true value of T_c for thick clouds.

During initial processing of the data, it was determined that the maximum emittance found using T_t was ~0.86, except for those cases with cloud cover too dense for complete penetration of the lidar beam. To identify and correct the exceptions, a new estimate of T_t was computed whenever T_c was adjusted as explained above. This new estimate, T_t', is determined from the following formula, which forces the cloud to have the maximum observed emittance:

$$B(T_t') = [B(T) - 0.14B(T_s)]/0.86.$$

The resulting value was then compared to T_t. If $T_t' < T_t - 3$ K, then T_t is reset to T_t'. The 3 K allowance (~0.5 km) is made to account for uncertainties in the lidar-determined cloud-top, due to time averaging and unknown penetration depth in thicker cloud. The result was then compared to the tropopause temperature using the assumptions that the cloud occurs in the troposphere and the tropopause temperature is the coldest in the troposphere. If T_t is colder, it is reset to equal the tropopause temperature. The value of z_t was then adjusted to correspond to the final value of T_t.

It is also assumed that

$$\epsilon_b = 1 - \exp(-\tau_e/\mu), \quad (2)$$

where τ_e is the IR absorption optical depth a $= \cos\theta$. Based on the results of Platt and Ste (1980), it is expected that the viewing zenith dependence of ϵ_b will not depart significantly fron Values of beam emittance derived with AVHRR may be adjusted to the GOES viewing zenith with this relationship.

The vertical emittance from (2) is

$$\epsilon_a = 1 - \exp(-\tau_e).$$

It is assumed here that scattering effects are negl in the upwelling direction. Thus, τ_e is equivale the IR absorption optical depth and ϵ_a is equal t vertical emittance.

b. *VIS reflectance and optical depth calculation*

Values of clear-sky reflectance ρ_s and clear-sky D_s were computed for each region using the 0.01° sky albedo, α_s, map of the IFO area (42°N–4 87°W–92°W) constructed by Minnis et al. (1990) GOES data at each half hour. Clear-sky reflectanc any latitude λ and longitude ϕ of the grid at tim estimated as

$$\rho_s(\lambda, \phi, t, \theta_0, \theta, \psi) = \alpha_s(\lambda, \phi, t, \theta_0)\chi_s(\theta_0, \theta, \psi)$$

where χ_s is the anisotropic reflectance factor with given by the model of Minnis and Harrison (19 D_s was determined by ρ_s using the VIS calibra The value of θ_0 varies by a few degrees over th time period, while the values of α_s were normali a single value of solar zenith angle designated θ account for these variations, $\alpha_s(t, \theta_0) = \theta_0)\mu_0/\mu_{0_t}$, where $\mu_{0_t} = \cos\theta_{0_t}$. The clear-sky diffu bedo is

$$\alpha_{sd} = \int \alpha_s(\theta_0)\mu_0 d\mu_0 \Big/ \int \mu_0 d\mu_0,$$

integrated over $\mu_0 = 0, 1$. The value of α_{sd} is set to $\alpha_s(57°)$ in this study since the full range of zenith angles is not observed at the time and la of the IFO, the true value of α_{sd} is usually equi to α_s measured at $\theta_0 \approx 53°$, and 57° is the l observed θ_0 for this dataset.

Cloud reflectance, ρ_c, is estimated with a vari the simple physical model used by Platt et al. (1 That is,

$$\rho = T_a\rho_c + \rho_s T_c T_u + \alpha_{sd}(1 - \alpha_d)(1 - T_c - \alpha_c)$$

where ρ is the measured reflectance, α_c is the albedo at θ_0, χ_c is the anisotropic reflectance fact the cloud, and $\rho_c = \alpha_c\chi_c(\theta_0, \theta, \psi)$.

This model assumes that all ozone absorption above the cloud (first term) and all Rayleigh and sol scattering is confined to the layers below the The second term in (5) accounts for direct sol diation, which passes through the cloud, reflects the surface, and passes back through the cloud

direction of the satellite. The third term accounts for the radiation that passes down through the cloud via multiple scattering, reflects diffusely from the surface below the cloud, and returns through the cloud scattered in the direction of the satellite.

Using the parameterization of Rossow et al. (1988), the transmittance of the air above the cloud is

$$\Upsilon_a = \exp[-u(0.085 - 0.00052u)(1/\mu_0 + 1/\mu)],$$

where u is the ozone abundance in cm-STP. The value used here, $u = 0.32$ cm-STP, is the average of the midlatitude winter and summer standard atmospheres above 10 km from McClatchey et al. (1973). Platt et al. (1980) implicitly assumed that $\Upsilon_a = 1$. The current model accounts for ozone absorption in the Chappius bands.

The transmittance of the cloud to direct solar radiation at θ_0 is

$$\Upsilon_c = \exp(-\tau_v/2\mu_0), \quad (6)$$

(see Platt et al. 1980). Similarly, the direct transmittance from the surface through the cloud along the satellite line of sight is

$$\Upsilon_u = \exp(-\tau_v/2\mu).$$

The visible optical depth is reduced by a factor of two for the direct transmittance because at least half of the radiation scattered out of the beam is actually diffracted in the forward direction (Takano and Liou 1989a). Clear-sky reflectance along the satellite line of sight is ρ_s and α_{sd} is the effective clear-sky albedo to diffuse radiation directly below the cloud. Due to the relative homogeneity of clear-sky reflectance over the IFO region, it is assumed that α_{sd} and ρ_s may be computed from the same data. The albedo of the cloud to diffuse radiation is α_d.

In addition to values for the clear-sky terms, the solution of (5) for ρ_c requires specification of τ_v and χ_c. VIS optical depth is estimated by iteration on (5) using a linear interpolation of the relationships between μ_0 and α_c for randomly oriented hexagonal columns (length, 125 μm; width, 50 μm) in Fig. 4 of Takano and Liou (1989b). Similar interpolations are used to estimate $\alpha_d(\tau_v)$, where

$$\alpha_d(\tau_v) = \int_0^1 \alpha_d(\tau_v, \mu_0)d\mu_0 \Big/ \int_0^1 \mu_0 d\mu_0.$$

For a given measurement, (5) is solved iteratively using an initial guess of cloud albedo such that $\Upsilon_c = \Upsilon_u = 1 - \alpha_c$. A value for τ_v is determined from this initial guess using the theoretical data. A limit of 20 iterations is imposed to achieve an absolute difference of less than 0.001 between the guess and the computed value of α_c. Generally, fewer than five iterations are required. Since α_c must be greater than zero, α_c is set to 0.001 for initial guesses that are less than or equal to zero. If $\tau_v < 0$, $\alpha_d < 0.001$, or $\alpha_c \leq 0.001$ after any iteration, it is assumed that τ_v is indeterminate and the data are not used. The causes for these indeterminate cases (e.g., shadowing of the surface by adjacent clouds or inadequate specification of the cloud reflectance anisotropy) are discussed later.

A value for χ_c, which depends on τ_v and the cloud microphysics, is needed to determine α_c from ρ_c. No models of χ_c are currently available for ice clouds in terms of τ_v. Because of favorable angles Platt et al. (1980) were able to assume that $\chi_c = 1$. However, most empirical and theoretical bidirectional reflectance models for cloudy scenes (e.g., Suttles et al. 1988) reveal a systematic decrease in χ_c with θ_0 for the angles used in this study. The cloudy scene bidirectional reflectance model developed by Minnis and Harrison (1984b) is used initially to estimate χ_c. That model's reflectance anisotropy is similar to other empirical and theoretical models (Stuhlmann et al. 1985). The inclusion of all cloud types in its derivation should produce a reflectance pattern that combines the scattering properties of both ice and liquid water clouds. New values of χ_c, derived after the initial analysis, are used to reanalyze the data to provide better estimates of VIS optical depth.

The data were preprocessed to define limits to eliminate pixels containing low clouds and those scenes containing only thick clouds. Underlying low clouds confuse the interpretation of cirrus radiances. Thick clouds increase the uncertainty in the determination of T_c, T_t, and ϵ_b. A simple filter of the form,

$$\epsilon_b = 1 - \exp(-k\alpha_c/\mu), \quad (7)$$

where k is a regression coefficient, was used to eliminate low clouds. This formula gives a first approximation to the relationship between ϵ_b and cloud albedo. The rationale for its use and the details of the filtering are described in appendix A. The data were also screened for partially cloud-filled pixels as detailed in appendix B.

c. *Results and discussion for midcloud temperature emittances*

All results discussed in this section are based on $T_z = T_c$ in (1). Examples of the two-dimensional GOES histograms used in this analysis are shown in Figs. 4a and 4b for 1500 UTC over FMC. The latter represents a cirrus case (see Fig. 1) on 28 October, while the former, taken during the previous day, is typical of clear conditions. Maximum clear-sky reflectance for this hour is denoted with the dashed line in Fig. 4a. Some of the cold, apparently cloudy pixels in Fig. 4b are no brighter than the clear pixels in Fig. 4a. Moreover, some of these pixels are actually darker than the cloud-free pixels. Depending on χ_c and τ_v, some of the cold, dim pixels yield a positive value of α_c in the solution of (5). Those pixels with indeterminate α_c and $T < T_s - 3$ K are hereafter referred to as "dark" pixels.

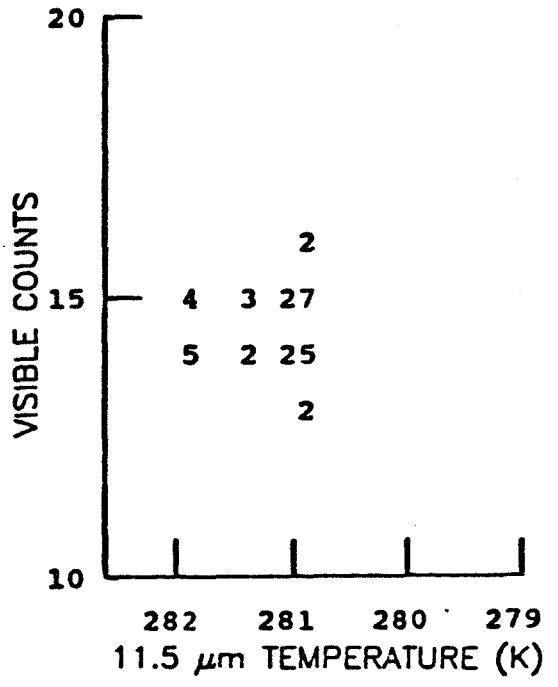

FIG. 4a. VIS–IR histogram of GOES pixels over FMC at 1500 UTC 27 October 1986 (numbers denote frequency of occurrence of temperature-count pairs).

They are not used to solve (7). Their impact and origins are discussed in section 4d. The cloud emittances are plotted in Fig. 5a against the measured reflectances for the case in Fig. 4b. Eliminating the dark pixels and applying (5) to the data in Fig. 5a yields the cloud albedo values. Averaging the emittances for a given albedo produces the mean values and the standard deviations plotted in Fig. 5b. The solid line represents the solution to (7) using the average value of $k = 5.1$. The mean beam emittance and VIS optical depths for the data used in Fig. 5b are $\bar{\epsilon}_b = 0.38$ and $\bar{\tau}_v = 0.59$.

The data from FMC in Fig. 5b for this hour are compared to those from MAD and WAU shown in Fig. 6. Apparently, the clouds over WAU are much denser than those over MAD, while the MAD observations are similar to those over FMC. Values of T_c differed by only 1 K among the sites, while T_t ranged from 225 K at WAU to 217 K at MAD. Depolarization ratios derived from the lidar returns indicated intermittent liquid layers during the morning of 28 October, especially at ~1500 UTC. Those liquid layers may be the source of the larger emittances over WAU. Data from all three sites were combined, averaged, and fit with (7) yielding $k = 5.6$. The scatter in the means between the sites at a given hour is of the same order as that for different hours at the same site as seen in Fig. 7 for FMC at 3 times during 28 October.

1) GOES-SURFACE LIDAR RESULTS

A summary of the results for the case study 27–28 October is given in Table 2. Cloud-top heights range from 9.5 to 11.0 km at all three sites. The cloud-center temperatures vary by about 25 K. Cloud optical depths were much greater over WAU than over the other sites. Dark pixels were found more often over FMC and MAD than over WAU.

Due to dropouts, the only data available for 1500 UTC during the primary IFO cirrus days occurred on 28 October. Data from other days were available for most of the afternoon hours. The combined datasets permitted coverage of the full range of emittances at a given hour as illustrated in Fig. 8 for 2000 UTC. Data for all of the hours used in the case study and the entire IFO analyses are shown in Figs. 9a and 9b, respectively. The clouds over the area during 27–28 October were generally thinner with lower emittances than most of those observed during the other days. The combined datasets (Fig. 9b) yield a large number of samples for $\epsilon_b < 0.5$ and $\epsilon_b > 0.8$ and relatively few for intermediate values of ϵ_b. Apparently, the cirrus, which occurred during the IFO, tended to be either very thick or rel-

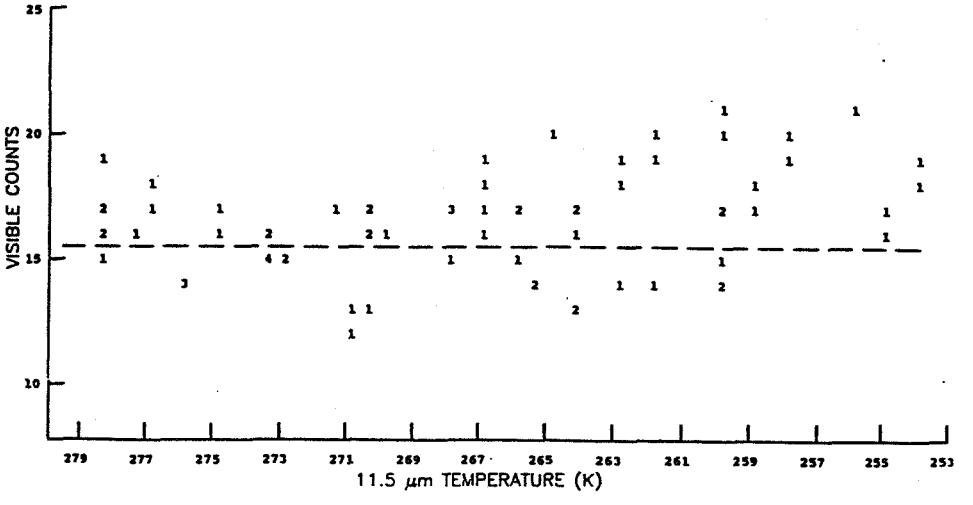

FIG. 4b. VIS–IR histogram of GOES pixels over FMC at 1500 UTC 28 October 1986. Dashed line refers to maximum clear-sky count.

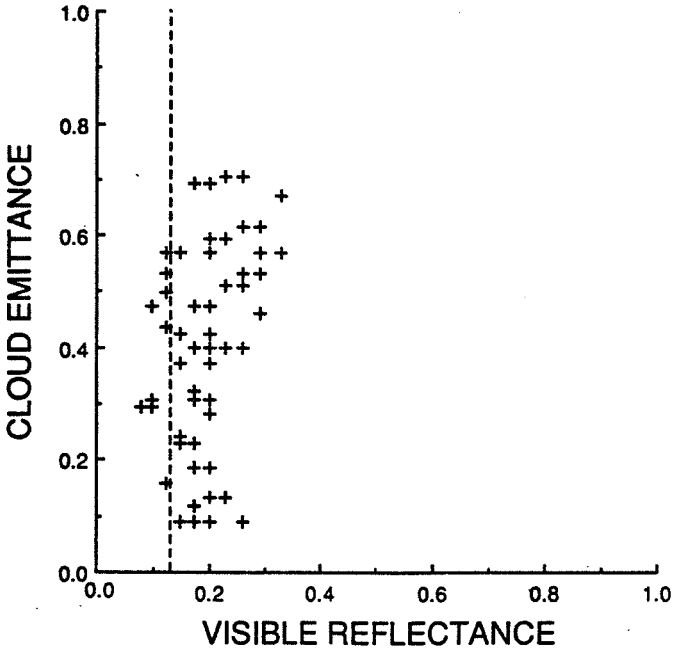

FIG. 5a. Cloud emittances and observed reflectances for $T < T_s - 3$ K derived from Fig. 4b. Dashed line refers to maximum clear-sky reflectance.

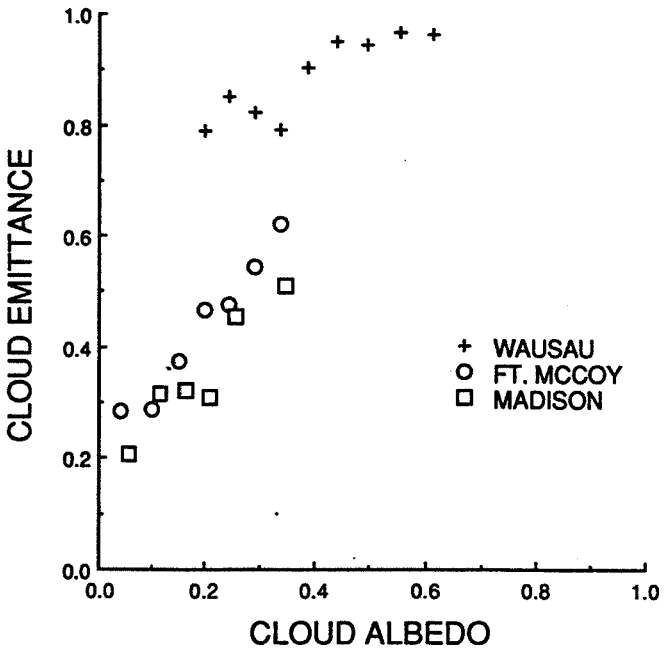

FIG. 6. Average cloud emittance versus cloud albedo at 1500 UTC 28 October 1986 over three sites from GOES VIS–IR data.

atively thin. Perhaps, a longer time period would produce more uniform sampling. No data are found for $\epsilon_b < 0.08$ since no clouds are recognized if $T > T_s - 3$ K.

Table 3 summarizes the values of τ_v derived from all of the GOES-surface IFO data (Fig. 9b) and from case study data only (Fig. 9a) for each relevant time. The average scattering angles, Θ, between the sun, satellite, and scene are also listed in Table 3. Visible optical depths observed during the case study are less than half of those observed for all of the IFO cirrus days.

The mean vertical emittance is given as a function of temperature in Fig. 10. The dashed line corresponding to the results from Fig. 7a of Platt et al. (1987) is included for comparison. Although there is a general increase in ϵ_a with increasing cloud temperature, the

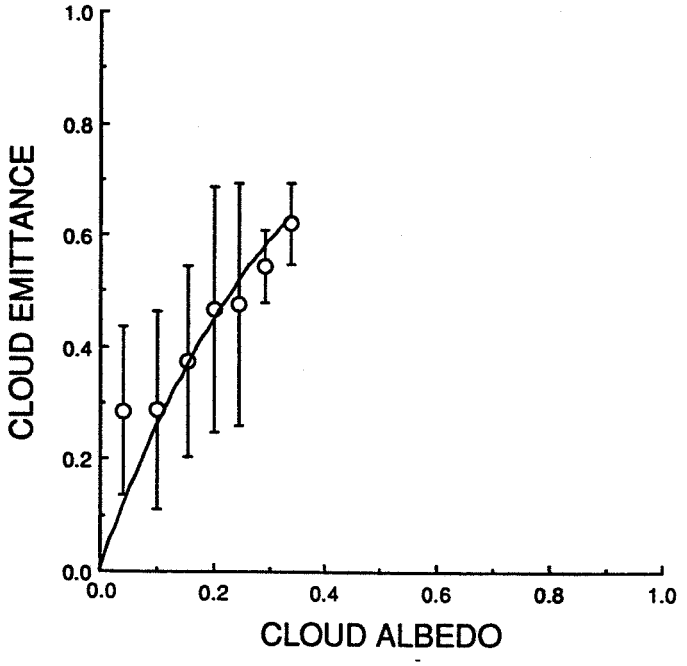

FIG. 5b. Cloud albedos and mean cloud emittances derived from Fig. 5a without "dark" pixels. Vertical lines represent standard deviations. The curved line denotes the regression fit to Eq. (7).

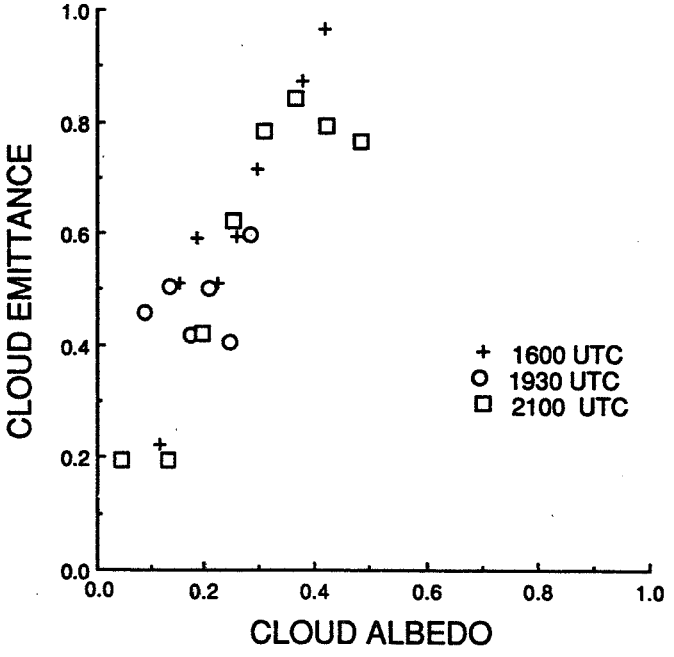

FIG. 7. Average cloud emittance and albedo at three times during 28 October 1986 over FMC from GOES VIS–IR data.

TABLE 2. Observed and computed cloud properties for October 1986 case study.

Site (Day)	Time (UTC)	T_s (K)	z_t (km)	h (km)	T_c (K)	T_t (K)	τ_e	τ_v	Dark pixel (%)	τ'_v	
FMC (27)	2030	287.7	9.6	1.1	227.8	225.1	0.11	0.23	4	0.20	1
	2100	286.9	10.3	1.6	228.7	220.3	0.19	0.52	0	0.55	2
(28)	1330	278.3	9.5	2.1	237.9	227.7	0.22	0.12	0	0.22	1
	1400	279.7	11.0	1.3	231.6	216.8	0.14	0.16	5	0.21	1
	1430	280.5	11.2	1.5	230.0	215.6	0.18	0.32	11	0.38	2
	1500	281.6	10.1	1.3	239.4	222.5	0.31	0.62	7	0.65	1
	1600	283.0	10.0	3.0	240.1	223.2	0.80	1.77	0	1.61	2
	1700	287.9	10.4	1.9	223.0	219.6	0.23	0.95	0	0.74	3
	1900	285.4	10.8	2.1	227.5	217.1	0.23	0.64	0	0.45	1
	1930	285.5	10.9	2.6	228.9	216.6	0.41	0.99	3	0.79	1
	2000	285.9	11.0	1.9	224.4	216.3	0.41	1.05	0	0.87	1
	2030	284.8	10.9	1.7	220.7	216.4	0.62	1.78	6	1.55	1
	2100	280.9	10.7	2.4	230.7	216.7	0.79	1.41	5	1.53	2
	2130	281.2	10.8	2.2	226.3	216.4	0.44	0.75	11	1.33	2
	2200	276.8	10.9	2.4	221.7	216.1	0.32	0.30	0	0.87	2
MAD (28)	1330	278.4	10.8	3.4	237.9	217.9	0.16	0.18	3	0.35	2
	1500	280.2	10.8	4.2	242.8	217.7	0.24	0.65	2	0.68	2
	1600	281.7	10.6	3.7	241.9	218.5	0.58	1.18	0	1.07	1
	1700	284.8	10.5	4.3	240.4	218.8	0.40	0.98	0	0.75	1
	1800	289.1	9.8	3.2	229.4	224.6	0.14	0.95	0	0.75	5
	1930	287.7	10.7	1.8	222.1	217.3	0.10	0.26	3	0.13	1
	2000	286.5	10.7	1.8	221.7	217.1	0.10	0.55	7	0.43	4
	2030	286.6	10.7	3.1	223.3	217.1	0.34	0.86	3	0.76	2
	2100	286.0	10.5	2.4	223.3	217.2	0.29	0.56	33	0.59	1
	2130	284.5	10.8	4.0	232.2	216.4	0.55	0.46	3	0.73	1
	2200	281.1	10.5	4.2	237.4	216.8	0.44	0.27	13	1.24	2
WAU (28)	1500	279.0	9.8	3.2	238.0	225.0	1.67	3.20	0	3.50	2
	1600	282.5	10.1	3.1	238.0	222.4	1.40	2.42	0	2.19	1
	1700	287.1	10.1	3.9	235.0	222.3	1.21	2.52	0	1.91	1
	1800	288.4	10.3	4.1	231.0	220.3	1.13	3.13	0	2.35	4
	1900	285.7	11.0	0.8	217.1	216.4	0.19	0.77	0	0.55	3
	1930	283.9	10.9	2.1	226.4	216.6	0.30	1.03	0	0.82	2
	2000	284.4	10.9	2.9	236.1	216.5	1.04	2.42	0	1.93	1
	2030	285.4	10.7	3.1	231.0	216.9	1.34	3.73	0	3.11	2
	2100	284.1	10.6	3.2	234.0	217.0	0.36	1.43	7	1.66	2
	2130	279.7	11.0	1.0	217.0	216.0	0.29	0.45	1	0.76	2

values derived for the case study are generally lower than the IFO means. The case study averages parallel those found by Platt et al. (1987) using ground-based observations in Australia. The mean value of ϵ_a found here for the case study results is 0.33, the same as that from Platt et al. (1987).

Cloud thickness versus T_c is shown in Fig. 11. Maximum average thickness is found at $T_c \approx 232$ K for the IFO and at $T_c \approx 241$ K for the case study. The case study values of h increase nearly monotonically with T_c. The IFO results show a tendency towards thinner clouds for $T_c < 220$ K and for $T_c > 240$ K. The thickest clouds were observed during 22 October and 1 November. During the case study, the observed clouds were 2.6 km thick on average compared to a mean thickness of 4.2 km during the remaining cirrus days of the IFO.

Cloud IR volume absorption coefficient, $\sigma_a = \tau_e/h$, is plotted against T_c in Fig. 12. The results reveal a trend of increasing extinction with T_c in the IFO data (correlation coefficient of 0.71). The average value σ_e is 0.20 for the case study data.

The variation of vertical emittance with T_c for IFO data differs from that found for the case study a Platt et al. (1987), probably because of substan differences in cloud depths. This difference in thickn is evident in Fig. 11 where the case study data, a sub of the IFO data, are also consistent with the result Platt et al. (1987), probably because of substan ume absorption coefficients in Fig. 12 are not as v behaved as emittance and cloud thickness when c sidered as a function of T_c. Except for the highest a lowest temperatures (which are poorly sampled), for the case study data is close to that observed by P et al. (1987). Differences between the IFO and c study data are also seen in the behavior of σ_a suggest that thickness is not the only discrepancy between case study and other IFO clouds. Vertical distributi of nongaseous cloud water content and particle sha sizes, and phase may also affect these differences.

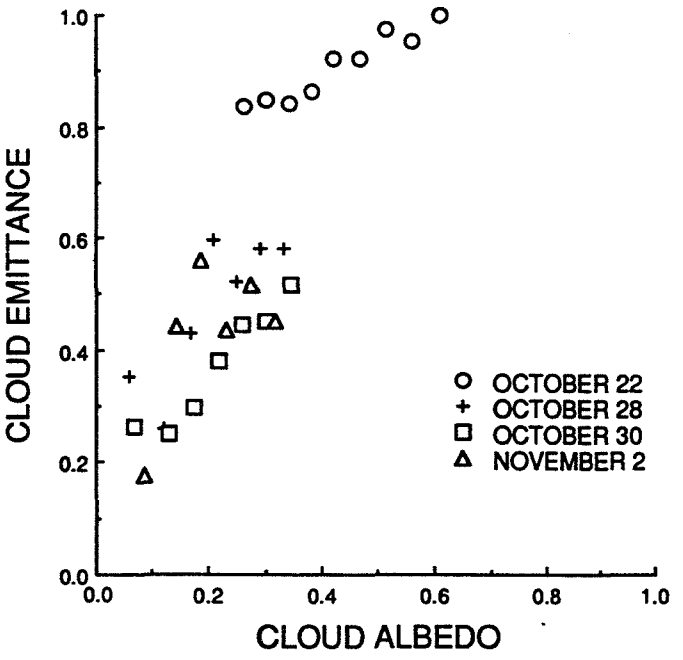

FIG. 8. Average cloud emittances and albedos from GOES at 2100 UTC over FMC during different IFO days.

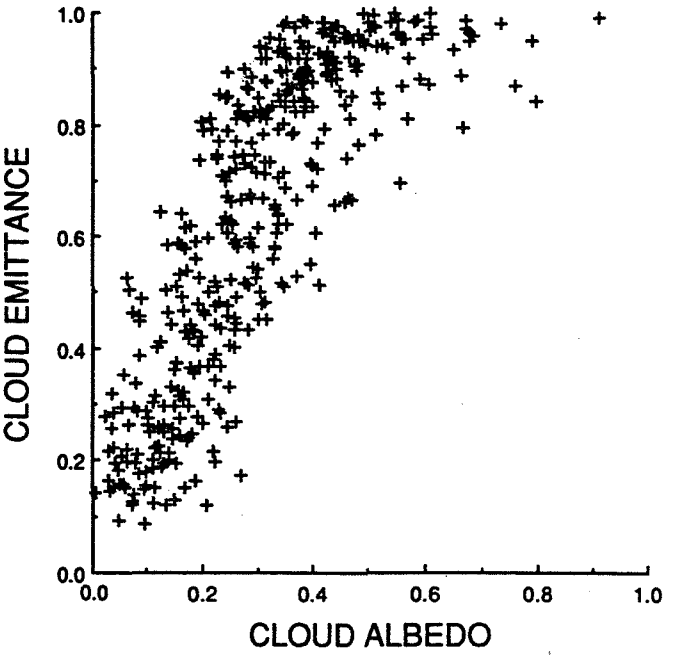

FIG. 9b. Same as Fig. 9a, except for all IFO scenes.

2) GOES/ER-2 CLOUD PARAMETERS

Table 4 lists the data and derived parameter values for the five cirrus matches between the GOES and ER-2 lidar for the case study days. Data taken during 27 October were located just outside the northwestern boundary of the IFO area. On 28 October the ER-2 was over Lake Michigan at ~1600 UTC, while it was near FMC at 1800 UTC. The three scenes at 1600 UTC correspond to small contiguous areas. The small optical depths indicate that the aircraft also sampled relatively thin clouds during the case study.

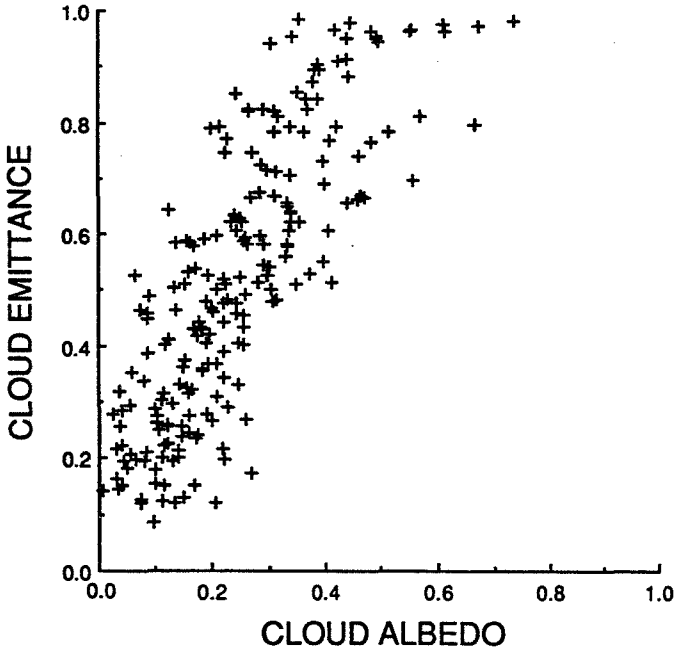

FIG. 9a. Average cloud emittance versus cloud albedo for all case study scenes from GOES over surface sites where $T_z = T_c$.

3) CLOUD PARAMETERS FROM AVHRR DATA

Figure 13 presents the averaged cloud emittance-albedo pairs derived from both AVHRR and GOES data taken for the 0.25° × 0.35° area over WAU on 28 October. Although the relative viewing angles were within ±8° for the two satellites, the absolute viewing conditions were different. The GOES viewed the region from the south, while the AVHRR viewed from the north with the solar plane almost midway between the two views. Discrepancies in the albedo range may be due to this misalignment (some dark pixels were found in the GOES results). Resolution differences, however, would tend to produce a smaller range in both albedo and emittance for the GOES (8 km) relative to the AVHRR (1 × 4 km^2) radiances as observed in Fig. 13. In general, the GOES data are very close to the AVHRR results except for the smaller values of α_c. The latter may be affected by the presence of "dark" pixels. The values for the AVHRR VIS and IR optical depths are ~10% greater than their GOES counterparts.

Another comparison of GOES and AVHRR results is given in Fig. 14 for data taken over WAU 2 November. The AVHRR viewed the scene with $\theta = 18°$ and $\psi = 38°$. The squares correspond to AVHRR data as reduced for the given viewing angles. AVHRR emittances corrected to the GOES viewing zenith angle using (2) are denoted with the crosses. The range in α_c is smaller for GOES than for the AVHRR, consistent with the resolution differences. In this case, the

TABLE 3. Reflectance parameters computed for all GOES-surface lidar data.

Time (UTC)	Cases (IFO)	θ (°)	ψ (°)	Θ (°)	Nominal (using χ_c) All data (IFO) τ_v	ξ	Case study τ_v	ξ	Reanalyzed (using χ'_c) All data (IFO) τ'_v	ξ'	Case study τ'_v	
1330	4	80.2	106.6	109	1.28	1.17	0.15	0.83	0.28	1.61	0.28	1.
1400	3	75.6	112.6	117	2.21	1.42	0.17	1.12	3.22	2.32	0.21	1.
1430	2	71.3	118.6	124	1.07	1.79	0.32	1.72	1.35	2.22	0.38	2.
1500	3	67.9	125.7	131	1.72	2.02	1.72	2.02	1.87	2.15	1.87	2.
1600	5	61.0	140.0	146	2.93	2.50	1.82	2.11	2.64	2.25	1.64	1.
1630	2	57.8	147.7	153	2.59	1.85	—	—	3.06	2.18	—	-
1700	6	57.6	156.6	160	2.58	2.90	1.57	2.93	1.96	2.21	1.20	2.
1800	6	57.3	174.1	173	2.43	2.96	1.95	6.21	1.92	2.33	1.48	4.
1830	1	56.1	177.1	175	3.65	2.06	—	—	3.88	2.19	—	-
1900	7	59.9	169.0	168	1.62	3.12	0.69	3.43	1.82	2.12	0.49	2.
1930	4	61.1	160.8	162	1.73	2.74	0.75	2.76	1.34	1.97	0.57	1.
2000	8	65.0	153.6	154	2.07	2.68	1.69	2.87	2.27	2.26	1.35	2.
2030	5	68.3	146.5	147	1.56	2.55	1.87	2.37	1.33	2.23	1.59	2.
2100	6	72.8	140.3	140	1.07	2.07	1.02	2.19	1.17	2.24	1.12	2.
2130	4	76.2	133.6	132	1.12	1.29	0.55	1.25	0.81	2.23	0.94	2.
2200	5	81.2	128.1	125	0.80	0.84	0.28	0.70	1.04	2.30	0.80	2.
Totals and means	71	67.2	145.4	—	1.69	2.13	1.04	2.17	1.80	2.19	1.11	2.

AVHRR data produce a much lower minimum cloud albedo. The application of (2) appears to have produced very similar emittances for the two datasets, although there is a 20% difference in the average values of τ_e. The mean VIS optical depths differ by a factor of 2.

All of the coincident AVHRR and GOES data are summarized in Table 5. The AVHRR IR optical depths are consistently greater than the corresponding GOE values by ~0.1. This difference indicates the possibili of a calibration offset in the thermal channels. Despi this obvious bias, the good relative agreement in Fi 14 between the corrected AVHRR emittances and th GOES emittances suggests that (3) is a reasonable ap proximation to the IR absorption optical depth. An IR scattering effects that are ignored here are apparentl

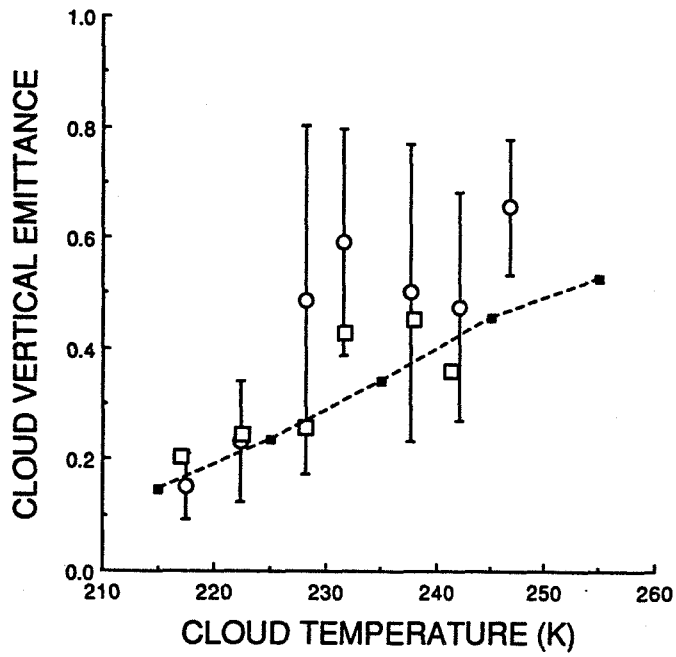

FIG. 10. Variation of cloud vertical emittance with cloud-center temperature for all IFO (circles) and case study (squares) data from GOES over surface lidar sites. Vertical lines denote standard deviations. Dashed line adapted from Platt et al. (1987).

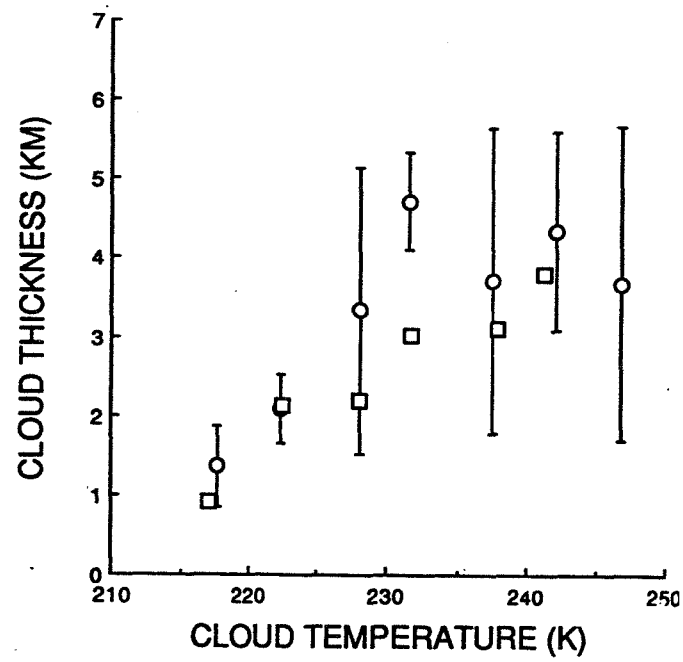

FIG. 11. Variation of cloud thickness with cloud-center temperatur for all IFO (circles) and case study (squares) data from GOES ove surface lidar sites. Vertical lines denote standard deviations.

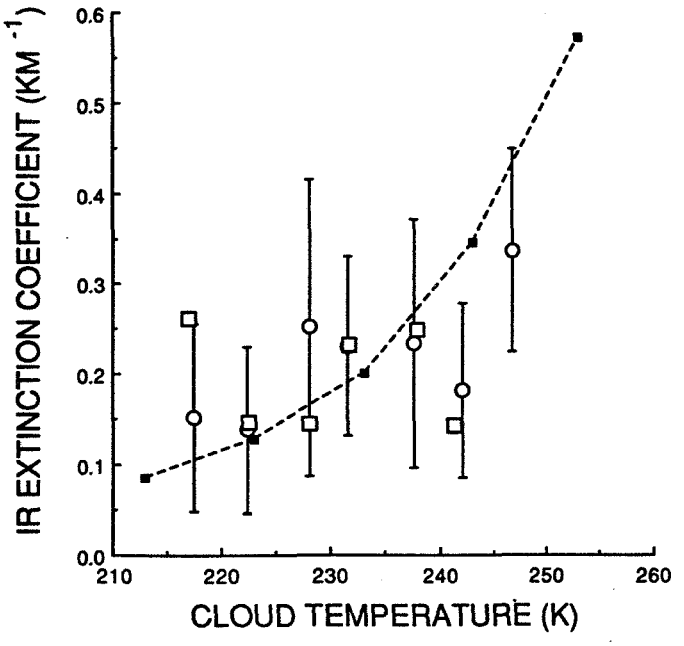

FIG. 12. Variation of infrared volume extinction (absorption) coefficient with cloud-center temperature for all IFO (circles) and case study (squares) data from GOES over surface lidar sites. Vertical lines denote standard deviations. Dashed curve adapted from Platt et al. (1987).

insignificant compared to the other error sources. Differences between the GOES and AVHRR values of τ_v vary from scene to scene. Even when the times and angles are very close and the data appear similar as in Fig. 13, there are substantial differences in τ_v. Over FMC during 28 October, there is good agreement between the parameters however. The outstanding differences may be attributable to a number of factors that are discussed in section 3e.

d. Results and discussion for cloud-top temperatures with GOES

The analyses discussed above were also performed for the GOES-derived emittances for $T_z = T_t$. A plot of all of the mean cloud emittance-albedo pairs is shown in Fig. 15. The largest concentrations of data are found for $\epsilon_b(T_t) < 0.8$. In general, α_c is greater for a given value of ϵ_b than it is in Fig. 9b. Cloud-top emittance tends to plateau at $\epsilon_b \approx 0.86$, while cloud-center emittance appears to level at $\epsilon_b \approx 0.98$. The lower emittances lead to diminished values of τ_e relative to those derived for T_c.

The emittance ratio, $r_\epsilon = \epsilon_b(T_t)/\epsilon_b(T_c)$, was computed for discrete intervals of T_c. Mean values and standard deviations of these ratios are shown in Fig. 16. The emittance ratio increases almost linearly with decreasing cloud center temperature. Standard deviations about a given mean ratio are less than 0.1. The emittance ratio is close to unity for $T_c < 215$ K.

The well-correlated variation of r_ϵ suggests the possibility that T_t as well as T_c may be retrieved with VIS–IR radiance pairs. This ratio integrates many of the other parameters examined earlier. For example, cloud thickness in Fig. 11 is least at the highest altitudes and increases before leveling or even decreasing for temperatures around 235 K. For the highest clouds, there is little difference between T_c and T_t because the clouds are not very thick. Since cloud depths are greater at lower altitudes, it is possible to sense radiation from areas deep within the cloud thereby causing greater differences between T_c and T_t. As the depth of the cloud decreases, the ratio should approach unity. At higher temperatures ($T_c > 250$ K), the relationship of r_ϵ to T_c may not be as well defined because liquid water becomes more common and the mean cloud depth may not be dependent on T_c. Whether the relationship shown in Fig. 16 is typical for all observing angles is also unknown. Additional sampling from other angles and over a wider variety of temperatures would help to better define the relationship between r_ϵ and T_c. However, the results shown in Figs. 11, 12, and 16 suggest that it may be possible to obtain reasonable estimates of h and T_t over a limited range of T_c.

e. Emittance uncertainties

The parameter values derived here are subject to considerable uncertainty as evidenced by the results in Table 5 and the large standard deviations in earlier figures. Potential sources of error abound in an analysis of this type due to the large number of variables and the nonuniformity of cirrus clouds.

Parameters derived from the lidar essentially provide

TABLE 4. Observed and computed cloud properties for case study ER-2 data.

Day	Time (UTC)	Lat. (°N)	Lon. (°W)	T_s (K)	T_c (K)	h (km)	τ_e	τ_v	ξ	Dark pixel (%)	τ'_v	ξ'
27	1830	45.8	93.1	290.0	225.0	0.5	0.12	0.69	5.73	0	0.46	3.86
	1900	45.3	92.5	288.5	234.0	0.5	0.14	0.51	3.43	0	0.39	2.64
	1930	44.9	91.1	288.4	234.0	0.5	0.24	0.73	2.91	3	0.61	1.68
28	1600	44.6	87.0	283.0	229.0	3.7	0.43	0.86	1.99	0	0.84	1.95
	1600	44.5	87.1	283.0	229.0	3.7	0.42	0.92	2.12	0	0.91	2.10
	1600	44.5	87.1	283.0	229.0	3.7	0.45	1.00	2.21	0	0.99	2.21
	1800	43.6	89.4	288.9	228.0	1.5	0.28	0.90	3.23	0	0.69	2.57

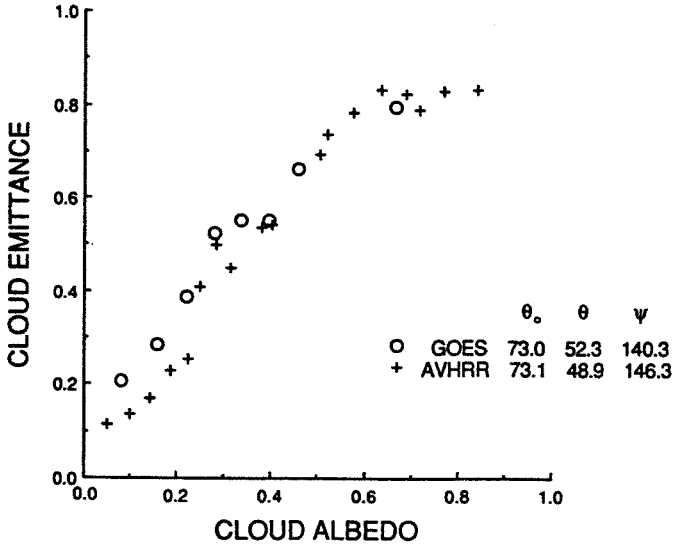

FIG. 13. Comparison of cloud albedos and emittances derived from 28 October 1986 GOES and AVHRR data taken at ~2100 UTC over WAU.

a two-dimensional view of the cirrus clouds. The validity of the assumption that z_c, h, and z_t represent the average cloud heights within the large areas covered by the strip of pixels is difficult to evaluate. One means of estimating how well the lidar data represent the large-area cloud characteristics is to examine the differences between the strip of pixels and surrounding areas. The rms difference between the emittances for the strip and the box containing the strip is 0.05 or 7%. This difference is equivalent to a ±0.7 km variation in cloud-center height between the strip and the box. Changes of 2 km in cloud-center altitude during a given half hour are common as seen in Fig. 1. The variations in the small-scale lidar data are greater than those in the large-scale satellite data as expected.

Assuming that the large-scale differences are representative of the lidar-satellite scale differences, it is estimated that the use of lidar data to set z_c causes an uncertainty in ϵ_a of ±10% based on an average value for ϵ_a of 0.62. Note that no clouds with $\epsilon_b < 0.1$ were included in the analysis because of the cloud-detection threshold of 3 K. A conservative estimate of the uncertainty in T_s is ±2 K. Inclusion of this error raises the overall uncertainty in ϵ_a to ±13%. This uncertainty in ϵ_a is equivalent to a ±20% uncertainty in τ_e for a given scene over the range of optical depths considered here. The AVHRR–GOES comparisons are, on average, within this uncertainty level. The average IR optical thickness is 0.96 for all 71 scenes. From the strip and box comparison, it is also estimated that z_t and h have uncertainties of ±0.7 km.

Another source of uncertainty in ϵ_a is the use of a mean cloud height for the entire scene. This error source may be examined by performing a pixel-by-pixel analysis on a scene that varies systematically with time. One example is the cloud over FMC between 2020 and 2050 UTC. The GOES pixels from the corresponding wind strip data were averaged in lines perpendicular to the wind vector. Using the wind speed, these averaged pixels were converted to times and aligned with the lidar-defined cloud parameters. The results shown in Fig. 17 indicate good alignment between the two datasets. In this case, it appears that the lidar data provide an accurate cross section of the cloud. The GOES reflectance increases as the cloud thickens and T increases as z_c lowers. Equations (1) and (5) were applied to each average pixel using T_c derived from Fig. 17 to determine τ_e and τ_v. Figure 18 shows the variation of the parameters with time. Although the thin part of the cloud is detected with the IR data, a value for τ_v is not computed since the reflectances are lower than that for clear skies. Nevertheless, the mean values for τ_e and ϵ_b derived on a pixel-by-pixel basis are 0.59 and 0.54, respectively, compared to 0.62 and 0.59 derived for the entire scene using a mean value of z_c. This comparison suggests that the error in ϵ_b for using the mean cloud height is around 10% with a slight tendency to bias the values to the high end because of nonlinear effects. While these results may not represent all cases, they indicate that the use of a mean cloud height for the analysis is a reasonable approach.

4. Relationship between VIS and IR parameters

a. Scattering efficiency ratio

For a given cloud particle with cross-sectional area $2\pi a^2$, the VIS scattering cross section is

$$\beta_v = Q_{sca} 2\pi a^2,$$

and the IR absorption cross section is

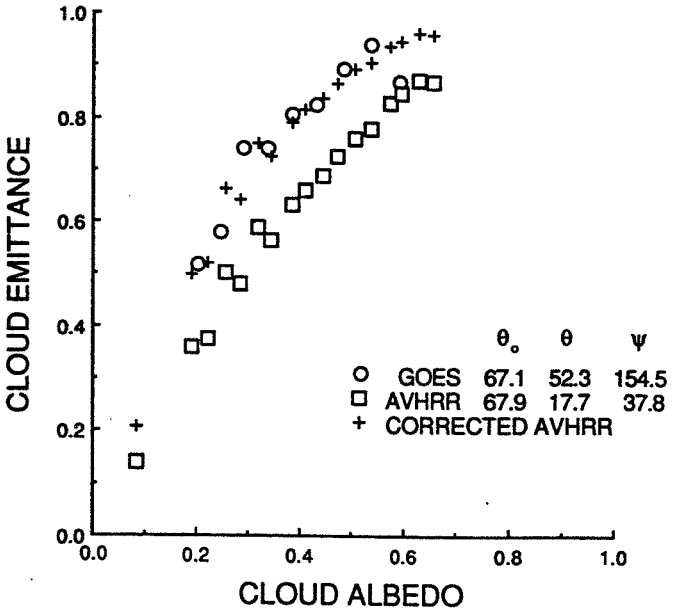

FIG. 14. Same as Fig. 13, except for 2 November 1986 at ~2000 UTC.

TABLE 5. Comparison of AVHRR- and GOES-derived cloud parameters.

		AVHRR Parameters							GOES Parameters						
Site (Day)	T_c (K)	Time (UTC)	Θ (°)	τ_e	τ_v	ξ	ξ'	Dark pixel %	Time (UTC)	τ_e	τ_v	ξ	Dark pixel %	τ_v'	ξ'
FMC															
(28)	231	2100	141	0.83	1.47	1.95	1.96	0	2100	0.72	1.36	1.79	3	1.48	1.94
(30)	223	2042	127	0.25	0.35	1.13	1.79	18	2030	0.17	0.63	3.50	3	0.57	3.12
(2)	230	2006	92	0.49	1.18	1.94	1.36	5	2000	0.39	0.97	2.42	0	0.80	1.98
WAU															
(28)	234	2100	142	0.31	1.69	3.50	21.4	0	2100	0.26	0.78	2.20	6	0.89	2.41
(2)	230	2006	98	1.34	4.61	3.21	1.78	0	2000	1.16	3.26	2.72	0	2.48	2.09

$$\beta_e = Q_{abs} 2\pi a^2,$$

where the VIS scattering efficiency is Q_{sca}, the IR absorption efficiency is Q_{abs}, and the effective particle radius is a. The extinction optical depth for a given wavelength, λ, is

$$\tau(\lambda) = \beta(\lambda) \int N(z) dz,$$

where the integral is over some finite height, β is the extinction optical depth, and $N(z)$ is the number density of particles at z. If it is assumed for a given cloud that the VIS extinction is due entirely to scattering, the IR extinction is due entirely to absorption, and the extinction coefficients are constant, then the scattering-to-absorption ratio is

$$\xi = Q_{sca}/Q_{abs} = \beta_v/\beta_e = \tau_v/\tau_e.$$

Therefore, if ξ and τ_v are known, then the value of τ_e may be determined. This efficiency ratio forms the basis of the ISCCP cloud-height correction algorithm. The values of Q_{sca} and Q_{abs} depend primarily on the particle size in terms of the size parameter, $2\pi a/\lambda$, and the index of refraction. Mie scattering calculations of Q_{sca} and Q_{abs} indicate that ξ for the wavelengths of interest may vary from ~5 for $a = 2.0$ μm to ~2.4 for $a = 10.0$ μm (Sassen 1981). The value of ξ asymptotically approaches 2.0 for very large particles; i.e., $2\pi a/\lambda \gg 1$ (e.g., Hansen and Travis 1974). Platt et al. (1987) have presented some theoretical results that indicate ξ is also a function of particle shape and may have values slightly less than 2.0.

For each satellite-lidar dataset in this study, the scattering efficiency ratio is computed for all of the pixels, N, having a discrete value of ρ as follows.

$$\xi = \sum_{i=1}^{N} (\tau_v/\tau_{e_i})/N. \quad (8)$$

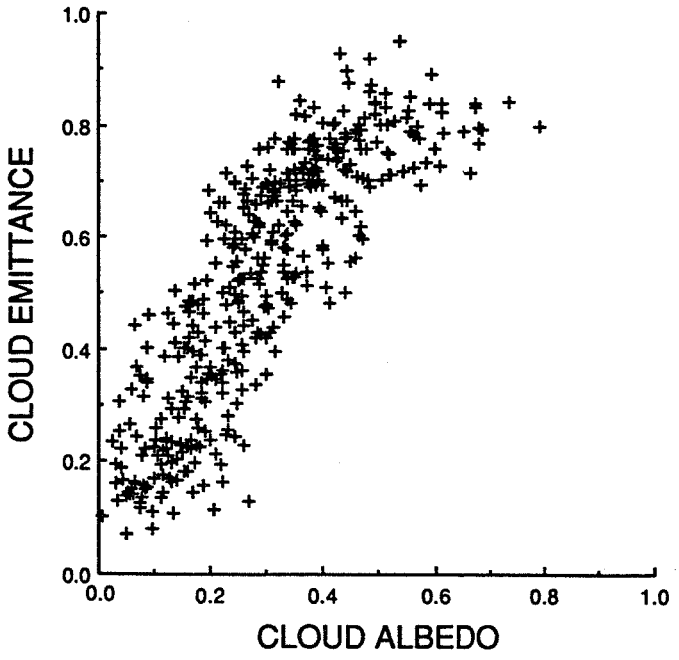

FIG. 15. Same as Fig. 9b, except $T_2 = T_c$.

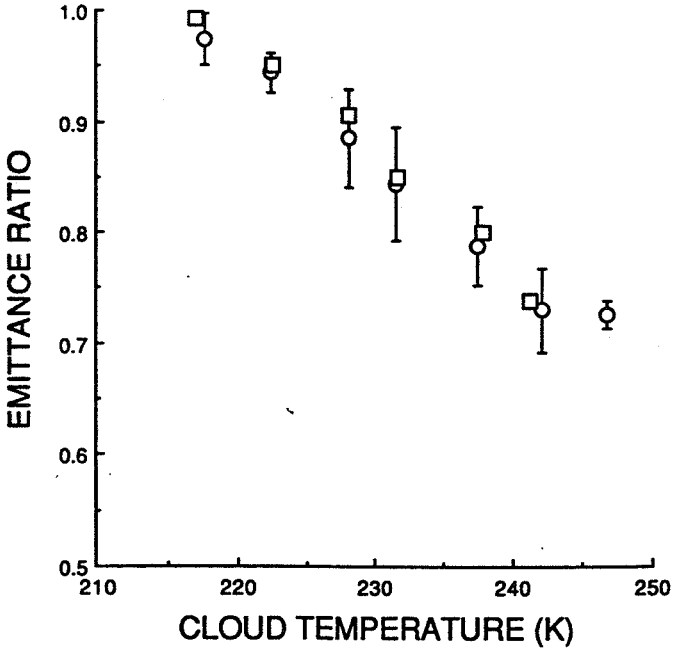

FIG. 16. Variation of ratio of cloud-top emittance to cloud-center emittance on cloud-center temperature for all IFO (circles) and case study (squares) data from GOES over surface lidar sites. Vertical lines denote standard deviations.

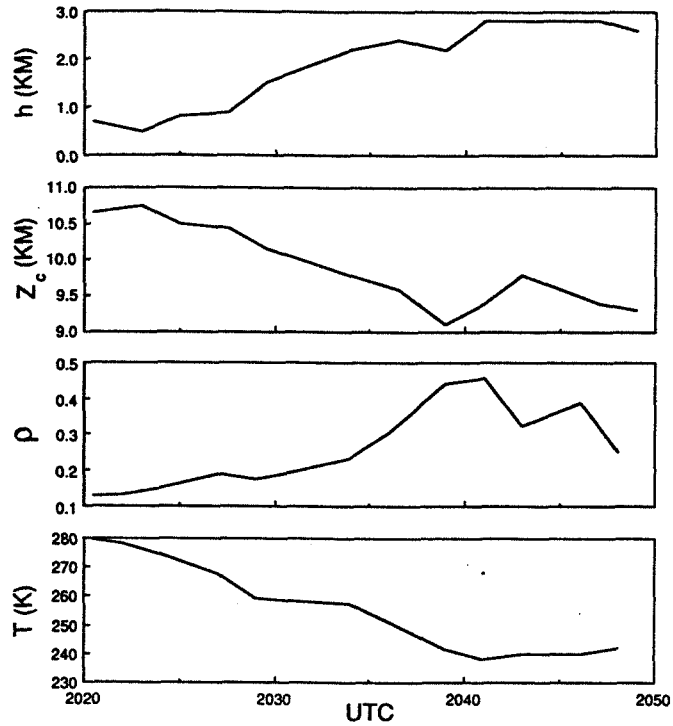

FIG. 17. Comparison of GOES and lidar observations along wind vector over FMC during 28 October 1986.

Only one temperature, T_c, is used to compute τ_e for a given dataset since only one average cloud height is derived for each time. Changes in the actual cloud height and thickness within the scene (e.g., Fig. 1) tend to introduce variations in τ_e for a given reflectance. Thus, the mean value of ξ is computed for each cloud reflectance value to minimize the effects of cloud height variability.

Visible optical depths for the case study GOES data are given in Table 2. Tables 3–5 summarize the results of applying (8) to all of the data. Despite the differences between the values of τ_v for IFO and case study results in Table 3, two similarities are quite evident in a comparison of the respective scattering efficiencies. For both datasets, the scattering efficiency appears to increase with decreasing θ_0 and increasing Θ. At high values of θ_0, ξ is well below the expected limit of 2. The average values of ξ are also very close, 2.17 and 2.13, for the case study and IFO, respectively. In Table 4, the greatest values of ξ also occur near local noon (1800 UTC).

b. Reanalyzed visible data

The temporal dependencies of τ_v and ξ are not realistic. They are primarily due to shortcomings in the analysis treatment of χ_c. The anisotropy of the reflected radiation field for real clouds depends on the optical thickness, incident radiation, microphysical properties of the cloud, and the morphology of the cloud field. The value of χ_c used here is fixed for a given set of angles and represents an empirical average for all cloud types. The average cloud optical depth in the bidirectional reflectance model used here is probably clos 10, while τ_v for the clouds analyzed in this stud generally smaller than 2. Since cirrus clouds are only type considered here and the angles are fixed a given hour, it is likely that χ_c will be biased w respect to local time. There will also be random err in χ_c due to variations in microphysics, morpholo and cloud optical depth for a given hour. The m nitudes of these errors are currently unknown, but potentially large. Assuming that the time sampl represents a random sampling of χ_c, the averages various parameters derived from all times should relatively unbiased.

Using the assumption that the mean value of ξ independent of time, new values of χ_c were determir from (5) using the observations of τ_e and the me scattering ratio of 2.13. These new values were averag at each time. The means, denoted as χ_c', are given Table 6 with the mean nominal values from the bi rectional reflectance model. The results indicate m anisotropy in the cirrus reflectance pattern than in t empirical model. The data of Takano and Liou (198 indicate that reflectance anisotropy diminishes w increasing optical depth for scattering by hexagoi columns. Thus, the smaller optical depths of the clou here compared to those for the clouds in the empiri model are probably responsible for the larger range χ_c' compared to χ_c.

To eliminate the temporal (angular) dependence τ_v, the data were reanalyzed using χ_c'. The values the visible optical depth and the scattering ratios c termined from the reanalysis are listed in Tables 2 and denoted with the primed variables, τ_v' and ξ', spectively. Values of ξ' for the AVHRR data we computed by changing the nominal values of χ_c so th the derived value of τ_v' for the AVHRR data was equ to τ_v' for the corresponding GOES data. In general, t

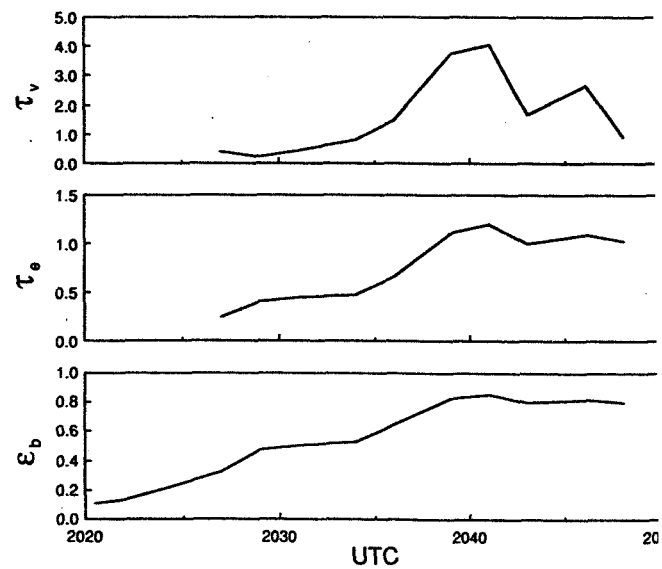

FIG. 18. Cloud optical properties derived from Fig. 17.

TABLE 6. Anisotropic reflectance factor comparison.

Time (UTC)	Number of pixels	χ_c (nominal)	χ_c' ($\xi = 2.13$)	Mean difference	Standard deviation
1330	213	0.823	0.618	0.205	0.104
1400	177	0.864	0.735	0.129	0.050
1430	113	0.896	0.809	0.087	0.113
1500	177	0.922	0.896	0.026	0.079
1600	215	0.980	1.034	−0.054	0.123
1630	146	1.002	0.912	0.090	0.044
1700	212	1.020	1.195	−0.175	0.264
1800	158	1.050	1.206	−0.156	0.348
1830	72	1.061	1.025	0.036	0.000
1900	262	1.029	1.214	−0.185	0.220
1930	236	1.008	1.147	−0.139	0.206
2000	245	0.982	1.091	−0.109	0.164
2030	290	0.953	1.008	−0.055	0.103
2100	222	0.918	0.890	0.028	0.093
2130	283	0.882	0.713	0.069	0.154
2200	210	0.843	0.579	0.264	0.082

new mean optical depths in Tables 2 and 3 have been increased for hours near the terminator and decreased near noon. The temporal dependence of the scattering efficiency ratios has been effectively eliminated for the IFO averages, while some tendency for maximum values near noon remains for the case study results. Resulting means of ξ' are not equal to 2.13 because of the nonlinearities in the solution of (5) and (8) and because four additional scenes were eliminated due to filtering. In Table 4, all of the optical depths and ratios were decreased yielding a mean value for ξ' of 2.43. The new values of χ_c for the AVHRR data (Table 5) reduced the differences between the GOES and AVHRR scattering efficiency ratios with respective means of 2.31 and 2.35 for the five values of ξ'. The greatest difference between the two datasets is found for FMC during 30 October when almost 20% of the AVHRR data are classified as dark pixels.

Mean values of τ_v' were computed for discrete intervals of cloud thickness. The results shown in Fig. 19 reveal a strong, almost linear, dependence of τ_v' on cloud thickness. This apparent relationship lends further support to the potential for deriving cirrus depth from the VIS–IR radiance data. Figure 20 shows the variation of mean ξ' with IR optical depth. The standard deviations of the IFO data are denoted with the vertical lines. The case study averages (squares) vary from 1.79 to 2.54, while the IFO means (circles) range from 1.91 to 2.33. There is good consistency between the IFO and case study results for $\tau_e < 1.0$. Clouds with $\tau_e > 1.0$ were undersampled during the case study (Fig. 9a). These results show no indication of a dependence of ξ' on τ_e.

Average scattering efficiencies were also computed for discrete levels of T_c (Fig. 21). For $T_c > 230$ K, $\xi' \approx 2.0$. Despite the large standard deviations, the mean value of ξ' appears to increase with decreasing temperature for $T_c < 230$ K. At $T_c = 217$ K, the mean

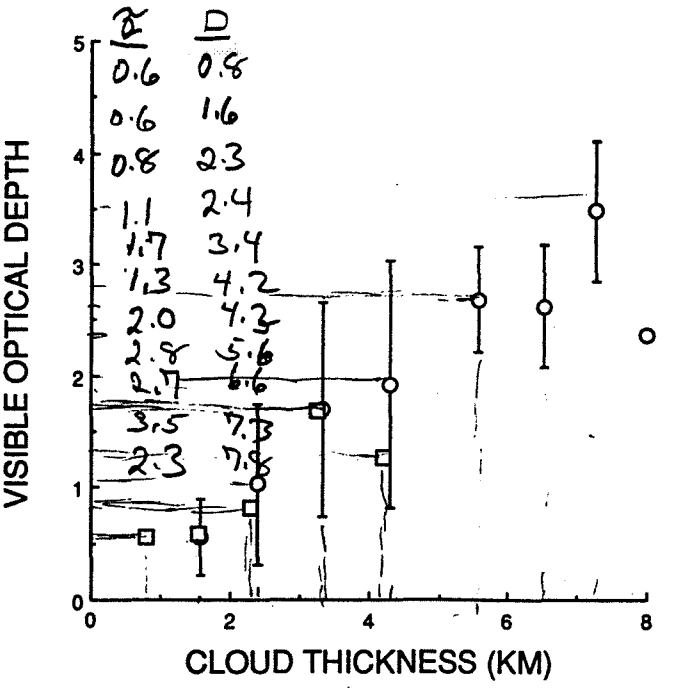

FIG. 19. Variation of cloud visible optical depth with cloud thickness for all IFO (circles) and case study (squares) data from GOES over surface lidar sites. Vertical lines denote standard deviations.

scattering efficiency ratio reaches a maximum of ~2.6 for the IFO data. To determine if there is a significant difference between the results for cold and warm cirrus clouds, average values for ξ' were computed for $T_c \leq 230$ K and for $T_c > 230$ K. For the thirty cases with $T_c \leq 230$ K (cold clouds), the mean value of ξ', $\overline{\xi'}$ is 2.43 with a standard deviation of 0.89. For the other

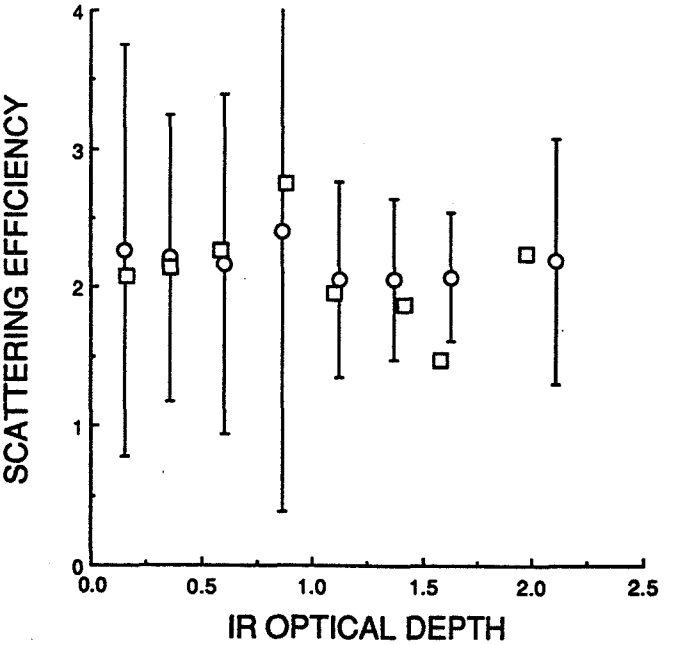

FIG. 20. Variation of mean scattering efficiency ratio with infrared optical depth for all IFO (circles) and case study (squares) data from GOES over surface lidar sites. Standard deviations denoted by vertical lines.

37 scenes (warm clouds), the mean scattering efficiency ratio is 2.11 with a standard deviation of 0.71. Application of sampling theory with an assumption of normal distributions yields $\bar{\xi}' = 2.43 \pm 0.17$ for the cold clouds and $\bar{\xi}' = 2.11 \pm 0.12$ for the warm clouds. (The mean for all 67 cases, 2.25, differs from that in Table 3 because of different averaging techniques.) Using a two-tailed Student t-test, it was found that the cold-cloud ($T_c \leq 230$ K) ratios are different from the warm-cloud values at the 90% confidence level. The mean ratio for the warm clouds is not significantly different from 2.0, the lower limit expected for large particles.

As noted earlier, the value of ξ is highly dependent on the particle size. Neglecting the effects of particle shape, it may be concluded from these results that large particles are the dominant scatterers in the clouds for $T_c > 230$ K. At colder cloud temperatures, smaller particles (e.g., $a < 20$ μm) apparently contribute more to the scattering. Thus, the average particle size in the colder clouds must be significantly less than the warmer clouds. Figure 21 suggests that the proportion of small particles in the clouds increases as the cloud-center temperature decreases. These findings are consistent with the results of Platt and Dilley (1981) who determined that the lidar-measured backscatter-to-extinction ratio is relatively constant for $T_c > 233$ K. The value of that ratio changes abruptly to a new value at temperatures slightly less than 233 K. Heymsfield and Platt (1984) were able to show that the number density of large particles in cirrus clouds decreased substantially when the temperature dropped below −40°C. The VIS extinction coefficients derived from the GOES data are

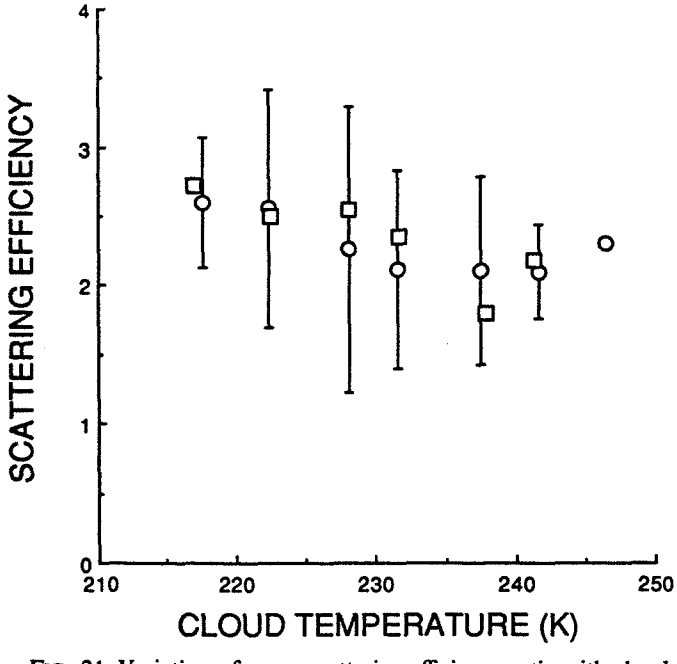

FIG. 21. Variation of mean scattering efficiency ratio with cloud-center temperature for all IFO (circles) and case study (squares) data from GOES over surface lidar sites. Vertical lines denote standard deviations.

0.41 km^{-1} and 0.45 km^{-1} for $T_c \leq 230$ K and $T_c > 23$(K, respectively. These values fall in the range of value: computed by Heymsfield and Platt (1984), but show less dependence on temperature.

Although particle size is very important in the determination of ξ, Platt et al. (1987) have presentec theoretical results indicating that ξ is also a functior of particle shape. The results of Heymsfield and Plat (1984) show that ice crystal habits change significantly when the cloud temperature drops below 233 K. Thus both factors, smaller crystals and shape changes, may explain the increase in ξ for $T_c < 230$ K observed in the current dataset. Microphysical measurements using probes sensitive to small ice particles are needed tc further clarify these results.

c. *Assumptions for visible optical depth calculations*

The determination of τ_v' relies on the assumptions that the clouds can be modeled as plane parallel entities, that (5) is an adequate parameterization of a more exact radiative transfer model, and that the cloud albedo model, or the implied scattering phase function, is appropriate for the clouds studied here. The lidar plots in Figs. 1 and 2 show considerable structure in the clouds observed during 28 October. Such morphology is probably typical of most of the cirrus clouds observed during the IFO. Thus, the clouds do not appear to be plane-parallel and homogeneous. Because exact modeling of the nonhomogeneous clouds is not possible at this time, no attempt is made to estimate the effects of cloud morphology on the derived values of VIS optical depth.

One means of evaluating the parameterization is to compare the results of (5) with values of τ_v derived for each scene with a detailed radiative transfer model using the scattering phase function that produced the cloud albedo model applied in (5). Takano et al. (1989) computed τ_v for several of the IFO scenes using a three-level adding–doubling radiative transfer model with two different scattering phase functions. One of the phase functions was the same as that used to derive the cloud albedo model employed here. The other was for ice spheres with areas equivalent to the hexagonal columns used in the first phase function. Takano et al. (1989) used a Lambertian surface with an albedo of 0.11 to simulate the Wisconsin land areas. They determined the value of τ_v for 16 scenes during the case study period by matching the reflectance of the adding–doubling model at the GOES angles to the mean GOES-derived reflectance of the square area around each lidar site. The pixels in the same areas (which include the strips analyzed earlier) were analyzed with the parameterization using the values of χ_c'.

A comparison of the results showed that the average value of τ_v for the radiative transfer model using hexagonal crystals was 0.95 compared to an average of 0.99 for the parameterization. The rms difference was

17%. Although the 0.04 mean difference is not statistically significant, it is expected for several reasons. The Takano et al. (1989) results include all of the pixels in the region, while the results from (5) exclude all dark pixels. Furthermore, the radiative transfer model does not include ozone absorption. Exclusion of the dark pixels and inclusion of ozone absorption would both tend to increase the mean model-derived optical depth by a few percent. The rms differences are most likely due to the use of a Lambertian surface albedo in the adding–doubling model and the use of a fixed value of χ_c' for each hour in (5). The mean value of ξ for the model results was 2.55 compared to 2.56 for the parameterization. From these comparisons it is evident that (5) is quite adequate for parameterizing the detailed radiative transfer model for the range of optical depths seen in the case study. In addition, the good agreement between the average derived values of ξ' over land and water at the same hour (i.e., 1600 UTC) in Table 4 indicates that (5) is useful over a reasonable range of surface albedos.

The cirrus clouds observed during the IFO contained mixtures of hexagonal columns, plates, and aggregates of various sizes and shapes (Kajikawa and Heymsfield 1989). Even water droplets were found in some of the warmer cirrus clouds (Sassen et al. 1990). In this study, the visible radiances have been treated as if they were reflected from a cloud composed entirely of one size of hexagonal columns. Although exact evaluation of the uncertainty in τ_v due to the use of the single phase function is not possible, some inferences may be drawn from the results to make a qualitative assessment of the hexagonal column, cloud-albedo model.

One indication of the reasonability of the model used here is that the mean value of ξ is close to the limit of 2.0 expected for large particles, especially for the warmer clouds. An examination of the results of Takano et al. (1989) reveal that the mean value of τ_v derived with the equivalent ice-sphere model was 30% greater than that for the hexagonal column model. The resulting mean value of ξ for the ice spheres is 2.9. These results indicate that the ice-crystal model is more appropriate than the spherical model for interpreting the cirrus reflectance data.

The adding–doubling model of Takano and Liou (1989b) was used to calculate the cloud reflectances for the angles corresponding to GOES and AVHRR in Table 5 using the values of τ_v' and the hexagonal column phase function. The resulting reflectances at the GOES angles were ratioed to the corresponding reflectances at the AVHRR angles. For the three cases in which the GOES and AVHRR angles differed significantly (30 October and 2 November), the average ratio for the adding–doubling results was 1.6 compared to 1.3, the mean ratio of the GOES and AVHRR values of χ_c'. About half of the difference in the mean ratios may be due to the uncertainties in the values of χ_c' for each individual case. Thus, the actual difference in the ratios may be as small as 0.15. This limited result suggests that the actual scattering by the cirrus clouds may be less anisotropic than expected for the hexagonal crystal model. Although discrepancies between the microphysical characteristics of the actual and modeled clouds are likely to cause differences between the observed and modeled radiation fields, some of the tendency for more diffuse reflectance from the cirrus may be due to shadowing effects as discussed below. A more complete analysis using much more data is required to better define typical cirrus reflectance anisotropy and the single scattering phase function that accounts for it. Given the current knowledge of cirrus cloud radiative properties, however, the cloud albedo model used in (5) appears to be adequate for computing τ_v'.

d. Dark pixels

It is possible that the "dark" pixels noted earlier may be caused by the extreme reflectance anisotropy expected for very thin clouds. For small values of τ_v and $\Theta \sim 120°$, there should be very little reflection from the cloud in the direction of the satellite as compared with its albedo to upwelling diffuse radiation from the surface. Thus, the pixel may appear darker than a clear scene for the same viewing and illumination conditions.

Examples of the variations of ρ as a function of α_c computed with (5) are shown in Fig. 22a for WAU at 1400 and 1800 UTC. The corresponding values of ρ_s are 0.13 and 0.16, respectively, with $\alpha_{sd} = 0.11$. The relationship between cloud albedo and optical depth depends on the solar zenith angle resulting in a divergence of the curves at larger values of α_c. Additional calculations were performed for $\mu_0 = 0.4$; $\chi_c = 1$; and $\rho_s = 0.04, 0.08, 0.16, 0.32$, and 0.64; with $\alpha_{sd} = 0.92\rho_s$.

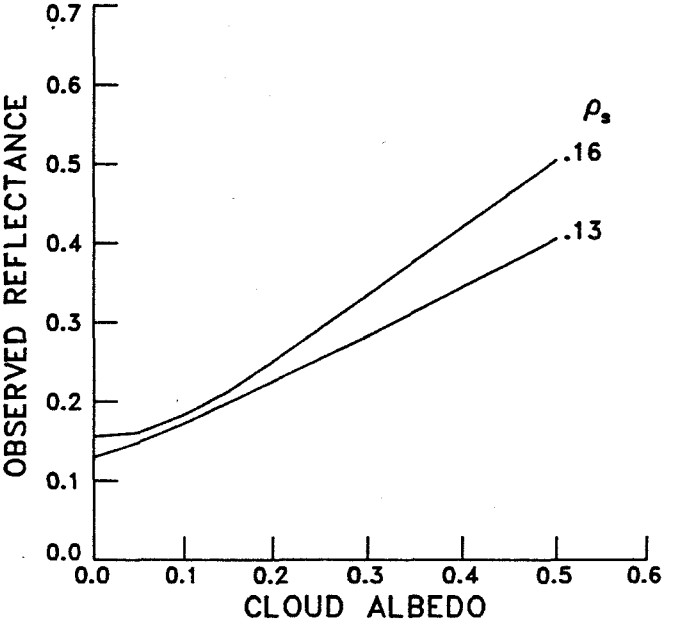

FIG. 22a. Theoretical top-of-the-atmosphere visible reflectance over WAU for 1400 UTC ($\rho_s = 0.13$) and for 1800 UTC ($\rho_s = 0.16$).

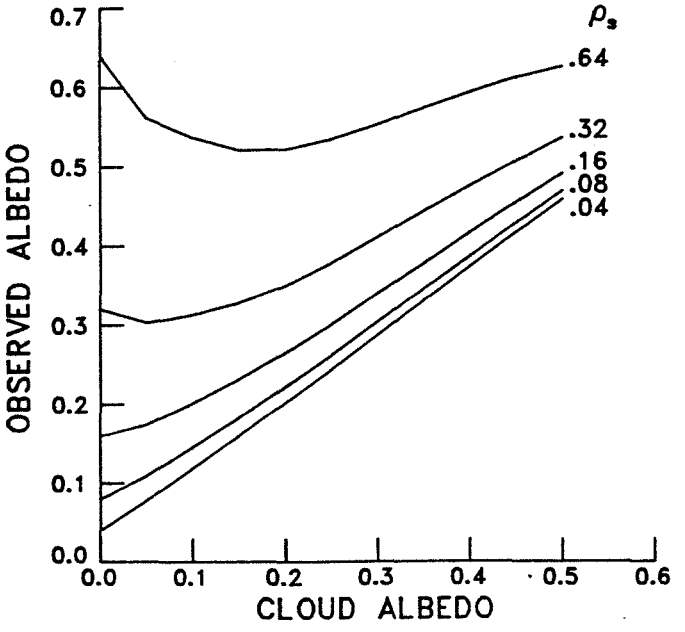

FIG. 22b. Theoretical top-of-the-atmosphere visible albedos for various surface albedos.

The results are shown in Fig. 22b. For relatively dark surfaces, the measured reflectance increases monotonically with α_c. Over bright surfaces, the reflectance actually decreases first, then increases at greater cloud albedos. A dark surface contributes little to the upward flux, while the opposite is true for bright surfaces. The increased reflectance of a cloud to diffuse radiation tends to trap some of the reflected radiation from the surface. For thin clouds over bright surfaces, this effect can result in a reflectance that is lower than that observed for the clear-sky case. Additional calculations for other solar zenith angles indicate that the insertion of the thin cirrus cloud above the bright surface decreases the albedo at lower sun angles, making the discrimination of clear and cloudy skies more difficult over deserts and other bright scenes. It is possible that this effect may also be important at certain angles and values of χ_c over dark surfaces.

Although such a mechanism may cause some pixel darkening, it is probably not the primary cause. Cloud shading is more likely to be the predominant cause of dark pixels. For example, at altitudes of 10 km, a 2 km thick cloud can cast a shadow that has its leading edge removed at least 8 km horizontally on the surface from the position of the cloud's leading edge for $\theta_0 \geq 45°$. Thus, the cloud and the portion of the surface affected by direct transmission through the cloud can easily be offset by one or more GOES pixels. The projected line of sight from the satellite through a cloud will not line up with the cloud's shadow unless $\Theta \approx 180°$. In most instances, therefore, the direct transmission from the surface through the viewed cloud will come from the shadow of a different cloud. The diffuse reflectance will result from the combined effects of the various clouds in the vicinity. For a homogeneous cloud field, an optically thick viewed cloud, or $\Theta = 180°$, such effects are negligible. Figures 1, 2, and 17 provide ample evidence that the clouds observed during the case study are neither optically thick nor homogeneous. In an inhomogeneous cloud field, it is possible to observe a surface darkened by the shadow of a thick cloud through a thin cloud that produces little scattering of its own in the direction of the satellite. Thus, to the viewer in space a pixel appears to be a cloud by virtue of its cold temperature, but is darker than expected for a clear scene.

This effect may be examined quantitatively by considering (5). Use of that model implicitly assumes a homogeneous cloud field. To consider an inhomogeneous cloud field, let τ_s replace τ_v in (6), where τ_s is the VIS optical depth of the cloud casting a shadow onto the surface in the line of sight of the observed cloud that has optical depth τ_v. Since the diffuse radiation emerging from the bottom of the clouds and reflecting from the surface is coming from all of the clouds in the field, let α_c in the third term of (5) be replaced by the average albedo of the observed and the shading cloud. The results of solving this inhomogeneous version of (5) for two different observed clouds are displayed in Fig. 23. The circles represent $\tau_s = \tau_v$. Viewing angles were fixed at $\theta = 52°$ and χ_c varied with θ_0, which changed with time as in the lower halves of Tables 3 and 6. Clear-sky reflectance is denoted with the dashed horizontal line.

The greatest effects of cloud inhomogeneities are seen for $\tau_v = 0.25$. Both shading clouds cause dark pixels for $\theta_0 < 81°$. Some dark pixels occur for $\tau_s = \tau_v$ for $\theta_0 < 60°$. Calculations using smaller μ_0's produced no dark pixels. The thickness of the shading cloud becomes more important as μ_0 increases. The impact of shading on the observed cloud having $\tau_v = 1$ is less pronounced with little likelihood of dark pixels for the range of μ_0

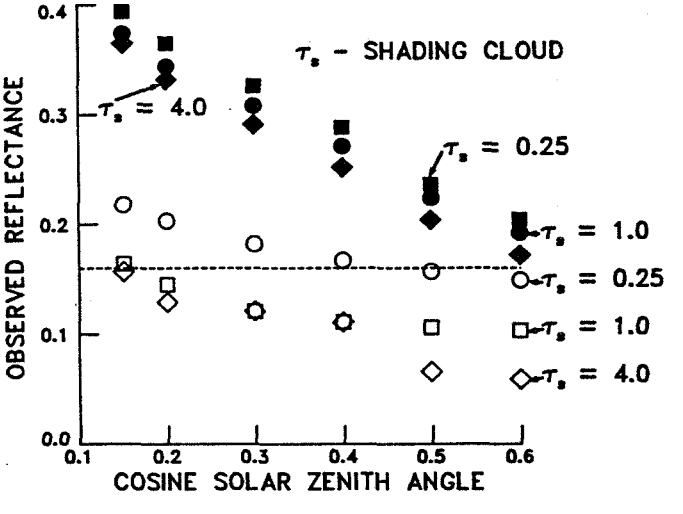

FIG. 23. Effect of cloud shading on observed reflectance. Optical depth of observed cloud is τ_v. Solid symbols, $\tau_v = 1$. Open symbols $\tau_v = 0.25$. Dashed line is clear-sky reflectance.

considered. Shading by the thin cloud ($\tau_s = 0.25$) actually increases the observed reflectance for all cases using $\tau_v = 1$. As τ_v increases to larger values, the impact of τ_s will become negligible. This lack of a shadowing effect for thicker clouds suggests that the observed reflectance may be biased toward a value that is lower than expected when the scene contains both optically thick ($\tau_v \geq 2$) and thin clouds, even if no dark pixels occur.

Shadowing effects can be observed in the data shown in Fig. 18. Dark pixels corresponding to the thinnest part of the cloud are seen before 2027 UTC. The next few pixels to the right are detectable but τ_v is much less than τ_e. The VIS optical depth for the pixels corresponding 2040 UTC is more than three times the value of τ_e, suggesting enhanced reflectance. In this figure, the sun would be located approximately to the right of the figure at $\theta_0 = 68°$. With a cloud top near 11 km, the thickest part of the cloud would cast a shadow approximately 28 km to the left or to the position corresponding to 2025 UTC. The view from the satellite is at a 35° angle, not perpendicular, to the solar plane. Thus, the surface in the line of sight of the cloud at 2025 UTC would correspond to the 2020 UTC position. That surface would be shaded by a cloud with $\tau_e \approx 0.5$ or $\tau_v \approx 1.0$ assuming that Fig. 18 is an accurate cross section of the cloud. A dark pixel would be expected at 2020 UTC based on the results in Fig. 23. The first visibly detectable cloud coincides with $\tau_e \approx 0.3$ at 2027 UTC. Its value of τ_v is much less than the expected value of 0.6.

While the shading can explain the darker pixels, it does not account for the excessively bright ones at 2040 UTC. For these bright pixels, it is instructive to refer to the cloud structure in Fig. 1. The vertical thickness of the cloud changes rapidly so that the pathlength of the incident solar radiation through the cloud is not necessarily $h\sec\theta_0$. The pathlength may be substantially increased because of the cloud structure. For example, the sun angle may coincide with the right arm of the "V" defining the cloud centered at 2035 UTC in Fig. 1. This effect would tend to cause a cloud to appear brighter than expected for the observed τ_e. In this case, the shadowing and enhancement effects apparently cancel to yield a reasonable value of ξ' for the whole scene.

The occurrence of dark pixels is shown in Fig. 24 as a function of ϵ_b. Most of the dark pixels are found at emittances corresponding to $\tau_e < 0.2$. Some, however, are found for $\tau_e = 0.5$. Very few dark pixels were observed near noon when $\Theta > 160°$. Most were found in the midmorning and late afternoon when shading conditions were favorable. The dark pixels comprise only 3% of the data considered here. This percentage belies the importance of this effect since shading will occur in many instances without producing the easily detectable dark pixels. The shading effect will tend to reduce the observed reflectance causing an underestimation of the cloud's thickness and emittance. Cloud shadows or their absence will also affect the interpretation of reflectance anisotropy. Their presence at high solar zenith angles will yield lower than normal values of τ_v.

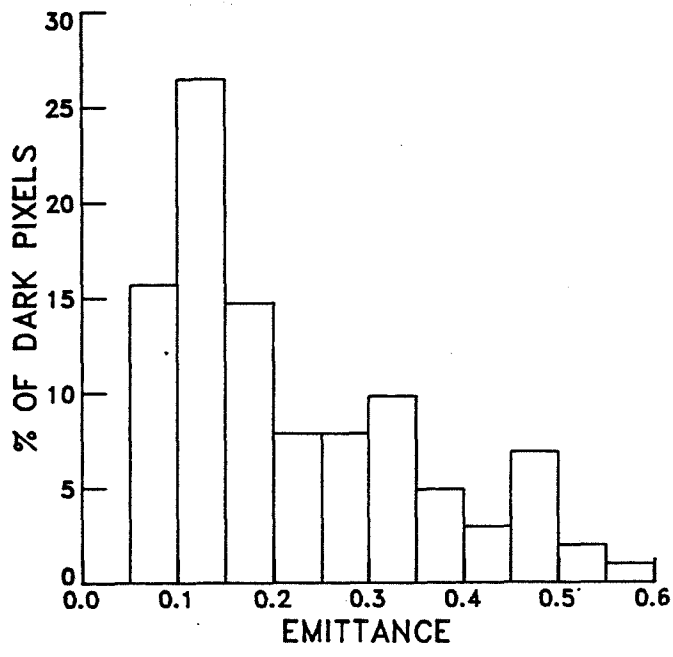

FIG. 24. Percentage of total number of "dark" pixels as a function of effective beam emittance, ϵ_b.

5. Conclusion

The cirrus clouds observed during the case study days are similar to those observed in previous research. By comparison, however, they are not necessarily typical of midlatitude cirrus clouds since their bulk properties are significantly different from those observed during other IFO cirrus days.

The analysis performed in this study using a combination of ground-based and satellite instrumentation yields some results that are similar to earlier studies that utilized other combinations of platforms and instruments. This consistency of results for different approaches lends a higher degree of confidence to the common findings. In addition, the combined datasets used here have provided some valuable new insights into the problem of determining cirrus cloud properties using VIS and IR radiance pairs from satellites.

The determination of cloud-top emittance or actual cloud-top temperature appears to be feasible based on the results of this study. Previously, what has been termed cloud-top temperature in emittance-adjusted, VIS-IR retrievals is closer to cloud-center temperature. The emittance ratio and the dependence of cloud thickness on cloud-center temperature derived here may be utilized in a scheme to estimate cloud thickness. This latter parameter will be useful for computing radiative divergence for observed cirrus clouds.

The results indicate that scattering efficiencies are greater for colder clouds. This finding holds promise for improvements in determining the IR optical depth from reflected VIS data. Additional study, however, is required to confirm this conclusion.

From the examination of the reflectance data and scattering efficiencies it is concluded that much work remains to adequately describe the scattered radiation field for real cirrus clouds. Both theoretical and empirical bidirectional reflectance models should be developed for clouds composed of realistic particle shapes. As in the ISCCP model, the patterns should be developed for various optical depths. Those models will require confirmation with the aid of further observational data. The effects of cloud particle scattering in IR radiative transfer should also be examined observationally.

Cloud shadows are a problem for the interpretation of cloud reflectances, especially for cirrus. The effects are not limited to large solar zenith angles. Relatively high viewing zenith angles can produce situations that result in the viewing of shadows, even for the near-zenith sun. It is apparent that analysis of a single pixel is most sensitive to shadowing problems. Some of the effects may be diminished through averaging over several pixels. Other approaches to deal with shading need to be developed. Validations of cirrus scattering calculations must also consider these effects. The problem of shadows is not as important over water because of the low surface albedo. Other problems in remote sensing of clouds such as partially cloud-filled pixels have not been considered here. Future research efforts should address these other factors.

Acknowledgments. The contributions of Messrs. P. Heck, R. Wheeler, and G. Gibson of Lockheed Engineering and Sciences Company to the satellite data reduction and graphics are deeply appreciated. We also thank Ms. S. Morgan of Computer Sciences Corporation for her assistance in reducing the GOES data. Discussions with Dr. B. A. Wielicki of NASA Langley Research Center were also quite helpful. We would also like to thank Drs. K. N. Liou and Y. Takano of the University of Utah for making their radiative transfer model available. The Madison lidar measurements were supported by ARO Grant DAAG29-84-K-0069, ONR Grant N00014-87-K-0436, and NASA Grant NAAG1-882.

APPENDIX A

Low and thick cloud filtering

The presence of low clouds contaminates the data since the analysis is predicated on the presence of only one cloud layer (the cirrus layer may contain two or more distinct sublayers). The cloud heights are defined for the upper-level cloud (generally, $z_b > 4$ km) detected by the lidar. In some instances, the occurrence of low clouds was either noted by the lidar operators or evident in the backscatter intensity plots. In other cases, the visual observations were not recorded or the low clouds were located within the satellite-defined area around the site, but beyond the observer's horizon. The datasets containing low clouds must either be eliminated or the pixels contaminated by low clouds must be removed. Elimination of all datasets containing low clouds would substantially reduce the number of samples.

In order to define a simple preprocessing filter, it is first assumed that $\alpha_c \propto \tau_v$ for small optical depths. It is also assumed that, to a first approximation, $\rho = T_a\alpha_c + \rho_s(1 - \alpha_c)^2$ and $\alpha_c = \rho_c$. Using the definition of ξ (§ 3e) and (4), it can be shown that

$$\epsilon_b = 1 - \exp(-k\alpha_c/\mu), \tag{7}$$

where k is the constant of proportionality. Values for k are determined in the following manner. For a given site and time, ϵ_b is computed with (1) for each cloudy pixel having $D > D_s$ and $T < T_s - 3$ K. The mean emittance is then computed for each value of D corresponding to the approximated value of α_c. Equation (7) is solved for k using each albedo-emittance pair. An average value of k is then computed for a specified subset of the data. This procedure is applied using $T_z = T_c$.

To filter the data, it is assumed that low clouds are generally brighter than cirrus, but their emittances depend on albedo, as in (7), in the same manner as cirrus. Thus, if a maximum cloud albedo is known for a given cirrus emittance, then it may be assumed that any pixels brighter than that maximum contain some low clouds. The values of those maximum albedos, α_{max}, must be estimated here. To determine those maximum values, the histograms were first filtered manually to obtain a set containing no low clouds. The maximum albedo for each temperature (emittance) was extracted for every histogram at a given time. Data taken on 22 October 1986, were used in the analysis. All maxima for a given time were compared to determine the greatest values for that time. Very little dependence on time was found in this comparison. Therefore, the maxima from all hours were combined. The resultant values were then used to solve (7) for k using a least-squares regression fit. The results were averaged to obtain the coefficient, k_{max}, which is used to define the maximum cloud albedo for a given emittance. The results of this process yield $k_{max} = 2.4$. Thus, for a given time, (7) may be solved for α_{max} using k_{max} and the emittance. Any pixel with $\alpha_c > \alpha_{max} + 0.025$ is assumed to contain low clouds and is eliminated from further processing. The 0.025 increment is an estimate of the uncertainty in α_{max} resulting from the use of an approximation.

An example of this filtering is shown in Fig. A1 for the data over FMC at 1930 UTC 28 October when low clouds were noted in the observer's log. Crosses represent individual pixels. The solid line represents α_{max}

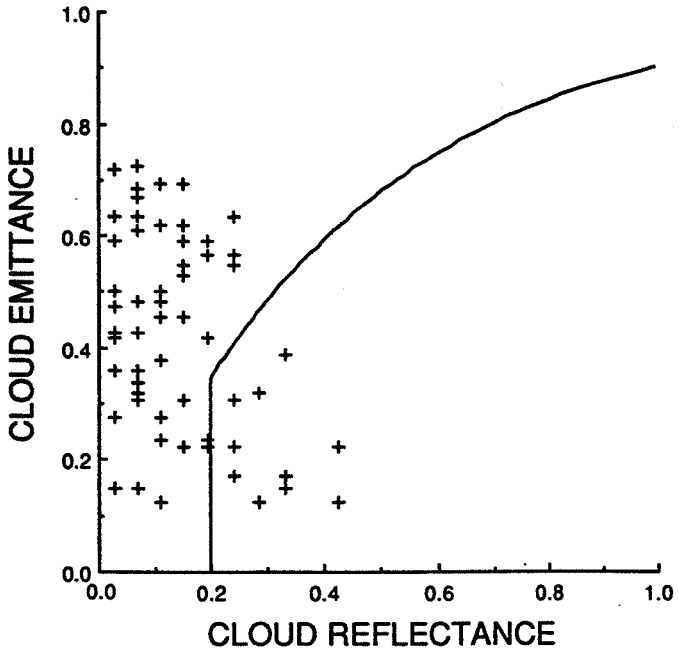

FIG. A1. Example of low-cloud filter application over FMC at 1930 UTC 28 October 1986. All data to right of solid line correspond to low clouds.

computed using k_{max}. The vertical line, $\alpha_{max} = 0.20$, is used at low reflectances because of larger uncertainties at those reflectance levels. This value is based on a visual inspection of the data that contained low clouds. The filtering process eliminates the pixels that clearly contain low clouds (i.e., those to the right of the line). Some pixels containing both low and high clouds, however, may remain in the data.

All cases having $\tau_v > 5.0$ were also removed from the dataset. This arbitrary limit was imposed to minimize the uncertainties in τ_e, τ_v, and subsequent values of ξ. The absolute error in derived optical depth increases with increasing emittance. The value of T_c is also more uncertain for thick clouds than thinner clouds. Thus, errors in emittance are greater for these thick clouds. Their removal does not significantly affect the trends in the results. Inclusion of the thick clouds, however, greatly increases the noise in the data. No case study scenes were affected by the thick-cloud elimination.

APPENDIX B

Partially cloud-filled pixels

The use of (7) or (8) implicitly assumes that the pixel is completely filled with cloud. While it is likely that some of the pixels are partially clear, definitive means for determining which are overcast and which are partly cloudy are unavailable. Platt (1. .., proposed a bispectral method to discriminate partly cloudy pixels from those containing thin clouds. His technique requires uniform blocks of constant height and thickness for detection of partly cloudy pixels. Detection of thin clouds allows variable thicknesses, but not heights. As seen in Figs. 1 and 2, real cirrus clouds are anything but uniform and constant in altitude and depth. An actual cloud field may also contain broken clouds with variable optical depths. The nonuniformity of such real clouds blurs the distinction between the linear relationship for partly cloudy pixels and the exponential dependency for variable thickness overcast pixels. Over land the ISCCP algorithm uses a threshold of 6 K colder than the clear-sky temperature to determine cloudy pixels (Rossow et al. 1988). Because of the low spatial variability in T_s over the land areas in this study, it is assumed here that pixels colder than $T_s - 3$ K are overcast. The data are not used, however, if there is evidence of any significant breaks in the ceiling from the lidar displays or if the mean IR optical depth is less than 0.1. Very few breaks were seen over the sites on 28 October. The cirrus observed on 27 October were mostly scattered leading to the selection of only two scenes for that day.

APPENDIX C

List of symbols

a	particle radius
B	Planck function at 11.5 μm
D, D_s	observed and clear-sky visible counts
h	cloud thickness
k, k_{max}	albedo coefficient, albedo coefficient for maximum cloud albedo
Q_{abs}, Q_{sca}	absorption and scattering efficiencies
r_ϵ	cloud-top and -center emittance ratio
T, T_s	observed and clear-sky 11.5 μm equivalent blackbody temperatures
T_c, T_t	cloud-center and -top 11.5 μm equivalent blackbody temperatures
T_a	clear-sky temperature estimated from surface data
T_z, T_g	air temperatures at altitude z and at the surface
t	time
u	ozone abundance
z_b, z_c, z_t	cloud-base, cloud-center, and cloud-top altitudes
α_c, α_d	cloud and diffuse cloud albedos
α_s, α_{sd}	clear-sky albedo, clear-sky diffuse albedo
α_{max}	maximum albedo for high clouds at a given emittance
β, β_v, β_e	extinction, scattering, and absorption cross sections
γ	density of particles in the medium
ϵ_a, ϵ_b	vertical emittance, beam emittance
Θ	single-scattering angle
θ, θ_0	viewing zenith angle, solar zenith angle
λ	latitude or wavelength
μ, μ_0	$\cos\theta$, $\cos\theta_0$
ξ	scattering efficiency ratio
ρ, ρ_s, ρ_c	observed, clear-sky, and cloud visible reflectance
σ_e	volume extinction coefficient

τ_e, τ_v	infrared absorption and visible scattering optical depths
τ_s	visible scattering optical depth of shading cloud
$\Upsilon_a, \Upsilon_c, \Upsilon_u$	ozone, downward cloud, and upward cloud transmittances
ϕ	longitude
χ_s, χ_c	clear-sky and cloud anisotropic reflectance factors
ψ	relative azimuth angle
IFO	Intensive Field Observations (19 October–2 November 1986)
IR	infrared window (11.5 μm)
FMC	Ft. McCoy, Wisconsin
UTC	Coordinated Universal Time
MAD	Madison, Wisconsin
WAU	Wausau, Wisconsin
VIS	visible (0.65 μm)

REFERENCES

Grund, C. J., and E. W. Eloranta, 1990: The 27–28 October 1986 FIRE IFO cirrus case study: optical properties of cirrus clouds measured by the high spectral resolution lidar. *Mon. Wea. Rev.*, **118**, 2344–2355.

Hahn, C. J., S. G. Warren and J. London, 1988: Surface synoptic cloud reports for Wisconsin, 86 Oct–Nov 3. Cooperative Inst. for Research in Environ. Sci., Campus Box 449, Univ. of Colorado, Boulder, CO, 15 pp.

Hansen, J. E., and L. D. Travis, 1974: Light scattering in planetary atmospheres. *Space Sci. Rev.*, **16**, 527–610.

Heymsfield, A. J., and C. M. R. Platt, 1984: A parameterization of the particle size spectrum of ice clouds in terms of the ambient temperature and the ice water content. *J. Atmos. Sci.*, **41**, 846–855.

Kajikawa, M., and A. J. Heymsfield, 1989: Aggregation of ice crystals in cirrus. *J. Atmos. Sci.*, **46**, 3108–3121.

Liou, K. N., 1973: Transfer of solar irradiance through cirrus cloud layers. *J. Geophys. Res.*, **78**, 1409–1418.

——, 1986: Influence of cirrus clouds on weather and climate processes: a global perspective. *Mon. Wea. Rev.*, **114**, 1167–1199.

——, and G. D. Wittman, 1979: Parameterization of the radiative properties of clouds. *J. Atmos. Sci.*, **36**, 1261–1273.

McClatchey, R. A., R. W. Fenn, J. E. A. Selby, F. E. Volz and J. S. Garing, 1973: Optical properties of the atmosphere (3rd edition). AFCGRL-72-0497, 113 pp. [NTIS-N73-18412.]

Minnis, P., and E. F. Harrison, 1984a: Diurnal variability of regional cloud and clear-sky radiative parameters derived from GOES data, Part I: analysis method. *J. Climate Appl. Meteor.*, **23**, 993–1011.

——, and ——, 1984b: Diurnal variability of regional cloud and clear-sky radiative parameters derived from GOES data, Part III: November 1978 radiative parameters. *J. Climate Appl. Meteor.*, **23**, 1032–1051.

——, E. F. Harrison and G. G. Gibson, 1987: Cloud cover over the eastern equatorial Pacific derived from July 1983 ISCCP data using a hybrid bispectral threshold method. *J. Geophys. Res.*, **92**, 4051–4073.

——, P. W. Heck and E. F. Harrison, 1990: The 27–28 October 1986 FIRE Cirrus IFO case study: cloud parameter fields derived from satellite data. *Mon. Wea. Rev.*, **118**, 2426–2446.

Paltridge, G. W., and C. M. R. Platt, 1981: Aircraft measurements of solar and infrared radiation and the microphysics of cirrus cloud. *Quart. J. Roy. Meteor. Soc.*, **107**, 367–380.

Platt, C. M. R., 1973: Lidar and radiometric observations of cirrus clouds. *J. Atmos. Sci.*, **30**, 1191–1204.

——, 1979: Remote sounding of high clouds, I: calculations of visible and infrared optical properties from lidar and radiometer measurements. *J. Appl. Meteor.*, **18**, 1130–1143.

——, 1983: On the bispectral method for cloud parameter determination from satellite VISSR data: separating broken cloud and semitransparent cloud. *J. Climate Appl. Meteor.*, **22**, 429–439.

——, and A. C. Dilley, 1979: Remote sounding of high clouds: II. Emissivity of cirrostratus. *J. Appl. Meteor.*, **18**, 1144–1150.

——, and G. L. Stephens, 1980: The interpretation of remotely sensed high cloud emittances. *J. Atmos. Sci.*, **37**, 2314–2322.

——, and A. C. Dilley, 1981: Remote sounding of high clouds: IV. Observed temperature variations in cirrus optical properties. *J. Atmos. Sci.*, **38**, 1069–1082.

——, and ——, 1984: Determination of cirrus particle single-scattering phase function from lidar and solar radiometric data. *Appl. Opt.*, **23**, 380–386.

——, D. W. Reynolds and N. L. Abshire, 1980: Satellite and lidar observations of the albedo, emittance, and optical depth of cirrus compared to model calculations. *Mon. Wea. Rev.*, **108**, 195–204.

——, J. C. Scott and A. C. Dilley, 1987: Remote sounding of high clouds, VI. Optical properties of midlatitude and tropical cirrus. *J. Atmos. Sci.*, **44**, 729–747.

Reynolds, D. W., and T. H. Vonder Haar, 1977: A bispectral method for cloud parameter determination. *Mon. Wea. Rev.*, **105**, 446–457.

Rossow, W. B., L. C. Garder, P. Lu and A. Walker, 1988: International Satellite Cloud Climatology Project (ISCCP), Documentation of cloud data. *WCRP* Report WMO/TD-No. 266, 122 pp. [Available from Dr. W. B. Rossow at NASA Goddard Space Flight Center, Institute for Space Studies, 2880 Broadway, New York, NY, 10025.]

Sassen, K., 1981: Infrared (10.6 μm) scattering and extinction in laboratory water and ice clouds. *Appl. Opt.*, **20**, 185–193.

——, C. J. Grund, J. Spinhirne, M. Hardesty and J. M. Alvarez, 1990: The 27–28 October 1986 FIRE IFO cirrus case study: a five lidar view of cirrus cloud structure and evaluation. *Mon. Wea. Rev.*, **118**, 2288–2312.

Shenk, W. E., and R. J. Curran, 1973: A multispectral method for estimating cirrus cloud top heights. *J. Appl. Meteor.*, **12**, 1213–1216.

Schiffer, R. A., and W. B. Rossow, 1983: The International Satellite Cloud Climatology Project (ISCCP): the first project of the World Climate Research Progamme. *Bull. Amer. Meteor. Soc.*, **64**, 779–784.

Spinhirne, J. D., D. L. Hlavka and W. D. Hart, 1988: ER-2 lidar observations from the October 1986 FIRE cirrus experiment. NASA TM 100704, 49 pp. [NTIS-N89-21444.]

Starr, D. O'C., 1987: A cirrus-cloud experiment: intensive field observations planned for FIRE. *Bull. Amer. Meteor. Soc.*, **68**, 119–124.

Stephens, G. L., 1980: Radiative properties of cirrus clouds in the infrared region. *J. Atmos. Sci.*, **37**, 435–446.

Stuhlmann, R., P. Minnis and G. L. Smith, 1985: Cloud bidirectional reflectance functions: a comparison of experimental and theoretical results. *Appl. Opt.*, **24**, 396–401.

Suttles, J. T., R. N. Green, P. Minnis, G. L. Smith, W. F. Staylor, B. A. Wielicki, I. J. Walker, D. F. Young, V. R. Taylor and L. L. Stowe, 1988: Angular radiation models for earth-atmosphere system: Volume I–Shortwave radiation. NASA RP 1184, 144 pp. [NTIS-N88-27677.]

Takano, Y., and K. N. Liou, 1989a: Radiative transfer in cirrus clouds: I. Single scattering and optical properties of oriented hexagonal ice crystals *J. Atmos. Sci.*, **46**, 3–20.

——, and ——, 1989b: Radiative transfer in cirrus clouds: II. Theory and computation of multiple scattering in an anisotropic medium. *J. Atmos. Sci.*, **46**, 21–38.

——, K. N. Liou and P. Minnis, 1989: Cirrus optical depth retrieval from satellite-measured bidirectional reflectance. *AMS Symp. on Role of Clouds in Atmos. Chem. and Global Climate*, Anaheim, CA, Amer. Meteor. Soc., 178–180.

CIRRUS CLOUD OPTICAL AND MORPHOLOGICAL VARIATIONS WITHIN A MESOSCALE VOLUME

By
Walter W. Wolf

A THESIS SUBMITTED IN PARTIAL FULFILLMENT OF THE
REQUIREMENTS FOR THE DEGREE OF

Master of Science
(Atmospheric and Oceanic Sciences)

at the
UNIVERSITY OF WISCONSIN – MADISON
1996

Abstract

Cirrus cloud optical and structural properties were measured above southern Wisconsin in two time segments between 18:07 and 21:20 GMT on December 1, 1989. These clouds were measured using the University of Wisconsin–Madison Volume Imaging Lidar (VIL), the University of Wisconsin–Madison High Spectral Resolution Lidar (HSRL), and the VISSR Atmospheric Sounder (VAS) situated on GOES. The VIL imaged the cirrus cloud structure within a mesoscale volume and detected cirrus cloud cover percentages of 81.5% and 76.8% for the two time periods. A series of RTIs were created from the VIL cirrus scans to simulate many vertically pointing lidars situated across the wind. The cloud cover percentages for the individual RTIs ranged from 54.7% to 100%. The variation of the cirrus cloud features across the wind indicate the sampling errors associated with point measurements when they are used to describe the mesoscale cirrus cloud structure. The average cloud length along the wind was 130 km while the average cloud length across the wind was 14 km. The distance between clouds was 273 km along the wind and 24 km across the wind.

A new technique was used to calculate the cirrus cloud visible aerosol backscatter cross sections for a single channel elastic backscatter lidar. Cirrus clouds were viewed simultaneously by the VIL and the HSRL. This allowed the HSRL aerosol backscatter cross sections to be directly compared to the VIL single channel backscattered signal. This first attempt resulted in an adequate calibration. The calibration was extended to all the cirrus clouds in the mesoscale volume imaged by the VIL. This enabled the VIL backscattered signal to be converted into aerosol backscatter cross sections at a resolution of 2 to 3 km along the wind direction and a 60 m resolution both horizontally across the wind and in the vertical. Usage of a constant aerosol backscatter phase function (0.0499 sr^{-1}) enabled the calculation of extinction cross sections at each data point in the VIL observed mesoscale volume. This allowed for the cirrus cloud visible scattering optical depths to be calculated throughout the imaged volume. The VIL volume was viewed from the position

of the GOES to directly compare the VIL visible scattering optical depths to the VAS infrared absorption optical depths. The resulting ratio of the visible scattering optical depths to the infrared absorption optical depths was approximately 2:1.

Acknowledgments

I would like to thank Dr. Edwin W. Eloranta for his patience and guidance throughout this ordeal. What can I say Ed. You believed in me when perhaps I didn't believe in myself. Your comments, criticisms, and 'suggestions' helped to bring this work together. You have shown me the correct way to do science. (By the way, I hope this section does not need any corrections.)

I would like to thank Dan Forrest whose vast computer knowledge helped me out of many situations. His ability to see the root of a problem, or even the obvious which I often missed, has kept me on the right track. I guess that is what friends are for.

Antti and Paivi Piironen, without you two this thesis would not have been completed. While putting this work together, it was the small details which caused the most trouble. Antti, thanks for all of the programs; Paivi thanks for keeping my facts straight.

Dr. Donald Wylie, thanks for your cooperation with the satellite data. There is still a lot of work to be done.

I would like to thank Professors Steve Ackerman, William Smith, and Roland Stull for reading this work and for their helpful comments and suggestions.

I would also like to thank my parents, Joseph and Carole Wolf, because they started all of this many years ago. Thanks for the love and support throughout the years.

Last, but certainly not least, I would like to sincerely thank my wife Michelle for all the love and support she has given me over the years. She was always there when I started questioning whether it was all worth it. Her devotion and unselfishness made the extra hours a little easier to handle. Maybe I will be home at a reasonable hour now ... maybe.

Funding for this research has been provided by the NASA Grant NaG–1–882, Office of Naval Research Grant N0014–93–1–G013, Office of Naval Research Grant

F19628–91–K–0007, and the Office of Naval Research Grant N00014–91–J–1558.

Contents

1 Introduction

Cirrus clouds have a direct impact on the radiation balance of the Earth-Atmosphere system. These clouds reflect a portion of the incoming solar radiation and partially absorb the outgoing infrared radiation. The reflection of the incoming solar radiation reduces the energy added to the system. The partial absorption of the outgoing infrared radiation reduces the energy lost to space. This occurs because the cirrus clouds absorb the upwelling infrared radiation and radiate energy at longer wavelengths (associated with the lower temperatures at the cirrus cloud heights) in all directions. The energy radiated downward by the cloud is put back into the system, warming the levels beneath the cloud, while a reduced amount of upwelling infrared radiation leaves the system. Since the effective temperature of the planet is dependent upon the balance between the incoming and outgoing radiation, the change in the radiation balance caused by cirrus clouds has to be understood to predict future climate change.

The cirrus cloud morphological and optical properties alter the Earths radiation balance. The cloud structural properties which affect the radiation balance are: the cloud height, latitude, and the frequency of cloud occurrence. The height of the cirrus cloud governs its radiative temperature. Since the cirrus cloud height, the insolation, and the Earths surface temperature are functions of latitude, the effect of cirrus clouds on the radiative balance also changes with latitude (Platt (1981), p. 674-676). The frequency of occurrence of the cirrus clouds will control the overall impact of these clouds on the radiative balance. The more often cirrus clouds occur, the greater their effect will be on the global energy balance. The optical properties of the cirrus clouds moderate both the incoming and the outgoing radiation. The scattering properties of ice crystals at visible wavelengths control the amount of downwelling solar radiation reaching the lower atmosphere while the absorptive and scattering properties of the ice crystals at infrared wavelengths governs the amount of infrared radiation escaping to space.

Climatologies have been compiled to determine the cirrus cloud frequency

around the planet. Although there have been many cloud climatologies over the years, few have dealt with cirrus cloud coverage. One of the first extensive cloud climatologies to include cirrus clouds was compiled by London (1957). He assembled a large number of surface cloud observations from the Northern Hemisphere recorded in the 1930's and the 1940's and separated them according to cloud types, one of which was cirrus clouds. Recent climatologies have been compiled by Barton (1983), Woodbury and McCormick (1986), Prabhakara et al. (1988), Wylie and Menzel (1989), and Warren (1985). While the instruments and techniques used in these studies differ, each of these climatologies is limited by a lack of detailed global coverage. One cirrus climatology which was not regionally limited was compiled by Wylie et al. (1993). This four year cloud climatology used the NOAA polar orbiting HIRS (High resolution Infrared Radiation Sounder) multispectral infrared data. The cirrus clouds, detected using the CO_2 slicing technique (Smith and Platt (1978), p. 1797–1798), were present in 42% of the satellite observations on the average.

Cirrus cloud climatologies have been compiled from ground based point measurements and area averaged satellite data. The satellite and ground based instruments measure different atmospheric scales. The satellite climatology compiled by Wylie et al. (1993) averages 20 km by 20 km pixels containing cirrus clouds to produce 2^o latitude by 3^o longitude grids. The ground based point measurements observed only a small portion of the atmospheric structure (which may or may not contain cirrus clouds) which is advected over the instrument position. The cirrus cloud structure on a scale between the point measurements and the area averaged satellite measurements, the mesoscale, is unknown. In some cases, the mesoscale cirrus cloud structure has been inferred from point measurements. To ascertain the variability of the cirrus clouds on this intermediate scale, and thereby the accuracy of cirrus cloud point measurements in determining the overall cirrus cloud structure, cirrus clouds have to be measured throughout a mesoscale volume. One instrument capable of making these measurements is a volume imaging lidar.

The cirrus cloud optical properties, which depend directly upon the particle

composition, shape, size, and number density, also affect the Earths radiation budget. In situ measurements have been used to determine the cirrus cloud particle composition, size, shape, and number density. Cirrus clouds consist of ice crystals with maximum lengths typically in the range of 20-2000 μm (Liou (1986), p. 1172). These crystals are large compared to visible wavelength radiation and are approximately equal to or greater than the wavelengths of infrared radiation.

A relationship has been used by climate modelers to parameterize the cirrus cloud visible and infrared optical properties. From Mie theory, as a spherical particle becomes large compared to the wavelength of the incident light, the scattering efficiency of the particle converges to two while the absorption efficiency of the particle converges to one (Liou (1980), p. 139). Since the cirrus cloud ice crystals are large compared to the wavelength of visible radiation and since the complex part of the index of refraction (which is associated with absorption by the particle) at visible wavelengths is small, scattering will dominate the interaction of solar radiation with the ice crystals. At infrared wavelengths, absorption will dominate the interaction between the ice particles and the radiation since the cirrus cloud ice crystals are highly absorbing at 10 μm (Dorsey (1940), p. 491). Due to the differing radiative properties of the ice crystals at the two wavelengths, the cirrus cloud optical properties at visible and infrared wavelengths has be related through Mie theory by a ratio of efficiencies, the scattering efficiency divided by the absorption efficiency. This ratio is approximately two when the particle absorption equals the particle emission at infrared wavelengths. This efficiency ratio can also be stated in terms of the cirrus cloud optical depth at the two different wavelengths: the visible scattering optical depth divided by the infrared absorption optical depth multiplied by a ratio of visible extinction efficiency to the infrared extinction efficiency. Both models and cirrus cloud measurements have been used to test this optical depth relationship for nonspherical ice crystals. A model Minnis (1991) used three size distributions of hexagonal ice crystals and calculated a ratio for the optical depths ranging from 2.06 to 2.22. For these calculations, it was assumed that the extinction efficiencies at the two wavelengths were equal.

Measurements from a FIRE (First ISCCP Cloud Climatology Project) IFO (Intensive Field Operation) which used ground based and satellite based instruments suggested a 2.13 ratio between the visible and infrared optical depths for the cirrus clouds (Minnis et al. (1990)). To calculate the visible optical depths for the FIRE data from the measured visible radiances, the ground albedo and the cloud cover within each pixel had to be known. Measurements by Platt et al. (1980) from a ground based lidar and satellite radiometers suggested a ratio less than 2.0. A method is described in this thesis which allows for the calculation of the visible optical depths for cirrus clouds in a mesoscale volume using a ground based volume imaging lidar. Knowledge of the cirrus cloud visible optical depths over a mesoscale region allows for a direct comparison with the cirrus cloud infrared optical depths measured by satellite radiometers for the same region. This method of comparing the cirrus clouds on the mesoscale can also be used to validate the cirrus cloud detection techniques from satellite radiometers.

This thesis quantitatively describes the variability of the cirrus cloud optical and morphological properties within a mesoscale volume measured by the University of Wisconsin Volume Imaging Lidar (VIL). The cirrus cloud cover within the measured volume is calculated and compared to cirrus cloud point measurements made with the University of Wisconsin High Spectral Resolution Lidar (HSRL). The difference between the point and area cloud covers is used to illustrate the importance of sampling errors in single point measurements when they are used to describe cirrus clouds throughout a mesoscale volume. This is accomplished by estimating the change in solar flux at the surface of the Earth using the difference in the average cloud cover detected by the two lidars and the measured cirrus cloud visible optical depths. The visible scattering properties of the cirrus clouds are also calculated throughout the mesoscale volume. This is achieved by directly calibrating the VIL backscattered signal to the cirrus cloud aerosol backscatter cross sections measured by the HSRL. This is possible since both instruments were aligned to simultaneously view the same cirrus clouds. The variability of the cirrus cloud aerosol backscatter cross sections will be determined

using the calibrated VIL signal within the mesoscale volume. The cirrus cloud visible scattering properties can then be used to calculate the visible optical depth of the cirrus clouds in the volume. These visible optical depths will then be directly compared to the infrared optical depths for the cirrus clouds calculated from VAS (VISSR Atmospheric Sounder) radiance measurements. The ratio of the visible and infrared optical depths is compared to Mie theory and results from previous experiments.

2 Instrumentation

The instruments used in this study are the University of Wisconsin High Spectral Resolution Lidar (HSRL), the University of Wisconsin Volume Imaging Lidar (VIL), and the VISSR (Visible and Infrared Spin Scan Radiometer) Atmospheric Sounder (VAS) situated on the GOES satellite. These instruments were part of CRSPE (University of Wisconsin–Madison Cirrus Remote Sensing Pilot Experiment) (Ackerman et al. (1993)).

2.1 HSRL

The HSRL is a dual channel vertically pointing lidar with high spectral resolution. This instrument makes point measurements (line measurements in time) of the atmospheric structure advected over its position by the wind. The HSRL transmits radiation at a wavelength of 532 nm and was used to determine the visible aerosol backscatter cross sections per unit volume, optical depths, and if the particulate and gaseous absorption are negligible, aerosol backscatter phase functions. The HSRL has an advantage over single channel lidar systems because it separates the backscattered radiation into a part due to aerosols and a part due to molecules. This separation is possible because the signal backscattered from the molecules is Doppler broadened while the larger, bulkier aerosols have little effect on the wavelength of the scattered light. This two channel approach enables

a direct calculation of the atmospheric extinction and aerosol backscatter cross sections per unit volume. The advantage of this system over a single channel lidar system can be seen by first examining the single channel lidar equation and then the dual channel lidar equation. The equation for a single channel lidar system is:

$$P(R) = \frac{E_o c A_r}{2R^2} [\beta'_a(180, R) + \beta'_m(180, R)] \exp^{-2\int_0^R \beta_\epsilon(r')dr'} + M(R) + b \quad (1)$$

where:

R	=	range (m)
$P(R)$	=	power incident on (and within the field of view of) the receiver within the spectral bandpass of the instrument (W)
E_o	=	transmitted energy (J)
c	=	speed of light (m s^{-1})
A_r	=	area of the receiver (m^2)
$\beta'_a(180, R)$	=	aerosol backscatter cross section per unit volume (m^{-1} sr^{-1}) where:

$$\beta'_a(180, R) = \beta_a(R) \frac{P_a(180, R)}{4\pi} \quad (2)$$

$\beta_a(R)$	=	aerosol scattering cross section per unit volume (m^{-1})
$\frac{P_a(180,R)}{4\pi}$	=	aerosol backscatter phase function (sr^{-1})
$\beta'_m(180, R)$	=	molecular backscatter cross section per unit volume (m^{-1} sr^{-1}) where:

$$\beta'_m(180, R) = \beta_m(R) \frac{3}{8\pi} \quad (3)$$

$\beta_m(R)$	=	molecular scattering cross section per unit volume (m^{-1})
$\frac{3}{8\pi}$	=	molecular backscatter phase function (sr^{-1})
$\beta_\epsilon(R)$	=	extinction cross section per unit volume (m^{-1})
$M(R)$	=	multiple scattering contribution incident on the receiver within the field of view of the instrument (W)
b	=	background radiation incident on the receiver within the bandpass and field of view of the receiver (W)

Equation 1 contains two unknowns, $\beta'_a(180, R)$ and $\beta_\epsilon(R)$ (since $\beta_m(R)$ can be calculated from a radiosonde profile). This equation can be solved by either finding a relationship between $\beta'_a(180, R)$ and $\beta_\epsilon(R)$ or by using a calibration source to directly determine one of these two variables. In the former case, the Klett method has been used to solve the lidar equation. This method assumes a power law relationship between $\beta'_a(180, R)$ and $\beta_\epsilon(R)$ (Klett (1981)):

$$\beta'_a(180, R) = const \cdot \beta^k_\epsilon(R) \tag{4}$$

where k, which is generally in the interval $0.67 \leq k \leq 1.0$ (Klett (1981), p. 212), depends on both the lidar wavelength and various aerosol properties which include the aerosol shape, composition, and number distribution. The power law relationship can be substituted into the differential form of the logarithmic lidar equation:

$$\frac{dS(R)}{dR} = \frac{1}{\beta'_a(180, R)} \frac{d\beta'_a(180, R)}{dR} - 2\beta_\epsilon(R) \tag{5}$$

where:

$$S(R) = \ln(\frac{R^2 P(R)}{E_o}) \tag{6}$$

to get the following nonlinear ordinary differential equation:

$$\frac{dS(R)}{dR} = \frac{k}{\beta_\epsilon(R)}\frac{d\beta_\epsilon(R)}{dR} - 2\beta_\epsilon(R). \tag{7}$$

This equation has the same form as the Bernoulli equation and is easily solved. If k is assumed to be a constant, then the solution to Equation 7 is:

$$\beta_\epsilon = \frac{\exp[(S - S_m)/k]}{\left\{\beta_{m\epsilon}^{-1} - \frac{2}{k}\int_r^{r_m} \exp[(S - S_m)/k]dr'\right\}} \tag{8}$$

where $S_m = S(r_m)$ and $\beta_{m\epsilon} = \beta_\epsilon(r_m)$ (Klett (1981), p. 213). This solution assumes that the backscatter by the atmospheric aerosols dominates the molecular backscatter. At 1064 nm, the wavelength of the VIL, this assumption is valid and Equation 8 can be used to solve the lidar equation. To maintain the stability and accuracy of the solution, Equation 8 has to be integrated backwards from far ranges. The dependence of this form of the solution on $\beta_{m\epsilon}$ decreases with decreasing r.

Equation 1 can also be solved by using a calibration source. Previous studies have used the lidar signal above or below cirrus clouds as the calibration source. It has been assumed that the backscattered radiation at the chosen height was the result of only molecular scattering (Sassen (1989)). This method used a constant multiple scattering correction factor and made an additional assumption for a constant backscatter to extinction ratio for the cirrus particles. Uncertainties in this method are largely due to aerosols in the calibration layer which cause a larger than expected signal for the molecular backscatter. This leads to smaller than expected aerosol backscatter cross sections which cause underestimates in the cirrus cloud visible optical depth calculations.

For the two channel approach used by the HSRL, Equation 1 was separated into two equations: one for molecular backscatter and one for aerosol backscatter (Shipley et al. (1983)):

$$N_m(R)R^2 = \frac{N_o c}{2} A_r \beta_m(R) \frac{3}{8\pi} \exp^{-2\int_0^R \beta_\epsilon(r')dr'} \tag{9}$$

$$N_a(R)R^2 = \frac{N_o c}{2} A_r \beta_a(R) \frac{P_a(180,R)}{4\pi} \exp^{-2\int_0^R \beta_\epsilon(r')dr'} \tag{10}$$

where:

$N_m(R)$	=	number of incident photons on the receiver per unit time which were scattered by molecules from range R
$N_a(R)$	=	number of incident photons on the receiver per unit time which were scattered by aerosols from range R
N_o	=	number of transmitted photons
$\beta'_m(180,R)$	=	molecular backscattering cross section per unit volume (m^{-1} sr^{-1}) which depends upon the pressure and temperature of the air with height:

$$\beta'_m(180,R) = \frac{p(R)C_{air}}{T(R)} \tag{11}$$

where:

$p(R)$	=	air pressure at range R (Pa)
$T(R)$	=	air temperature at range R (^{o}K)
C_{air}	=	$4.51944 \cdot 10^{-9}$ ^{o}K Pa^{-1} m^{-1} sr^{-1} (at 532 nm).

A rawinsonde profile gives the needed information to solve Equation 11. Using the calculated $\beta_m(R)$ at each range (using Equation 3 and Equation 11), $\beta_\epsilon(R)$ can be determined by inverting Equation 9:

$$\beta_\epsilon(R) = -\frac{1}{2}\left[\frac{d(\ln(N_m(R)R^2)))}{dR} - \frac{d(\ln(\beta_m(R))}{dR}\right]. \tag{12}$$

Equation 11 gives a calibrated target at every range. This calibration target can be used to solve for the aerosol backscatter cross section per unit volume by

taking the ratio of the two scattering equations (Equation 9 and Equation 10) and rearranging terms:

$$\beta'_a(180, R) = \beta_m(R)\frac{3}{8\pi}\frac{N_a(R)}{N_m(R)}. \tag{13}$$

If gaseous and particulate absorption are negligible (extinction is just a result of scattering processes) then the aerosol scattering cross section is:

$$\beta_a(R) = \beta_\epsilon(R) - \beta_m(R). \tag{14}$$

The integration of $\beta_\epsilon(R)$ with range determines the aerosol visible optical depth (τ_v):

$$\tau_v = \int_0^R \beta_\epsilon(r')dr'. \tag{15}$$

Knowledge of $\beta_a(R)$ enables the calculation of the aerosol backscatter phase function:

$$\frac{P_a(180, R)}{4\pi} = \beta_m(R)\frac{3}{8\pi}\frac{N_a(R)}{\beta_a(R)N_m(R)}. \tag{16}$$

This set of equations shows the advantage of the HSRL over a single channel lidar system. The HSRL configuration allows for the direct calculation of the cirrus cloud visible optical depth, aerosol backscatter cross sections, and aerosol backscatter phase functions (if gaseous and particulate absorption are negligible).

2.2 VIL

The VIL is an elastic backscatter lidar which measures the three dimensional atmospheric structure. This instrument scans the atmosphere in both azimuth and elevation angles using a wavelength of 1064 nm. The VIL typically scans the

atmospheric structure in two directions, parallel and perpendicular to the wind direction at the cirrus cloud heights. A series of cross wind scans enables a three dimensional reconstruction of the cirrus clouds. This three dimensional view, using the advection of the clouds by the wind as the third dimension, reveals the cirrus mesoscale cloud morphology.

For CRSPE, the VIL scanned the atmosphere at approximately 9° a second with a time resolution of 85 seconds between consecutive scans. A typical VIL cirrus scan can be seen in Figure 1. The top cloud picture is a cross wind scan and the bottom picture is an along wind scan. The cross wind scan started at 357° (north), scanned overhead, and ended at 177°. This is called the cross wind scan because it was almost perpendicular to the wind direction at the cirrus cloud heights (the wind was approximately from the west-northwest at the cirrus cloud heights). After the completion of the cross wind scan, the azimuth angle of the system was rotated 90° to begin the along wind scan. This scan started at 267°, scanned overhead, and completed at 87° (toward the east). This X scan was performed almost continuously for a three hour time period (18:08 - 21:20 GMT). For CRSPE, the VIL scanned 120 km of the atmosphere in the horizontal extent with a maximum distance between data points of 60 m.

The two VIL scan directions allow for two different views of the cirrus clouds. Precipitation from the cirrus clouds can be seen in the along wind scan due to the wind shear at the cirrus cloud heights. This can be seen in the bottom picture in Figure 1. The slope of the cirrus clouds with distance results from wind shear. The along wind scan also shows the cirrus clouds which will be advected over the VIL at later times. The cross wind scans show the cirrus cloud structure perpendicular to the wind. The cirrus clouds seen in the cross wind scans during this experiment usually had a higher degree of spatial variability than those observed in the along wind scans. These variations across the wind would not be seen by a vertically pointing ground based instrument.

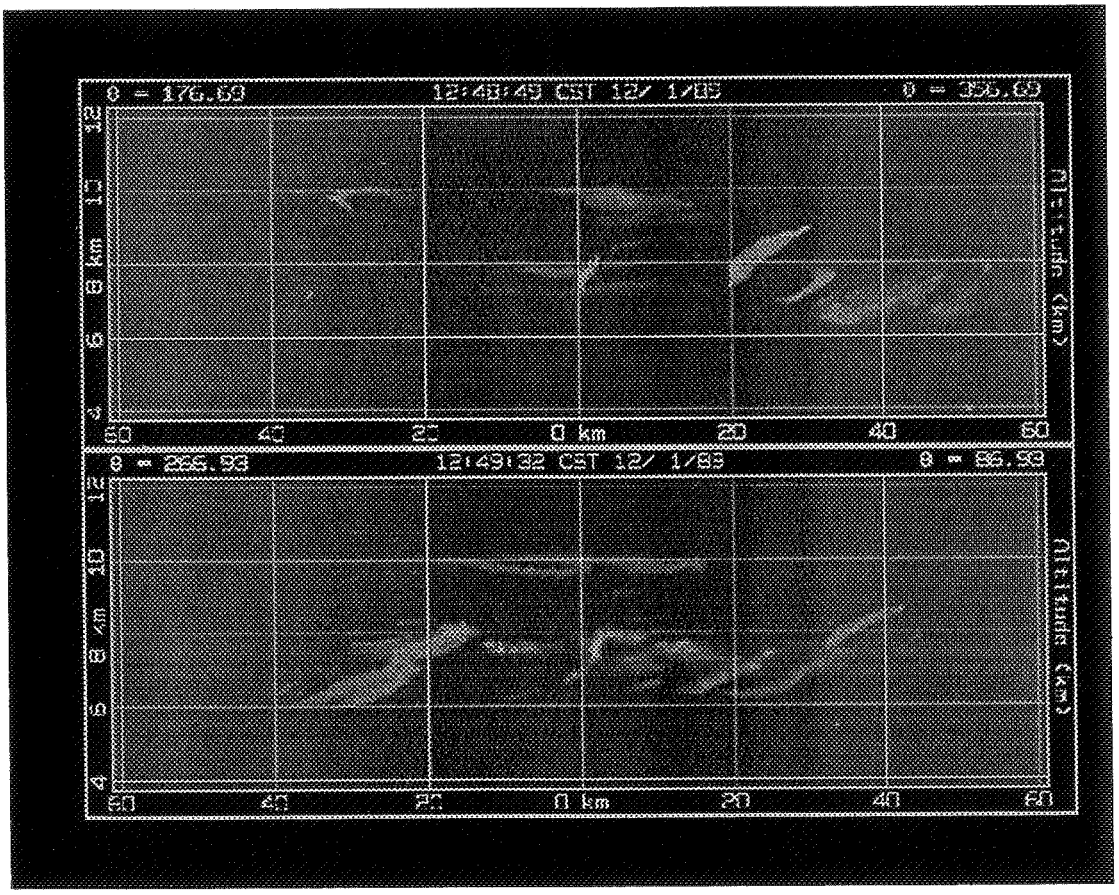

Figure 1: Typical cirrus clouds seen from 18:08 to 19:24 GMT. The x-axis is the distance from the VIL and the y-axis is height. The top picture is a cross wind scan; scanning from the North (357°) to the South (177°). The bottom picture is an along wind scan, scanning from West (267°) to East (87°). The scan times are given in local time (CST). Both scans show the cirrus cloud variability. Precipitating cirrus clouds are seen in the along wind scan.

2.3 VAS

The VAS, a radiometer on the GOES satellite, detects infrared radiation in 12 spectral bands that lie between 3.9 and 15 μm at 7 km or 14 km resolution (depending on the detector used) while also measuring at visible wavelengths with a 1 km resolution. The infrared channels have a 7 km resolution at nadir above the equator and a 10 km resolution viewing the atmosphere above Madison, Wisconsin. The upwelling longwave radiation in the 11 μm channel was used to determine the cirrus cloud infrared emissivity and optical depth. The upwelling radiation was converted into a temperature for each pixel using Planck's Radiation Law. The cirrus infrared emissivity was then calculated using the following equation:

$$\epsilon_{ir} = \frac{T_{sfc}^4 - T_{sat}^4}{T_{sfc}^4 - T_{cld}^4} \tag{17}$$

where:

T_{sfc} = brightness temperature for a clear pixel
T_{sat} = brightness temperature detected by the radiometer
T_{cld} = temperature at the mid-cloud height.

T_{sfc} used in Equation 17 was determined from a satellite pixel where it was assumed that no clouds were present (a clear pixel). Clear pixels were determined with help from the VIL since subvisible cirrus clouds were present during the experiment. The cirrus mid-cloud heights were calculated from the VIL cross wind scans. The cloud temperatures associated with the cirrus mid-cloud height were determined from coincident rawinsonde measurements. The rawinsondes were launched from the HSRL site during this experiment.

2.4 Instrumentation Locations

For CRSPE, the VIL was located near Pine Bluff, Wisconsin (43.06° N Latitude and 270.30° E Longitude) while the HSRL was located to the east in Madison,

Wisconsin (43.08° N Latitude and 270.58° E Longitude). The HSRL was located a distance of 24 km from the VIL at an azimuth of 87° (1.26 km North and 23.97 km East of the VIL). One of the VIL scan planes was aligned over the position of the HSRL viewing the same cirrus clouds as the HSRL. In relation to Pine Bluff, Wisconsin, the VAS was situated at a zenith angle of 52.90°, an azimuth angle of 244.58°, and a distance of 38017.73 km. The time periods of the experiment under investigation are from 18:07 to 19:24 GMT and from 19:29 to 21:20 GMT on December 1, 1989. The separation of the time periods was a result of a break in the VIL data set. The wind speed, wind direction, temperature, and pressure at the cirrus cloud heights were determined from coinciding rawinsonde profiles. There were four rawinsondes launched from Madison, Wisconsin on December 1, 1989, two of which were used: 18:00 GMT and 21:24 GMT. To create individual profiles between these times, the rawinsonde data was linearly interpolated between the 18:00 and 21:24 profiles.

Three remote sensing instruments were used to determine the cirrus cloud optical and structural properties. The VIL was used to determine the cirrus cloud structural properties since it viewed the three dimensional cirrus cloud structure. Cirrus cloud cover percentages and horizontal structure functions were calculated from the three dimensional data. The VIL area averaged cirrus cloud structure was compared to the cirrus cloud structure measured by the HSRL. This allowed for the determination of the sampling errors associated with cirrus cloud point measurements. To calculate the cirrus cloud optical properties, all three remote sensing instruments were used. The HSRL was used to calibrate the VIL to determine the visible cirrus cloud optical properties throughout a mesoscale volume. The VAS was used to determine the infrared cirrus cloud optical properties for the same volume.

3 Cirrus Cloud Mesoscale Structure

Many previous measurements of the cirrus cloud morphology have been made using ground based vertically pointing instruments. These cloud measurements were aligned along the wind due to the advection of atmospheric structure over the instrument. Attempts by these point measurements to represent the general cirrus cloud structure relied on the uniformity of the clouds throughout the area under consideration. If the cirrus clouds varied significantly across the wind, then point measurements along the wind could not be used to represent the large scale cirrus cloud structure. The VIL cirrus cloud scans were used to observe the cirrus cloud structure in an atmospheric mesoscale volume. Cirrus cloud structural variations within this volume were used to determine the cirrus cloud variability and the sampling errors associated with cirrus cloud point measurements.

During CRSPE, the VIL scanned a volume of the atmosphere containing cirrus clouds. Each cross wind scan showed a two dimensional picture of the cirrus clouds. A time series of cross wind scans revealed the three dimensional cloud structure where it was assumed that there was no time variation during the advection of the cirrus clouds by the wind. Once a cirrus cloud threshold value was chosen for the VIL data within the volume, the cloud cover percentage and horizontal structure within the mesoscale volume could be calculated from consecutive cross wind scans. A cirrus cloud threshold denotes the smallest backscattered signal considered to be from a cirrus cloud. A threshold value was determined by examining a histogram of the VIL backscattered signal from the cirrus cloud heights, 6 to 11 km, for the time periods under consideration (Figure 2). A clear distinction between cirrus cloud backscatter and the background aerosol backscatter was seen. The range squared, energy normalized VIL data greater than the chosen threshold value (3.48 in Figure 2) was assumed to have been backscattered from the cirrus cloud ice crystals. Backscatter values smaller than the threshold were considered to be the result of non-cirrus aerosols and molecules. Since the threshold was chosen from a series of VIL cross wind scans, the cirrus cloud threshold value was constant for

the whole data set. Only data within a horizontal distance of 30 km from the VIL was used in the cirrus cloud determination. The 30 km distance was chosen to retain a consistent threshold value throughout the data set. When the distance to the scatterers becomes large, the VIL signal becomes instrument limited causing the thinner cirrus clouds to go undetected. The calculations of the cirrus cloud structure are done in the following subsections.

3.1 Horizontal Cirrus Cloud Structure

The cirrus cloud threshold determined in the previous section allows the cirrus cloud structure to be examined. To calculate the cirrus cloud cover percentage within the mesoscale volume, RTI (Range Time Indicator) profiles were created at 100 m intervals along the VIL cross wind scan up to a distance of 30 km from the VIL. A RTI is a plot of the backscattered signal where time is the x-axis and altitude is the y-axis. A total of 601 RTIs were created for each time period. Consecutive points in each RTI were separated by 85.5 seconds, the time between consecutive cross wind scans. The cross wind scan time separation was converted into a distance by using the average wind speed measured by the rawinsonde at the cirrus cloud heights. An average wind speed of 35 ms^{-1} resulted in a distance between scans of approximately 3 km. The RTIs simulated 601 vertically pointing lidar systems situated across the wind at 100 m intervals. The cloud cover percentage from each RTI shows the cloud cover that would be observed by a vertically pointing lidar system at that position. To determine the presence of cirrus clouds, the VIL backscattered signal between the heights of 6 and 11 km in each simulated vertical profile was compared to the cirrus cloud threshold value. If any of the data points between the given heights for each vertical profile (for each simulated RTI) had a value greater than the cirrus cloud threshold value, then that RTI point contained cirrus clouds. Otherwise the point was labeled clear.

The cloud cover percentage calculated from the simulated RTIs was used to determine the spatial variability of cirrus clouds within a mesoscale volume. A direct

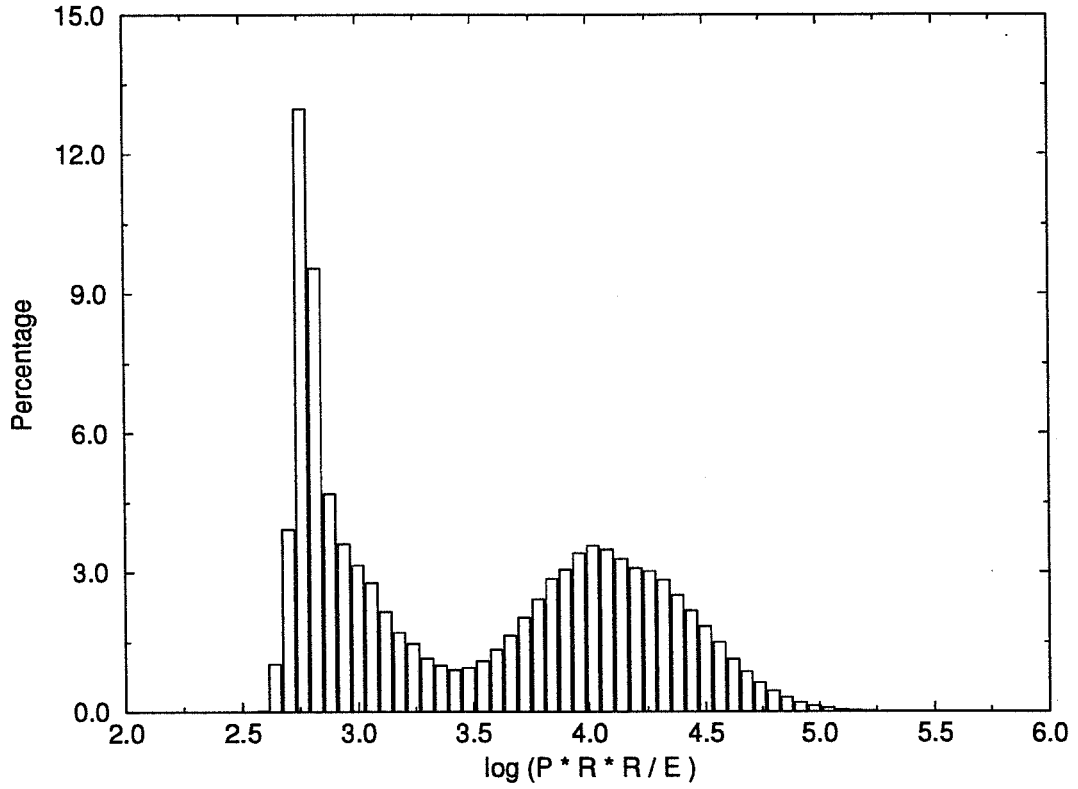

Figure 2: 50 point histogram of the VIL signal from the cirrus cloud heights, 6 km to 11 km. The x-axis is the logarithm of the VIL range square corrected, energy normalized signal. The y-axis is the percentage of points in each interval. Notice the local minimum near 3.5. This shows a clear separation between the cirrus cloud ice crystal backscatter and the background aerosol and molecular backscatter at 1064 nm.

comparison of average cloud cover seen by the VIL and the cloud cover detected by individual VIL RTIs shows the difference between point and area measurements of the cirrus cloud structure. Cirrus cloud-nocloud structure functions was calculated to determine the horizontal dimensions of the cirrus clouds and the distance separating the individual cloud structures. A cross wind structure function was used to determine the separation between and length of the cirrus clouds across the wind. An along wind structure function was used to determine the length of the cirrus clouds and the distances separating these clouds along the wind.

A three hour time period on December 1, 1989 was investigated. As described earlier, this three hour data set was split into two sections which were chosen as a result of the continuity of the VIL data. The first time period extended from 18:08 to 19:24 GMT and the second from 19:29 to 20:21 GMT on December 1, 1989. The earlier period contained a large amount of scattered cirrus clouds while the later period had some scattered cirrus clouds early but at 20:30 GMT a widespread precipitating cirrus cloud deck was advected into the region.

3.1.1 Cirrus Cloud Cover Percentage

Cirrus cloud cover percentages were calculated for the VIL simulated RTIs and the HSRL RTI for the two time periods. To compare the VIL and HSRL cloud cover percentage values, the HSRL data had to be shifted upwind to the position where the same cirrus clouds occurred in the VIL scans. This time shift ($\sim$10 minutes) was used to match the two data sets. The shift was determined from the distance between the two systems and the average wind speed at the cirrus cloud heights. The average wind direction at the cirrus cloud heights, determined by the rawinsonde, was used to calculate the direction to shift the HSRL data upwind. The HSRL shifted RTI and VIL simulated RTI cirrus cloud cover percentages were then compared for the two data periods.

For the first time period (18:08-19:24 GMT), broken cirrus clouds were advected into the region from 278° to 297° at wind speeds ranging from 26 ms^{-1} to

40 ms^{-1}. Cirrus cloud cover percentages were calculated for the 60 km of VIL vertical profiles spaced every 100 m (Figure 3). The individual RTIs show cirrus cloud cover percentages ranging from 54.7% 17.2 km south of the VIL to 100% both directly above the VIL and 30 km to the north of the VIL. The mean cloud cover was 81.5% for the mesoscale volume. The maximum difference in cloud cover between two RTIs in the 60 km spread was 45.3%. The maximum cloud cover difference between two RTIs 10 km apart was 27.8%. For the same time period, the time shifted HSRL data had a cloud cover percentage of 100%. Since the VIL along wind scan was not perpendicular to the wind axis, the cirrus clouds seen by the HSRL passed 5.54 km to the north of the VIL.

There are a couple of interesting features to note in Figure 3. A cloud cover percentage of 100% was seen directly above the VIL. This maximum was the result of a very thin cirrus cloud layer located at a height of 10 km, the tropopause. This high cloud cover percentage was the result of specular reflection from ice crystals. Specular reflection occurs when higher than normal signal is backscattered to the receiver due to specific ice crystal orientations. When the cirrus cloud ice crystals are in the form of plates they can become positioned such that their flat surfaces are parallel to the ground. This plate orientation causes enhanced laser backscatter when the lidar at the ground is viewing vertically. Directly above the VIL specular reflection occurred but the backscattered signal off the vertical did not show this enhanced backscatter. This reveals the importance of tilting the receiver of a vertically pointing lidar system slightly off of the vertical. For this early time period, the HSRL saw 100% cirrus cloud cover due to the oriented ice crystals. The VIL also detected signal from this height but the backscatter signal was smaller than the threshold value, causing the VIL to miss these clouds (except for the cases where specular reflection occurred). During this experiment, the HSRL was tilted off of the vertical to remove the occurance of specular reflection. The 100% cirrus cloud cover percentage seen by the HSRL shows that specular reflection was a problem and that the HSRL receiver was not tilted as far off of the vertical as was originally thought.

A second interesting feature in Figure 3 was the variation of the cirrus clouds within the volume. By comparing the cirrus cloud cover at 17.2 km and 24.7 km to the south of the VIL, a cloud cover difference of 27.8% was seen. This difference shows the variability of cirrus clouds across a short distance (7.5 km) even when the cloud cover is averaged in time. This cirrus cloud variability shows possible sampling errors when point measurements are used to represent the cirrus cloud cover over an area. A point measurement made at either 17.2 km or 24.7 km south of the VIL could not accurately describe the general cirrus clouds structure within a mesoscale volume. This reveals the difficulties encountered when using a single vertically pointing system to describe the cirrus cloud spatial structure over a large area. The variation of cirrus clouds within a small region suggests a need to view cirrus clouds throughout the mesoscale volume.

Since cirrus clouds affect the incoming solar radiation, an error in the cirrus cloud cover percentage will result in changes in the calculated visible radiative flux reaching the surface of the Earth. The magnitude of the change in the calculated visible radiative flux will determine whether the cirrus cloud cover needs to be considered when discussing climate warming. To estimate the magnitude of this change in the incoming solar flux, consider a simple calculation for the change in the direct solar flux due to an incorrect cirrus cloud cover percentage:

$$\Delta F = \mu_o \frac{r_o^2}{r^2} \mid S_{con} \Delta P_{clr} + S_{con} \Delta P_{cld} T \mid \tag{18}$$

where:

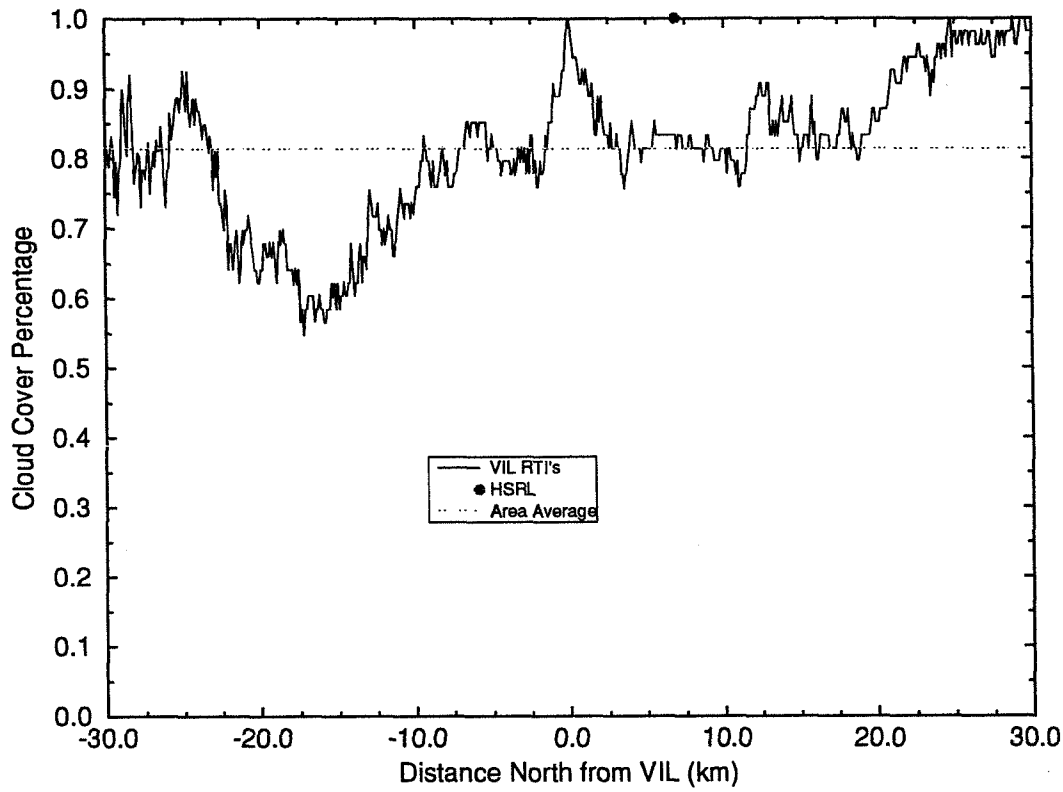

Figure 3: Cloud cover percentages calculated for 601 simulated RTIs for the time period 18:08 to 19:24 GMT on December 1, 1989. The x-axis is the distance from the VIL (north is positive). The y-axis is the cloud cover percentage. The solid line is cloud cover percentages for each VIL simulated RTI (consecutive RTIs are separated by 100 meters). These cloud cover percentages are aligned along the wind resulting in a time average of the cirrus clouds for each RTI. The solid circle is the time shifted HSRL cloud cover percentage. The dashed line is the average VIL cloud cover percentage for this time period. Note the specular reflection directly above the VIL.

S_{con} = mean annual solar constant (1380 W m^{-2})
ΔP_{clr} = change in percentage of sky which is clear ($-\Delta P_{cld}$)
ΔP_{cld} = change in percentage of sky which is cloudy
T = transmission through the cloud ($\exp(-\tau_{vis})$)
τ_{vis} = visible scattering optical depth
μ_o = cosine of the solar zenith angle
r_o = mean Earth-Sun distance
r = actual Earth-Sun distance

On the right hand side of Equation 18, the first term is the change in radiance produced from the transmission of the solar radiation through the cloudless atmosphere while the second term is the change in radiance error produced from the transmission of solar radiation through the cirrus clouds. The absolute value was taken because we are only interested in an estimate of the magnitude of the change of the incoming solar radiation, not whether warming or cooling would occur. For the Earth, μ_o is described as the following:

$$\mu_o = \sin\delta \sin\phi + \cos\delta \cos\phi \cos\omega \tag{19}$$

where ϕ is the latitude and δ is the solar declination angle which is defined as:

$$\delta = 23.45 \sin(\frac{360^o}{365}(d_n + 284)) \tag{20}$$

with d_n as the day of the year. The hour angle, ω, is defined as:

$$\omega = -15^o H \tag{21}$$

where H is number the of hours from local noon. $\frac{r_o^2}{r^2}$ can be rewritten in the following form:

$$\frac{r_o^2}{r^2} = 1 + 0.033\cos(\frac{360^o d_n}{365}) \quad (22)$$

Equations 18 to 22 were used to estimate a change in the direct visible radiative flux seen at the surface of the earth due to an incorrect cirrus cloud cover. The cloud cover percentage error used for the first time period was the difference between the minimum and maximum VIL RTI cloud cover percentages. The HSRL cloud cover percentage for the same cirrus cloud deck was not used because of possible contamination by specular reflection. The absorption of solar radiation by the atmospheric constituents was neglected in these calculations. For the first time period, the transmissivity of the cirrus clouds at solar wavelengths was defined by the cirrus cloud visible optical depth measured by the HSRL, $\tau_{vis} = 0.257$.

An estimate of the change in solar flux at the surface of the earth for Madison, Wisconsin at 13:00 GMT on December 1, 1989 was calculated using Equation 18. For this time period, a 45.3% difference in cirrus cloud cover resulted in a change of 58.18 Wm^{-2} seen at the surface of the Earth. The magnitude of this error was approximately 14 times greater than the effects due to the doubling of CO_2, 4 Wm^{-2}. Obviously an incorrect cloud cover will have an important effect on both the radiative balances occurring in the atmosphere and the models simulating the radiative and dynamical structure of the Earth's atmosphere. Even though Equation 18 does not incorporate the Earth's surface albedo or absorption by atmospheric gases, it does show the need for the accurate simulation of cirrus clouds and their global coverage.

For the later time period (19:29 to 21:20 GMT), scattered cirrus clouds were present until 20:30 when a widespread, three kilometer thick, cirrus cloud deck was advected into the region from approximately 277°. The area averaged cloud cover for the VIL was 76.8%, 4.7% smaller than the previous time period. The HSRL cloud cover was 67.9% (Figure 4), resulting in a cloud cover difference between the two systems of 8.9%. The minimum cloud cover detected by a VIL RTI was 59.0%, from 0.7 to 1.0 km north of the system. The maximum detected cloud cover was 100%, 29.8 km to the north. A maximum cloud cover difference of

41.0% was seen between the VIL RTIs. The maximum cirrus cloud cover difference detected between RTIs separated by 10 km was 30.8%. Again large variations in the cloud cover were noticed depending on the location of a vertically pointing lidar. Specular reflection does not have as large of an effect on the cloud cover percentages because most of the cirrus clouds were lower and optically thicker than the previous time period. Also, the thin cirrus layer at the tropopause was not detected after 20:00 GMT.

By using Equation 18 for Madison, Wisconsin at 14:30 GMT on December 1, 1989, with an average $\tau_{vis} = 0.428$ for the cirrus clouds (measured by the HSRL), a change of 12.36 Wm^{-2} was seen at the surface of the Earth. This value was approximately five times smaller than the previous time period. The early time period had a large cloud cover difference and small optical depth. The latter had a smaller cloud cover difference and a larger optical depth. It also had less incident solar radiation due to the time of day. There were compensating effects during the second time period due to the larger optical depth and the smaller cloud cover difference. The larger cirrus cloud optical depth reduced the incoming solar radiation more than the earlier time period but the smaller cirrus cloud cover percentage difference decreased the effect of the cirrus clouds on the radiation balance. The change in the radiative flux caused by cirrus clouds for either time period would dominate the atmospheric temperature increases caused by the doubling of CO_2. This implies that knowledge of the spatial structure is very important in understanding the radiative effects of cirrus clouds on the climate.

As was previously shown, cirrus clouds can vary significantly over a mesoscale area. Very precise point measurements of cirrus clouds will not give reliable statistics of the cirrus clouds due to the cloud sampling errors. Better instruments which only measure a vertical profile through the atmosphere would not be able to accurately describe the influence of the cirrus cloud spatial structure on the climate because of the sampling errors. Even a very long time average would not give an accurate description of the cirrus clouds. The long time average would be biased because the clouds have to be advected over the instrument. The cross wind

cirrus cloud variation would not be detected, and, as shown previously, this can be significant (especially if the cirrus clouds tend to align along the wind direction). Although the VIL has been used to determine the cirrus cloud spatial structure throughout a mesoscale volume, the effects of this cirrus cloud variation on the Earth's radiation balance has yet to be determined.

In some models which simulate the effects of cirrus clouds on the Earth's radiation balance, the three dimensional cirrus clouds have been averaged to produce a cirrus cloud layer with the equivalent radiative properties, an 'equivalent uniform layer'. This reduction in complexity of the cirrus cloud radiative properties can be achieved for the radiative effects of the cirrus clouds at one wavelength of radiation according to the mean value theorem. Complexities arise in this process when the radiative effects of the cirrus clouds has to be described at two different wavelengths, say at both visible and infrared wavelengths. In this case, the radiative effects at both wavelengths have to be matched within the equivalent uniform layer of cirrus clouds, which may not be possible. Even if an equivalent uniform layer was used, the radiative properties of the cirrus clouds may be reproduced but the dynamical structure of the atmosphere would not be reproduced. Since clouds are an integral part of the atmosphere they affect both the radiative balance and the dynamical structure. An equivalent uniform cloud field will not have the same dynamical effect as multi-layered scattered cirrus cloud field. As an example, if a previously uniform cirrus cloud field was evaporating and breaking up, then there would be regions of subsidence within the cloud field. This will not be simulated in a model using an equivalent uniform layer as a parameterization for cirrus clouds.

3.1.2 Structure Functions

A cirrus cloud-nocloud horizontal structure function was calculated for the three hour time period, 18:08 - 21:20 GMT (Figure 5), using the following equation:

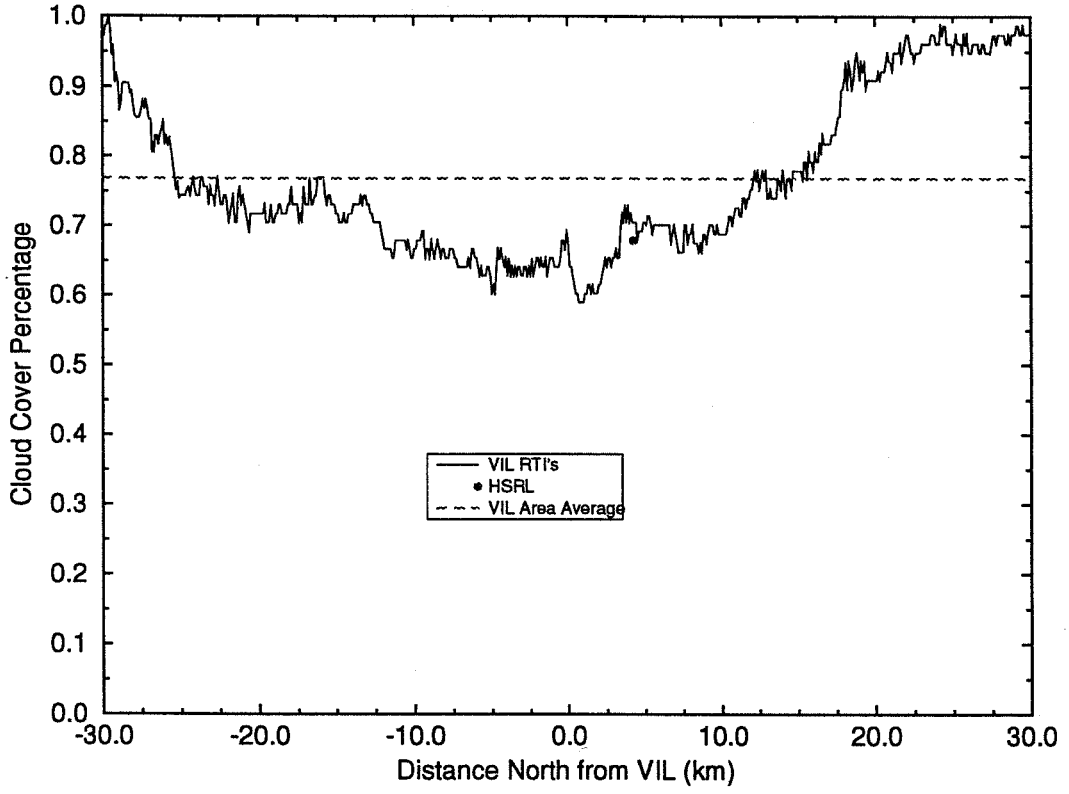

Figure 4: Same as Figure 3 except for the time period from 19:29 to 21:20 GMT on December 1, 1989.

$$SF_{AA}(l) = \frac{1}{N-l} \sum_{k=0}^{N-l-1} [A_k - A_{k+l}]^2 \tag{23}$$

where:

A_k	=	the cloud-nocloud value (either 1 or 0) at point k
A_{k+l}	=	the cloud-nocloud value (either 1 or 0) value at the point $k + l$
l	=	lag
N	=	number of points

A maximum in the structure function shows a negative correlation between points separated by the lag, i.e. length of the cloud; a relative minimum indicates a positive correlation between points separated by the lag, i.e. the distance between clouds (except at zero separation which is defined to be zero). For the structure function, the width (or length) of the cloud occurs at a local maximum. This was not the half-width of the cloud because if the lag was equal to half the cloud length, an increase in the lag would cause an increase in the structure function. Structure functions were determined both along and across the wind. For the structure functions aligned with the wind, the lag was a function of time. This lag was converted into a distance using the average rawinsonde measured wind speed at the cirrus cloud heights. The along wind structure function was used to determine the length of the cirrus clouds and distance between cirrus clouds. For the cross wind structure functions, the lag was a function of distance. The cross wind structure functions shows the the length of the cirrus clouds and the distance between clouds across the wind.

A series of along wind structure functions were calculated for the 60 km of VIL data for the combined 3 hour time period (Figure 5). The plotted structure functions consist of individual structure functions 25 km north and south of the VIL, a structure function for the cirrus clouds occurring directly above the VIL, and an area averaged structure function. A large amount of variation between

the individual structure functions was seen in Figure 5. The along wind structure function 25 km to the north revealed approximately a 6 km (3 minute) length for the cirrus clouds. This structure function had very little variation because 25 km to the north of the VIL the sky had over 95% cloud cover as seen in Figures 3 and 4. The structure function 25 km to the south of the VIL showed a separation between clouds of approximately 262 km (125 minutes) with a cirrus cloud length of 147 km (70 minutes). The cirrus clouds directly overhead had a separation of 262 km (125 minutes) with a 141 km (67 minutes) cloud length. The average structure function for the mesoscale region imaged by the VIL revealed a 273 km (130 minutes) separation between clouds and an average cloud length of 130 km (62 minutes). Smaller scale oscillations were embedded on the individual structure functions. These oscillations show small scale variations in the cirrus features. The effects of the area averaging can be seen in the average structure function where the small scale oscillations have been smoothed out. The half width of the cirrus cloud, 65 km, shows the average distance that a satellite has to move its field of view along the wind direction to view the ground. If a vertically pointing system were used to determine the cirrus cloud structure, the result would be a single structure function defining the whole region. As was seen here, this would not be representative of the volume.

The average cross wind structure function is shown in Figure 6. This structure function increases slowly with the lag because a greater percentage of the cirrus clouds occurred to the north of the VIL. The movement of a widespread cirrus cloud deck from the northwest into a region which previously contained scattered cirrus clouds biased the structure function to larger lag distances. The average cross wind structure function shows cirrus clouds with lengths of 14 km and 43 km. The distance between cirrus clouds was 24 km. As expected, the cross wind structure function was very different than the along wind structure function during this time period. The length of the cirrus clouds along the wind was about 9 times larger than the cirrus cloud length across the wind. The difference in the

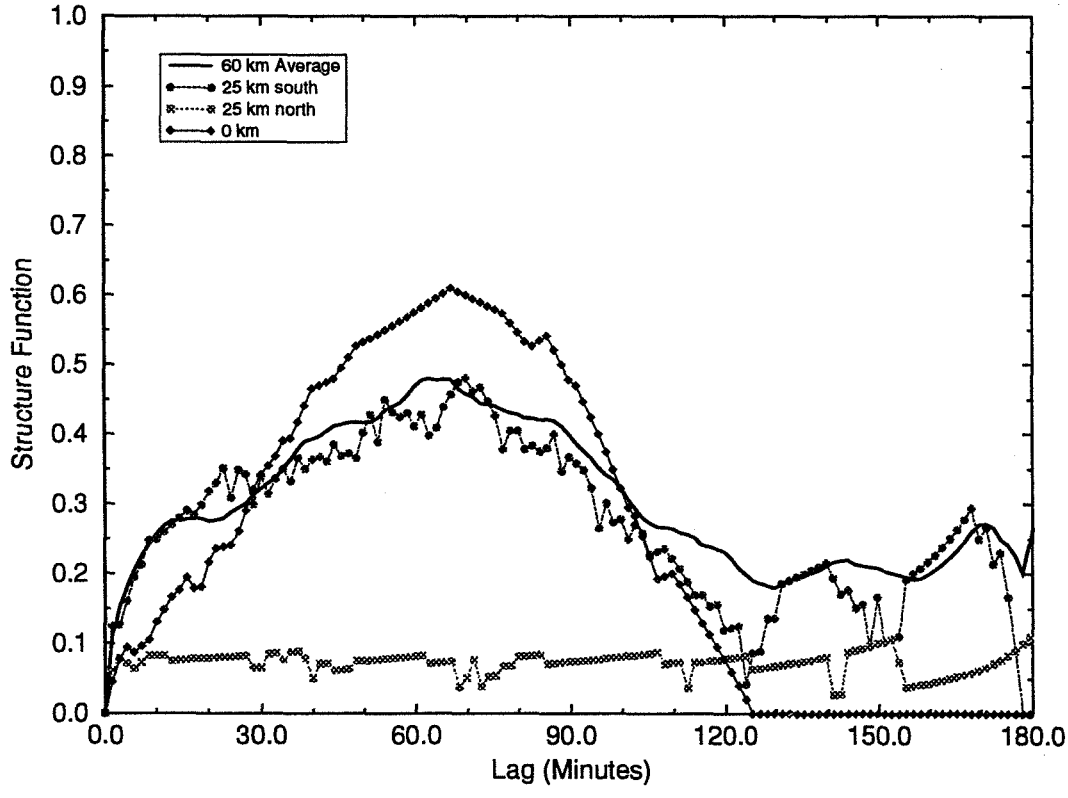

Figure 5: Along wind structure functions for December 1, 1989, from 18:08 to 21:20 GMT, calculated from the VIL simulated RTIs. The x-axis is the lag in the structure function in minutes (1 minute is approximately 2100 meters). The y-axis is the cloud-nocloud structure function. Plotted are: the average along wind structure function for the 60 km spread (thick solid line), structure function for a RTI 25 km south of the VIL (circles), structure function for an RTI 25 km north of the VIL (squares), VIL structure function for a RTI directly overhead (diamonds). More detailed explanations are in the text.

average structure functions for the two scan directions results in an aspect ratio (length/width) of 9:1 for the cirrus clouds. This aspect ratio suggests that, for this experiment, the cirrus clouds tended to be aligned along the wind. A longer time period has to be analyzed to get a better understanding of the average cirrus cloud horizontal structure.

To get a statistically accurate measurement of the distance between clouds the structure function has to become either independent of the lag or a constant which is periodic with the lag. This was only seen for the individual cirrus cloud structure function 25 km to the north of the VIL. The other structure functions gave local measurements of the cirrus cloud structure since the structure function varied with the lag. A longer time period is needed to get better cloud cover statistics for the structure function calculations. This process can be performed on the FIRE II VIL data set.

3.2 Vertical Cirrus Cloud Structure

The vertical cirrus cloud structure during the two time periods was very complex. From 18:08-19:24 GMT, there was mostly scattered optically thin cirrus clouds which occurred both individually and in layers as seen in Figure 1. The lowest level clouds occurred at a height of 6 km while the highest cirrus clouds were seen at 10 km. The uppermost clouds occurred at the tropopause and consisted of ice crystals as seen by the specular reflection from the layer (as described in Section 3.1.1). The majority of the cirrus clouds occurred between the heights of 6 and 9 km, often overlapping at different levels. Occasionally, a precipitating cirrus cloud advected into the region at a height of 8 km between 25 km north and 25 km south of the VIL. These precipitating cirrus clouds are seen in the bottom half of Figure 1, the along wind scan. Virga fell approximately 2 km from these clouds before evaporating. Most of the cirrus clouds during this time period were seen north of the VIL.

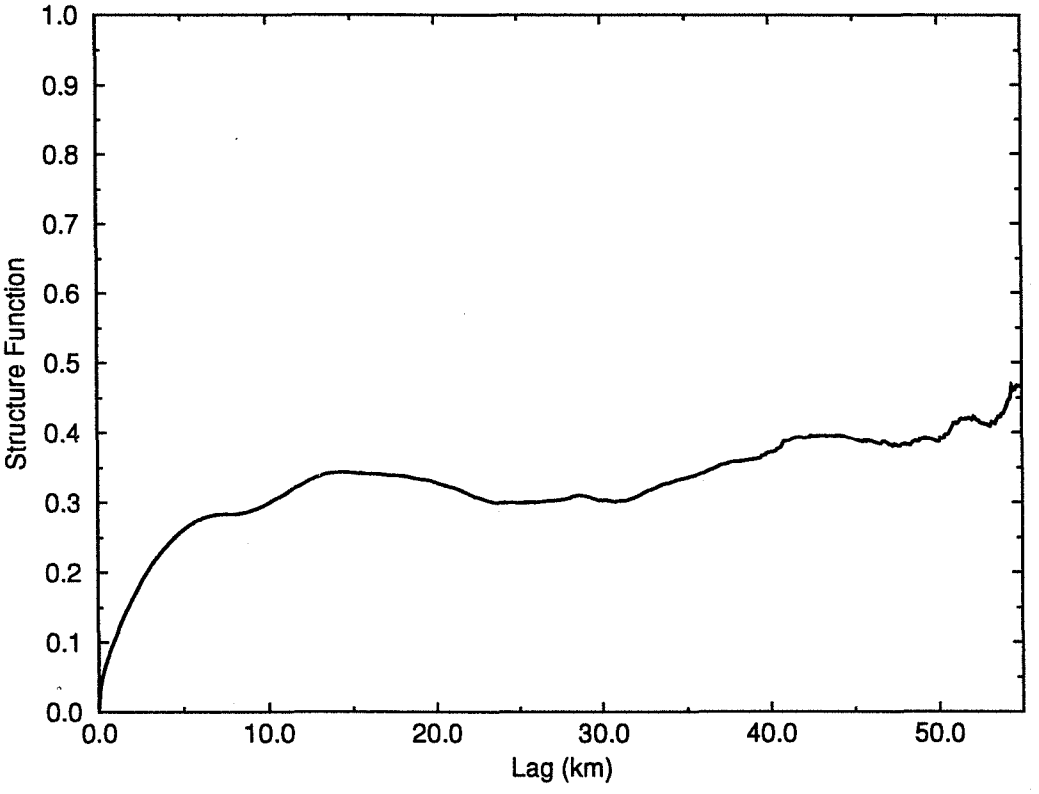

Figure 6: Cross wind structure function for December 1, 1989, from 18:08 to 21:20 GMT, for the 60 km of VIL data. The x-axis is the lag in the structure function in distance (km). The y-axis is the cloud-nocloud structure function. This plot shows the average cross wind structure function for the 3 hour time period. The minimum around 24 km shows the average distance between the cirrus clouds. The peak determines an average cirrus cloud cross wind length of 14 km.

For the second time period, 19:29 to 21:20 GMT, the cirrus clouds were more widespread. At 19:30 GMT, the cirrus clouds were similar to the earlier period with scattered thin cirrus clouds throughout most of the region. Again, these clouds often occurred in multiple layers. At 19:40 a precipitating cirrus cloud layer at a height of 8 km between 20 and 40 km to the south of the VIL moved into the region (Figure 7). This layer lasted for about one hour with virga falling 1 to 2 km below the precipitating layer. At 20:30 GMT, an extensive precipitating cirrus cloud deck advected into the region between 20 km south and 30 km north of the VIL (Figure 8). The precipitating layer occurred between heights 8.5 and 9.5 km with ice crystals falling to a height of 6 km. As the time period progressed, the cirrus cloud deck increased in optical thickness. Both to the north and south of the cirrus cloud deck multiple layers of thin cirrus clouds were seen. Also in Figure 8, the attenuation of the VIL signal can be seen. This loss of signal occurs between 7 km and 9 km further than 40 km north of the VIL and further than 30 km south of the VIL. The cirrus cloud layer at the tropopause was visible until 20:00 GMT.

3.3 Cloud Structure Summary

It has been shown that cirrus clouds are very complex in both the horizontal and vertical directions. These clouds are not homogeneous in either direction and can not be assumed so. Their complex structure needs to be viewed throughout a mesoscale sized volume to accurately describe the cirrus cloud spatial structure. These clouds have to be accurately described to understand the radiation balance in the Earth's atmosphere. The data set studied was only for a three hour time period. To better understand the general properties of the cirrus cloud spatial structure, a larger set of cirrus cloud data needs to be analyzed.

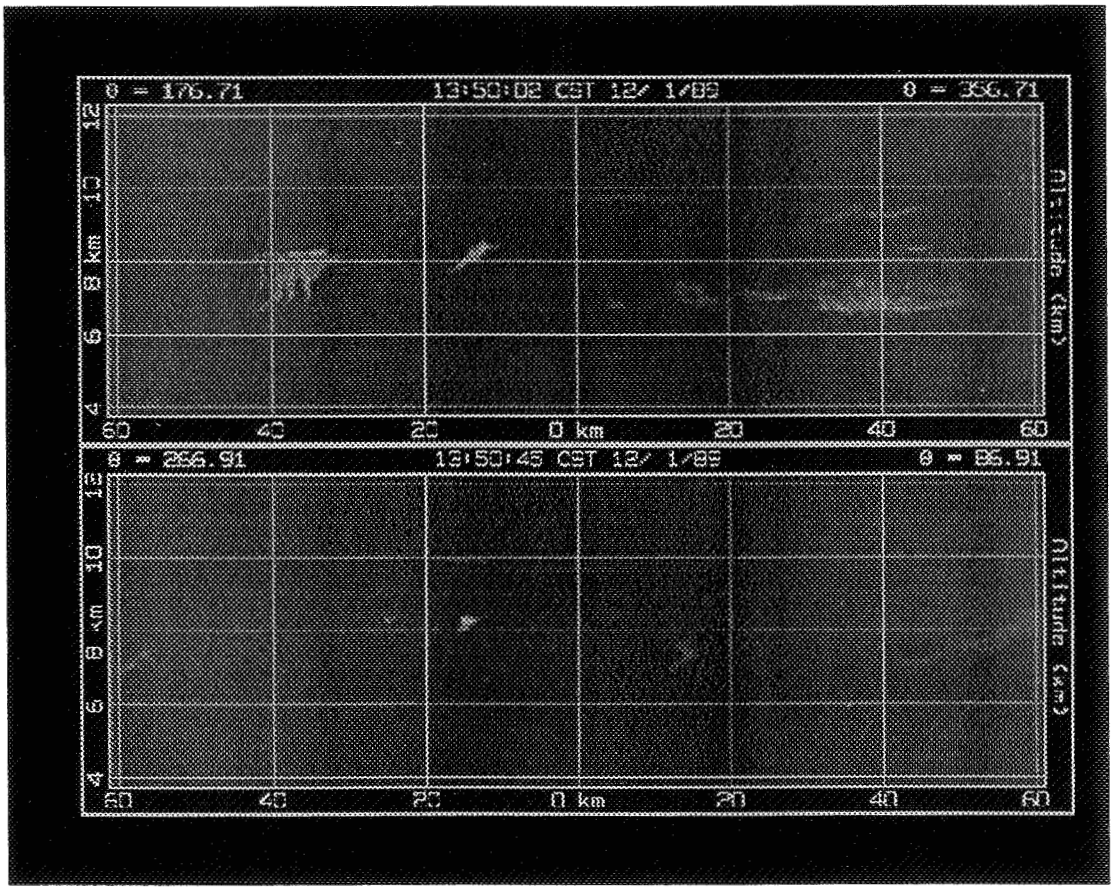

Figure 7: Typical cirrus clouds seen from 19:29 to 20:15 GMT. The x-axis is the distance from the VIL and the y-axis is altitude. The top picture is a cross wind scan, scanning from the North (357°) to the South (177°). The bottom picture is an along wind scan, scanning West (267°) to East (87°). The scan times are given in local time (CST). Both scans show the cirrus cloud variability.

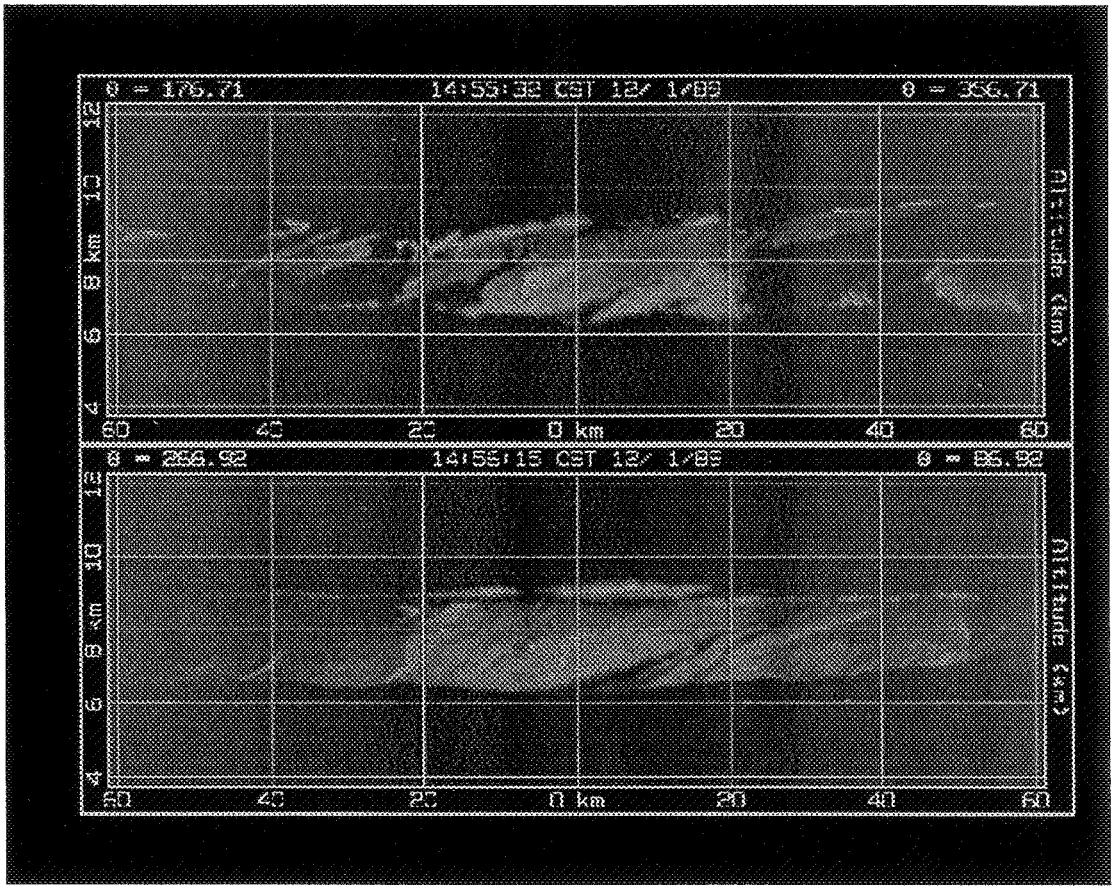

Figure 8: Same as Figure 7 but for the time period of 20:30 to 21:20 GMT. The precipitation from the cirrus clouds is easily seen in the along wind scan. Note the effects of attenuation at the longer slant paths in the bottom scan between 20 and 60 km West of the VIL near a height of 8km (also between 40 and 60 km East of the VIL at the same heights).

4 Cirrus Cloud Visible Optical Properties

Examination of the cirrus cloud structure has shown the advantages of a volume scanning system and the difficulties encountered by a vertically pointing instrument when attempting to describe the cirrus cloud spatial structure across a mesoscale volume. As shown by the simple radiative transfer calculations, the cirrus cloud optical properties play an important role in the radiation balance within the Earth-Atmosphere system. Like the cirrus cloud spatial structure, the cirrus cloud optical properties at visible and infrared wavelengths may vary significantly across a mesoscale volume. The visible optical depth influences the amount of solar radiation which passes through the cirrus clouds and reaches the lower levels of the Earth's atmosphere. The infrared optical depth moderates the amount of infrared radiation lost to space through these clouds. To understand the effects of cirrus clouds on the Earth's radiative budget, the cirrus cloud optical properties have to be known.

Previous attempts to determine the cirrus cloud visible optical depth, to compare to the cirrus cloud infrared optical depth, have been made using satellite based radiometers and ground based lidars. The calculations using satellite data could not independently determine the cirrus cloud visible optical properties since additional measurements of the cloud coverage and cloud types within each pixel were needed. These calculations also needed measurements of the reflectivity of the Earth's surface at the visible wavelengths for each pixel. Errors also occurred in the visible optical depth calculations due to poor calibrations of the visible channels. The visible channels were calibrated at the ground and the calibration has degraded over time. Ground based lidars have also been used to determine the cirrus cloud visible optical properties. The measurements by a vertically pointing lidar are limited by the instrument viewing capability. These lidars only observe the cirrus clouds advected over their position producing biased results due to the cirrus cloud spatial variability and the possible preferential alignment of the cirrus clouds. A volume scanning ground based lidar needs to view a large enough

volume of the atmosphere to remove pixel alignment errors associated with the direct comparison of the cirrus clouds viewed by the scanning lidar and the satellite radiometer (described in Section 5).

A new technique to calculate the cirrus cloud visible optical properties throughout a mesoscale volume is described in the following section. This method uses coincident cirrus cloud measurements from two ground based lidar systems, the VIL and the HSRL. The cirrus cloud visible aerosol backscatter cross sections calculated from the HSRL data are used to calibrate the VIL backscattered signal. The VIL cirrus cloud scans will then be used to extend the calibration to a mesoscale volume. This new calibration method, which uses data from two lidar systems, was attempted without previous knowledge of the errors associated with this calibration process.

4.1 Calibration Technique

The VIL and HSRL were aligned to view the same cirrus clouds during CRSPE. This alignment allowed the cirrus clouds to be used as a calibration target for the single channel VIL data. This calibration scheme was possible because the HSRL unambiguously determined the aerosol backscatter cross sections throughout the depth of the cirrus cloud as described in Section 2.1. The HSRL $\beta'_a(180, R)$ were directly correlated to the VIL backscattered signal for the simultaneously measured cirrus clouds. This was achieved using a cirrus cloud point comparison applied between the VIL backscattered signal and the HSRL $\beta'_a(180, R)$.

Before the VIL backscattered signal could be calibrated, corrections had to be made to the VIL data. The VIL backscattered signal which was at the limit of detectability of the receiver had to be removed from the data set. If these system limited points were included in the VIL–HSRL comparison, an erroneous VIL signal calibration would result. The technique to remove the instrument limited data points is described in Appendix A. After the system limited points were removed from the data set, the VIL signal had to be corrected for angular

dependencies in the data and/or possible temporal variations in the receiver (field of view changes or a change in gain of the avalanche photo–diode). This was accomplished by normalizing the VIL backscattered signal to a low level aerosol layer. This normalization technique, which required a spatially and temporally uniform aerosol layer to relate the VIL backscattered signal throughout time and space, is described in Appendix B.

After the corrections were made to the VIL data, a cirrus cloud point comparison between the VIL corrected raw signal and the HSRL $\beta'_a(180, R)$ was achieved. The VIL data which viewed the clouds over the HSRL were converted into an altitude verses time profile (RTI) simulating the HSRL data set. The HSRL RTI and VIL simulated RTI are shown in Figure 9. To create the VIL RTI, the backscattered signal was converted from spherical coordinates into cartesian coordinates. The VIL data was then averaged in distance around the HSRL site (24 km to the East of the VIL) to match the one minute averaging of the HSRL profiles. The average wind speed at the cirrus cloud heights was used with the averaging time of the HSRL data to determine the VIL averaging distance ($\sim$ 2 km). Errors between the positioning of the VIL and HSRL vertical profiles were caused by misalignments between the VIL along wind scan plane and the HSRL position (due to VIL scan angle errors). A cross correlation between the HSRL RTI and VIL RTI cloud points was calculated to find the best fit between the two profiles. The position of the peak in the cross correlation was compared to the position of the peak of an autocorrelation of the HSRL RTI data points. The difference between the peak positions for the two correlations revealed shifts between the two RTIs. For the 19:29-21:20 GMT time period, the VIL data was shifted one point (60 m) in the vertical and one point (one scan, 85 seconds or approximately 3 km) in the horizontal compared to the HSRL data. The horizontal and vertical shifts between the data sets can result from: misalignment between the VIL scan direction and the wind direction, scan angle errors, and/or inconsistent time measurements between the two systems. The misalignment of the VIL scan direction in relation to the wind direction can lead to significant errors if there are large spatial variations

in the cirrus cloud optical and structural properties. The associated errors result from the differences in the spatial averaging used to produce the HSRL and the VIL simulated vertical profiles. The HSRL data were averaged along the wind axis while the VIL data were averaged along the cirrus cloud scan axis; the two profiles were produced from different sections of the atmosphere. (The variations of the cirrus cloud particles and the associated errors are discussed at the end of this section.) Another problem can be the misalignment of the VIL along wind scan. Slight scan angle miscalculations will lead to relatively small distance errors. A 0.5° error in the scan angles (azimuth and/or elevation) will lead to a 200 m error in scan position with regards to the HSRL profile. This can easily account for the vertical shift between the two data sets. A third problem resulted from differing time records between the two systems. The HSRL clock times were taken from the telephone. The times were given to the minute so they were ± 30 seconds. The telephone time was then stored in a Whole Sky Imager computer. Over a two week period, this clock drifted tens of seconds. Therefore the HSRL times are believed to be ± 1 minute. The VIL times were set from the radio every day resulting in less than 5 seconds of error. A 1 minute error between the two data sets is approximately a 2 km error in the cirrus cloud comparison. The shift of the VIL simulated RTI in relation to the HSRL RTI can be accounted for by these errors.

The resulting profiles, HSRL RTI and the shifted VIL simulated RTI, were compared on a point by point basis. The result of this comparison can be seen in Figure 10. A straight line of slope one which best fits the cirrus cloud backscatter data was also plotted. This best fit straight line was used to calibrate the VIL data; it related the VIL backscattered signal directly to the cirrus cloud aerosol backscatter cross sections per unit volume calculated from the HSRL data. A one-to-one relationship was expected because of the assumption that the scattering by the ice particles was independent of the wavelength of the incident visible radiation.

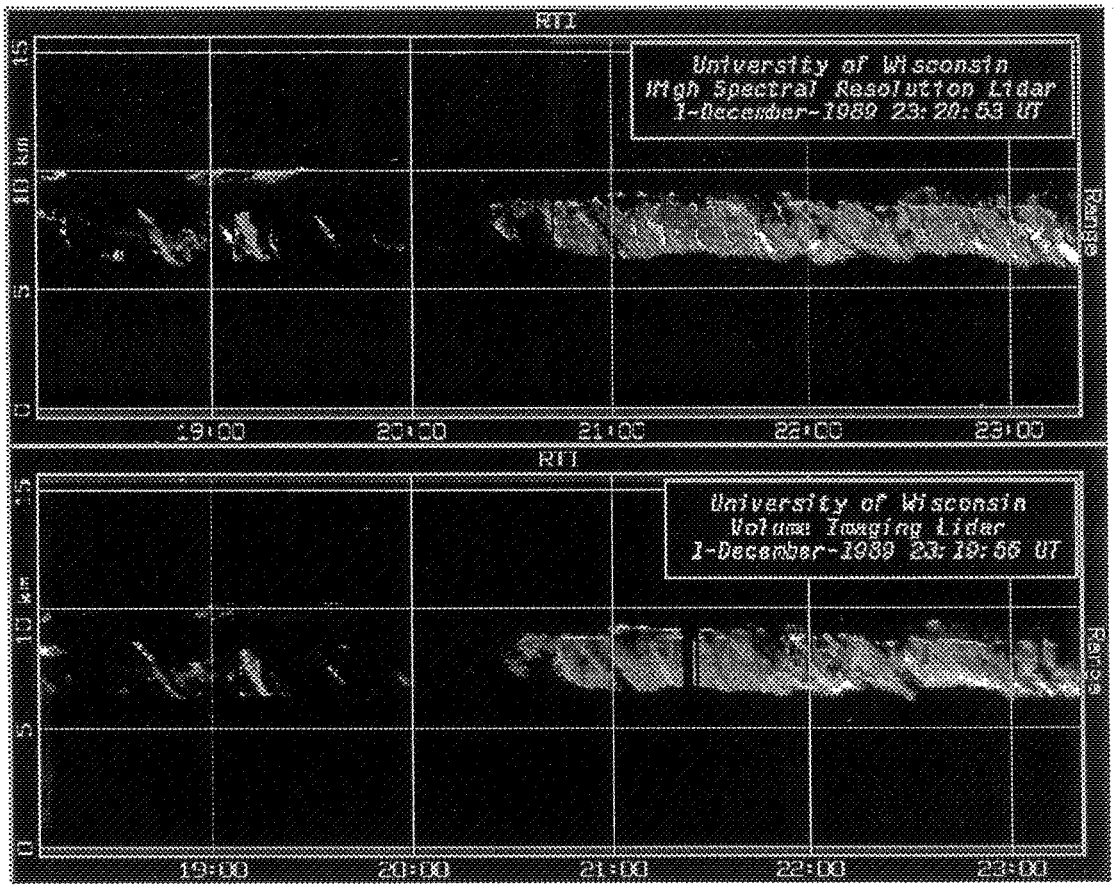

Figure 9: Comparison of cirrus clouds over Madison, Wisconsin from 18:08 to 23:20 GMT. The x-axis is time and the y-axis is altitude. The top picture is the HSRL RTI. The bottom picture is a VIL RTI 24 km East of the VIL over the HSRL. The VIL RTI is a synthetic RTI created from the VIL cirrus cloud scans to simulate the HSRL RTI. These two RTIs were used for the cirrus cloud point comparison between the two lidar systems.

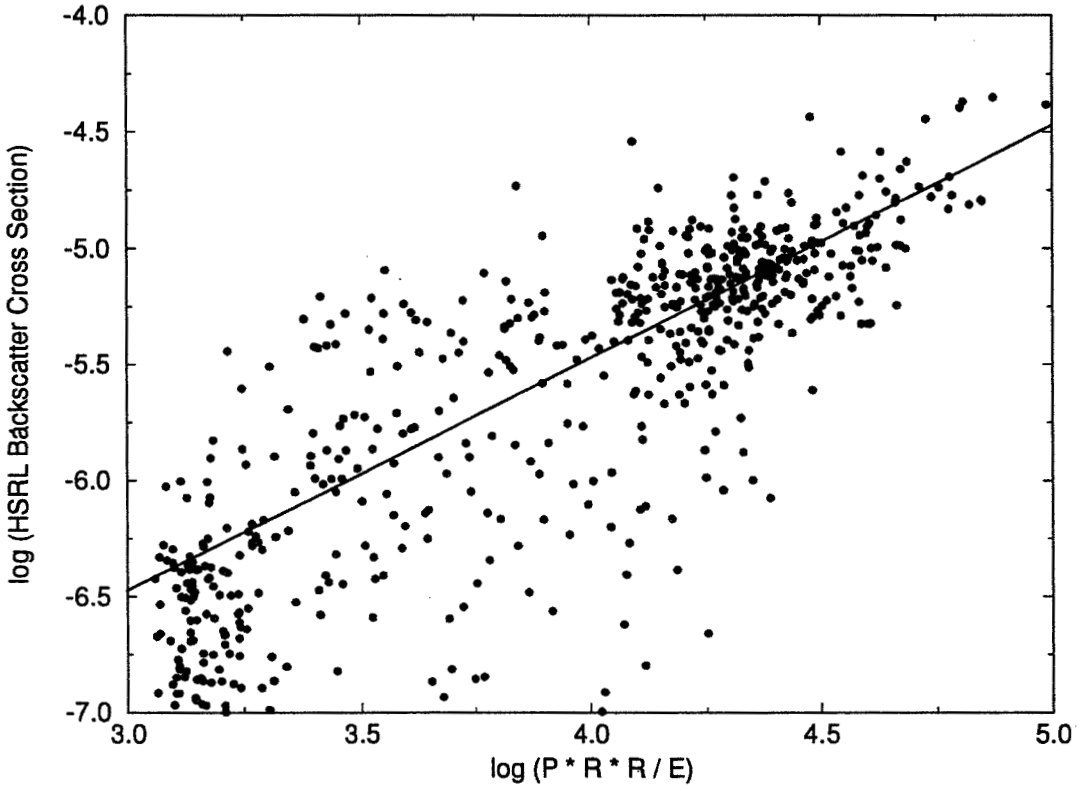

Figure 10: VIL–HSRL cirrus cloud data point comparison on December 1, 1989 from 19:29 to 21:20 GMT. The x-axis is the logarithm of the VIL range squared corrected, energy normalized signal. The y-axis is the logarithm of the HSRL aerosol backscatter cross sections. Since the VIL signal was not corrected for losses due to attenuation, only the bottom 1.5 km of the cirrus clouds was used in this comparison. The cirrus cloud threshold value used in Section 3 is located at 3.48. A straight line best fit to the cirrus cloud particles is also plotted.

In Figure 10, the VIL signal contains backscatter from both aerosols and molecules. For this comparison, the molecular backscatter at 1064 nm was small compared to backscatter from the cirrus cloud ice crystals and was neglected. (The molecular signal was about twenty times smaller than the background aerosol signal at the cirrus cloud heights for the 1064 nm wavelength radiation (see Section 4.2).) The signal from non-cirrus aerosols can be seen at the lower end of the plot in Figure 10. No VIL data had values less than 10^3 m^2 sr^{-1}. This was a result of the dynamic range of the VIL; data with values smaller than 10^3 m^2 sr^{-1} from a horizontal distance of 24 km could not be separated from the noise in the data system.

The VIL raw data in Figure 10 was not corrected for attenuation. To avoid attenuation problems in the initial calibration, the point comparison was only performed on the bottom 1.5 km of the cirrus clouds where attenuation was assumed negligible. This assumption would not be valid if the cirrus cloud was 1.5 km thick (with a cloud base at 6 km), had an average $\beta'_a(180, R)$ of $1 \cdot 10^{-4}$ m^{-1} sr^{-1}, and was viewed at an elevation angle of 4° out to 60 km. The optical depth would be 2 through the bottom 1.5 km of the cirrus clouds for this situation. For the cirrus clouds in this study, the average cirrus $\beta'_a(180, R)$ (from Figure 13) was $1 \cdot 10^{-5}$ m^{-1} sr^{-1}. This would give an optical depth of 0.2 only at far ranges (greater than 50 km) and low elevation angles. So for a distance of 24 km the assumption of negligible attenuation through the bottom 1.5 km of the cirrus clouds (in the vertical) was valid.

The bottom 1.5 km of the cirrus cloud seen by the VIL was calibrated using the HSRL $\beta'_a(180, R)$. The result of the calibration can be seen in Figure 11. Here the VIL signal at each point was transformed into a $\beta'_a(180)$. To calibrate the VIL data throughout the depth of the cirrus clouds, corrections had to be made for signal loss due to attenuation. The technique to correct for the attenuation in the VIL data is described in Appendix C.

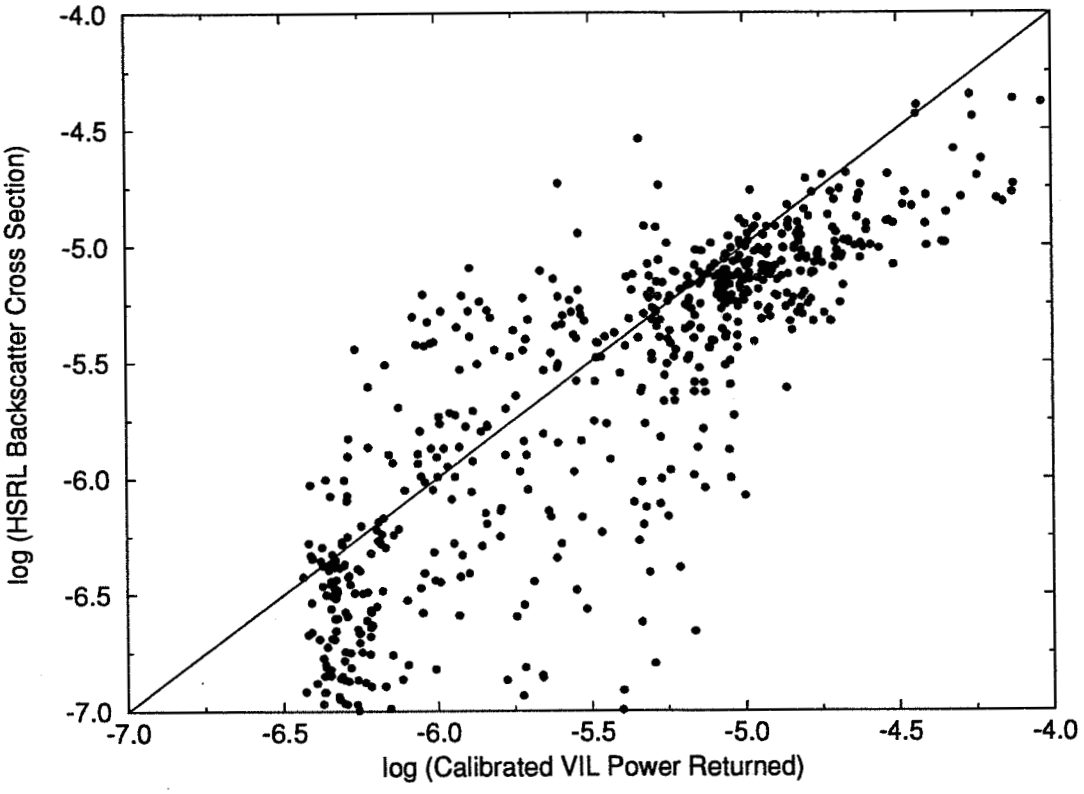

Figure 11: Same as Figure 10 except the calibrated VIL $\beta'_a(180, R)$ is compared to the HSRL $\beta'_a(180, R)$. A one to one line is plotted for reference.

4.2 Calibration Results

The results of the calibrated, attenuation corrected VIL data between the heights of 6 to 9 km above the HSRL are seen in Figure 12. The point comparison between the HSRL $\beta'_a(180)$ and the calibrated VIL $\beta'_a(180)$ shows more scatter than the comparison for the data between the heights of 6 and 7.5 km. This was a result of the misalignment errors between the two profiles described earlier and the usage of a bulk aerosol backscatter phase function for the correction of the attenuation in the VIL signal.

The lowest $\beta'_a(180)$ detected by the VIL at a horizontal distance of 24 km was approximately $3 \cdot 10^{-7}$ m^{-1} sr^{-1} (-6.5 in Figure 12). The VIL data centered around a value of $5.0 \cdot 10^{-7}$ m^{-1} sr^{-1} (-6.3) corresponded to non-cirrus aerosol backscatter. Little correlation was expected in this range because of the wavelength dependence of the scattering at the two lidar wavelengths by the non-cirrus aerosols. The $\beta'_a(180)$ centered around $1.0 \cdot 10^{-5}$ $m^{-1}sr^{-1}$ (-5.0) correspond to the backscatter by cirrus cloud ice particles. In Figure 12, the VIL calibrated $\beta'_a(180)$ are approximately 1.5 times greater than the HSRL $\beta'_a(180)$. This was a result of the VIL signal being corrected for multiple scattering while the HSRL signal was not. If a multiple scattering correction factor of 0.5 was included in the calculation of the HSRL $\beta'_a(180, R)$ (similar to the VIL multiple scattering correction), then $N_a(R)$ in Equation 10 would increase resulting in an increase in $\beta'_a(180, R)$.

The calibration of the VIL data was extended to the cross wind scans for the two time periods. This extension produced aerosol backscatter cross sections for the mesoscale volume at a resolution of 2-3 km parallel to the wind (a function of the wind speed and the scanning rate of the VIL) and a resolution of 60 m in both the cross wind scan direction and the vertical. To determine whether the VIL calibrated $\beta'_a(180)$ for the mesoscale volume had a similar distribution to the VIL simulated RTI and HSRL RTI $\beta'_a(180)$ distributions, 50 point histograms of the data between the heights of 6 km and 11 km were computed. To create the VIL

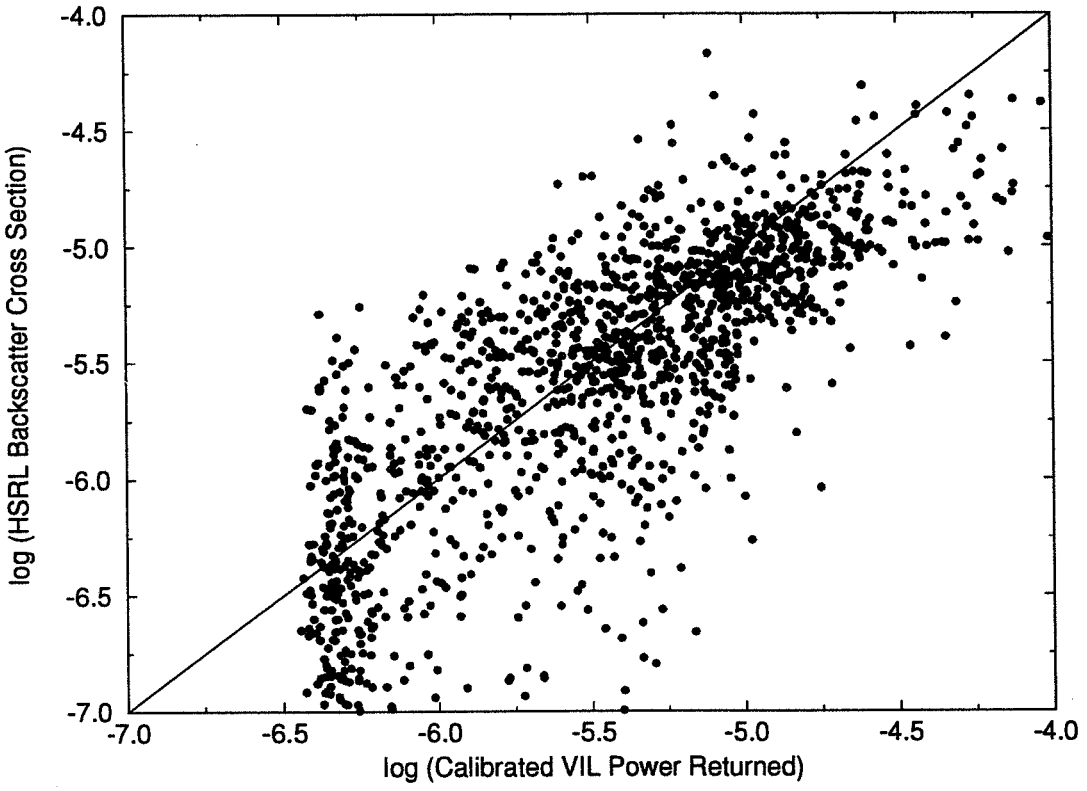

Figure 12: VIL–HSRL cirrus cloud data point comparison on December 1, 1989 from 19:29 to 21:20 GMT. The x-axis is the logarithm of the calibrated VIL aerosol backscatter cross sections. The y-axis is the logarithm of the HSRL aerosol backscatter cross sections. The point comparison is for data between 6 km and 9 km in height, the depth of the cirrus cloud layer. A one to one line is plotted for reference.

histograms, the molecular $\beta_m(180, R)$ was calculated using Equation 11 (for 1064 nm) and subtracted from the VIL calibrated backscattered signal. This allowed for the VIL and HSRL $\beta'_a(180)$ distributions for the atmospheric aerosols to be compared.

The resulting histograms are seen in Figure 13. A peak occurs in all three histograms near $8 \cdot 10^{-6}$ $m^{-1}sr^{-1}$ (-5.2). This peak was associated with the cirrus ice particle $\beta'_a(180)$. In all three histograms, the range of $\beta'_a(180)$ for the ice crystals spanned from $1 \cdot 10^{-6}$ to $1 \cdot 10^{-4}$ $m^{-1}sr^{-1}$. The peak at the smaller $\beta'_a(180)$, which represents the non-cirrus aerosols, occurred near $1.5 \cdot 10^{-7}$ m^{-1} sr^{-1} for the HSRL RTI and the VIL data from the mesoscale volume. The non-cirrus aerosol peak for the VIL RTI, which occurred at $5.0 \cdot 10^{-7}$ $m^{-1}sr^{-1}$, shows the loss of signal at far ranges for the VIL. For $\beta'_a(180)$ below $3.8 \cdot 10^{-7}$ $m^{-1}sr^{-1}$ (neglecting attenuation affects), the VIL receiver was not sensitive enough to detect the radiation backscattered from a horizontal distance of 24 km. The $\beta'_a(180)$ limit of detectability for a distance of 6 km can be seen in the histogram of the VIL data for the mesoscale volume. The smallest detectable $\beta'_a(180)$ was $1.25 \cdot 10^{-7}$ $m^{-1}sr^{-1}$ (-6.8) as seen in Figure 13. Some HSRL $\beta'_a(180)$ were smaller than $1.0 \cdot 10^{-7}$ $m^{-1}sr^{-1}$. This was a result of incomplete separation between the aerosol and molecular channels for regions with small aerosol backscatter. This incomplete separation even led to some negative HSRL $\beta'_a(180)$ beneath the cirrus cloud layer. This problem has been removed in a new configuration of the HSRL (Piironen and Eloranta (1993)). Figure 13 also shows a relative minimum value for the $\beta'_a(180)$ near $1.0 \cdot 10^{-6}$ $m^{-1}sr^{-1}$ for all three histograms. This relative minimum shows a clear separation between the background aerosol backscatter and the ice particle backscatter. This minimum value coincides with the threshold value used for the cirrus cloud determination in Section 3. At 1064 nm, the molecular backscatter cross section at a height of 6 km (calculated from the coincident rawinsonde density profile) was $6.44 \cdot 10^{-9}$ $m^{-1}sr^{-1}$. A typical aerosol backscatter cross section taken from the cirrus volume was $1.58 \cdot 10^{-7}$ $m^{-1}sr^{-1}$. By comparing these two values,

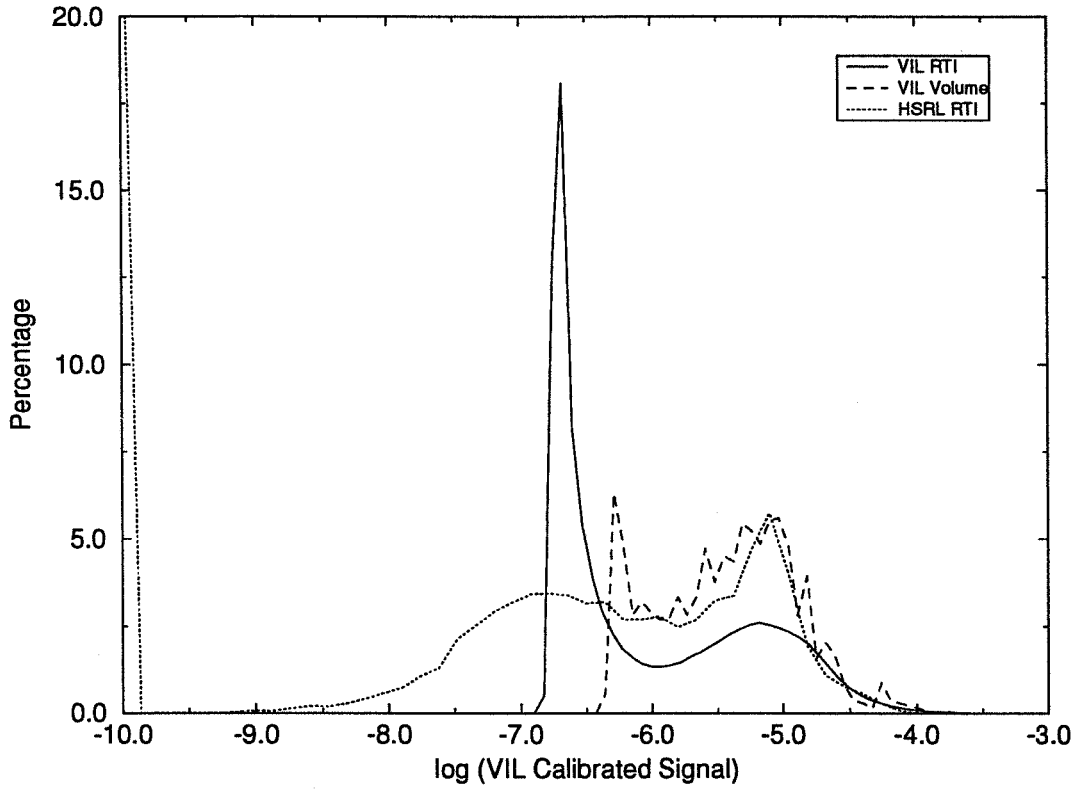

Figure 13: 50 point histograms of $\beta'_a(180)$ between heights of 6 km and 11 km from 19:29 to 21:20 GMT on December 1, 1989. The x-axis is the logarithm of $\beta'_a(180)$ and the y-axis is the percentage of points falling within each interval. Histograms of the HSRL $\beta'_a(180)$ (short dash), vertical profile of VIL $\beta'_a(180)$ over the HSRL position (24 km to the East of the VIL (solid line)), and the VIL $\beta'_a(180)$ throughout a mesoscale volume produced from consecutive VIL cross wind scans (long dash) are shown. The cirrus cloud threshold value used in Section 3 coincides with a value of $1.0 \cdot 10^{-6}$ m^{-1} sr^{-1}.

it was determined that the signal backscattered by the background aerosols at a wavelength of 1064 μm was at least a factor of twenty greater than the molecular backscatter at the cirrus cloud heights during this experiment.

Although the peak at the ice crystal backscatter cross sections coincides for the three histograms, large variations are seen in the calibration plot between the VIL and the HSRL (Figure 12). The scatter seen in Figure 12 can result from variations in the $\frac{P_a(180,R)}{4\pi}$ throughout the cirrus mesoscale volume, misalignments between the two lidar systems, and/or signal noise. The $\frac{P_a(180,R)}{4\pi}$ are dependent on the shape (or type) of the ice crystals scattering the laser light. The $\frac{P_a(180,R)}{4\pi}$ for different types of ice crystals can change by 0.048 sr^{-1} as calculated by Takano and Liou (1989) (the values for the ice crystal $\frac{P_a(180,R)}{4\pi}$ varied between 0.037 and 0.085 sr^{-1}). If the cirrus $\frac{P_a(180,R)}{4\pi}$ changed significantly over the volume, then the actual $\beta'_a(180)$ will change along with the $\frac{P_a(180,R)}{4\pi}$ causing errors in the attenuation correction technique. A second cause for the errors in the calibration may be a result of the variations of the ice crystal $\beta'_a(180)$ across the cirrus clouds.

The variation of the $\beta'_a(180)$ for visible wavelengths within the cirrus clouds will give an estimate on the allowable error between the VIL scan plane and the HSRL position. If the cirrus particles vary significantly from point to point then the alignment of the VIL has to be precise. If, on the other hand, the $\beta'_a(180)$ for the cirrus particles vary slowly within the cloud, then small alignment errors will be acceptable. To determine the variation of the ice crystal $\beta'_a(180)$ between the cirrus cloud data points in the scanned mesoscale volume, autocorrelations of the along wind and cross wind cirrus scans were calculated.

During the first time period (18:07-19:24 GMT) scattered cirrus clouds occurred throughout the mesoscale volume. Along the wind, there was 95.6% correlation between cirrus cloud $\beta'_a(180)$ for data points separated by 100 meters in the horizontal. For a 200 meter horizontal separation, there was an 89.5% correlation between cirrus cloud points. At 500 meters, there was a 73.9% correlation and at a distance of 1000 meters, the correlation dropped to 55.9%. In the vertical, for data points separated by 60, 120 and 240 meters, there was an 82.9%, 58.9%, and

a 31.4% correlation between the ice crystal $\beta'_a(180)$, respectively. The cirrus cloud $\beta'_a(180)$ correlations were also calculated for the VIL cross wind scans. For a 100 meter horizontal separation along the scan plane, there was a 94.6% correlation. At 200 meters, an 88.2%, at 500 meters, a 73.2% correlation, and at 1000 meters, a 54.6% correlation between the cirrus cloud $\beta'_a(180)$. In the vertical, at a 60 meter interval, there was a 79.0% correlation, 120 meters, a 49.1% correlation, and at 240 meter separation, a $\beta'_a(180)$ correlation of 29.3% was seen.

For this time period, the horizontal and vertical correlations were similar for the along and cross wind VIL scans. Good correlation existed for points separated by 100 to 200 meters. When the length of the correlation was extended to 500 and 1000 meters, the variation between data points became significant. The high correlation at 100 and 200 meter separations in the horizontal suggest that small azimuth angle alignment errors between the two systems can be tolerated. If the misalignments between the two profiles was as large as 1000 meters, then the resulting calibration would be very poor. In the vertical, only a maximum error of 60 m could be tolerated when generating a calibration for the VIL. The vertical cirrus cloud $\beta'_a(180)$ correlations changed more rapidly than the horizontal correlations. This was due to the vertical wind shear within the cirrus cloud. For the first time period, the larger separation lengths had correlations less than 50% for the cirrus ice crystal $\beta'_a(180)$. A calibration for the VIL could not be produced for larger separation lengths in the horizontal and the vertical due to the cirrus cloud $\beta'_a(180)$ variations.

For the second time period (19:29-21:20 GMT), the cirrus clouds were more spatially uniform due to the presence of a cirrus cloud deck. For the along wind scan, at 100, 200, 500, and 1000 meter separations, correlations of 94.8%, 89.3%, 78.6%, and 67.9% were seen, respectively. In the vertical, at 60, 120, and 240 meter data point separations, correlations of 84.2%, 64.4%, and 45.3% were seen, respectively. For the cross wind scan, at 100, 200, 500, and 1000 meter separation between points, correlations of 95.2%, 89.3%, 75.6%, and 59.4% between the cloud data points existed. In the vertical, for 60 meter data point separation, an 82.1%

correlation was seen while at 120 meters a 59.0% correlation occurred. At a 240 meter separation in the vertical, a correlation of 36.1% was detected. During this time period, the correlation values along the wind were higher than those in the cross wind scans for the larger distances between data points. This was a result of the widespread cirrus cloud deck over most of the region at this time which had an aspect ratio of 9:1.

For the VIL RTI simulating the HSRL RTI during the first time period, the correlation between cloud points was calculated. The correlation was computed along the wind direction with a separation between points (scans) in the horizontal of approximately 3 km and with a 60 meter data point separation in the vertical. In the horizontal, correlations of 76.3%, 48.2%, 18.1%, and 15.5% were seen at 1, 2, 5, and 10 scan separations (points). In the vertical, correlations of 89.2%, 71.0%, and 52.7% were seen at 60, 120, and 240 meter separations, respectively. For the second time period, correlations of 83.3%, 65.6%, 46.9%, and 36.1% were seen for 1, 2, 5, and 10 scan separations respectively. In the vertical, separations of 60, 120, and 240 meters resulted in 88.9%, 73.3%, and 55.1% correlations between the cirrus cloud aerosol backscatter cross sections, respectively. Higher correlations were seen in the vertical because these points were taken from a single cirrus cloud scan while the horizontal data points were taken from consecutive scans. The vertical correlations were similar to the previously calculated values as would be expected. There was very little correlation between the cirrus cloud particulate $\beta'_a(180)$ in the horizontal because of the large distances separating consecutive data points and the 2 km averaging along the scans to produce each profile. The second time period had higher correlations in the horizontal than the first time period. This was a result of a widespread cirrus cloud deck which occurred during the second time period while the earlier period had scattered cirrus clouds throughout the region. The scattered cirrus clouds created a situation which made it difficult to produce a VIL RTI to match the HSRL RTI. The cirrus cloud deck on the other hand had more uniformity which allowed for greater scan angle errors between the two systems. Also, the VIL scan plane was more closely aligned with the wind

direction at the cirrus cloud heights during the later period.

The cirrus cloud $\beta'_a(180)$ correlations revealed the types of error which would occur due to misalignments between the viewing positions of the two lidars. If large scan angle errors were present (greater than 1^o), then the cirrus cloud point comparison between the HSRL RTI and the VIL simulated RTI would be poor due to the variation of the $\beta'_a(180)$ within the cirrus clouds. For acceptable calibration results, the VIL azimuth angle errors have to be less than 0.5^o and the elevation angle errors have to be less than 0.25^o.

For the two time periods, the cirrus cloud $\beta'_a(180)$ correlation values were similar but the calibration plots were not. The attempted calibration plot for the first time period (18:08 to 19:24 GMT) was very poor and as a result was not shown. The difference between the two time periods was the direction of the cirrus cloud advection and the widespread cirrus cloud deck throughout the later period. The clouds during the first time period were advected into the region from 283^o while the clouds during the second time period came from 277^o (on average). This difference of 6^o between the wind direction and the VIL along wind scan direction result in point comparison errors in the calibration plot. The errors occurred when the VIL data was averaged along the scan plane to simulate the HSRL data (which was averaged along the wind direction). Since the VIL was averaged over the same distance as the HSRL profile (2 km), the offset between the VIL and HSRL data points at the end of the averaging length (1 km from each system) was 200 meters for the later time period and 300 meters for the early time period. The aerosol backscatter cross section correlation values across the wind dropped approximately 14% at the end of the averaging distances for the given time periods. This reduction in correlation, along with the scattered cirrus clouds, made the production of a VIL calibration plot from the first time period data impossible. This shows the importance of either aligning the VIL along the wind or using smaller averaging times in determining the cirrus cloud visible optical properties from the HSRL.

5 Visible vs. Infrared Optical Depths

From Mie theory, in the limit of completely absorbing particles at 10.6 μm which are also large compared to visible wavelengths, the ratio of the visible scattering efficiency to the infrared absorption efficiency is expected to be 2:1. This ratio (Q_{vscat}/Q_{irabs}) has been used to describe the radiative properties of cirrus cloud ice crystals (Minnis (1991), p. 83). This efficiency ratio can also be written as the ratio of the visible scattering optical depth to the infrared absorption optical depth times an extinction efficiency ratio ($\frac{\tau_{vscat}Q_{vext}}{\tau_{irabs}Q_{irext}}$). Since the ice crystals were assumed to be large compared to both visible and infrared wavelengths, the extinction efficiency ratio was one and the optical depth of cirrus clouds at the two wavelengths are directly related. A relationship of this type allows for a simple parameterization for the cirrus cloud optical properties at the two wavelengths. Measurements of the optical depth at one wavelength allows for the optical properties of the cirrus clouds at the second wavelength to be calculated. Previous modeled ratios for cirrus cloud $\frac{Q_{vscat}}{Q_{irabs}}$ range from 1.8:1 to 4:1 (Minnis et al. (1993), p. 1281).

Few coincident measurements of the cirrus clouds optical depth at both infrared and visible wavelengths have been made to test the optical depth ratio determined from theory. Platt et al. (1980) made simultaneous measurements of cirrus clouds using a ground based lidar and a satellite based infrared radiometer. The ratio of the optical depths at the two wavelengths measured by Platt was less than 2. The cirrus clouds were observed within a 10 km by 10 km volume using a single channel lidar. The visible optical depths were determined with the aid of a calculated backscatter to extinction ratio for the cirrus clouds. Measurements of cirrus cloud optical properties were also made during a FIRE IFO using ground based and satellite measurements. The mean ratio of the visible scattering optical depth to infrared absorption optical depth for the cirrus clouds observed during the IFO was 2.13 (Minnis et al. (1990)). The cirrus clouds were observed using a satellite based visible radiometer. The visible optical depths were calculated from

these visible radiances using an iteration technique where the cloud albedo was linearly related to the cosine of the solar zenith angle. The cloud cover percent and cloud type within each pixel had to be known.

A method is described in this section to calculate the area averaged ratio of the $\frac{\tau_{Vscat}}{\tau_{IRabs}}$ for cirrus clouds. This method used VIL data calibrated using the method described in Section 4 and the VAS 11 μm radiance measurements. The visible scattering optical depths were determined by integrating the VIL calibrated visible extinction cross sections (calculated using Equations 12 and 14) in distance along a ray from the GOES point of view. The infrared absorption optical depth was calculated from the VAS infrared emissivities which were determined using Equation 17. The mid-cloud height used in Equation 17 was determined by the VIL and the temperature at the mid-cloud height was measured with the rawinsonde.

The VAS on GOES imaged the atmosphere over Wisconsin once every half hour. To compare the visible and infrared optical depths, the VIL mesoscale volume was viewed from the position of the GOES satellite. This was possible because the VIL imaged the cirrus clouds throughout the mesoscale volume. The resulting VIL volume can be viewed from any direction because the $\beta_\epsilon(R')$ are known at each data point within the volume (calculated from the $\beta'_a(180, R')$ using the bulk backscatter phase function as described earlier). For an accurate lidar and satellite cirrus cloud comparison, the VIL cirrus cloud volume was broken into one hour time periods around each VAS picture. To match the cirrus clouds in the GOES infrared image to the picture created from the VIL data, the clouds viewed by the VIL were shifted in position to the point where they would have occurred at the time of the VAS picture. The translation of the cirrus clouds was made under the assumptions that the cirrus clouds were advected at the speed of the wind at their heights and that the cirrus clouds did not change over a half hour period. The magnitude and direction of the shift was a result of the wind speed and direction at each cirrus cloud level and the time difference between the scan where the cirrus clouds occurred and the VIL scan at the time of the VAS snapshot.

To convert the VIL data within the volume into visible scattering optical depths, a ray tracing technique was used to integrate the VIL extinction cross sections between the satellite position and the ground. Rays were traced to the ground for each VIL area which had a resolution of 1.0 km by 1.0 km. The VIL extinction cross sections were integrated along each ray to determine the optical depth of the cirrus clouds for each visible pixel. The pixels were then averaged to create grids the size of the VAS infrared radiometer pixels, approximately a 10 km resolution above Madison, Wisconsin. The resulting averaged visible scattering optical depths were directly compared to the VAS infrared absorption optical depths calculated using the following equation (where ϵ_{ir} is calculated in Equation 17):

$$\tau_{ir} = -\ln(1 - \epsilon_{ir}). \tag{24}$$

The VAS infrared radiance satellite image was directly compared to the VIL visible optical depth simulated satellite image. The VIL visible optical depth image was position shifted to achieve the best cloud correlation between the two pictures to correct for cloud position errors in the VAS image due to satellite registration errors (this correlation was done by eye). A visible to infrared optical depth comparison was calculated for the pixels with high cloud cover percentages. The resulting comparison is shown in Figure 14. A line with a slope 2:1 is shown for reference. It should be noted that this optical depth comparison was achieved using an upper limit on $\beta'_a(180)$, not a limit on the attenuation correction factor. This upper limit of $\beta'_a(180)$ did not remove a significant number of overcorrected data points which resulted from the attenuation correction. This leads to some overestimations of the visible optical depths especially at larger optical depths.

In Figure 14, the optical depth ratio from different cirrus cloud types is represented by different symbols. The clouds labeled as '1935 A' were thin nonprecipitating cirrus clouds which often occurred in overlapping layers. The ratio for these clouds was close to 2:1 with a slight tendency for the ratio to be less than 2:1. An example of these clouds is seen in Figure 7 between 20 and 50 km to the

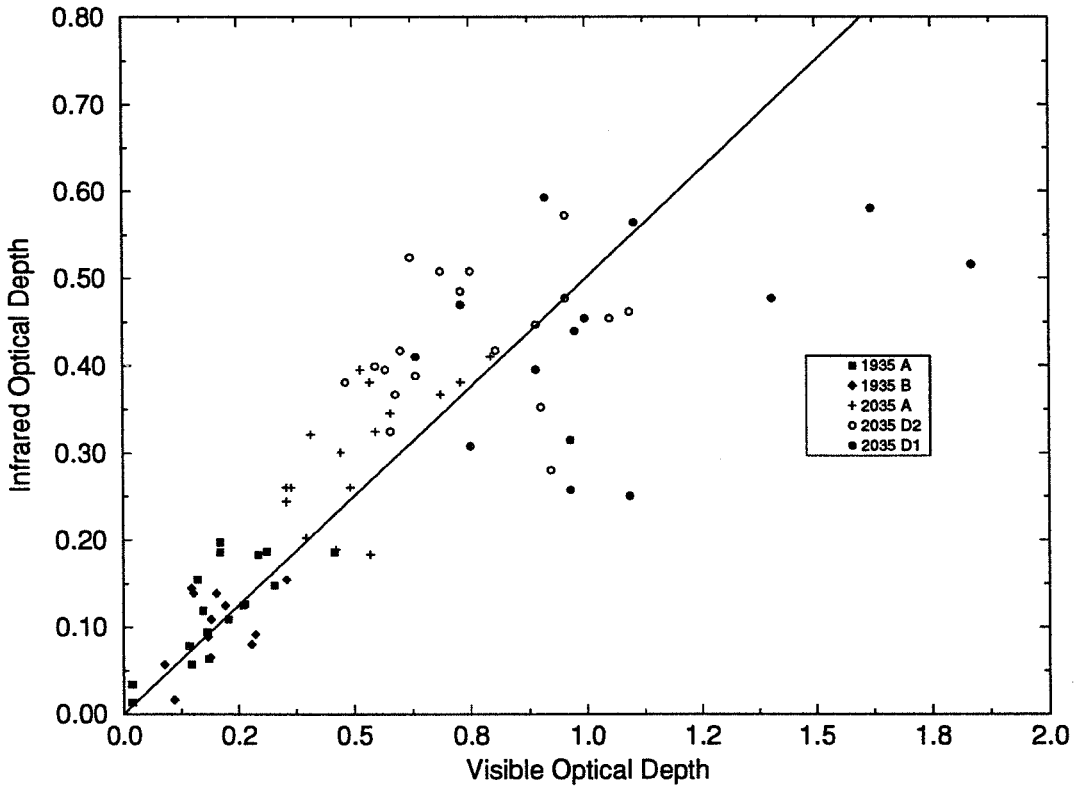

Figure 14: VIL visible scattering optical depths verses VAS infrared absorption optical depths for the same cirrus cloud pixels from 19:29 to 21:20 GMT on December 1, 1989. The x-axis is the VIL visible scattering optical depths. The y-axis is the VAS infrared absorption optical depths. The different symbols represent different cirrus cloud types described in the text.

north. The second cloud type, '1935 B', was a band of precipitating cirrus clouds occurring between 30 and 40 km south of the VIL in Figure 7. These clouds also show an optical depth ratio close to 2:1. Both of these cloud types had visible optical depths less than 0.5. The remaining sets of clouds were thick precipitating cirrus clouds where the optical depths often became large. Extensive virga fell from these optically thick cirrus clouds to a height of 6 km. The cirrus clouds described as '2035 A' were precipitating bands occurring ahead of a large cirrus cloud deck. The optical depth ratio for these clouds tended to be less than 2:1. A fourth type of ice cloud was labeled '2035 D2'. These were clouds in the center of a large precipitating cirrus cloud deck. The optical depth ratios for these clouds also tended to be less than 2:1. Some of the cirrus clouds were too optically thick for the VIL signal to penetrate at longer slant paths. This led to smaller than expected visible optical depths which resulted in a ratio of less than 2:1. The last group of cirrus were labeled '2035 D1'. This group consisted of three cirrus cloud cross wind scans within the large precipitating cloud deck which had vertically thin layers of high backscatter. The optical depth ratios for these clouds ranged from 2:1 to 3:1. Optical depth ratios greater than 2:1 can result from: specular reflection in the VIL data, pixel misalignments between the two images, incorrect averaging of the VIL data, instability in the VIL attenuation correction procedure, and smaller than expected scattering particles.

Specular reflection in the three cross wind scans could not have caused the thin regions of high backscatter. The increased backscatter layer extended over a horizontal range of 40 km. The ice crystal orientation would have had to change with the VIL scan angle to cause specular reflection for the whole range (which was highly unlikely). A second possible error was the allocation of the cirrus clouds into the different cirrus cloud pixels. This can result in an increase or a decrease in the optical depth ratio depending on which satellite pixel the cirrus clouds fell. The magnitude of these allocation errors are currently under investigation. Another cause for an optical depth ratio greater than 2:1 could be the result of the averaging technique to produce the visible optical depths at the 10 km scale. For each satellite

pixel, the average infrared radiance was measured. This was converted into an effective temperature which was then used to calculate the infrared optical depth. The visible optical depths were produced at a 1 km scale by averaging the extinction cross sections at each level and then integrating them with height. The 1 km visible optical depth pixels were then averaged together to produce a 10 km scale image. Since the effect of the optical depth on the transmitted radiation was nonlinear, the VIL extinction cross sections should have been averaged over the 10 km infrared image. A probable error in the optical depth comparison was the instability in the VIL attenuation correction technique. This effect only becomes important for the clouds with large optical depths since the corrections at the smaller optical depths were minimal. One last error could result if the scatterers were not large compare to both the 11 μm and 0.5 μm radiation. If the particles were spherical and consisted of ice, then the scatterers with radii between 0.1 μm and 4 μm would cause an optical depth ratio greater than 2:1.

Some other errors associated with this visible to infrared optical depth comparison are scattering of the infrared wavelength radiation by the cirrus cloud ice particles (especially at larger infrared optical depths), the assumption that the upwelling infrared radiation has a T^4 dependence, and the attenuation of the VIL signal through thick cirrus such that the VIL signal does not penetrate through the clouds. If infrared radiation was scattered by the cirrus cloud or reflected from the cloud base, less infrared radiation from beneath the cloud would reach the satellite radiometer. This would reduce the radiance detected by the radiometer which would result in a calculated cirrus cloud emissivity which would be larger than the actual cirrus cloud infrared emissivity. The higher cloud emissivity would result in a larger optical depth which would result in an optical depth ratio smaller than 2:1. The assumption that the upwelling infrared radiation has a T^4 dependence will result in an error in the calculated emissivities of approximately 3%. Another problem was the incomplete penetration of the cirrus cloud by the VIL. For the VIL, total penetration of the cirrus clouds is needed to make accurate calculations of the visible scattering optical depths across the mesoscale volume. Incomplete

penetration would cause an underestimation in the thickness of the cirrus clouds which would result in underestimations of the visible scattering optical depths. This underestimation of the cloud depth would also lower the optical depth ratio.

When comparing the VIL optical depth image to the VAS infrared radiance image, large variations were seen in the visible image while very little variation between pixels was seen in the infrared satellite image. This relative uniformity in the satellite infrared image was a result of the large area covered by each pixel and the smearing that occurred between pixels. This pixel smearing was due to the response rate of the infrared detector and the sampling rate of the VAS. Also, the calculation of the emissivity was strongly dependent on the choice of surface temperature and mid-cloud temperature as seen in Equation 17. A lower haze layer or subvisible cirrus clouds which were undetected in the satellite image would cause lower than expected surface temperatures which would decrease the cirrus cloud emissivity.

The technique described here to compare the visible scattering optical depth to the infrared absorption optical depth removes ambiguities associated with the previous visible to infrared optical depth comparison. The cirrus clouds were compared on the same scale removing horizontal homogeneity assumptions. The cirrus clouds were viewed from the same direction at the same resolution removing angular viewing effects. Since both systems viewed the cirrus cloud horizontal structure, the pixel alignment between the two images could be done. The cirrus cloud base, top, and mid-cloud height were determined for each cloud pixel from the VIL data. This removed the uncertainty of the mid-cloud height in determining the mid-cloud temperature used to calculate the cirrus infrared emissivities. For the time periods studied here, the VIL was able to detect subvisible cirrus clouds. These clouds, not seen in the infrared channels, would have been ignored in the determination of a surface temperature from a clear pixel which was used in the calculation of the cirrus cloud infrared emissivities. This removed some of the surface temperature uncertainties. At visible wavelengths, the ground albedo was needed for cirrus cloud albedo calculations from satellite based visible radiometers.

The calculation of the visible optical depth from the VIL did not need ground albedo values because the visible optical depth of the cirrus was directly determined from the integration of the cirrus visible extinction cross sections along the line of sight of GOES. The bulk cirrus cloud backscatter phase function used by the VIL was determined from the HSRL enabling the technique to be self contained.

Although it was not done in this study, the level of the cloud where maximum scattering occurs can be determined by integrating the VIL extinction cross section along a viewing angle using the ray tracing technique. The height can be compared to the mid-cloud height to calculate the errors associated with the usage of the mid-cloud temperature in determining the cirrus infrared emissivity and optical depth.

6 Conclusion

Cirrus clouds were viewed using the University of Wisconsin Volume Imaging Lidar, University of Wisconsin High Spectral Resolution Lidar, and the VAS radiometer situated on GOES. The VIL imaged the cirrus clouds within a mesoscale volume. The HSRL measured the visible scattering properties of the cirrus clouds. The VAS radiance measurements were used to calculate the infrared absorption properties for the cirrus clouds.

The backscattered radiation detected by the VIL was used to determine the horizontal and vertical structure of the cirrus clouds. The presence of cirrus clouds was determined by choosing a threshold value from a histogram of the VIL backscattered signal between heights of 6 and 11 km. The backscattered radiation in each VIL profile was compared to the threshold value to determine cirrus cloud cover percentages and structure functions. The cirrus cloud cover percentages ranged from 54.7% to 100% for simulated vertical profiles across the wind created from the VIL cross wind scans. For the two time periods studied, the area averaged cirrus cloud cover percentages were 81.5% and 76.8%. Differences in the average cloud cover were seen between the VIL area measurements and HSRL

vertical profiles. The maximum cloud cover difference of 45.3% between two VIL RTIs during the first time period was used as a cirrus cloud cover error to estimate a resulting change in the incoming solar radiation. This cloud cover error, along with an average cirrus cloud optical depth of 0.257, resulted in an estimated change in the direct solar flux of 58.18 W m^{-2} seen at the surface of the Earth. For the second time period, a cloud cover difference of 8.9% between the VIL and HSRL, associated with a cloud optical depth of 0.428, resulted in a 12.36 W m^{-2} difference in direct solar flux seen at the surface of the Earth. The errors due to the incorrect cirrus cloud cover would dominate the increase in the planetary effective temperature resulting from the doubling of CO_2, especially in the case of spatially scattered, optically thin cirrus clouds. This implies that the variability of the cirrus clouds throughout a mesoscale volume has to be measured to understand the effects of these clouds on the Earth's radiation balance. Sampling errors associated with point measurements make them poor indicators of the cirrus cloud area averaged values.

The cirrus cloud horizontal and vertical structure was also examined. Structure functions were used to determine the cirrus cloud length, width, and the separation between clouds. The cirrus cloud average length along the wind was 130 km and its length across the wind averaged 14 km. The average distance between clouds along the wind was 273 km while across the wind it was 24 km. In this experiment, the cirrus clouds were typically aligned along the wind direction with an aspect ratio of approximately 9:1. Preferential alignment of cirrus clouds implies that point measurements which rely on cloud advection may not even detect cirrus clouds if large variations exist across the wind. Examination of the vertical cloud structure showed many instances of multi-layered and/or precipitating cirrus clouds. The complexity of the vertical structure shows the dependence of cloud formation on the dynamical situation in the atmosphere.

A method was described to calculate the cirrus cloud visible optical properties across a mesoscale volume. This was possible because an experiment was run where the VIL along wind scan plane crossed over the HSRL position resulting in

coincident cirrus clouds measurements. The HSRL cirrus cloud aerosol backscatter cross sections were used to directly calibrate the VIL backscattered signal. A point comparison was made for the HSRL aerosol backscatter cross sections and the VIL data (which was normalized to a low level aerosol layer to remove angular dependencies). This initial comparison was computed for the signal backscattered from the bottom 1.5 km of the cirrus clouds where it was assumed that the attenuation in the VIL signal was negligible. A best fit straight line was used to calibrate the VIL backscattered signal into aerosol backscatter cross sections per unit volume. The calibrated VIL signal was then attenuation corrected using a forward integration of the single channel lidar equation. To forward integrate the lidar equation, extinction cross sections at each data point and a multiple scattering correction factor were needed for the VIL data. Extinction cross sections were created from the VIL calibrated aerosol backscatter cross sections using a single aerosol backscatter phase function for the whole volume calculated from the HSRL data (assuming negligible molecular extinction within the cirrus cloud compared to the aerosol extinction at 1064 nm). A multiple scattering correction factor of 0.5 was used to correct the backscattered signal to account for one half of the original scattered light being diffracted by the ice particles and staying within the receiver field of view. After the VIL signal was attenuation corrected, the resulting calibrated VIL cirrus cloud aerosol backscatter cross sections were compared to the original HSRL aerosol backscatter cross sections. An adequate correlation resulted between the two sets of aerosol backscatter cross sections. The largest errors in the calibration technique resulted from VIL scan angle errors leading to misalignments between the two vertical profiles, misalignments between the VIL scan direction and the wind direction, and the usage of a bulk aerosol backscatter phase function in the VIL attenuation correction technique. The alignment of the VIL scan and the HSRL vertical profile was critical since the calibration technique was dependent upon both system viewing the same cirrus cloud.

The calibration technique was used to convert the VIL signal in both scan directions into aerosol backscatter cross sections per unit volume. The calibrated

cross wind VIL data was used to calculate the visible scattering optical depth of the cirrus clouds within the mesoscale volume assuming no changes in the cirrus clouds as they were advected by the wind (over a half hour period). The visible optical depths were calculated by integrating the VIL cirrus cloud extinction cross sections along a path through the VIL observed volume traced by a ray from the position of the GOES satellite. This allowed for a direct comparison of the VIL visible scattering optical depths and VAS infrared absorption optical depths. The ratio of the VIL visible scattering optical depth to the VAS infrared absorption optical depth was approximately 2:1 (especially for thin cirrus clouds) although variations did occur. The 2:1 ratio value agrees with previous measurements by Minnis (1990). When making this optical depth comparison, the cirrus clouds detected by the VIL had to be correctly allocated into the different pixels to enable an accurate comparison with the infrared image. This process was hampered by the lack of variation in the infrared image compared to the visible cirrus cloud image.

The technique to compare the visible scattering to infrared absorption optical depths can also be used to compare the cloud cover determined from the VIL to the cloud cover calculated from the satellite infrared radiometer data using the CO_2 slicing technique. This comparison would be used to test the accuracy of the satellite based cirrus cloud climatologies. The cirrus cloud albedo and mid-cloud height calculations from satellite based radiometers can also be tested. The level of maximum scattering within a cirrus cloud can also be determined and compared with the cirrus mid-cloud heights throughout the mesoscale volume. Although these comparisons are not encompassed in this thesis they can easily be accomplished with the tools available.

This first attempt at a calibration of the VIL backscattered signal by the HSRL aerosol backscatter cross sections shows promise. Some of the inherent problems in this technique were revealed. Improvements are being made to both the VIL and the HSRL. This will result in more accurate measurements which will lead to a better understanding of the cirrus cloud optical and structural properties. The cirrus cloud detection technique and the VIL calibration technique should be

attempted on a large cirrus cloud data set to achieve a statistical representation of the cirrus cloud optical and structural properties.

A Removal of System Limited Data Points

To correctly calibrate the VIL data, the system limited data points had to be removed from the data set. At far ranges the backscattered radiation can not be separated from the system noise because the VIL signal decreases due to the range squared dependence and attenuation. When the VIL raw data is corrected for the range squared dependence, the places where the VIL signal increases monotonically as a function of the range is where the signal could not be separated from the noise as seen in Figure 15. This limit of detectability occurs where the VIL signal starts to increase with range around bin 250. The large increase in the signal around the range bin 500 was the result of radiation backscattered from a cirrus cloud.

To remove the noise dominated points, the points where the raw signal was within the noise regime had to be determined. At far ranges, the raw backscattered signal becomes linear with range when the backscattered power is plotted on a natural log scale. This was a result of both the attenuation of the transmitted pulse in the atmosphere and the range squared decrease of the signal. Shot noise occurs along with the raw signal. If the shot noise was random, as expected, then the noise should occur as a Gaussian distribution about the raw data. This would not affect the slope of the VIL data with range in Figure 15. So, if the VIL raw data was sorted according to their magnitudes and replotted on a log-linear plot, then the signal which was small and could not be separated from the noise would appear as a straight line at the lower signal magnitudes (Figure 16).

This process was applied to each VIL raw profile where the VIL backscatter signal was sorted according to their magnitudes. The sorted values were approximated using a straight line median fit. The straight line median fit was first applied to the whole sorted profile. The points occurring above the fit had large signal backscatter and were remove from the sorted set. The remaining sorted points were then refitted using a straight line median fit. After a number of successive fits, where a chosen threshold was met, the remaining points consisted only of the small signal values which could not be separated from the noise (they appear as

a straight line in Figure 16). These noise points were discarded from the original data set. For the shot used in Figure 15 and Figure 16, over one half of the data points had to be discarded. The remaining data points are the signal backscattered by aerosols and molecules in the atmosphere.

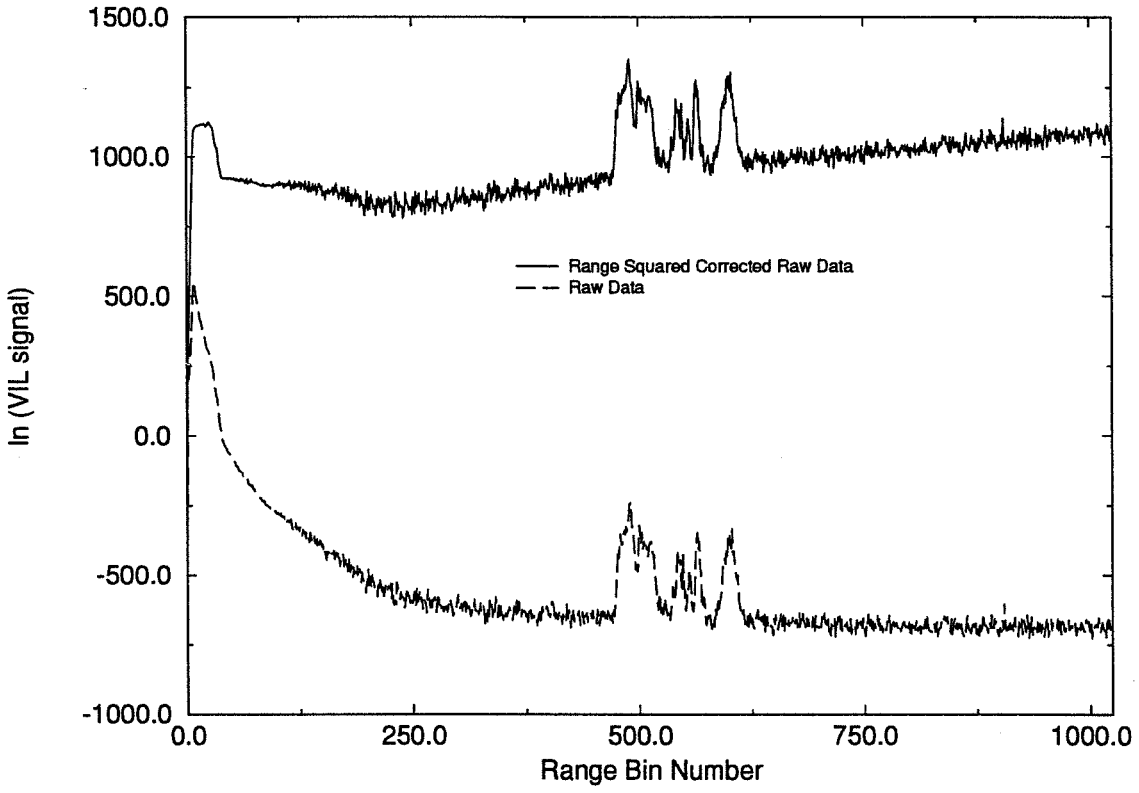

Figure 15: Removal of the noise points from the VIL raw data. The x-axis is the range bin number and the y-axis is 128 · ln (P / E) for the raw data and 128 · ln (P * R * R / E) for the range squared corrected raw data. The solid line is the range squared corrected VIL profile. The long dashed line is the VIL raw data profile.

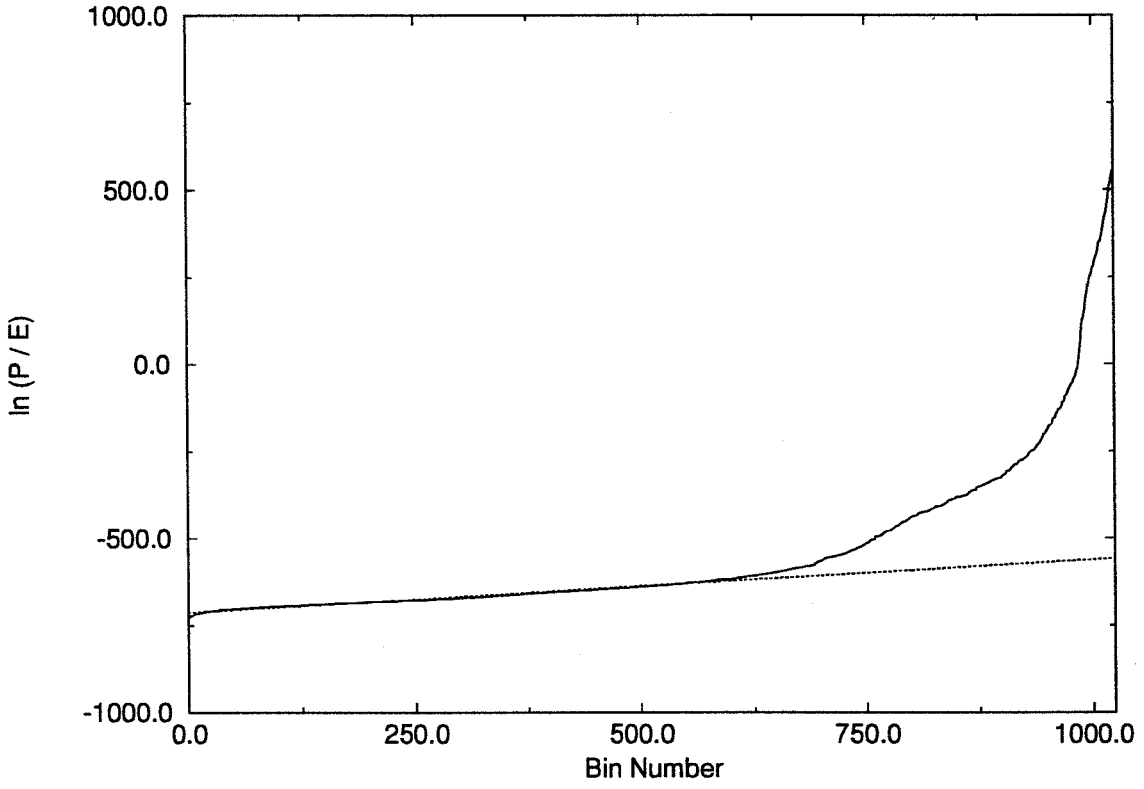

Figure 16: Removal of the noise points from the VIL raw data. The x-axis is the sorted bin number. The y-axis is 128 · ln (P / E). The solid line is sorted VIL raw data (sorted according to magnitudes). The dashed line is the straight line median best fit to the sorted noise points.

B Data Normalization

Since the VIL mechanical axis was not aligned with its optical axis during this experiment, alignment errors were a problem for the VIL. The VIL signal varied when the system mirrors were scanned in angle as a result of partial blocking of the transmitted beam (an example is baffle blocking of the transmitted pulse). Other signal variations can also result from changes in the gain of the avalanche photodiode over time and/or field of view changes in the receiver. To remove these dependence, each VIL scan was normalized to a low level aerosol layer situated between 1 km and 2 km above the ground. Only backscattered signal falling within a bounded aerosol region were used in the data normalization. The region was bounded by a minimum and maximum height along with a minimum and maximum distance from the VIL. The minimum and maximum heights were determined by the size of the aerosol layer. The minimum range from the VIL was determined by the extent of the system overlap regime. A maximum range of 10 km was chosen to stay well above the minimum detectable signal for the VIL. The median backscattered signal from the bounded aerosol layer for each lidar profile was set equal to the median backscattered signal in the normalization regime. This normalization technique removed both the time and angular dependence of the cirrus clouds scans with the assumption that the aerosol layer did not change in time. If the aerosol layer did not have temporal and spatial uniformity, errors would result from the normalization process. Nonuniformities would cause variations in the cirrus cloud backscatter which are the result of data processing and not cirrus cloud variability. The aerosol layer used for the VIL data normalization was detected by the HSRL and appeared uniform in time. Additional errors can also result if too much outgoing signal was blocked before it left the transmitter. When this occurred, the radiation backscattered from the atmosphere was too small to be separated from the noise. These system limited data points were removed from the data set as described in Appendix A.

C Attenuation Correction

To correct for the attenuation in the VIL signal, the optical depth between the VIL and each point in the profile has to be known (Equation 1). To determine the optical depth between the VIL and each data point, the extinction cross section at each point has to be determined. Since the VIL data was converted into aerosol backscatter cross sections, these values were used to calculate the extinction cross sections. The aerosol backscatter cross sections were first converted into aerosol scattering cross sections using Equation 2 assuming no absorption and additional knowledge of a bulk $\frac{P_a(180,R)}{4\pi}$ for the mesoscale volume. The average bulk $\frac{P_a(180,R)}{4\pi}$ calculated with the HSRL was used as the bulk $\frac{P_a(180,R)}{4\pi}$ for the mesoscale volume. Since no absorption at visible wavelengths by the cirrus ice crystals was assumed, Equation 14 relates the aerosol scattering cross sections to the extinction cross sections. A forward integration was performed on the resulting extinction cross sections to determine the attenuation between the VIL and each data point. The attenuation to each point was used to correct the existing VIL $\beta'_a(180, R)$ for signal loss. In this analysis, a multiple scattering correction was included. The attenuation along each profile was corrected by a multiple scattering factor of 0.5 which decreased the attenuation by a factor of 2 (Eloranta and Shipley (1982)). This correction factor was a result of half of the light attenuated by the cirrus cloud ice particles being diffracted in the forward direction. This diffraction peak stayed close to the initial beam and further scattering of this light by other particles resulted in greater backscatter at the receiver.

The bulk $\frac{P_a(180,R)}{4\pi}$ for cirrus cloud particles was calculated by the HSRL for each cirrus profile. These bulk $\frac{P_a(180,R)}{4\pi}$ were averaged over the 3 hour time period resulting in a $\frac{P_a(180,R)}{4\pi}$ of 0.0499 sr^{-1}. This value fell within the expected range of $\frac{P_a(180,R)}{4\pi}$ as described by Takano and Liou (1989). Their results give values of $\frac{P_a(180,R)}{4\pi}$ for thin plates (0.025 sr^{-1}), ice columns (0.038 sr^{-1}), and thick plates (0.087 sr^{-1}). (Plates were detected at the tropopause as noted by the specular reflection described previously.) This average $\frac{P_a(180,R)}{4\pi}$ was used to correct all of

the VIL data for attenuation.

The method of a forward integration of the backscattered signal was first used to correct radar backscatter for attenuation. Hitschfeld and Bordan (1954) were one of the first to test the forward integration method. Klett (1981) showed the instability of this forward integration for large optical depths. In this study, if the one way optical depth of the cirrus cloud along each VIL profile became greater than 0.7, then the attenuation correction at further ranges (or larger optical depths) was considered to be unstable. This choice in the one way visible optical depth was chosen on the assumption of a 10% error in the VIL aerosol backscatter cross sections. The attenuation correction (using an optical depth of 0.7) of the data with a 10% error would result in a 40% error in the attenuation corrected signal.

References

[1] Ackerman, Steve A., Eloranta, Ed W., Grund, Chris J., Knuteson, Robert O., Revercomb, Henry E., Smith, William L., and Donald P. Wylie (1993): University of Wisconsin Cirrus Remote Sensing Pilot Experiment. *Bulletin of the American Meteorological Society*, **74**, p. 1041–1049.

[2] Barton, I. J. (1983): Upper Level Cloud Climatology from an Orbiting Satellite. *Journal of the Atmospheric Sciences*, **34**, p. 758–765.

[3] Cess, R. D. et al. (1990): Intercomparison and Interpretation of Climate Feedback Processes in 19 Atmospheric General Circulation Models. *Journal of Geophysical Research*, **95(D10)**, p. 16601–16615.

[4] Dorsey, N. Ernest (1940): "Properties of Ordinary Water–Substance." Reinhold Publishing Corporation, New York.

[5] Eloranta, E. W. and S. T. Shipley (1982): A Solution for Multiple Scattering. "Atmospheric Aerosols: Their Formation, Optical Properties, and Effects." Spectrum Press, Hampton, Va, p. 227–237.

[6] Grund, Christian John (1987): Measurement of Cirrus Cloud Optical Properties by High Spectral Resolution Lidar. Ph.D Thesis, University of Wisconsin–Madison, 92 pp.

[7] Klett, James D. (1981): Stable Analytical Inversion Solution for Processing Lidar Returns. *Applied Optics*, **20**, p. 211–220.

[8] Liou, Kuo-Nan (1980): "An Introduction to Atmospheric Radiation." Academic Press, San Diego, California.

[9] Liou, Kuo-Nan (1986): Review: Influence of Cirrus Clouds on Weather and Climate Processes: A Global Perspective. *Monthly Weather Review*, **114**, p.

1167–1199.

[10] London, J. (1957): A Study of the Atmospheric Heat Balance. Final Rep., Contract AF19(122)–165. Dept. of Meteorology and Oceanography, New York University, 99 pp. [AST1A 117227, Air Force Geophysics Laboratory, Hanscom AFB, Mass 01730.]

[11] Minnis, Patrick, Young, David F., Sassen, Kenneth, Alvarez, Joseph M., and Christian J. Grund (1990): The 27–28 October 1986 FIRE IFO Cirrus Case Study: Cirrus Parameter Relationships Derived from Satellite and Lidar Data. *Monthly Weather Review*, **118**, p. 2402–2425.

[12] Minnis, Patrick (1991): Inference of Cirrus Cloud Properties from Satellite–Observed Visible and Infrared Radiances. Ph.D. Thesis, Department of Meteorology, University of Utah, 161 pp.

[13] Minnis, Patrick, Liou, Kuo-Nan, and Yoshihide Takano (1993): Inference of Cirrus Cloud Properties Using Satellite-observed Visible and Infrared Radiances. Part I: Parameterization of Radiance Fields. *Journal of the Atmospheric Sciences*, **50**, p. 1279–1304.

[14] Piironen, P. and E. W. Eloranta (1993): Demonstration of an Iodine Absorption Filter Based High Spectral Resolution Lidar. Submitted to *Optics Letters*, on September 2, 1993.

[15] Platt, C. M. R. (1979): Remote Sounding of High Clouds: I. Calculation of Visible and Infrared Optical Properties from Lidar and Radiometer Measurements. *Journal of Applied Meteorology*, **18**, p. 1130–1143.

[16] Platt, C. M. R. and A. C. Dilley (1979): Remote Sounding of High Clouds: II. Emissivity of Cirrostratus. *Journal of Applied Meteorology*, **18**, p. 1144–1150.

[17] Platt, C. M. R.,Reynolds, David W., and N. L. Abshire (1980): Satellite and Lidar Observations of the Albedo, Emittance and Optical Depth of Cirrus Compared to Model Calculations. *Monthly Weather Review*, **108**, p. 195–204.

[18] Platt, C. M. R. (1981): The Effect of Cirrus of Varying Optical Depth on the Extraterrestrial Net Radiative Flux. *Quarterly Journal of the Royal Meteorological Society*, **107**, p. 671–678.

[19] Prabhakara, C., Fraser, R. S., Dalu, G., Wu, Man-Li C., Curran, R. J., and T. Styles (1988): Thin Cirrus Clouds: Seasonal Distribution Over Oceans Deduced from Nimbus–4 IRIS. *Journal of Applied Meteorology*, **27**, p. 379–399.

[20] Ramanathàn, V., Pitcher, Eric J., and Maurice L. Blackmon (1983): The Response of a Spectral General Circulation Model to Refinements in Radiative Processes. *Journal of the Atmospheric Sciences*, **40**, p. 605–630.

[21] Sassen, Kenneth and Byung Sung Cho (1991): Subvisual–Thin Cirrus Lidar Dataset for Satellite Verification and Climatological Research. *Journal of Applied Meteorology*, **31**, p. 1275–1285.

[22] Shipley, S. T., Tracy, D. H., Eloranta, E. W., Trauger, J. T., Sroga, J. T., Roesler, F. L., and J. A. Weinman (1983): High Spectral Resolution Lidar to Measure Optical Properties of Atmospheric Aerosols. 1: Theory and Instrumentation. *Applied Optics*, **23**, p. 3716–3724.

[23] Smith, W. L. and C. M. R. Platt (1978): Comparison of Satellite-Deduced Cloud Heights with Indications from Radiosonde and Ground-Based Laser Measurements. *Journal of Applied Meteorology*, **17**, p. 1796–1802.

[24] Starr, David O'C. and Donald P. Wylie (1990): The 27–28 October 1986

FIRE Cirrus Case Study: Meteorology and Clouds. *Monthly Weather Review*, **118**, p. 2259–2287.

[25] Takano, Yoshihide and Kuo-Nan Liou (1989): Solar Radiative Transfer in Cirrus Clouds. Part I. Single–Scattering and Optical Properties of Hexagonal Ice Crystals. *Journal of the Atmospheric Sciences*, **46**, p. 3–19.

[26] Warren, S. G., Hahn, C. J., Chervin, R. M., and R. L. Jenne (1986): Global Distribution of Total Cloud Cover and Cloud Type Amounts over Land. NCAR Tech. Note NCAR/TN273+STR, [Available from National Center for Atmospheric Research, Boulder, CO 80307, NTIS DE87006903/XAB.] 228 pp.

[27] Woodbury, Gerard E., and M. P. McCormick (1986): Zonal and Geographical Distributions of Cirrus Clouds Determined by SAGE Data. *Journal of Geophysical Research*, **91**, p. 2775–2785.

[28] Wylie, D. P., and W. P. Menzel (1989): Two Years of Cloud Cover Statistics Using VAS. *Journal of Climate*, **2**, p. 380–392.

[29] Wylie, D. P., Menzel, W. P., Woolf, Harold M., and Kathy I. Strabala (1993): Four Years of Global Cirrus Cloud Statistics Using HIRS. Submitted to the *Journal of Climate* July 1993.

UNIVERSITY OF JOENSUU
DEPARTMENT OF PHYSICS
VAISALA LABORATORY

DISSERTATIONS 6

A High Spectral Resolution Lidar Based on Absorption Filter

Paivi Piironen

ACADEMIC DISSERTATION

To be present, with the permission of the Faculty of Science of the University of Joensuu, for public criticism in Auditorium P1 of the University of Joensuu, Tulliportinkatu 1, Joensuu, on October 14th, 1994, at 12 noon.

JOENSUU 1994

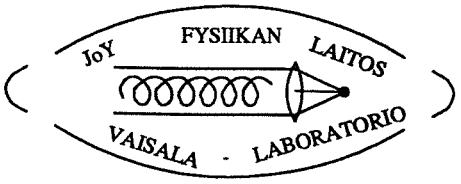

UNIVERSITY OF JOENSUU
DEPARTMENT OF PHYSICS
VAISALA LABORATORY

DISSERTATIONS 6

A HIGH SPECTRAL RESOLUTION LIDAR BASED ON AN IODINE ABSORPTION FILTER

PAIVI PIIRONEN

Joensuu 1994

Contents

Preface

This work was carried out in Space Science and Engineering Center of University of Wisconsin (Madison, USA) during years 1991-1994. I would like to thank Dr. Ed Eloranta for serving as my supervisor. Ed's enthusiasm, knowledge, Finnish "sisu", and aim at perfection and honest science will never stop amazing me. Ed's support, criticism, and suggestions during this work are greatly appreciated.

Special thanks go to Dan Forrest for his work on the software development. With his magical touch to the programming Dan helped me on the controlling of the HSRL and his wonderful RTI-displays made possible the real time visualization of the lidar data. Also thanks go to Jim Hedrick for his work on the mechanics and Jim Rose for his work on the electronics.

I would also like to thank Prof. Jyrki Kauppinen (University of Turku, Finland) and Dr. Erkki Kyrölä (Finnish Meteorological Institute, Finland) for their comments on the manuscript. Thanks to Kari Hassinen (University of Joensuu, Finland) for technical help on printing this thesis.

Very special thanks go to my husband Antti for his support during these years. During last years we have shared ideas and sleepless nights while working on our theses. I also wish to thank my parents for all the support and showing me the value of hard work.

The support for my work was provided by the University of Joensuu, Finland. The HSRL was supported by the Naval Research Laboratory, U.S. Department of Navy, under grant N00014-93-1-G013, by National Aeronautics and Space Admin., under grant NAG-1-882, and by Department of Energy, under grant DE-FG02-90ER61058.

Madison, August 1, 1994

Päivi Piironen

Päivi Piironen
University of Wisconsin–Madison
Space Science and Engineering Center
1225 West Dayton Street
Madison, WI 53706, USA

Keywords: High Spectral Resolution Lidar, lidar, iodine absorption, optical parameters of atmosphere, error analysis

Abstract

A High Spectral Resolution Lidar (HSRL) that uses an iodine absorption filter and a tunable, narrow-bandwidth Nd:YAG laser is demonstrated. The iodine absorption filter provides better performance than the Fabry-Perot etalon that it replaces. This study presents an instrument design that can be used as a basis for a design of simple and robust lidar for the measurements of the optical properties of the atmosphere. The HSRL provides calibrated measurements of the optical properties of the atmospheric aerosols. These observations include measurements of aerosol backscatter cross section, optical depth, backscatter phase function, depolarization, and multiple scattering. The errors in the HSRL data are discussed and the effects of different errors on the measured optical parameters are shown.

This is a personal reprint. The bibliographical information for the original publication is following:

Julkaisija Publisher	Joensuun yliopisto University of Joensuu
Toimittaja Editor	FT Timo Jaaskelainen
Exchange	Joensuu University Library, exchange P.O.Box 107, FIN-80101 JOENSUU, FINLAND Fax: +358-73-151-2691
Sale	Joensuu University Library, sale of publications P.O.Box 107, FIN-80101 JOENSUU, FINLAND Fax: _358-73-151-2691 Email: lavikainen@joyl.joensuu.fi

UDK	535.2:551.510.4:551.508.5
ISSN	1236-4673
ISBN	951-708-268-1

Original print by: Joensuun yliopiston monistuskeskus 1994

1 Introduction

The climate models used for modeling the transport of the short and longwave radiation in the atmosphere require a knowledge of the aerosol and cloud optical properties. Because the optical properties of cirrus clouds are not well known, the measurements of cloud optical depth, phase function, and particle size provide important information. Clouds affect the radiative balance of the earth and its atmosphere by reflecting incoming solar radiation and trapping outgoing longwave radiation. Cirrus clouds have been found to have an important role on this process[1,2]. Cirrus clouds consist of large, nonspherical ice crystals and they are generally found between altitudes of 4 and 15 km. Compared to water clouds, cirrus clouds are generally optically thin. Studies based on climate models suggest that presence of cirrus may produce either a heating or cooling effect depending on the cloud optical properties and altitude[1,2].

The University of Wisconsin High Spectral Resolution Lidar (HSRL) measures optical properties of the atmosphere by separating the Doppler-broadened molecular backscatter return from the unbroadened aerosol return. The molecular signal is then used as a calibration target which is available at each point in the lidar profile. This calibration allows unambiguous measurements of aerosol scattering cross section, optical depth, and backscatter phase function. Also measurements of depolarization and multiple scattering can be performed. In this study, clear air aerosols, stratospheric aerosols, and cloud particles are all referred to as aerosols. Similar measurements of cloud optical parameters can be made with a Raman-lidar[3,4], but because the Raman backscatter cross section is about 1000 times smaller than the Rayleigh backscatter cross section, the HSRL has a significant signal strength advantage over the Raman-technique. Another advantage of the HSRL is that it can provide daytime measurements while sky noise background limits the measurements of the weak Raman signal to night time.

The basic idea of an HSRL was originally presented by Fiocco and DeWolf[5]. They proposed the measurements of atmospheric aerosols by interferometrically separating the backscatter signal. They demonstrated the principle of an HSRL with laboratory measurements of scattering from natural aerosols and artificially produced dense fog. A later experiment with the HSRL technique was performed by Schwiesow

and Lading[6], who used Michelson interferometers in an attempt to measure atmospheric temperature. Their evaluation showed that a Michelson interferometer based measurements would theoretically produce accurate measurements of atmospheric temperature, but development of a functional system was limited by the quality of available optical components.

An investigation done by Shipley *et al.*[7] for a shuttle borne lidar experiment to measure global distribution of aerosols and their effects on the atmospheric heat budget started the University of Wisconsin HSRL research. The demonstration of the first University of Wisconsin HSRL was published by Shipley *et al.*[8]. The paper by Sroga *et al.*[9] presented the first results measured with the same system. The transmitter was based on a dye laser that operated at 476.8 nm wavelength. This laser provided only a 2–4 mW output and it operated at 100 Hz repetition rate. The backscatter signal was collected by a 0.35 telescope with a 320 μrad receiver field of view. The filtering of the solar background was performed by using an interference filter and three low resolution etalons with a total bandpass of 2 pm. The separation between aerosol and molecular backscatter signals was based on a high resolution etalon with $\sim$ 0.5 pm bandpass. The HSRL was mounted in an aircraft. The system pointed down to ground and it therefore covered only about 2 km measurement range. The range dependence of the receiver spectrometer bandpass due to the angular sensitivity of the etalon transmission complicated the measurements.

The aircraft system was later modified for ground based operations and the changes were reported by Grund[10]. The problems due to the range dependence of the spectrometer bandpass were reduced by using a fiber optics scrambler[12]. The transmitter laser was changed to a CuCl laser operating at 510.6 nm wavelength. The laser output power was 50 mW at 8 kHz repetition rate. The receiver telescope and the high resolution etalon remained the same, but the number of low resolution etalons was decreased to two providing a 2.5 pm bandpass. This system was capable of measuring cirrus cloud optical parameters up to $\sim$ 12 km altitude. Later, the development of lasers enabled the use of an injection seeded, frequency doubled Nd:YAG-laser (532 nm) as the HSRL transmitter. The new laser provided a 0.7 W output at 4 KHz repetition rate. This change was reported by Grund and Eloranta[11].

After all the development in the HSRL, problems with the insufficient calibration accuracy and environmental sensitivity of the system operation remained. The HSRL produced accurate measurements of clear air and thin cirrus, but the measurement accuracy was not sufficient for the cases where the aerosol signal was large compared to the molecular signal. Eventhough the measurement accuracy was not high enough to provide direct measurements of the optical depth profile inside a cloud, the total cloud optical depth was obtained. The cloud optical depth was determined from the decrease in the molecular signal across the cloud. The calculations of optical depth profile inside a cloud were made by assuming a constant backscatter phase function with altitude. The measured molecular profile was fitted with a profile derived from the known molecular backscatter cross section that had been corrected for the atmospheric extinction. The extinction profile was obtained by applying the Bernoulli solution to the aerosol backscatter profile[12]. The measured optical depth was used as a constraint.

The accuracy of the HSRL calibration was improved and the sensitivity for environmental changes was reduced in the next University of Wisconsin HSRL (Eloranta and Piironen[13]). In order to make the system operation more stable, the system was moved to a temperature controlled and vibrationally isolated environment. Participation in field experiments was made possible by moving the lidar to a semitrailer. The diameter of the receiver telescope was increased to a 0.5 m and the field of view was decreased to 160 μrad. A new photon counting data system was designed and extensive computer control of the system operations was implemented. Depolarization and multiple scattering measurement capabilities were added. With the improved system, the measurements of cloud optical properties were performed at altitudes up to $\sim$ 30 km.

During the 18 first years of the University of Wisconsin HSRL, the separation between aerosol and molecular scattering was based on a Fabry-Perot etalon with a 0.5 pm bandpass. With this etalon, the signal was divided into two channels. The signal reflected from the etalon surface was measured with one channel. This channel contained the the wings of the molecular spectrum and the part of the aerosol spectrum that did not pass the high resolution etalon. The other channel was used to measure

the part of the aerosol spectrum and the central part of the molecular spectrum that transmitted through the etalon. The basic idea of the spectral separation of a high resolution etalon based HSRL is presented in Fig 1.

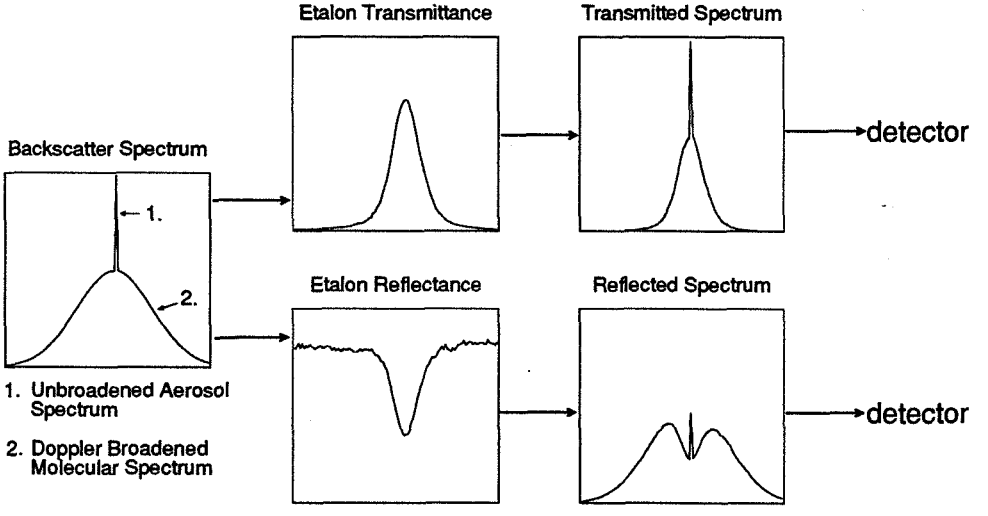

Figure 1. The spectral response of a high resolution etalon based HSRL. The received signal is a combination of the Doppler-broadened molecular backscatter spectrum and the unbroadened aerosol spectrum. The aerosol signal and the center of the molecular signal that transmits through the etalon is detected with one channel. The other channel detects the signal reflected from the etalon.

For the aerosol backscatter signal, only a $\sim$ 2:1 separation ratio between aerosol and molecular channel is achieved by a etalon. The Fabry-Perot etalon based HSRL produces accurate measurements of clear air, thin cirrus, and stratospheric aerosols. However, when the system is used to probe dense water clouds, the aerosol signal becomes on the order of 10^3 larger than the molecular return. Therefore, the inversion coefficients used to separate the aerosol and molecular signals must be known with better than 0.01% accuracy or otherwise some of the aerosol return will appear in the separated molecular return. Since the inversion coefficients for the etalon based system are known with only $\sim$ 0.1% accuracy, the measurements of dense water clouds are subject to error. The performance of a Fabry-Perot etalon is limited by its finesse and the angular distribution of incoming light. The etalon must be operated in pressure and temperature controlled environment, since better than a 0.1 mbar

pressure tuning accuracy and 0.1 °C temperature stability are required to keep the filter performance stable.

Shimizu *et al.*[14] proposed the use of an narrow-band atomic absorption filter in an HSRL and She *et al.*[15] reported high spectral resolution lidar measurements of temperature and aerosol extinction coefficient made by using a barium atomic absorption filter. These studies, and later studies from the same group[16,17], have shown, that an absorption filter provides a high rejection against aerosol scattering and therefore it makes the separation between molecular and aerosol scattering easier. Another advantage of an absorption filter is the stability of the absorption characteristics[14]. Furthermore, the transmission characteristics of an absorption filter are not dependent on the mechanical alignment of the filter[14] or the angular dependence of the incoming light. Also, a wide dynamic range in rejection against aerosol scattering is achieved by simply changing the vapor pressure[14] or the length of the cell.

This study presents an HSRL employing an iodine absorption filter. The spectrum of the $B^3\Pi^+_{ou} \rightarrow X^1\Sigma^+_g$ electronic transition in molecular iodine has more than 22 000 absorption lines in the visible wavelengths[18], and 8 of them are easily reached by thermally tuning a frequency doubled Nd:YAG laser output[19]. Compared to the barium, the advantage of iodine is that instead of requiring a dye laser, a narrow bandwidth, frequency doubled Nd:YAG laser can be used. Also, a strong absorption is obtained in a short cell at room temperature. Even though iodine has extensive hyperfine structure, the absorption line width is similar to the barium line width, which is broadened by operating at a temperature of ~500 °C.

A large number of iodine absorption lines have been used as reference for Doppler-limited spectroscopy studies and also numerous spectroscopic studies of the line structure and hyperfine structure have been performed. Liao and Gupta[20] reported a use of an iodine absorption vapor cell as a narrow band filter for fluorescence spectroscopy. Lately Miles *et al.*[21] reported the measurements of flow field properties based on an iodine absorption filter and Filtered Rayleigh Scattering technique. The first iodine absorption filter based HSRL is presented here.

The basic idea of an iodine absorption filter based HSRL is presented in Figure 2. The received backscatter signal is divided to two channels. One channel detecting

a sample from the total backscatter spectrum and the other channel the spectrum filtered by the iodine absorption filter. This signal contains information about the wings of the molecular spectrum and a small aerosol cross-talk signal. The first measurements made with the iodine absorption based HSRL were presented by Piironen and Eloranta[22].

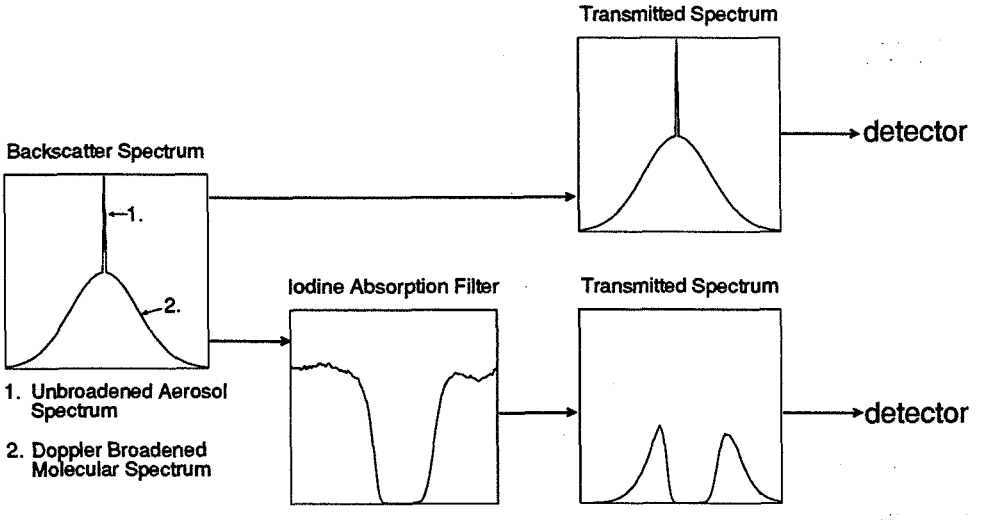

Figure 2. The spectral response of an iodine absorption filter based HSRL. The detected backscatter spectrum is divided to two channels. One containing the information from the total backscatter spectrum and the other the wings of the molecular spectrum and a small aerosol cross-talk.

The work presented in this thesis is organized as follows. A short introduction to the HSRL theory is given in Chapter 2. After that, the instrumentation of the new iodine absorption based HSRL is given in Chapter 3. This chapter also presents the basic principles of the polarization and multiple scattering measurements. A more detailed description of the iodine absorption cell is given in Chapter 4. The system calibration and laser wavelength locking are discussed in Chapter 5. In Chapter 6, examples from the data obtained with the new HSRL are given. This chapter gives a more detailed description of the depolarization measurements and also shows the effects of multiple scattering on the measured depolarization ratio. In addition to the depolarization measurements, the measurements of scattering ratio, aerosol backscatter cross section, and optical depth are discussed. The measurements show, that the

use of an iodine absorption filter enables accurate measurements of cloud optical parameters. Because the cross talk between channels can be accurately corrected and because the 160 μrad field of view of the HSRL effectively suppresses multiple scattering, the optical depth inside a cloud can be measured. This makes future studies of scattering phase function possible. As a final example from the HSRL measurements the Chapter 6 shows an atmospheric temperature profile obtained by the HSRL. The accuracy of the HSRL measurements is discussed in Chapter 7 and the error analysis is presented.

2 Lidar theory of the HSRL

The lidar equation of a monostatic lidar system can be presented in the following form

$$N(R) = \frac{N_o}{R^2}\frac{cA}{2}[\beta_a(R)\frac{P_a(\pi,R)}{4\pi} + \beta_m(R)\frac{P_m(\pi,R)}{4\pi}]e^{-2\tau(R)} + M(R) + B, \qquad (1)$$

where

$N(R)$ = number of photons incident on the receiver field of view from range R per data bin length,

N_o = number of transmitted photons,

c = speed of light,

A = area of the receiver telescope,

$\beta_a(R), \beta_m(R)$ = aerosol and molecular scattering cross sections per unit volume, respectively,

$\frac{P_a(\pi,R)}{4\pi}, \frac{P_m(\pi,R)}{4\pi}$ = normalized backscatter phase function due to aerosol and molecular scattering, respectively,

$\tau(R)$ = one way optical depth between lidar and backscatter volume at range R,
$= \int_0^R \beta_\epsilon(r')dr'$, where
$\beta_\epsilon(R)$ = total extinction cross section per unit volume,

$M(R)$ = multiple scattering contribution incident on the receiver per data bin length,

B = number of background photons incident on the receiver per data bin length.

Equation (1) demonstrates that the lidar return depends on both the local value of the backscatter cross section and on the optical depth between the lidar and backscattering volume at range R. A conventional single channel lidar provides a single measurement of N(R) at each range, and therefore it does not provide enough information to solve the lidar equation for extinction or backscatter cross section. The knowledge about the relationship between the backscatter cross section and extinction has to

be known or assumed and an estimate of a boundary value has to be given (see for example Klett[23]).

In order to make measurements of extinction and backscatter cross section, the HSRL measures two signals which can be processed to present lidar returns from aerosol and molecule backscattering. The separation between the aerosol and molecular scattering is possible, because the signal backscattered from air molecules is Doppler-broadened, while the signal from more massive, slowly moving aerosols remains spectrally unbroadened.

In the case of the HSRL, two separate lidar equations can be written

1) For aerosols

$$N_a(R) = F(R)\frac{N_o c A}{2R^2}\beta_a(R)\frac{P_a(\pi, R)}{4\pi}e^{-2\int_0^R \beta_\epsilon(r')dr'} \tag{2}$$

2) For molecules

$$N_m(R) = F(R)\frac{N_o c A}{2R^2}\beta_m(R)\frac{3}{8\pi}e^{-2\int_0^R \beta_\epsilon(r')dr'}, \tag{3}$$

The molecular backscatter phase function is here replaced with its analytical value $\frac{3}{8\pi}$. The term F(R) is an overlap term, that is a function of receiver and transmitter geometry[8]. Because the molecular scattering cross section is a function of the air density and can be calculated from the Rayleigh scattering theory using an independently measured atmospheric density profile, the equation (3) is well defined and it can be solved for the extinction. The molecular scattering cross section provides a calibration target which is available at each point of the lidar return.

Following optical parameters can be obtained from the separated lidar signals:

1) Aerosol to molecular backscatter ratio (scattering ratio) SR(R)

$$SR(R) = \frac{N_a(R)}{N_m(R)}. \tag{4}$$

Notice that, the backscatter ratio measurement is not dependent from the overlap term, and therefore measurements of backscatter ratio for the overlap region can be performed. The same effect can be seen later on the aerosol backscatter cross section and depolarization ratio determination.

2) Aerosol backscatter cross section

The properties of the molecular scattering are well known and therefore, the atmospheric density can be used to compute the molecular scattering cross section per unit volume β_m. From Rayleigh scattering theory[24], the molecular scattering cross section per unit volume is

$$\beta_m(R) = \mathcal{N}_m(R)\frac{d\sigma_R(\pi)}{d\Omega}, \tag{5}$$

where

$\mathcal{N}_m$ = number of gas molecules per unit volume

$\frac{d\sigma_R(\pi)}{d\Omega}$ = differential Rayleigh scattering cross section at scattering angle π per average gas molecule

For mixture of atmospheric gases below 100 km altitude[24],

$$\frac{d\sigma_R(\pi)}{d\Omega} = 5.45[\frac{\lambda(\mu m)}{0.55}]^{-4}10^{-28}cm^2sr^{-1}. \tag{6}$$

The number of gas molecules per unit volume can be calculated from the atmospheric pressure P(R) and temperature T(R).

$$\mathcal{N}_m(R) = \frac{P(R)}{T(R)}\frac{N_A}{R_a}, \tag{7}$$

where

P(R) = atmospheric pressure at range R

T(R) = atmospheric temperature at range R

N_A = Avogadro's number

R_a = gas constant of dry air

Thus, by using the previous equations, the molecular scattering cross section per unit volume can be written in the following form.

$$\beta_m = \frac{C_{air}P(R)}{T(R)}, \tag{8}$$

where

C_{air} $= 3.786 \times 10^{-8} KhPa^{-1}m^{-1}$ at 532 nm (from Eq. 5)

$P(R)$ = atmospheric pressure

$T(R)$ = atmospheric temperature

The aerosol backscatter cross section can be calculated by using the backscatter ratio and the calculated value of β_m

$$\beta_a(R)\frac{P_a(\pi,R)}{4\pi} = SR(R)\beta_m(R)\frac{3}{8\pi}. \tag{9}$$

3) The optical depth of a layer between ranges R_1 and R_2

$$\tau(R_2) - \tau(R_1) = \int_{R_1}^{R_2} \beta_\epsilon(r')dr' = \frac{1}{2} ln \left[\frac{\beta_m(R_2)}{\beta_m(R_1)}\frac{R_1^2}{R_2^2}\frac{N_m(R_1)}{N_m(R_2)}\frac{F(R_1)}{F(R_2)}\right]. \tag{10}$$

4) Total extinction cross section

The average value of total extinction cross section is a range derivative of the optical depth

$$< \beta_\epsilon > = < \frac{\partial\tau(R)}{\partial R} > = \frac{\tau(R_2) - \tau(R_1)}{R_2 - R_1}. \tag{11}$$

5) Backscatter phase function

The backscatter phase function, $\frac{P_a(\pi,R)}{4\pi}$, can be calculated from the following equation

$$\frac{P_a(\pi,R)}{4\pi}a(R) = \beta_m(R)\frac{3}{8\pi}\frac{SR(R)}{\beta_\epsilon(R)}, \tag{12}$$

where

$a(R)$ = single scattering albedo.

For water and ice clouds and most aerosols, the single scattering albedo at the wavelength of 532 nm can be assumed to be unity and therefore the backscatter phase function can be measured.

6) Linear depolarization ratio

The discrimination between water and ice clouds can be made from the depolarization properties of the backscatter signal. The linear depolarization ratio can be given as follows.

$$\delta_{a,m}(R) = N_{(a,m)\perp}(R)/N_{(a,m)\parallel}(R), \tag{13}$$

where $N_\perp$ and $N_\parallel$ are the number of incident on the receiver perpendicular and parallel to the receiver polarization axis, respectively. In the case of the HSRL, separate depolarizations of aerosol and molecular backscattering can be measured.

7) Cloud particle size

By measuring the signal strength variations as a function of field of view, the size of the cloud particles can be measured. The multiple scattered lidar return is a function of receiver field of view, particle size, range from lidar and the optical depth of the cloud. In the HSRL, the multiple scattering information along with the simultaneous single scattering measurement are used to calculate the cloud particle size.A detailed description of the multiple scattering approximation used for the HSRL measurements is presented by Eloranta[25,26] and Eloranta and Shipley[27].

3 Instrumentation

3.1 Introduction

3.1.1 An overview of the high resolution etalon based system

In the earlier versions of the University of Wisconsin HSRL, the separation between aerosol and molecular backscatter signals was made with a high resolution etalon with ~ 0.5 pm bandpass. The Figure 3 shows the receiver of the etalon based system[13]. The backscattered light was collected by the receiver telescope and directed through a fiber optics scrambler. The fiber optics scrambler was used to reduce the range dependence of the receiver spectrometer bandpass due to the angular sensitivity of the etalon transmission[12]. After collimation, the signal was prefiltered with an interference filter and a pair of low resolution etalons. After passing the dual aperture, the light was directed to the high resolution etalon. The high resolution etalon was slightly tilted with respect to the optical axis. This allowed the light that did not pass through the etalon to be reflected back to the dual aperture and to the molecular channel photodetector (PMT1). The light that passed through the high resolution etalon was detected with the aerosol channel photodetector (PMT2). The signal detected with the aerosol channel was a combination of aerosol backscatter spectrum and the center of molecular backscatter spectrum. The signal detected with the molecular channel was a combination of the wings of the molecular spectrum and the part of the aerosol backscatter spectrum that did not pass the high resolution etalon.

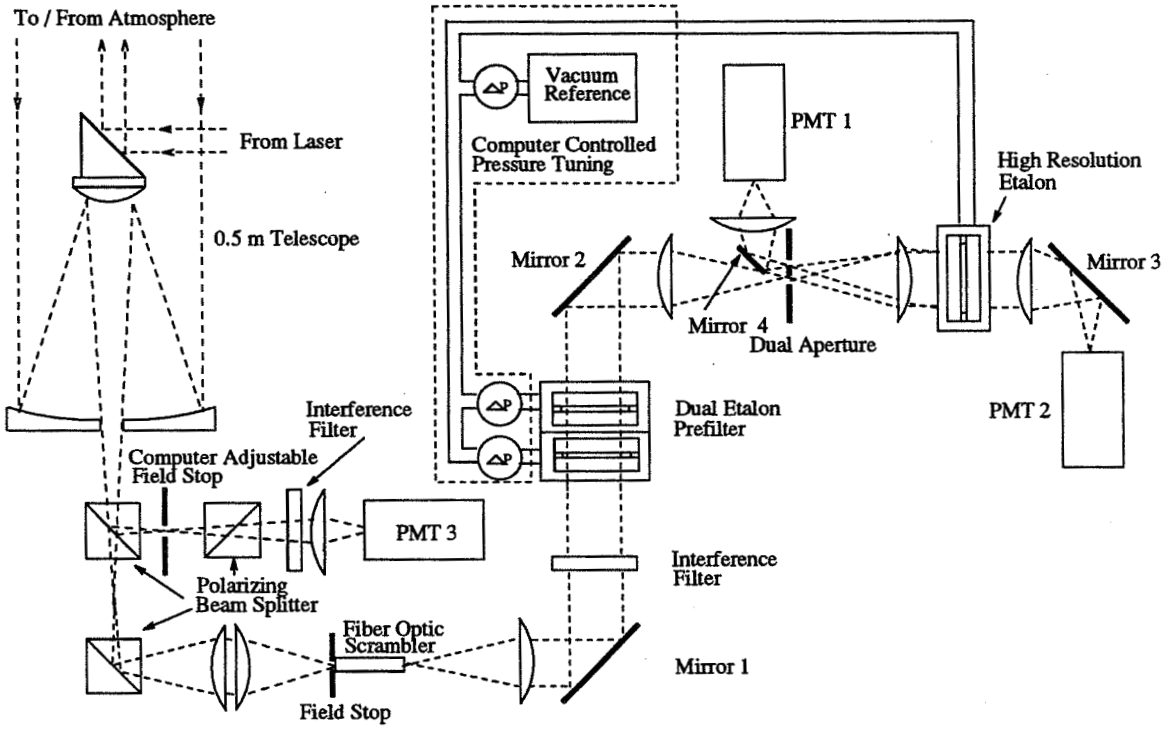

Figure 3. The receiver of the high resolution etalon based system. The backscatter signal is collected with a telescope. The fiber optics scrambler reduces the range dependence of the receiver spectrometer bandpass due to the angular sensitivity of the etalon transmission. The signal is background filtered with a interference filter and a pair of low resolution etalons. The separation between aerosol and molecular backscatter signals is done in the high resolution etalon. The part of the spectrum that transmits the etalon is combination of aerosol backscatter spectrum and the center of molecular backscatter spectrum (PMT2). The signal detected with PMT1 is a combination of the wings of the molecular spectrum and the part of the aerosol backscatter spectrum that did not pass the high resolution etalon.

3.1.2 A short introduction to the improvements

The instrument has been modified to measure polarization and a separate channel has been added to measure both polarization and signal amplitude variations as function of receiver field of view. These modifications allow discrimination between ice and water clouds and measurements of multiple scattering. Along with these modifications, the high resolution etalon, used in the earlier versions of the HSRL, has been

replaced with an iodine absorption filter. Also, the system has been redesigned for use in a semitrailer. Other changes include new data acquisition system, temperature controlled environment for the receiver optics, and improved optical design. The system parameters of the HSRL are summarized in Table 1.

The changes to the HSRL have improved the measurement capabilities of the HSRL. With the new HSRL, the measurements of the optical parameters of the atmosphere below 35 km can be made and therefore, the measurements can cover clouds from water clouds to high altitude cirrus clouds and also measurements of stratospheric aerosol layers can be performed. Clouds with optical depths up to ~ 3 can be measured. This means that most of the cirrus cloud cases can be fully observed and the cloud bases of the thick water clouds can be measured up to 300-500 m inside the cloud. This has been achieved by using a high pulse repetition rate, small pulse energy per laser pulse, and very fast photon counting electronics. Furthermore, the averaging time required for a good signal to noise ratio has been decreased by improving the optical transmission of the system. The use of the iodine filter, the controlling of the pressure of the etalons and the temperature of the optics, and the locking of the laser wavelength to an iodine absorption peak have increased the stability and the reliability of the system. Therefore, the need for frequent calibrations is eliminated and a stable operation can be maintained over a long period of time. The enhanced calibration technique has improved the accuracy of the HSRL calibrations.

Table 1. HSRL specifications (April 26, 1994)

Transmitter	
Wavelength	532 nm
Pulse duration	$\sim$ 130 ns
Pulse repetition rate	4 kHz
Average power	$\sim$ 0.2 W (seeded)
Frequency stability:	
Without I_2-locking	$\sim$ 100 MHz/hour (= 0.09 pm/h)
With I_2-locking	$\lambda\pm$ 0.052 pm
Receiver	
Telescope	
Type	Dall-Kirkham
Diameter	0.5 m
Focal length	5.08 m
Wide field of view channel	
Filter bandwidth	1.0 nm
Field of view	computer adjustable 0.21 $\rightarrow$ 4.0 mrad
Polarization rejection	$\sim 1\times10^{-3}$
Aerosol+molecular channel	
Filter bandwidth	8 pm
Field of view	0.160 mrad
Polarization rejection	$\sim 1\times10^{-3}$
Molecular channel	
Filter bandwidth	1.8 pm
Field of view	0.160 mrad
Polarization rejection	$\sim 1\times10^{-3}$
Photon counting data system	
Number of counters	3 (wfov, aerosol+molec., molec.)
Number of data buffers	6 (2 polarizations per channel)
Minimum bin width	100 ns
Number of bins	8192/channel
Max. rate of counters	$\sim 10^9$ Hz, tested to 350 MHz
Embedded computer	Intel i960CA
System control	Sun Sparc II

3.2 Transmitter

3.2.1 Transmitter laser

As a transmitter, the University of Wisconsin HSRL uses a continuously pumped, Q-switched, injection seeded, frequency doubled Nd:YAG laser operating at a 4 kHz pulse repetition rate[12] (Figure 4). The host cavity is based on a Quantronix model 116 laser. The quarter waveplates on either side of the Nd:YAG-rod are used to generate circularly polarized light in the rod in order to eliminate the spatial hole burning. The narrow bandwidth single frequency operation is achieved by injecting the cw-output of a diode pumped monolithic Nd:YAG ring laser (a modified Lightwave model S-100 seedlaser) into the host cavity through a partially transmitting rear mirror. Measurements have shown, that less than 100 MHz/h frequency drift is achieved. The 4 kHz pulse repetition rate is achieved by using an acousto-optic Q-switch.

The output of the laser is externally doubled by a KTP crystal. The frequency doubled output of the laser is tunable over a 124 GHz frequency range by controlling the temperature of the seedlaser diode. The original analog temperature controlling circuit of the seedlaser has been modified and connected to the microprocessor to allow remote control of the seedlaser Nd:YAG crystal temperature.

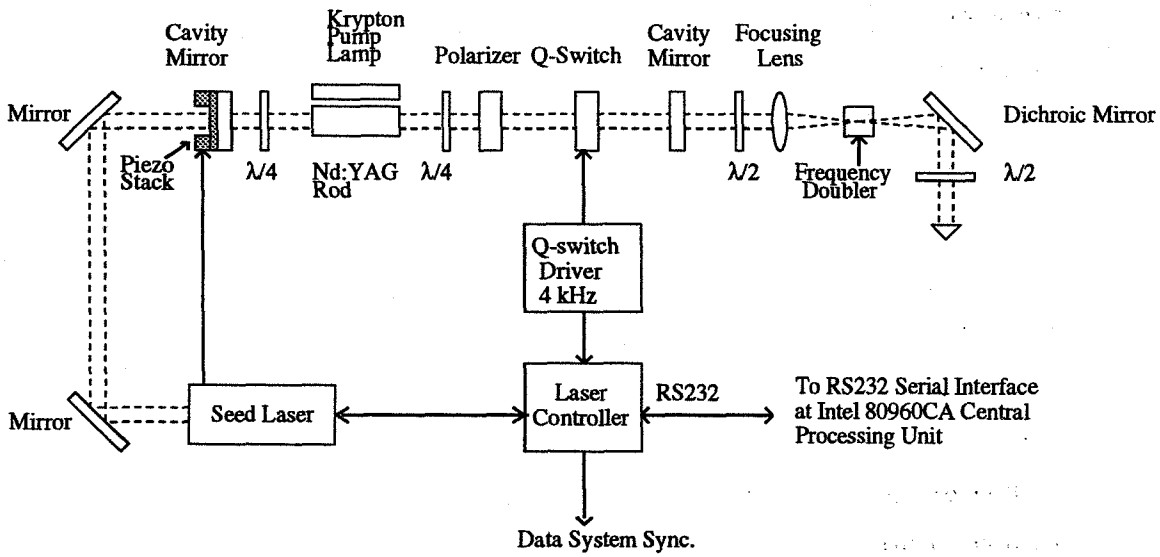

Figure 4. The HSRL transmitter laser.

After frequency doubling, the 532 nm and 1064 nm beams are separated by a harmonic beam separator. Because up to 15% of the residual 1064 nm beam is reflected from the beam separator, a second harmonic beam separator in the laser output (Figure 5) is used to provide more efficient filtering. The remaining 1064 nm beam is cleaned by a spatial filter. The spatial filter also cleans a halo of broader bandpass radiation.

Successful injection seeding requires that overlap between seedlaser resonance frequency and the frequency of a host cavity longitudinal mode is achieved. When the frequency of a host cavity longitudinal mode is locked to the seedlaser resonance frequency, the pulse developing out from the seedlaser signal will saturate the homogeneously broadened gain medium preventing development of any other axial modes from the spontaneous emission. Therefore, because one longitudinal mode is amplified more than any other mode, a spectrally narrow bandwidth pulse is generated. Since the seedlaser emissions used for injection seeding are generally $\sim$ 10 orders of magnitude stronger than the spontaneous emission, the Q-switched pulse builds up sooner out of the seed emission than the spontaneous emission. The frequency locking between seedlaser and host cavity is realized by controlling the host cavity length with a piezoelectric translator.

Because the seeded pulse builds up more rapidly when the host cavity is tuned to the seed laser frequency, the time between the Q-switch opening and the subsequent laser pulse (the Q-switch buildup time) can be used to servo control the tuning of the host cavity[28]. The spectral purity of the outgoing laser pulse can also be monitored using the Q-switch buildup time. A microcontroller based feedback loop seeks to maintain the cavity length by dithering the rear mirror so that the minimum Q-switch buildup time is obtained. For each laser pulse, a small offset voltage is applied to the piezoelectric translator and the effects to the Q-switch buildup time are simultaneously monitored. Based on the Q-switch buildup time the mirror position is driven towards the minimum time. Statistics on the Q-switch buildup time is collected at 4 kHz rate, but the mirror position is dithered at $\sim$ 140 Hz. The amount of dither is calculated based on the seeding percentage. The observed Q-switch build up time is $\sim$ 4.5 μs and the difference between seeded and unseeded conditions is typically

$\sim$ 500 ns. Because the spectral purity of the transmitted laser beam is important for HSRL measurements and because some shots are unseeded, the information from the Q-switch build up time is used to trigger the data system only for seeded shots.

The frequency stability of a single-frequency laser is determined by the seedlaser and the stability of the frequency locking is affected by the environment. The injection seeded operation is easily interrupted by mechanical vibrations transmitted through the support structure or through the cooling water or hoses. The effects of change in the optical length of the cavity due to thermal expansions of the support structure and temperature changes in the laser rod are compensated by the active controlling of the main cavity length. The laser is installed on a Super-Invar breadboard supported by a thick honey comb table that is mounted into a vibration insulated frame. The invar breadboard and the honey comb table are isolated from each other by a rubber pad. The laser was delivered with a Super-Invar table, which is thermally stable, but it is found to be acoustically sensitive. The active controlling of the main cavity length already minimizes the effects of changing environmental temperature so that an acoustically more insensitive table might provide a better performance. The mechanical vibrations coming from the laser cooling pump and transmitted into the cavity by hoses and water are isolated by a pressure dumper in the cooling water line. Because the original pressure dumper did not offer enough isolation, an extra damping system was installed. Also extra long elastic plastic water hoses are used to further attenuate the vibrations coming from the laser cooling pump. Furthermore, the temperature of the surrounding environment is stabilized by controlling the air temperature around the laser. The wavelength locking of the laser output to a iodine absorption line is demonstrated later in Chapter 5.2.

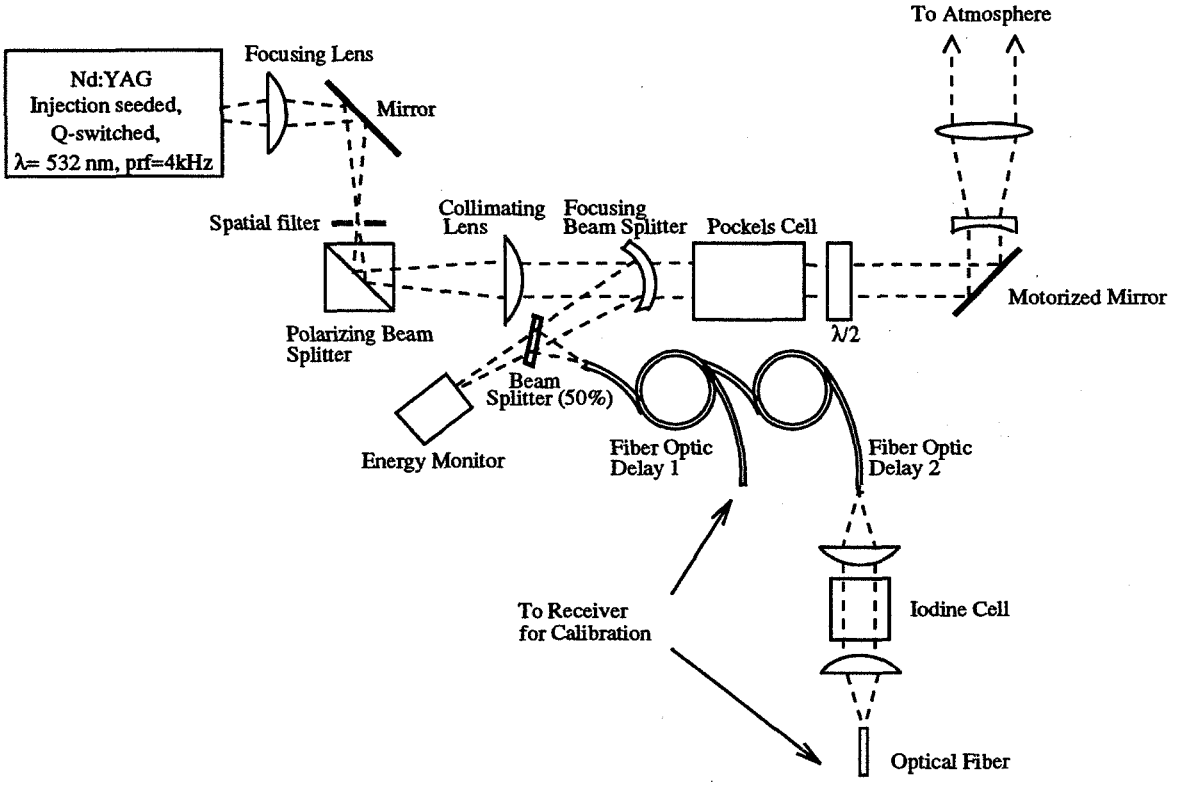

Figure 5. The HSRL transmitter setup. The HSRL transmitter employs an injection seeded, frequency doubled Nd:YAG laser. A Pockels cell in the output is used to rotate the polarization of the outgoing laser beam by 90 degrees for alternative laser pulses. An iodine absorption cell is used for the frequency locking of the laser wavelength. A sample of each laser pulse is directed to a pair of optical fibers, delayed, and injected back to the receiver for system calibrations. The length of the fibers is set so that the time-separated pulses can be recorded into the data profile.

3.2.2 Optics

A small amount (~2 %) of each transmitted laser pulse is directed into a pair of 100 m long optical fibers, delayed, and injected back to the receiver for system calibrations (see Figure 5). Since some of the laser shots are unseeded, the delay is necessary so that the measured Q-switch buildup time of each pulse can be used as a quality control to trigger the data system only for seeded shots. The length of the fibers is

set so that the time-separated pulses can be recorded in the data profile. The other ends of the calibration fibers are connected to a diffuse cylinder, which is located at the receiver such that the calibration light signals can be used to monitor system performance during data taking. Another 2 % of the laser light is taken into an energy monitor. The energy normalization of the received signal is realized by storing the energy of each laser pulse into the data record. A 4 cm long iodine cell is used for frequency locking of the laser. This cell provides $\sim$ 50 % absorption when the laser is tuned to the absorption peak. The frequency locking to the iodine peak is described later in Chapter 5.2.

Because the HSRL measures depolarization of the clouds and uses this information to separate between water and ice clouds, the polarization stage of the outgoing laser beam has to be well controlled. The output of the laser is linearly polarized and the orientation of the polarization vector is set perpendicular to the plane of the hypotenuse of the polarization cube. The use of the polarization cube guarantees that the residual cross-polarized component is cleaned out from the outgoing laser beam. In order to be able to use the same receiver optics and the same detector for both polarization components, the polarization of the outgoing laser pulse is rotated by 90 degrees for alternative laser pulses by a Pockels cell. The accuracy of the Pockels cell rotation is measured by observing the light coming from the Pockels cell through a polarizing cube with a photodetector. These calibrations show that the residual cross polarization can be reduced to 0.1 % of the parallel component. The calibration accuracy is limited by the 0.1 % rejection accuracy of the polarizing cube. The timing of the voltage switching between laser pulses is synchronized with the Q-switch signal and the controller electronics assures that the proper Pockels cell voltage is applied in time before the next laser shot. The final alignment between the transmitter and receiver polarization axes is performed by adjusting a half-waveplate and by using the atmosphere as a calibration target.

The use of small receiver field of views is made possible by decreasing the divergence of the outgoing laser beam with a beam expanding telescope (magnification 4x).

3.3 Receiver

3.3.1 Optics

The backscattered light is collected using a 50 cm diameter telescope (see Figure 6). To avoid specular reflection from horizontally oriented ice crystals, the system pointing direction is tilted by 4 degrees from the zenith. The signal polarized parallel to the receiver polarization axis and the signal perpendicular to that are separated by using a polarization cube (see Figure 6). This cube separates the signal to the WFOV-channel (PMT 3) and to the spectrometer-channels (combined aerosol+molecular channel (PMT1) and molecular channel (PMT 2)). An extra polarization cube for both channels is used to clean up the cross polarization component of the received signal down to a level that makes accurate depolarization measurements possible.

The multiple scattering properties can be studied by using the WFOV-channel, while simultaneously measuring the single scattering return with the spectrometer channels. A stepper motor driven aperture for the WFOV-channel enables field of view variations between 0.224 and 4 mrad. An interference filter with 1 nm bandpass is used for the background filtering. Because the field of view can be wide and the filter bandpass is broad, the WFOV measurements are currently limited to night time. The field of view of the spectrometer channels is 160 μrad, which further decreases the background sky noise and multiple scattering effects to the measured signal.

In order to achieve daytime measurements with the spectrometer channels, a low resolution etalon pair and an 1 nm interference filter are used to suppress the background solar radiance. The bandpass of the etalon pair is $\sim$9 pm, which is about 3 times the width of the expected Doppler broadened molecular spectrum. The length of the spacers is chosen so that only one common transmission order for the etalon pair occurs inside the interference filter bandpass. The bandpass of the low resolution etalon pair is wider than in earlier systems[8,12] in order to decrease the system sensitivity for the drift between transmitter wavelength and the etalon transmission maximum. The effects of environmental changes to the etalon performance are eliminated by mounting each etalon into a separate pressure and temperature controlled chamber. A third etalon chamber is used as a pressure reference. The absolute pressure in reference chamber and the differential pressures in each etalon chamber are

maintained by a computer controlled servo loop. The etalons are operated near the pressure where the changes in tuning gas density with temperature are cancelled by the thermal expansion of the etalon spacers[29]. Nitrogen is used as a tuning gas.

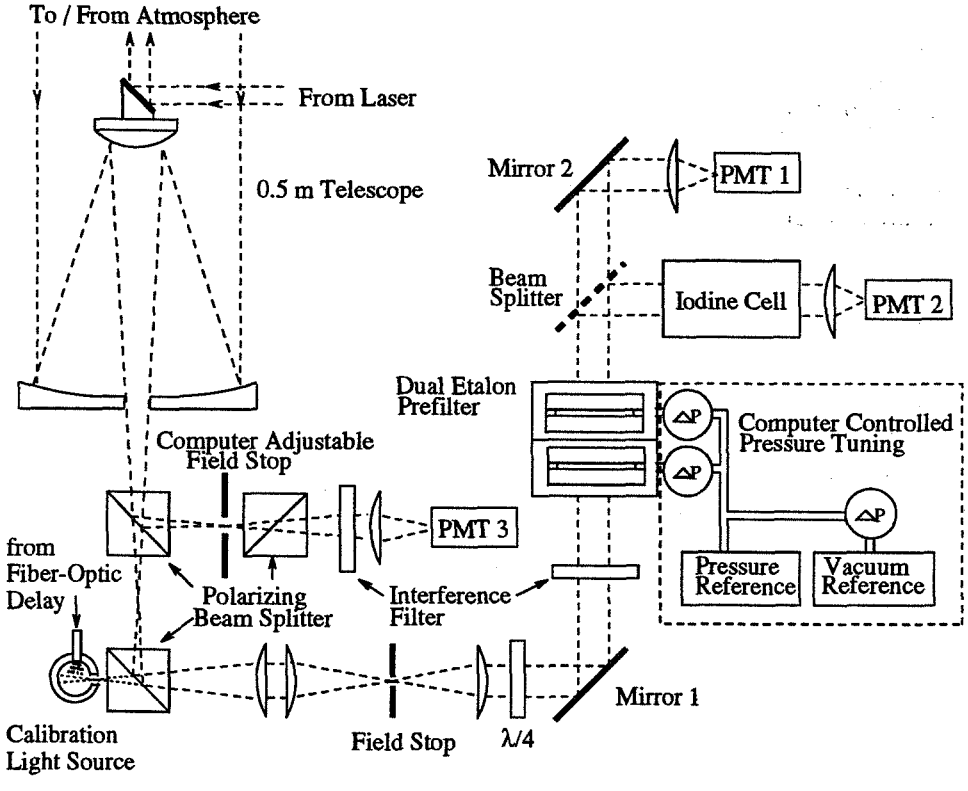

Figure 6. A polarizing prism at the output of the telescope separates the orthogonally polarized signals between wide field of view channel (PMT3) and the spectrometer channels (PMT1 and PMT2). Since the polarization of the transmitted laser pulse is rotated by 90^o between laser pulses, each channel alternatively receives perpendicular and parallel components. The received backscatter signal is prefiltered with an interference filter and a low resolution etalon pair before being directed into a beam splitter. The signal detected with PMT1 contains the information about the total aerosol and molecular backscatter signal. The signal directed through the iodine cell and detected by PMT2 is a combination of a amount of aerosol backscatter signal which passes through the absorption cell and the wings of the molecular backscatter signal.

After background filtering, the signal is divided into two channels by a beam splitter. The signal detected with the PMT1 (combined aerosol+molecular channel) contains the information about the total aerosol and molecular backscatter signal. The signal directed through the 43 cm long iodine cell and detected by the PMT2 (molecular channel) is a combination of the small amount of aerosol backscatter signal, which passes through the absorption cell, and the wings of the molecular backscatter signal (see Figure 7). The iodine absorption cell is described in more detail in Chapter 4.

A beamsplitter with a 30/70 (trans./refl.) splitting ratio is used to divide the signal between PMT1 and PMT2. The beam splitting ratio is chosen from the commercially available beamsplitters so that a good photon counting statistics with both channels is achieved when the system is tuned to the iodine absorption peak. Some beamsplitter types have poor transmission and reflection efficiencies and therefore part of the signal is lost in the beamsplitting process. Because good system transmission is important, a beam splitter with a high transmission and reflection efficiencies was chosen.

The beam splitters are highly polarization sensitive elements. When linearly polarized laser beam interacts with atmospheric aerosols and molecules, the backscatter signal consist of two perpendicularly polarized components. Therefore, the polarization sensitivity of the beamsplitter transmission and reflection has to be taken into account. The polarization sensitivity of the beamsplitter performance is noted as a problem in a system described by Krueger *et al.*[17]. The advantage of the HSRL is that the received signal is polarization filtered and therefore the light coming from the atmosphere to the beam splitter is always incident with the same polarization. On the contrary, the light from the current calibration light source is polarized orthogonally to the lidar signal and therefore the polarization sensitivity of the beam splitter creates a problem. This problem is solved by generating a circularly polarized light for the beamsplitter with a $\frac{\lambda}{4}$-waveplate.

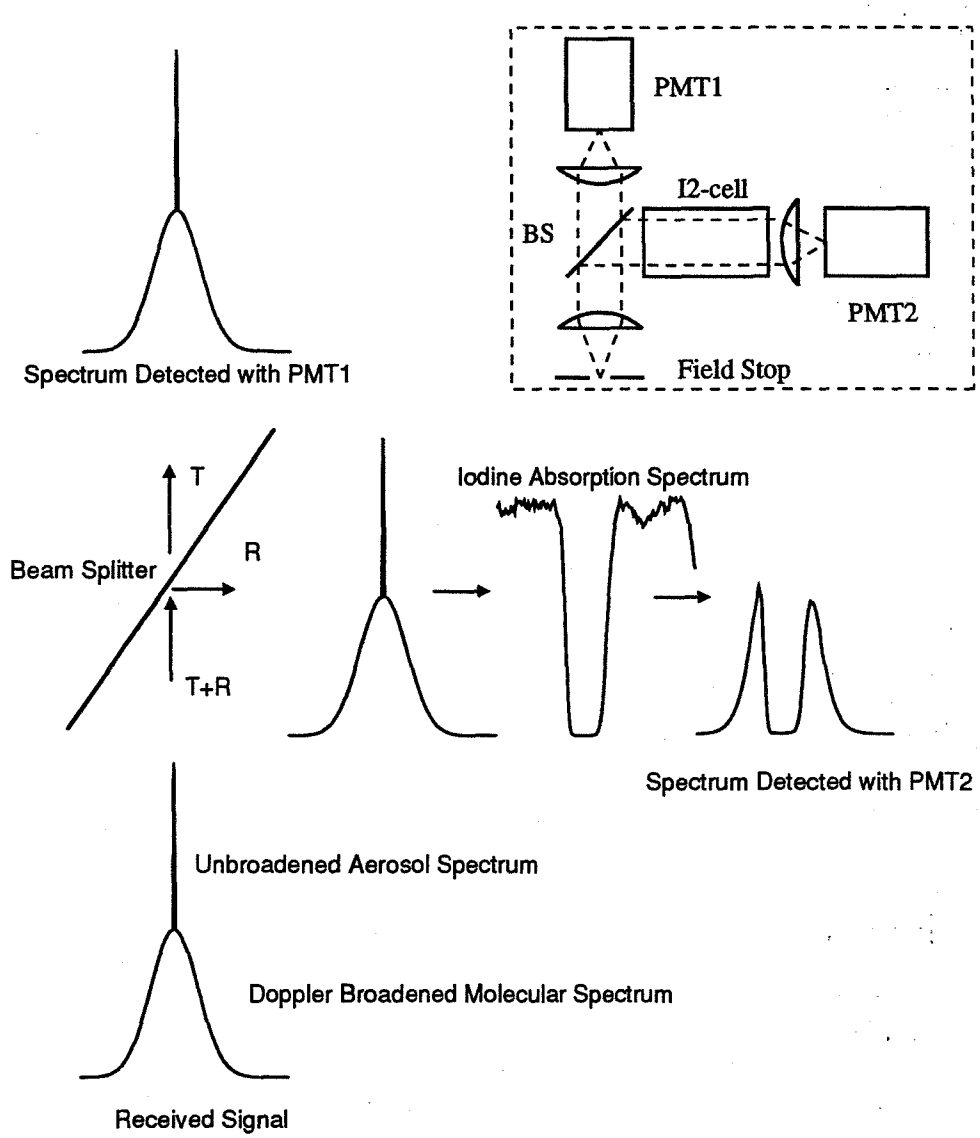

Figure 7. The spectral response of the HSRL receiver. The insert figure at the upper right corner shows a simplified setup of the spectrometer channels. The light that passes the field stop contains information about the Doppler-broadened molecular spectrum and the aerosol backscatter spectrum. The signal is divided into two parts with the beam splitter. The signal, which is transmitted through the beam splitter is detected with PMT1 and it contains information from the total backscatter signal. The signal, that reflects from the beam splitter is directed through an iodine absorption cell. In this process, the aerosol backscatter signal is attenuated in the iodine absorption line. Also the central parts of the molecular spectrum are filtered out and therefore the signal detected with PMT2 is a combination of the wings of the molecular spectrum and that part of the aerosol backscatter signal that passes through the cell.

3.3.2 Data system

In order to increase the dynamical range of the HSRL, new photon counting electronics were designed (Figure 8). The photon counting data system has three counters and each counter has 2 buffers, one for each polarization. Counting rates have been tested up to 350 MHz, but counters are designed to operate up to ~1 GHz. The 100 ns bin width enables a 15 m range resolution. The 4 kHz laser repetition rate enables the use of 2333 range bins, which can be used to probe the atmosphere up to 35 km. The limiting factor of the data system is the photomultipliers (EMI 9863B/100), which allow counting only up to 15 MHz without significant pile-up effects. The PMT's are pile-up and afterpulse tested and both corrections are included to the data processing. The corrections are discussed later in this chapter.

Computer control of the system is made by using Intel 80960CA embedded processor. The user interface is realized by using a Sun Sparc Station II. In addition to the data taking and the communication with the Sun, the system processor is used to control HSRL operation including pressure controlling of the etalons, timing of the Pockels cell voltage, controlling of the seedlaser temperature, controlling of the system shutters and relays, and controlling of the WFOV aperture.

Most of the HSRL-operations are computer controllable from a menu interface. System performance can be followed from real time displays. The real time Range Time Indicator (RTI) displays for the raw and/or inverted data are used to display the incoming data so that altitude, variability, thickness and depolarization of the cloud layer can be observed when the clouds move over the lidar site. Similar displays for the cloud optical properties (optical depth, aerosol backscatter cross section, phase function) can be shown.

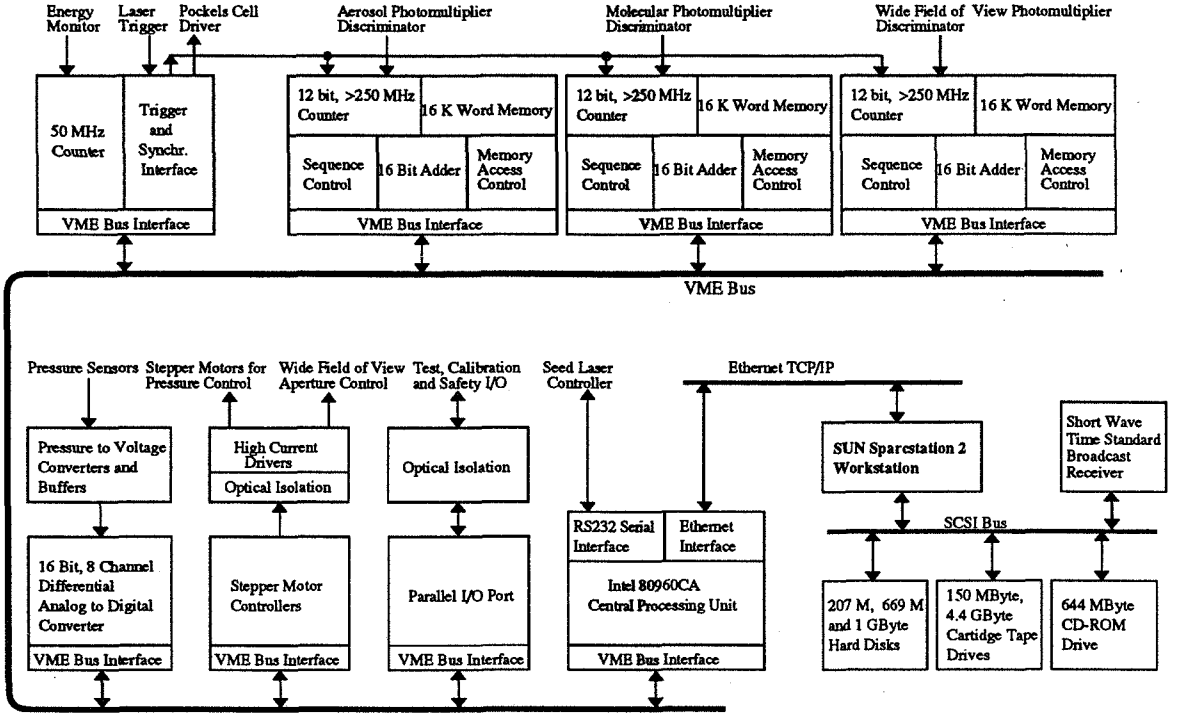

Figure 8. The HSRL data acquisition system.

The new counter design has improved the background light measurement accuracy of the HSRL. Instead of interrupting the data taking every 3.5–7 min for background and calibration checks (as was made with the system described by Grund[10]), the new HSRL is capable of measuring the background light simultaneously with the data. The maximum resolution of the data system is increased from 256 to 4096 range bins per channel. In the HSRL, the amount of background light in the measurement is calculated from the measured profile by using the upper altitudes of the lidar profile. The signal together with the background light is saved and therefore different kind of background corrections can be studied. Currently, the measured HSRL profiles are background corrected by assuming the signal above ~33 km to be background. By averaging the upper range bins together, the average amount of background in the measurement is calculated. The disadvantage of the current background correction method is that some of the signal can still be originated from Rayleigh scattering

leading into an overestimate of the amount of background light for altitudes 33 km or higher. A development of a background correction method that removes the Rayleigh scattering contribution from the background is currently in progress.

Photomultiplier afterpulsing can be seen as multiple output counts for a single input photon[30]. The afterpulsing could be caused by positive electron production in the dynode chain. The afterpulse pulses are time delayed compared to the signal from incident photon and the time delay is proportional to the path length for electron propagation. The signal originated from a short light pulse and measured with the HSRL can be presented in following form

$$< S(t) >= \int_0^{t+dt} S(t')\Phi(t-t')dt', \tag{14}$$

where

$< S(t) >$	= signal measured with the HSRL
S(t')	= signal incident on the receiver
Φ	= signal responce function, that contains the laser pulse width, datasystem bin width and afterpulsing of the photomultiplier

The afterpulse probability distributions were measured by illuminating the photomultiplier photocathode with a short duration laser light pulse. Pulse counting rates less than one count per 100 ns long data bin per pulse were used. A large number of laser pulses were averaged (~1 hour average). The probability distributions were calculated from the background corrected data. The amount of background light was calculated from the end of data record and the average value was subtracted from data. The measured afterpulse probability distributions of two photomultiplier tubes are presented in Figure 9. The afterpulse probability distribution was found to be different for each tube and therefore a separate correction for each tube had to be implemented to the signal analysis program. With a known afterpulse probability distribution function, the afterpulse contribution can be removed from the measured signal by using deconvolution. The effect of afterpulse correction to the measured signal is presented in Figure 10.

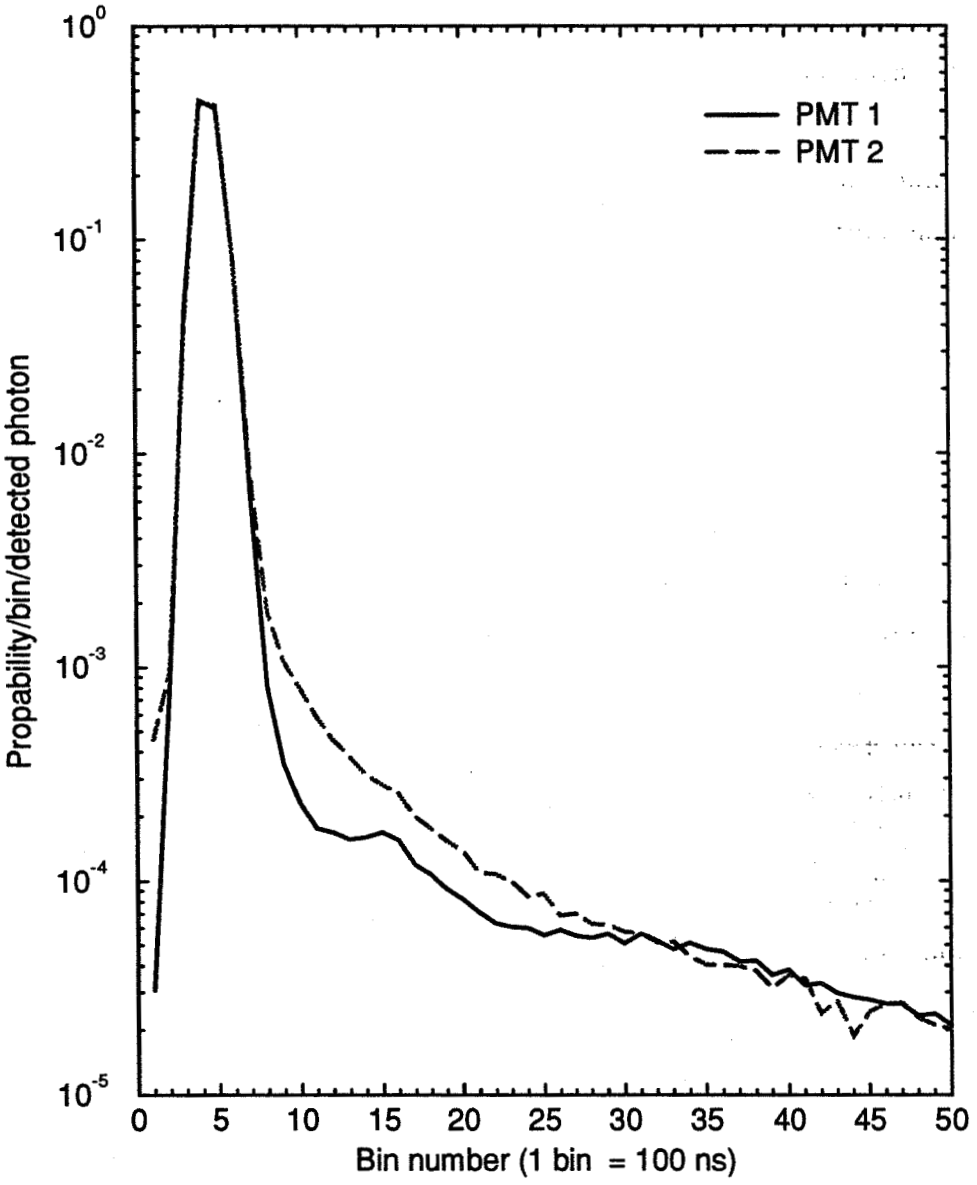

Figure 9. The temporal distributions of two EMI 9863B/100 photomultiplier tubes. The temporal distribution of the measured photons is a convolution of the laser pulse width, bin width of the data system, and the afterpulsing of the photomultiplier. The laser pulse is located in the first bins and the afterpulse can be seen as a decaying tail. The afterpulse distribution of the PMT1 shows better afterpulse behavior than the PMT2.

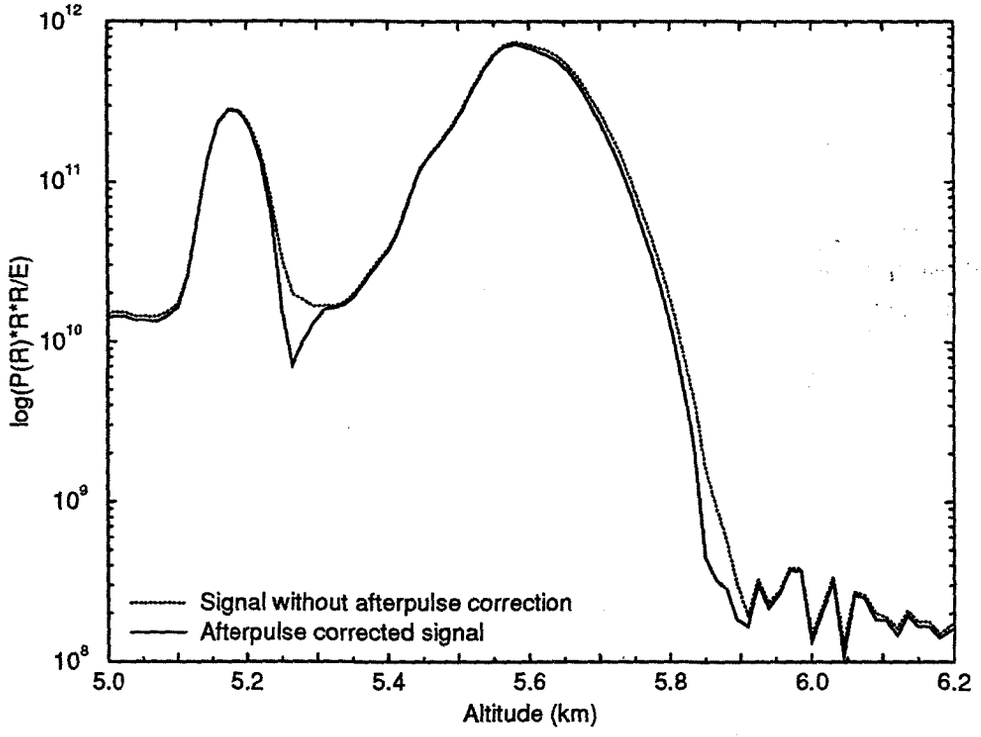

Figure 10. The effect of afterpulse correction to the measured aerosol signal in the case of thick water cloud (at 5.6 km) with an ice crystal precipitation at 5.1 km. The afterpulsing increases the aerosol signal at the end of the cloud, and therefore the geometrical thickness of the clouds is underestimated. The effect of afterpulsing to the molecular signal is similar, and thus a slight overestimate of the optical depth of the cloud is made, if the afterpulse correction is not performed.

The pulse pile-up is seen when all time separated photons are not distinguishable and they overlap. This causes a nonlinear response. In order to be able to separate between counts, a minimum separation time between two pulses is required for them to be distinguished. This time is called resolving time (or dead time). Since the time interval distribution of photons that reach the photomultiplier follow a Poisson distribution, the probability P_o that a pulse overlaps with another pulse inside a certain time interval is given by the following formula[31]

$$P_o = 1 - e^{-R\tau} \tag{15}$$

where

τ = resolving time

R = average count rate

In order to obtain the resolving time (dead time) of the photomultipliers, the photomultiplier responses to different count rates were tested. First, light level is set to level which is high enough to generate a pile-up. Then the photomultiplier response to different light levels is measured by changing the light intensity with neutral density filters and recording the signal change. In order to be able to define the resolving time of the photomultiplier, the photon counting was modeled. The pulses coming from the photomultiplier were treated as Poisson distributed signals. The resolving time that produced the best fit between simulated and measured results was used for the pile-up correction. All photomultipliers were found to have $\sim$ 13 ns resolving time. The pile-up correction has to be performed before the afterpulse correction or any other corrections, because the pile-up effect is nonlinear. The pile-up is affected by the signal strength, signal background and afterpulsing and therefore, data has to contain the information from all these factors when the correction for pile-up is performed.

In order to make the pile-up correction for data, the following equation was used

$$N = N_o e^{-R\tau} \tag{16}$$

where

N = measured counts

N_o = actual counts

τ = resolving time

R = average count rate = $\frac{N_o}{dt}$

This equation is solved iteratively for N_o, so that

1. $N_o(1) = \mathrm{N}$
2. New $N_o(i+1) = Ne^{\frac{N_o(i)}{dt}\tau}$, where dt = bin length [s]

3. Step 2 is repeated until N_o converges

The effect of pile-up correction to the measured signal is presented in Figure 11.

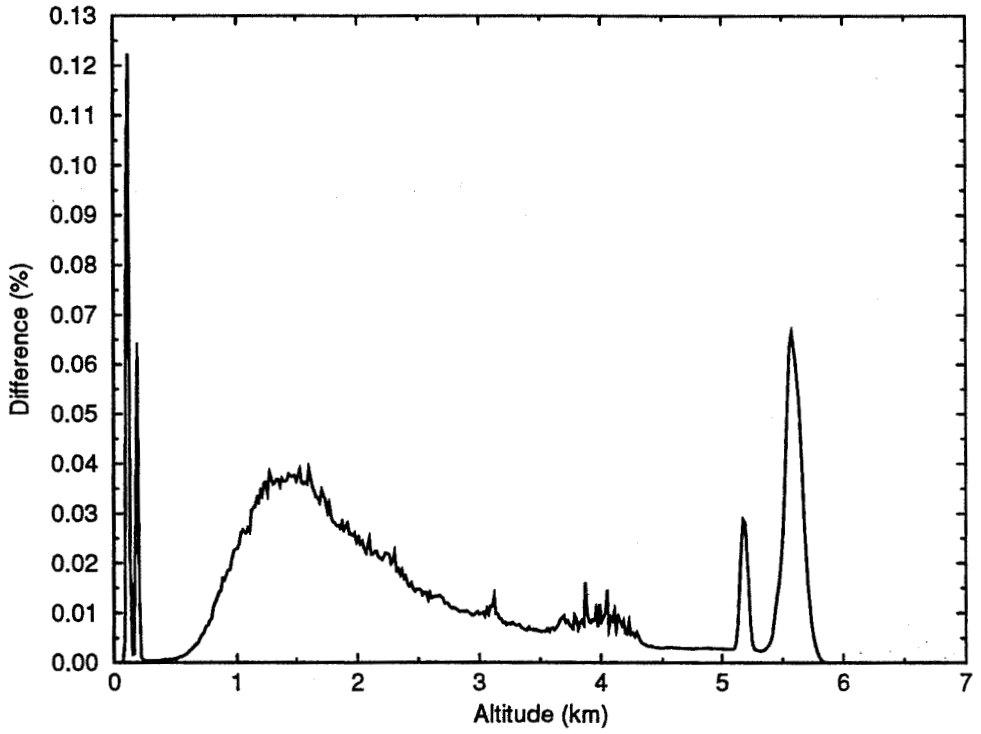

Figure 11. The effect of pile-up correction to the measured aerosol signal in the case of thick water cloud (at 5.6 km) with an ice crystal precipitation at 5.1 km. The calibration fiber signals are shown as spikes at altitudes $\sim$ 0 km. The maximum number of photons measured for the water cloud is 0.68 photons/100 ns bin and after pile-up correction 0.75 photons/100ns bin are observed. Even with this low count rates the effect of pile-up is $\sim$ 10% and therefore, the pile-up correction is very important when strong returns from clouds are studied.

4 Iodine absorption filter

In order to overcome the limited capability of the high resolution etalon to separate between aerosol and molecular scattering and to increase the system stability and reliability, an iodine absorption filter was constructed. For the first HSRL measurements a 43 cm long cell was made. The cell was made from glass tubing with an attached side arm. Optical quality end windows with anti-reflection coatings were epoxed to the ends. The cell with iodine crystals in a side arm was evacuated and kept at 27 °C. Transferring of the iodine from the absorption cell into the vacuum pump was prevented by evacuating the cell through a cold trap and cooling the side arm with liquid nitrogen. Although the iodine cell can be operated at room temperature, the operating temperature of the cell has to be controlled, because the vapor pressure of iodine is very temperature sensitive[32]. In the HSRL, the cell temperature is maintained with ±0.1 °C accuracy by operating the cell in temperature controlled environment.

The iodine spectrum is measured by scanning the laser wavelength by changing the temperature of the seedlaser under computer control. A small amount of laser light is directed into a 100 m long fiber optic delay (Fiber 1 in Figure 4) and sent to the receiver to create a calibration light source. The temperature-wavelength dependence of the scan was determined by using the free spectral range of the high resolution etalon as a reference. This could be made, because the free spectral range of the etalon can be calculated when the length of the etalon spacers is known and the spacing of two (or more) etalon transmission peaks in temperature units can be measured. The calibration was made by simultaneously measuring the transmission spectrum of the high resolution etalon and iodine absorption filter. The simultaneous measurement of the high resolution etalon and iodine absorption filter transmissions was made by measuring the signal reflected from the high resolution etalon (Figure 12) and the signal transmitted through the absorption cell. The pressure in etalon was held constant while the laser wavelength was scanned. The spectrum was normalized by measuring the cell transmittance without the iodine cell.

A part of the measured iodine spectrum is presented in Figure 13. The measured spectrum was compared with a published spectrum[18] and an ~0.01 pm wavelength

agreement in relative line positions was observed. The linearity of the temperature scan was confirmed from the free spectral range information of high resolution etalon by performing the scan over more than one free spectral range. Single mode operation between two seedlaser mode hops can be maintained over 20 GHz range (at 1064 nm) and within this range two high resolution etalon free spectral ranges can be covered. During a mode hop the laser frequency jumps back about 10 GHz.

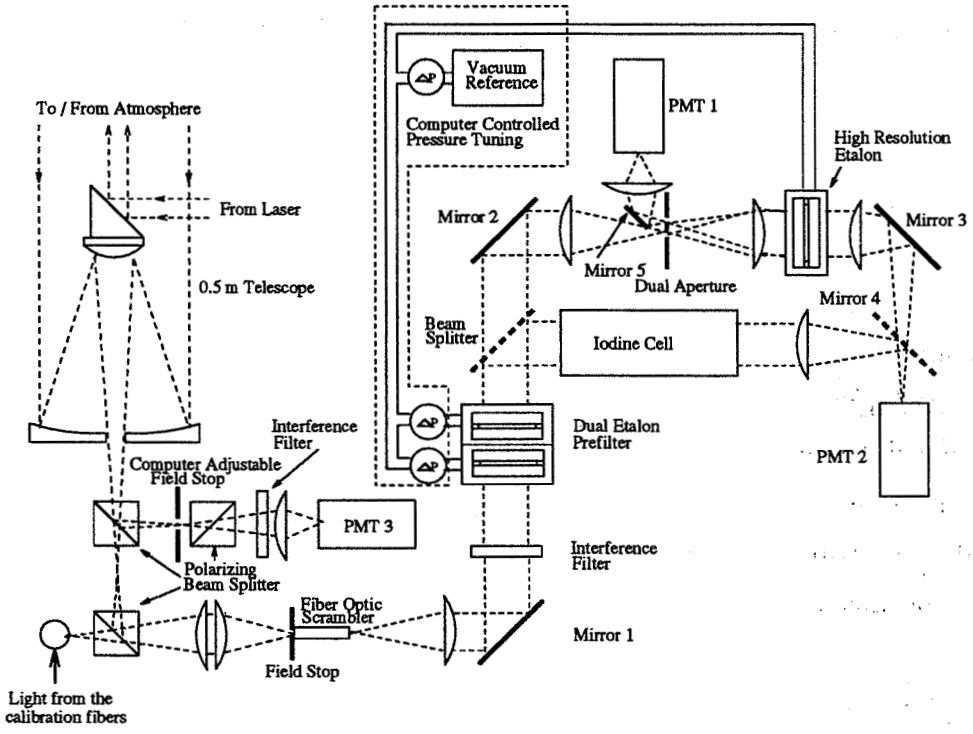

Figure 12. The HSRL receiver used for iodine spectrum calibrations. The same receiver setup was used for the first HSRL measurements with the iodine absorption filter. For data taking the transmission of the high resolution etalon was tuned out from the peak and the etalon was used as a reflector. When the beamsplitter and the mirror 4 are removed from the system, the system returns back to the old HSRL receiver.

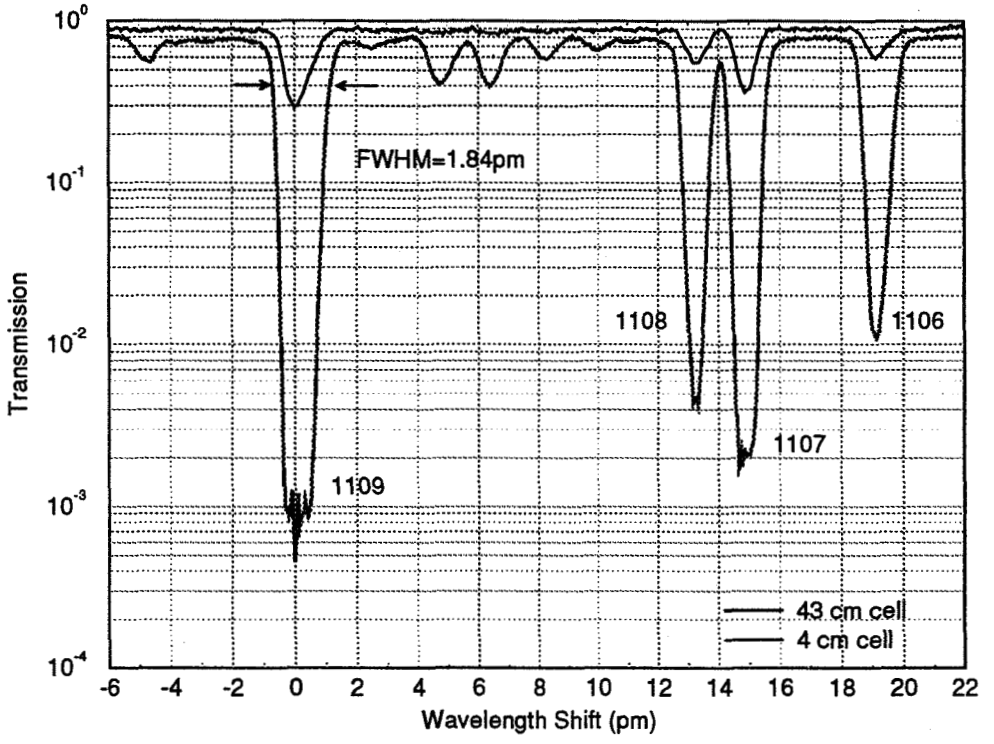

Figure 13. Transmission of a 4 cm and 43 cm iodine cells as a function of wavelength shift. The identification line numbers are from Gerstenkorn and Luc[18].

For initial HSRL measurements the line 1109 (peak wavelength 532.26 nm)[18], which is well isolated from the neighboring lines, was chosen. The full width half maximum width of the line is ~1.8 pm and the peak transmission is ~ 0.08%. The hyperfine structure of the peak 1109 defines the asymmetric shape of the absorption peak[33]. In fact, the line 1109 is a combination of two rotational vibrational transitions with different hyperfine structures.

The iodine absorption cell provides a robust filter for the HSRL, because it is not dependent on the mechanical alignment of the filter or the angular dependence of the incoming light. Another advantage is the stability of the absorption characteristics. This provides a stable long term operation. The strength of observed absorption line is dependent on the line strength, and the length, temperature, and pressure of the cell. By controlling the operating environment and with a nearly leak proof system, the

current iodine cell is operated for several months without any maintenance. During this time, a small change in absorption strength and line width were observed due to a small leak that was caused by the iodine penetrating through a hose. Also the iodine was found to condense into the walls of the cell, but even during a long period of time, the amount of condensation has been small and $\sim$ 10% extra absorption is observed. The condensation can be prevented by operating the tip of the side arm couple degrees below the cell temperature. The problems with reactive iodine penetrating through the hoses can be prevented by using a sealed all-glass cell. In a short term operation, the stability of the absorption characteristics has proven to be so good that a system calibration scans from different days can be used for the calculations of the system calibration coefficients. This requires, that the alignment of the receiver optics is stable.

An absorption filter offers a high rejection against aerosol scattering and therefore it makes the separation between aerosol and molecular scattering easier. Also, a wide dynamic range in rejection against aerosol scattering is achieved by simply changing the vapor pressure or the length of the cell. Comparison between high resolution etalon and iodine absorption filter performance is presented in Figure 14. A 2:1 separation between molecular and aerosol scattering by the etalon (Figure 14.b) is measured compared to a 1000:1 separation in the iodine cell when operated at 27 °C (Figure 14.a). The molecular transmission in Figure 14.a and Figure 14.b is calculated by using the Doppler-broadened molecular spectrum at -65 °C. This temperature is close to the lowest temperature measured at the tropopause and this gives the smallest transmission through the iodine absorption cell. The molecular transmission of the high resolution etalon and the iodine absorption filter are similar (Figure 14.c). Due to wide absorption line width, the molecular transmission of the iodine filter is more dependent on the air temperature than the etalon. The temperature dependence of the cell transmission is modeled by using the table values of iodine vapor pressure[32] (Figure 14.d). Calculations show, that by changing the cell temperature from 27 °C to 0 °C, the online transmission can be tuned from 0.08% to 60%.

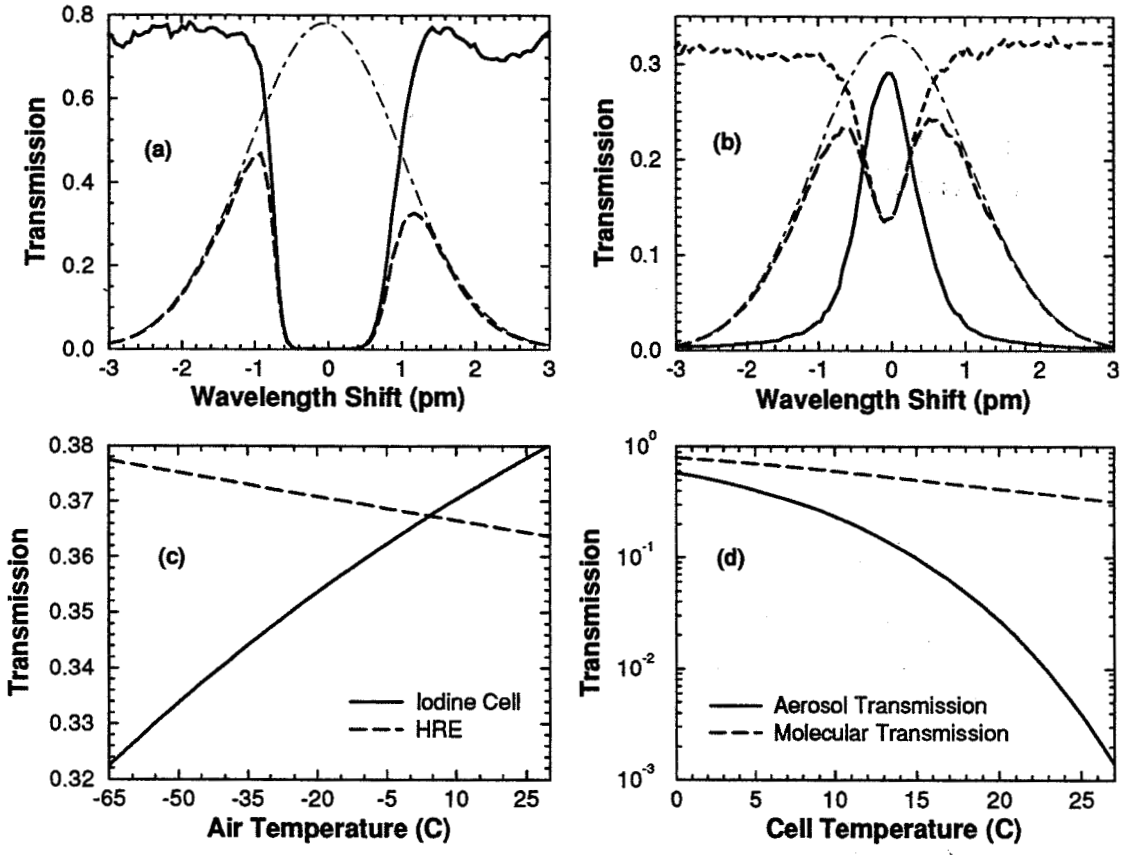

Figure 14. (a) Transmission of 43 cm cell (solid line) together with the molecular transmission (dashed line) at -65 °C air temperature as a function of wavelength shift. Dot-dashed line shows the calculated molecular spectrum at -65 °C. (b) Etalon transmission (solid line) and calculated molecular transmission (dashed line) as a function of wavelength shift. Dot-dashed line shows the calculated molecular spectrum at -65 °C. (c) Comparison of molecular transmission of high resolution etalon and iodine cell as a function of air temperature. (d) Iodine cell aerosol and molecular transmission as a function of cell temperature.

5 Calibration and tuning

5.1 Calibration theory

The HSRL measures optical properties of aerosols by using the backscatter from atmospheric molecules as a calibration target. In the receiver the signal is separated into two separate signals: one proportional to total aerosol and molecular scattering and the other containing the molecular backscattering together with a small aerosol cross talk component. The measured signals are

$$S_{a+m}(R) = \eta[N_a(R) + N_m(R)] \tag{17}$$

$$S_m(R) = \eta[C_{am}N_a(R) + C_{mm}(R)N_m(R)], \tag{18}$$

where

S_{a+m}	= signal measured with the combined channel (PMT1 in Figure 6)
S_m	= signal measured with molecular channel (PMT 2 in Figure 6)
N_a, N_m	= total number of aerosol and molecular backscatter photons incident on the receiver field of view
C_{am}	= aerosol transmission of the molecular channel relative to the combined channel
C_{mm}	= molecular transmission of the molecular channel relative to the combined channel
η	= system efficiency factor that includes the optical transmission of the combined channel and its photomultiplier quantum efficiency

These two equations can be solved to present the separated aerosol and molecular backscatter signals.

$$N_m(R) = \frac{S_m(R) - C_{am}S_{a+m}(R)}{\eta(C_{mm}(R) - C_{am})} \tag{19}$$

$$N_a(R) = \frac{S_{a+m}(R) - \eta N_m(R)}{\eta} \tag{20}$$

The calibration coefficients C_{am} and C_{mm} are obtained from a system calibration scan. For calibration the system input aperture is uniformly illuminated with a diffuse

light. The receiver spectral transmission function is measured by scanning the laser wavelength over an 11 pm wavelength range around the selected iodine absorption peak and recording the signals (originated from calibration fiber 1 and calibration fiber 2) with both spectrometer channels (PMT1 and PMT2 in Figure 6). A calibration scan is performed before and after each dataset. When system is running for a long period of time (time $\sim$ 3 hours) the system operation is interrupted and a calibration scan is performed. An example from a calibration scan is presented in Figure 15. In addition to the information on the system spectral transmission, the calibration signals contain information on the beamsplitting ratio between channels. Since the signal measured through the iodine cell is flat at the top of the iodine absorption peak, the determination of the wavelength of the absorption maximum is based on the signal from the reference iodine cell (4 cm cell in Figure 5, calibration fiber 2) and measured with the PMT1. Otherwise, the signals from the first calibration fiber are used for the calibration coefficient calculations.

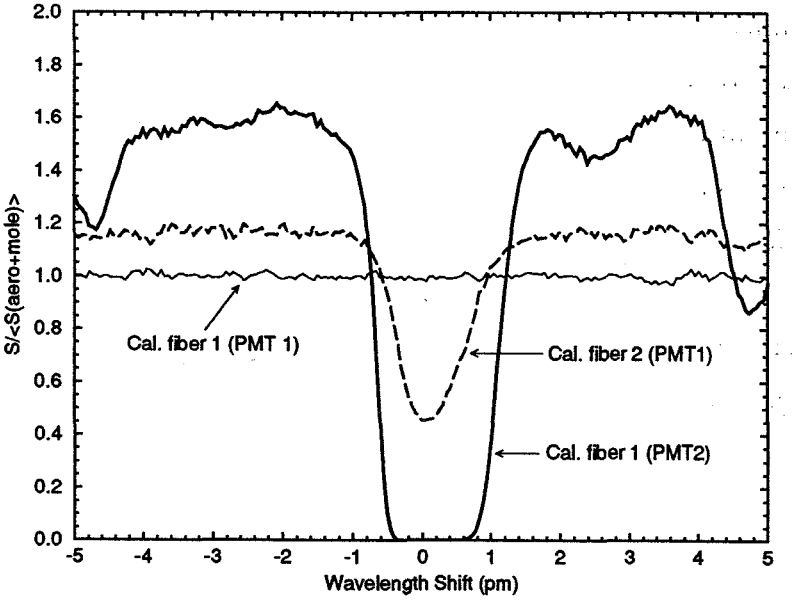

Figure 15. An HSRL calibration scan. The calibration fiber 1 signal that is detected with PMT2 shows the iodine absorption spectrum of the 43 cm long iodine cell. The calibration fiber 2 signal detected with PMT1 presents the absorption spectrum of the 4 cm long reference cell. The signal from calibration fiber 1 and detected with PMT1 is used as a reference.

Since the Doppler-broadening of the aerosol backscatter is negligible, the spectral distribution of the aerosol backscatter can be assumed to be similar to the spectral distribution of the transmitter laser. The measured calibration signals can be presented as a convolution between laser spectral distribution and spectral bandpass of each channel. Therefore, the fraction of the total aerosol backscatter detected by the molecular channel (C_{am}) can be directly obtained from the calibration signals.

$$C_{am} = \frac{S_m(\text{at peak})}{S_{a+m}(\text{at peak})}, \tag{21}$$

where

$S_m =$ calibration fiber 1 signal detected with the PMT2 at the iodine absorption peak

$S_{am} =$ calibration fiber 1 signal detected with the PMT1 at the iodine absorption peak.

The fraction of the total molecular backscatter measured by the molecular channel (C_{mm}) is calculated by convoluting the measured filter function with the calculated molecular spectrum.

$$C_{mm} = \frac{\sum_{n=1}^{N} S_m(\lambda_n) M_{spect}(\lambda_n) \Delta\lambda}{\sum_{n=1}^{N} S_{a+m}(\lambda_n) M_{spect}(\lambda_n) \Delta\lambda}, \tag{22}$$

where

S_m = calibration fiber 1 signal detected with the PMT2 (filter function for molecular channel convoluted with the laser spectrum)

S_{a+m} = calibration fiber 1 signal detected with the PMT1 (filter function for aerosol + molecular channel convoluted with the laser spectrum)

M_{spect} = calculated molecular spectrum

N = number of points in calibration scan

λ = wavelength

$\Delta\lambda$ = the wavelength difference between two points in the calibration scan

The divisor on the Eq. 22 is presented as a convolution aerosol and molecular channel. Therefore, the divisor presents the amount of molecular spectrum seen with the combined aerosol and molecular channel. The dividend of the Eq. 22 describes the molecular signal detected through the iodine absorption cell. The molecular spectrum model used in the calculation is presented in a paper by Yip and Nelking[34] and it includes the effects of Brillouin scattering as a function of temperature and pressure.

The accuracy of the calibration coefficients is mainly limited by the photon counting statistics. Because the signal transmitted through the absorption peak is small, the error due to photon counting statistics dominates the error in the determination of C_{am}. Therefore, the accuracy of the C_{am} is improved by increasing the photon counting statistics at the absorption peak. Three different ways to increase the photon counting statistics can be considered. First, the signal at the absorption peak can be increased by scaling the light with neutral density filters while scanning. Second, the amount of aerosol backscatter signal can be further decreased into a point where the effects of the photon counting statistics are negligible. Third, longer averaging time can be used.

The disadvantage of using neutral density filters is that the filters have to be well calibrated and the change in the value of neutral density filter has to recorded into the data so that the signal can be reconstructed back to the absorption spectrum. The disadvantage of the longer absorption cell is that the increased cell length will further decrease the amount of transmitted molecular signal. Also the spectral purity of the laser limits the observable absorption strength. In order to be able to obtain a good photon counting statistics for the signal of the whole absorption peak, a long averaging time is required and therefore the total calibration time would be unreasonable long ($\sim$ 1h) and during this time the laser has time to drift. The drift in the laser output wavelength during the scan effects the width of the measured absorption spectrum.

The current HSRL uses a calibration procedure, where the absorption spectrum is first measured by scanning the laser wavelength so that $\sim$ 1% photon counting accuracy is achieved for the spectrum around the absorption peak. In order to obtain

a high photon counting statistics in short period of time, the light from the calibration fibers is optimized so that maximum number of photons is detected with small pile-up effects at the detectors. During the scan the location of the peak absorption maximum is detected from the signal through the 4 cm long reference iodine absorption cell. After completing the scan, the seedlaser temperature is set back to the maximum and by using a tuning program (described in more detail in Chapter 5.2) the laser wavelength is kept at the absorption peak until better than 3% photon counting statistics is obtained. With this procedure the effects due to a shift in the laser output wavelength to the width of the absorption spectrum can be minimized and the photon counting errors in the determination of the C_{am} can be reduced from about 20% to 3% within $\sim$ 10 min averaging time.

The atmosphere provides the best reference when the accuracy of the HSRl calibrations is studied. Figure 16 presents an HSRL calibration which is performed simultaneously with data taking. Two different cases are studied. First, a calibration from a thick water cloud is shown. Second, a calibration from clear air is presented. In order to detect the possible range dependence of the calibration, lidar returns from different altitudes are studied. The comparison between calibrations from atmosphere and from the calibration light source also recovers possible misalignments of the system.

The system calibration signal from the iodine absorption spectrum presents a calibration from a pure aerosol target. The agreement between system calibration and atmospheric calibration from a thick water cloud can be seen from Figure 16. Both signals are defined from the ratio of the signal detected through the iodine cell to the signal detected with the combined aerosol+molecular channel. The background corrected, energy normalized signals are used. The data is averaged over a 90 m range. An expected calibration curve from a pure molecular target can be calculated by convoluting the measured iodine absorption spectrum with the calculated molecular spectrum. The calculated molecular calibration together with a measured atmospheric calibration from different altitudes are presented in Figure 16.b-d. The measured absorption spectrum is presented as a reference. For the calculated molecular calibration, the atmospheric temperature, and therefore the width of the Doppler-

broadened molecular spectrum, is calculated by using the temperature values obtained by a radiosonde measurement. The signals from higher altitudes are disturbed by the low photon counting statistics, but otherwise a good agreement between system calibration and atmospheric calibration is obtained and no range dependence in the system calibration is observed. The range dependence of the atmospheric calibration would show up as a noticeable deviation from the system calibration.

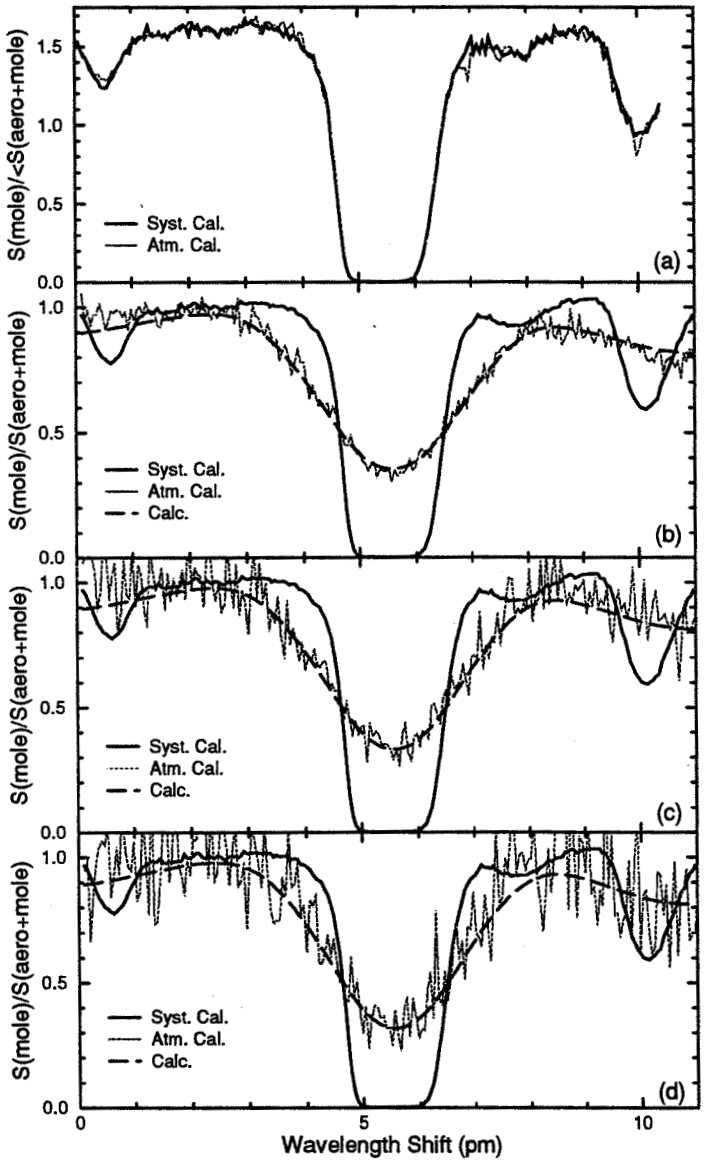

Figure 16. A HSRL calibration scan together with a simultaneous calibration from the atmosphere. Figure (a) shows a calibration from a thick water cloud (thin dashed line) together with a system calibration scan (thick solid line). In figures (c)-(d), the dashed line shows a clear air calibration at 3175 m (b), 5510 m (c), and 7550 m (d). The temperatures at these altitudes were -11 °C (b), -32 °C (c), and -45 °C (d), respectively. The long dashed line presents the expected molecular return. The measured calibration scan is presented as a reference (solid line).

5.2 The laser wavelength locking into the iodine absorption peak

The system calibration is sensitive to the drifts between the transmitter wavelength and the receiver bandpass transmission maximum. The measurements show that the seedlaser drifts at ~100 MHz/h rate. In order to achieve a stable long term operation without frequent calibrations, the wavelength of the transmitter laser is locked to the iodine absorption peak. Wavelength locking to the Doppler-broadened iodine absorption line was used because it requires much less power than a locking into a hyperfine structure of the iodine absorption line with Doppler-free technique[33]. Compared to the wavelength locking with a high resolution etalon, the advantage of the locking to an iodine absorption peak is that, iodine peak provides an absolute frequency reference. Another technique to lock the laser output wavelength to the Doppler-broadened iodine absorption line was reported by Arie and Byer[35]. They use Fourier transformation spectroscopy to lock the laser to the center of the Doppler-broadened peak. This method does not require any dither of the laser frequency, but it is more complex.

In the HSRL, the absorption spectrum of the 4 cm long iodine absorption cell is used to provide information about the absorption peak maximum. The absorption peak of the 43 long iodine absorption cell cannot be used as a reference for the wavelength locking because the saturation of the absorption at the peak causes the flat shape of the peak, and because the signal at the peak is small due to the strong absorption. Therefore it does not provide good photon counting statistics for the locking. The length of the reference cell is chosen so that the absorption is $\sim$ 50%. The cell transmission has to be high enough to provide a good photon counting statistics within a short averaging time.

The locking of the laser wavelength to the iodine absorption peak is performed by using an automatic controlling program that works as follows. First, the location of the absorption maximum is detected during a calibration scan. After completing the scan, the program automatically sets the seedlaser temperature to the observed peak. In order to keep the laser wavelength locked to the maximum absorption wavelength, the seedlaser temperature is dithered around the optimum temperature

and information about the ratio of signal from the second calibration fiber to the signal from the first calibration fiber detected with PMT 1 (see Figure 17) is gathered. The seedlaser temperature is kept at temperature that produces the minimum ratio. The basic idea of the tuning program is presented in the following.

The tuning procedure has four steps. First, information about the ratio between calibration fibers is gathered for the seedlaser temperature (T(peak)) that was detected to produce the minimum ratio. Then, a temperature T=T(peak)+dT is applied and the change in the ratio is observed. After gathering enough statistics ($\sim$ 30 s), the seedlaser temperature is returned back to the temperature T(peak) and a new value for the ratio at this temperature is measured. After this, the optimum temperature is detected by finding the temperature that produces the minimum ratio. If the temperature T=T(peak)+dT produced a smaller ratio, then that temperature becomes to the new optimum temperature T(peak). If the ratio for temperature T=T(peak)+dT was not better, the dithering to temperature T=T(peak)-dT is performed and the procedure is repeated. The wavelength dither corresponds to temperature change of 0.009 °C (0.052 pm). A time history of the dither temperatures for a 9 hour run shows that, the seedlaser temperature is dithered between 3 temperatures under typical operating conditions.

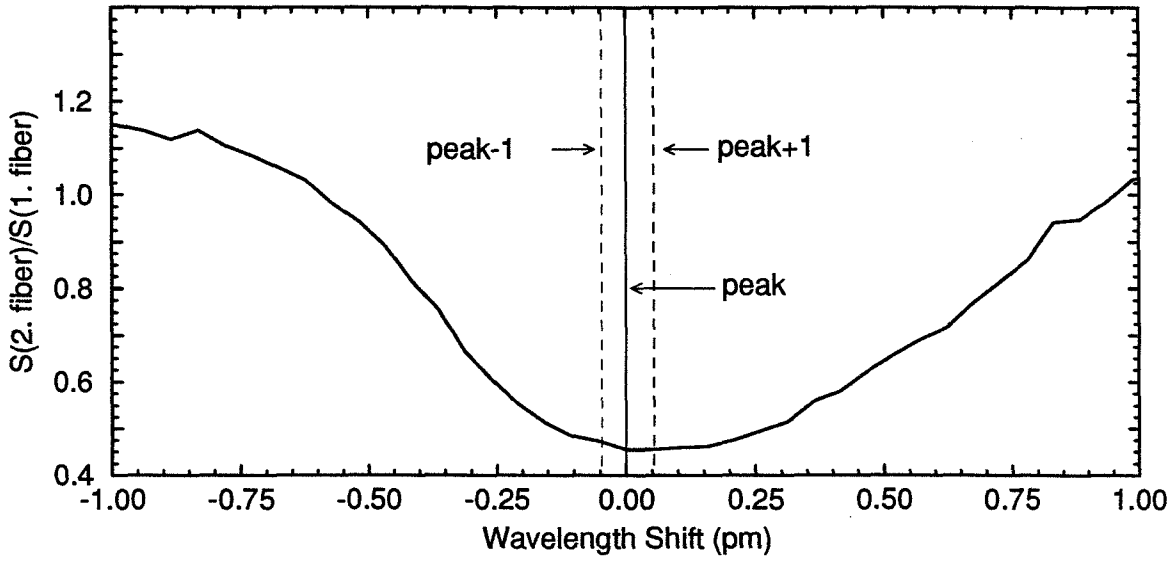

Figure 17. Signal for the frequency locking of the laser. An expanded view from the peak shows that as the temperature is changed in either direction from the detected peak, a change in the ratio is noticed.

Because the absorption peak of the 43 cm long absorption cell is flat around the maximum absorption wavelength, the error due to tuning to the amount of aerosol detected in the molecular channel (C_{am}) is comparable to the photon counting statistics. On the other hand, the error due to dithering to the amount of detected molecular signal in the molecular channel (C_{mm}) is a combination of photon counting statistics and the error between the convoluted signals at different dithering wavelengths. The errors in C_{mm} due to tuning as a function of atmospheric temperature are presented in Figure 18. Figure 18 shows the error in the determination of C_{mm}, when the laser wavelength is tuned off by ± 0.052 pm, but the calculation of C_{mm} is made for the peak wavelength. Also the error due to dithering is shown. The asymmetry of the absorption spectrum makes the errors due to the tuning asymmetric. The total effect of the tuning procedure to the measured profiles has to be calculated as a weighted average of the errors at different dithering wavelengths, because the tuning program is realized so that the laser spends 2/3 of the time at the wavelength that produces

the minimum ratio and 1/3 of the time doing the dithering. Therefore, the total error due to dithering is better than 0.1%, when measurement period is long compared to the dither time. In principle, the error due to wavelength locking can be eliminated by inverting the data by using different calibration coefficients for different dithering wavelengths. This has not been accomplished yet.

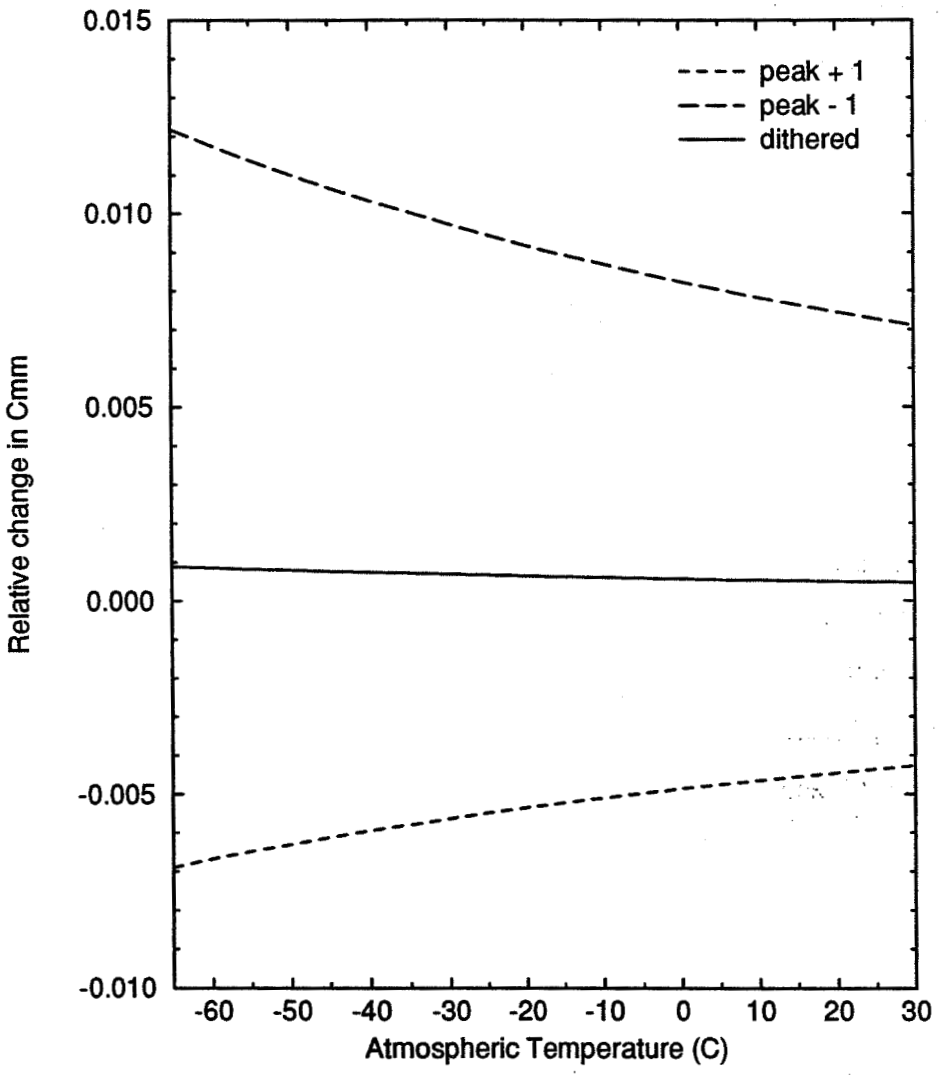

Figure 18. The errors in C_{mm} due to the tuning. Error when the seedlaser temperature is detuned from the optimum temperature by ± one step (0.009 °C) and when the seedlaser temperature is dithered, but the inversion is performed by using the observed peak value.

6 Measurements

Starting from July 1993, the iodine absorption filter based HSRL has been operated at the University of Wisconsin-Madison campus. During this time the HSRL has been routinely operated and the stability and reliability of the system have been tested. As a result, a dataset consisting of $\sim$ 30 different cirrus cloud cases has been obtained with a simultaneous NOAA-11 and/or NOAA-12 satellite overpasses. As an example from the data collected with the HSRL a dataset from November 11, 1993 is shown. This dataset contains a meteorologically interesting case: a cirrus cloud, supercooled water cloud, and ice crystal precipitation together with a strong low level aerosol structure. Figures 19 - 25 present Range Time Indicator (RTI) pictures from the data. Both raw and inverted data are shown along with depolarization and optical depth. The pictures are generated from the background corrected, energy normalized, and range square corrected data.

For the RTI's of the inverted data, the aerosol and molecular signals are separated by using Equations 19 and 20. The optical depth is obtained from the ratio of the inverted molecular profile to the return predicted for the pure molecular scattering (Eq. 10). The color scale shows the signal strength and the white areas are regions where the backscatter signal is larger than the maximum color scale value. The black areas indicate that the signal is smaller than the smallest color scale value.

The Figure 19 shows the raw lidar return detected with the combined aerosol and molecular channel. This profile is similar to the profile obtained with a conventional single channel lidar: the signal from small amounts of aerosol scatterers is dominated by the scattering from molecules, and therefore all aerosol structures are not clearly visible. The ability of the HSRL to separate aerosol and molecular scattering can be seen from the RTI picture of the inverted aerosol signal Figure 20. After inversion, the aerosol structures are more visible and they do not have the decrease with altitude caused by the atmospheric density profile. The ability of the iodine absorption filter to reject aerosol scattering is visible from the RTI of the raw molecular signal (see Figure 21): only a small aerosol cross-talk for the densest parts of the clouds is observed and this is easily removed by the inversion, as can be seen from Figure 22. The phase of the water at different layers can be seen from the depolarization RTI's. Figure

23 shows the raw depolarization observed with the combined aerosol and molecular channel. The inverted aerosol depolarization is shown in the Figure 24. From these pictures, a cirrus cloud at $\sim$ 8 km (depolarization ratio $\sim$ 40%) and a supercooled water cloud at 5 km (depolarization ratio $\sim$ 1 %) with ice crystal precipitation can be easily separated. For low level aerosols (0-3.7 km), a two layer polarization structure is seen. The small increase in water cloud depolarization as a function of cloud height is an indicator of multiple scattering. The low molecular depolarization is presented in Figure 25. The low depolarization ratio values with small signal to noise ratio show up in the picture as noise.

The optical depths on the different parts of the data set can be seen from the Figure 26. The optical depth of the cirrus cloud between 7 and 10 km is $\sim$ 0.4. The water cloud at $\sim$ 5 km has an optical depth of 2.5-3. The extinction through the ice crystal precipitation below the water cloud and the extinction through the water cloud can be seen as a change in the color scale as a function of altitude. The optical depth of the ice crystal precipitation is $\sim$ 0.1.

A more detailed analysis of the dataset is presented in the following sections. First, the depolarization measurements are discussed in Chapter 7.1. The effects of multiple scattering to the depolarization measurements are shown. The measurements of the cloud particle sizes are not included to this study. The depolarization data from August to November 1993 is analyzed and a summary from the observed depolarizations as a function of atmospheric temperature is given. Second, an example from a measurement of scattering ratio, aerosol backscatter cross section, and optical depth is given together with error estimates for the optical depths (see Chapter 7.2). The temperature dependence of the Doppler-broadened molecular spectrum enables the measurements of the atmospheric temperature by the HSRL. Preliminary results from a temperature measurement are presented in Chapter 7.4.

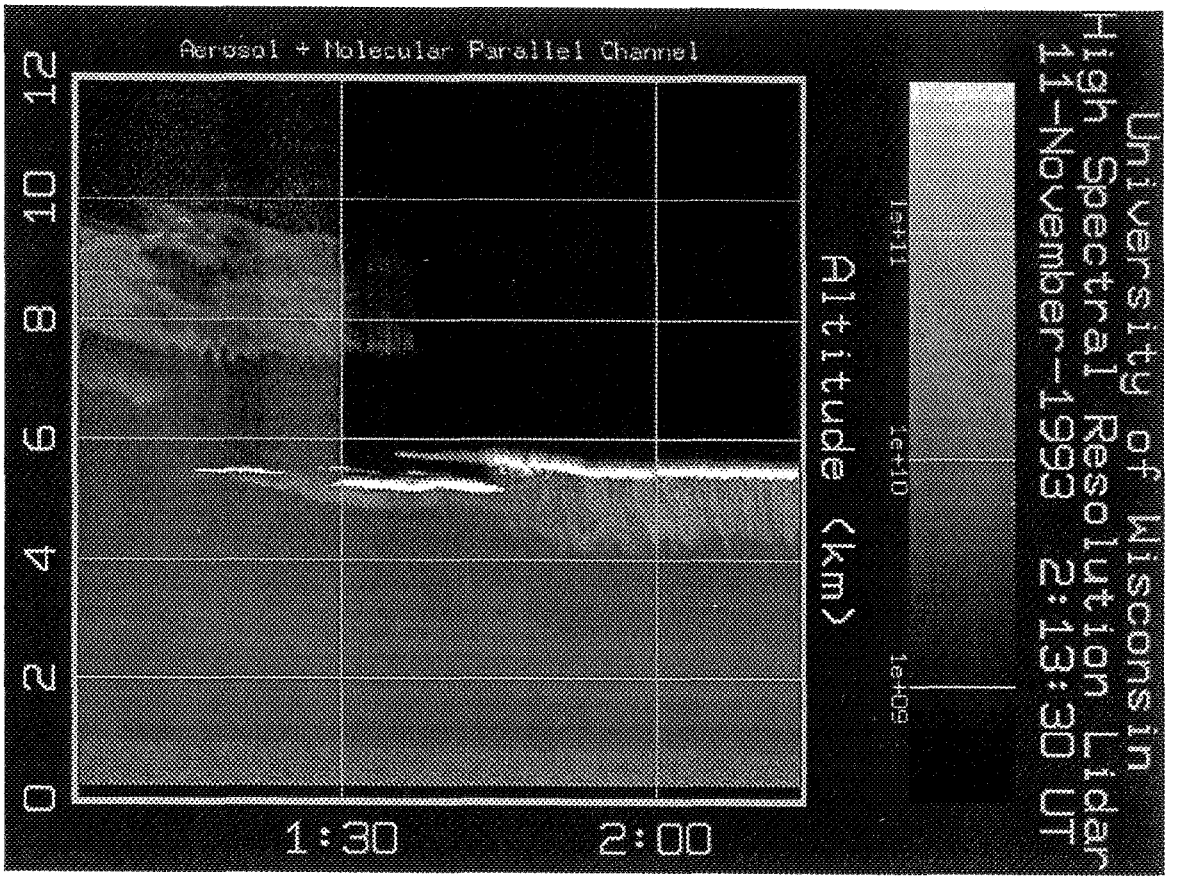

Figure 19. The raw lidar return presenting the combined aerosol and molecular channel return. A water cloud layer with an ice crystal precipitation are seen at 5 km. Above the water cloud, a cirrus cloud can be seen. The low level aerosol structure between 0 and 3.7 km is hardly visible because it is damped by the molecular backscatter signal.

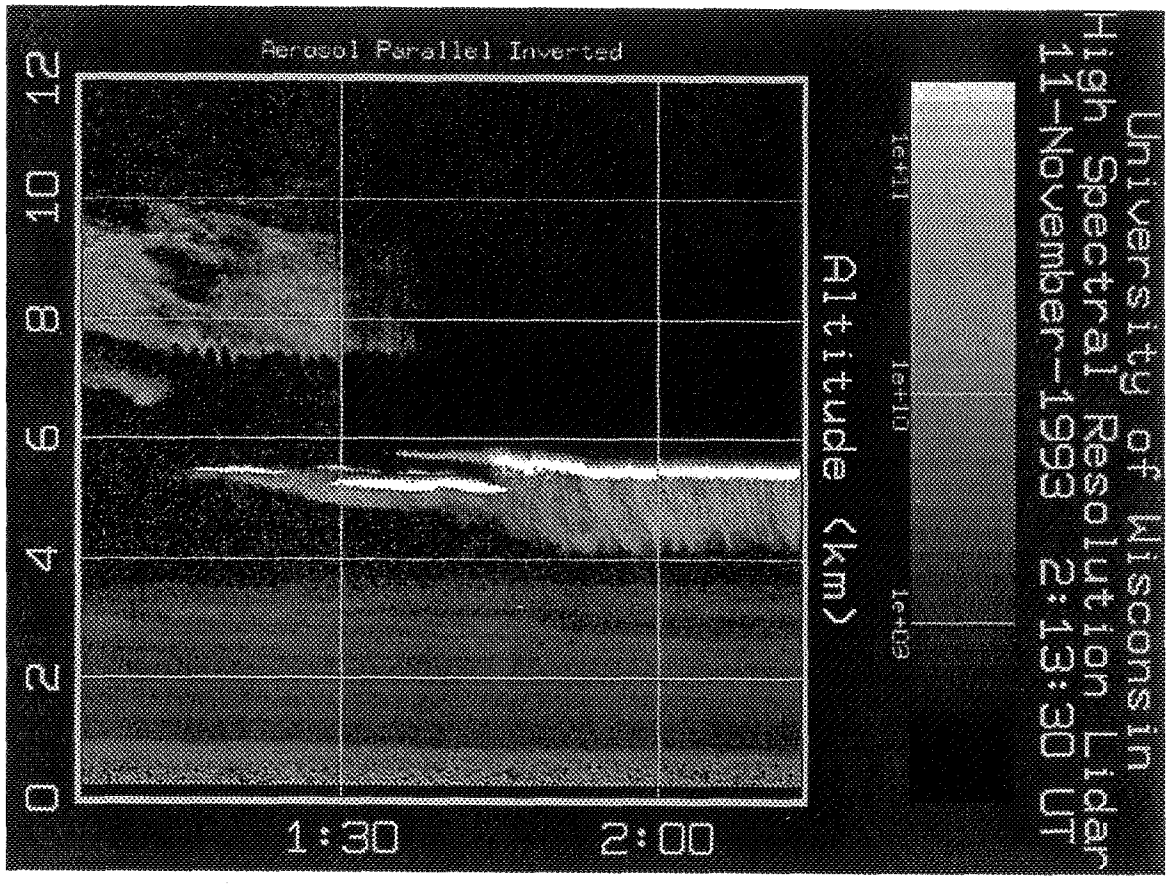

Figure 20. The inverted aerosol profile. After separating the aerosol and molecular backscatter returns, the layers where the aerosol backscatter signal is small compared to the molecular signal are clearly visible. The largest difference is seen for the low level aerosol layer between 0 and 3.7 km.

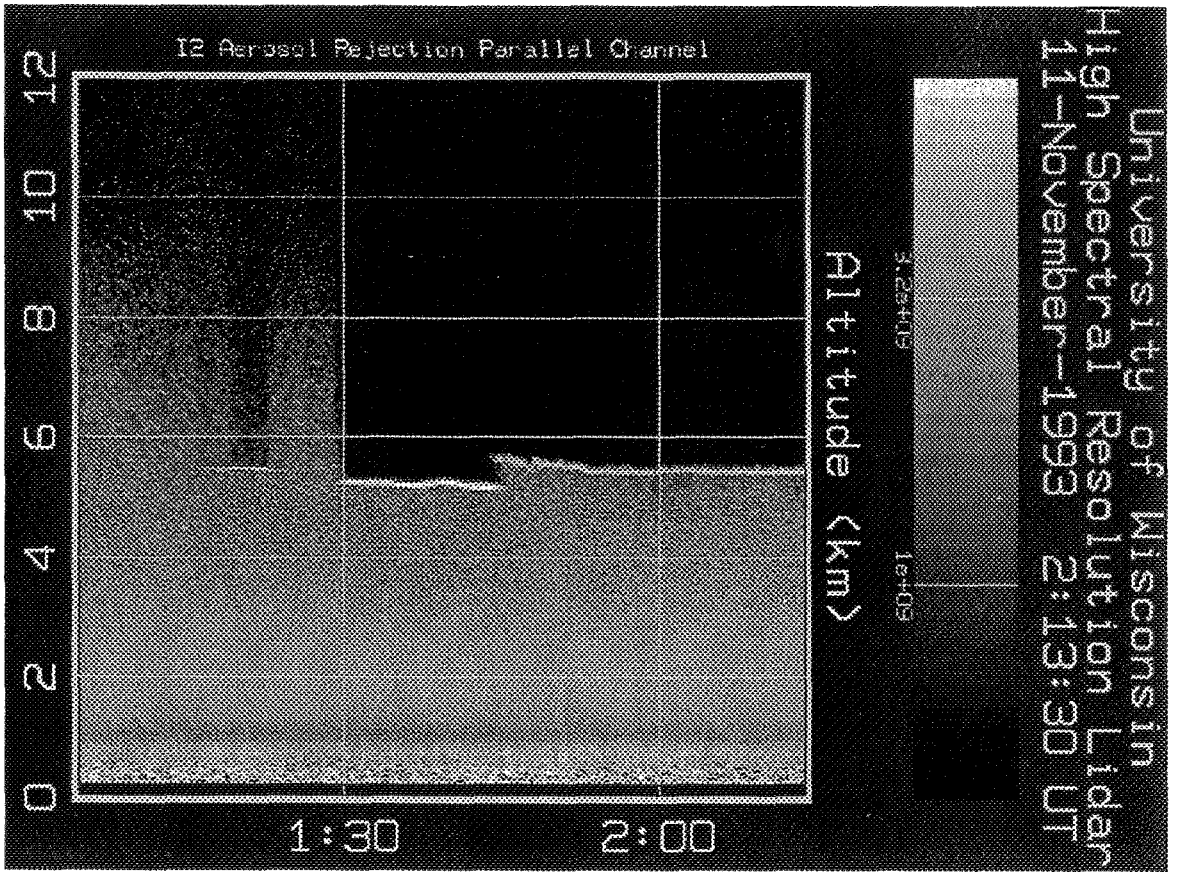

Figure 21. The raw molecular return. A small aerosol cross talk signal is visible for the densest parts of the water cloud at $\sim$ 5.5 km. The dark areas indicate that very little or no return through parts of the water cloud is observed.

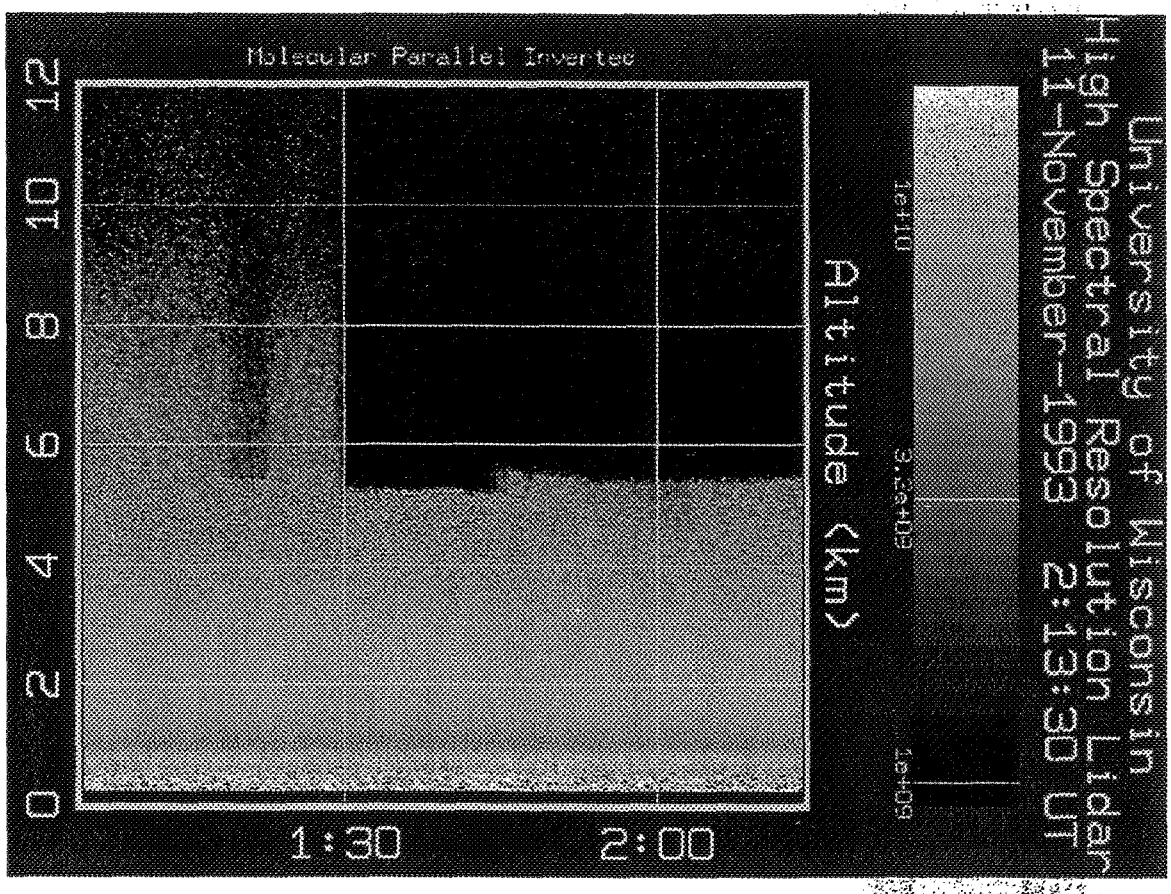

Figure 22. The inverted molecular profile. After the inversion, the cross talk that was visible in Figure 21 cannot be seen and the inverted molecular profile therefore presents the atmospheric extinction at various points of the dataset. The inaccuracy of the overlap correction can be seen as a darker line at $\sim$ 1 km.

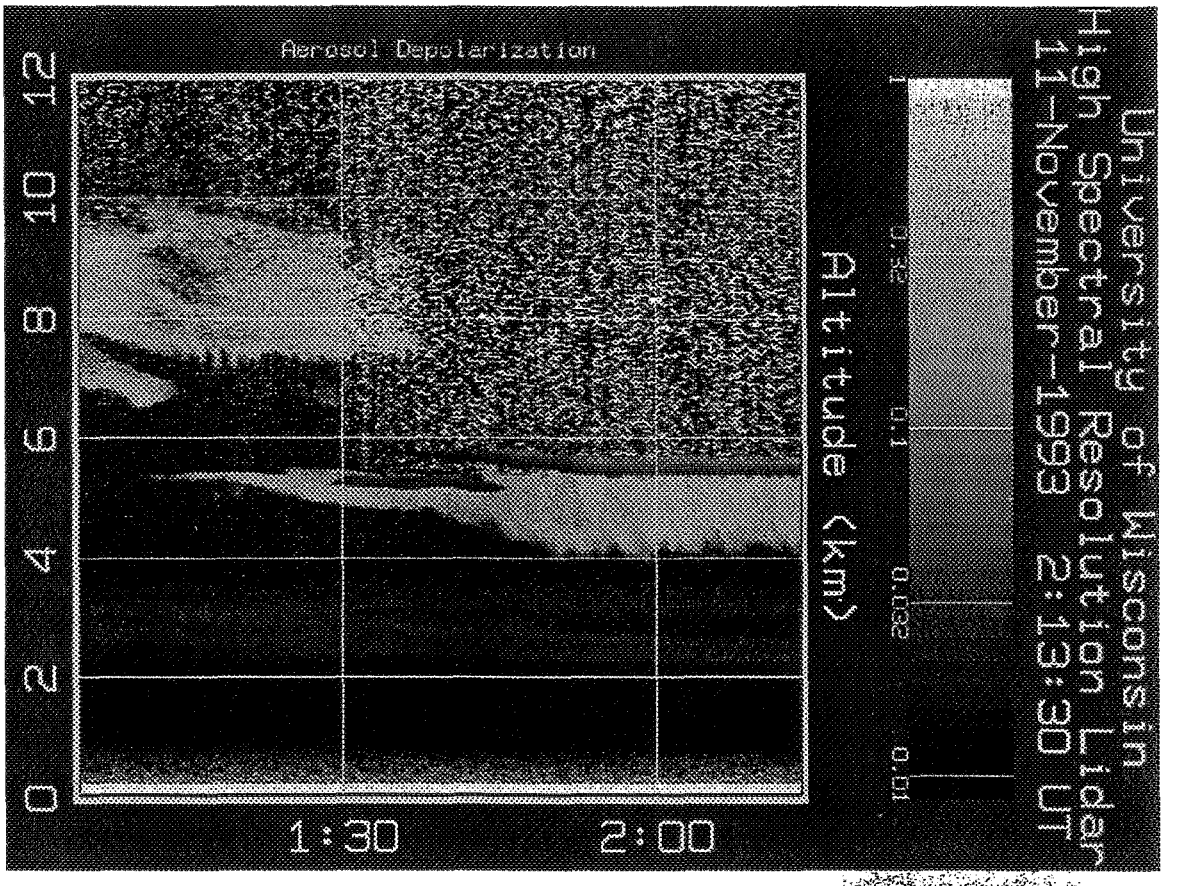

Figure 23. The raw aerosol depolarization combined with the molecular depolarization. The picture shows the depolarization ratio that is seen with a lidar that cannot separate the aerosol and molecular backscatter signals. The depolarizations for altitudes with low aerosol content are dominated by the molecular depolarization. The parts of the cirrus cloud and parts of the ice crystal precipitation between 4 and 5.5 km show depolarization ratios that are $\sim$ 10%, and those layers could be expected to contain mixture of ice and water. Some parts of aerosol layer between 2 and 3.7 km show depolarization of $\sim$3.5 %. The water cloud at 5.5 km has $\sim$1% depolarization. The increase in the water cloud depolarization as a function of altitude is due to the multiple scattering.

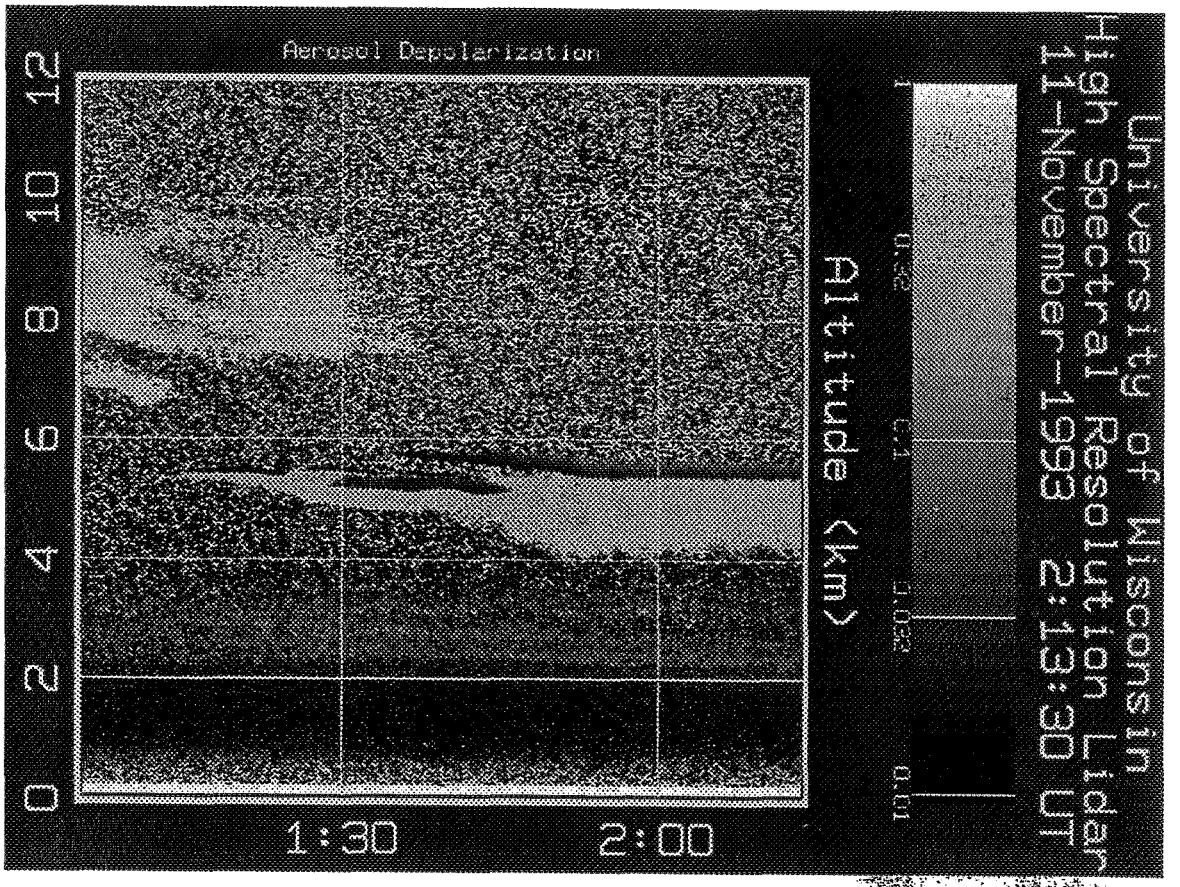

Figure 24. The inverted aerosol depolarization. After inversion, the cirrus cloud depolarization of $\sim$ 40% indicates pure ice depolarization. The ice crystal precipitation falling out from the water cloud show similar depolarizations values. The low level aerosol structure shows a two layer polarization structure. A $\sim$1% depolarization ratio for the layer between 0.5-2 km is observed indicating nearly spherical particles. The depolarization of the layer between 2 and 3.7 km shows a $\sim$ 5% depolarization.

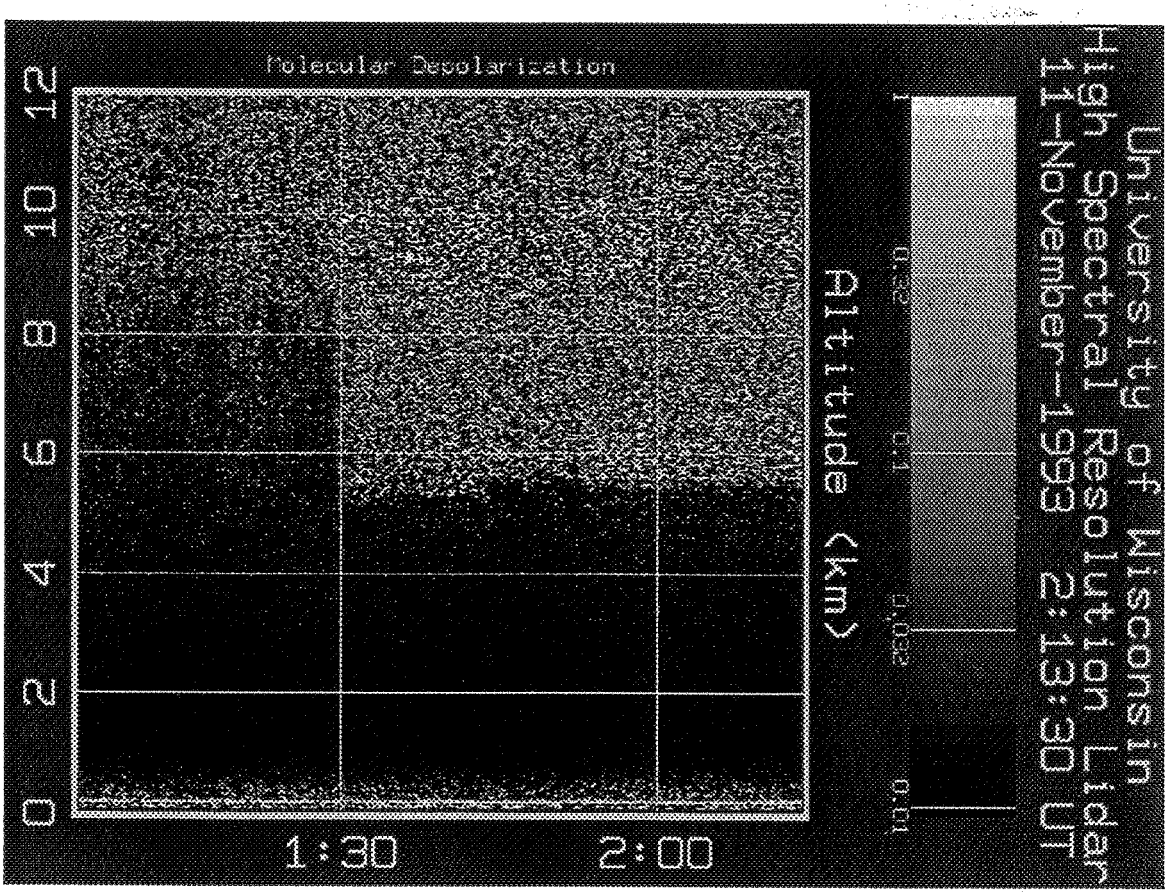

Figure 25. The inverted molecular depolarization. A less than 1% molecular depolarization is observed. The increase in the depolarization variations at the higher altitude is due to the low signal to noise ratio.

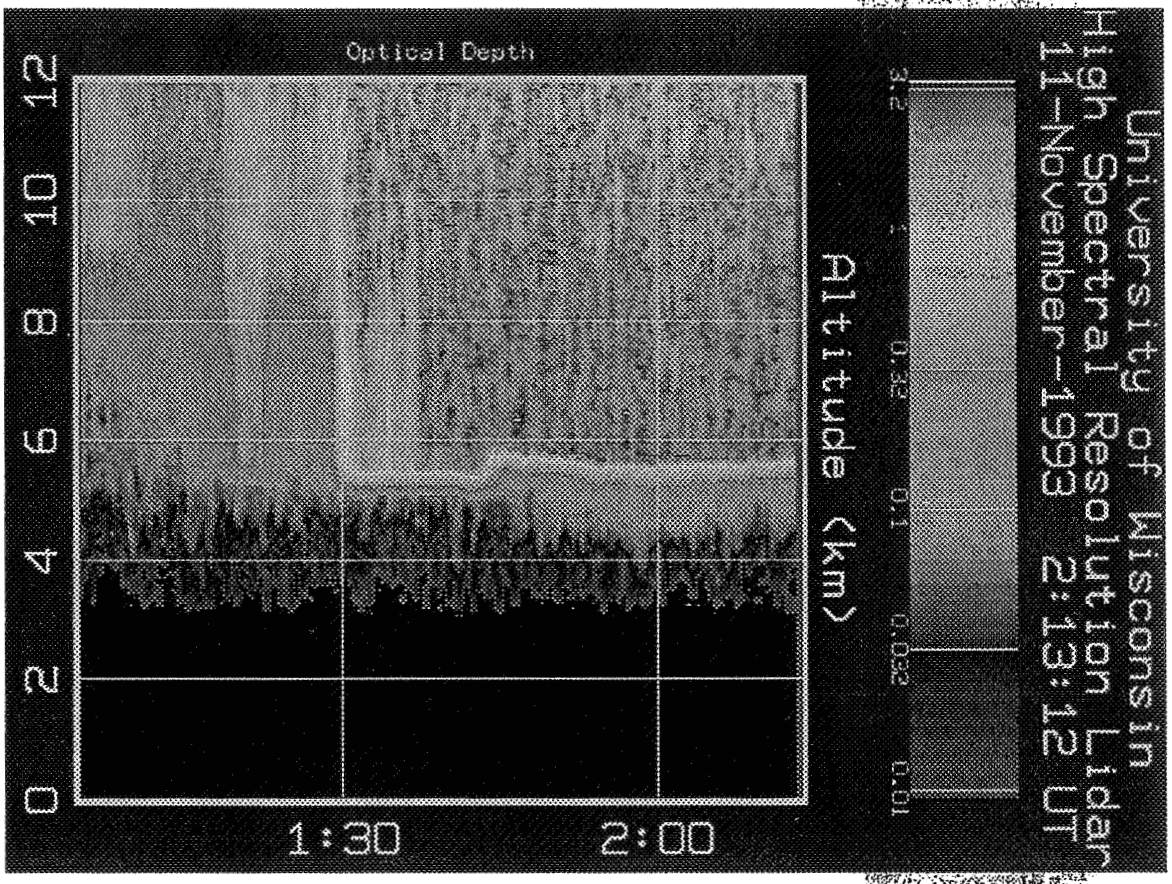

Figure 26. The optical depth. The optical depth above 3 km is shown. The optical depth of the cirrus cloud between 7 and 10 km is ~ 0.4. The water cloud at ~ 5 km has a optical depth of 2.5-3. The extinction through the ice crystal precipitation below the water cloud and the extinction through the water cloud can be seen as a change in the color scale. The optical depth of the ice crystal precipitation is ~ 0.1.

6.1 Depolarization ratio

Lidar measurements of atmospheric depolarization can be used to distinguish between liquid and solid phases of water in the atmosphere[36–38]. The quantity to describe the degree of polarization is the linear depolarization ratio δ

$$\delta = \frac{I_\perp}{I_\parallel}, \tag{23}$$

where $I_\perp$ and $I_\parallel$ are the measured perpendicular and parallel backscatter intensities in respect to the transmitter polarization axis. The backscatter signal of a linearly polarized laser beam from spherical particles is totally linearly polarized ($\delta = 0$). The particles can be assumed to be spherical in case of wet haze, fog, cloud droplets, and small raindrops. The depolarization of the pure molecular atmosphere is nonzero, because of the anisotropy of the air, and therefore a 0.37–0.4 % depolarization for the Cabannes line is expected[39,40]. The depolarization of the molecular return that includes the Cabannes line and the rotational Raman lines is $\sim 1.5\%$[40]. If particles are nonspherical (as ice crystals, snow flakes or dust particles) or if the backscatter signal has a multiple scattering contribution, the backscattered signal contains a cross-polarized component ($0 < \delta < 1$). A specular reflection from a oriented ice crystal layer provides a small depolarization, which therefore can be misinterpreted as the backscatter signal from a water cloud, but the off vertical pointing direction of the HSRL is expected to prevent this.

Lidar studies of atmospheric polarization have been traditionally based on a technique, where a linearly polarized laser beam is sent to the atmosphere and the received polarization components are separated by a polarization cube and detected by a pair a photomultiplier tubes, one for each polarization component. This method requires a precise calibration of the receiver in order to avoid the problems due to differences between channels in optics, and in photomultiplier sensitivity.

In the new HSRL (see Figs. 5 and 6), the polarization measurements are made by using one transmitter laser and one detector for both polarization components. The transmitted laser beam is linearly polarized, and for polarization measurements the polarization of the transmitted laser beam is rotated by 90 degrees on alternative laser pulses by a Pockels cell. In the receiver, the signal parallel to the transmitter

polarization axis and the signal perpendicular to that are separated and cleaned by a polarization cube pair. Since the polarization of the transmitted laser shot alternates between two subsequent laser shots, the same detector can accurately measure both polarization components and therefore no calibration of the receiver is required. The 250 μs time separation between laser pulses insures, that both depolarization components are measured from the same atmospheric scatterers. The depolarization variations as a function of field of view can be studied with the new WFOV-channel. The effects of specular reflection from a horizontally oriented crystal layer are minimized by tilting the receiver by 4 degrees from the zenith. With the HSRL, separate measurements of aerosol and molecular depolarizations can be made.

Depolarization measurements are affected by presence of multiple scattering when a lidar is used to probe dense clouds. Because the amount of detected multiple scattering is dependent from the cloud particle size, range from the cloud, optical depth of the cloud, and the field of view of the system, typical systems with 1-5 mrad field of views have difficulties separating between water and ice for dense clouds. In order to separate between water and ice for optically thick clouds, the HSRL uses a 160 μrad field of view for the spectrometer channels.

Figure 27 represents an example of the multiple scattering effect on the measured depolarization. Figure 27.a. shows the measured energy and range square corrected signals from a supercooled water cloud with ice precipitation. For the WFOV-channels, 0.22, 0.65, 1.1, and 1.6 mrad field of views are used. The WFOV-channel measurements are then compared to the measurements of the 0.16 mrad field of view channels. The amount of multiple scattering in the signal is calculated from the ratio of the WFOV-signal to the signal simultaneously measured with the narrow field of view channel (see Figure 27.b.). Figure 27.c shows the depolarization ratios for different field of views and the Figure 27.d shows the ratio of the WFOV depolarization to the narrow field of view depolarization. For the optically thin ice crystal precipitation layer, the change in depolarization as a function of field of view is hardly noticeable. The change from ice to water shows up as a drop in the depolarization ratio. All field of views show a low depolarization for the water cloud base but as soon as the signal penetrates deeper into the cloud, an increase in the depolarization

as a function of field of view can be observed. Inside 300 m the multiple scattering effects in the cloud will increase the depolarization of the larger field of views up to the level which is comparable with the observed ice crystal depolarization and therefore, the separation between ice and water becomes impossible. The low values of depolarization observed with the narrow field of view channel and with the smallest WFOV field of view show that the narrow field of view effectively suppresses the effects of multiple scattering. Therefore, the HSRL signals from these field of views can be used to separate between ice and water clouds even for optically thick clouds. On the other hand, information from depolarization and signal strength variations as a function of field of view can be used to verify multiple scattering calculations.

Theoretically, the depolarization of the spherical dropplets should be zero, but the depolarization ratios observed for the water cloud at 5.5 km is ~2 %. In the cases of water clouds with an ice crystal precipitation, the non-zero values of depolarization ratio can be explained by the presence of ice. Because the water cloud is precipitating ice, there has to be some ice mixed with water in the cloud. The scattering from the cloud base is $\sim$ 20 times larger than signal from ice crystal precipitation. Based on this ratio, $\sim$ 2 % ($\sim$ 1/20 x ice depolarization of 40 %) depolarization for the cloud base depolarization can be expected due to the presence of ice crystals with $\sim$ 40 % depolarization.

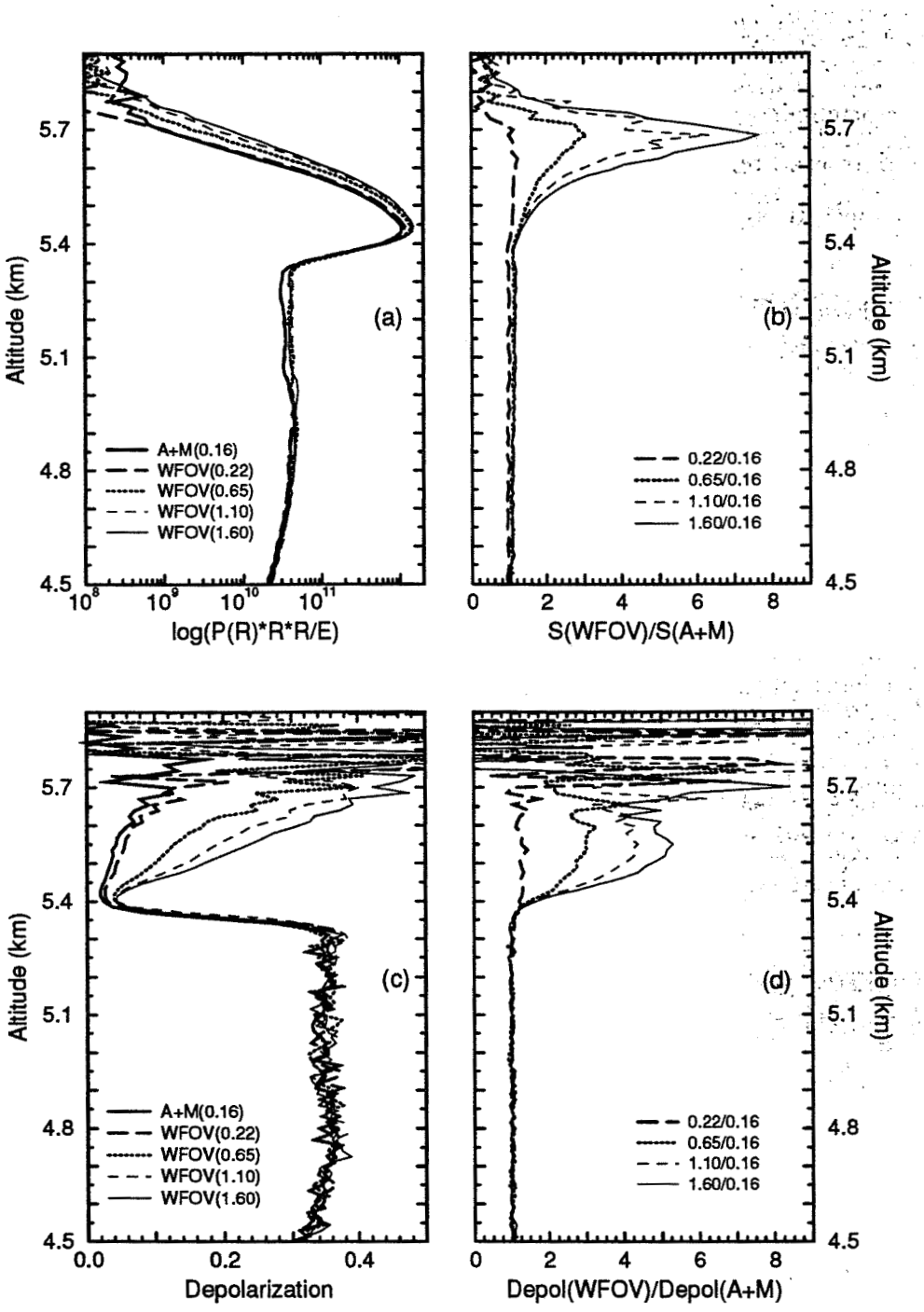

Figure 27. Effects of multiple scattering on depolarization in the backscatter return from a water cloud at 5.5 km with ice crystal precipitation between 4.5 and 5.3 km. Data obtained on November 11, 1993 02:04-02:14 UT. (a) Measured signals. (b) Ratios of measured WFOV signals to 0.16 mrad field of view signal. (c) Measured depolarization ratios. The cloud base depolarization of the smallest field of view at 5.4 km is $\sim$ 2 %. (d) Ratios of the measured WFOV depolarizations to the depolarization of the 0.16 mrad field of view channel.

The capability of the HSRL to distinguish between aerosol and molecular scattering allows separate polarization measurements. This is important when layers with a low aerosol content are studied. The effects of the molecular scattering on the observed depolarization can be seen by comparing the raw and inverted aerosol depolarization ratios. For the cases where the amount of aerosol scatterers is small, the signal from molecular scattering dominates the depolarization picture (see Figure 23). Therefore, aerosol depolarizations similar to the molecular depolarization can be seen and also parts of the cirrus cloud and ice crystal precipitation show depolarization ratios which are close to the depolarization of the supercooled water or mixture of ice and water (green areas in the raw aerosol depolarization RTI). After inversion a clear difference in the depolarizations is seen: the depolarization of the low level aerosols is better defined and the depolarization of the cirrus shows that the cloud contains pure ice crystals (Figure 24). Therefore, a clear separation between ice and water can be based to the depolarization ratios calculated from the inverted aerosol profiles. The effect of the inversion to the depolarization ratio is also visible from the Figures 28 – 29.

The profile of the raw aerosol depolarization shows the depolarization of the combined aerosol+molecular channel and therefore, it shows the depolarization ratio which is seen with a conventional single channel lidar. The raw molecular depolarization contains the depolarization component of the aerosol cross talk together with the molecular depolarization. In the same figure, the separated aerosol and molecular signals are shown with the inverted aerosol and molecular depolarizations. Figure 28 shows a two layer water cloud with an ice crystal precipitation. The peaks of the water clouds are observed at 5.2 and 5.6 km and the corresponding low depolarization values are 1–2 %. A small increase in the depolarization with penetration depth is observed. The values of raw depolarization of the ice crystal precipitation are close to those of water and ice mixture, but the inverted depolarization ratios show a clear ice depolarization. After inversion the increase in aerosol depolarization at 2–3.7 km is also very clear. The Figure 29 shows a water cloud layer at 5.4 km with a more dense ice crystal precipitation. With increased backscatter signal from ice, the value of raw depolarization ratio indicates clear ice and therefore the effects of molecular

depolarization do not show up so clearly, eventhough a change in depolarization ratio is observed after the inversion.

The depolarization observed in the clear air is 0.7–0.8 %, when the observations are made without the low resolution etalons. When the low resolution etalons are used, the depolarization is 0.55–0.6 %. The expected value for the molecular depolarization of the Cabannes line is $\sim$ 0.4 and $\sim$ 1.44 for the Cabannes line[39,40] and rotational Raman lines[40]. The HSRL observations show a 1.5 % depolarization for the signal from the rotational Raman lines and Cabannes line. Because the system filter bandpass admits a small fraction of the rotational Raman lines (75 % depolarization) and simultaneously blocks part of the Cabannes line, the molecular depolarization value measured by the HSRL is larger than the expected Cabannes line depolarization. The amount of transmitted rotational Raman signal is temperature dependent. A model to calculate the expected depolarization was written. This model includes the rotational Raman spectrum for nitrogen and oxygen, molecular spectrum including effects of Brillouin scattering, and spectral transmissions of different filters. The polarization that correspond to different atmospheric temperatures can be calculated. The ratio of rotational Raman signal to Rayleigh signal is chosen so, that a 1.44 % depolarization for the clear air is observed. These calculations show, that a 0.56 –0.62 % depolarization is expected for the case where no low resolution etalons were used. A 0.402 –0.425 % depolarization is expected, when one or two etalon are used. The depolarization observed with the HSRL are larger than the expected values. The cause of the additional depolarization in the HSRL measurements is currently unknown.

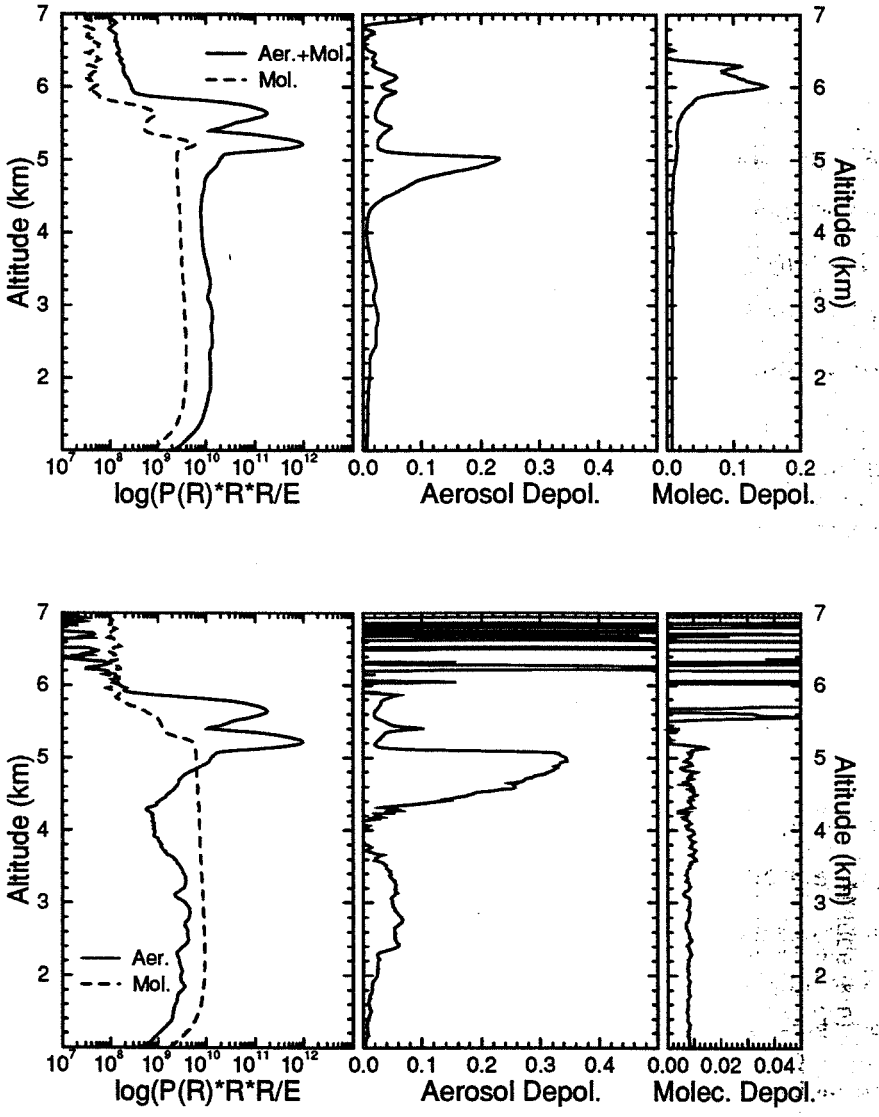

Figure 28. Raw and inverted depolarization ratios of clear atmosphere with ice crystal precipitation and two water cloud layers above it (November 11,1993 01:35-01:47 UT). The upper set shows the raw aerosol and raw molecular profiles together with the depolarizations. The lower set shows the inverted profiles with the inverted depolarizations. The water clouds are observed at 5.2 and 5.6 km altitudes. The low water cloud depolarization values can be observed from the aerosol depolarization figures. The small increase in water cloud depolarization as a function of penetration depth is due to the multiple scattering. The weak signal from the ice crystal precipitation is visible 4.3-5.1 km. Because of the low ice crystal content, the raw depolarization ratios of the ice crystal precipitation shows values that would indicate mixed phase, but after the inversion a clear ice crystal depolarization is visible. The clear air aerosol depolarization is less than 6%. The observed molecular depolarization is 0.8 %.

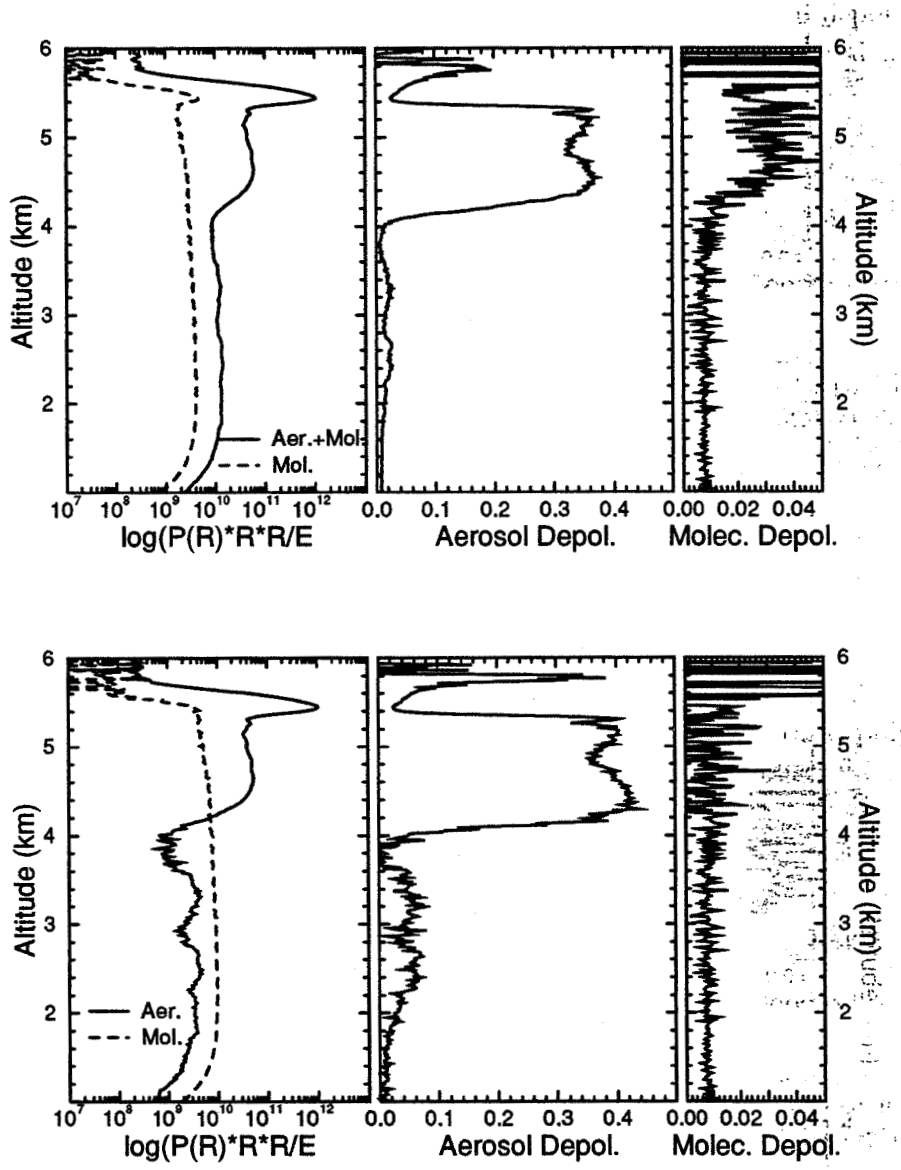

Figure 29. Raw and inverted depolarization ratios of a thin cirrus cloud and a thin water cloud with an ice crystal precipitation (November 11,1993 01:55-02:01 UT). The upper set shows the raw aerosol and molecular profiles along with the raw depolarization ratios. The lower set shows the inverted profiles with the inverted depolarization ratios. The water cloud at 5.5 km has a low depolarization value ~1.5% at the cloud base and it increases towards the cloud top due to the multiple scattering. The dense ice crystal precipitation is visible between 4 and 5.4 km. Because the ice crystal content of the precipitation is large compared to the molecular backscatter, only small difference between raw and inverted aerosol depolarizations is observed. The raw molecular depolarization shows a small increase for the cloud, but after the inversion a constant 0.8% depolarization is observed.

The depolarization data for cirrus clouds obtained between August and November 1993 have been analyzed. A summary of the observed depolarization ratios as a function of temperature are presented in Figure 30. In this study only clouds with scattering ratios greater than 0.5 were used. This was made in order to fully separate cloud depolarizations from noisy clear air depolarizations. The values of clear air depolarizations are low and affected by the photon counting statistics. Because the HSRL measurements have shown, that the scattering ratios of clear air aerosol and stratospheric aerosols can exceed values 1-3, the use of the scattering ratio of 0.5 does not guarantee a clear separation between clouds and clear air aerosols. On the other hand, the scattering ratios of the cirrus clouds can be below 1. Therefore, a visual separation between cirrus clouds and clear air aerosols is made and only the cloud altitudes are included to the study. In this study, 2 min averaging times for the data were used. By using a short averaging time, the errors due to temporal changes of the atmosphere were minimized. The atmospheric temperatures were obtained from radiosonde measurements and temperature intervals of 5 °C were used. Water clouds at cirrus cloud altitudes were separated from ice clouds based on the depolarization ratio values. Clouds with depolarization ratio values less than 15 % were classified as water clouds.

The high depolarization values of the cirrus clouds are easily separable from the water cloud depolarizations. The average cirrus cloud depolarization varies from 33% to 41% showing an increase towards the colder temperatures. Part of this can be expected to be from different shape, size, and orientation of the ice crystals at different temperatures[41,42]. The size and shape of the ice crystals have been found to be different at different temperatures and the crystals have been found to have a preferred orientation. A similar increase in cloud depolarization towards colder temperature was observed by Platt *et al.*[43]. His study was made for midlatitude and tropical cirrus and the depolarization values for temperatures from -30°C to -10 °C were lower, ranging from ~0.15 to ~ 0.25. The cirrus cloud depolarizations measured with the HSRL do not show any depolarization values below 20% for the temperatures from -30 to -10 °C. The system used by Platt had a 2.5 mrad field of view, and the low depolarization values are possibly caused by multiple scattering from water

clouds. The HSRL measurements have shown that when the depolarization of a water cloud is measured with a system with $\sim$ 1.0 mrad field of view, the effects of multiple scattering are large enough to cause depolarization values of $\sim$ 20%, and therefore the separation between water and ice becomes impossible. Also the HSRL measurements show a substantial probability of observing water at temperatures from -30 to 0 °C.

In 45% of the cases simultaneous observations of water cloud layers at the cirrus cloud altitudes were made. The Figure 30 shows, that supercooled water clouds at cirrus cloud altitudes are found at temperatures as low as -35 °C. Above 0°C temperature the low depolarization values indicate pure water, and the presence of cirrus disappears. The water cloud depolarizations are below 10 % and they contain the effects of multiple scattering. When the same clouds are studied with a NOAA-11 or NOAA-12 satellite, the simultaneous appearance of the water and ice cannot be noticed. On the satellite measurements, the cloud types are separated by using the information on the temperature. Therefore, if satellite data is used for cirrus optical depth studies, a supercooled water cloud layer mixed with ice cannot be easily separated and water will increase the optical depth value determined for the cirrus cloud. The depolarization ratio knowledge of the cloud measured with a lidar can be used to separate the water from ice and therefore separate optical depth measurements for both constituents can be performed.

The initial measurements have shown that the HSRL is capable of measuring cirrus cloud particle sizes. These measurements together with phase function measurements can be used for further studies of the cloud particle size effects on the depolarization ratio[26].

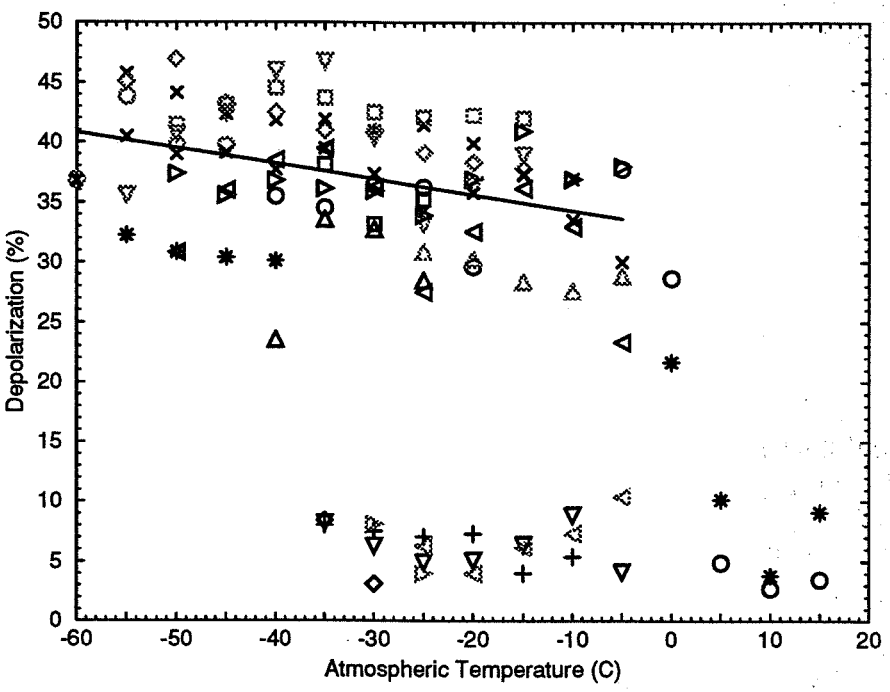

Figure 30. Cirrus cloud and supercooled water cloud depolarization as a function of temperature observed between August 2 and November 11, 1993. The depolarization values below 10% are indication of water clouds and higher depolarization values indicate the presence of ice.

6.2 Measurements of scattering ratio, aerosol backscatter cross section, and optical depth

Two examples from the measured scattering ratio, aerosol backscatter cross section and optical depth profiles for the November 11, 1993 dataset are presented in figures 31 and 32. The cloud altitude and geometrical thickness of the clouds can be seen from the inverted aerosol profile. The inverted molecular signal shows the extinction in the signal through the atmosphere. This can be compared to the predicted Rayleigh return, calculated from the radiosonde data. The unsmoothed profiles are used. The Figure 31 shows a thin cirrus cloud case and the Figure 32 presents a water cloud together with a thin cirrus cloud. The water cloud is seen at 5.2 km altitude and the cirrus cloud can be found ranging from 7 to 9.2 km. The measured signals show the large dynamical range achieved in HSRL measurements: signal strength variations over four decades are seen.

The scattering ratio is calculated from the ratio of inverted aerosol profile to the inverted molecular profile. The measured scattering ratios for the whole dataset vary from $\sim 10^{-3}$ to $\sim$1000. The maximum scattering ratio is 10 for the case presented in Figure 31 and $\sim$300 for the water cloud case in Figure 32.

The aerosol backscatter cross section is obtained from the scattering ratio and an estimate for the atmospheric density profile. The values of aerosol backscatter cross section change from $\sim 10^{-6} m^{-1} sr^{-1}$ for cirrus and ice precipitation to $\sim 10^{-4} m^{-1} sr^{-1}$ for water cloud. The observed aerosol backscatter values of the clear air are between 10^{-6} and $10^{-7} m^{-1} sr^{-1}$.

The total optical depths are calculated from the ratio of the inverted molecular signal to the return predicted for the pure molecular scattering. They range from 0.5 to 2.5 for this dataset. The Figure 31 shows a optical depth of 0.5 for the cirrus cloud and a optical depth 1.4 is observed for the case in Figure 32. The water cloud optical depth is 1 and the cirrus cloud gives an optical depth of 0.4. With the laser power used for this measurement, the optical depth of 2.5 is the upper limit of the current system. By increasing the laser output power larger optical depths can be measured. Because the cross talk between channels is small and it can be accurately corrected, and also because the 160 μrad field of view of the HSRL effectively suppresses multiple

scattering, the optical depths inside a cloud can be measured.

The accuracy of the optical depth measurements can be seen from the Figure 33. The leftmost graph shows the error in the optical depth measurement of a thin cirrus cloud and rightmost graph shows the error when a cirrus cloud of optical depth ~ 1 is studied. The errors presented here are root mean square errors and they consist of photon counting, background correction, calibration, and wavelength tuning errors. The signals are spatially averaged with a 150 m filter and the filtering is taken into account in the error analysis. The accuracy of the optical depth measurements is limited by the photon counting statistics. This can be seen from the error bars, which are on the same order as the signal fluctuations. The accuracy of the HSRL measurements can be increased by increasing the signal strength and/or by using a constrained nonlinear fit to the inverted molecular profile.

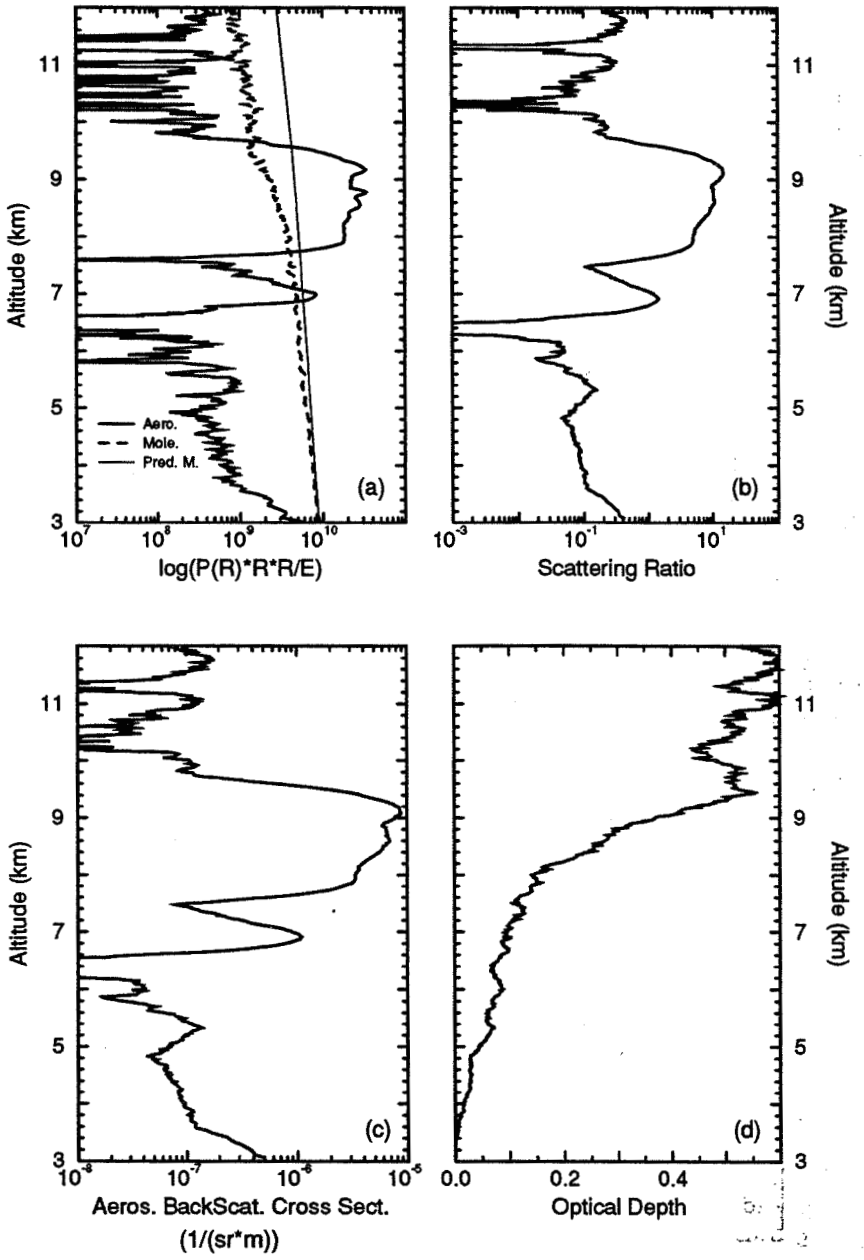

Figure 31. The measured scattering ratio, aerosol backscatter cross section and optical depth profiles of a thin cirrus cloud between 6.5 and 10 km (November 11, 1993 01:05-01:09 UT). (a) The inverted aerosol and molecular profiles along with a calculated molecular profile. The difference between the calculated and measured profiles shows the extinction. (b) The scattering ratio values are ranging from ~0.1 (clear air between 3 and 6.5 km) to 10 (cirrus cloud at 10 km). (c) The aerosol backscatter cross section of the cirrus cloud is $\sim 5{\cdot}10^{-6} m^{-1} sr^{-1}$ and $\sim$ for $10^{-7} m^{-1} sr^{-1}$ the clear air between altitudes 3 and 6.5 km. (d) The optical depth between 3 and 11 km is 0.55. The optical depth of the cirrus cloud is 0.4.

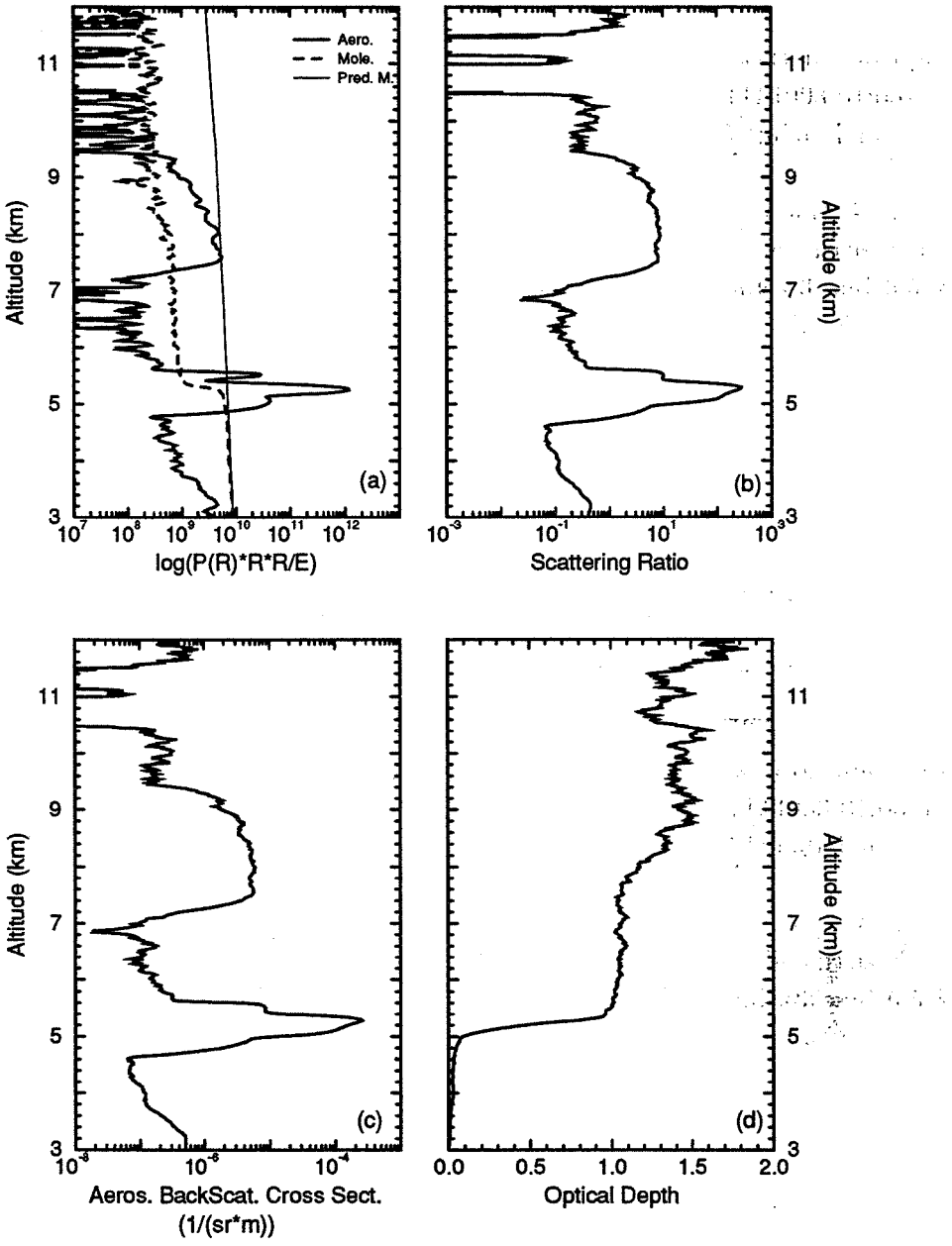

Figure 32. Scattering ratio, aerosol backscatter cross section and optical depth profiles of a thin cirrus cloud between 7 and 9.2 km and a water cloud with an ice crystal precipitation at 5.2 km (November 11, 1993 01:29-01:34 UT). (a) The inverted aerosol and molecular profiles along with the calculated molecular profile of the clear air. (b) Scattering ratio of the water cloud is $\sim$ 300 and 10 for the cirrus cloud. (c) The observed aerosol backscatter cross sections are ranging from $10^{-7} m^{-1} sr^{-1}$ for the clear air to $2{\cdot}10^{-4} m^{-1} sr^{-1}$ for the water cloud. (d) The optical depth is 1 for the water cloud and 0.4 for the cirrus.

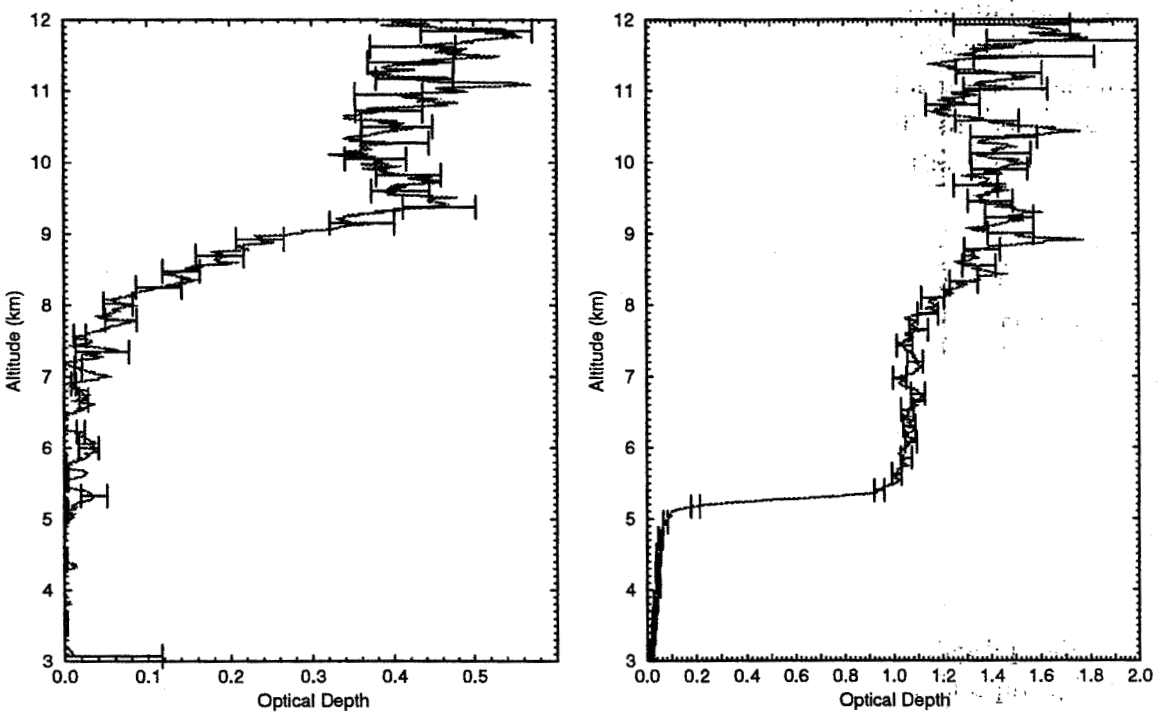

Figure 33. The root mean square errors in the optical depth measurement. A thin cirrus case (November 11, 1993 01:05-01:09 UT) (leftmost graph) and a cloud layer of optical depth of 1.4 (November 11, 1993 01:29-01:34 UT) (rightmost graph). The cases are the same as in Figure 29. The error bars are of the same order as the signal fluctuations indicating that the optical depth measurements are mostly limited by the photon counting statistics.

6.3 Measurements of atmospheric temperature

The temperature dependence of the Doppler-broadened molecular spectrum enables the measurements of the atmospheric temperature by a HSRL. The capability to measure the temperature would eliminate the possible errors due to the difference between the radiosonde reading and the current temperature over the lidar site. For this purpose, the temperature measurement capabilities of the University of Wisconsin HSRL were studied. The presence of clouds and strong layers of clear air aerosols will affect the shape of the molecular spectrum measured with the HSRL. The temperature measurement method presented in the following was used to test the capabilty of the HSRL to accurately measure the molecular spectrum width for layers with small aerosol content.

Lidars have been used for the measurements of the atmospheric temperature profile by many lidar groups. The technique proposed by Strauch *et al.*[44] and Cooney[45] allows calibrated temperature measurements by using the rotational Raman spectrum of nitrogen. With this technique about 1 °C temperature accuracy at low altitudes is achieved. Kalshoven *et al.*[46] demonstrated a differential absorption lidar method for temperature measurements. They used 2 laser wavelengths and O_2-absorption lines to measure atmospheric temperature up to 1 km altitude with 1 °C accuracy. Later Endemann and Byer[47] reported simultaneous measurements of atmospheric temperature and humidity with a continuously tunable IR-lidar. They used a three-wavelength differential absorption lidar technique and water vapor absorption lines. With this technique a 2.3 °C absolute accuracy was achieved. In addition to Raman and differential absorption lidar techniques, Keckhut *et al.*[48] used Rayleigh scattering lidar to measure atmospheric temperature for altitudes 30–70 km.

The temperature measurements made with a high resolution lidar have been reported by Alvarez *et al.*[16]. Their temperature measurement is based on the two barium absorption filters with different bandpasses. Because the strength of the signal received through an absorption cell is proportional to the width of the Doppler-broadened spectrum, the information of the signal strength together with a theoretical calculation for the Doppler-broadened Rayleigh-Brillouin spectrum can be used for the determination of the atmospheric temperature. Their latest measurements have

shown that only a 10 °C accuracy is achieved for profiles up to 5 km.

The preliminary measurements of the atmospheric temperature made with the University of Wisconsin HSRL have been based on one iodine absorption filter. For temperature measurements the system transmission spectrum is measured by scanning the laser wavelength over the iodine absorption spectrum, similarly as in the system calibration scan. For one temperature profile, data from 5 calibration scans were averaged. This was done to increase the signal to noise ratio of the measurement. The measured profile was calculated by averaging the signal over a 300 m range with 1 km steps.

The signal from atmosphere and detected through the iodine absorption cell is a convolution of the Doppler-broadened molecular spectrum and the iodine absorption spectrum. The Brillouin modified approximation for the Doppler-broadened spectrum was used to calculate the molecular line shapes at temperatures ranging from -70 to +30 °C with 1°C resolution. The calculated line shapes were convoluted with the measured iodine absorption spectrum. In order to define the atmospheric temperature at certain altitude, a least square fit was used to fit the measured profile to the calculated profile. The temperature that produced the best fit defined the temperature of that altitude. Figure 34 shows an example of the received signal from 8 km altitude observed through the iodine absorption cell normalized by the signal observed with the channel without iodine absorption filter. The iodine absorption spectrum is shown as a reference. The modeled molecular profile is shown for the temperature that produced the best fit. The best fit was found at -47°C temperature.

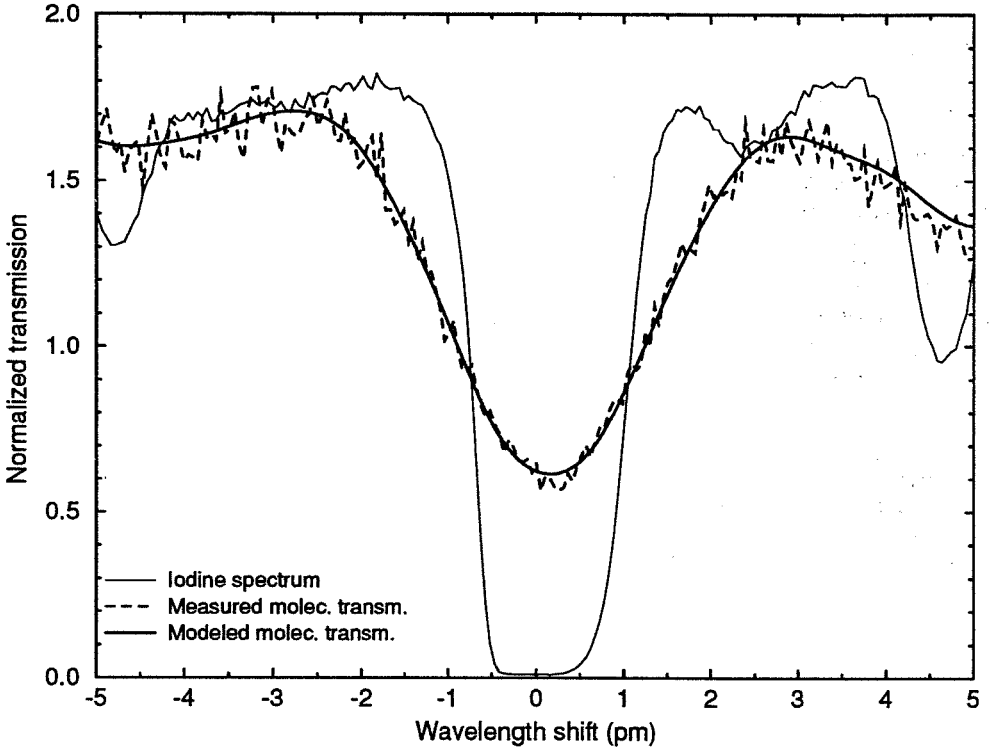

Figure 34. The HSRL signal from 8 km altitude observed through the iodine absorption filter normalized by the signal measured simultaneously without the iodine absorption filter. The iodine absorption spectrum is plotted for reference. The modeled molecular transmission is shown for the temperature that produced the best fit between measured and calculated molecular transmissions. The best fit was obtained at -47°C temperature.

The sensitivity of the molecular transmission of the iodine absorption filter to the width of the molecular spectrum is illustrated in Figure 35. The figure shows the effect of incorrect temperature to the fit. For this figure, the modeled molecular transmissions were subtracted from the modeled molecular transmission at -47 °C temperature. The temperature difference of 5 °C is displayed. The Figure 35 shows that a clear difference between temperatures is achieved, but because the differences are small, the accurate measurements of atmospheric temperature by the scanning technique are difficult to obtain.

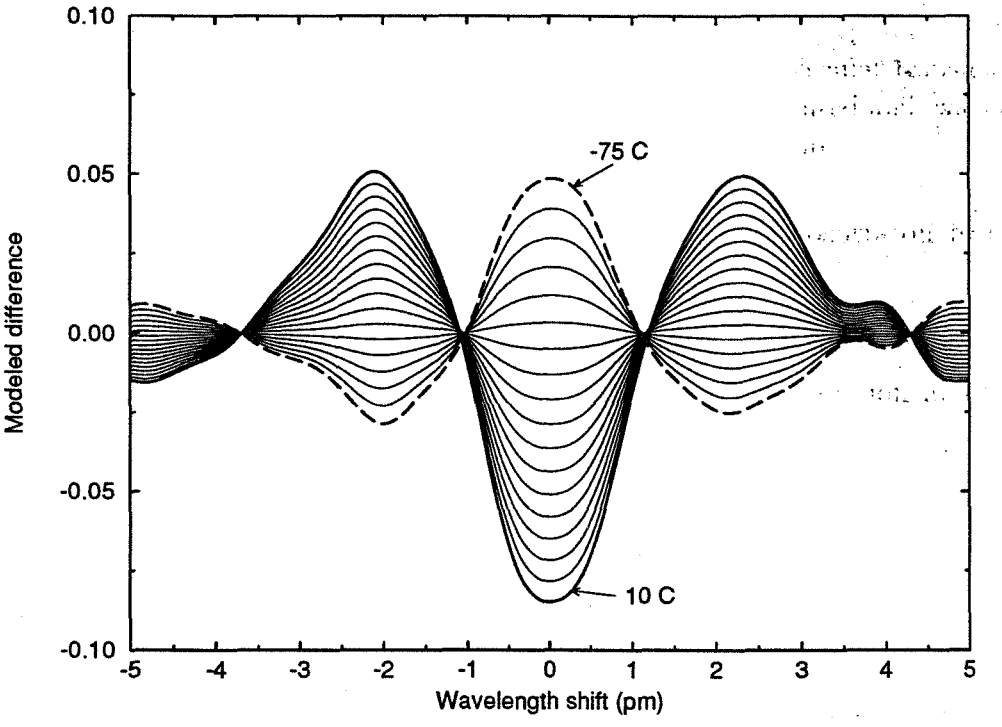

Figure 35. The sensitivity of the molecular transmission to the temperature. The difference in modeled molecular transmission to the molecular transmission at -47°C is shown with 5°C temperature steps.

A temperature profile measured on February 27, 1994, in Madison between 00:00 and 03:00 UT is presented in Figure 36. For the comparison the radiosonde temperature profiles from nearest weather stations are presented. The stations at Green Bay (WI, 180 km northeast from Madison), Peoria (IL, 350 km south from Madison), and St. Cloud (MN, 450 northwest from Madison) provided a radiosonde profile at 00:00 UT. The temperature values measured by the HSRL agree with the temperatures measured with the radiosondes. For the profile between 4 and 8 km the observed rms temperature differences are 2.97, 7.08, and 5.52 °C between HSRL and the weather stations. The rms difference between weather stations is 7.06 °C. For low altitudes, the largest difference between profiles is observed. This is expected because of the synoptic scale variations in weather conditions between different locations.

For altitudes between 6-8 km, a good agreement between HSRL measurement and the central Minnesota (St. Cloud) radiosonde profile is seen. These altitudes had a low aerosol content providing scattering ratio of ~ 0.02. The temperatures above 8 km show a big deviation from the radiosonde temparatures. This is due a strong aerosol layer, that disturbs the HSRL temperature measurement. The scattering ratio of the aerosol layer above 8 km was ~ 0.3. Also the measured temperature values for altitude between 2 and 3.5 km are colder than the radiosonde values. This is due to presence of a low level aerosol layer with scattering ratio of ~ 0.1 The presence of aerosols deepens the measured spectrum and therefore a fit into this spectrum underestimates the temperature. Therefore, if the temperatures are going to be measured in the presence of aerosols, the effect of the aerosol signal has to be separated from the molecular contribution.

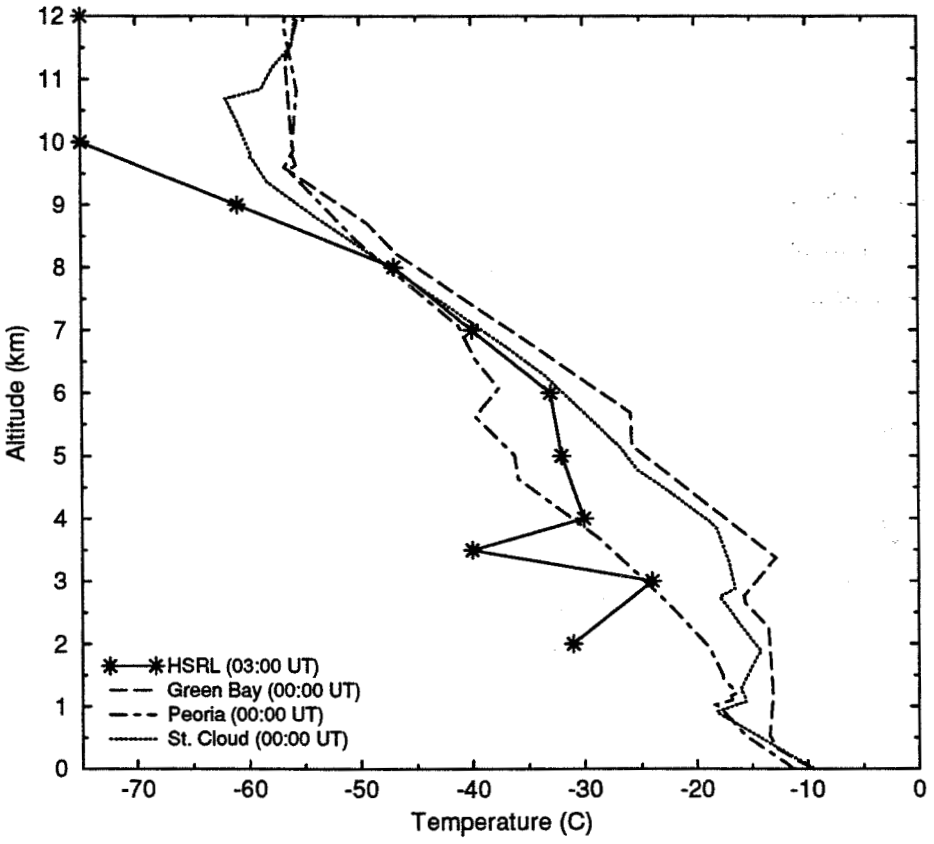

Figure 36. A temperature profile obtained with the HSRL on February 27, 1994. The temperature profile obtained with radiosondes show the atmospheric temperature measured at the closest weather stations. A good agreement between HSRL and radiosonde observations is observed between altitudes of 4 and 8 km. These are altitudes with a low aerosol backscatter content.

7 Error analysis

7.1 Error sources

The signal detected with a photon counting system is a combination of backscatter signal, background light, and internal noise in the photodetector. The lidar equation (Eq. (1)) shows that the amount of received signal is determined by the number of transmitted photons, scattering cross section, backscatter phase function, area of the telescope, transmission of the receiver optics, and the sensitivity of the detectors. On the other hand, the HSRL measurements are dependent on the system calibration coefficients (Eqs. (17) and (18)). The errors in the HSRL measurements can be divided into 5 main categories:

1. errors due to photon counting statistics
2. errors due to changes in system calibration coefficients
3. errors in the background subtraction
4. errors due to a multiple scattering contribution
5. errors in the atmospheric temperature profile used to compute the molecular density

The error in the photon counting process is proportional to the square root of the measured signal. The errors due to photon counting statistics that are induced to the calibration coefficients were discussed in Chapter 5.

The system detection efficiency is a combination of the system transmission and the photomultiplier quantum efficiency. The system detection efficiency affects the amount of detected signal and therefore, it is directly related to the photon counting statistics. A model to calculate the expected system transmission was developed. This model includes the spectral transmission of interference filters, etalons, and iodine absorption cell, transmissions and reflections of optical components (lenses, mirrors, cubes, etalon chamber windows) and photomultiplier quantum efficiencies.

The transmittance and reflectance values of different optical components were confirmed with measurements. The calculated transmission efficiencies were compared with the measured values. For this study, a clear air case was chosen. Because the properties of molecular scattering are well known, the lidar equation for molecular scattering (Eq. 3) can be solved for the number of photons expected for the pure molecular return.

In order to predict the expected molecular return, the calculated system transmission was convoluted with the calculated molecular spectrum at a 5 km reference altitude. The temperature for the Doppler-broadened molecular spectrum calculation was taken from a radiosonde profile. By calculating the ratio of measured to expected number of photons given by the lidar equation, the actual system transmission was estimated. The two way extinction between lidar and the backscatter volume was assumed to $\sim$ 1. The comparison between expected and measured detection efficiency values is given in Table 2. This comparison was made without using the low resolution etalons. Each etalon decreases the transmission by a factor of $\sim$ 2.

Table 2. HSRL detection efficiency

Channel	Calculated (%)	Measured (%)
Aerosol+Molecular	0.78	0.6
Molecular	0.44	0.36
WFOV	4.4	3.4

The transmission efficiency values show $\sim$ 25 % difference between calculated and measured values. A $\sim$ 10% error can be made by assuming the extinction between lidar to 1. Also the uncertainty on the transmission and reflectance values of optical components affect the calculation. The largest uncertainty is the quantum efficiency of the photomultipliers. The value 0.12 is taken from the manufacturers specification, but only a 0.03 change in the quantum efficiency would correct the difference. The transmissions and reflectances of the receiver components that affect to the detection efficiency are listed in Table 3. The transmission and reflection numbers of some components are confirmed with a measurement and rest of the values are obtained from the manufacturers specifications.

Table 3. Transmission / Reflection losses in HSRL components. The source for the transmission and reflection values is manufacturers specification (spec.) or a measurement (meas.).

Channel	Component	R or T (%)	Source	Total(%)
ALL				
	Telescope mirrors (2)	R = 90.0	meas.	R= 81.0
	Interference filter (1)	T= 50.0	meas.	T=50.0
	Polarizing cubes (2/channel)	T=99.0	spec.	T=99.0
		R=93.0	spec.	R=93.0
	PMT quantum efficiency	QE= 12.0	spec.	QE= 12.0
A+M, M				
	Etalon chamber windows (3)	T= 90.0	meas.	T= 73.0
	Mirrors (2 /channel)	T= 90.0	meas.	T= 81.0
	Lenses (3 / channel)	T=99.4	spec.	T=98.2
A+M				
	Beam splitter	T=30.0	meas.	T=30.0
M				
	Beam splitter	R=70.0	meas.	R=70.0
	Iodine absorption cell	T(cell)=80.0	meas.	T=80.0
		T(mol.)~30.0	calc.	T=30.0
WFOV				
	Lens	T=99.4	spec.	T = 99.4
Total eff.				
	Aerosol+Molecular Channel			0.78
	Molecular Channel			0.44
	WFOV Channel			4.4

The reflectivity of the telescope mirrors is limited by the reflectivity of the aluminum coating. The poor transmission values of the etalon chamber windows and the mirrors have a big effect on the detection efficiency, because they lose $\sim$ 41% of the received signal. These components are taken from the old system and they are not optimized for the current operating wavelength. In order to increase the system performance, these components are going to be replaced in near future.

The errors due to change in the system calibration coefficients are mainly caused by change in the transmission-receiver wavelength tuning and change in the system alignment. These errors can be calculated by a partial differentiation.

A change in atmospheric temperature and pressure affects the amount of detected molecular signal. Therefore, if the radiosonde profile is not valid for the measure-

ment conditions, an error is generated in the calculated molecular signal. The width of the Doppler-broadened spectrum directly affects the calibration coefficient C_{mm}. This affects to the amount of molecular signal subtracted from the signal detected with the combined aerosol+molecular channel. In Brillouin spectrum and molecular backscatter cross section calculations, the effects of changing atmospheric conditions are minimized by using the current radiosonde data from the nearest weather stations. By comparing temperature and pressure readings from the closest radiosonde stations, an $\sim$ 1-5 % difference between stations is observed. This due to the geographic separation between weather stations. Because the lidar is located between these stations, the error is expected to be smaller.

In addition to the atmospheric temperature and pressure changes, the effects of the wind on the measurement has to be considered because the high wind velocities can shift the Doppler-broadened spectrum with respect to the laser wavelength. A bulk shift in respect to the radiated spectrum is an indicator of wind, while the line broadening is associated with the random thermal motions of the molecules (and aerosols). If the line center of the Doppler-broadened spectrum is shifted in respect to the transmitted wavelength, the system calibration will be in error. The Doppler-shift for the backscatter signal can be calculated from

$$\frac{\Delta\nu}{2\nu_o} = \frac{v}{c}, \tag{24}$$

where

$\Delta\nu$ = wavenumber shift

$2\nu_o$ = wavenumber of the laser line center

v = molecular velocity

c = velocity of light

The wind velocities measured by a radiosonde can be used as an estimate for the horizontal wind. The maximum horizontal wind velocities are generally smaller than 70 m/s at cirrus cloud altitudes, and the maximum vertical winds are normally below 1 m/s in troposphere. Therefore, the maximum wind to the lidar pointing direction θ (θ = 4 degrees from the zenith) is $v_l = v_x sin\theta + v_y cos\theta$, which corresponds to a

velocity of 5.9 m/s. The shift in the spectrum is 19.8 fm, which is much smaller than the current 0.052 pm detection accuracy of the molecular spectrum. Also the horizontal wind speeds are generally much lower[49], and therefore, the effects due to wind to the HSRL measurements are negligible, but caution is required if larger zenith angles of the pointing direction are considered.

The uncertainty in transmitter-receiver peak transmission tuning can be seen as a shift in the transmitter wavelength in respect to the spectral transmission maximum of the receiver. This effects the amount of detected molecular signal, but if the drift is large, a change in the amount of detected aerosol is observed. The drift also affects the system transmission. In the current HSRL, the effects of a drift between transmitter and receiver wavelengths are minimized by locking the transmitter laser wavelength to the iodine absorption peak (see Chapter 5.2). The effects of the wavelength locking to the measured signal were also discussed in Chapter 5.2.

In addition to the previous errors, the system calibration is affected by all misalignments of the system. The error due to a system misalignment can be divided into three different categories:

1. alignment error in the receiver optics
2. alignment error between transmitter and receiver pointing direction
3. an error in the compensation for the beamsplitter polarization dependence

A small alignment error (off focus, off axis or misalignment in system pointing direction) can lead situations, where part of the backscattered light is lost in the optics, detector, or atmosphere. This can easily lead into a range dependence of the received signal. This affects the inversion and furthermore, the measured optical depth. A misalignment also affects the total system transmittance and the signal to noise ratio of the measured signal. System pointing instabilities make the overlap correction of the received signal difficult. The overlap region is the close distance range where the overlap of the receiver field of view and the transmitted beam is incomplete. The effect of misalignment between transmitter end receiver pointing directions is largest for the overlap region. The effects vary daily depending from

the accuracy of the alignment between transmitter and receiver pointing direction. Large receiver field of views are less critical for the alignment errors. The signal measured with the large field of views of the WFOV channel can be used to align the small field of view channels. In the HSRL, the alignment between transmitter and receiver pointing directions is performed as follows. A corner cube is used to direct the outgoing laser beam to the receiver. The beam is aligned to the center of the receiver aperture by adjusting the turning mirror on the top of the telescope secondary mirror. Then the corner cube is removed and the signal from the atmosphere is used to verify the alignment. The signal of the large field of view of the WFOV-channel is compared to signal of the combined channel. If the channels are properly aligned and if the transmitter and receiver pointing directions are the same, the slopes of the signals are similar for the altitudes above the overlap region and therefore, the ratio between WFOV-channel signal to the spectrometer channel signal is constant. The alignment of the smallest WFOV channel aperture can be verified similarly by comparing the signal from the larger aperture to the signal from the smallest WFOV aperture. The effects of alignment errors on the system measurement accuracy are not included to the error analysis, because with a careful alignment the errors can be minimized.

The accuracy of the background correction is mostly affected by the photon counting statistics. The effects of photon counting on the measured background are decreased by summing at least 66 range bins together. The background correction method used in HSRL measurements was described earlier in Chapter 3.2.2. In addition to the photon counting statistics, the accuracy of the background correction is affected by the slight tendency to overestimate the number of background counts for altitudes close to 33 km. Eventhough atmospheric density, and therefore the amount of Rayleigh scattering, decreases rapidly with the range, some of the signal that is measured into the upper range bins of the HSRL can still be due to Rayleigh scattering. Therefore, when those range bins are used to calculate the number of background counts, the background is slightly overestimated due to the Rayleigh signal.

The effects of the multiple scattering on the received lidar signal are usually neglected and the received signal is assumed to be single scattered. A lidar return from

water and thick cirrus clouds usually encounters large optical depths within a short distance of the cloud boundary and therefore, many of the received photons are likely to be from multiple scattering. The effect of multiple scattering to the lidar signal is dependent from the receiver field of view, cloud particle size, range from the lidar, and the optical depth of the cloud. The effect of multiple scattering can be seen in the lidar profile as a reduction in the rate of attenuation of the signal. In depolarization, the effect of multiple scattering will show up as an increase in the depolarization ratio towards the cloud top. The HSRL measurements have shown, that the effect of multiple scattering on the smallest field of view signals is small, because the depolarization ratio values observed for the water clouds are low.

The current HSRL profiles are not corrected for multiple scattering contributions. An inversion program that accounts multiple scattering effects is currently in progress. The magnitude of the error caused by assuming the signal to be originated from single scattering depends from the field of view of the receiver, optical thickness of the cloud, size of the cloud particles, and penetration depth. The clear air aerosols and thin cirrus layers have a small or no multiple scattering effect. Because of the large particle size of ice crystals, the signal from thick cirrus clouds contains a multiple scattering contribution even for the small field of views. The multiple scattering from water cloud droplets is distributed to the larger field of views. The amount of multiple scattering on the measured signal can be estimated from the paper by Eloranta and Shipley[27].

7.2 Effects of different errors on the measured optical parameters

The effects of different errors on the inverted aerosol and molecular return and to the measured optical parameters were calculated by partially differentiating Equations (19), (20), and (4)–(13). The error analysis is made for the data obtained on November 11, 1993. A section of the data for a thin two-layer cirrus cloud structure is analyzed. The case is the same as shown in Figure 31. The thin cirrus cloud case is chosen for this study for two reasons. First, the backscatter signal from thin high altitude cirrus is small. Therefore, an error analysis made for the thin cirrus tests the measurement sensitivity of the system. Second, if accurate measurements of thin cirrus clouds can be made within short averaging time, then the HSRL can be considered for studies of contrail formed cirrus. The short averaging time is important for the contrail studies, because they drift rapidly with the wind and only a limited number of samples from one contrail can be obtained.

Information from cloud optical properties can be obtained by comparing the HSRL measurements with satellite observations. Thus, the averaging time of the HSRL data has to be close to the time resolution of a satellite image. The use of the short averaging times also prevents the smoothing of the the lidar signal so that the rapid changes in cloud structure in both time and altitude remain in the data. For this study, the 3 min averaging time was chosen to study the errors in the inverted aerosol and molecular returns, inverted aerosol and molecular depolarization ratios, backscatter ratio, optical depth, and aerosol backscatter cross section. Because the measurement of the backscatter phase function is difficult due to uncertainty in the extinction cross section determination, the 6 min averaging time was used for error analysis of the phase function measurement.

The error analysis presented here shows the total errors together with the partial errors. All errors are calculated as mean square errors (see Equations 26-35) and presented as fractional root mean square errors (see Figures 37- 44). The partial errors in Figures 37- 44 present the effects of errors on the photon counting of the combined channel and the molecular channel, error in the molecular backscatter cross section per unit volume due to the uncertainty in temperature and pressure profiles,

and errors in the calibration coefficient determination. The error estimate calculations include the photon counting error, error in the background correction, error due to the uncertainty in the temperature and pressure profiles measured with a radiosonde, and errors due to the tuning of the laser wavelength. The errors due to system alignment and the error due to multiple scattering effects are not included to this error analysis. Also the error in the determination of the range R is negligible.

The errors in background correction are assumed to be from photon counting statistics. The uncertainty of 2 % for the temperature profiles is used. The error in pressure profile is estimated to 1 mbar of the radiosonde pressure reading at each altitude. The error is due to the geographic separation between closest weather stations. This is estimated from the radiosonde measurements from the closest weather stations. The uncertainty on the molecular spectrum calculation is estimated with the 2% uncertainty on the atmospheric temperature. The error on the calibration coefficient C_{mm} determination is a combination of the photon counting error, uncertainty of the molecular spectrum, and the error caused by tuning of the laser wavelength. The accuracy of the calibration coefficient C_{am} determination is limited by the photon counting statistics. The error in the molecular backscatter cross section per unit volume measurement depends on the errors in the atmospheric temperature and pressure.

The error in the molecular profile can be given as

$$
\begin{aligned}
(\Delta N_m(R))^2 = \; & \left(\frac{\partial N_m(R)}{\partial S_m(R)}\right)^2 (\Delta S_m(R))^2 + \left(\frac{\partial N_m(R)}{\partial S_{a+m}(R)}\right)^2 (\Delta S_{a+m}(R))^2 + \\
& \left(\frac{\partial N_m(R)}{\partial C_{mm}(R)}\right)^2 (\Delta C_{mm}(R))^2 + \left(\frac{\partial N_m(R)}{\partial C_{am}}\right)^2 (\Delta C_{am})^2 + \\
& \left(\frac{\partial N_m(R)}{\partial B_{a+m}}\right)^2 (\Delta B_{a+m})^2 + \left(\frac{\partial N_m(R)}{\partial B_m}\right)^2 (\Delta B_m)^2; \qquad (25)
\end{aligned}
$$

which leads to equation

$$\left(\frac{\Delta N_m(R)}{N_m(R)}\right)^2 = \frac{C_{am}(R)^2 \Delta S_{a+m}(R)^2}{\left(S_m(R) - B_m(R) - C_{am}(R)\left(S_{a+m}(R) - B_{a+m}(R)\right)\right)^2} + \frac{\Delta S_m(R)^2}{\left(S_m(R) - B_m(R) - C_{am}(R)\left(S_{a+m}(R) - B_{a+m}(R)\right)\right)^2} + \frac{\Delta C_{am}(R)^2}{\left(C_{mm}(R) - C_{am}(R)\right)^2} + \frac{\Delta C_{mm}(R)^2}{\left(C_{mm}(R) - C_{am}(R)\right)^2} + \frac{C_{am}(R)^2 \Delta B_{a+m}(R)^2}{\left(S_m(R) - B_m(R) - C_{am}(R)\left(S_{a+m}(R) - B_{a+m}(R)\right)\right)^2} + \frac{\Delta B_m(R)^2}{\left(S_m(R) - B_m(R) - C_{am}(R)\left(S_{a+m}(R) - B_{a+m}(R)\right)\right)^2} \quad (26)$$

$\Delta S_m(R)$ and $\Delta S_{a+m}(R)$ are the photon counting errors. $\Delta C_{am}(R)$ and $\Delta C_{mm}(R)$ the errors in the calibration coefficient determination. The background correction errors are given by $\Delta B_m(R)$ and $\Delta B_{a+m}(R)$. The error analysis made for the calibration coefficients show that C_{mm} can be determined with better than 5 % accuracy and C_{am} with a better than 2 % accuracy.

The effects of different errors on the inverted molecular return are shown in Figure 37. The errors in inverted molecular return are dominated by the photon counting statistics and the determination of the calibration coefficient C_{mm}. The error due to the measurement accuracy of the aerosol signal is negligible. The errors in the C_{am} determination have only a small effect on the inverted molecular return.

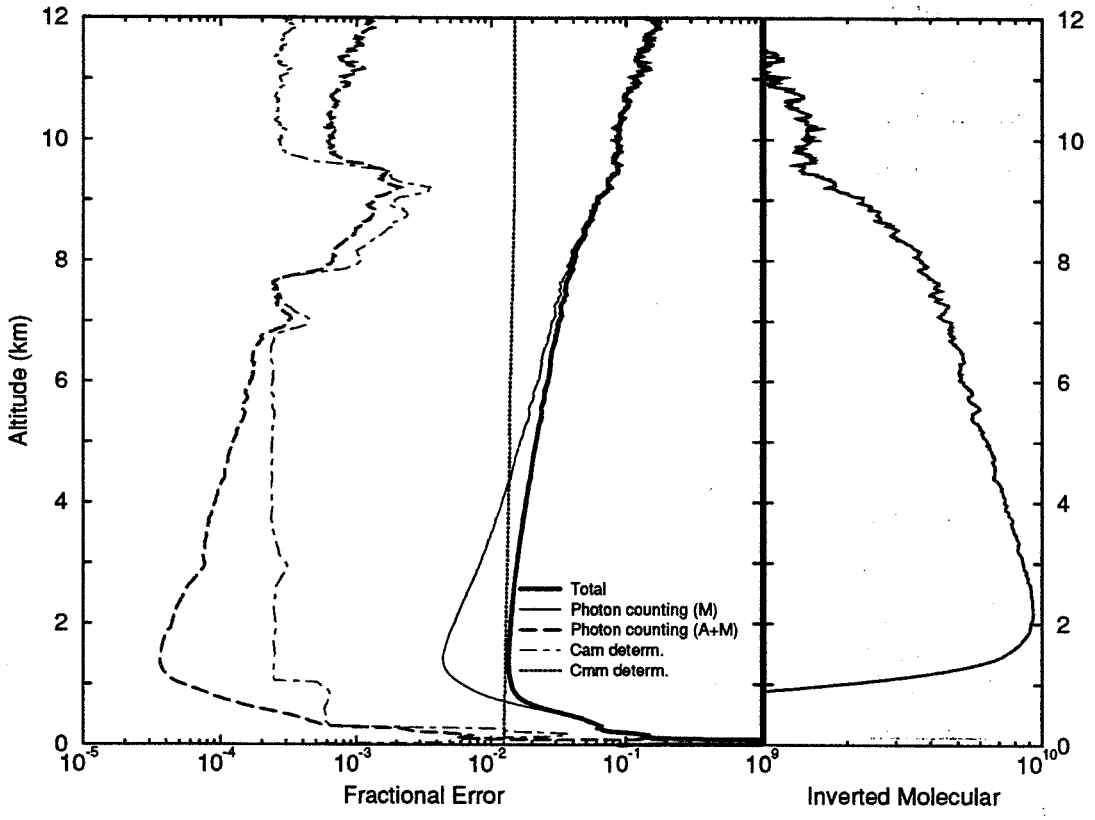

Figure 37. The effects of different errors on the inverted molecular profile (November 11, 1993, 01:05-01:08 UT). Data from a thin cirrus cloud is analyzed by using a 3 min. averaging time. The measured molecular profile (rightmost graph) presents the signal variations as a function of altitude. The extinction due to the thin cirrus cloud is observed between 6.5 and 10 km. The accuracy of the inverted molecular return determination is mostly limited by the photon counting statistics and the determination accuracy of the calibration coefficient C_{mm} (leftmost graph). The large errors shown in the overlap region below 2 km are due to a focus error and incomplete overlap of the receiver field of view and transmitted laser beam.

The error in the measured aerosol profile can derived similarly to the molecular profile

$$(\Delta N_a(R))^2 = \left(\frac{\partial N_a(R)}{\partial S_m(R)}\right)^2 (\Delta S_m(R))^2 + \left(\frac{\partial N_a(R)}{\partial S_{a+m}(R)}\right)^2 (\Delta S_{a+m}(R))^2 + \left(\frac{\partial N_a(R)}{\partial C_{mm}(R)}\right)^2 (\Delta C_{mm}(R))^2 + \left(\frac{\partial N_a(R)}{\partial C_{am}}\right)^2 (\Delta C_{am})^2 + \left(\frac{\partial N_a(R)}{\partial B_{a+m}}\right)^2 (\Delta B_{a+m})^2 + \left(\frac{\partial N_a(R)}{\partial B_m}\right)^2 (\Delta B_m)^2 \quad (27)$$

This differential equation can be expanded to following form

$$\left(\frac{\Delta N_a(R)}{N_a(R)}\right)^2 = \frac{C_{mm}(R)^2 \Delta S_{a+m}(R)^2}{\left(S_m(R) - B_m(R) - C_{mm}(R)\left(S_{a+m}(R) - B_{a+m}(R)\right)\right)^2} + \frac{\Delta S_m(R)^2}{\left(S_m(R) - B_m(R) - C_{mm}(R)\left(S_{a+m}(R) - B_{a+m}(R)\right)\right)^2} + \frac{\Delta C_{am}(R)^2}{\left(C_{am}(R) - C_{mm}(R)\right)^2} + \frac{\Delta C_{mm}(R)^2}{\left(C_{am}(R) - C_{mm}(R)\right)^2} + \frac{C_{mm}(R)^2 \Delta B_{a+m}(R)^2}{\left(S_m(R) - B_m(R) - C_{mm}(R)\left(S_{a+m}(R) - B_{a+m}(R)\right)\right)^2} + \frac{\Delta B_m(R)^2}{\left(S_m(R) - B_m(R) - C_{mm}(R)\left(S_{a+m}(R) - B_{a+m}(R)\right)\right)^2} \quad (28)$$

The accuracy of the inverted aerosol return is mostly affected by the determination accuracy of the inverted molecular return (photon counting statistics and C_{mm} determination accuracy) and the photon counting statistics of the combined aerosol and molecular channel (see Figure 38). For the cases of small aerosol backscatter content, large errors in the determination of the aerosol return are made when short averaging times are used. The errors are caused by subtracting a large amount of molecular signal from the combined channel signal that contains the strong molecular signal together with a small aerosol contribution. Therefore, the statistics of the molecular signal dominates the aerosol backscatter signal determination. The determination of clear air aerosols requires longer averaging times in order to achieve reliable results. On the other hand, the measurements of cloud aerosols can be done with $\sim$ 1.0% accuracy (7-10 km).

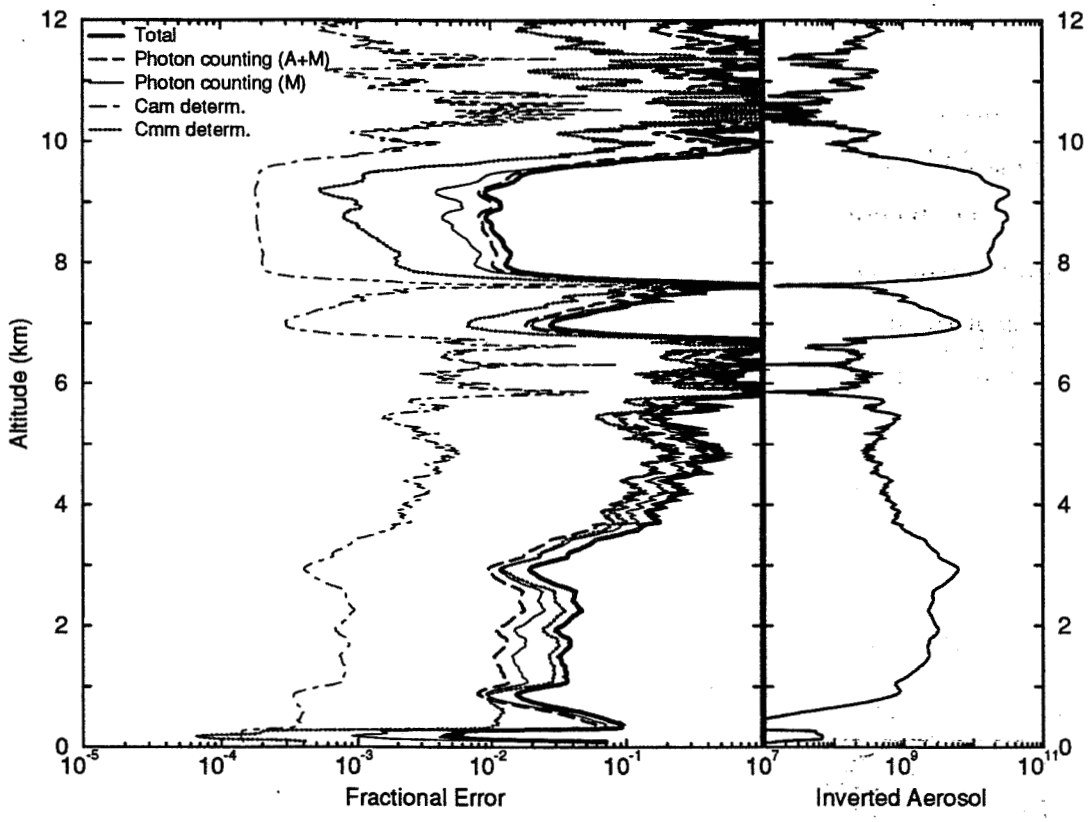

Figure 38. The effects of different errors on the inverted aerosol profile in case of a thin cirrus cloud (November 11, 1993, 01:05-01:08 UT). Averaging time of the data is 3 min. The measured aerosol profile (rightmost graph) shows the signal variation as function of altitude. The thin cirrus layer is observed between 6.5 and 10 km and a strong aerosol layer is seen between 0 and 3.5 km. The measurements of the aerosols are limited by the accuracy of the molecular profile measurements (leftmost graph). The 3 min averaging time provides 1-5% accuracy for thin cirrus cloud and strong aerosol layer measurements, but a longer averaging time is required for the measurements of the clear air aerosols.

Using the calculated errors for the measured aerosol and molecular profiles, the errors in the determination of the optical parameters (see Chapter 2) can be calculated as follows.

The errors in the determination of inverted aerosol and molecular returns have a direct effect on the accuracy of the backscatter ratio (or scattering ratio) determination (Figure 39). Therefore, the error in the backscatter ratio is

$$(\Delta SR(R))^2 = \left(\frac{\partial SR(R)}{\partial N_a(R)}\right)^2 (\Delta N_a(R))^2 + \left(\frac{\partial SR(R)}{\partial N_m(R)}\right)^2 (\Delta N_m(R))^2, \qquad (29)$$

The effects of errors on photon counting, background correction, and calibration can be derived by combining the previous equation with the equations (26) and (28). Similar derivations of the differential errors can be made for the optical parameters given in following.

For the cases of a low aerosol backscatter content, the errors in the backscatter ratio are dominated by the errors in the aerosol return determination. For a stronger aerosol backscatter return from a cloud, the errors due to molecular return determination are on the same order or higher than the errors due to aerosol return determination. The backscatter ratios of the thin cirrus and strong aerosol layers can be determined with better than 10% accuracy, but measurements of the clear air require longer averaging times.

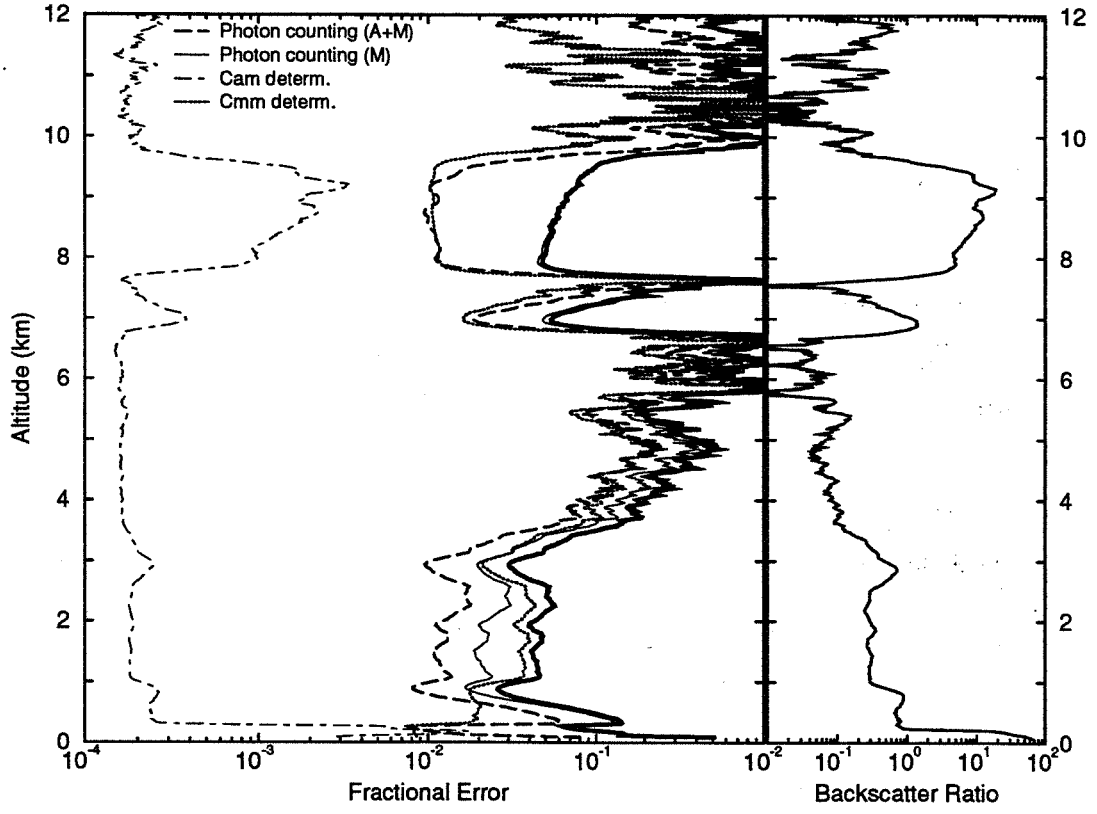

Figure 39. The effects of different errors on the backscatter ratio in case of a thin cirrus cloud (November 11, 1993, 01:05-01:08 UT). Averaging time of the data is 3 min. The backscatter ratio profile (rightmost graph) shows the ratio of the aerosol return to the molecular return as a function of altitude. Backscatter ratios ~0.1 to 20 are observed. The errors in the backscatter ratio measurement (leftmost graph) are determined by the accuracy of the aerosol and molecular return measurements. For the altitudes with a low aerosol content, the error in backscatter ratio is limited by the accuracy of the aerosol backscatter return measurement. For the cirrus cloud the accuracy depends on the goodness of the molecular backscatter profile measurement.

The error in optical depth can be approximated as sum of error in the molecular scattering cross section per unit volume and error in the molecular return determination.

$$(\Delta\tau(R))^2 \approx 2\left(\frac{\partial\tau(R)}{\partial\beta_m(R)}\right)^2(\Delta\beta_m(R))^2 + 2\left(\frac{\partial\tau(R)}{\partial N_m(R)}\right)^2(\Delta N_m)^2 \tag{30}$$

Error in the molecular scattering cross section per unit volume $\Delta\beta_m(R)$ is determined by the uncertainties in the radiosonde based measurement of the atmospheric temperature and pressure.

$$(\Delta\beta_m(R))^2 = \left(\frac{\partial\beta_m(R)}{\partial T(R)}\right)^2(\Delta T(R))^2 + \left(\frac{\partial\beta_m(R)}{\partial P(R)}\right)^2(\Delta P(R))^2 \tag{31}$$

Error in optical depth measurement is dominated by the error in the determination of the molecular return and the uncertainty on the density profile measured by a radiosonde (see Figure 40). For this study, a 2% error in the temperature profiles is assumed. The closest radiosonde measurement site is Green Bay (WI), which is $\sim$ 180 km northeast from the lidar. Because the weather conditions can vary between the lidar site and the closest weather station, larger errors in the temperature profile are possible. The effects of errors on the atmospheric density profile can be minimized by making radiosonde measurements on the lidar site.

The figure shows, that with 3 min averaging time the cloud optical depths can be detected with $\sim$ 10 % accuracy. This accuracy is sufficient when clouds with optical depths greater than 1 are measured. For situations where optical depth is less than 1, a longer averaging time is required.

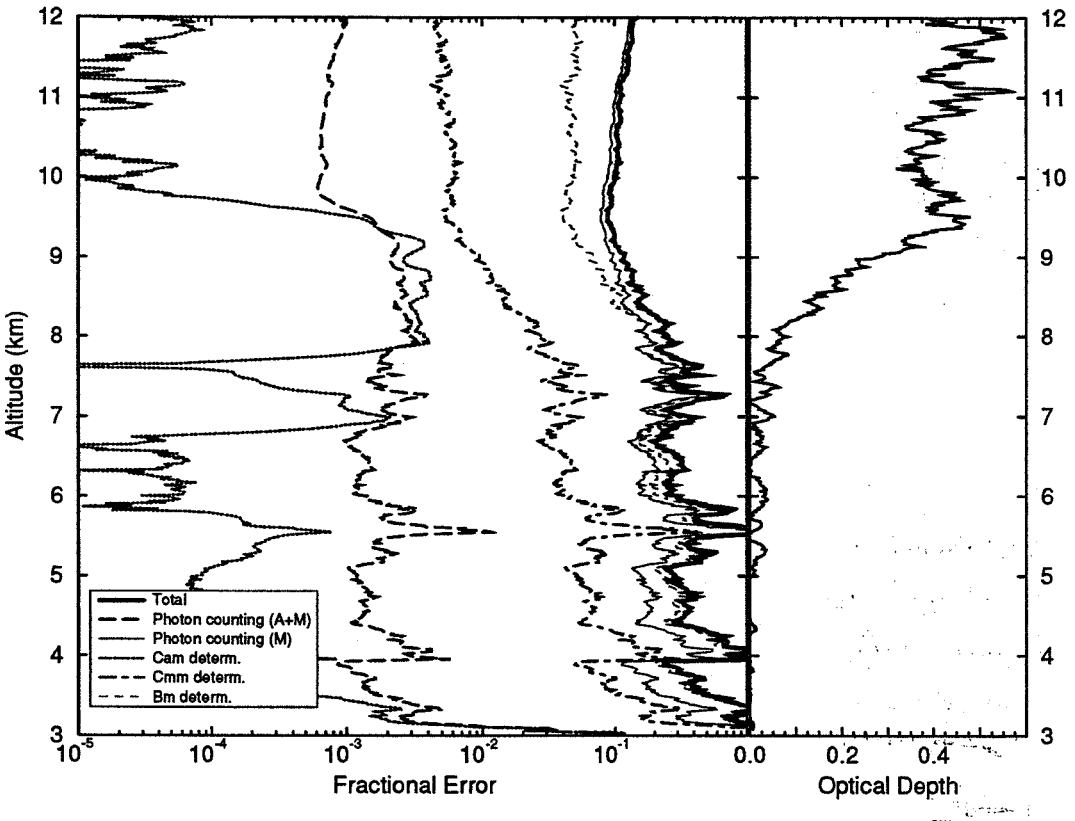

Figure 40. The effects of different errors to the optical depth in case of a thin cirrus cloud (November 11, 1993, 01:05-01:08 UT). Averaging time of the data is 3 min. The optical depth profile (rightmost graph) shows the variation of the optical depth as a function of altitude. Optical depth of 0.5 is measuered for the range from 3 to 12 km and optical depth of 0.4 is observed for the cirrus cloud between 6.5 and 10 km. The errors in the measurement of the optical depth below 6.5 km are dominated by the inaccuracy of the radiosonde profile (leftmost graph) and the photon counting statistics of the molecular channel. The error in the calibration coefficient C_{mm} determination also has a significant effect on the total error. The optical depth of the thin cirrus cloud can be measured with $\sim$ 10% accuracy.

The accuracy of the aerosol backscatter cross section measurement is limited by the accuracy of the molcular backscatter cross section per unit volume determination and the accuracy of the backscatter ratio.

$$\left(\Delta\beta_a(R)\frac{P_a(\pi,R)}{4\pi}\right)^2 = \left(\frac{\partial\beta_a(R)\frac{P_a(\pi,R)}{4\pi}}{\partial\beta_{m(R,T,P)}}\right)^2 (\Delta\beta_{m(R,T,P)})^2 + \left(\frac{\partial\beta_a(R)\frac{P_a(\pi,R)}{4\pi}}{\partial SR(R)}\right)^2 (\Delta\, SR(R))^2 \qquad (32)$$

The effects of different errors on the aerosol backscatter cross section are shown in Figure 41. This figure shows, that the measurements are mostly limited by the photon counting statistics, but also the uncertainty on the $\beta_m(R)$ determination has a significant effect. The aerosol backscatter cross sections of clouds and strong aerosol layers can be observed with better than 10 % accuracy, but the measurements of clear air aerosol backscatter cross sections require longer averaging time.

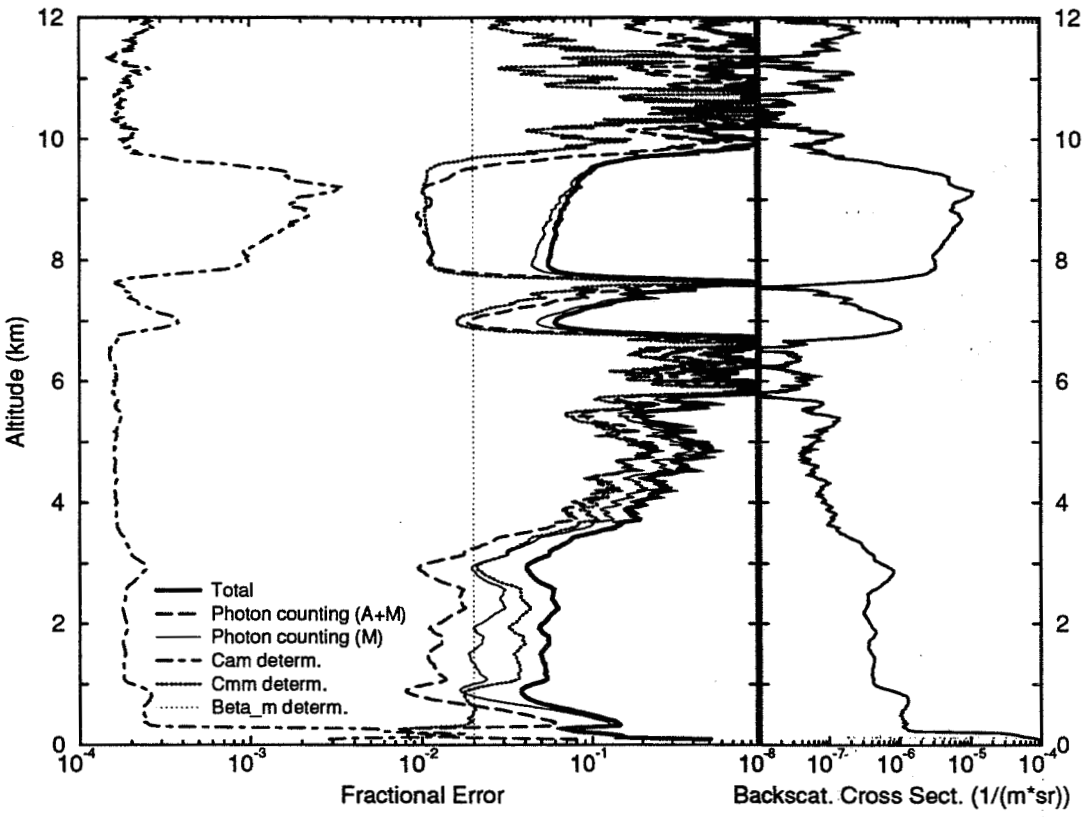

Figure 41. The effects of different errors to the aerosol backscatter cross section in case of a thin cirrus cloud (November 11, 1993, 01:05-01:08 UT). Averaging time of the data is 3 min. The aerosol backscatter profile is presented as a function of altitude (rightmost graph) and the backscatter cross section values range from $\sim 10^{-7}$ to $10^{-5} 1/m$. The aerosol backscatter cross section of the cirrus cloud (6-10 km) and the strong aerosol layer between 1 and 3.7 km can be determined with 4-10 % accuracy, but the measurements of the aerosol backscatter cross section of the clear air require a longer averaging time (leftmost graph).

The error in the phase function is affected by the errors on determinations of the molecular scattering cross section per unit volume, the aerosol and molecular profile, and the extinction cross section. These errors can be further divided to the photon counting errors, errors in the calibration coefficient determination, and errors in the background subtraction.

$$\left(\Delta\frac{P_a(\pi,R)}{4\pi}\right)^2 = \left(\frac{\partial\frac{P_a(\pi,R)}{4\pi}}{\partial\beta_m(R)}\right)^2 (\Delta\beta_m(R))^2 + \left(\frac{\partial\frac{P_a(\pi,R)}{4\pi}}{\partial SR(R)}\right)^2 (\Delta SR(R))^2 + \left(\frac{\partial\frac{P_a(\pi,R)}{4\pi}}{\partial\beta_\epsilon(R)}\right)^2 (\Delta\beta_\epsilon(R))^2 \quad (33)$$

Because the extinction section is a range derivative of the optical depth, the determination accuracy of the molecular profile limits the phase function measurements. For this study, the accuracy of the phase function determination is estimated for a 6 min section of the thin two-layer cirrus cloud. The statistics obtained within 3 min averaging time is not sufficient for the measurements of phase function profiles.

The accuracy of the phase function value determination can be seen from Figure 42. The cloud phase function can be observed with 10-20% accuracy when 6 min averaging time is used. By increasing the averaging time or the signal strength, accurate measurements of cloud phase function profiles can be made.

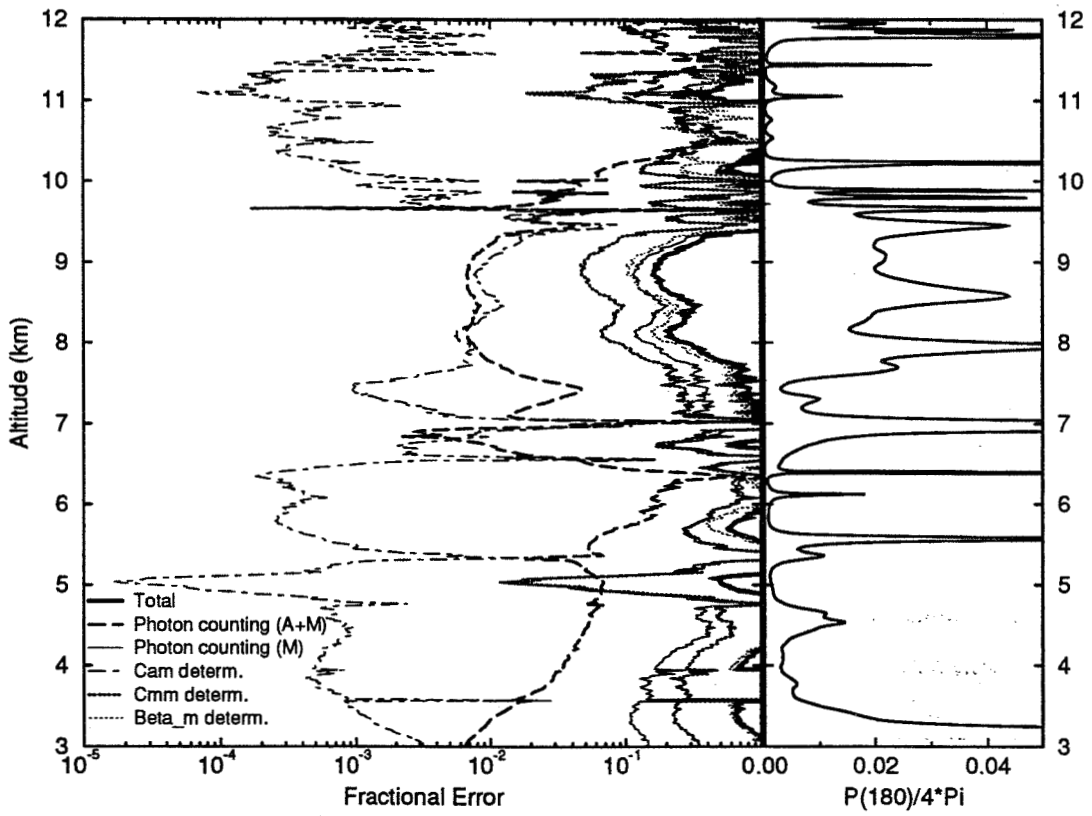

Figure 42. The effects of different errors on the phase function in case of a thin cirrus cloud (November 11, 1993, 01:05-01:11 UT). The 6 min averaging time is used. The phase function profile is presented as a function of altitude and the average phase function of the cirrus cloud layer between 7.5 and 10 km is 0.02 (rightmost graph). The accuracy of the phase function measurements is determined by the photon counting statistics, determination accuracy of the calibration coefficients, and accuracy of the molecular scattering cross-section per unit volume (leftmost graph). The accuracy achieved within 6 min averaging provides phase function measurements with $\sim$ 20% accuracy for the cloud layer.

Error in the inverted depolarization ratio can be presented as a sum of errors in the parallel channel and the perpendicular channel signals.

$$(\Delta\delta_{a,m}(R))^2 = \left(\frac{\partial\delta_{a,m}}{\partial N_{a,m\perp}}\right)^2 (\Delta N_{a,m\perp})^2 + \left(\frac{\partial\delta_{a,m}}{\partial N_{a,m\parallel}}\right)^2 (\Delta N_{a,m\parallel})^2 \quad (34)$$

The Fig 43 shows that the accuracy of the depolarization measurements is mostly limited by the accuracy of the perpendicular channel signal. The errors in the perpendicular channel signal determination are dominated by the photon counting statistics. The Figure 43 shows that short averaging times provide accurate measurements of cloud depolarization, and therefore reliable separation between water and ice clouds can be based on the depolarization measurements of the HSRL. Also reliable depolarization measurements of strong aerosol layers can be performed.

Figure 44 presents the errors in the molecular depolarization ratio. The measurements of molecular depolarization ratio can be performed with better than 10 % accuracy for the altitudes between 0.8 and 4 km. Reliable measurements of molecular depolarization for higher altitudes require longer averaging times. By using long averaging times the effects of atmospheric temperature on the measured depolarization can be studied.

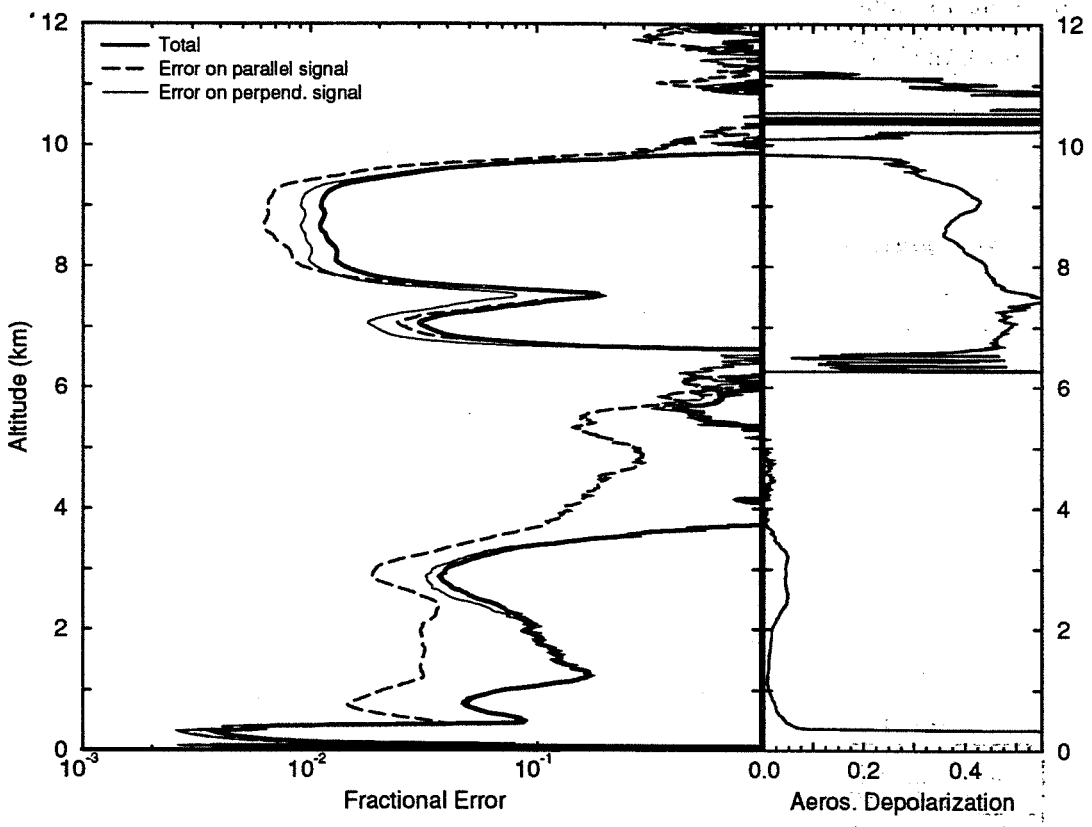

Figure 43. The effects of different errors to the inverted aerosol depolarization ratio in case of a thin cirrus cloud (November 11, 1993, 01:05-01:08 UT). Averaging time of the data is 3 min. The depolarization profile shows the variations of the inverted aerosol depolarization as a function of altitude (rightmost graph). A $\sim$ 40% cirrus cloud depolarization is observed (6.5 - 10 km) and the depolarization of the strong aerosol layer is $\sim$ 5%. The measurements of the inverted aerosol depolarization ratio are limited by the accuracy of the perpendicular signal (leftmost graph). The depolarizations of clouds can be measured with $\sim$1 % accuracy. The depolarizations of strong aerosol layers are obtained with better than 10% accuracy.

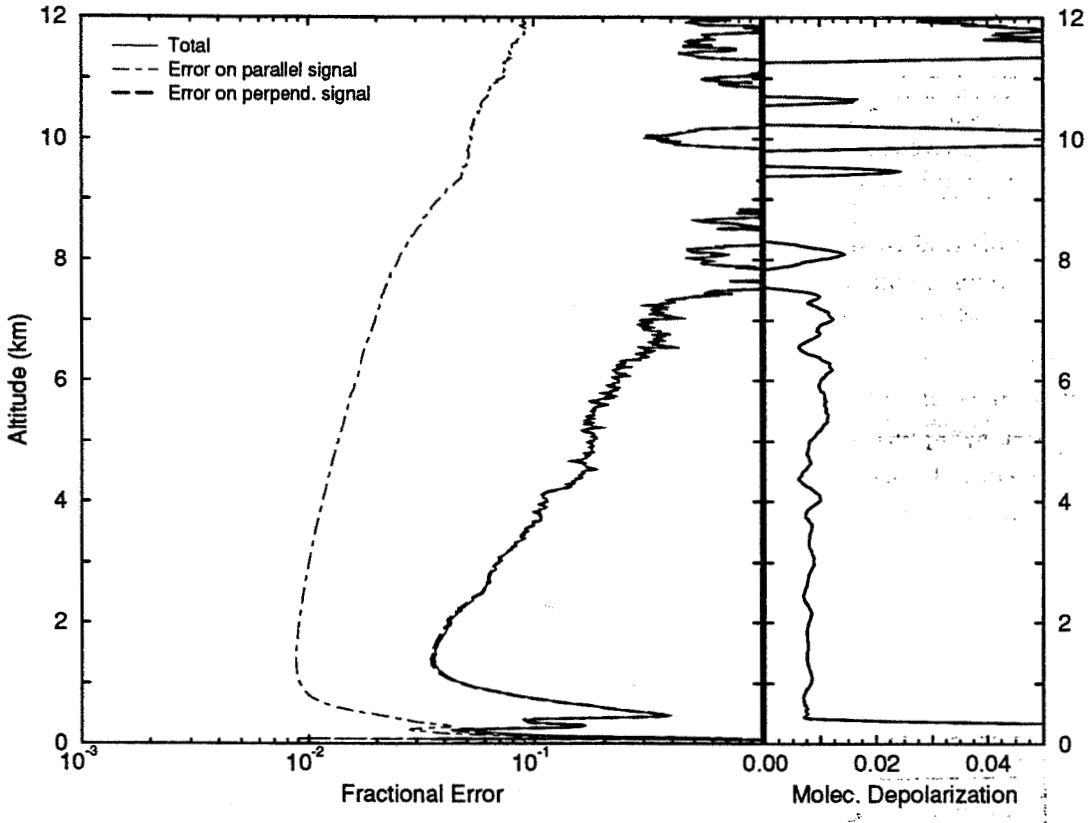

Figure 44. The effects of different errors on the inverted molecular depolarization ratio in case of a thin cirrus cloud (November 11, 1993, 01:05-01:08 UT). Averaging time of the data is 3 min. The depolarization profile shows the variations of the inverted molecular depolarization as a function of altitude (rightmost graph). A 0.8 % depolarization is observed from 0.5 to 7 km. The measurements of the molecular depolarization are limited by the accuracy of the perpendicular signal measurement (leftmost graph). For altitude between 0.8 and 4 km better than 10% accuracy is achieved. Measurements molecular depolarization for the higher altitudes require longer averaging times.

8 Conclusions

The work presented in this thesis has shown that the installation of the iodine absorption filter has substantially improved the performance of the University of Wisconsin-Madison High Spectral Resolution lidar (HSRL). The new system design that includes the iodine absorption filter, polarization, and multiple scattering measurement capabilities is shown. The high resolution etalon, that was used in the earlier system to separate between aerosol and molecular scattering, provided only 1:2 separation for the aerosol backscatter signal between channels. The iodine absorption filter has been shown to suppress the aerosol backscatter signal on molecular channel down to 0.08% and therefore the aerosol cross talk signal on the molecular signal can be easily removed even for optically thick clouds. In the etalon based system, the determination of the system calibration terms was sufficient to provide accurate inversions only for the clear air aerosols and thin cirrus clouds. The use of the iodine absorption filter has also improved the robustness of the HSRL, reduced the complexity of the system, and increased the optical transmission of the system, so that accurate measurements of the optical depth, backscatter cross section and phase function can be made. Also the simultaneous measurements of depolarization and multiple scattering are performed. The HSRL implementation shows a depolarization measurement technique that uses the one transmitter laser and one detector to measure both polarization components. Therefore, no calibration of the receiver is required. The multiple scattering measurements are realized with a separate channel that allows measurements of signal strength variations as function of field of view simultaneously with the measurements of the narrow field of view channels.

The iodine absorption filter provides an absolute wavelength reference for the HSRL measurements. The iodine absorption line observed through a cell with 50% transmission on the line center is used for the wavelength locking of the HSRL transmitter laser. This provides stable operation over a long period of time without a need for frequent calibrations. Measurements have shown that the laser wavelength is maintained within $\pm$ 0.052 pm.

The stability and reliability of the system have been tested by operating the iodine absorption based HSRL at the University of Wisconsin-Madison campus. Start-

ing from July 1993, the HSRL has been routinely operated and data from different atmospheric conditions have been recorded. This dataset contains $\sim$ 30 cirrus cloud cases. The measurements show that accurate measurements of optical properties of the atmosphere can be performed. The improved measurement accuracy has made possible to measure optical depth profiles inside the clouds. The current HSRL can be used to probe clouds that have optical depths up to $\sim$ 3. This means that most of the cirrus cloud cases can be fully observed and the bases of thick water clouds can be measured up to 300–500 m inside the cloud. This has been achieved by using the iodine absorption filter, high laser pulse repetition rate, small pulse energy per laser pulse, and very fast photon counting data system. The measurement accuracy of the HSRL is high enough to provide accurate measurements of optical parameters of clouds and strong clear air aerosol layers within 3 min averaging time, but the accurate measurements of clear air optical parameters require longer averaging times. The clear air optical parameters can be measured up to 35 km. The error analysis shows that accuracy of the HSRL measurements is mostly limited by the photon counting statistics. The system performance can be increased by increasing the system detection efficiency or/and increasing the transmitted laser power. The greatest improvement would be a photodetector with higher quantum efficiency and faster count rate capability.

The depolarization data obtained by the HSRL shows the ability of the HSRL to distinguish between water and ice clouds. It is shown, that the 160μrad field of view of the spectrometer channels effectively suppresses the multiple scattering effects on the measured depolarization ratio. Therefore, a reliable separation between water and ice clouds is possible. The HSRL measurements have shown, that traditional systems with 1–5 mrad field of views cannot reliably separate between water and ice, because the depolarization observed with a 1 mrad field of view is comparable to the ice depolarization within a small penetration depth from the water cloud base due to the multiple scattering. The error analysis shows, that the depolarization of the clear air aerosol layers can be observed with better than 10 % accuracy. The accuracy of the cloud depolarization measurements is better than 1 %. The measurements of depolarizations of weak aerosol layers and molecular backscatterer are limited by the

photon counting statistics.

The study of the cloud depolarizations between August 2 and November 11, 1993 shows that in 45 % of cirrus cloud cases simultaneous observations of supercooled water at cirrus cloud altitudes were made. The average cirrus cloud depolarization is shown to increase from 33% at -5°C temperature to 41% at -60°C. The observed behavior is different than observed by Platt *et al.*[43]. The depolarization observed by Platt *et al.* ranged from ~15% to ~40% between temperatures from -10 to -60 °C. The largest difference between the HSRL measurements and Platt's measurements is observed for the temperature range from -30 to -10 °C, where Platt observed low cirrus cloud depolarizations. The low values of depolarization in Platt's measurement are most probably caused by multiple scattering from supercooled water droplets, because the system used for this measurement had a 2.5 mrad field of view. The HSRL measurements show that supercooled water clouds have been found at temperatures as low as -40°C and pure water clouds have been found at temperatures above 0°C. No water has been found at temperatures below -40°C and the presence of cirrus disappears at temperatures above 0°C. In the HSRL measurements, the cirrus cloud depolarization ratios for all temperatures are close to the values observed for the temperatures without supercooled water clouds. The small difference in the observed depolarization as a function of temperature may be a result of different shapes, sizes, and orientations of the ice crystals at different temperatures.

The depolarization of the molecular backscatter is ~0.7–0.8%, when measured without the low resolution etalons. When the low resolution etalons are used, a ~0.55–0.6% depolarization is measured. The depolarization measured for the signal from the Cabannes line and the rotational Raman lines is 1.5 % without any spectral filters. The measured molecular depolarization value is larger than the expected 0.4 % depolarization of Cabannes line. The system filter bandpass admits a small fraction of the rotational Raman lines and blocks part of the Cabannes line and therefore an increase on the depolarization ratio is observed due to the presence of the highly depolarized rotational Raman lines. The model calculation for the depolarization transmission of the system show, that a 0.56 –0.62 % depolarization is expected for the case where no low resolution etalons were used. A 0.402 –0.425 % depolarization

is expected, when one or two etalon are used. The depolarization observed with the HSRL are larger than the expected values. The cause of the small difference between expected and measured depolarization values is currently unknown. The further analysis of the depolarization measurement accuracy of the HSRL requires an advanced study of effects of the iodine spectrum and rotational Raman lines to the depolarization.

The HSRL measurements require a knowledge of the atmospheric temperature profile. The atmospheric temperature profile measured with the HSRL shows that the HSRL can be used to measure temperature with a high enough accuracy so that the measured temperature profiles can be used for the analysis of the HSRL data. Therefore, the requirement for radiosonde measurements of atmospheric temperature could be eliminated. Before the temperature measurements with the HSRL can be routinely performed, the effects of aerosol backscatter signal to the molecular transmission of the iodine absorption filter have to be removed.

This study has provided an instrument basis for a design of a simple and robust lidar for the measurements of the optical properties of the atmosphere. The University of Wisconsin HSRL provides a unique instrument for the measurements of the cloud optical properties and the data measured with the HSRL provides useful information that can be used for the climate models that study the effects of clouds to the earths atmosphere.

References

[1] Stephens, G. L. and P. J. Webster, "Clouds and climate: Sensitivity of simple systems," *J. Atm. Sci.*, **39**, 235–247, 1981.

[2] Liou, K.-N., "Influence of cirrus clouds on weather and climate processes: A global perspective," Monthly Weather Review, **114**, 1167–1192, 1986.

[3] Ansmann, A., U. Wandinger, M. Riebesell, C. Weitkamp, and W. Michaelis, "Independent measurements of extinction and backscatter profiles in cirrus clouds by using a combined Raman elastic-backscatter lidar," *Appl. Opt.* , **31**, 7113–7131, 1992.

[4] Whiteman, D. N., S. H. Melfi, and R. A. Ferrare, "Raman lidar system for the measurements of water vapor and aerosols in the Earth's atmosphere," *Appl. Opt.* , **31**, 3068–3082, 1992.

[5] Fiocco, G. and J. B. DeWolf, "Frequency spectrum of laser echoes from atmospheric constituents and determination of aerosol content of air," *J. Atm. Sci.*, **25**, 488–496, 1968.

[6] Schwiesow, R. L. and L. Lading, "Temperature profiling by Rayleigh-scattering lidar," *Appl. Opt.* , **20**, 1972–1979, 1972.

[7] Shipley, S. T., J. H. Joseph, J. T. Trauger, P. J. Guetter, E. W. Eloranta, J. E. Lawler, W. J. Wiscombe, A. P. Odell, F. L. Roesler, J. A. Weinman, "The evaluation of a shuttle borne lidar experiment to measure the global distribution of aerosols and their effect on the atmospheric heat budget," Final report on NASA grant NSG 1057, 1975 pp. 150.

[8] Shipley, S. T., D.H. Tracy, E. W. Eloranta, J. T. Trauger, J. T. Sroga, F. L. Roesler, and J. A.Weinman, "High resolution lidar to measure optical scattering properties of atmospheric aerosols. 1: Theory and instrumentation," *Appl. Opt.* **22**, 3716–3724, 1983.

[9] Sroga, J. T., E. W. Eloranta, S. T. Shipley, "F. L. Roesler, and P. J. Tryon, High spectral resolution lidar to measure optical scattering properties of atmospheric aerosols. 2: Calibration and data analysis," *Appl. Opt.* , 22, 3725–3732, 1983.

[10] Grund, C. J., "Measurement of cirrus cloud optical properties by high spectral resolution lidar," Ph.D. Thesis, Department of Meteorology, University of Wisconsin-Madison, 1987.

[11] Grund, C. J., E. W. Eloranta, "Fiber-optics scrambler reduses the bandpass range dependence of Fabry-Perot etalons used for spectral analysis of lidar backscatterer," *Appl. Opt.* **30**, 2668, 1991.

[12] Grund, C. J. and E. W.Eloranta, "University of Wisconsin High Spectral Resolution Lidar," *Optical Engineering*, **30**, 6–12, 1991.

[13] Eloranta, E. W. and P. K. Piironen, "Adaptation of the University of Wisconsin High Resolution Lidar for polarization and multiple scattering measurements," Sixteenth International Laser Radar Conference, Cambridge, Massachusetts, July 20-24, 1992, NASA Conference Publication 3158, 353–356, 1992.

[14] Shimizu, H., S. A. Lee, and C. Y. She, "High spectral resolution lidar system with atomic blocking filters for measuring atmospheric parameters," *Appl. Opt.* **22**, 1373–1391, 1983.

[15] She, C. Y., R. J. Alvarez II, L. M. Caldwell, and D. A. Krueger, "High-spectral-resolution Rayleigh-Mie lidar measurements of aerosol and atmospheric profiles," Opt. Lett. **17**, 541–543, 1992.

[16] Alvarez, R. J. II, L. M. Caldwell, P. G. Wolyn, D. A. Krueger, T. B. McKee, and C. Y. She, "Profiling temperature, pressure, and aerosol properties using a high spectral resolution lidar employing atomic blocking filters," *J. Atm. Ocean. Techn.* **10**, 546–556, 1993.

[17] Krueger, D. A., L. M. Caldwell, R. J. Alvarez II, and C. Y She, "Self-consistent method of determining vertical profiles of aerosol and atmospheric properties using a high spectral resolution Rayleigh-Mie lidar," *J. Atm. Ocean. Techn.* **10**, 533–545, 1993.

[18] Gerstenkorn, S. and P. Luc, *Atlas du spectre d'absorption de la molecule d'iode* (Centre National de la Recherche Scientifigue, Paris, 1978).

[19] Harrison, J. A., M. Zahedi, and J. W. Nibler, "Use of seeded Nd:YAG lasers for high-resolution spectroscopy," Opt. Lett. **18**, 149–151, 1993.

[20] Liao, K. H. and R. Gupta, "I_2 vapor cell as narrow band optical filter," *Rev. Sci. Instr.*, **49**, 867–869, 1978.

[21] Miles, R. B., J. N. Forkey, and W. R. Lempert, "Filtered Rayleigh Scattering measurements of supersonic/hypersonic facilities," AIAA 17th Aerospace Ground Testing Conference, July 6-8, 1992, Nashville, TN (USA).

[22] Piironen, P. and E. W. Eloranta, "Demonstration of a high spectral resolution lidar based on an iodine absorption filter," Opt. Lett. bf 19, 234–236, 1994.

[23] Klett, J. D., "Stable analytical inversion solution for processing lidar returns," *Appl. Opt.* **20**, 211–220, 1981.

[24] Hinkley, E. D. (editor), "Laser Monitoring of the Atmosphere," Springer-Verlag, New York, 1976.

[25] Eloranta, E. W. "Calculation of doubly scattered lidar returns," Ph. D. Thesis, Department of Meteorology, University of Wisconsin, 1972.

[26] Eloranta, E. W., "A practical model for the calculation of multiply scattered lidar returns," Optical Society of America, Remote Sensing of the Atmosphere, Topical Meeting, Salt Lake City, Utah, March 8-12, 1993, pp. ThE20-1.

[27] Eloranta, E. W. and S. T. Shipley, "A solution for multiple scattering," *in Atmospheric Aerosols: Their Formation, Optical Properties, and Effects,* Spectrum Press, Hampton, Virginia, 1982.

[28] *Model S100 Injection Seeding System*, Lightwave Electronics Corporation, California, USA, 1989.

[29] Grund, C. J., F. L. Roesler, and E. W. Eloranta, "Thermally induced spectral drift cancellation in pressure-tuned Fabry-Perot etalons," *Appl. Opt.* , **27**, 662–663, 1988.

[30] Sroga, J. F., "Remote measurerements of aerosol scattering properties by an airborne high spectral resolution lidar," Ph. D. Thesis, University of Wisconsin-Madison, 1983.

[31] *How to perform photon counting using photomultiplier tubes*, Hamamatsu, Technical Information, No. ET-06/Feb 1990.

[32] *TRC thermodynamic tables (Non-hydrocarbons)*, (College Station, Tex. : Thermodynamics Research Center, Texas A & M University, 1986), pp. k-190, ka-190.

[33] Arie, A. and R. L. Byer, "Laser heterodyne spectroscopy of $^{127}I_2$ hyperfine structure near 532 nm," *J. Opt. Soc. Am. B.*, **10**, 1990–1997, 1993.

[34] Yip, S. and M. Nelking, "Application of kinetic model to time-dependent density correlations in fluids," *Physical Review*, **135**, A1241–A1247, 1964.

[35] Arie, A. and R. L. Byer, "Frequency stabilization of the 1064-nm Nd:YAG lasers to Doppler-broadened lines of iodine," *Appl. Opt.* , **32**, 7382–7386, 1993.

[36] Scotland, R. M., K. Sassen, and R. Stone, "Observations by lidar of linear depolarizations of hydrometeors," *J. Appl. Meteor.*, **10**, 1011–1017, 1971.

[37] Sassen, K. "The polarization lidar technique for cloud research: a review and current assessment," *Bull. Am. Meteor. Soc.*, **72**, 1848–1866, 1991.

[38] Pal, S. R. and A. I. Carswell, "Polarization properties of lidar backscattering from clouds," *Appl. Opt.* , **12**, 1530–1535, 1973.

[39] Rowell, R. L. and G. M. Aval, "Rayleigh-Raman depolarization of laser light scattered by gases," *J. Chem. Phys.*, **54**, 1960–1964, 1971.

[40] Young, A. T., "Rayleigh scattering," *Physics Today*, January 1982, 42–48, 1982.

[41] Liou, K.-N. and H. Lahore, "Laser sensing of cloud composition: a backscatter depolarization technique," *J. Appl. Meteor.*, **13** 257–263, 1974.

[42] Kumai, M., "Formation of ice crystals and dissipation of supercooled fog by artificial nucleation, and variations of crystal habit at early growth stages," *J. Appl. Meteor.*, **21**, 579–587, 1982.

[43] Platt, C. M. R., J. C. Scott, and A. C. Dilley, "Remote sensing of high clouds. Part VI: Optical properties of midlatitude and tropical cirrus," *J. Atm. Sci.* **44**, 729–747, 1987.

[44] Strauch, R. G., V. E. Derr, and R. E. Cupp, "Atmospheric temperature measurement using Raman backscatter," *Appl. Opt.* , **10**, 2665–2669, 1971.

[45] Cooney, J., "Measurements of atmospheric temperature profiles by Raman backscatter" *J. of Appl. Meteor.*, **11**, 108–112, 1972.

[46] Kalshoven, J. E., Jr., C. L. Korb, G. K. Schemmer, and M. Dombrowski, "Laser remote sensing of atmospheric temperature by observing resonant absorption of oxygen," *Appl. Opt.* , **20**, 1967–1971, 1981.

[47] Endemann, M. and R. L. Byer, "Simultaneous measurements of atmospheric temperature and humidity using a continously tunable IR lidar," *Appl. Opt.* , **20**, 3211–3217, 1981.

[48] P. Keckhut, A. Hauchecorne, and M. L. Chanin, "A critical review of the database acquired for the long-term surveillance of the middle atmosphere of the French Rayleigh lidars," *J. Atm. Ocean. Techn.*, **10**, 850–867, 1993.

[49] Heymsfield, A. J., "Precipitation development in statiform ice clouds: A microphysical and dynamical study," *J. Atm. Sci.*, **34**, 367–381, 1977.

The 5–6 December 1991 FIRE IFO II Jet Stream Cirrus Case Study: Possible Influences of Volcanic Aerosols

KENNETH SASSEN, DAVID O'C. STARR, GERALD G. MACE, MICHAEL R. POELLOT, S. H. MELFI, WYNN L. EBERHARD, JAMES D. SPINHIRNE, E. W. ELORANTA, DONALD E. HAGEN, AND JOHN HALLETT

Reprinted from JOURNAL OF THE ATMOSPHERIC SCIENCES, Vol. 52, No. 1, 1 January 1995
American Meteorological Society

The 5–6 December 1991 FIRE IFO II Jet Stream Cirrus Case Study: Possible Influences of Volcanic Aerosols

KENNETH SASSEN,* DAVID O'C. STARR,† GERALD G. MACE,# MICHAEL R. POELLOT,@ S. H. MELFI,† WYNN L. EBERHARD,& JAMES D. SPINHIRNE,† E. W. ELORANTA,** DONALD E. HAGEN,†† AND JOHN HALLETT##

*Meteorology Department, University of Utah, Salt Lake City, Utah
†NASA Goddard Space Flight Center, Greenbelt, Maryland
#Meteorology Department, The Pennsylvania State University, University Park, Pennsylvania
@Atmospheric Sciences Department, University of North Dakota, Grand Forks, North Dakota
&NOAA Environmental Technology Laboratory, Boulder, Colorado
**Meteorology Department, University of Wisconsin, Madison, Wisconsin
††Physics Department, University of Missouri, Rolla, Missouri
##Desert Research Institute, Reno, Nevada

(Manuscript received 14 January 1994, in final form 25 May 1994)

ABSTRACT

In presenting an overview of the cirrus clouds comprehensively studied by ground-based and airborne sensors from Coffeyville, Kansas, during the 5–6 December 1992 Project FIRE IFO II case study period, evidence is provided that volcanic aerosols from the June 1991 Pinatubo eruptions may have significantly influenced the formation and maintenance of the cirrus. Following the local appearance of a spur of stratospheric volcanic debris from the subtropics, a series of jet streaks subsequently conditioned the troposphere through tropopause foldings with sulfur-based particles that became effective cloud-forming nuclei in cirrus clouds. Aerosol and ozone measurements suggest a complicated history of stratospheric–tropospheric exchanges embedded within the upper-level flow, and cirrus cloud formation was noted to occur locally at the boundaries of stratospheric aerosol-enriched layers that became humidified through diffusion, precipitation, or advective processes. Apparent cirrus cloud alterations include abnormally high ice crystal concentrations (up to ~600 L^{-1}), complex radial ice crystal types, and relatively large haze particles in cirrus uncinus cell heads at temperatures between −40° and −50°C. Implications for volcanic–cirrus cloud climate effects and usual (nonvolcanic aerosol) jet stream cirrus cloud formation are discussed.

1. Introduction

A major focus of climate research is, of necessity, the climatological characterization of the current state of the cloudy atmosphere. Such knowledge is requisite in order to assess the validity of cloud predictions from global general circulation models and also, in general, to better understand the effects of cloud radiative forcing and feedbacks on climate, present or future. The essentially continuous observations provided by earth-orbiting satellites obviously have significant advantages in this endeavor, and the International Satellite Cloud Climatology Project (ISCCP) represents a long-term program to employ satellite data to gain knowledge of the amounts and types of cloud cover (Schiffer and Rossow 1983). Unfortunately, whereas cirrus clouds are certainly an important component of this dataset, it is recognized that they represent a particularly difficult cloud category to detect and categorize. This is because cirrus clouds are composed of relatively dilute assemblies (i.e., in comparison to water clouds) of complexly shaped ice crystals that are by definition optically thin in the visible and greybody emitters in the infrared spectral regions (Platt et al. 1987).

To help overcome the deficiencies in our basic knowledge of cirrus clouds and improve our ability to characterize them from satellite radiance measurements, the First ISCCP Region Experiment (FIRE) has been established (Cox et al. 1987). The initial Intensive Fields Observation (IFO) program was conducted over central and southern Wisconsin in October–November 1986 and utilized three research aircraft and an array of four ground-based lidar systems. (For a description of prior case study findings based on aircraft, lidar, and satellite studies, see the November 1990 special issue of *Monthly Weather Review*.) The IFO II program recently took place during November–December 1991 and brought together an even greater collection of state of the art in situ and

Corresponding author address: Dr. Kenneth Sassen, Department of Meteorology, University of Utah, 819 William C. Browning Building, Salt Lake City, UT 84112.

TABLE 1. Specifications of the FIRE IFO II remote sensing systems, as configured during the experiment at Coffeyville, Kansas. Entries v, h, and c refer to vertical, horizontal, and circular polarization properties.

	University of Utah PDL	NOAA WPLDL	NASA RAMAN	NASA ER-2 CALS	PSU W-band radar
Transmitter					
Type	NdYAG	CO_2	XeF	NdYAG	Clystron
Wavelength (μm)	0.532	10.6	0.351	0.532	3.2×10^4
Peak energy (J)	0.5	1.0	0.045	0.04	200
Pulse length (ns)	7	300	20	5.0	500
Maximum PRF (Hz)	10	10	400	5.0	20×10^3
Beamwidth (mrad)	0.45	0.05	~0.5	1.0	4.36
Polarization	v	c	—	v	v
Receiver					
Diameter (m)	0.35	0.25	0.76	0.15	0.91
Beamwidth (mrad)	0.3–4.0	0.05	2	1.4	4.36
Polarization	$v + h$	—	—	$v + h$	v
Detectors	2	1	8	2	1
Scanning (° s^{-1})	(Manual)	30	(Fixed)	(Fixed)	(Fixed)
Data handling					
Range resolution (m)[a]	6.0	75	75	7.5	75
Number of channels	2	1	8	2	1
Samples per channel	2048	20	600	3072	506
Pulses averaged	1–10	1–10	23200	1	1000–20000
Data quantities[b]	P, δ	P, β_π, V	P, β_π, σ_π, w	P, δ	Z_e

[a] Effective minimum resolution.

[b] Relative returned power P; backscatter cross section β_π; linear depolarization ratio δ; radial Doppler velocity V; extinction cross section σ_π; water vapor mixing ratio w; equivalent radar reflectivity factor Z_e.

TABLE 2. Special aerosol, ozone, and microphysical apparatus deployed on the indicated Project FIRE aircraft, providing data used in this study.

University of North Dakota Citation	
Ozone	
Manufacturer/model	Scientrex/LOZ3
Type	Chemiluminescent
Range	0.2 to 400 ppb
Resolution	0.1 ppb
Accuracy	±10%
Response	1 s
Condensation Nuclei	
Manufacturer/model	TSI/3760
Type	Alcohol condensing
Range	$0–10^4$ cm^{-3}
Resolution	1 cm^{-3}
Accuracy	±6%
Response	2 s
Replicator	
Manufacturer/model	Desert Research Institute
Type	Continuous Formvar
Range	~10–1000 μm
NCAR Saberliner	
Tandem electric aerosol classifiers	
Manufacturer	UMR
Range	0.01–0.5 μm
Resolution	±5%
Accuracy	±5%
Response	2 min

remote sensing instruments for studying cirrus clouds over Coffeyville, Kansas.

It is the early results from an interesting IFO II cirrus cloud case study involving a significant departure from the conditions encountered during the IFO I that are reported here. The global atmospheric effects created by the explosive June 1991 eruptions of the Philippine volcano Pinatubo presented an opportunity to investigate the possible effects on cirrus cloud formation of stratospherically derived volcanic aerosols (Sassen and Horel 1990; Mohnen 1990; Sassen 1992). Beginning on the evening and dawn of 4 December 1991, spectacular twilight effects indicative of a sudden increase in volcanic aerosols were noted by IFO observers. These kinds of events accompanied the latitudinal redistribution of the Pinatubo debris as spurs of stratospheric aerosols were lifted from the tropical zonal belt, aided by jet stream circulations in both hemispheres (GVN Bulletins 1991–1993). The series of jet streak cirrus cloud systems that were subsequently studied over southeastern Kansas yielded indications of unusual cloud properties, suggesting a link between the volcanic aerosols, tropopause-folding effects, and cirrus cloud formation. In this paper we focus attention on the connections between the observed vertical atmospheric structure, stratospheric–tropospheric aerosol content, and the resultant cirrus cloud properties. At

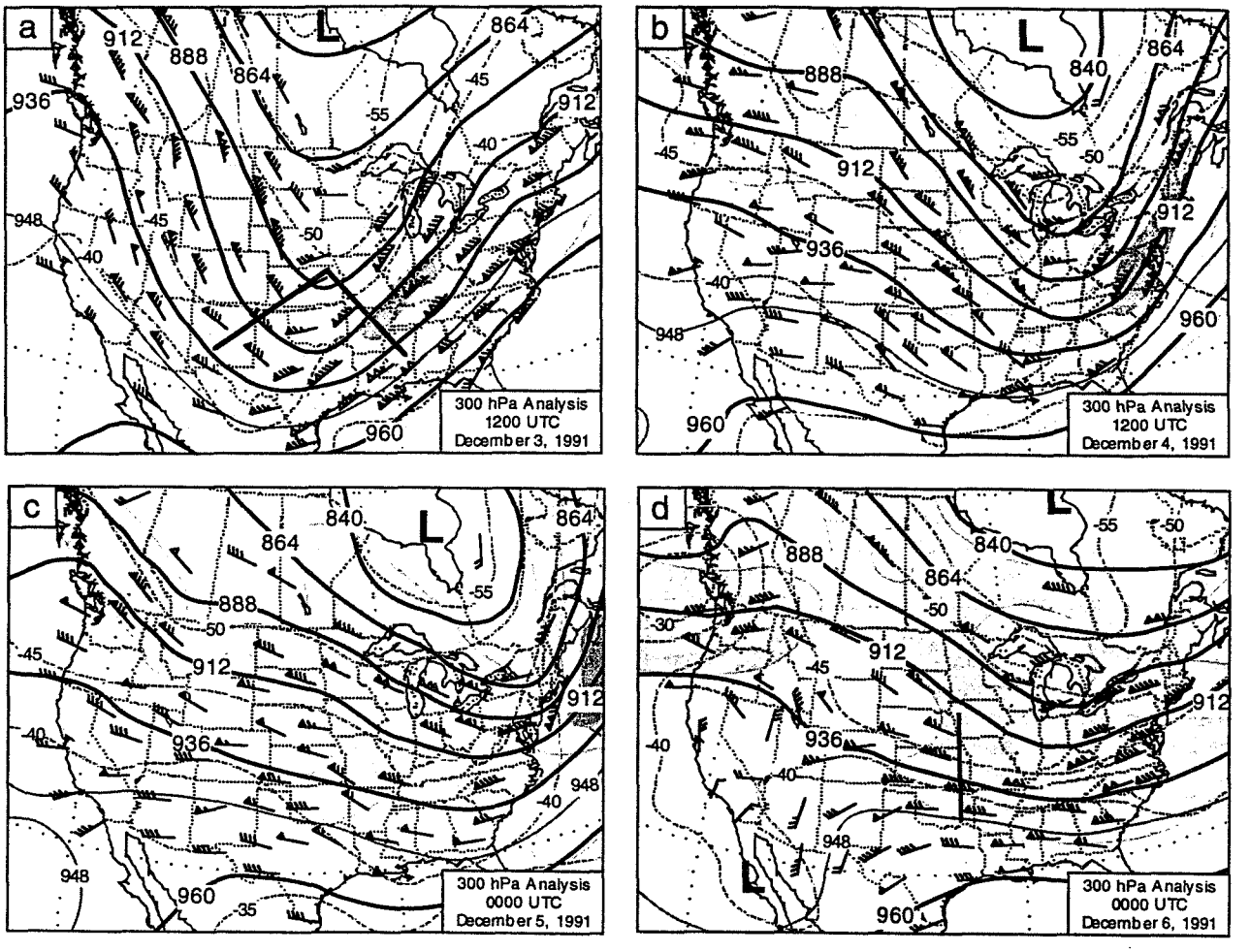

FIG. 1. 300-mb analyses constructed using conventional radiosonde data for (a) 1200 3 December, (b) 1200 4 December, (c) 0000 5 December, and (d) 0000 6 December. Solid lines are geopotential heights in 240-m intervals, thin stippled lines are isotherms at 5°C intervals, and light- and heavy-shaded areas correspond to 35–55 m s^{-1} and >75 m s^{-1} wind speeds, respectively. The thick solid lines in (a) and (d) denote the cross sections in Figs. 2 and 5, respectively.

the same time, the unique IFO II observing capabilities are highlighted. More detailed experimental and model findings will be given in subsequent case study papers.

2. The Intensive Field Observation II experiment

Unlike the IFO I that featured a mesoscale (~100 km) array of four lidar ground stations and often wide-ranging aircraft operations, the second field experiment emphasized aircraft missions that were closely coordinated with an extensively instrumented central Hub site at the Coffeyville airport (37.10°N, 95.58°W), along with two nearby (~20 km) remote sensing stations positioned along the expected mean cirrus cloud wind direction. This change in emphasis reflected the attitude that the benefits accrued by overlapping the instrument cloud coverage to yield synergistic multi-wavelength, multitechnique datasets outweighed any advantages of a more dispersed deployment, even given the spatial variability of cirrus cloud systems. A primary reason for the choice of this midwestern site was the availability of data from the initial installations of the developing National Weather Service (NWS) wind profiler network. These measurements provide highly useful dynamical information related to mesoscale cirrus cloud formation and were supplemented by special project wind profilers and rawinsonde (CLASS) soundings, as well as enhanced western to central regional NWS rawinsonde operations. A secondary purpose was to allow for the possible investigation of different types of cirrus than were studied during IFO I, including late-season convective anvil outbreaks and cirrus associated with subtropical jet streams.

The participating instrumentation supporting the Hub scientific objectives can be characterized as a model of modern research capabilities: three cloud microphysical–radiation aircraft, plus an overflying ER-

2 remote-sensing platform; four lidar systems encompassing polarization diversity, Raman, high spectral resolution, and infrared Doppler techniques; special sondes to measure vertical atmospheric structure, ozone, and ice crystal types; dedicated microwave wind and RASS temperature profilers; and an unparalleled variety of passive remote sensors, including the initial Spectral Radiation Experiment (SPECTRE) deployment (Ellingson et al. 1993). Since the full extent of these research capabilities will be illuminated in following IFO-II case study papers, only the specifications of the major instruments yielding available datasets pertinent to this research are outlined here.

The specifications and data quantities gathered by the Coffeyville Hub and ER-2 active remote sensors utilized here are listed in Table 1. These include the University of Utah Polarization Diversity Lidar (PDL), the NOAA Wave Propagation Laboratory CO_2 Doppler lidar (Post et al. 1992), the NASA Goddard Space Flight Center water vapor/nitrogen Raman (Whiteman et al. 1992) and downward-looking ER-2 polarization cloud lidar (CLS) systems, and the Pennsylvania State University W-band radar. A coaligned (PRT-5 type) narrowbeam (0.14°) midinfrared (9.5–11.5 μm) radiometer was also operated with the PDL unit to measure the effective atmospheric window brightness temperature of the clouds plus atmosphere. Also stationed at the Hub site was a developmental high spectral resolution lidar (HSRL) from the University of Wisconsin at Madison. The lidar systems at the two nearby ground sites were the University of Wisconsin volume imaging lidar (VIL—see Eloranta and Forrest 1992) and the NASA Langley Research Center polarization scanning lidar. In addition to the standard parameters of state and cloud microphysical instrumentation aboard the NCAR King Air and Saberliner and the University of North Dakota Citation aircraft, special cloud microphysical and aerosol sensors were deployed in order to focus attention on the nucleation mechanisms and the shapes of the cirrus particles (see Table 2).

3. Vertical atmospheric and aerosol structures

Over the case study period from 0000 (all times UTC) 5 December to 2400 6 December 1991, three separate occurrences of cirrus clouds were comprehensively studied from the Hub site. However, for the current purposes it is useful to begin our examination of the local atmospheric and aerosol vertical structures at 0000 3 December, just prior to the spectacular twilight observations on the evening of 3 December and dawn of 4 December. During the early portion of the case study period (0000 3 December–0000 5 December), the upper-tropospheric flow pattern over North America was dominated by a single high-amplitude trough–ridge system. As shown in Fig. 1a, at 1200 3 December a deep trough at 300 mb extended from a low near Hudson Bay though the central United States and into northern Mexico. A southwesterly jet stream with a speed maximum of 75 m s^{-1} extended from central Mexico into the Canadian Maritime Provinces, and a northwesterly jet (60 m s^{-1} maximum) reached from the Gulf of Alaska to the desert Southwest of the United States. Locally in southeastern Kansas, 3 December began as a cold dreary day, with frozen precipitation of various kinds giving way to a broken low-level cloud deck that dissipated before sunset.

Analysis of this system has been performed by compositing NWS rawinsonde data (processed at full vertical resolution), Project FIRE CLASS rawinsonde data, and NWS Wind Profiler Demonstration Network (WPDN) horizontal wind data. Figure 2 shows the thermodynamic and wind structure of the system along a cross section "folded" across the trough axis roughly normal to the axis of the jet stream (see Fig. 1a). An elevated frontal zone associated with the most intense region of cyclonic shear vorticity in the northwesterly jet extended from the trough axis southwestward. Isentropic potential vorticity (IPV) in this cross section exhibits a large discontinuity near the frontal interface extending down to near the 500-mb level. This feature

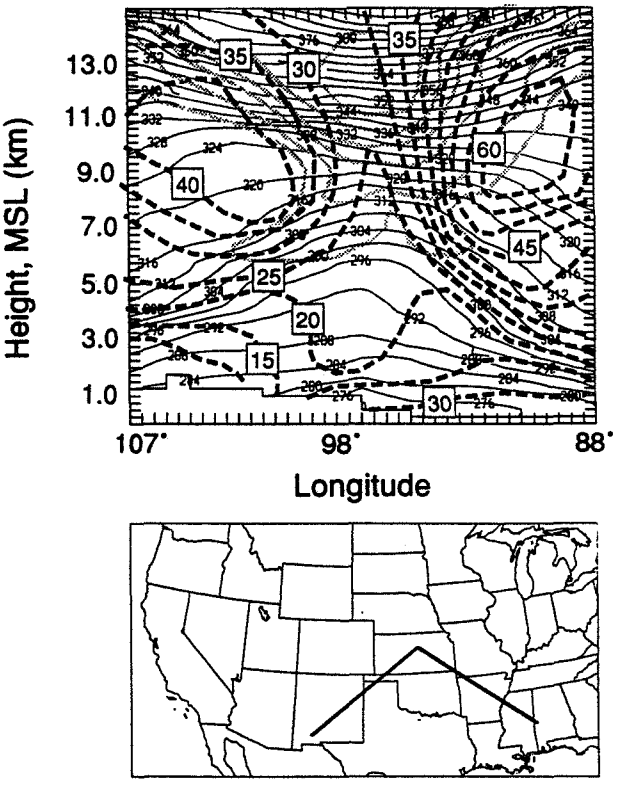

FIG. 2. Vertical cross section along the solid line segments in the map below and in Fig. 1a for 1200 UTC 3 December, centered around the upper-level trough axis. Contours are horizontal wind speed (heavy dashed lines) in m s^{-1} with an interval of 5 m s^{-1}, potential temperature (thin solid lines) at 2 K intervals, and isentropic potential vorticity (light solid lines), where the outer and inner contours are 100 and 600 ($\times$ 10^{-7} K mb^{-1} s^{-1}).

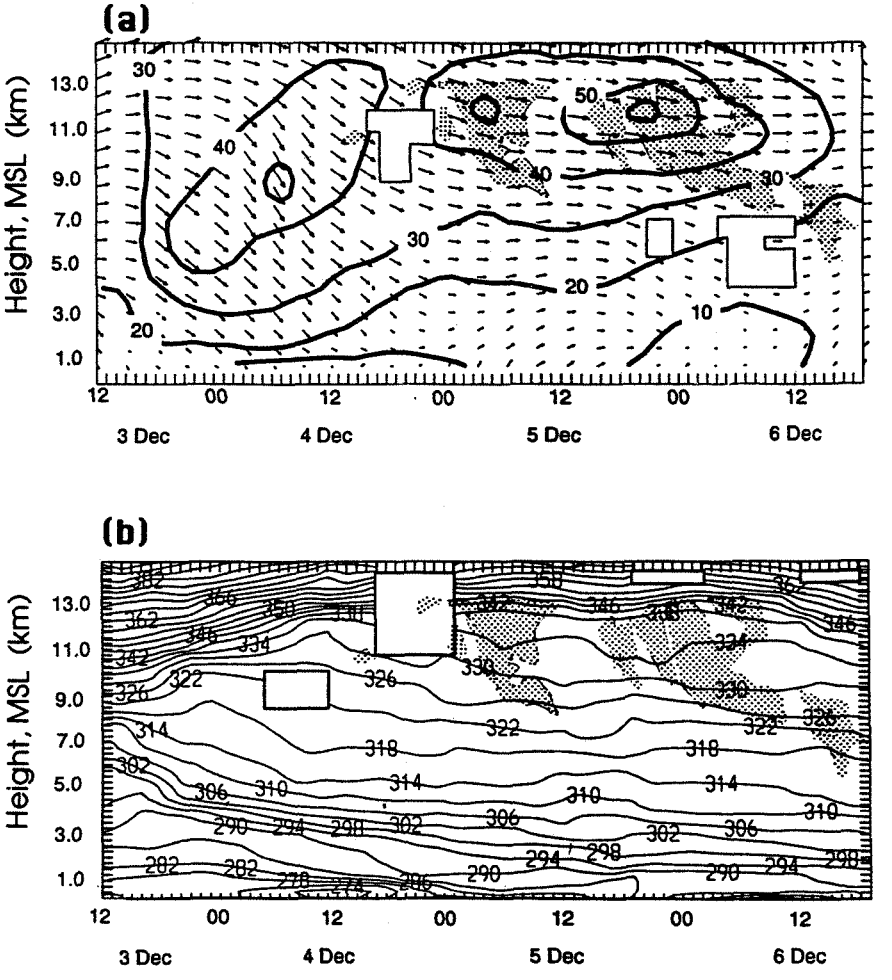

FIG. 3. Time–height cross sections of (a) horizontal wind velocity and (b) potential temperature over Coffeyville, Kansas, from 1200 3 December to 1800 6 December. (Rectangular blocks represent areas lacking sufficient data to complete the displays.) Stippling depicts the approximate cirrus cloud boundaries measured by the Hub remote sensors over the entire period.

has been shown to be indicative of an intrusion of stratospheric air into the middle and upper troposphere, otherwise known as a tropopause fold (Danielson 1968; Shapiro 1976), in association with intense upper-tropospheric baroclinic zones. Among other things, tropopause folds have been documented as a mechanism for injecting stratospheric aerosols of volcanic origin into the troposphere (Shapiro et al. 1984). Assuming that widespread enhanced aerosol loading existed in the lower stratosphere as a result of the Pinatubo eruptions (see below), it is not unlikely that stratospheric aerosols could have been deposited into the middle and upper troposphere over a large portion of the western and southwestern United States by this active fold event.

The spatial extent of the elevated frontal surface becomes evident in light of Fig. 3. These time–height cross sections of potential temperature and horizontal wind over Coffeyville show the elevated frontal surface in the northwesterly flow upstream of the trough axis for a 78-h period beginning 1200 3 December. The layer of enhanced static stability, defined by the 294 and 306 K isentropes, was continuously observed at lower levels with the passage of time and could still be recognized as a distinct entity 36 h later. Given a mean advective speed of 20 m s^{-1}, the longevity of this feature suggests an along-trajectory length scale of more than 2500 km. This illustrates the large geographical extent of this feature. Note that the boundaries of all cirrus clouds observed over this 4-day period by the Hub lidar and radar systems (see next section) are also shown as the stippled areas in these figures.

By 4 December (Fig. 1b), the jet–trough system had propagated eastward, resulting in a more zonal flow pattern over much of western North America. This process is also evident in the time–height cross sections shown in Fig. 3. Winds over Coffeyville veered from westerly to northwesterly from 1200 3 December to 1200 4 December, while the tropopause heights cor-

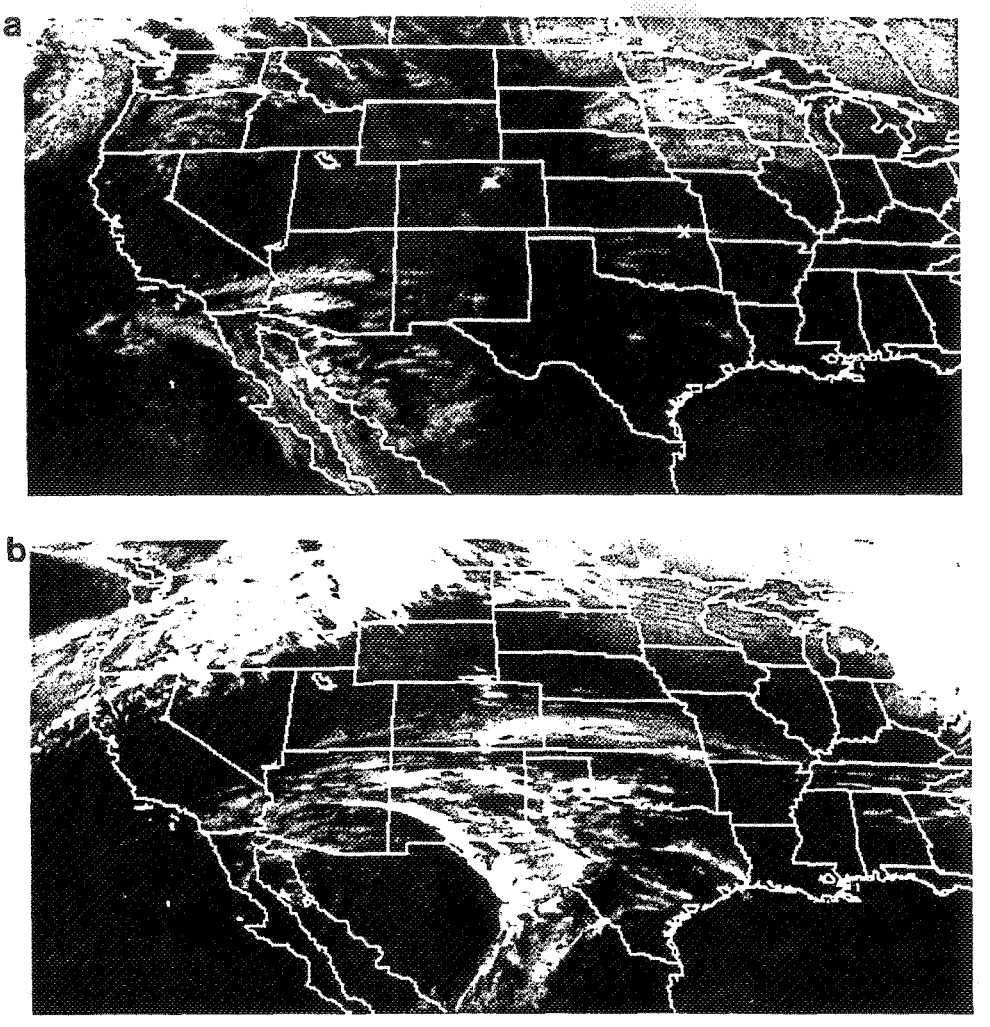

FIG. 4. Large-scale GOES satellite infrared imagery for (a) 0600 5 December and (b) 0000 6 December. The x symbol locates the Coffeyville site in southeastern Kansas. (Images courtesy of P. Minnis.)

respondingly increased from about 8 to 12 km. However, a closed low pressure system, which appears to have played a role in moisturizing the upper-tropospheric flow and the subsequent production of cirrus clouds over the southern Great Plains, began intensifying to the west of the Baja peninsula.

By 0000 5 December, a subtropical jet stream extended from the Four Corners region eastward along the Kansas–Oklahoma border (Fig. 1c). As depicted schematically in Fig. 3 and as shown in the satellite imagery of Fig. 4, cirrus clouds existed locally at and below the level of maximum wind along the anticyclonic shear side of the jet axis. The position of the cirrus relative to the upper-tropospheric flow is qualitatively in line with theoretical expectations of reduced static stability and upward motion below the level of maximum wind in the right-rear quadrant (i.e., entrance region) of a jet streak (Mattocks and Bleck 1986). Although the corresponding vertical cross-sectional analysis (not shown) failed to reveal local near-tropopause baroclinic zones or a "classic" fold event associated with this cirrus-generating feature (e.g., see Keyser and Shapiro 1986), there is a suggestion of a layer of enhanced static stability defined by the 318 and 326 K isentropes (Fig. 3) corresponding to the cirrus cloud-base region.

The thermodynamic and wind structure of the next jet streak (centered at 2000 5 December and 12.0 km over Coffeyville; Fig. 3a) was considerably more intense and better defined. The vertical cross section normal to the upper-tropospheric air flow at 0000 6 December (Fig. 5) reveals a weak elevated frontal zone bounded by the 320 and 328 K isentropes that is well correlated with the region of largest cyclonic shear vorticity associated with the jet streak. Corresponding values of isentropic potential vorticity depict a discontinuity from tropospheric to stratospheric values along the frontal interface that is strongly suggestive of a

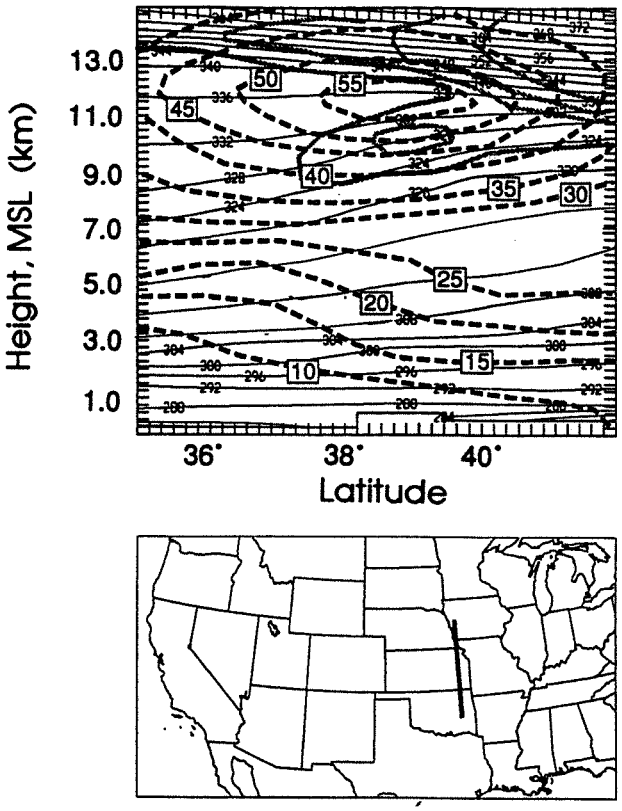

FIG. 5. As in Fig. 2 except for 0000 6 December along the heavy solid line segment depicted in Fig. 1d.

folded tropopause over central and northern Kansas. Satellite imagery (Fig. 4b) shows that the cirrus clouds observed during this period (see also Fig. 3) were part of an elongated shield of cirrus that extended eastward from the closed low near southern California (Fig. 1d), which appears to have been orographically enhanced over central Colorado. The base of the cirrus clouds observed over Coffeyville (~37°N) at this time was at 8.5 km with tops near 13 km. The lower cirrus layer height corresponds to the upper portion of the elevated frontal zone and the southern extent of the stratospheric potential vorticity in the cross section. Additionally, data from an ozonesonde launched at about this time (Fig. 6c) reveals a well-defined spike in the ozone profile centered at 8.75 km. Based on this analysis, we conclude that the cirrus observed over Coffeyville on the night of 6 December, and likely on 5 December as well, existed within a layer bounded from below by the elevated frontal surface and above by the tropopause, such that the cirrus clouds were in direct contact both with stratospheric air at the tropopause and with a layer of midtropospheric air of very recent stratospheric origin.

The layer of enhanced static stability attributed to this upper front continues to be evident in the potential temperature cross sections at 1200 6 December and 1800 6 December (not shown), although the frontal zone appears to be disconnected from the tropopause, and the IPV discontinuity is no longer clearly evident. This 6-hour period roughly brackets the third cirrus event of this case study.

Views of the changes in the stratospheric–volcanic aerosol scattering properties derived from the nocturnal Raman lidar measurements over the corresponding period are given in Figs. 7a–d (see also Ferrare et al. 1992). This data sequence reveals that the main body of the aerosol layer was present close to the bottom of the stratosphere over the period and also illustrates the relatively rapid height increase in the lower aerosol boundary over the night of 4 December in connection with the local deamplification of the upper-level pattern. The presence of upper-tropospheric cirrus clouds, which are at times only narrowly separated from the

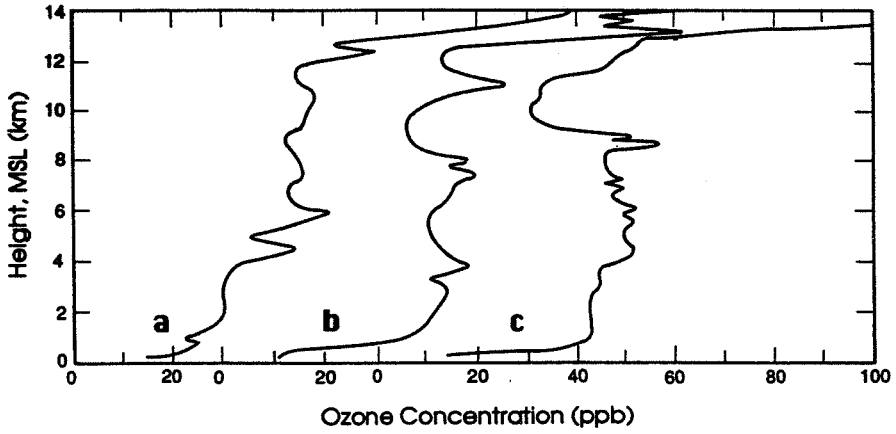

FIG. 6. Sequence of vertical ozone profiles (in parts per billion by volume) measured by ozonesondes launched daily at about 0000 on (a) 4, (b) 5, and (c) 6 December from Coffeyville, Kansas. Curves (b) and (c) are each shifted to the right by 30 ppb.

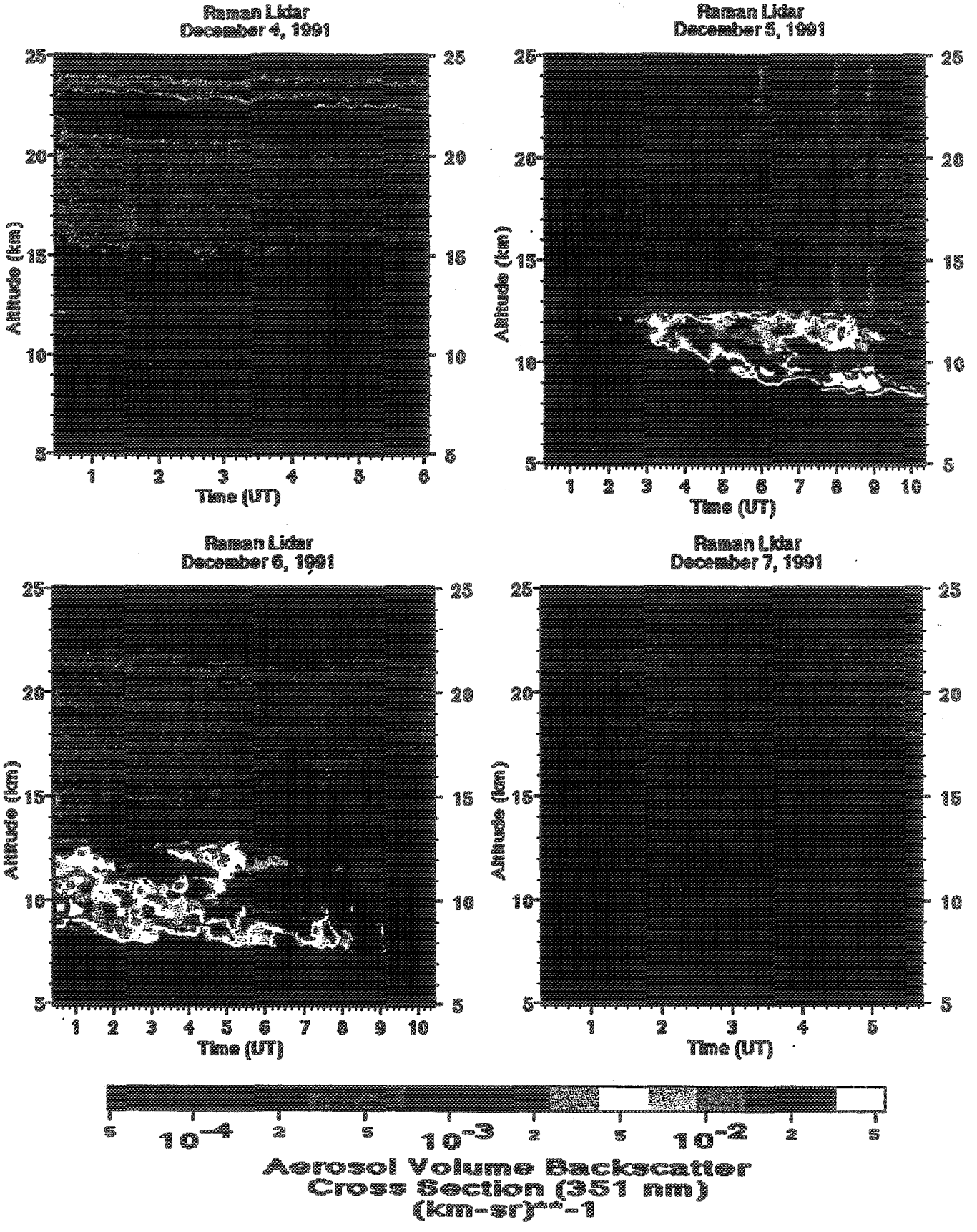
Raman Lidar
December 4, 1991
Raman Lidar
December 5, 1991
Raman Lidar
December 6, 1991
Raman Lidar
December 7, 1991
Altitude (km)
Time (UT)
Aerosol Volume Backscatter
Cross Section (351 nm)
(km-sr)^-1

stratospheric volcanic aerosol layer, are also indicated in *b* and *c*. For comparison, time-averaged aerosol backscattering profiles derived from both day and night CO_2-lidar measurements bracketing the case study period are provided in Fig. 8. Although the backscattering properties of atmospheric aerosols at the laser wavelengths of 0.531 and 10.6 μm can differ, both lidars indicate similar temporal variations in the stratospheric aerosol. In addition, the CO_2-lidar data clearly show the major post-Pinatubo enhancement of tropospheric aerosols (Post et al. 1992), where the day to day aerosol variations between 8.0 and 13.0 km (i.e., in the cirrus cloud developmental region) are particularly significant. Finally, the 3-day sequence of local vertical ozone profiles in Fig. 6 also provides evidence for variable regions of enhanced ozone concentrations within the troposphere. These direct indications of stratospheric–tropospheric air exchanges suggest that a variety of upwind mixing processes were active in the upper air flow pattern that swept over the IFO II project area, even through only two tropopause folds were identified locally in our previous analyses.

In the following section, detailed cloud remote sensing and supporting in situ data are examined to investigate the possible effects of the jet streak dynamical processes on cirrus cloud formation and structure.

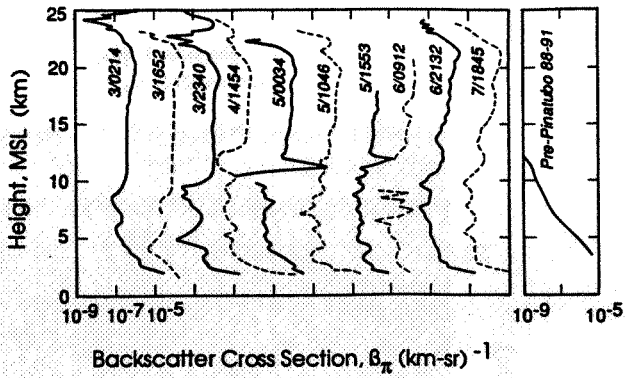

FIG. 8. Aerosol backscatter cross sections through the troposphere and lower stratosphere obtained at the 10.6-μm CO_2 lidar wavelength at the indicated day/time, illustrating the considerable extend and variability of volcanic aerosol content during the case study period (compare with the long-term average pre-Pinatubo profile obtained from Boulder, Colorado, at extreme right). (Note that the peaks near 11.5 km at 0034 and 1553 5 December are due to diffuse cirrus clouds.) Starting from the left, each profile is shifted by one division to the right.

4. Remote sensing and in situ cloud measurements

a. 0000–1000 5 December cirrus clouds

As can be seen schematically in Fig. 3, although thin scattered cirrus clouds began to make their initial appearance by midday on 4 December, it was not until the arrival of the jet streak after sunset that local cirrus cloud development became significant (Fig. 4). The passage of this cirrus streak is illustrated in Fig. 9, with PDL time–height displays of range-normalized returned power (P) and linear depolarization ratio (δ, the ratio of the cross to parallel polarized signals returned from the vertically polarized laser pulse) and coaligned narrowbeam midinfrared radiometer atmospheric brightness temperature T_{eff}. As is also apparent in the lower-resolution Raman lidar data (Fig. 7b), the most long-lived feature of this cloud system was a diffuse tropopause-topped cirrus layer, which sporadically increased in vertical extent through the action of fallstreaks, only to subsequently fade back to near the tropopause. During its most active precipitating stage at ~0600, however, this layer appears to have spawned a convective cirrus cloud layer ranging in height from 8.5 to 9.5 km. Prior cirrus research suggests that a conditioning of subcloud air through precipitation and evaporation processes can lead to this result (Starr and Cox 1985; Sassen et al. 1990). The NASA Raman water vapor data in this case (Fig. 10) confirm a gradual downward sloping moistening of a dry layer from about 7.0–9.0 km (possibly representing an elevated frontal zone).

The lower cirrus layer, on the other hand, produced considerably stronger laser backscattering, which was at times highly depolarized, and can be associated with the highest measured values of T_{eff}. As shown in the top panel of Fig. 9, T_{eff} gradually increased from the atmospheric background temperature of −70°C to −60°C at about 0600 (i.e., until the lower cirrus layer started to become established). Thereafter, even as the upper layer diminished in thickness, T_{eff} approached −40°C on two occasions (~0750 and 0850) when relatively deep and strongly scattering fallstreaks developed in the trailing cirrus layer. Higher-resolution details of the lower cloud structures are provided in Fig. 11, where a series of convective ice-phase uncinus cells ($\delta \approx 0.45$) with trailing crystal fallstreaks are found in (a), a strongly scattering region displaying a fine structure of mammatus-like protrusions and a highly depolarizing ($\delta = 0.6$–0.7) cloud-top region in (b), and in (c) is shown a highly supercooled (~ −35°C) liquid-phase altocumulus cloud ($\delta \leq 0.05$) that developed just below the cirrus cloud trailing edge (apparently in re-

FIG. 7. Raman lidar height–time displays of volume backscatter cross sections (km sr)$^{-1}$ in the 0.351-μm aerosol channel, collected over the indicated times on the consecutive nights of 4–7 December [(a)–(d), respectively]. The logarithmic backscatter scale (inserted at bottom) was chosen to characterize both the volcanic aerosol content and the generally diffuse upper-tropospheric cirrus clouds present on the nights of 5 and 6 December. Note that the vertical stripes above the cirrus clouds in (b) are due to detector noise associated with the strong signal attenuation produced by regions of the cloud layer.

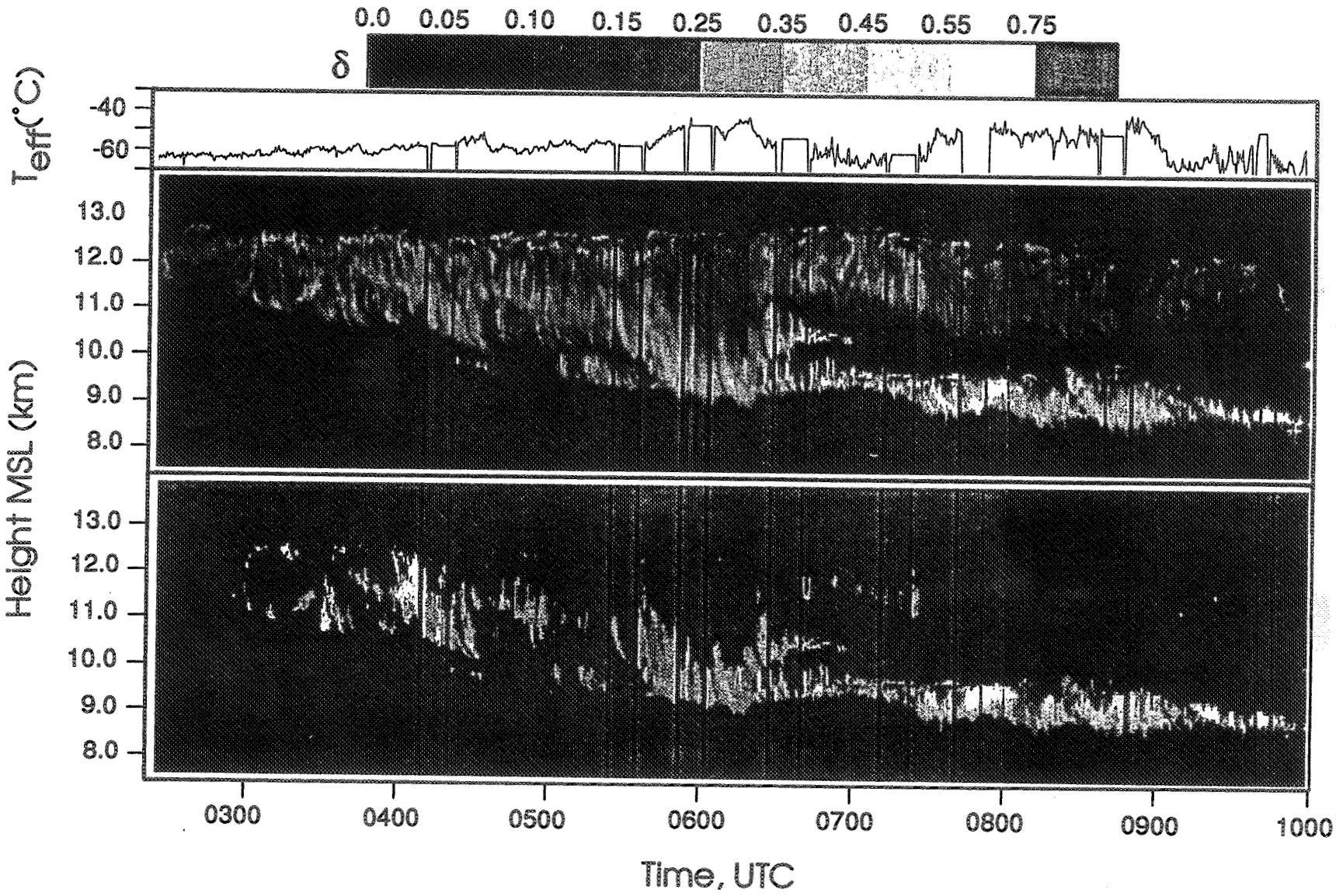

FIG. 9. Polarization lidar HTI display of relative range-normalized backscattered power P (top, based on a logarithmic grayscale) and linear depolarization ratios (bottom, see δ key at top) of the cirrus clouds studied on the night of 5 December. The panel at top provides the effective atmospheric window infrared brightness temperatures T_{eff} measured by a coaligned narrowbeam radiometer (except during the intermittent 10-Hz PDL data files, where frequent recording errors occurred). Note that the δ value display is incomplete because noise- or molecular scattering–dominated signals are rejected during analysis (and assigned the middle-gray background shown at the right end of the δ-value key).

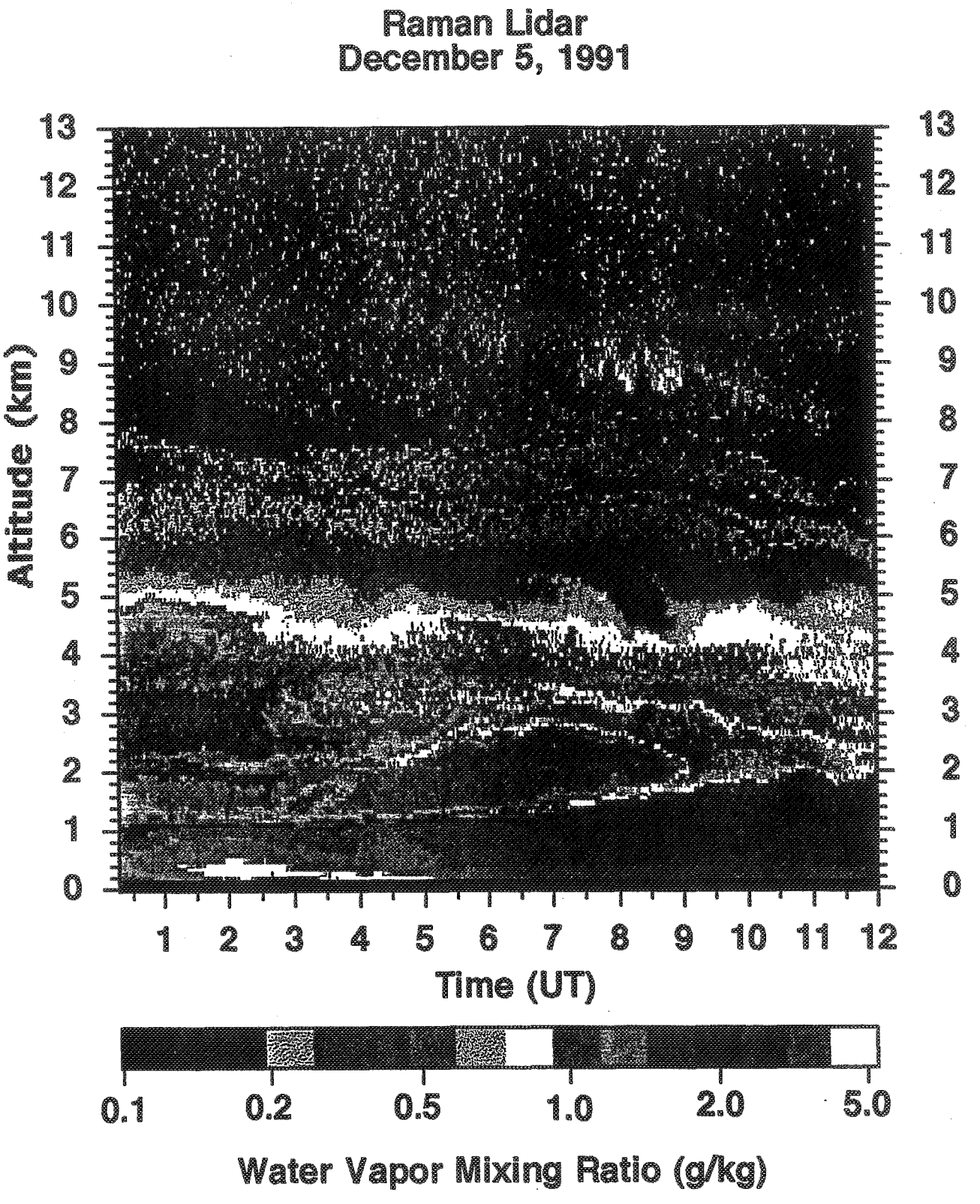

FIG. 10. Raman lidar HTI display of water vapor mixing ratio in g kg^{-1} (see key at bottom) on the night of 5 December. Note the descending layer of humidity just below the cirrus cloud, which produced sufficient attenuation to generate the erroneous signals above ~10 km. Considerable boundary-layer water vapor structure is present.

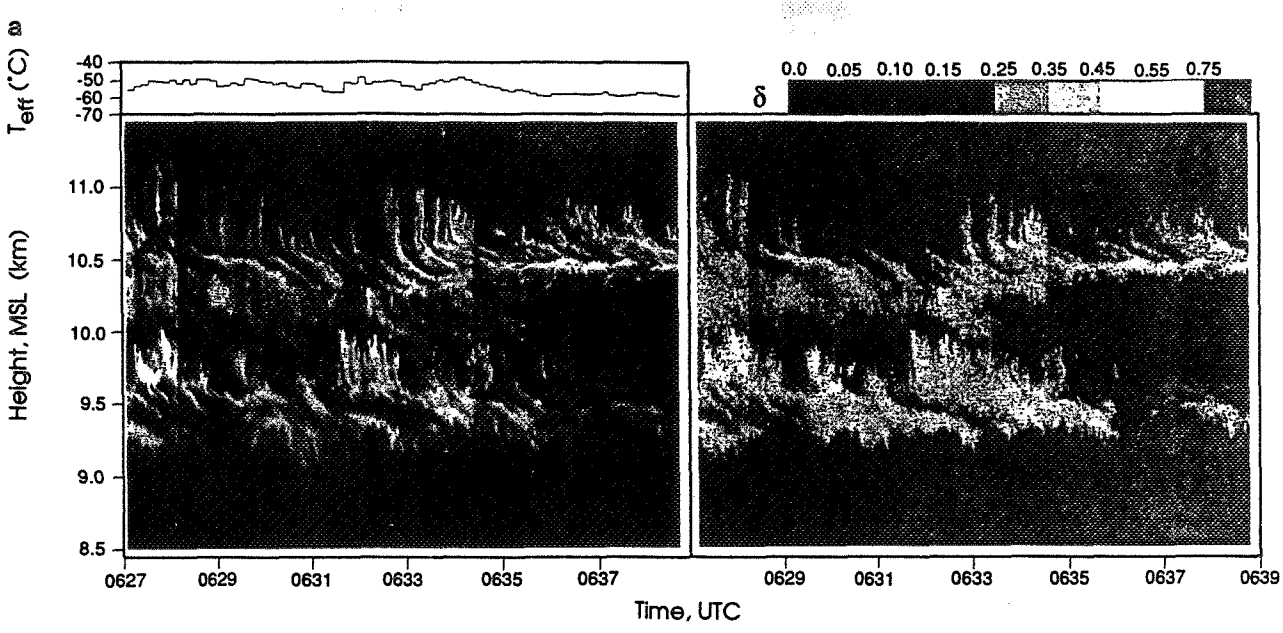

FIG. 11. High resolution height–time PDL displays of relative returned energy and depolarization (right of each pair) illustrating the highly structured convective lower cirrus layer at the indicated times on 5 December. Shown in (a) are numerous sheared fallstreaks emanating from two layers of uncinus cells, (b) a dense and highly depolarizing region above mammatus-like structures, and (c) the brief appearance of a highly supercooled altocumulus ($\delta \leq 0.05$) cloud just below the trailing edge of the cirrus cloud base.

sponse to the humidification caused by prior cirrus particle evaporation), only to be disrupted by plumes of ice crystals resulting from cirrus particle-seeding effects. Note that values of T_{eff} are relatively high in the deep fallstreaks of (a) and (b) and much lower in the dissipating cirrus cloud trail in (c), although the passage of the supercooled altocumulus cloud seems to have caused a small increase in effective temperature. Views such as these illustrate that it is the accumulation of cirrus uncinus fallstreaks that often defines the base of a cirrus cloud layer (see Sassen et al. 1990).

A Citation aircraft mission, involving racetrack patterns 10–15 km long and an Eulerian spiral descent was conducted in close support of the Hub site from 0612–0847. (The excellent aircraft navigation was confirmed by the sighting of the green PDL laser beam at one point just off the wing tip over the Hub!) Figure 12, which superimposes the corrected aircraft altitude flight pattern on an expanded PDL lidar returned power display, reveals that the platform sampled both the tenuous upper and denser lower layers. The corresponding time plots of aircraft air T and dewpoint T_d temperatures, 2D-C probe ice particle mean size d and concentration N_i, and condensation nuclei CN and ozone concentrations are provided in the panels below the lidar display. Note that the cirrus precipitation-induced humidification of the subcloud region shown by the Raman water vapor profiles (Fig. 10) is also indicated by the differences in the dewpoint measurements at ~9.0 km obtained during the ascent and later descent legs through the developing lower cirrus cloud layer. The in situ and remote cloud measurements are generally in quite good agreement in defining the cirrus cloud boundaries, although strong optical attenuation in the developing lower layer partially blocked the probing of the upper layer at those times corresponding to the highest observed T_{eff} values (see top panel of Fig. 11b). The combined evidence shows that the two cloud layers have dissimilar microstructures, with the higher cirrus displaying much lower ice crystal concentrations and different crystal shapes (according to the lidar δ values). In addition, at cloud top at 0751, FSSP particle concentrations (not shown) of ~0.2 cm^{-3} are found without any indications of ice crystals at a temperature of −64°C, indicating quite small ice or haze particles. The 2D-C probe ice crystal concentrations in the lower cloud often reach 200 L^{-1} and actually peak at ~600 L^{-1} (2-s averages are given in Fig. 12), which represents the highest value by far measured by any aircraft during the campaign (or elsewhere to the best of our knowledge). The photomicrograph examples of ice particles captured by a Formvar replicator device from 0800 to 0815 given in Fig. 13 indicate complicated radial particle shapes (that were generally too fragile to survive impaction intact), which can be said to be in keeping with the strong laser depolarization ($\delta \approx 0.65$) noted at this time and altitude (see Fig. 11b).

The variations in CN counts and ozone concentrations in the bottom panel of Fig. 12 have important implications for these unusual cirrus cloud properties. We provide these data in Fig. 14 in terms of vertical

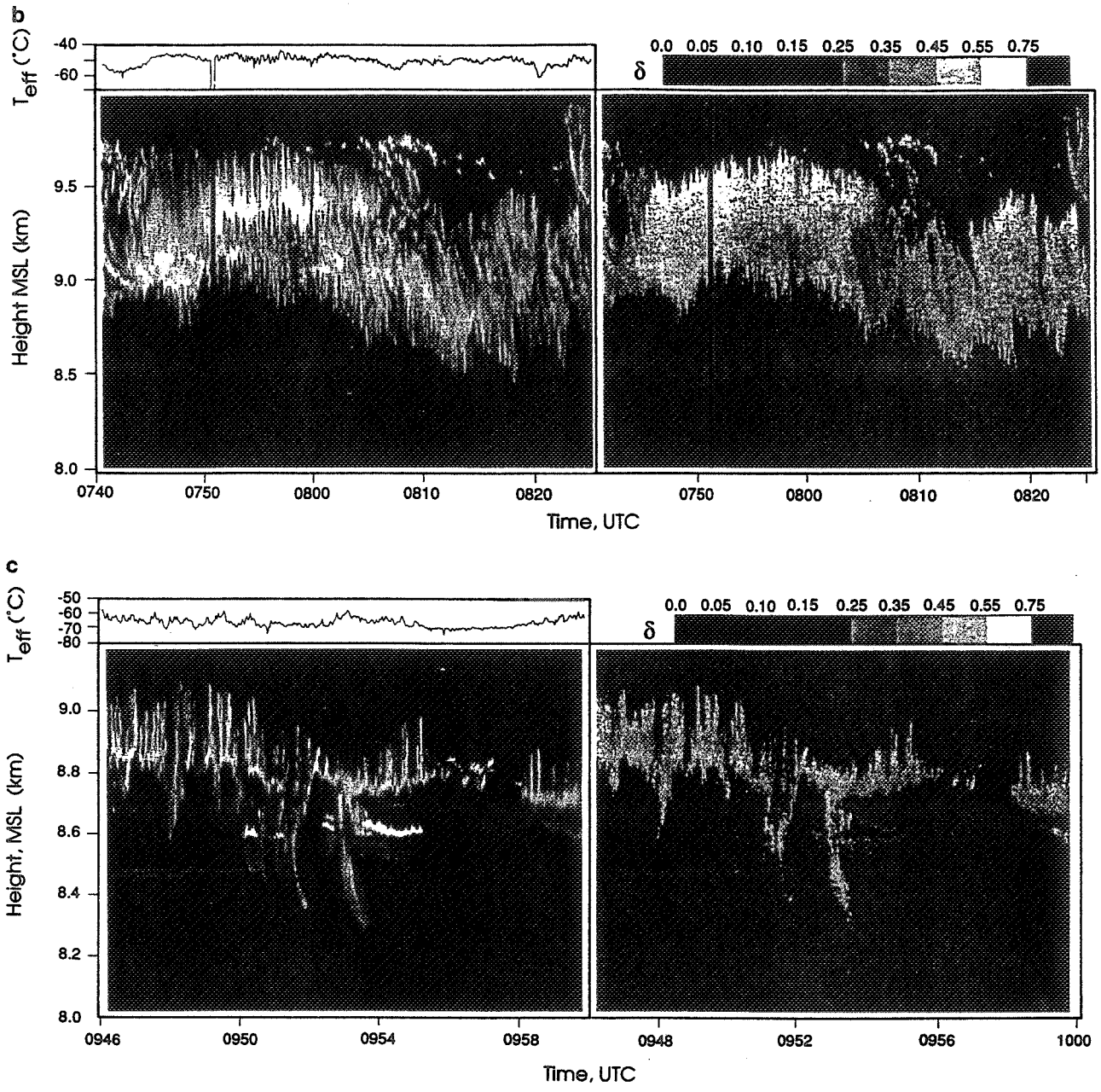

profiles obtained during the ascent (0612–0750) and descent (0751–0847) portions of the flight. It is apparent that CN counts are significantly enhanced in the height interval 7.0–11.0 km encompassing the lower cirrus cloud layer, with offscale counts of >1000 cm^{-3} at ~9.0 km present during the descent spiral. Figure 15 more directly illustrates the association of the high ice crystal concentrations with the upper portion of the aerosol layer. The ozone profiles (Fig. 14) tend to dip in the layer containing the greatest CN counts, but they also show increased concentrations of >20 ppb toward the top of the elevated aerosol layer. While the ascent and descent ozone profiles are similar, and are comparable to Fig. 6b data, those for the CN are sufficiently different to suggest considerable spatial variability in the aerosol distribution. (Note also the significant CN variations along the nearly level flight segment in Fig. 12 from 0805–0830.) In summary, the evidence presented here and in section 3 indicates an association between the formation and maintenance of the lower cirrus layer with the cirrus particle evaporation-induced humidification of a region containing elevated ozone

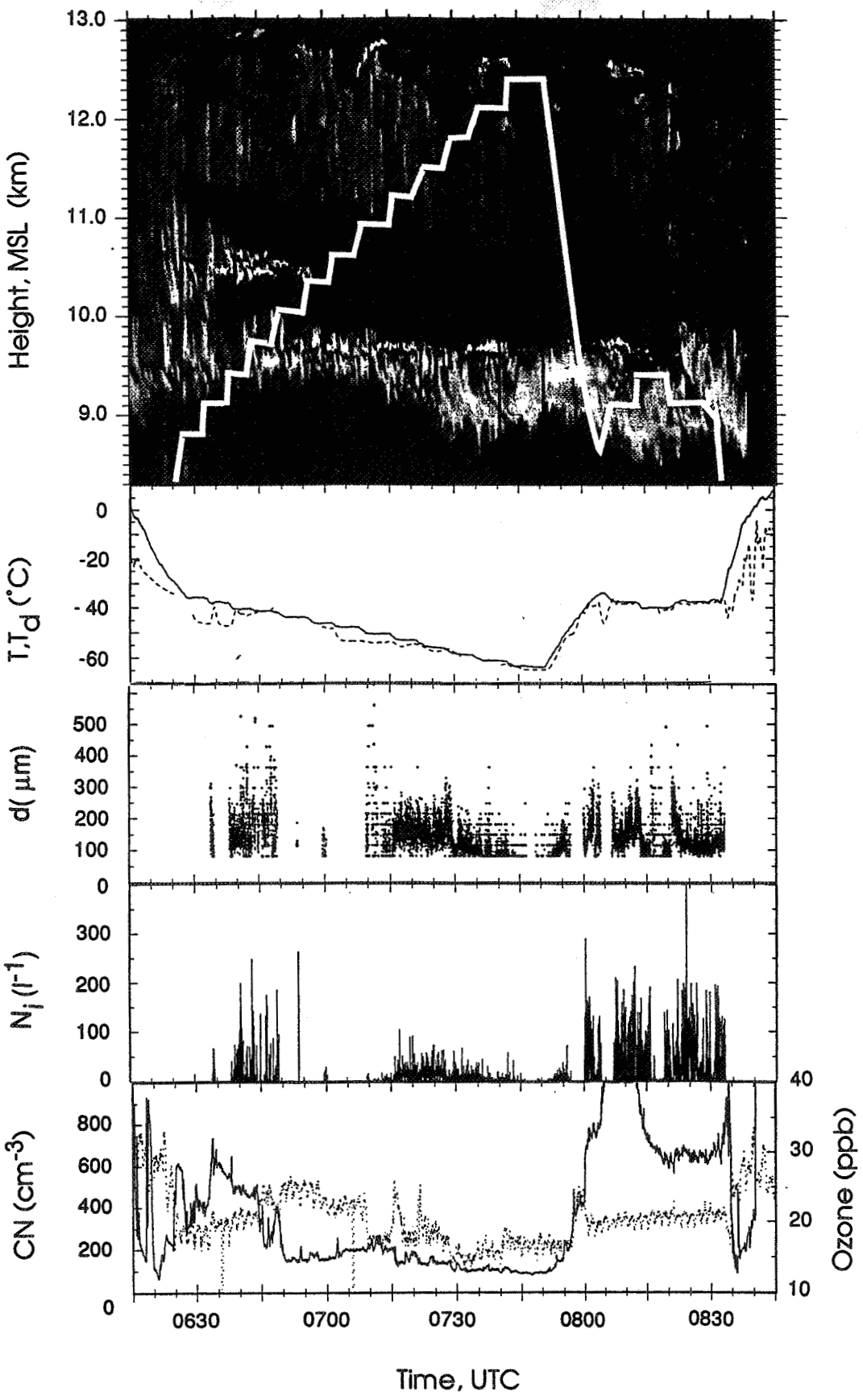
Height, MSL (km)
13.0
12.0
11.0
10.0
9.0
T,T_d (°C)
0
-20
-40
-60
d(μm)
500
400
300
200
100
0
N_i (l^-1)
300
200
100
0
CN (cm^-3)
800
600
400
200
0
Ozone (ppb)
40
30
20
10
0630
0700
0730
0800
0830
Time, UTC

and aerosol concentrations of probable stratospheric origin.

b. 1800 5 December–0800 6 December cirrus clouds

A number of airborne missions in the vicinity of the Hub were conducted early during this period as thin cirrus clouds initially made their appearance, but generally the missions were performed prior to the local occurrence of the deep jet streak cirrus cloud band (see Figs. 3 and 4). We again utilize Citation measurements from a mission featuring a step pattern between the Hub and Parsons (30 km to the northeast) sites from 1756 to 2023 5 December. In addition, downward-looking lidar data from the ER-2 platform obtained during a transit from Coffeyville to the Texas Gulf region are presented, since this dataset uniquely portrays the large-scale geographical distribution of volcanic aerosols (below the 20-km flight altitude) at ~2000 corresponding to the approximate time of the local jet maximum. Specialized aerosol measurements collected by the NCAR Saberliner are also given to further explore the issue of the nature of the aerosol.

The Citation data plots in Fig. 16 provide the same information as in Fig. 14, showing the height dependencies in CN and ozone concentrations during the ascent and descent legs. (Since zenith-pointing lidar data for this mission are incomplete, a combined display as in Fig. 12 is not available.) As in the previous Citation mission, greatly enhanced CN counts are found in the altitude interval 7.5–10.0 km, and Fig. 17 shows that the cirrus cloud region is again associated with the top of the aerosol-enriched layer. Moreover, thin strongly enriched aerosol layers between 10.2 and 12.2 km are embedded in the upper cirrus. Ozone concentrations (Fig. 16) display peaks near the main aerosol layer base and top, as well as near the Citation ceiling altitude, where it appears that ozone just above the tropopause was sampled. Additional aerosol information derived from the University of Missouri/Rolla mobile aerosol sampling system (as described in Hagen et al. 1992) during overlapping Saberliner missions is included in Table 3. These samples were taken below the cirrus cloud base in relatively dry air with relative humidities of ~25%: the average aerosol total mass (derived from four size distribution measurements and assuming unit density) was 0.1 $\mu g\ m^{-3}$. Of the three measurements of aerosol-soluble mass fraction (assuming the presence of either ammonium sulfate R_{AMS} or sulfuric acid $R_{H_2SO_4}$) obtained within the aerosol layer (compare sample heights with Fig. 16), one is significantly elevated ($R_{AMS} = 0.22$) above the usual tropospheric values of a few percent or less. The lower soluble mass fractions are consistent with previous measurements made in the altitude range 7.0–10.0 km over the central United States using bag samples processed in a laboratory-based continuous flow thermal diffusion chamber facility (Hagen et al. 1990). The measurement exhibiting the highest soluble mass fraction may suggest aerosols resulting from volcanic activity, or perhaps may be of aircraft exhaust origin.

The ER-2 CLS height-distance display of Fig. 18 covers 640 km of lower stratospheric and tropospheric aerosol and cloud returns along a north–south flight track at ~95°W latitude from Coffeyville (left) to near Houston, Texas. Note that the atmospheric cross section in Fig. 5 corresponds to a portion of this flight track and reveals the relationship between the high altitude aerosols and clouds (colored blue and white, respectively) and the vigorous jet streak defined by the 0000 6 December synoptic analysis. The lidar aerosol backscatter (at 0.53-μm wavelength) illustrates the enrichment of aerosols at the base of the stratosphere caused by the jet stream circulation. This is a powerful representation of the vertical and latitudinal redistribution of volcanic aerosols from the tropical belt into which the debris were originally injected. The wedged-shaped region of enhanced aerosols extending just above the gradually lowering surface of the tropopause (from 17.0 to 15.5 km, center to left) appears to be tenuously connected to the higher stratospheric aerosol layer at a distance of ~500 km (not shown) and also appears to slope downward toward the cirrus cloud tops ("overexposed" white regions in this image to highlight aerosol scattering) about 150 km north of Coffeyville.

The subsequent local development of the jet streak cirrus band (see Fig. 4b for satellite view) is traced in the PDL height–time returned power and δ displays of Fig. 19. Based on a 6-year lidar record of Project FIRE Extended Time Observations (ETO) of cirrus clouds collected at Salt Lake City, Utah, such complex cirrus structures containing an abundance of generating features within swirling layers are quite unusual. Effective infrared window brightness temperatures (top panel) are correspondingly variable in response to the variations in total physical cloud thickness and the accumulations of fallstreak particles. Sometimes $T_{eff} \approx -35°C$ are encountered. Also, in contrast to the displays of Fig. 9, unusually high δ values are now sometimes found in generating areas in the usually diffuse upper cirrus regions. Moreover, the sporadic occurrence of low δ (≤ 0.15) values in association with the

FIG. 12. Combined PDL lidar and University of North Dakota Citation aircraft data displays from the mission in support of the Hub remote sensors on the night of 5 December. At top is a height–time display of returned energy, with the Citation flight track shown superimposed in white, in situ data panels of air T and dewpoint temperature T_d (dashed), ice crystal mean diameter d and concentration N_i (derived from the 2D-C probe), and condensation nuclei CN and ozone (dashed, in parts per billion by volume) concentrations.

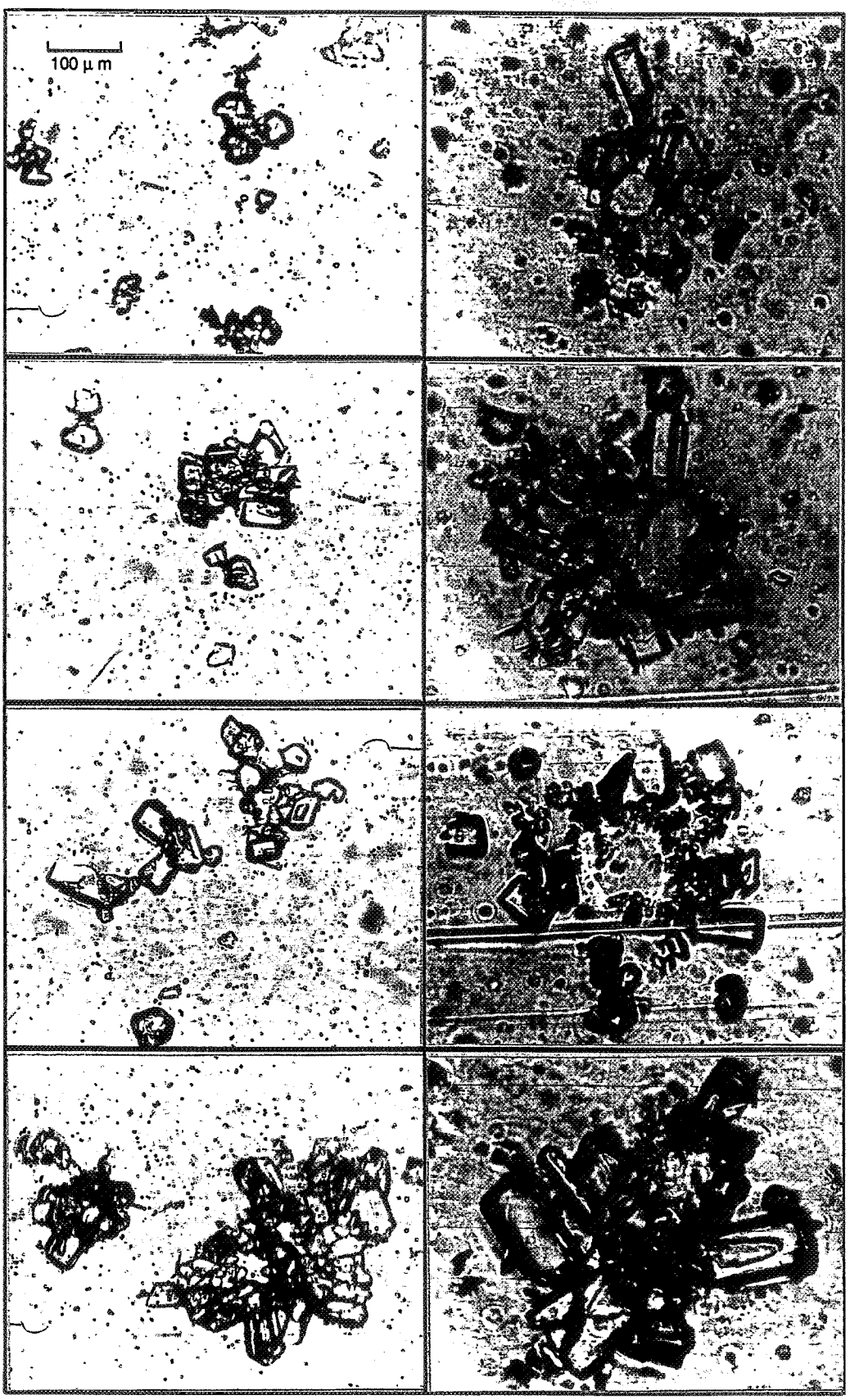
100 μm

lower cirrus generating regions (at and below about 10.5 km) indicate the effects of spherical scatterers that appear to be intimately involved in the generation of the cirrus particle fallstreaks defining the cirrus cloud base. Given in Fig. 20 are higher-resolution displays of three such regions, which clearly identify the Mie scattering effects of rapidly growing haze particles in generating cell heads (Sassen 1992), despite the extremely low temperatures approaching −50°C (see figure caption). Although in the infrared window region the verniers of haze particles do not appear to have provided T_{eff} signatures (Fig. 20c), certainly the accumulations of ice crystals nucleated from them are associated with sufficient mass to significantly increase the T_{eff} produced by the entire depth of the cloud layer (Figs. 20a–b).

It is interesting to note that supercooled sulfuric acid droplets at temperatures as low as −48°C have been reported on the basis of in situ measurements in regions of the upper troposphere likely affected by tropopause folds (Yamato and Ono 1989). Comparison with the in situ CN profiles obtained earlier strongly suggest that these cirrus cloud features are the result of contamination from relatively large cloud-forming nuclei of volcanic origin. Although the low δ-value cell-top generating structures were not consistently observed, their association with crystal fallstreaks, which are long-lived, suggest their great importance to the formation and maintenance of the lower cirrus layer.

c. 1200–1700 6 December cirrus clouds

The properties of the final cirrus cloud system of the case study period differ sharply from those described above, although Fig. 3 suggests that this relatively low-level cirrus (or altostratus) cloud mass represents a continuation of the precipitating cloud trail of the cirrus described above. The structure of this cirrus mass is best represented in the W-band (3.2-mm wavelength) PSU radar height–time display of Fig. 21, because this optically thick cloud, along with some lower stratus clouds, often produced strong optical attenuation of the lidar signals. This radar cloud image shows a succession of ice crystal fallstreaks emanating from generating cells at an altitude ~9.0 km, generally producing echoes significantly stronger and lower than those measured earlier.

Although the radar echo cloud-top heights lie close to the peak of enhanced CN counts measured ~20 h earlier by the Citation, more contemporaneous aerosol data are available from the NCAR Saberliner Hub mission from 1430 to 1630, in which CCN concentrations were measured by the University of Missouri/Rolla CCN counter. CCN counts in excess of 300 cm^{-3} were obtained throughout the cloud layer from 6.0 to 9.0 km, but at an altitude of ~7 km the number exceeded 1000 cm^{-3}. The significance to cloud formation of this great concentration of cloud-forming particles was subsequently revealed by the volume imager lidar (VIL) scans given in Fig. 22. Although these west–east VIL scans portray the cloud conditions only in the vicinity of the Hub (~11 km to the northeast of the VIL site), the scans reveal the presence of strongly attenuating cirrus or altostratus (Fig. 22a, left) and supercooled liquid altocumulus cloud layers, which were initially found embedded in the ice clouds (Fig. 22a, right) and later, alone, produced streaks of ice virga (Fig. 22b, right). Polarization lidar and aircraft measurements over the Hub confirm the predominantly liquid cloud phase of the altocumulus, which at an altitude of ~7.0 km corresponds to the peak in the CCN concentration profile measured by the Saberliner.

5. Discussion

We have provided indirect evidence for cirrus cloud formation and maintenance processes contaminated by relatively abundant volcanic cloud-forming nuclei, but fundamental questions must be addressed to justify this linkage between sulfur-based aerosols of stratospheric origin and cirrus cloud microphysics. Fortunately, recent research has already produced the framework to evaluate this interplay of rather exotic cloud processes. These studies include polarization lidar measurements of lower stratospheric volcanic aerosols and tropopause-topped corona-producing cirrus clouds, laboratory aerosol scattering simulations, and numerical model findings concerning the basic nature of cirrus particle nucleation at temperatures typical of the upper troposphere.

Two pathways from sulfuric acid droplet aerosol to cirrus cloud ice crystal have recently received experimental and theoretical attention. Although in either case it is unknown whether the stratospheric aerosol can serve as an efficient heterogeneous ice nuclei, cloud modeling evidence (Heymsfield and Sabin 1989; Sassen and Dodd 1989) has illustrated that at temperatures colder than −35° to −40°C the homogeneous freezing of solution droplets growing in updrafts likely represents an effective process to generate ice crystals. In

FIG. 13. Sequence of photomicrographs of Formvar-preserved ice crystals obtained from the Citation during the traverse of the lower cirrus cloud layer (see Fig. 12). The crystals at left were collected at a temperature of ~ −40°C from 0800–0802 as the aircraft first penetrated the cloud top, while those at right at −37.7°C from 0818–0820 during a leg at 9.45 km. These complex column/sector radial crystals generated the unusually strong laser depolarization shown in Fig. 11b. The cause of the unusual impacted-particle ringed structures, particularly evident at right, is uncertain. A 100-μm scale is inserted at top left for reference.

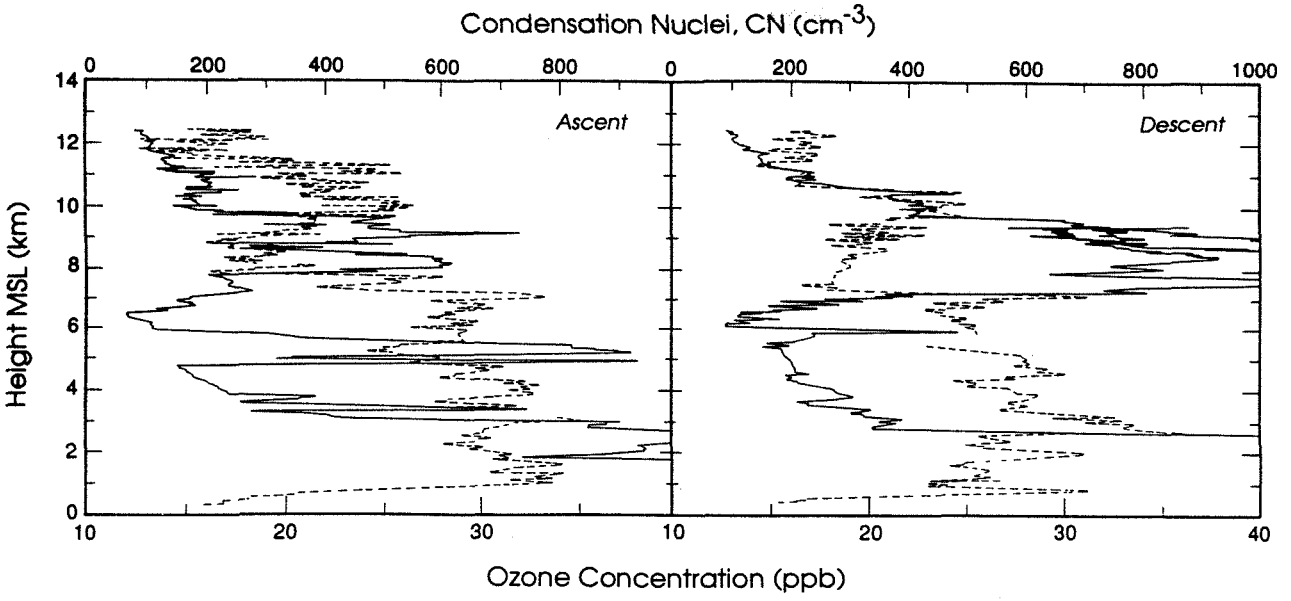

FIG. 14. Comparison of vertical profiles of condensation nuclei and ozone (dashed) concentrations measured by the Citation during the ascent (left) and descent portions of the Hub mission on the night of 5 December.

dealing with an aerosol of stratospheric origin either under background (e.g., see Friend et al. 1973; Bigg 1975) or volcanically perturbed conditions, the sulfuric acid droplets can either directly or indirectly participate in the ice nucleation process after tropospheric alteration. Evidence for the direct homogeneous freezing of sulfuric acid droplets, following a dilution in solution strength from water vapor diffusional growth in the vicinity of the tropopause, comes from polarization lidar

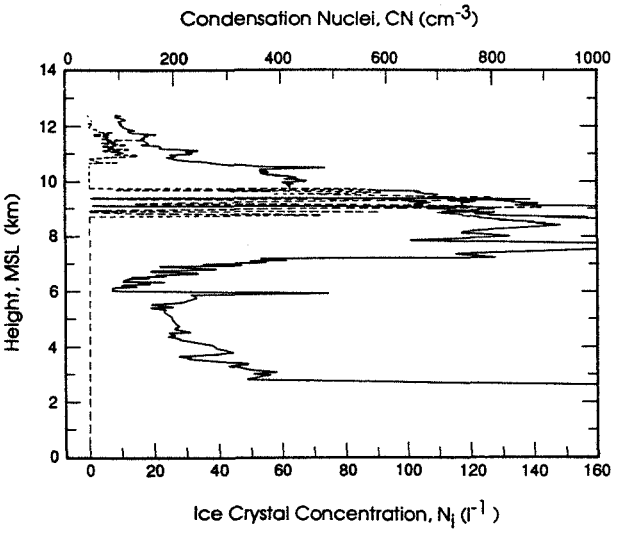

FIG. 15. Vertical profiles of 2D-C probe ice crystal (dashed) and condensation nuclei concentrations obtained during the Citation descent spiral over the Hub from 0753–0804 5 December, illustrating the connection between the cirrus particles and the elevated CN counts near the top of the aerosol layer.

studies of corona-producing cirrus clouds (Sassen 1991). These high cold clouds of relatively small (10–30 μm) particles produce relatively strong ($\delta \approx 0.55$–0.75) laser depolarization, indicative of complexly shaped ice crystals. Presumably these are radial particles that have a polycrystalline structure due to the effects of the coating of liquid sulfuric acid, which is excluded to the surface of the ice germ during drop freezing under the observed environmental conditions (Th. Peter 1992, personal communication).

The indirect path from sulfuric acid droplet to ice crystal involves the homogeneous freezing of haze particles formed on ammonium sulfate cloud condensation nuclei CCN that were derived from acid droplets. The chemistry of this process leading to the neutralization of the acid solution readily follows when droplets, especially if they are evaporating, are exposed to ammonia gas to produce ammonium sulfate crystals (e.g., see Rubel and Gentry 1985). Since ammonia gas is generated at the earth's surface primarily through biological activity (Georgii and Müller 1974) and is consumed photochemically in the stratosphere, this CCN creation process could become significant within tropopause folds where the ammonia gas enhancement of stratospheric air would favor ammonium sulfate CCN production. In support of this view, polarization lidar studies of an unusual lower-stratospheric volcanic aerosol plume affected by tropopause folding activity (Sassen and Horel 1990) yielded depolarization values consistent with partially crystallized sulfuric acid droplets created in the laboratory (Sassen et al. 1989). However, since sufficient time and ammonia gas concentrations may not be available to completely neu-

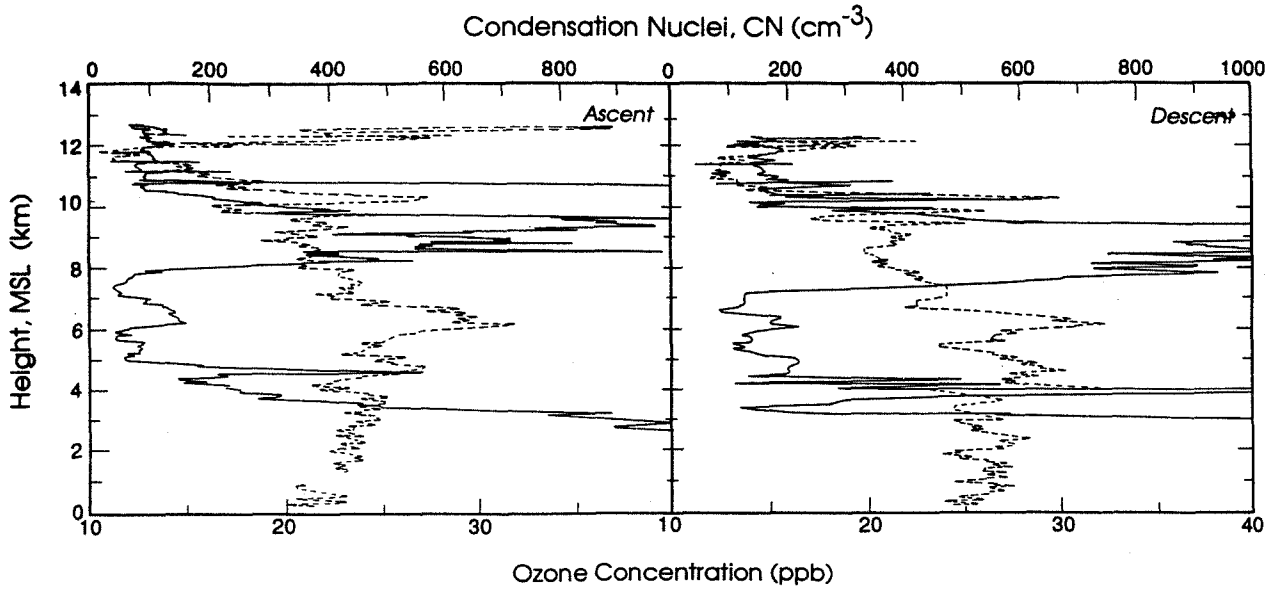

FIG. 16. Comparison, as in Fig. 14, of vertical profiles of CN and ozone (dashed) concentrations obtained during the ascent (left) and descent flight segments of the Citation mission of the afternoon of 5 December.

tralize the acid droplet population, it remains ambiguous which solution droplet freezing process would dominate cirrus cloud particle production following the type of stratospheric–tropospheric exchanges indicated here.

Although the distinction between these two nucleation processes is not of great significance to the current study in relation to the documentation of the appropriate atmospheric structures and the resultant effects on cirrus cloud properties, the lidar depolarization data suggest that both ice nucleation mechanisms may have been active at times. If we equate the atypically high δ values with a dominance of the complicated ice crystal shapes generated from the homogeneous freezing of sulfuric acid droplets, and the unusually low δ values with haze particles derived from relatively large ammonium sulfate CCN particles to yield the variety of crystal shapes commonly observed in cirrus, then the PDL depolarization data could be applied to discriminating the two particle-forming mechanisms at temperatures ≤ -40°C. We note that $\delta \geq 0.55$ were measured only occasionally but predominantly within generating regions near the tops of the lower and upper cirrus cloud layers on the nights of 5 and 6 December, respectively, whereas the strongly scattering $\delta \leq 0.1$ cell heads were found only on 6 December at the tops of the fallstreaks forming the lower layer. This great diversity in lidar depolarization suggests that the stratospheric aerosol content within the cirrus cloud altitude range was variable in time and space.

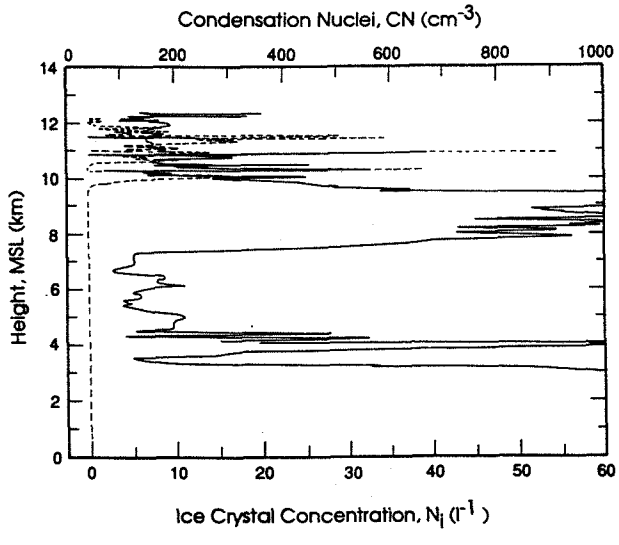

FIG. 17. Vertical profiles of ice crystal (dashed) and CN concentrations, as in Fig. 15, measured from 1915–2021 5 December during the spiral descent of the Citation.

TABLE 3. Soluble mass fraction analysis of aerosol samples collected in situ on 5 December by the NCAR Saberliner assuming the presence of ammonium sulfate (R_{AMS}) or sulfuric acid ($R_{H_2SO_4}$) solutions; N denotes the total CN concentration as measured with a TSI CN counter.

Time (UTC)	Altitude (m)	N (cm^{-3})	R_{AMS}	$R_{H_2SO_4}$
1544	8300	1100	0.10	0.072
1604	9100	1100	0.041	0.030
2028	8850	1800	0.22	0.160

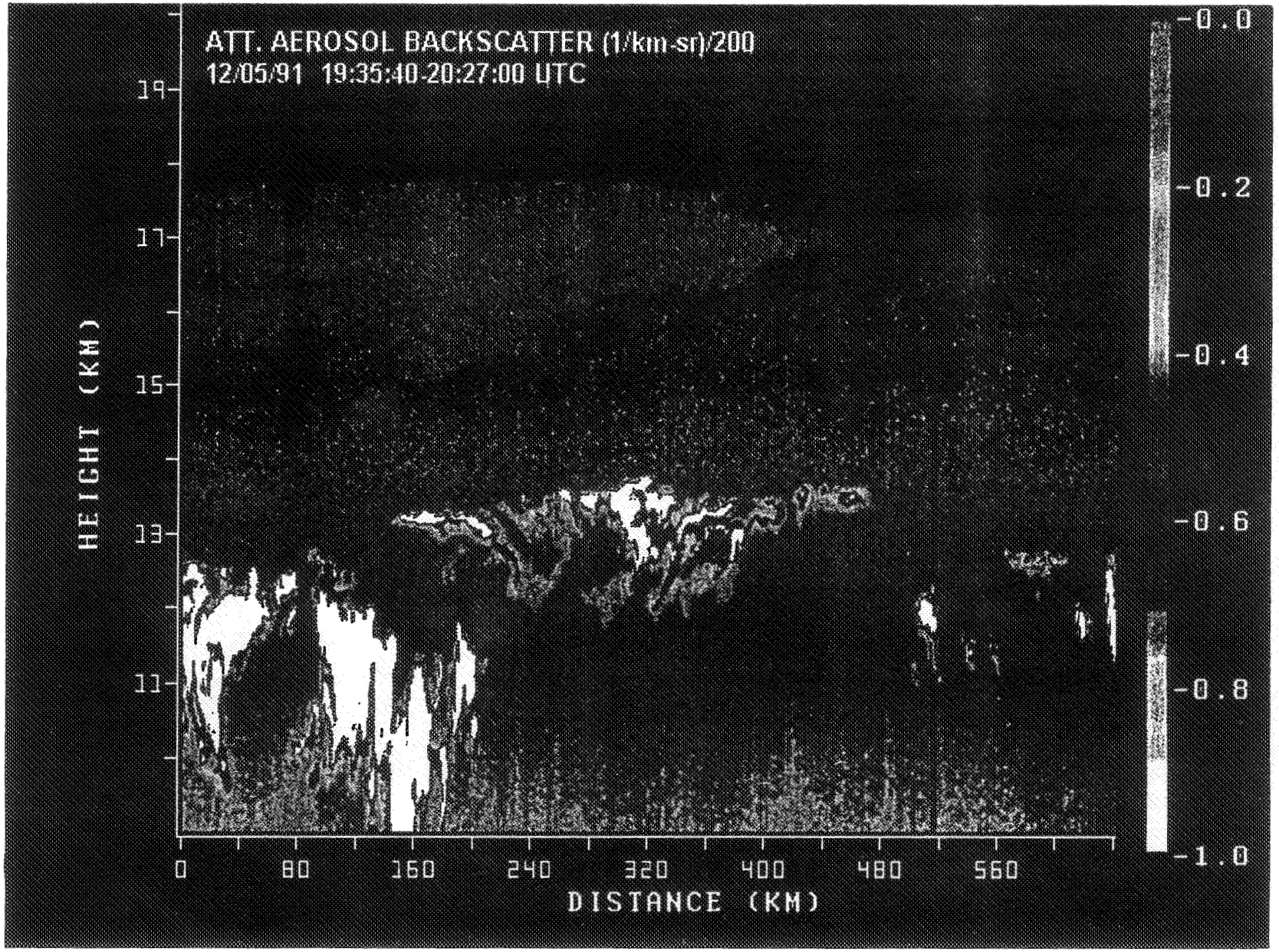

FIG. 18. Height vs distance display of attenuated backscatter coefficients (see key) obtained by the downward-looking ER-2 lidar system from Coffeyville (0-km distance) south to the Houston area. This display has been adjusted to bring out the relatively weak backscattering from lower-stratospheric/upper-tropospheric aerosols, and thus "overexposes" the patchy cirrus clouds also sampled.

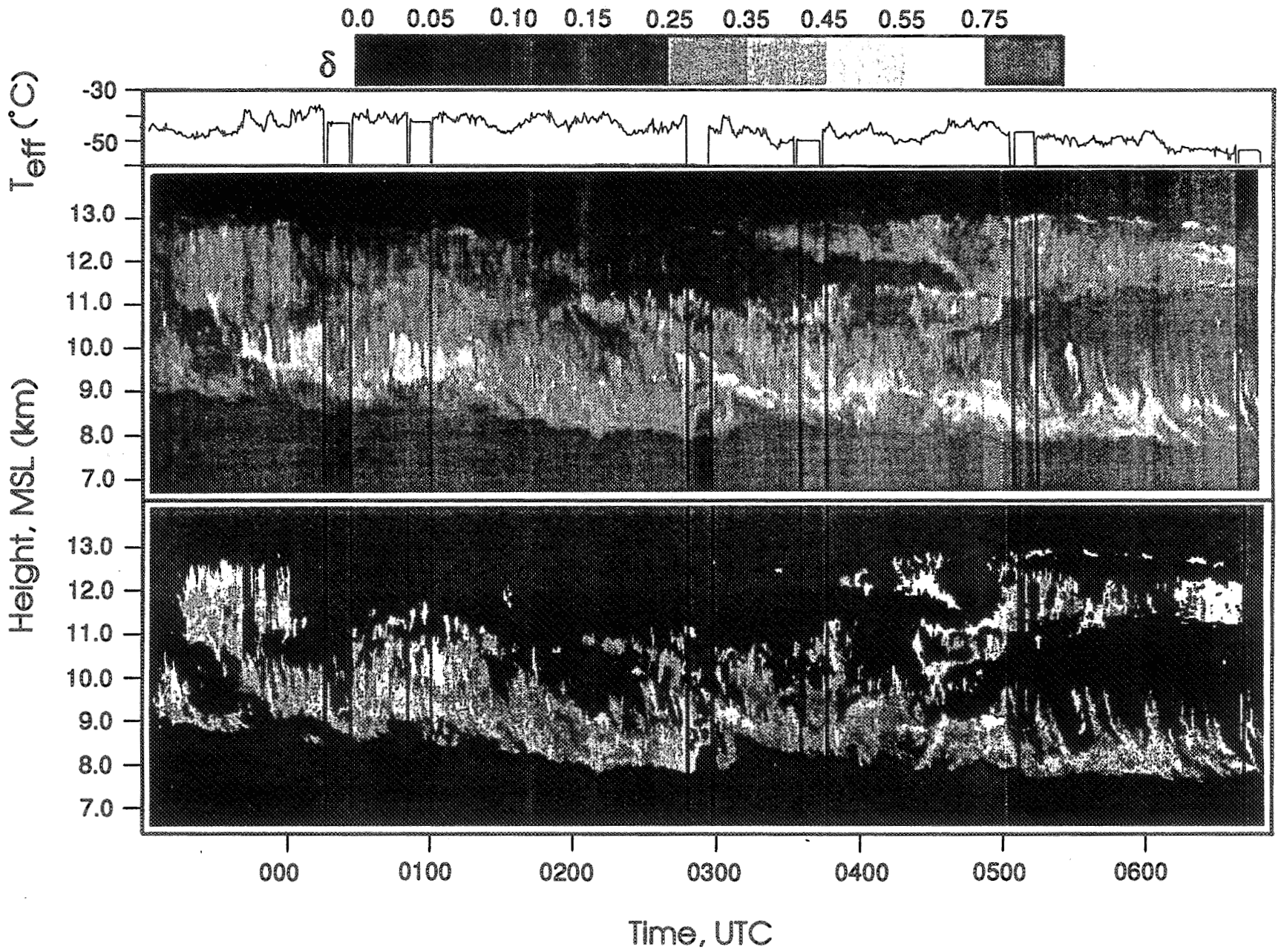

FIG. 19. Polarization lidar HTI displays of relative returned lidar energy (top) and linear depolarization ratios (see at top key) of the cirrus observed on the evening and night of 5–6 December. Infrared radiometer brightness temperatures T_{eff} are shown in the top panel.

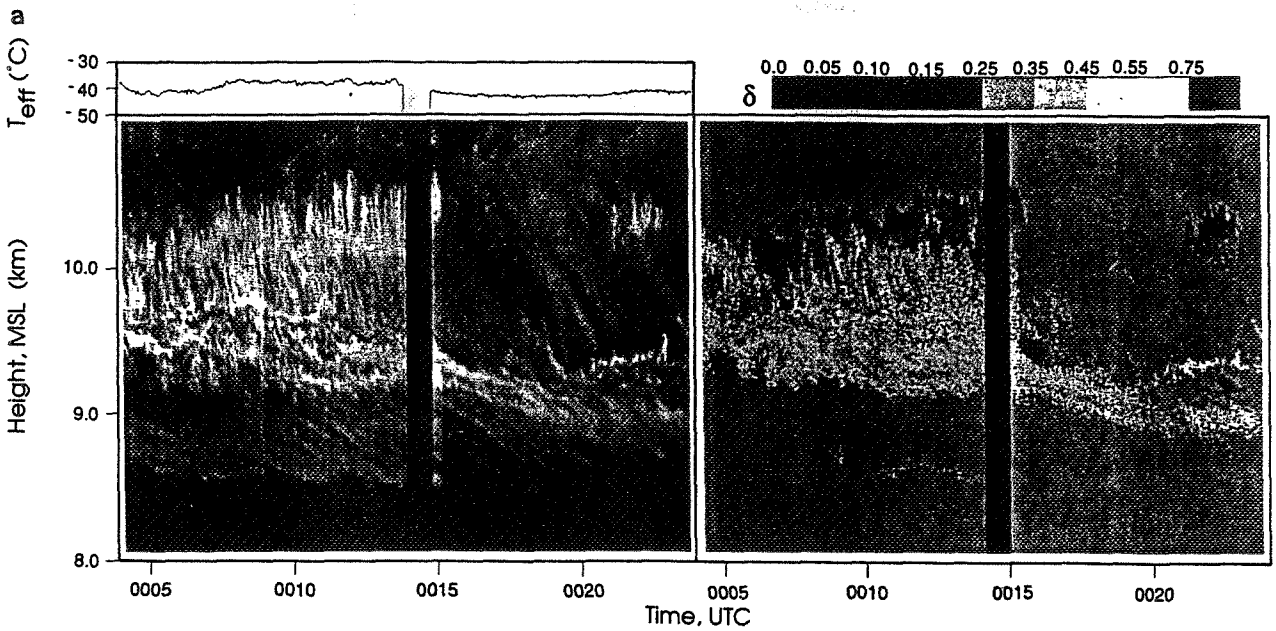

FIG. 20. Details of the high-resolution PDL returned energy and depolarization displays (as in Fig. 11) expanded from Fig. 19 at the indicated times on 6 December, showing complexes of cirrus uncinus cell heads composed mostly of haze droplets with $\delta \leq 0.1$ and the streamers of ice crystals nucleated from them. The uncinus cell head minimum temperatures are −47.3°, −43.0°, and −47.8°C in (a)–(c), respectively.

In terms of the time–height analysis of Fig. 3, it is obvious that opportunities for stratospheric–tropospheric exchanges were provided locally by the passage of jet streaks. A question must be addressed, however, before these changes in atmospheric structure can be related to the formation of cirrus clouds—that is, how are the relatively dry mixed parcels humidified sufficiently to bring about the aerosol growth and ice crystal nucleation processes involved in cirrus generation? We believe that a variety of mixing processes were involved in preparing the stratospheric aerosol for their role as cirrus cloud nuclei. Most notably, the obvious connection between cirrus cloud generation and the boundaries of the elevated frontal zones, as well as the tropopause itself, shows that turbulent and diffusion processes were effective in activating some of the aerosol particles. The local humidification of the mixed stratospheric–tropospheric layers caused by cirrus precipitation and evaporation processes is also clearly indicated and may have aided in the formation of altocumulus at the trailing edges of the cirrus cloud masses. However, since not all of the observed clouds can be linked to identifiable atmospheric structures of recent stratospheric origin, despite the presence at times of greatly elevated CN concentrations, it would appear that advective processes acting on more mixed parcels contained enriched aerosol levels were also prevalent. The in situ aerosol data suggest that considerable spatial inhomogeneity in the aerosol field was present, while at the same time the CO_2-lidar observations demonstrate that the upper troposphere contained a greatly enhanced aerosol content over typical pre-Pinatubo conditions throughout the case study period. This suggests that prolonged stratospheric–tropospheric mixing had taken place in the upstream flow that subsequently swept over the Hub. A long fetch of modified stratospheric air would have had opportunities to become moisturized. For example, according to satellite imagery, large-scale cirrus generation in this case was facilitated by an upwind closed low pressure system over the Baja Peninsula and by orography in the western United States (see Fig. 4).

6. Conclusions

This intensively studied case study from the Project FIRE IFO II campaign has provided an opportunity to examine the effects of a series of jet streaks on the formation of cirrus clouds at midlatitudes. The linkage between jet stream dynamics and cirrus clouds has long been recognized on the basis of satellite imagery (Whitney et al. 1966), and the characteristics of the cirrus have recently been the subject of numerical studies (Durran and Weber 1988).

In this case, however, remote and in situ aerosol and ozone measurements have illustrated that the microphysical processes involved in the formation and maintenance of jet stream cirrus clouds could have been significantly altered by contamination from decaying volcanic debris within six months of the massive Mt. Pinatubo eruptions. Indicated cirrus cloud alterations include abnormally high ice crystal concen-

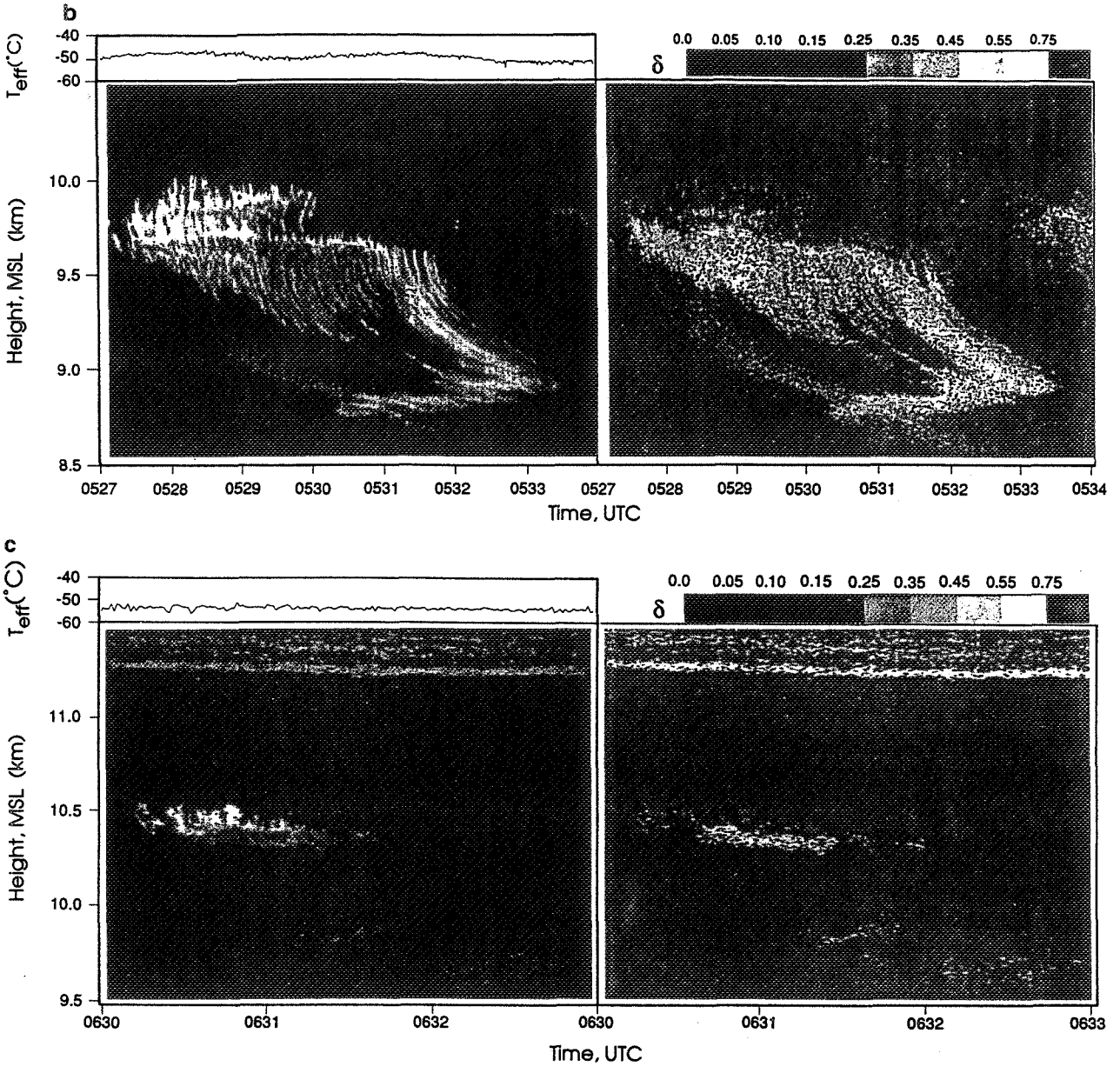

FIG. 20. (*Continued*)

trations (up to ~600 L^{-1}), perhaps unique radial ice crystal shapes, and relatively large haze particles in cirrus uncinus cell heads at temperatures approaching −50°C. These unusual cloud microphysical properties appear to have resulted both from the previous modification of the middle and upper troposphere caused by upwind tropopause foldings and from direct contact with the tropopause and elevated frontal zones. In essence, the local jet streak dynamical processes acted on an atmospheric environment already altered by stratospheric–tropospheric exchanges embedded in the upper-level flow. Although previous lidar research has suggested that the locally observed vertical distribution of volcanic aerosols was influenced by upstream tropopause foldings (Post 1986; Sassen and Horel 1990), it can now be concluded that the continued mixing and dynamical processes experienced by such regions can serve to humidify and condition the aerosol, particularly at the mixed tropospheric–stratospheric interfaces, to make them effective cirrus particle-forming nuclei. The in situ data further suggest that relatively small (on the order of tens of kilometers) aerosol-contaminated parcels were contained within the advecting air flow, presumably the result of the breakup of aging elevated frontal zones that could not be satisfactorily resolved in the available synoptic

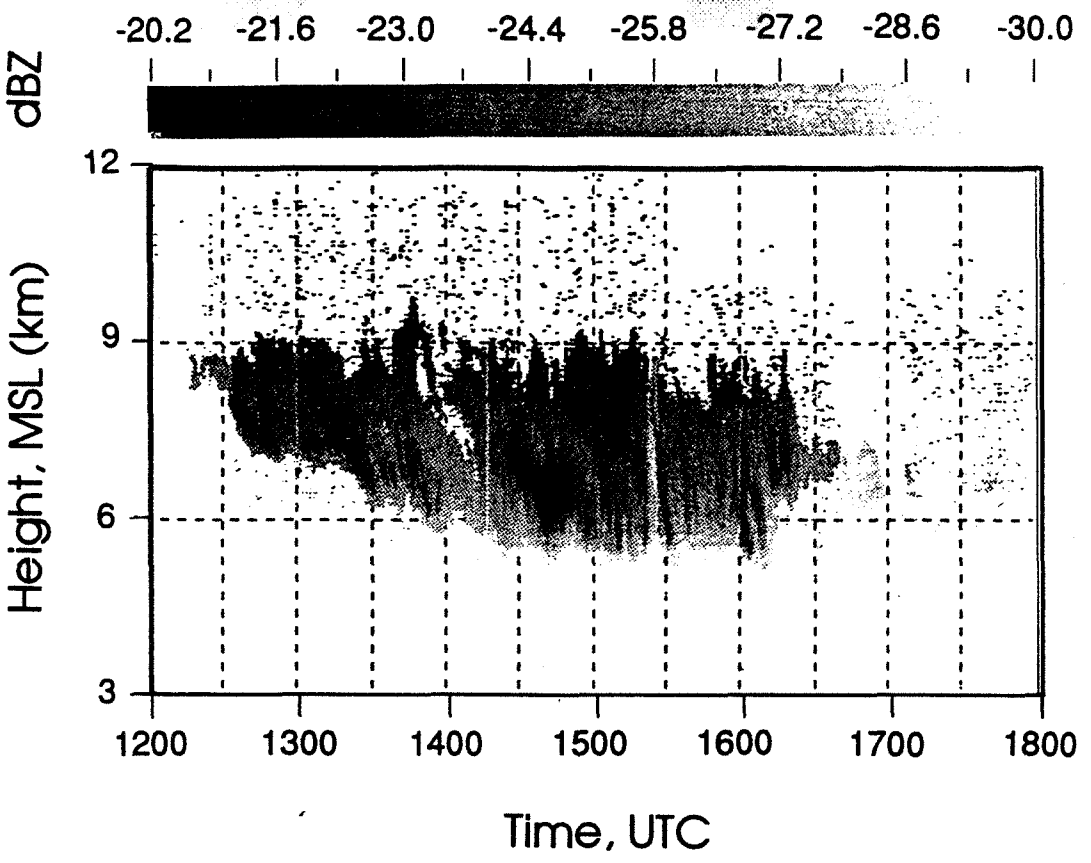

FIG. 21. Height–time radar-reflectivity greyscale display (in dBZ, see key at top) of the cirrus over the Hub during the indicated period on 6 December, as measured by the Pennsylvania State University 94-GHz radar.

data. Interestingly, aircraft ozone concentrations in these parcels tend to be inversely related to CN counts, except at the aerosol-layer boundaries where ozone enhancement was observed, which is suggestive of possible ozone depletion via interactions with the aerosols of stratospheric origin (Hofmann and Solomon 1989; Rodriguez et al. 1994). Basically, these atmospheric conditions were fortuitously observed over the Hub site due to the relative consistency in the upper-level flow over the project area during the case study period.

These findings have implications for "normal" cirrus clouds that form in association with jet streams, and also perhaps for deep tropospheric storm systems that develop along upper-level fronts (Martin et al. 1993). Cirrus cloud–stratospheric aerosol effects need not occur solely in connection with jet streams, however, a fact that has major implications for cirrus cloud formation models ranging from the cloud to GCM scales. Even though the background (i.e., volcanically unperturbed) lower-stratospheric aerosol content is considerably more innocuous, mixing processes provide the upper troposphere with a steady source of aerosols from above (Reiter 1972; Kent et al. 1991). There is already evidence from pre-Pinatubo lidar studies that those midlatitude cirrus with cloud tops extending just above the tropopause have unusual cloud properties, including the generation of corona displays and strong backscattering and depolarization (Sassen 1991). The data presented here from the morning hours of 5 December show what appears to be an analogous occurrence, except that this cirrus layer formed well below the tropopause (and possible corona effects could not be assessed). Cirrus ice particle nucleation from the homogeneous freezing of diluted sulfuric acid droplets of stratospheric origin is indicated to yield a polarization lidar scattering signature when such particles predominate in the cloud (although their presence may go unnoticed when mixed with other particles). The ice crystal photomicrographs in Fig. 13 provide tantalizing indications of the complex nature of the particles that result from the acid droplet freezing process.

It is clear that the apparently distinct nucleation mechanisms involved in the formation of tropopause-topped and some jet stream cirrus clouds from sulfur-based particles have climatic implications, as shown schematically in Fig. 23. In this flow chart the aerosol mixing may be due to gradual turbulence–diffusion or relatively rapid tropopause folding effects, and the moisturizing process to create cirrus particles can in-

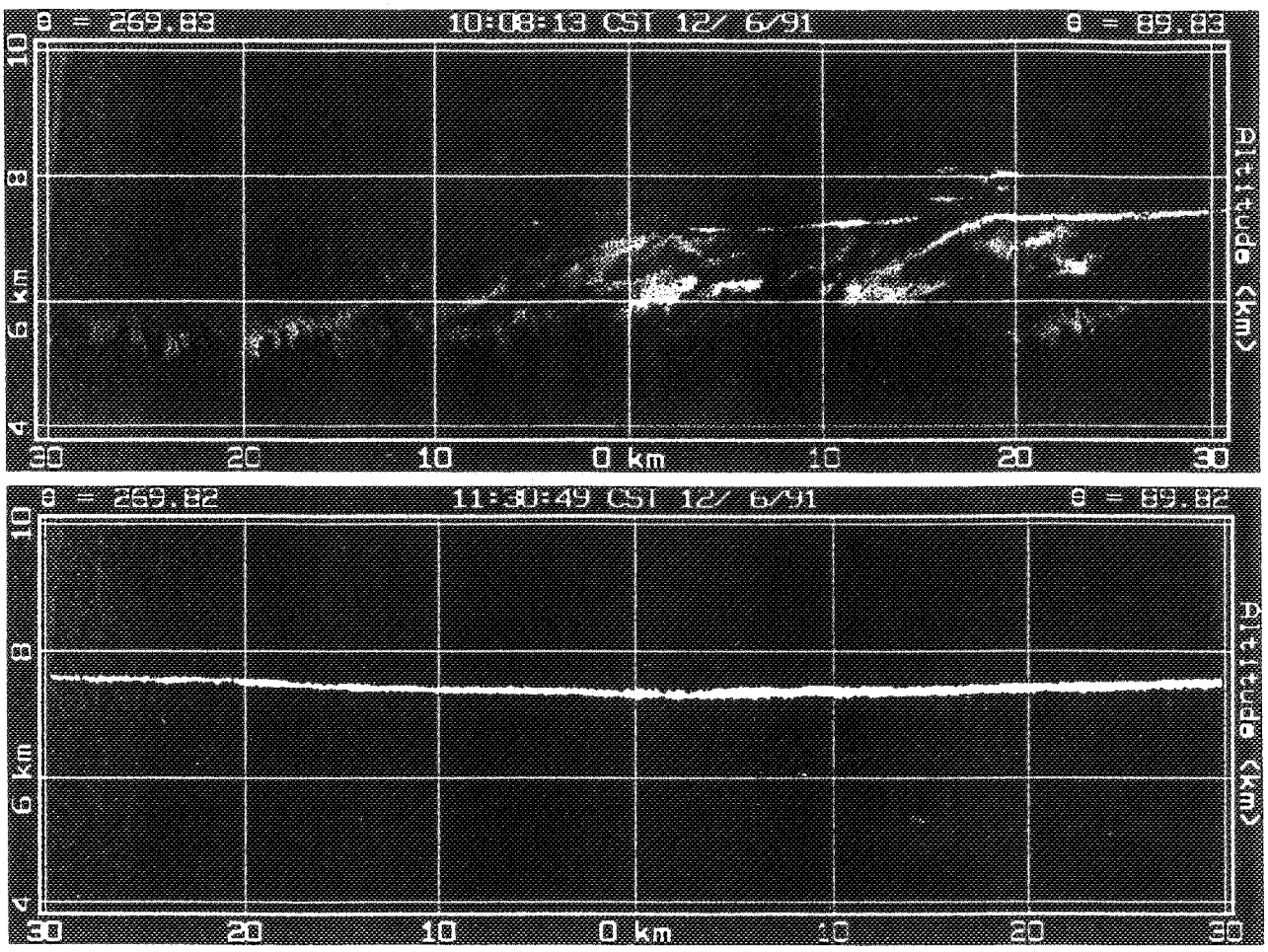

FIG. 22. Volume imager lidar range–height scan displays of the cirrus and altocumulus clouds in the vicinity of the Hub site, collected at (a) 1608 and (b) 1731 6 December. These clouds often produced strong optical attenuation that restricted the depth of lidar probing. This is evident in the left side of the top display, where only the cloud-base region with mammatus-like protrusions was penetrated by the laser.

volve aerosol sedimentation through the hydropause or uplift in connection with jet streaks or other dynamical processes, such as in closed low pressure systems. The key to understanding the climatic effects of volcanically altered cirrus, however, lies in the exact changes that occur in cloud microphysical properties. Although radiative transfer simulations have generally indicated that optically thin cirrus clouds in the upper troposphere contribute to the greenhouse warming effect (e.g., see Liou 1986), the opposite effect, a cooling from increased cirrus cloud solar scattering, could reinforce the albedo increase caused by volcanic aerosols in the stratosphere (Minnis et al. 1993). Assuming, for example, that larger and more abundant CCN are introduced into cirrus cloud altitudes, one might expect from modeling studies that the cirrus would be produced more readily (i.e., at lower relative humidities) and be longer lasting (i.e., drawing from an enlarged CCN population to replenish losses from crystal precipitation). Alternatively, greatly increased CCN concentrations could lead to more gravitationally stable cirrus clouds composed of more numerous small crystals with quite different radiative properties. A further complication is the unusually complex shape of these cirrus crystals, which, according to previous research (Sassen 1991), tends to produce relatively small and highly depolarizing particles near cloud tops until additional diffusional or aggregational growth with other particles causes a change in cloud-scattering properties. Detailed cloud microphysical–radiative simulations tailored to the haze and ice cloud alterations induced by sulfur-based aerosols, using reasonable size distributions, are required to solve this problem, and it is encouraging that first steps in this direction have already been made (Jensen and Toon 1992).

Finally, we note from Fig. 23 that the fate of the stratospheric aerosol in the middle and upper troposphere is likely to be a relatively rapid removal through precipitation processes. In situ measurements have

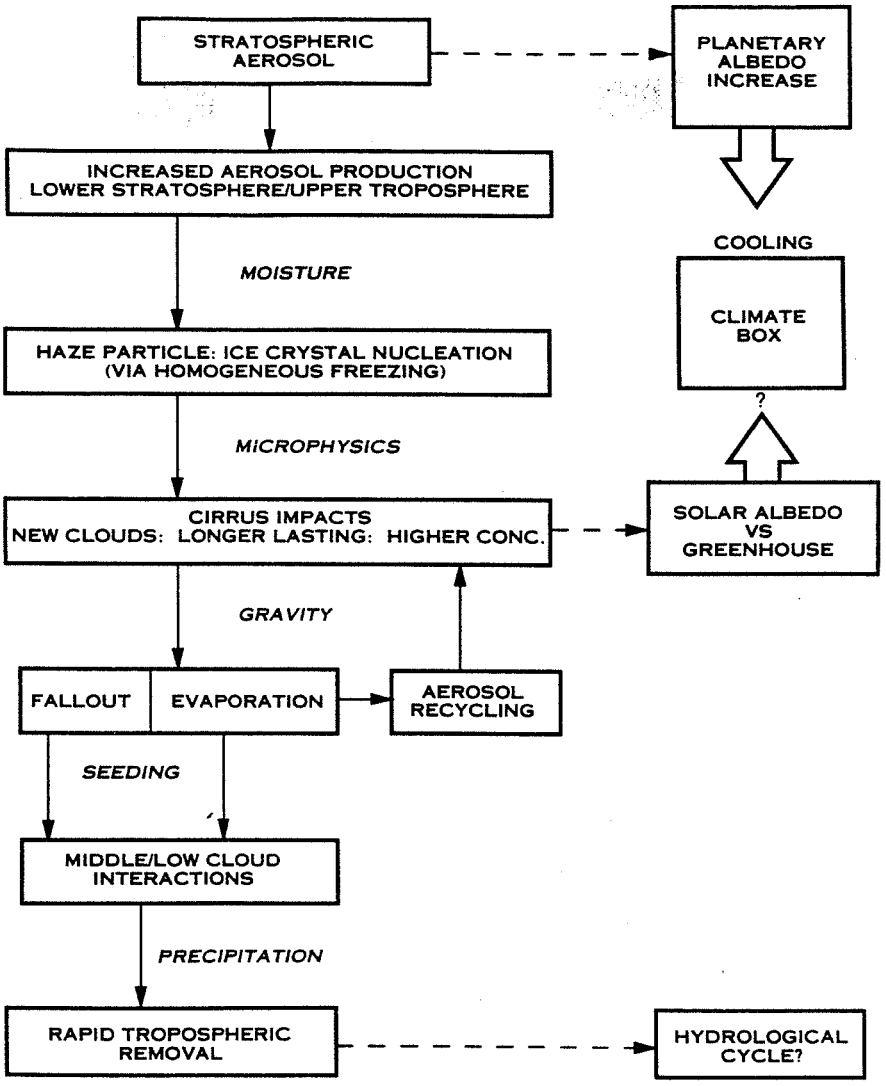

FIG. 23. Schematic representation of the possible climatic effects (right) produced by an influx of volcanic stratospheric aerosols into the troposphere.

shown the significant decline in the sulfuric acid aerosol that occurs in the midtroposphere (Yamato and Ono 1989), a phenomenon that is also suggested by satellite studies (Kent et al. 1991). Although the stratospheric CCN introduced into lower tropospheric clouds may be overwhelmed by the abundant background CCN population derived from the surface, and thus be of little consequence to climate, it is possible that precipitation could be enhanced from cirrus particle seeding effects, thereby affecting the hydrological cycle. This lies clearly outside the scope of this paper, but we can point out that a similar hypothesis was suggested many years ago in connection with the fallout of meteoric dust introduced into the upper atmosphere following major meteor showers (Bowen 1956).

Acknowledgments. Support for the University of Utah FIRE IFO research came from NSF Grant ATM-8914348, which also partially supported the NCAR aircraft operations, and NASA Grant NAG-1-1314: PDL development from DOE Grant DE-FGO2ER1059 of the Atmospheric Radiation Measurement program, which, along with a grant from the NOAA Climate and Global Change Program, also supported the NOAA WPL field operations: University of North Dakota Citation operations from NASA Grant NAG-1-1351: University of Missouri aerosol-sampling efforts from NSF Grant ATM-8820708: and for Pennsylvania State University NASA Grant NAG-1-1095 and a graduate student fellowship from NASA Goddard SFC (for G. G. Mace). Project FIRE NASA funding was provided by the Office of Space Science and Applications under the direction of Dr. J. T. Suttles.

The authors wish to thank the personnel at GSFC (Dave Whiteman, Rich Ferrare, Keith Evans) and San-

dia National Laboratory (John Goldsmith, Scott Bisson, Marshall Lapp) who were responsible for the GSFC Raman lidar data acquisition and analysis, and numerous other FIRE investigators who contributed to the project and made their data available.

REFERENCES

Bigg, E. K., 1975: Stratospheric particles. *J. Atmos. Sci.*, **32,** 910–917.

Bowen, E. G., 1956: The relation between rainfall and meteor showers. *J. Meteor.*, **13,** 162–166.

Cox, S. K., D. S. McDougal, D. A. Randall, and R. A. Schiffer, 1987: FIRE—The First ISCCP Regional Experiment. *Bull. Amer. Meteor. Soc.*, **68,** 114–118.

Danielson, E. F., 1968: Stratospheric–tropospheric exchange based upon radioactivity, ozone, and potential vorticity. *J. Atmos. Sci.*, **25,** 502–518.

Durran, D. R., and D. B. Weber, 1988: An investigation of the poleward edges of cirrus clouds associated with midlatitude jet streams. *Mon. Wea. Rev.*, **114,** 702–714.

Ellingson, R. G., and Coauthors, 1993: The Spectral Radiation Experiment (SPECTRE): Clear-sky observations and their use in ICRCCM and ITRA. *IRS' 92: Current Problems in Atmospheric Radiation,* S. Keevallik and O. Kamer, Eds., A. Deepak, 451–453.

Eloranto, E. W., and D. K. Forrest, 1992: Volume imaging lidar observations of the convective structure surrounding the flight path of an instrumented aircraft. *J. Geophys. Res.*, **97,** 18 383–18 394.

Ferrare, R. A., S. H. Melfi, D. N. Whiteman, and K. D. Evans, 1992: Raman lidar measurements of Pinatubo aerosols over southeastern Kansas during November–December, 1991. *Geophys. Res. Lett.*, **19,** 1599–1602.

Friend, J. P., R. Leifer, and M. Trichon, 1973: On the formation of stratospheric aerosols. *J. Atmos. Sci.*, **30,** 465–479.

Georgii, H. W., and W. J. Müller, 1974: On the distribution of ammonia in the middle and lower troposphere. *Tellus,* **26,** 1–2, 180–184.

Global Volcanism Network, *Bulletin of the Smithsonian Institution 1991–1993:* Vols. 17–19 [Available from the American Geophysical Union, Washington, DC.]

Hagen, D. E., A. J. Heymsfield, M. B. Trueblood, and J. Podzimek, 1990: Measurements of upper-tropospheric aerosol characteristics: Implications for cirrus clouds. *Proc. Conf. on Cloud Physics,* San Francisco, CA, Amer. Meteor. Soc. 475–478.

——, M. B. Trueblood, and P. D. Whitefield, 1992: A field sampling of jet exhaust aerosols. *Particulate Sci. & Technol.*, **10,** 53–63.

Heymsfield, A. J., and R. M. Sabin, 1989: Cirrus crystal nucleation by homogeneous freezing of solution droplets. *J. Atmos. Sci.*, **46,** 2252–2264.

Hofmann, D. J., and J. Soloman, 1989: Ozone destruction through heterogeneous chemistry following the eruption of El Chichon. *J. Geophys. Res.*, **94,** 5029–5041.

Jensen, E. G., and O. B. Toon, 1992: The potential effects of volcanic aerosols on cirrus cloud microphysics. *Geophys. Res. Lett.*, **19,** 1759–1762.

Kent, G. S., M. P. McCormick, and S. K. Schaffner, 1991: Global optical climatology of the free tropospheric aerosol from 1.0-μm satellite occultation measurements. *J. Geophys. Res.*, **96,** 5249–5267.

Keyser, D., and M. A. Shapiro, 1986: A review of the structure and dynamics of upper-level frontal zones. *Mon. Wea. Rev.*, **114,** 452–499.

Liou, K. N., 1986: Influence of cirrus clouds on weather and climate processes: A global perspective. *Mon. Wea. Rev.*, **114,** 1167–1199.

Martin, J. E., J. D. Locatelli, and P. V. Hobbs, 1993: Organization and structure of clouds and precipitation on the Mid-Atlantic coast of the United States. Part VI: The synoptic evolution of a deep tropospheric frontal circulation and attendant cyclogensis. *Mon. Wea. Rev.*, **121,** 1299–1316.

Mattocks, C., and R. Bleck, 1986: Jet streak dynamics and geostrophic adjustment processes during the initial stages of lee cyclogensis. *Mon. Wea. Rev.*, **114,** 2033–2056.

Minnis, P., E. F. Harrison, L. L. Stowe, G. G. Gibson, F. M. Denn, D. R. Doelling, and W. L. Smith Jr., 1993: Radiative climate forcing by the Mount Pinatubo eruption. *Science,* **259,** 1411–1415.

Mohnen, V. A., 1990: Stratospheric ion and aerosol chemistry and possible links with cirrus cloud microphysics: A critical assessment. *J. Atmos. Sci.*, **47,** 1933–1948.

Platt, C. M. R., J. C. Scott, and A. C. Dilley, 1987: Remote sounding of high clouds. Part VI: Optical properties of midlatitude and tropical cirrus. *J. Atmos. Sci.*, **44,** 729–747.

Post, M. J., 1986: Atmospheric purging of El Chichón debris. *J. Geophys. Res.*, **91,** 5222–5228.

——, C. J. Grund, A. O. Langford, and M. H. Proffitt, 1992: Observations of Pinatubo ejecta over Boulder, Colorado, by lidars of three different wavelengths. *Geophys. Res. Lett.*, **19,** 195–198.

Reiter, E. R., 1972: *Atmospheric Transport Processes, Part 3: Hydrodynamic Tracers.* U.S. Atomic Energy Commission Critical Review Series, USAEC Report TID-24868, 212 pp. [NTIS TID-25731.]

Rodriguez, J. M., M. K. W. Ko, N. D. Sze, and C. W. Heisey, 1994: Ozone response to enhanced heterogeneous processing after the eruption of Mt. Pinatubo. *Geophy. Res. Lett.*, **21,** 209–212.

Rubel, G. O., and J. W. Gentry, 1985: Onset of particle crystallization resulting from acid droplet ammonia gas reactions. *J. Aerosol Sci.*, **18,** 23–27.

Sassen, K., 1991: Corona-producing cirrus cloud properties derived from polarization lidar and photographic analyses. *Appl. Opt.*, **30,** 3421–3428.

——, 1992: Evidence for liquid-phase cirrus cloud formation from volcanic aerosols: Climatic implications. *Science,* **257,** 516–519.

——, and G. C. Dodd, 1989: Haze particle nucleation simulations in cirrus clouds and applications for numerical and lidar studies. *J. Atmos. Sci.*, **46,** 3005–3014.

——, and J. D. Horel, 1990: Polarization lidar and synoptic analyses of an unusual volcanic aerosol cloud. *J. Atmos. Sci.*, **47,** 2881–2889.

——, H. Zhao, and B.-K. Yu, 1989: Backscatter laser depolarization studies of simulated stratospheric aerosols: Crystallized sulfuric acid droplets. *Appl. Opt.*, **28,** 3024–3029.

——, C. J. Grund, J. Spinhirne, M. Hardesty, and J. M. Alvarez, 1990: The 27–28 October 1986 FIRE IFO cirrus case study: A five lidar overview of cloud structure and evolution. *Mon. Wea. Rev.*, **118,** 2288–2311.

Schiffer, R. A., and W. B. Rossow, 1983: The International Satellite Cloud Climatology Project (ISCCP): The first project of the World Climate Research Programme. *Bull. Amer. Meteor. Soc.*, **64,** 779–784.

Shapiro, M. A., 1976: The role of turbulent heat flux in the generation of potential vorticity in the vicinity of upper-level jet stream systems. *Mon. Wea. Rev.*, **104,** 892–906.

——, R. C. Schnell, F. P. Parungo, S. J. Oltmans, and B. A. Bodhaine, 1984: El Chichón volcanic debris in an Arctic tropopause fold. *Geophys. Res. Lett.*, **11,** 421–424.

Starr, D. O'C., and S. K. Cox, 1988: Cirrus clouds. Part II: Numerical experiments on the formation and maintenance of cirrus. *J. Atmos. Sci.*, **42,** 2682–2694.

Whiteman, D. N., S. H. Melfi, and R. A. Ferrare, 1992: Raman lidar system for the measurement of water vapor and aerosols in the earth's atmosphere. *Appl. Opt.*, **31,** 3068–3082.

Whitney, L. F., Jr., A. Timchalk, and T. I. Gray Jr. 1966: On locating jet streams from TIROS photographs. *Mon. Wea. Rev.*, **94,** 127–138.

Yamato, M., and A. Ono, 1989: Chemical and physical properties of stratospheric aerosol particles in the vicinity of tropopause folding. *J. Meteor. Soc. Japan,* **67,** 147–165.

Reprinted from MONTHLY WEATHER REVIEW, Vol. 118, No. 11, November 1990
American Meteorological Society

The 27–28 October 1986 FIRE IFO Cirrus Case Study: Cloud Optical Properties Determined by High Spectral Resolution Lidar

C. J. GRUND AND E. W. ELORANTA

University of Wisconsin–Madison, Department of Meteorology, Madison, Wisconsin

(Manuscript received 17 February 1989, in final form 12 June 1990)

ABSTRACT

During the FIRE cirrus IFO, the High Spectral Resolution Lidar (HSRL) was operated from a roof top site on the University of Wisconsin–Madison campus. Because the HSRL technique separately measures the molecular and cloud particle backscatter components of the lidar return, the optical thickness is determined independent of particle backscatter. This is accomplished by comparing the known molecular density distribution to the observed decrease in molecular backscatter signal with altitude. The particle to molecular backscatter ratio yields calibrated measurements of backscatter cross section that can be plotted to reveal cloud morphology without distortion due to attenuation. Changes in cloud particle size shape and phase affect the backscatter to extinction ratio (backscatter-phase function). The HSRL independently measures cloud particle backscatter phase function. This paper presents a quantitative analysis of the HSRL cirrus cloud data acquired over an ~33 hour period of continuous near-zenith observations. Correlations between small-scale wind structure and cirrus cloud morphology have been observed. These correlations can bias the range averaging inherent in wind profiling lidars of modest vertical resolution, leading to increased measurement errors at cirrus altitudes. Extended periods of low intensity backscatter were noted between more strongly organized cirrus cloud activity. Optical thicknesses ranging from 0.01–1.4, backscatter-phase functions between 0.02–0.065 sr^{-1}, and backscatter cross sections spanning 4 orders of magnitude were observed. The altitude relationship between cloud top and bottom boundaries and the cloud optical center altitude was dependent on the type of formation observed. Cirrus features were observed with characteristic wind drift estimated horizontal sizes of 5 km–400 km. The clouds frequently exhibited cellular structure with vertical to horizontal dimension ratios of 1:5–1:1.

1. Introduction

Determinations of the optical properties, structure, and the vertical and horizontal extent of cirrus clouds have broad applications in remote sensing and the atmospheric sciences. Cirrus clouds reflect incoming solar radiation and trap outgoing terrestrial radiation; thus, the global energy balance depends upon the optical and morphological characteristics of these clouds. Scattering and absorption by cirrus clouds affect measurements made by many satellite-borne and ground-based remote sensors. Scattering of ambient light by the cloud, and thermal emissions from the cloud, can increase measurement background noise. Multiple scattering processes can adversely affect the divergence of optical beams propagating through these clouds.

Predicting the effects of greenhouse gasses, aerosols, albedo changes, and solar fluctuations on climate requires the development of models that accurately account for the highly variable, nonlinear influence of clouds on radiative balance. Models of the feedback mechanisms between cirrus clouds and earth's climate can be tested and improved by studying time series of cloud formation, maintenance, and dissipation processes. Good models require good initialization data and must generate realistic cloud radiative properties. Spatial and temporal histories of the optical and morphological characteristics of real clouds are required to fulfill these needs.

Because of its precise ranging capabilities, spatial resolution, and sensitivity, lidar has played an important role in the detection, depiction, and characterization of cirrus clouds (Evans et al. 1966; Platt et al. 1987; Sassen et al. 1990), and for the verification of cloud heights derived from satellite-borne sensor measurements (Wylie and Menzel 1989). Lidar systems that make one measurement at each range can adequately determine backscatter intensity distributions for optically thin clouds; however, they cannot independently determine absolute optical quantities. As optical thickness increases, simple plots of lidar backscatter intensity may produce a distorted representation of cloud morphology, and can produce serious errors in cloud altitude determinations. This is because the lidar return signal from any range depends on both the backscatter cross section and the optical depth to that range. Single-channel lidar systems may not separately measure backscatter and extinction. In order to pro-

Corresponding author address: Dr. Christian J. Grund, Department of Meteorology, University of Wisconsin–Madison, Madison, WI 53706.

duce calibrated measurements, single-channel lidar retrieval techniques must be constrained by additional information or assumptions about the optical properties or distribution of the scatterers (Spinhirne et al. 1980; Klett 1981; Weinman 1984; Eloranta and Forrest 1986). Direct measurements require the determination of a signal intensity calibration at each range.

The High Spectral Resolution Lidar (HSRL) has been specifically designed (Shipley et al. 1983; Sroga et al. 1983) to produce calibrated measurements of aerosol and cloud particle optical depth, extinction corrected cloud morphology, and backscatter phase function. The HSRL spectrally separates molecular backscatter from cloud particle and aerosol backscatter. This is possible because thermal agitation Doppler broadens the backscattered spectrum from molecules. Small aerosols and cloud particles that contribute significantly to the backscatter are more massive than molecules and thus exhibit slower Brownian drift velocities that produce insignificant broadening of the scattered spectrum. Using the known distribution of molecular scattering cross section to provide a calibration reference at every range, extinction is unambiguously determined from the observed range dependent decrease in molecular backscatter intensity. The ratio of measured aerosol to molecular backscatter intensity provides the aerosol backscatter cross section at each range. Because aerosol and gaseous absorption are negligible at the HSRL wavelength, the backscatter phase function can be directly measured. A more detailed description of the HSRL theory and the definitions of lidar measured quantities may be found in the Appendix.

HSRL measurements of cirrus cloud optical properties were first acquired (Grund 1987) during the FIRE Intensive Field Observations (Starr 1987). In this paper we discuss the application of the HSRL to cirrus cloud measurements and provide a comprehensive survey of the cirrus cloud optical properties determined during the case study period.

2. System characteristics

Using a multietalon pressure-tuned Fabry-Perot spectrometer, the HSRL simultaneously observes the lidar return in two channels. The spectrally narrow "aerosol channel," centered on the transmitted wavelength, is most sensitive to aerosol scattering and to the central region of the Doppler-broadened molecular spectrum. With a prominent notch in the center of its bandpass, the spectrally wider "molecular channel" accepts the entire Doppler-broadened molecular spectrum, while rejecting much of the aerosol scatter. Thus, the signal in each channel represents a different linear combination of the aerosol and molecular scattering contributions to the lidar return. Complete separation of the two channel signals requires the determination of a 2×2 matrix of inversion coefficients. The two coefficients, which represent the aerosol backscatter transfer function for each channel, are determined b diffusely filling the receiver telescope with attenuate laser light and observing the response of the two chan nel signals to a spectral scan of the receiver (Grun 1987). The coefficients that represent the molecula backscatter transfer function for each channel are cal culated from the calibration scan convoluted with model of the molecular backscatter spectrum (Yip an Nelkin 1964), corrected for temperature and pressur at each altitude. Table 1 summarizes the HSRL syster characteristics at the time the case study data was ac quired.

Data acquisition and control of the multietalo spectrometer and scanning mirror system are accom plished by a DEC 11/73 computer running a multiuse operating system. Real time and time-averaged displa of range square and log corrected data is provided b an in A-scope. Data are acquired in 4 second "shots of 32 000 accumulated, range-resolved lidar profile Each shot is written to magnetic tape for later pro cessing.

The tapes are subsequently written to a 2.6 gigabyt capacity write once optical disk, which facilitates re peated access to individual segments of large dataset Calibration and data analysis are performed on a VA 11/751 computer, which has on-line image display an graphics capability.

TABLE 1. Summary of HSRL operating parameters during th 1986 FIRE cirrus IFO. Because of the narrow spectral bandwidt narrow field of view, high repetition rate, and photon counting de tection scheme, the HSRL was capable of measuring cirrus clou optical properties under day or night conditions, while maintainir eye-safe operations.

	HSRL Receiver	
Telescope:	Primary diameter	.35 m
	Secondary diameter	.114 m
	Focal length	3.85 m
	F.O.V. (full width)	320 mR
Interference filter:	FWHM	1 nm at 510.6 nm
Pre-filter etalons:	Plate diameter	50 mm
	Etalon spacers	1.003, .726 mm
	Combined FWHM	2.5 pm
High resolution etalon:	Plate diameter	150 mm
	Etalon spacer	12.786 mm
	Bandwidth (FWHM)	.6 pm
Signal detection:	Photon counting	>10 mHz
Photomultiplier tubes:	EMI Gencom 9863B/100	low afterpulsing
	HSRL Transmitter	
	Laser, Wavelength	$CuCl_2$, 510.6 nm
	Transmitted beam diameter	30 mm
	Transmitted power	50 mW at 510.6 n
	Bandwidth (FWHM)	.4 pm
	Pulse repetition rate	8 kHz
	Pulse length	15 ns

3. Data analysis

In order to facilitate interpretation of the HSRL measurements by a varied community of cirrus researchers, we have chosen two forms for the representation of our data for this case study. The first, grey-scale imagery of the uninverted "aerosol channel" backscatter intensity, has the advantage of higher temporal resolution, but lacks a calibrated correction for extinction with range. The second data representation format, as contour plots of calibrated backscatter cross section, reveals the true distribution of backscattered intensity, but lacks the ability to depict the fine structural detail of the cirrus clouds. This resolution limitation was imposed by the low average power of the laser transmitter that necessitated time averaging to mitigate the effects of statistical noise in the inverted signals. We have chosen to reserve detailed calibrated analysis for this paper while presenting the more qualitative grey-scale imagery in the companion lidar intercomparison paper (Sassen et al. 1990).

Although the HSRL was primarily designed for the measurement of boundary layer aerosol properties, it has been successfully adapted to the task of cirrus cloud characterization (Grund 1987). Several difficulties arise when assessing cirrus cloud optical properties with the HSRL:

a) the signals are reduced by the additional range to the cirrus clouds (up to 15 km at zenith in midlatitudes);

b) the molecular scattering intensity is reduced by the lower air density at cirrus altitudes;

c) low temperatures at cirrus altitudes decrease the Doppler width of the scattered molecular spectrum making accurate separation from the unbroadened particulate scattering more difficult;

d) cloud backscatter intensities can be very large compared to molecular scattering thus requiring extreme accuracy (~0.1%) in the determination of the inversion coefficients; and

e) during daylight operations cirrus clouds scatter sunlight into the receiver field of view, increasing the background-light-induced noise. Aerosol scattering cross sections observed in previous operations rarely achieved even thin cirrus scattering cross section values.

To combat these problems, and still maintain reasonable calibration accuracy, time resolution, and measurement linearity, the following data processing algorithm has been applied:

a) A series of inverted molecular and aerosol profiles is generated with ~4 s time resolution. Because drifts in the system bandpass and receiver-transmitter tuning have nonlinear effects on the relative transmission of the receiver channels, a new set of separation coefficients is chosen for each of these profiles by the following method:

1) A synthetic calibration scan is produced for each shot by a linear interpolation in time between the adjacent calibration scans.
2) The spectral offset between the center of the receiver bandpass and the transmitted wavelength is estimated from observations of the ratio of the aerosol to molecular channel signals under uniform aperture illumination with transmitted laser light. This ratio is measured at ~2 min intervals during operations. The ratio is estimated for each shot time by an interpolating spline fit to the observations. Since the receiver–transmitter may exhibit relative drift of either sign, and the bandpass characteristics have a slight asymmetry, the sense of the tuning offset is assumed to be the same as the overall drift observed between the preceding and subsequent calibration scans. With the tuning drift determined, the inversion coefficients are calculated from the synthetic calibration scan and a model of the molecular scattering spectrum that includes the effects of Brillouin scattering.

b) Because the temporal and spatial distribution of extinction is highly variable in cirrus clouds, statistical fluctuations in lidar signals cannot be reduced by straight forward block averaging of profiles. The reason for this is evident in Eq. (A1). Because the signal from each range depends on an exponential term that varies from profile to profile, simple sums will exhibit a range dependent bias toward the shots with least attenuation (Milton and Woods 1987). To minimize this effect, inverted shots are initially summed only to the extent that the backscatter profile can be qualitatively discerned from noise (typically ~30 s). Subjective groups of these intermediate sums are formed by adding range resolved profiles together, as long as the backscatter profiles do not *appear* markedly different. Optical properties are determined from each of these grouped profiles, then combined in a time-weighted average to achieve the reported time resolution.

c) In calculating the optical properties, the inverted molecular signal has not been applied directly within the cirrus clouds. Instead, the HSRL molecular channel signal has been smoothed according to the following algorithm:

1) Regions dominated by Rayleigh scattering are determined both above and below the cloud (this is possible because first-cut HSRL backscatter cross section profiles clearly indicate regions of enhanced particulate scatter, even in the presence of a small cross-talk term).

2) In these regions, a least squares fit is produced from the observed separated molecular signal to the expected profile for a pure molecular scattering atmosphere calculated from a radiosonde profile of pressure and temperature. This is acceptable since the extinction contribution from particles is small and most

of the signal slope in the separated molecular profile is associated with the known decrease in density with height.

3) The clear-air observed signals are replaced with the smooth best fit estimates above and below the cloud.

4) The cloud optical thickness is determined from the decrease in the best fit molecular signal across the cloud determined in step 3, while accounting for the expected decrease in molecular cross section with altitude.

5) The vertical profile of extinction within the cloud is calculated from the separated particulate backscatter profile using a Bernoulli solution constrained by the optical thickness determined in step 4 and the assumption of a constant backscatter to extinction ratio. The Bernoulli technique is employed in this solution to reduce the logarithmic range derivative of the lidar Eq. (A1) to a first order equation which can be solved explicitly for the extinction profile, given the total optical thickness and an assumed power law relationship between backscatter and extinction (Weinman 1988).

6) The in-cloud molecular backscatter signal is replaced with a smooth estimate calculated from the extinction profile determined in step 5 and the known altitude distribution of the molecular scattering cross section $\beta_m(R)$ [see Eq. (A3)]. In this way, noise is removed from the molecular scattering profile, while the spatial distribution of extinction is closely maintained. Backscatter cross sections [Eq. (A5)] are calculated using this estimate of $P_m(R)$.

7) Backscatter phase functions are reported as bulk quantities calculated over the entire depth of cloud because the Bernoulli solution employed to mitigate the effects of noise assumes the backscatter to extinction ratio is constant.

Penetration of clouds, hence cloud-top altitudes, are assured in HSRL data by the presence of molecular backscatter signal from above the cloud. Molecular signal was clearly evident within the reported time resolutions throughout this case study period, suggesting confidence in the cloud-top altitudes indicated at the level of the minimum plotted backscatter cross section contours. Errors in optical thickness and backscatter phase function were determined by estimating the effects of photon counting statistics on both the range resolved signals and the uncorrelated background signal according to the methods detailed in Grund (1987).

Cirrus can sometimes form plate-like crystals that fall flat-face-down because of aerodynamics. Consequently, the HSRL was operated 3°–5° from zenith in order to minimize the impact of specular backscatter on the measurements of backscatter phase function and backscatter cross section. Specular backscatter enhancements by a factor of at least 13 have been observed, and larger enhancements seem possible. The e^{-1} full width of the forward scatter diffraction peak was ~1.5° (at 1.06 μm) suggesting a minimum crystal diameter of ~50 μm. Fortunately, at our operating wavelength, Ci size parameters are fairly large. This reduces the angular width of the diffraction peak so that the enhanced backscatter drops off rapidly with declination from zenith.

4. Lidar derived optical properties

Several periods of cirrus exhibiting differing optical and morphological characteristics were observed during the case study period. We will begin with a discussion of optically thin subvisual cirrus, proceed to a quantitative description of a mesoscale uncinus complex, continue with a comparison of altocumulus and ice cloud scattering properties, and conclude with the characterization of the optically thicker cirrus layer. Throughout this discussion we will refer to the optical properties defined in the Appendix. In addition, the reported optical thicknesses (τ) have had the effects of molecular extinction removed so that they represent only the attenuation due to particle scattering. Likewise, backscatter cross sections represent aerosol scattering quantities without molecular scattering contributions, and will be denoted $\beta_{a\pi}/4\pi$. Because we frequently observe correlations between small-scale wind features and lidar backscatter, isotachs are included on each backscatter cross section plot for reference. For a pictorial overview of the HSRL observations, the reader is directed to the lidar intercomparison paper elsewhere in this volume (Sassen et al. 1990).

a. Subvisible and background cirrus

The occurrence of *subvisible* cirrus has been a topic of interest in the last few years because of the potential effects on IR wavelength remote sensors. In addition to the attenuation provided by the cloud, thermal emissions from the cloud and ambient light scattered by the cloud can contribute to measurement background noise. Even tenuous clouds can develop significant optical thickness when probed by shallow angle or horizontally viewing long range sensors. In addition, low-level aerosol backscatter can complicate the retrieval of optical depth from simple lidar observations because calibrations often rely upon the determination of regions characterized by pure molecular scattering. Cloud visibility is a complicated property that depends on many factors including contrast, discernible structure, and sun angle in addition to optical thickness. However, in this paper, we will adopt the convention of Sassen et al. (1989) and consider clouds with a zenith angle $\tau \leq 0.03$ as subvisible. Within this case study period, several subvisible clouds were observed by the HSRL.

Figure 1 shows a contour plot of the $\beta_{a\pi}/4\pi$ of an isolated subvisible cirrus cloud. The contour interval

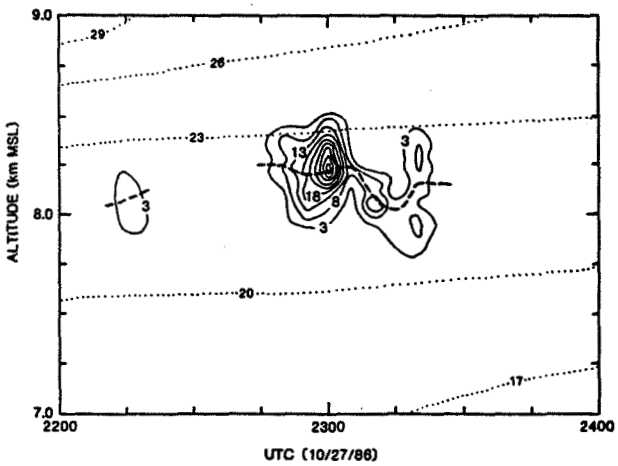

FIG. 1. Contour plot of the backscatter cross section (10^{-4} km^{-1} sr^{-1} in solid line) of a subvisible cirrus cloud. The dashed line indicates the optical midcloud height (see text). The average optical thickness of this cloud between 2245 and 2320 UTC was 0.03 with an average bulk backscatter phase function of 0.028 sr^{-1}. Isotachs (dotted line) are plotted in m s^{-1} from the Fort McCoy radiosondes launched at 2100 and 0000 UTC.

is 5.0 $(10)^{-4}$ km^{-1} sr^{-1} starting from 3.0 $(10)^{-4}$ km^{-1} sr^{-1}. The dashed line marks the optical midaltitude of the cloud; half the cloud optical depth is accumulated to either side of this line. This height was determined from the Bernoulli solution for the in-cloud extinction profile. The maximum value of $\beta_{a\pi}/4\pi$ measured in this cloud was 4.1 $(10)^{-3}$ km^{-1} sr^{-1} at 2301 UTC. Assuming negligible temporal evolution, translation with the 25 m s^{-1} ambient wind suggests a horizontal extent of ~60 km for this cloud. When the 2245–2322 data are averaged together, the mean optical thickness for this cloud was determined to be 0.03 ± 0.006. The bulk-average backscatter phase function for this cloud was found to be 0.028 ± 0.007 sr^{-1}. Backscatter intensification near 2300, 2310, and 2320 at ~8 km suggests this cirrus cloud was composed of ~5 km wide shallow cells or bands spaced ~20 km apart, imbedded in a less dense background cloud.

On two occasions during the case study, we have observed extended periods of enhanced backscatter with little apparent structure. Because the HSRL technique does not distinguish between backscatter from small aerosols (e.g., dust, H_2SO_4 droplets, etc.) and backscatter from cloud particles, we cannot be certain that these subvisible background veils are cirrus; however, because more dense cirrus are observed at the subvisible veil altitudes both before and after these observations, these features appear to be at least associated with cirrus. Regardless of particle identification, the existence of extended regions of elevated scatter at these altitudes have similar impacts on radiative balance and the operation of remote sensors.

A persistent region of enhanced backscatter of this type is evident in Fig. 2 from 8.5–13.8 km, and a two layer formation apparent in Fig. 3 between 7.0 and 13.8 km. Because of the small backscatter signals from these clouds, the range resolution has been degraded to ~900 m and temporal resolution has been reduced to 30–60 minutes. In higher time and spatial resolution images of the raw lidar data, these veils seem to be rather stable and are not seen to exhibit the cellular structure present in the subvisible cirrus of the type shown in Fig. 1. It is clear from these data that average backscatter cross sections of <1 $(10)^{-4}$ km^{-1} sr^{-1} can exist over extended regions even when structured clouds are not detected. Evidently, there must be several mechanisms for the generation and maintenance of subvisible clouds.

Because radiosonde humidity measurements do not often extend above ~10 km and are frequently unreliable at these altitudes, it is difficult to suggest particle composition from the availability of moisture for the formation of ice particles in these clouds. However, radiosondes launched from Platteville at 0000 and 0300 show consistently moist (RH with respect to ice >70%) regions from 8.8 km–9.5 km and 8.2 km–10.0 km, respectively. The 0900 and 1200 soundings indicated moist layers 7.2 km–10.2 km and 6.6 km–10.1 km, respectively, both with maxima RH with respect to ice in excess of 100%.

Between 0000 and 0400, the subvisible cloud exhibited an average optical thickness of 0.01 ± 0.004. From 0920 to 1140 the average optical thickness was 0.003 ± 0.002. Wind-drift estimates of the size of the features

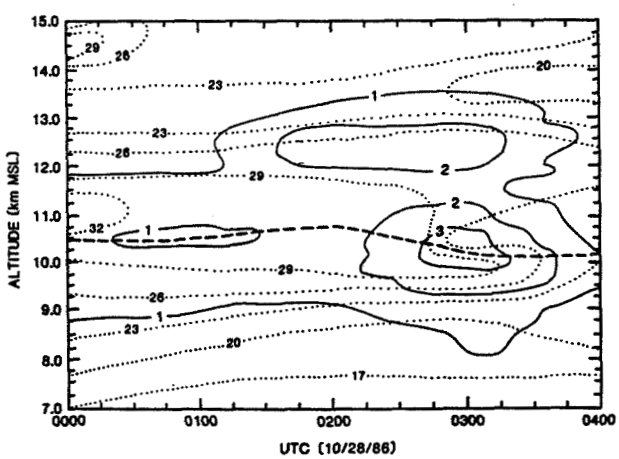

FIG. 2. Background veils of enhanced particle backscatter are frequently observed at cirrus altitudes. The average optical thickness of this layer was ~0.01. Backscatter cross section contours (solid line) are in units of 10^{-4} km^{-1} sr^{-1}, optical midcloud heights are plotted in dashed line, and isotachs are plotted in dotted line in m s^{-1} from the Fort McCoy radiosondes launched at 0000, 0300 and 0900 UTC (the 0600 radiosonde was not launched). Note the correlation between wind speed and backscatter cross section contour patterns. Correlations between wind velocity and backscatter distribution (e.g., 1000 UTC between 9 and 10.5 km) can bias wind profiles acquired from future space based Doppler lidars with insufficient vertical resolution (see text).

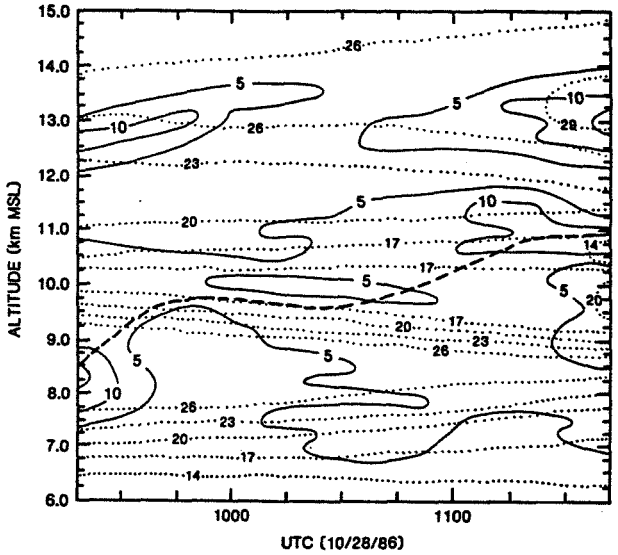

FIG. 3. A two-layer region of enhanced backscatter. Backscatter cross section contours (solid line) are in units of 10^{-5} km^{-1} sr^{-1}, optical midcloud heights are plotted in dashed line, and wind speeds are plotted in dotted line in m s^{-1} from the Fort McCoy radiosondes launched at 0900 and 1200 UTC. Backscatter cross section values are ~half of those shown in Fig. 2, and although the wind profiles are quite different, correlations between wind and backscatter are still evident.

depicted in Figs. 2 and 3 suggest that they extend for more than 400 km and 180 km, respectively. One implication of such large-scale optically thin clouds is that remote sensors attempting to view horizontally within such layers could easily encounter significant optical thickness, even though the cloud may not produce a visual manifestation. Another implication of such extensive cloud blankets is they can alter earth's radiative balance, if present on a global scale, while going undetected by space-borne passive remote sensors.

Isotachs plotted in Fig. 2 show a general correlation between wind speed maxima and backscatter cross section contours. Note the 26 and 29 m s^{-1} contours closely follow the pattern of backscatter cross section distribution. These apparent pattern correlations have been observed in several cases, though a consistent set of correlation characteristics has not been established. It is not clear whether the sheer is part of the cirrus generation mechanism or if cirrus formation and winds are both responding to the same environmental forcing.

Because wind-profiling Doppler lidars rely on backscatter from naturally occurring aerosols, correlations between wind sheer and the distribution of backscatter can bias vertically-averaged wind measurements of insufficient range resolution. As an example, a wind profiling lidar observing the 0200 profile between 7.5 and 14.5 km with 1 km resolution would produce an rms wind speed error of ~0.4 m s^{-1} due solely to range averaging with the maximum error of −1.2 m s^{-1} occurring at 9.8 km. When weighted by the backscatter cross section at each range, the 1 km averaged wind speed estimates produced rms errors exceeding 0.8 m s^{-1} with a peak error of 2.4 m s^{-1} at 8.6 km.

Figure 3 shows another example of a strong correlation between wind sheer and backscatter cross section. Note the packing of isotachs between 9.5 and 10.5 km coincident with the thin cloud region at 1000 UTC. When subjected to the above wind profiling lidar analysis, this data produced rms errors of ~0.5 m s^{-1} with a peak error of 1.7 m s^{-1} at 9.8 km due solely to the 1 km range averaging of the wind speeds between 6.5 and 14.5 km. Backscatter weighting of the range average produced an rms wind speed error of ~1.0 m s^{-1} with a peak error of −4.1 m s^{-1} at 9.0 km. A study of the effects of velocity-backscatter correlations and resolution specifications on wind profiling lidar measurements is reported in Grund et al. (1990).

b. Mesoscale uncinus complex (MUC)

Figure 4 presents a contour map of the absolute backscatter cross section from a mesoscale uncinus complex (MUC) observed between 0500 and 0900 UTC 28 October. For the basic structural description and a pictorial view of the relative backscatter from this mesoscale uncinus complex refer to Sassen et al. (1990). A series of uncinus generating cells is evident between 9.5 and 11.0 km, particularly between 0530 and 0700. Each of these cells is about 150 m thick. Cloud translation with the 10 km wind (20 ± 10 m s^{-1}) would suggest the cells are ~4–12 km across; thus, they have a height to width aspect ratio in the range ~1:50–1:180. Averaging times of ~12 minutes were chosen for each profile in this cross section so that ex-

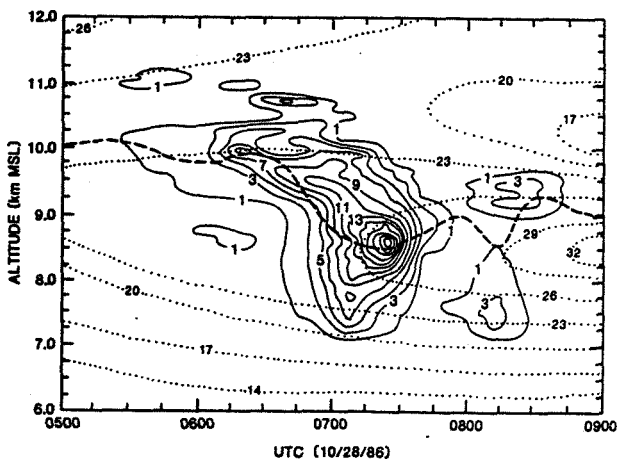

FIG. 4. Cr. : backscatter cross section (10^{-3} km^{-1} sr^{-1}, ——) and optical midcloud height (– – –) of a mesoscale uncinus complex. The average optical thickness of this system be.. .... 0600 and 0750 UTC was 0.58 ± 0.05 which varied from 0.09 ± 0.03 at 0750 U TC to 1.1 ± 0.3 at 0718 UTC. The bulk backscatter phase function averaged over the same time period was 0.042 ± 0.015 sr^{-1}. The MUC passed over Madison just ahead of a mesoscale wind jet. Again note the apparent association of wind speed (m s^{-1}, · · · · ·) with cirrus morphology. Isotachs were determined from the Fort McCoy radiosondes launched at 0300 and 0900 UTC.

pected signal-noise-induced errors in the average cloud-backscatter cross section were limited to ±15%. The maximum $\beta_{a\pi}/4\pi$ for this MUC was determined to be 0.024 km^{-1} sr^{-1} at 0722 near 8.7 km altitude, preceding the passage of a wind jet maximum of ~34 m s^{-1}. Both the Ft. McCoy and Platteville soundings at 0300 and 0900 (0600 was not acquired) indicate the regions above 7.4 km were consistently moist (>70% RH with respect to ice) and occasionally reached supersaturation as high as ~108% with respect to ice. The radiosonde profiles also show an abrupt decrease in relative humidity below 7.4 km suggesting the steep contour gradient at 0700 at 7.2 km altitude is related to rapid ice crystal evaporation in the dry environment beneath the complex. Analysis of the profiles averaged over the 0600–0750 period indicates this system had a mean optical thickness of 0.58 ± 0.05, which varied from 0.09 ± 0.03 at 0750 to 1.1 ± 0.3 at 0718. The bulk backscatter phase function averaged over the same time period was 0.042 ± 0.015 sr^{-1}.

Figures 5, 6, and 7 are the 0600, 0700, and 0800 GOES IR images covering the IFO study area that show the MUC passing directly over Madison (stationary white-on-black square in south–central Wisconsin). The relatively bright (cold) complex is embedded in a less intense eastward moving cloud band that extends ~NW–SE from a more extensive cloud shield covering northern Wisconsin. Cloud image tracking indicates the band is moving eastward at ~23 m s^{-1}, close to the wind-drift velocity at cirrus altitudes. The complex seems to be propagating southeastward as the band moves east. Radiosonde data show the 8.5 km wind backing from ~300° to ~270° as the complex passes; however, the winds show a slight but consistent veering with height above 8 km throughout this period. Figure 4 indicates the most optically dense cloud regions were near 8.5 km. Thus, the apparent southeastward propagation of the complex seems to be a displacement of the MUC generating region along the west wind-driven cloud band, rather than a translation of the complex with the ambient wind.

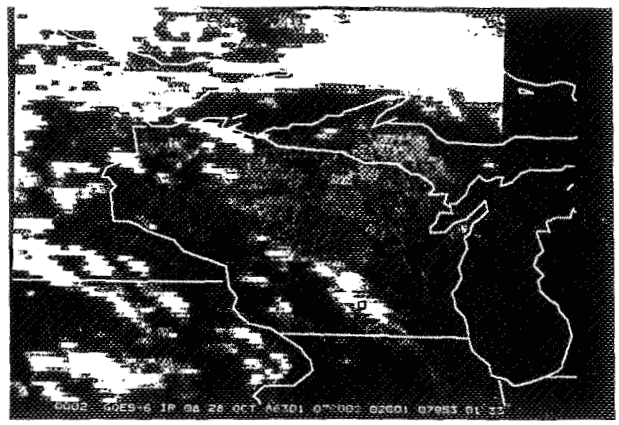

FIG. 6. The 0700 UTC GOES IR image shows the mesoscale uncinus complex (MUC) passing directly over the lidar site as it propagates southeastward along the eastward moving cloud band. The lidar time height cross section through the cloud band and MUC as it passed overhead was shown in Fig. 4.

Isotachs, interpreted from the 0300 and 0900 Ft. McCoy radiosonde data, show an apparent relationship between wind speeds and the MUC backscatter cross section distribution. Note the close proximity in time and altitude between the wind speed maximum and the backscatter cross section maximum. Also note that the cloud bottom occurs where the time height cross section indicates relatively steady winds. Further, the decrease in cloud top altitude seems to be related to the development of a wind minimum at 10.5 km. The jet and the wind minimum are of smaller scale than

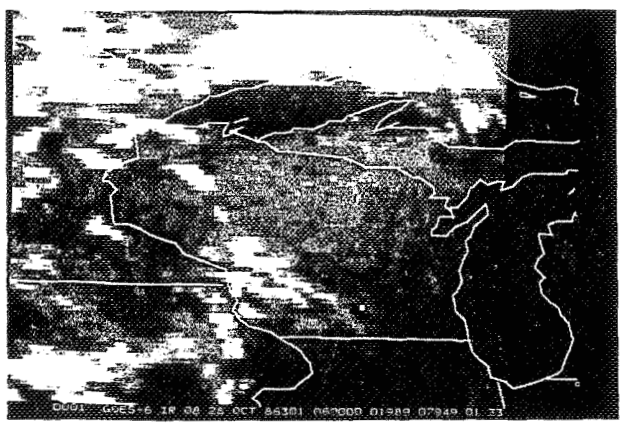

FIG. 5. The 0600 UTC GOES IR image showing the cirrus cloud band over Madison (white pixel in south–central Wisconsin) extending NW to SE from a larger cirrus shield covering northern WI. The relatively bright cloud regions just to the NW of Madison moved rapidly to the SE along the cloud band over the next two hours (see Fig. 6).

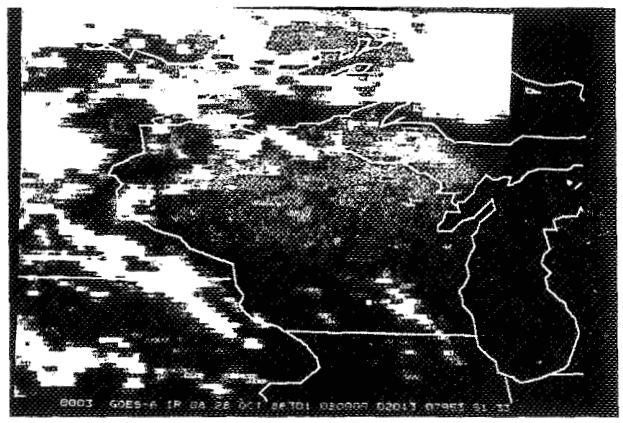

FIG. 7. The 0800 UTC GOES IR image shows the apparent dissipation of the MUC as it continues to propagate to the SE along the cloud band. The lidar (see Fig. 4) shows the backscatter structure of the cloud band following the MUC. Displacement estimates from Figs. 5–7 suggest the cloud band is moving eastward at ~23 m s^{-1}, in agreement with rawinsonde-determined winds at the lidar-determined cirrus altitudes.

the FIRE IFO radiosonde network. They appear strongly only in the Ft. McCoy soundings, and are just discernible in the Platteville sounding data; thus, no attempt has been made to interpolate the radiosonde data to Madison observation times. Future observations of this type would benefit from a more dense temporal and spatial net of wind observations.

The MUC observations also demonstrate the limitations inherent in interpreting cirrus cloud morphology strictly from zenith time height cross section measurements. If the wind sheer is deduced from the apparent slope of the virga trails, the wind maximum would be expected near the upper cloud level at ~10 km. In fact, the wind contours indicate the maximum of ~35 m s^{-1} near 8.5 km, decreasing to ~18 m s^{-1} at 10 km. Clearly, the time-height cross section of this complex does not represent a stationary phenomena translating with the ambient winds. Rather, in addition to translation, the clouds are undergoing significant evolution. Cloud genesis is probably related to circulations about the mesoscale jet, and the apparent shape of virga may be partially governed by the local distribution of moisture. Clearly, serious study of the morphology of such mesoscale phenomena can greatly benefit from the acquisition of real time three-dimensional lidar observations.

c. *Altocumulus versus cirrus*

From 1200 to 1500 UTC 28 October, a two-level cirrus–altocumulus formation was observed. Figure 8

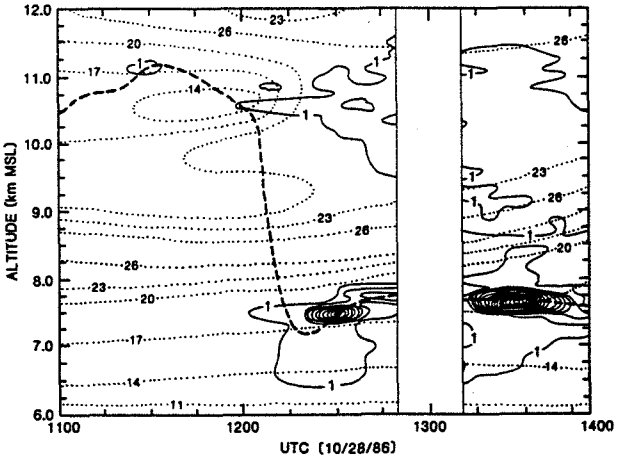

FIG. 8. Time height backscatter cross section (10^{-3} km^{-1} sr^{-1}, interval: 7 $(10)^{-3}$ km^{-1} sr^{-1}) of a two-layer cirrus formation with altocumulus embedded in the lower layer. The 1 $(10)^{-3}$ km^{-1} sr^{-1} contour near the ACu outlines what appears to be ice virga. The largest backscatter cross section observed during the case study (0.18 km^{-1} sr^{-1}) occurred ~1330 UTC at ~7.6 km. A table of localized backscatter phase function and optical thickness illustrating the differences in optical properties of ACu, ice virga, and the upper cloud layer may be found in Sassen et al. (1990). Isotachs are plotted in dotted line in m s^{-1} from the Forth McCoy radiosondes launched at 0900, 1200, and 1500 UTC.

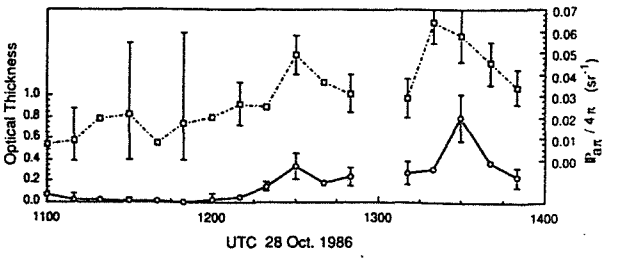

FIG. 9. Time history of the total cloud optical depth (——) and bulk normalized backscatter phase function (– · – ·, sr^{-1}) coincident with the backscatter cross sections plotted in Fig. 8. Ten minute averaging has been applied (see section 3) to smooth the data. The largest values of backscatter phase function values in this record coincide with the cirrus regions containing altocumulus cells.

highlights the dissimilarity in lidar backscatter between these cloud types. The lower layer cloud appears to be formed from a series of relatively dense altocumulus cells, each with a 0.5–1.0 km long ice crystal fallout tail. The identification of these clouds as ACu is inferred from an all-sky photograph taken at Wausau and the fact that similar cloud structure was observed at Ft. McCoy and Wausau lidar data around this time period (Sassen et al. 1990). Ice virga is inferred from the environmental temperature (−25° to −30°C) and from grey-scale images of lidar backscatter. Virga appears in these images as finely detailed striated sheets that deviate from vertical following the altitude profile of horizontal wind sheer. Translation with the wind speeds at 7.7 km would indicate the ACu were about 20 km across, yet they were ~200 m thick, producing a height to width ratio of only 1:100. As the ACu developed, Fig. 9 shows an increase in both the total cloud optical thickness and the backscatter phase function, while the optical midcloud altitude decreased from ~11 km to ~7.5 km. Note that the average cloud backscatter phase function peaks with the passage of each ACu cell. Because similar cloud features were also observed to produce little depolarization at Wausau and Ft. McCoy, we can infer, with some confidence, that the backscatter phase function peaks suggest these clouds are composed of supercooled spherical water droplets (see Sassen et al. 1990 for depolarization data and spatially localized backscatter phase functions).

The ACu bands at ~7.6 km produce significantly greater backscatter than either the 9–12 km cirrus or the lower level virga between 6.4 and 7.1 km. The $\beta_{a\pi}/4\pi$ maximum reached at 1419 exceeded 0.15 km^{-1} sr^{-1}, nearly an order of magnitude greater than the largest $\beta_{a\pi}/4\pi$ observed during this case study in any cirrus exhibiting significant vertical development. One reason for this is that ACu are primarily composed of supercooled liquid water droplets; because of optical surface wave phenomena, such droplets are more efficient at backscattering than nonspherical ice crystals. A second reason is that supercooled water droplets are necessarily quite small; whereas, once glaciation begins, cloud particles accumulate mass rapidly because of the

reduction of saturation vapor pressure with respect to ice. Hence, ice particle fall speeds rapidly exceed vertical atmospheric motion, and particle mass distributes over an extended column, decreasing the local backscatter intensity. The backscatter cross section will also diminish as growth processes redistribute water mass from many small particles to fewer but larger ice crystals with substantial fall speeds. This is because particle mass increases as the cube of the radius while the scattering cross section approximately follows the radius squared.

The ACu, when present, dominate the optical thickness profile. This effect is evident in the dramatic decrease of 4 km in the optical midcloud altitude between 1200 and 1215. Clearly, the occurrence of ACu can have significant impact on the radiative properties of the cloud independent of cloud top altitude and bottom altitudes.

d. Cirrostratus

From 1500 UTC 28 October to the end of the case study period, the cirrus observed over Madison assumed a distinct pattern of vertically developed cells with regions of enhanced backscatter appearing near both cloud top and cloud bottom (see Fig. 10). The vertical elongation of backscatter cross section contours suggests an upward and/or downward redistribution of cloud particles. The top and bottom cellular morphology of this layer is most evident ~1610 where an apparent generating region near cloud top produces a

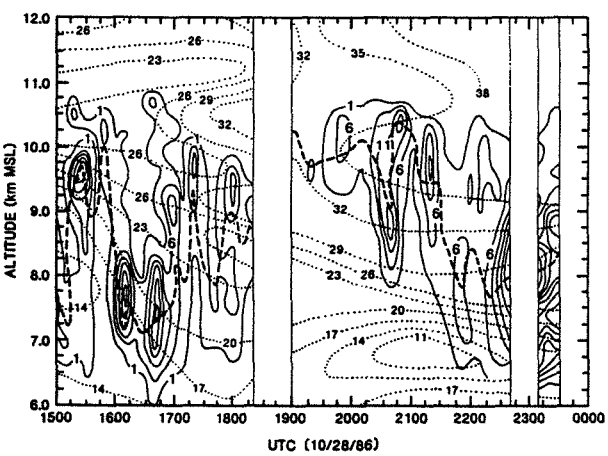

FIG. 10. From 1500 UTC until operations were terminated, a cirrostratus layer was observed over Madison which contained a distinct pattern of vertically developed cells evident in this time height backscatter cross section (10^{-3} km^{-1} sr^{-1}, ——) profile. Regions of intensified backscatter are found near both cloud top and cloud bottom. The optical midcloud height (- - -) tends to follow these regions independent of cloud top and bottom altitudes. The relatively cloud free period ~1900 UTC corresponds to the clear arc region noted in satellite imagery by Starr and Wylie (1990). Isotachs (· · · · ·) are plotted in m s^{-1} determined by radiosondes launched from Ft. McCoy at 1500, 1800, 2100, and 2400 UTC.

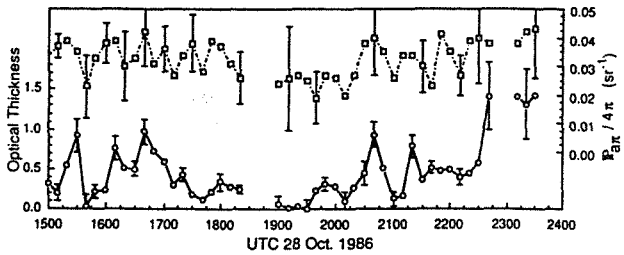

FIG. 11. Time history of the total cloud optical depth (——) and bulk normalized backscatter phase function (- · - · -, sr^{-1}) coincident with the backscatter cross sections plotted in Fig. 10. Peaks in the backscatter phase function tend to coincide with apparent generating regions while minima tend to occur between cells independent of cloud optical thickness suggesting different particle microphysics for the two regimes.

virga trail that extends to, and perhaps seeds, a second region of strong backscatter near ~7.5 km. The lower regions (at 1610 and 1640) also appear to be precipitating as evidenced by the vertical elongation of the cloud bottom backscatter cross section contours. Note that the midcloud altitude follows regions of enhanced backscatter very closely and that there is no obvious relationship between the appearance of these regions and either cloud top or cloud bottom altitudes. Thus, the structures that dominate cloud optical properties are not necessarily indicated by either the cloud boundaries or the physical midcloud altitude.

With the exception of two short periods, near 1540 and 1915, the cirrus optical thickness exceeded 0.1 forming an apparent cirrostratus layer (see Fig. 11). The gap in cloud cover at ~1900 corresponds to the passage of the clear arc identified from satellite imagery in Starr and Wylie (1990). Note that the peaks in backscatter-phase function (~0.038 sr^{-1}) tend to coincide with the occurrence of the regions of enhanced backscatter cross section independent of total optical thickness, while the regions between the cells usually produce the minima in the backscatter phase function values of ~0.02–0.026 sr^{-1}. This suggests differences in the microphysical properties for the particles associated with the cells compared with those of the surrounding cloud. One explanation may be that the lower regions of enhanced backscatter are areas of cloud particle generation that may contain an abundance of small supercooled water droplets (temperature at 7.5 km: ~ −30°C; at 9.5: ~ −45°C). Although the generation mechanism is unclear, an abundance of exceedingly small particles could also account for the observed backscatter-phase function effects (as well as low depolarization ratios, see Sassen et al. 1990). This issue cannot be resolved from in situ probe data because present instruments are incapable of resolving such small particles. However, Heymsfield et al. (1990) report observing clouds containing supercooled water droplets using aircraft borne in situ probes. In regions between the cells, it may be that sufficient time has elapsed so that the number density of droplets has been

substantially diminished by differential vapor pressure effects between ice and water, or the smallest of particles may have grown by some coalescence phenomena.

The modulation of the bulk backscatter-phase function also suggests that some of the apparent structure observed in the backscatter cross section plots is generated by microphysical changes and is not simply proportional to the distribution of cloud extinction cross section. This effect should be considered when deducing cloud morphological and optical characteristics from simple plots of lidar backscatter.

The backscatter contours in Fig. 10 indicate a large scale pattern of intensification with a period of about 45 minutes. However, an examination of the higher time resolution pictures of the raw laser returns reveals the clouds are composed of many repeated finer scale features. Figure 12 is an expanded scale view of the 1800 to 2230 time period that shows a striated 5 min structure imbedded in the larger scale organization. This pattern is most clearly developed between 2130 to 2230. Wind drift estimates would suggest that these features have a horizontal scale of about 9–11 km; thus, the height to width aspect ratio of the elementary structures is ~1:5; whereas the larger scale field of enhanced backscatter exhibits an aspect ratio of ~1:25.

5. Summary

The HSRL has been successfully adapted to the task of cirrus cloud optical property measurement. The transmitter configuration used to acquire the case study data produce ~50 mW of output power and achieved eye-safe, direct optical depth, and backscatter cross section measurements with 10 min averaging times. A new continuously pumped, injection seeded, frequency doubled Nd:YAG laser transmitter has recently reduced time-averaging constraints by a factor of ~10, while improving the aerosol-molecular signal separation capabilities and wavelength stability of the instrument (Grund and Eloranta 1990).

The cirrus cloud backscatter cross sections, optical thickness, and backscatter-phase functions have been determined for the 27–28 October 1986 segment of the HSRL FIRE dataset. Features exhibiting backscatter cross sections ranging over four orders of magnitude have been observed within this 33 hour period. Extended episodes of low backscatter cross section ($\sim 10^{-7}$ m^{-1} sr^{-1}) have been observed between structured cirrus clouds events.

During this period, cirrus clouds were observed with optical thicknesses ranging from 0.01 to 1.4. Bulk-av-

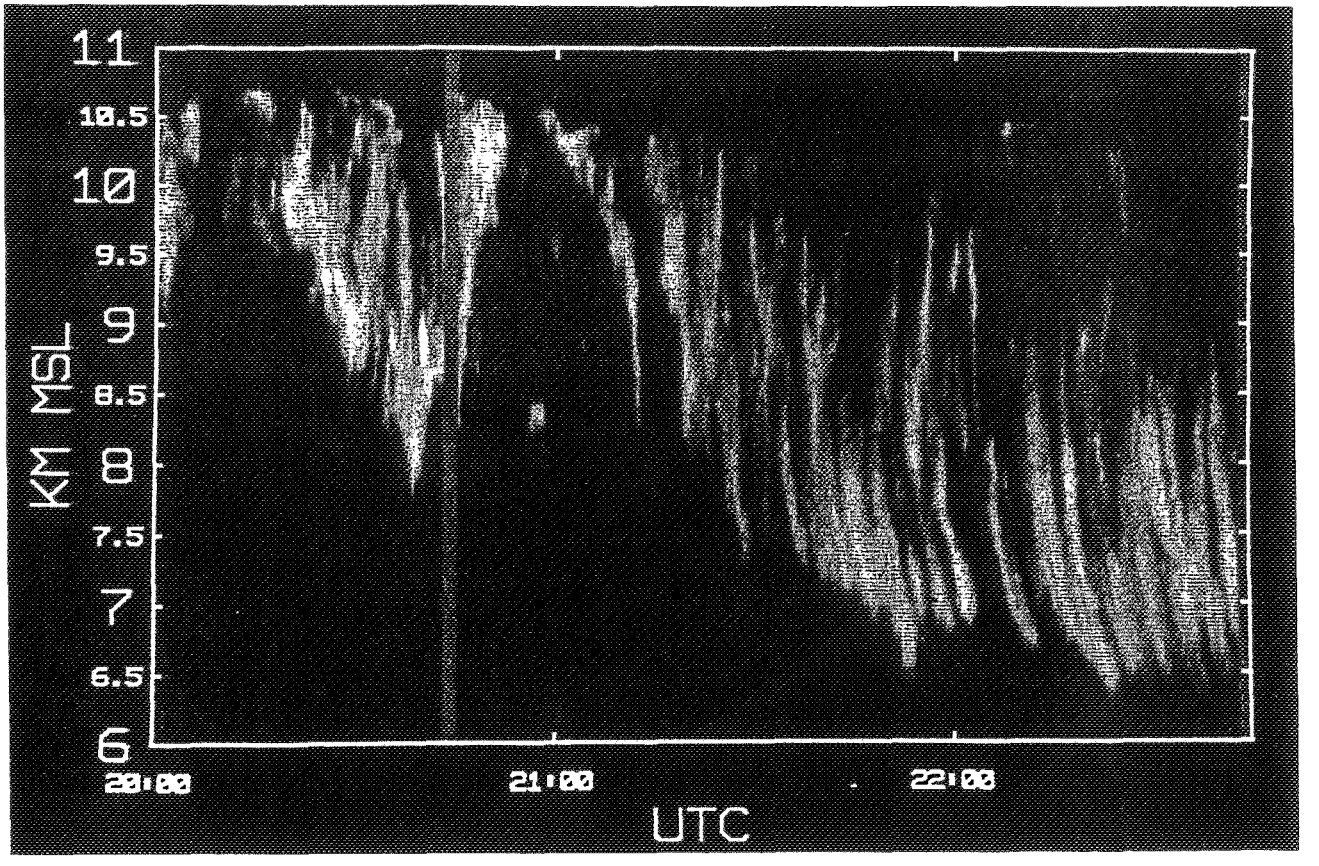

FIG. 12. Intensity modulated height time display of the log of the R^2 corrected HSRL aerosol channel signal. The image has 10 times the temporal resolution necessary to produce the calibrated attenuation corrected cross section plotted in Fig. 10. The image reveals an ~5 minute structure (~9–11 km wide) imbedded in the larger scale organization shown in Fig. 10.

erage backscatter-phase functions in the range of 0.02–0.065 sr^{-1} were also observed. A variety of cirrus cloud structures were observed with apparent sizes ranging from 5 to 400 km during this period that exhibited aspect ratios of from 1:5 to 1:1.

The altitude relationship between cloud top and bottom boundaries and the optical center of the cloud is influenced by the type of formation observed. ACu and uncinus generating regions tend to concentrate attenuation in regions of less than 200 m thickness that dominate the extinction profile, even when the generating cell caps an extended column of virga. Virga exhibits complicated fine scale structure, often lying in interleaved, sheared sheets. In cirrostratus, imbedded vertically-developed cells frequently occupy a significant altitude range, and create large spatial inhomogeneities in optical properties.

Cirrus morphology and generation processes appear to be related to the wind field, probably responding to secondary circulations. Better temporal and spatial resolution in wind measurements in future experiments would aid the understanding of cirrus generation and dissipation mechanisms.

Acknowledgments. We wish to thank Dr. D. O'C. Starr of NASA Goddard Space Flight Center for providing us with an analysis of the radiosonde data and Dr. D. P. Wylie of the University of Wisconsin for providing the GOES satellite images. Discussions with both Dr.'s Starr and Wylie proved invaluable in determining the meteorological processes related to the cirrus observations in this case study.

We also thank Daniel Forrest, Scott Kohn, and Sevtap Karakoy-Otles for providing important data analysis and programming support for this project.

Funding for HSRL development, data acquisition and the collection of cloud statistics has been provided under ARO Grant DAAG29-84-K-0069 and ONR Contract N00014-87-K-0436. Recent HSRL algorithm development, the incorporation of Brillouin scattering corrections in the molecular scattering model used to calibrate this data, and studies of the correlations between wind and backscatter cross section have been funded under AFGL contract F19628-87-0056. Analysis of HSRL FIRE related data is partially supported under NASA Grant NAG1-882.

APPENDIX

HSRL Theory

The basic principles inherent to all monostatic lidar systems are embodied in the lidar equation:

$$P(R) = E_0 \xi R^{-2}\left[\beta_a(R)\frac{\mathbb{P}_a(\pi, R)}{4\pi} + \beta_m(R)\frac{\mathbb{P}_m(\pi)}{4\pi}\right] \times \exp\left[-2\int_0^R \beta_\epsilon(r')dr'\right] + M(R) \quad \text{(A1)}$$

(after Collis and Russel 1976).

Here, $P(R)$ is the power incident upon the receiver from range R, E_0 is the energy of the transmitted pulse, $\xi = A_r(c/2)$ where A_r is the receiver area and c is the speed of light. The subscripts "a" and "m" denote aerosol and molecular scattering quantities. The term aerosol includes both small aerosol and cirrus cloud particles. $\beta_a(R)$ and $\beta_m(R)$ are the respective scattering cross sections per unit volume, $\mathbb{P}_a(\pi, R)/4\pi$ and $\mathbb{P}_m(\pi)/4\pi$ are the respective normalized backscatter-phase functions, $\beta_\epsilon(R)$ is the extinction cross section per unit volume, and $M(R)$ is the contribution from multiple scattering. The entire expression in the first set of brackets is the total normalized backscatter cross section per unit volume, $\beta_\pi(R)$. Both $\beta_\pi(R)$ and $\beta_\epsilon(R)$ are due to the effects of aerosols *and* molecules. The exponential term accounts for the two-way optical thickness between the lidar and the backscattering volume, where the optical thickness accumulated between range R_1 and R_2 is represented as:

$$\tau = \int_{R_1}^{R_2} \beta_\epsilon(r')dr'. \quad \text{(A2)}$$

Equation (A1) demonstrates that the lidar return depends upon both the local value of $\beta_\pi(R)$ *and* upon τ between the lidar and R. Only a single measurement of $P(R)$ is provided at each range by single-channel lidar systems, leading to ambiguities in the direct evaluation of β_π or β_ϵ. In fact, there are an infinite family of $\beta_\epsilon(R)$ profiles for which an increase in optical thickness with penetration depth is just cancelled by an increase in backscatter with range, rendering the medium invisible to single-channel lidar systems of low sensitivity (Grund and Eloranta 1987). In optically thicker cirrus clouds, the multiple scattering contribution $M(R)$ can further complicate matters by effectively increasing $P(R)$ in a way that depends upon the unknown spatial distributions of the angular scattering phase function and optical thickness between the lidar and the sensed volume (Eloranta and Shipley 1982).

As mentioned, several techniques have been employed to untangle β_π from β_ϵ. Each method requires significant assumptions about the distribution of scatterers and about the nature and profile of the particle backscatter to extinction ratio. The multiple scattering contribution, which can become large in returns from cirrus clouds, may be minimized by a narrow field of view (fov) design for the lidar system. This solution is often difficult to achieve and is therefore not frequently implemented; however, narrow fov is a necessary requirement for the high resolution spectrometer employed in the HSRL (see Table 1), thus the uncertainties caused by the effects of multiple scattering processes are greatly reduced in the data acquired with this system (Grund 1987).

Because the HSRL separately measures molecular and particulate backscatter, two lidar equations may be written that are coupled by the common unknown integral of extinction. Assuming $M(R)$ is negligible,

the molecular and particulate lidar equations may be written:

$$P_m(R)R^2 = E_0\xi\beta_m(R)\frac{3}{8\pi}\exp\left[-2\int_0^R \beta_\epsilon(r')dr'\right] \quad (A3)$$

and

$$P_a(R)R^2 = E_0\xi\beta_a(R)\frac{\mathbb{P}_a(\pi, R)}{4\pi}\exp\left[-2\int_0^R \beta_\epsilon(r')dr'\right] \quad (A4)$$

where the normalized molecular backscatter phase function ($\mathbb{P}_m(\pi)/4\pi$) has been replaced with its analytic value, $3/8\pi$.

Because the molecular scattering cross section (β_m) is determined by the profile of atmospheric density calculated from a convenient radiosonde (or from climatology), (A3) is completely defined, and may be solved explicitly for the extinction β_ϵ from the measured lidar return $P_m(R)$. The ambiguity in separating extinction from backscatter in single-channel lidar retrievals is eliminated by the HSRL technique since the system is effectively calibrated at each range with the return from the known molecular backscatter target.

The aerosol backscatter cross section is unambiguously determined from the ratio of (A4) to (A3):

$$\beta_a(R)\frac{\mathbb{P}_a(\pi, R)}{4\pi} = \beta_m(R)\frac{3}{8\pi}\frac{P_a(R)}{P_m(R)}. \quad (A5)$$

By solving (A3), the extinction cross section may be directly determined from the slope of the molecular backscatter return and a profile of molecular backscatter cross section calculated from the in situ density:

$$\beta_\epsilon(R) = -\frac{1}{2}\left[\frac{d\ln(P_m(R)R^2)}{dR} - \frac{d\ln(\beta_m(R))}{dR}\right]. \quad (A6)$$

In the absence of aerosol and gaseous absorption, $\beta_a = \beta_\epsilon - \beta_m$; therefore, the normalized backscatter phase function is uniquely determined from (A5) and the atmospheric density profile:

$$\frac{\mathbb{P}_a(\pi, R)}{4\pi} = \beta_m(R)\frac{3}{8\pi}\frac{P_a(R)}{[\beta_\epsilon(R) - \beta_m(R)]P_m(R)}. \quad (A7)$$

REFERENCES

Collis, R. T. H., and P. B. Russell, 1976: Lidar measurement of particles and gases by elastic backscattering and differential absorption. *Laser Monitoring of the Atmosphere*, Springer-Verlag, 71–151.

Eloranta, E. W., and S. T. Shipley, 1982: A Solution for Multiple Scattering. *Atmospheric Aerosols: Their Formation, Optical Properties and Effects*, Spectrum Press, 227–239.

——, and D. K. Forrest, 1986: Generation of attenuation corrected images from lidar data. *13th International Lidar Conf.*, Toronto, NASA Conference Pub. 2431, 3291–294.

Grund, C. J., 1987: Measurement of cirrus cloud optical properties by high spectral resolution lidar. Ph.D. thesis, University of Wisconsin–Madison, 92 pp.

——, and E. W. Eloranta, 1987: Optically significant cirrus clouds may be rendered "invisible" to space-borne simple lidar systems. Opt. Soc. Amer. *1987 Technical Digest Series*, **18**, 75–78.

——, and ——, 1990: High repetition rate continuously pumped injection seeded Nd:YAG laser extends High Spectral Resolution Lidar capabilities. Op. Soc. Amer. *1990 Technical Digest Series*, **4**, 368–371.

——, J. A. Weinman, and ——, 1990. Cirrus cloud velocity-backscatter correlations and instrument spatial resolution effects on remote wind sounding errors. Op. Soc. Amer. *1990 Technical Digest Series*, **4**, 158–161.

Klett, J. D., 1981: Stable analytic inversion solution for processing lidar returns. *App. Opt.*, **20**, 211–220.

Evans, W. E., E. J. Weigman, W. Viezee and M. G. H. Ligda, 1964: Performance specifications for a meteorological satellite lidar. NASA Report CR-760871, NTIS N66-2997, 174 pp.

Heymsfield, A. J., K. M. Miller and J. D. Spinhirne, 1990: The 27–28 October 1986 FIRE IFO cirrus case study: Cloud structure and composition from in situ measurements. *Mon. Wea. Rev.*, **118** 2313–2328.

Milton, M. J. T., and P. T. Woods, 1987: Pulse averaging methods for a laser remote monitoring system using atmospheric backscatter. *App. Opt.*, **26**, 2598–2603.

Platt, C. M. R., J. C. Scott and A. C. Dilley, 1987: Remote sounding of high clouds. Part VI: Optical properties of midlatitude and tropical cirrus. *J. Atmos. Sci.*, **44**, 729–747.

Sassen, K., M. K. Giffin, and G. C. Dodd, 1989: Optical scattering and microphysical properties of subvisual cirrus clouds and climatic implications. *J. Appl. Meteor.*, **28**, 91–98.

——, C. J. Grund, J. D. Spinhirne, J. M. Alvarez and M. J. Hardesty, 1990: The 27–28 October 1986 FIRE IFO cirrus case study: a five lidar overview of cloud structure and evolution. *Mon. Wea. Rev.*, **118**, 2288–2312.

Shipley, S. T., D. H. Tracy, E. W. Eloranta, J. T. Trauger, J. T. Sroga, F. L. Roesler and J. A. Weinman, 1983: High spectral resolution lidar to measure optical scattering properties of atmospheric aerosols. 1: Theory and instrumentation. *App. Opt.*, **22**, 3716–3724.

Spinhirne, J. D., J. A. Reagan and B. M. Herman, 1980: Vertical distribution of aerosol extinction cross section and inference of aerosol imaginary index in the troposphere by lidar technique. *J. Appl. Meteor.*, **19**, 426–438.

Sroga, J. T., E. W. Eloranta, S. T. Shipley, F. L. Roesler and P. J. Tryon, 1983: High spectral resolution lidar to measure optical scattering properties of atmospheric aerosols. 2: Calibration and analysis. *App. Opt.*, **22**, 3725–3732.

Starr, D. O'C., 1987: A cirrus-cloud experiment: intensive field observations planned for FIRE. *Bull. Amer. Meteor. Soc.*, **68**, 119–124.

——, and D. P. Wylie, 1990: The 27–28 October 1986 FIRE IFO cirrus cloud study: meteorology and clouds. *Mon. Wea. Rev.*, **118**, 2259–2287.

Weinman, J. A., 1984: Tomographic lidar to measure extinction coefficients of atmospheric aerosols. *App. Opt.*, **23**, 3882–3888.

——, 1988: The derivation of atmospheric extinction profiles and wind speed over the ocean from a satellite borne lidar. *App. Opt.*, **27**, 3994–4001.

Wylie, D. P., and W. P. Menzel, 1989: Two years of cloud cover statistics using VAS. *J. Climate*, **2**, 380–392.

Yip, S., and M. Nelkin, 1964: Application of a kinetic model to time-dependent density correlations in fluids. *Phys. Rev.*, **135**, A 1241–A 1247.